

Ahmednagar Jilha Maratha Vidya Prasarak Samaja's
New Arts, Commerce & Science College, Parner
INTERNAL QUALITY ASSURANCE CELL (IQAC)
Year 2023-24

3.3.1. Number of research papers per teachers in the Journals notified on UGC website during the year:

3.3.1.1. Number of research papers in the Journals notified on UGC website during the years:

Year	2023-24
Number	25

Sr. No.	Title of Paper	Name of Author/s	Department	Name of Journal	Year of Publication	ISSN Number	Is it listed in UGC care list? (Yes/No/-)	Link of Research Paper/ Journal website
1	Review On Principles Of Antioxidant Methods	Rani M. Shaikh & Rangnath K. Aher	Botany	Solovyov Studies ISPU Vol. 71, Issue 7, 19-27, 2023	2023	ISSN: 2076-9210	YES	https://shorturl.at/LrOlc
2	Critical Study of Challenges of Weeds to the farmers and use of Bio weedicides for sustainable Agriculture	Swati Rajesh Yeole, S. K. Aher and R. K. Aher	Botany	Inter. Jr of Advanced and Applied Research, Vol No 04 Issue No 30, 1-4, 2023	2023	ISSN: 2347-7075	YES	https://shorturl.at/AzpUk
3	Adivashichy	Deepak	Econo	IJAAR	Mar-	ISS	N	

	a Vividh Yojana-Ek Abhyas	Sontakke & Anil Pathade	mics	Vo1-5 Issue13 Mar-April2024	April 2024	N-234 7-707 5	O	
4	Ecological Crises in Amitav Ghosh's The Hungry Tide	A.V. More	English	Sanshodhak	2024	ISSN 2394-5990	Yes	
5	Exploring Farm Pond Patterns in Ahmednagar :Enhancing Agriculture Through Prtective Irrigation Strategies	Dr. Dattatray Sheshrao Ghungarde	Geography	Maharashtra Bhugolshashtra Sanshodhan Patrika	July-Dec 2023	0971-5785	No	
6	1.समकालीन समाज एवं लोकतंत्र के परिप्रेक्ष्य में मीडिया	Dr. V.S. Raut	Hindi	Akshara 10/Vol.II(A) Page No.191	Jan-2024	2582-5429	No	
7	1.समकालीन हिंदी साहित्य में समाज एवं लोक जीवन	Dr. H.Y. Gaikwad	Hindi	Akshara 10/Vol.II(A) Page No.173	Jan-2024	2582-5429	No	
8	1.हिंदी मीडिया में समाज और गणतंत्र	Prof. S.S. Arde	Hindi	Akshara 10/Vol.II(A) Page No.133	Jan-2024	2582-5429	No	
9	1.कुंवर नारयण की कविता में गणतंत्र	Prof. S.P. Tanpure	Hindi	Akshara 10/Vol.II(A) Page No.188	Jan-2024	2582-5429	No	
10	Microstructural, optical, and morphological	Lalita deshmkh S.L.Kadam	physics	Physica Scripta, 99, Page:	Feb-2024	-		https://doi.org./10.1088/1402-4896/ad24aa

	investigation s of SnO ₂ nanomaterial s grown by microwave assisted sol gel method			035925				
1 1	Bimetallic Co ₃ V ₂ O ₈ microstructur e: A versatile bifunctional electrode for supercapacit or and electrocataly sis applications	R.A. Kadam, M.A. Yewale, A.M. Teli ,Annu, U.T.Nakat, V. Kumar , S.L.Kadam , D.K.Shin	physics	Surfaces and Interfaces , 41 Page:103 267	Aug- 2023	-		https://doi.org/10.1016/j.surf.2023.103267
1 2	Sp here- shaped CuCo ₂ O ₄ nanostructur es battery type electrode for supercapacit or via hydrothermal synthesis approach	M.A. Yewale , R.A. Kadam, Umesh.T.Naka t, A.M. Teli , V. Kumar , S.A.Beknalkar, A.A. Jadhvar , S.L.Kadam , ,Nitin.T.Shela ke,D.K.Shin	physics	Colloids and Surfaces A:Physio chemical and Engineeri ng aspects ,679 Page:132 541	Oct- 2023	-		https://doi.org/10.1016/j.colsurfa.2023.132541
1 3	Effect of microwave annealing on Tin Oxide nanomaterial s	Lalita Deshmukh a,*, S.L. Kadam	physics	Materials Today: Procedin g	Aug- 2023			
1 4	Hydrotherma l Synthesis of Cobalt Vanadium Oxide (Co ₃ V ₂ O ₈) Hexagonal Disc for High- Performance Supercapacit ors	, A.A. Jadhvar , Nitin T.Shelake, M.A. Yewale , R.A. Kadam , S.L.Kadam , D.K.Shin	physics	Surfaces and Interfaces ,43 Page:103 519	Oct- 2023	-		https://doi.org/10.1016/j.surf.2023.103519
1 5	Synthesis and Characterizat ion of V ₂ O ₅ Nanorods Using Hydrotherma l Method for Energy	Rupin Ranu1,*, Kalyan B. Chavan2, Sachin V. Desarada3, V.K. Gade4 and S.L.	physics	Micro and Nanosyst ems	Oct- 2023			

	Application	Kadam5						
16	Wrapped Nanochain microstructures of Ni3V2O8 nanoparticles for supercapacitor applications using the hydrothermal method	M.A. Yewale , A.A. Jadhvar , R.B. Kharade , R.A. Kadam , V. Kumar , U.T.Nakat, , A.M. Teli , S.D.Dhasf, , D.K.Shin	physics	Journal of Energy storage ,73(2023) 109005	Sep-2023	-		https://doi.org/10.1016/j.est.2023.109005
17	Design and Development of Feedback Controller for Scanning Probe Microscopy Applications	Gaikwad S. B.1, Dr. S. L. Kadam2 , Dr. S. B. Iyyer3	physics	International Journal of Advanced Research in Science, Communication and Technology (IJARST)	March 2024	ISSN (Online) 2581-9429		www.ijarsct.co.in
18	Design and Simulation of 4 bit-Successive Approximation ADC	Suraj P. Gaikwad	Computer Science	International Advanced Research Journal in Science, Engineering and Technology (IARJET)	2023-24	ISSN (O) 2393-8021, ISSN (P) 2394-1588	YES	https://iarjset.com/wp-content/uploads/2023/04/IARJET.2023.10403.pdf
19	Secure Home Door Bell using Python and Raspberry Pi	Suraj P. Gaikwad	Computer Science	IOSR Journal of Electronics and Communication Engineering (IOSR-	2023-24	e-ISSN: 2278-2834, p-ISSN: 227	YES	https://www.iosrjournals.org/iosr-jecce/papers/Vol.%2018%20Issue%201/Ser-1/D1801012326.pdf

				JECE)		8-8735		
20	Sol-gel assisted beta-cyclodextrin coated MoO ₃ -Fe ₂ O ₃ nanocomposite for photodegradation of methylene blue dye	Dr. A. E. Athare	Chemistry	Journal of Sol-gel Science and Technology 110: 304-318	2024	1573-4846	Yes	https://doi.org/10.1007/s10971-024-06357-1
21	Ultrasonic wave-assisted synthesis of CeO ₂ -MoO ₃ nanocomposite for photofenton degradation of Rhodamine - B dye	Dr. A. E. Athare	Chemistry	Chemical Papers	2024	2585-7290	Yes	https://doi.org/10.1007/s11696-024-03479-2
22	Room temperature acetone sensing activity of beta-cyclodextrin coated MoO ₃ -ZrO ₂ nanocomposite	Dr. A. E. Athare	Chemistry	Surfaces and Interfaces 53 (2024) 105068	2024	2468-0230	Yes	https://doi.org/10.1016/j.surf.2024.105068
23	Architecture of gamma-WO ₃ nanosheets-like electrode material for super capacitor application	Dr. R. S. Diggikar	Chemistry	Journal of Mater Science: Mater Electron (2023) 34: 1735	2023	0957-4522	Yes	https://doi.org/10.1007/s10854-023-11081-7
24	Abhijat Marathi Bhasha Aani Pro. Hari Narke	Dr. H. S. Shelke	Marathi	Saksham Samiksha	Augest – Sept-2023	2231-4377	NO	
25	Aadhunik Tantradnyan Va Marathi Bhasha	Dr. H. S. Shelke	Marathi	Research Journey	January - 2024	2348-7143	NO	

REVIEW ON PRINCIPLES OF ANTIOXIDANT METHODS

Rani M Shaikh

P G Department of Botany and Research Center, New Arts, Commerce and Science College Parner, Tal- Parner, Dist- Ahmednagar, (M S),414 302.

Rangnath K Aher

P G Department of Botany and Research Center, New Arts, Commerce and Science College Parner, Tal- Parner, Dist- Ahmednagar, (M S),414 302

ABSTRACT

The antioxidant is defined as any substance that could put off or help oxidative harm by way of loose revolutionaries. The antioxidant inhibits the oxidative harm with the aid of unfastened revolutionaries through several mechanisms. The assets of the antioxidant are abundantly available in nature and may be set up in the diurnal food plan similar as fruit, veggies, seeds, nuts, leaves, roots, and barks. several principal composites related as antioxidants comparable as polyphenols, vitamins, and carotenoids. This composition provides a trendy summary of the most common in vitro patterns for determining antioxidant exertion. It emphasizes the operating principle, method, advantages, and drawbacks of various styles. The dedication of antioxidant exertion could not simplest comply with one single approach due to the diversity of antioxidant mode of conduct. accordingly, the selections of the applicable system of analysis need to be considered to achieve the reason of the exploration.

Key words: antioxidant activity, spectrometry, free radical , reactive oxygen species.

I. INTRODUCTION

The document of world health corporation (WHO) noted the burden of non-communicable diseases (NCDs) (e.g.cancer, cardiovascular sicknesses, continual respiration diseases, neurodegenerative sicknesses and diabetes) in many nations, as their numbers are regularly growing (Grosso G 2018). It money owed for almost -thirds of annual mortality, mainly in low- and center-income international locations (Engelgau M.M et al. 2018). The NCDs have been related with unhealthy existence such as imbalanced weight-reduction plan (excessive calories and fat intake) and mild physical pastime. Besides, the prevalence of NCDs has been related to oxidative stress, wherein the manufacturing of free radicals [reactive oxygen species (ROS) and reactive nitrogen species (RNS)] and the biological antioxidant defense gadget is not proportional (Sies H et al. 2005). ROS include superoxide anion radical (O_2^\bullet), singlet oxygen (1O_2), hydroxyl radical ($^\bullet OH$) and perhydroxyl radical (HO_2^\bullet) (Ahsan et al . 2003). RNS consist of radical nitrogen oxide ($^\bullet NO$), nitrogen dioxide ($^\bullet NO_2$), and non-radicals S-nitrosothiols, peroxyxynitrite ($ONOO^-$), nitroxyl anion (NO^-), nitrate (NO_3^-), nitrosonium cation (NO^+), dinitrogen trioxide (N_2O_3), dinitrogen tetroxide (N_2O_4), nitryl chloride (NO_2Cl), and nitrous acid (HNO_2) (Saddhe A.A et al.2019). The loose radicals are volatile, reactive, and have a tendency to capture other stable molecules. Consequently, if the number of loose radicals is in high concentration, the oxidative tissue harm can occur within the body (Huang Y.J and Nan G.X 2019).

Antioxidants are compounds which, found in meals or the human body in very Low concentrations, delay, control or save you oxidative processes leading to meals quality. Deterioration of food or the occurrence and propagation of degenerative illnesses within the organism. Some of techniques are concerned in the technique of inhibiting the oxidation By means of those antioxidant compounds (Shahidi F and Zhong Y 2015). Fats-soluble antioxidants are critical in preventing the peroxidation of polyunsaturated Fatty acids (PUFA) in biological membranes. Water-soluble antioxidants, like nutrition C, Play a key position in neutralising ROS within the hydrophilic segment. This evaluation provides a fashionable and updated evaluation of methods available for measuring Antioxidant activity and the chemistry precept behind them. Similarly, the maximum Critical advantages and shortcomings of each technique had been analysed and highlighted. Understanding the principle mechanisms, benefits and barriers of the dimension Assays is important for correct choice of technique(s) for legitimate evaluation of antioxidant Potential in practical applications.(Irina Georgiana Munteanu and Constantin Apetrei 2021).

The part of exogenous antioxidants comes into play when endogenous species are unfit to give full protection against the reactive oxygen. Vitamin C, vitamin E, vitamin D, vitamin K3, flavonoids, minerals and β - carotene are among the utmost effective and important exogenous antioxidants used as active constituents in utmost medicinals and food supplements. composites like butylhydroxytoluene, butylhydroxyanisole, gallates etc are among the synthetic exogenous antioxidants, while they can be attained from natural sources as well like flavonoids, vitamins, anthocyanins and some minerals (Litescu SC et al. 2011). In order to help dangerous goods of free revolutionaries in the body, also for the regression of food ingredients and fats, interest in the use of antioxidants is fairly adding (Molyneux P.2004).

II Benefits of antioxidants

The relation of antioxidants to the cancer prophylaxis, remedy, life and oxidative stress has gained notable attention in recent days (Kalcher K et al.2009). Recent studies suggest that the conditions related to oxidative stress like cancer, coronary heart complaint, hypertension, rotundity, diabetes and cataract are stylish defended by the use of vegetables, fruits and lower reused foods (Halvorsen.B.L et al.2002). This is made possible due to the positive health goods of vegetables and fruits containing salutary antioxidants. Walnuts, cranberries, blackberries, strawberries, blueberries, snorts, brewed coffee, cloves, grape juice, unsweetened chocolate are at the top of the food list containing antioxidants. On assaying 50 food particulars containing high quantum of antioxidants, 13 of them were spices, 5 were berries, 8 of them were vegetables and fruits, 5 were cereals and 4 of them were nuts (Halvorsen.B.L et al. 2006). Antioxidants regulate colorful oxidative responses naturally being in apkins. likewise, terminates or retards the oxidation process by scavenging free revolutionaries, chelating free catalytic essence and also by acting as electron benefactors.

A diet high in foods of animal origin and impregnated fats increases the threat of cardiovascular conditions and some cancers (Pierart Z.C et al.2006). which has generated interest in promoting the consumption of factory- deduced proteins (Espin J.C et al.2007). Legumes similar as cereals, fruits, and vegetables have health- promoting composites and nutritive value (Shetti A et al.2009). The nutritive quality and nutraceutical content associated with the antioxidant exertion of legumes similar as common bean are important sources of

nutritive factors (proteins, carbohydrates, fiber, vitamins, and some minerals). (Duarte-Martino HC et al.2012).

In vitro antioxidant methods through several mechanisms of actions makes the comparison of each antioxidant method impossible. However, the *in vitro* antioxidant approach can provide a measurement of the effectiveness of compounds. Generally, the assessment of *in vitro* antioxidant activity can be divided into two main mechanisms. The first category is assessment in relation to free radicals transfer (hydrogen atom transfer, single electron transfer, or the combination of both). The second category is related to the evaluation of the damaging effect on biological markers and substrates, which is based on lipid peroxidation (Litescu S C et al.2010). *In vitro* testing of antioxidants using free radical scavengers is relatively easy to perform. Among the free radical scavenging methods, the 1,1-diphenyl-2-picrylhydrazyl (DPPH) method is faster, simpler (i.e., does not require many steps and reagents) and less expensive than other test models. On the other hand, the decolorization assay of 2,2-azinobis(3-ethylbenzothiazoline-6-sulfonic acid) diamonium salt (ABTS) is applicable to both hydrophilic and lipophilic antioxidants.

III Discussion

1. *DPPH (2,2-diphenyl-1-picrylhydrazyl) Scavenging Activity*

The DPPH assay is very easy and rapid method for manual analysis of antioxidant content. This method can be used for solid or liquid samples and is applicable not only to specific antioxidants, but also to the total antioxidant capacity of the sample. The DPPH test is based on the ability of the stable free radical 2,2-diphenyl-1-picrylhydrazyl to react with a hydrogen donor (Inoue K et al 2005 and Fahey JW et al. 2002). The DPPH assay method is based on the depletion of DPPH, a stable free radical. The free radical DPPH with an odd number of electrons gives an absorption maximum at 517 nm (purple). When antioxidants react with DPPH, stable free radicals are reduced to DPPHH in the presence of hydrogen donors (e.g., free radical scavenging antioxidants), resulting in reduced uptake compared to DPPH. The radical form of DPPH-H causes a color change (yellowing) depending on the number of electrons captured. The stronger the discoloration, the higher the elasticity. This test is the most widely used model for evaluating the free radical scavenging activity of any new drug. The DPPH radical exhibits a strong absorption spectrum in the UV visible region. When a solution of DPPH is mixed with a solution of a substance capable of donating hydrogen atoms, it gives a reduced form (diphenylpicrylhydrazine; non-radical) that loses the purple color (pale yellow when picrylic acid groups are present). (Bondet V et al.1997). Approximately 4.3 mg of DPPH was dissolved in 3.3 ml of methanol and the tube was covered with aluminum foil to block light. 150 ml of DPPH solution was added to 3 ml of methanol and the absorbance at 517 nm was immediately measured as a control. Take 50 ml of compounds of varying concentrations and a standard compound (e.g. ascorbic acid) and bring to a volume of 150 ml with methanol. Each sample was then further diluted to 3 ml with methanol and DPPH was added to each 150 ml. The absorbance was taken after 15 minutes at 517 nm using methanol as blank on UV-vis spectrometer. The IC50 values for each drug compounds as well as standard preparation were calculated. The free radical scavenging activity was calculated using the following formula:

% scavenging=[Absorbance of control–Absorbance of test sample/Absorbance of control]×100 .The effective concentration of sample required to scavenge DPPH radical by 50% (IC50 value) was obtained by linear regression analysis of dose-response curve plotting between % inhibition and concentrations. The best way to compare antioxidant activity between samples is by using IC50 values. The inhibitory concentration value (IC50) is defined as the sample concentration required for 50% free radical inhibition. IC50 is determined in triplicate in the graph between residual free radical uptake and concentration in each assay. This test uses quercetin, 6-hydroxy-2,5,7,8-tetramethylchroman-2-carboxylic acid (Trolox), tocopherol and ascorbic acid as positive controls (Ferreira IC et al.2009 and Piljac-Zegarac J et al.2009). The DPPH Assay is a quick and simple test that provides reliable results. It is also widely used to screen for antioxidant properties because it only requires a UV-Vis spectrophotometer to operate. However, this method is sometimes complicated when a test compound has a spectrum overlapping the DPPH spectrum at 515 nm.

2. **FRAP (Ferric Reducing ability plasma)**

Assay Based on PubMed, the FRAP method has been described and used to measure the antioxidant efficacy in 3400 papers. In this method, the evaluation of antioxidant activity is characterized by the calculation of the low pH mixture of iron (III) and 2,3,5-triphenyl-1,3,4-triaza-2-azoniacyclopenta-1,4-dienechloride (TPTZ) reduction to its ferrous form (II), change the solution into violet-blue color. The changes was evaluated using spectrophotometer at the wavelength of 593 nm (Benzie I F.F and Strain J.J 1996). It has been applied to detect the antioxidant activity of honey (Moniruzzaman M et al.2016). FRAP method has some limitations. The antioxidant activity of slow-reacting compounds such as polyphenols cannot be accurately measured, nor can samples below the physiological pH value (pH 3.6) be measured and could give false-positive results if the samples have lower redox potential value than the redox pair Fe^{3+}/Fe^{2+} (Moniruzzaman .M et al.2016).

3. **TEAC (Trolox Equivalent Antioxidant Capacity)**

The data searching from PubMed shows that the TEAC assay has been utilized for measuring the antioxidant capacity, approximately 1100 papers.The principle of this method is based on the scavenging of stable ABTS+ (2,2'-azinobis(3-ethylbenzthiazoline-6-sulfonic acid) radical by antioxidants in comparison with Trolox. The reduction causes the color loss of ABTS. The color loss is measured at λ_{max} 750 nm. Generally, the polar analog of vitamin E, namely Trolox, is used to be the standard of the antioxidant calculation, and the result is interpreted as Trolox equivalents. The advantages of this method are simple, reproducible, a wide range of samples (e.g. a wide range of samples polarity (hydrophobic and hydrophilic compounds) (Awika J.M et al.2003). However, it should be noted that the different reaction rates between the antioxidants and ABTS radical, cause the different reaction times for the complete measurement of antioxidant capacity (Zheng.L et al.2016)

4. **ORAC (Oxygen Radical Absorbance Capacity)**

ORAC is one of the popular methods for determining the antioxidant activity according to the data from PubMed, where there are 1610 papers conducting this method. The measurement of antioxidant activity is based on the scavenging activity of oxyradical-induced oxidation of 2,2'-azo-bis-(2-methylpropionamide) dihydrochloride (AAPH) by samples with antioxidants. In this method, phycoerythrin or fluorescein is used as a target molecule. Over time, the fluorescent signal of these compounds will be lost when the antioxidant compounds

appear. When the solution tested containing antioxidant properties, the fluorescent reduction is inhibited and measured at the excitation wavelength of 485 nm and emission wavelength of 520 nm (Alam Md.N et al.2013 and Awika J.M et al.2003). The test uses Trolox as a reference standard, and the values usually expressed as Trolox Equivalent (TE).The antioxidant capacity results have a correlation with the total fluorescence area under reaction curves where the values of antioxidant are measured by subtracting the area with the blank, which contain no antioxidant (Apak R et al.2007). ORAC method is suitable to be conducted in a microtiter plate with constant temperature for automation of experiments in screening of biological samples matrices, relevant to *in vivo* conditions, considers both inhibition time and degree of inhibition of free radical action, and compliant for various sample matrices, including food (e.g., sorghum, orange juice, blueberries, nuts),pharmaceutical, and blood plasma (Alam Md.N et al.2013 and Prior R.L 2015). However, some difficulties occur when applying this method such as the control of ORAC reaction temperature, reagent concentration, and oxygen (Schaich K.M et al. 2015).

5. ***HORAC (Hydroxyl Radical Averting Capacity)***

The working principle of this assay is the measurement of the antioxidant activity by the calculation of the inhibitory activity of antioxidants against the oxidation of the fluorescent probe (fluorescein) by hydroxyl radicals. This radical is produced through the radical initiation process by the catalyzer hydrogen peroxide (H₂O₂) and Fenton reagent. Over time, the radicals bind the fluorescein, until the appearance of antioxidant, gradually preventing the oxidation of the probe (Borges R.S et al.2013). The standard of an antioxidant such as gallic acid is used to make the calibration curve. The value of antioxidants is then compared and correlated to the total area fluorescence decay curve (AUC) of the samples. The strong point of this assay is that the value of antioxidant capacity is directly calculated against the hydroxyl radicals produced from the breaking of the hydrophilic chain (Moharram H.A and Youssef M.M 2014). determining the antioxidant activity of vegetables (tomato, parsley, celery, chili pepper, radish, capsicum, eggplant, broccoli) (Číž M et al.2010).

6. ***CUPRAC (Cupric Ion Reducing Antioxidant Capacity)***

CUPRAC is one of electron-transfer based assay for measuring the antioxidant capacity. The method is based on the utilization of the pigment-oxidizing agent (chromogenic), namely bis-copper (II) neocuproine. When the antioxidants mix with the reagent, the reduction of chromogenic probe occurs and changes the color of the solution. The degree of color change is correlated with the concentration of antioxidants in the sample. The change is measured at a wavelength of 450 nm (Ozyürek M et al.2011). The CUPRAC method is simple and adjustable. It is beneficial for high-throughput screening of the antioxidants in matrices of food (egg white, whey protein, gelatin) and blood serum. It was also applicable to measure the hydrophilic and lipophilic antioxidant, due to the high solubility of the reagent in a polar and non-polar solvent (Cekiç S.D et al.2009). In addition, CUPRAC assay works at physiological pH (pH 7) compared to another the electron-transfer assay such as ABTS and FRAP (Apak R et al.2007).

7. ***Total Radical Trapping Antioxidant Parameter (TRAP)***

The TRAP method was firstly described by Wayner *et al.* to measure the total antioxidant capacity of blood plasma or serum (Wayner D.D et al et al.1985). This method is based on the generation of peroxy-radicals from 2,2'-azo-bis(2-amidinopropane) hydrochloride

(AAPH). The surface of the oxygen electrode can be used to monitor the lag time of oxidation. The induction period of APPH was measured to determine the ability of antioxidants to inhibit the oxidation. Then, the total antioxidant capacity of samples was measured by a comparison of the time interval of the reaction induction and the interval time generated by the reference compound, Trolox. It has been applied to measure the antioxidant activity of vegetables, berries, apple, banana, pepper, and green bean (Pellegrini N et al 2003). This method, however, has a significant drawback, such as lack of oxygen electrode stability. Therefore, some modification has been done by the addition of chemiluminescence such as R-phycoerythrin. This pigment is able to give a brief point where the reaction reaches the completion. The addition of the antioxidants could quench the chemiluminescence in the system (Huang D et al 2005).

8. **Folin-Ciocalteu method**

At present, the Folin–Ciocalteu test is commercially available from several important commercial societies, so this method is widely used to quantify polyphenols in plant-derived extracts (Blainski A et al. 2013), as well as in foods and beverages (Apak R et al. 2018). The pharmacopoeia includes the Folin–Ciocalteu test (Apak R et al. 2018), and Europe adopted it as an official procedure of measuring the total phenol contents in wines (European Community 1990). The Folin–Ciocalteu test is based on reducing the Folin–Ciocalteu reagent with phenolic compounds in an alkaline state. The exact chemical nature of the Folin–Ciocalteu reagent is not clearly defined, but it is believed that it may contain a complex of the phosphomolybdic/ phosphotungstic acid which are reduced to obtain a blue chromophore with the maximum absorption at 765 nm (Magalhaes L.M et al. 2008). The central molybdenum ion in the complex is accepted as a reducing site, where the Mo⁶⁺ ion is reduced to Mo⁵⁺ by accepting an electron donated by the phenolic antioxidant.

9. **TBARS (Thiobarbituric Acid Reactive Substances)**

TBARS is widely known as an assay for measuring the inhibition of lipid peroxidation product by antioxidant *in vitro*. This assay measures the susceptibility of the samples to the peroxy radical-induced by Cu²⁺/H₂O₂. When peroxidation occurs, the lipid peroxides and peroxy radicals are formed subsequently and decompose the lipid to create aldehydes and derivatives, such as 4-hydroxy-2-nonenal, malonic aldehyde (MDA), and hexanaldehyde (Singh S and Singh R P). This metabolite will react with TBA (thiobarbituric acid) and form red or pink chromophore. The changes of color are then measured at the wavelength of 530–540 nm. TBARS assay is comparable with other assays because it needs simple instrumentation, good reproducibility, adaptable for measuring lipophilic and hydrophilic antioxidant and suitable for running „high-throughput“ analysis (Ghani M.A et al. 2017). It has been used for determining the antioxidant activity in fried fast food, essential oils, and medicinal plants (Galego L et al. 2008 and Karagöz A et al. 2015). However, some drawbacks of this method have been described such as absorbance interference by samples containing aldehydes and sugars, unsuitable for measuring lipid peroxidation *in vivo*, takes longer time, and more complex preparation (Singh S and Singh R P and Ghani M.A et al. 2017).

IV Conclusion

This review is focused on the most common method of *in vitro* antioxidant activity. Each method has its advantages and disadvantages, depends on the characteristic of sample materials and mode of action of antioxidants. There is no single approach could describe all antioxidant activity. The evaluation of antioxidant activity should be carried out using several methods to measure the diverse inhibition mechanism of free radicals. Researchers have to critically consider the method of the antioxidant analysis before carried out that for the research purpose.

V References

1. Ahsan H, Ali A and Ali R 2003 Oxygen free radicals and systemic autoimmunity Clin. Exp. Immunol.131 398–404.
2. Alam Md N, Bristi N J and Rafiquzzaman Md ,2013. “Review on in vivo and in vitro methods evaluation of antioxidant activity”, Saudi Pharm. J21 143–52.
3. Apak R, Güçlü K, Demirata B, Özyürek M, Çelik S E, Bektaşoğlu B, Berker K I and Özyurt D 2007. Comparative evaluation of various total antioxidant capacity assays applied to phenolic compounds with the CUPRAC assay Molecules **12** 1496–547.
4. Apak, R.; Çapano şglu, E.; Shahidi, F. Measurement of Antioxidant Activity and Capacity—Recent Trends and Applications; John Wiley & Sons Ltd.: Hoboken, NJ, USA, 2018; pp. 1–283.
5. Awika J M, Rooney L W, Wu X, Prior R L and Cisneros-Zevallos L 2003. Screening methods to measure antioxidant activity of sorghum (*Sorghum bicolor*) and sorghum products J. Agric. Food Chem. 51 6657–62.
6. Benzie I F F and Strain J J 1996 The ferric reducing ability of plasma (FRAP) as a measure of “antioxidant power”: The FRAP assay Anal. Biochem.239 70–6
7. Blainski, A.; Lopes, G.C.; De Mello, J.C.P. Application and Analysis of the Folin Ciocalteu Method for the Determination of the Total Phenolic Content from *Limonium Brasiliense* L. Molecules 2013, 18, 6852–6865.
8. Bondet V, Brand-Williams W, Berset C. Kinetics and mechanisms of antioxidant activity using the DPPH free radical method. Food Sci Technol 1997;30:609-15.
9. Borges R S, Pereira G A N, Vale J K L, França L C S, Monteiro M C, Alves C N and Silva A B F da 2013. Design and evaluation of 4-Aminophenol and salicylate derivatives as free-radical scavenger Chem. Biol. Drug Des. 81 414–9.
10. Cekiç S D, Başkan K S, Tütem E and Apak R 2009. Modified cupric reducing antioxidant capacity (CUPRAC) assay for measuring the antioxidant capacities of thiol-containing proteins in admixture with polyphenols Talanta79 344–51.
11. Číž M, Čížová H, Denev P, Kratchanova M, Slavov A and Lojek A 2010 Different methods for control and comparison of the antioxidant properties of vegetables Food Control 21 518–23.
12. Duarte-Martino HC, Bigonha SM, De Morais CL, De Oliveira BR, Brunoro CN, Ramirez CL, et al. Nutritional and bioactive compounds of bean: Benefits to human health. In: Tunick MH, González DE, Mejía E. editors. Hispanic Foods: Chemistry and Bioactive Compounds (ACSSymposium). USA: American Chemical Society; 2012. p. 233-58.

13. Engulgau M M, Rosenthal J P, Newsome B J, Price L, Belis D and Mensah G A 2018. Non communicable diseases in low- and middle-income countries: a strategic approach to develop a global implementation research workforce *Glob. Heart* 13 131–7.
14. Espín JC, García-Conesa MT, Tomás-Barberán FA. Nutraceuticals: Facts and fiction. *Phytochemistry* 2007;68(22-24):2986-3008.
15. Fahey JW, Stephenson KK. Pinostrobin from honey and Thai ginger (*Boesenbergia pandurata*): A potent flavonoid inducer of mammalian phase 2 chemoprotective and antioxidant enzymes. *J Agric Food Chem* 2002;50(25):7472-6.
16. Ferreira IC, Aires E, Barreira JC, Estevinho LM. Antioxidant activity of Portuguese honey samples: Different contributions of the entire honey and phenolic extract. *Food Chem* 2009;114:1438-43.
17. Galego L, Almeida V, Gonçalves V, Costa M, Monteiro I and Matos F 2008; Antioxidant activity of the essential oils of *Thymbra capitata*, *Origanum vulgare*, *Thymus mastichina*, and *Calamintha baetica* *Acta Hort.* 765 325–34.
18. Ghani M A, Barril C, Bedgood D R and Prenzler P D 2017; Measurement of antioxidant activity with the thiobarbituric acid reactive substances assay *Food Chem.* 230 195–207.
19. Grosso G 2018; Dietary antioxidants and prevention of non-communicable diseases *Antioxidants (Basel)* 71-3.
20. Halvorsen BL et al. 2002; A systematic screening of total antioxidants in dietary plants. *The Journal of Nutrition* 132(3):461-471.
21. Halvorsen BL et al. 2006; Content of redox-active compounds (ie, antioxidants) in foods consumed in the United States. *The American journal of clinical nutrition* 84(1):95-135.
22. Huang D, Ou B and Prior R L 2005; The Chemistry behind Antioxidant Capacity Assays *J. Agric. Food Chem.* 53 1841–56.
23. Huang Y J and Nan GX 2019; Oxidative stress-induced angiogenesis *J. Clin. Neurosci.* 63 13–6
24. Inoue K, Murayama S, Seshimo F, Takeba K, Yoshimura Y, Nakazawa H. 2005; Identification of phenolic compound in manuka honey as specific superoxide anion radical scavenger using Electron Spin Resonance (ESR) and liquid chromatography with coulometric array detection. *J Sci Food Agric* 85:872-8.
25. Irina Georgiana Munteanu and Constantin Apetrei 2021, Analytical Methods Used in Determining Antioxidant Activity: A Review *y. Int. J. Mol. Sci.* 22, 3380.
26. Kalcher K et al. 2009; Electrochemical sensors and biosensors based on heterogeneous carbon materials *Monatshefte für Chemie-Chemical Monthly* 140(8):861-889.
27. Karagöz A, Artun F T, Özcan G, Melikoğlu G, Anıl S, Kültür Ş and Sütülpınar N 2015 In vitro evaluation of antioxidant activity of some plant methanol extracts *Biotechnol. Biotec. Eq.* 29 1184–9
28. Litescu S C, Eremia S and Radu G L 2010; Methods for the Determination of Antioxidant Capacity in Food and Raw Materials *Bio-Farms for Nutraceuticals* vol 698, ed M T Giardi, G Rea and B Berra (Boston, MA: Springer US) pp 241–9

29. Litescu SC et al.2011; Biosensors Applications on Assessment of Reactive Oxygen Species and Antioxidants. *Environmental Biosensors* .
30. Magalhaes, L.M.; Segundo, M.A.; Reis, S.; Lima, J.L. 2008, Methodological aspects about in vitro evaluation of antioxidant properties. *Anal. Chim. Acta* 613, 1–19.
31. Moharram H A and Youssef M M 2014;Methods for determining the antioxidant activity: A review *Alex. J. Fd. Sci. and Technol.*11 31–42.
32. Molyneux P. 2004; The use of the stable free radical diphenylpicrylhydrazyl (DPPH) for estimating antioxidant activity. *Songklanakarin J Sci Technol* 26(2):211-219.
33. Moniruzzaman, M, M I Khalil, S A Sulaiman, and S H Gan 2016. “Advances in the analytical methods for determining the antioxidant properties of honey: a review.” *Afr. J. Tradit. Complement. Altern. Med.* 9 36–42.
34. Ozyürek M, Güçlü K, Tütem E, Başkan K S, Erçağ E, Çelik S E, Baki S, Yıldız L, Karaman Ş and Apak R 2011; A comprehensive review of CUPRAC methodology *Anal. Methods*3 2439.
35. Pellegrini N, Serafini M, Colombi B, Del Rio D, Salvatore S, Bianchi M and Brighenti F 2003; Total antioxidant capacity of plant foods, beverages and oils consumed in Italy assessed by three different invitroassays *J. Nutr.*133 2812–9.
36. Pierart ZC, Rozowsky NJ. 2006; Papel de la nutricion en la prevencion del cancer gastrointestinal. *Rev Chil Nutr* 33(1):8-13.
37. Piljac-Zegarac J, Stipcevic T, Belscak A. 2009; Antioxidant properties and phenolic content of different floral origin honeys. *J Api Prod Api Med Sci* .1:43-50.
38. Prior R L 2015 Oxygen radical absorbance capacity (ORAC): New horizons in relating dietary antioxidants/bioactives and health benefits *J. Funct. Foods*18 797–810
39. Saddhe A A, Malvankar M R, Karle S B and Kumar K 2019; Reactive nitrogen species: Paradigms of cellular signaling and regulation of salt stress in plants *Environ. Exp. Bot.*161 86–97.
40. Schaich K M, Tian X and Xie J 2015; Hurdles and pitfalls in measuring antioxidant efficacy: A critical evaluation of ABTS, DPPH, and ORAC assays *J. Funct. Foods*14 111–25.
41. Shahidi, F.; Zhong, Y. Measurement of antioxidant activity. *J. Funct. Foods* 2015; 18, 757–781.
42. Shetti A, Keluskar V, Aggarwal A. Antioxidants enhancing oral and general health. *J Indian Acad Oral Med Radiol* 2009;21(1):1-6.
43. Sies H, Stahl W and Sevanian A 2005; Nutritional, dietary and postprandial oxidative stress *J. Nutr.*135 969–72.
44. Singh S and Singh R P, “In vitro methods of assay of antioxidants: an overview,” *Food Rev. Int.*24 392-414.
45. Wayner D D M, Burton G W, Ingold K U and Locke S 1985;Quantitative measurement of the total, peroxy radical-trapping antioxidant capability of human blood plasma by controlled peroxidation *FEBS Letters*187 33–7.
46. Zheng L, Zhao M, Xiao C, Zhao Q and Su G 2016; Practical problems when using ABTS assay to assess the radical-scavenging activity of peptides: importance of controlling reaction pH and time *Food Chem.*192 288–94.



Critical Study of Challenges of Weeds to the Farmers and Use of Bio Weedicides for Sustainable Agriculture

Ms. Swati Rajesh Yeole¹, Prof. Dr. S. K. Aher², Prin. Dr. R. K. Aher³

¹Research Scholar, Department of Botany, New Arts, Commerce and Science College, Parner District: Ahmednagar Pin Code:414302

²Research Guide, Department of Botany, New Arts, Commerce and Science College,

³Co- Guide, Department of Botany, New Arts, Commerce and Science College,

Corresponding Author- Ms. Swati Rajesh Yeole

Abstract:

Agriculture is considered as the one the prime source of livelihood to the farmers especially in rural part of India. The farmers are experiencing tremendous problems on account of weeds and it has affected enormously on the productivity in the agriculture sector. Weeds commonly called as undesirable plants growing along with the crop cultivated in the farm. It grows wildly in the farm and affects on the overall yield of crop. Weeds are also known as biggest threat to the farmers and it causes plenty of challenges in the process of sowing and reaping activity performed in the agriculture realm. There is need to exterminate the weeds from the crop and it also requires lot of labor and finance. Therefore, it is important that the farmers should use bio weedicide for minimizing soil erosion and achieve better productivity in the farm. The biggest difficulties faced by the farmers due weeds are: decrease in the productivity and economic loss. Bio weedicide is known as blessings to the farmers as it ensures systematic destruction of weeds. Hence, the farmers should avoid chemical weedicides and intensively use bio weedicides for environmental and agricultural protection.

This research paper primarily investigates challenges of weeds to the farmers and use of bio weedicides for better productivity, profitability, and sustainable development in agriculture.

Keywords: Weed, Agriculture, Weedicide, Challenges, Productivity and Profitability, Sustainable Agriculture.

1

Introduction:

Agriculture has played an important role in the life of people from ancient time. It is considered as prime source of livelihood to the people especially from rural part of India. The current population of India is 1,430,326,518 based on projections of the latest United Nations data. (<https://worldpopulationreview.com/countries/india-population>). It is apparent that India's population is equivalent to 17.76% of the total world population. India ranks number 1 in the list of countries (and dependencies) by population. Agriculture is one of the most useful and resourceful sources of self-employment to the people in India. Ratio of Decreasing land under cultivation and increasing population force us to focus on food security. To fulfill the need of food demand, security of food production by controlling weed has become a major

challenge to the farmers. The Gross Value Added (GVA) of agriculture and allied sectors in 2020-21 was 20.1%, it was 19% in 2021-22 and it again came down to 18.3% in 2022-23. (<https://newsonair.com/2023/03/22/parliament-session>). It is necessary to control the threats posed by the weeds to the farmers in the agriculture sector. There is presence of weeds in the farm and it causes lot of damage to yield taken by the farmers. It is essential to initiate effort to improved productivity in agriculture in India. Weeds are the most severe and widespread biological constraint to agricultural production systems and cause damage in cropped lands. There are plenty of consequences of weeds in the realm of agriculture and it has created serious concerns to the farmers community. It is apparent that the weeds reduce crop yield, availability of water and degrade quality of the produce besides raising cost of production. In

addition to yield and nutrient losses, weeds also harbor and serve as alternate hosts to several insect pests and diseases and may reduce land value. In the context of the problems created by the weeds to the crop, reviews on weed management in agroecosystems of India were made earlier (Joshi, 1971; Mukhopadhyay, 1993; Bhan and Sushilkumar, 1998; Yaduraju, 2012; Rao and Chauhan, 2015; Singh et al., 2016).

2. Weed as a natural competitor to food Crops: Challenge for farmers

It is clear that weeds have been biggest threats to the farmers. Man has selected his food crops from the thousands plant species that exist for their nutritional and flavor characteristic rather than through their ability to compete. Growing of crops, as part of agriculture for centuries, has changed the natural vegetation. It has been observed that weeds grow on soil along with crop plants naturally. But this growth of weed is not desirable in the monoculture system. These undesired plants deplete the nutrients, water and space allotted for the intended crop, and finally cause huge reduction in crop yield. It has also created plenty of apprehensions in the mind of farmers. Weeds, in crop field, reduce input efficiency, interfere with agricultural operations, impair quality and act as alternate hosts for several insect pests and diseases. Few weeds release toxic substance which affects the crop growth. The obvious effect of these traits is the hike in cost of cultivation by several folds. Along with this, weeds affect and interfere in the management of all the terrestrial and aquatic resources. They endanger the native biodiversity by choking and deliberate takeover of the native plants. The animals which depend on this native biodiversity for their survival are also getting affected. Therefore, weeds have become inevitable threat to the farmers especially in agriculture realm.

3. Most Common Crops and Types of Weeds in India:

The commonly cultivated crops in India are: Wheat, Cotton, Sugarcane, Groundnut, Soybean Grain (Wheat, rice, maize, pulses and millets), commercial crops (Jute, cotton, sugarcane, oil seeds and tobacco), plantations crops (rubber, coffee, tea, coconut), and horticulture crops (vegetables and fruits) are the four primary crops in India. (Rice, millets, wheat, pulses, and maize are all important food crops.

Sugarcane, horticulture, oil seeds, crops, coffee, tea, rubber, jute, and cotton; are important cash crops.). The farmers are toiling consistently and persistently to protect the crops the from the onslaught of the so-called weeds and its negative effects. Abundant information is available in India on weeds in rice (Rao and Nagamani, 2010; Subudhi et al., 2015), in wheat (Punia et al., 2017), cotton (Nalini et al., 2015), sugarcane (Jeyaraman et al., 2002), groundnut (Rajendran and Lourduraj, 1999), soybean (Panneerselvam and Lourduraj, 2000). A Weed Atlas for major weeds in major crops in 435 districts spread across 19 states of the country was published by DWR (Dixit et al., 2008). Eight hundred and twenty-six weeds species were reported to cause yield losses in India of which 80 and 198 were considered very serious and serious weeds respectively (Choudhury and Singh, 2015). Major weed species of India in different situations were given in the vision document of DWR (DWR, 2015). Major weeds are categorized into four groups: 1. Crop land weeds 2. Non-crop land weeds 3. Aquatic weeds 4. Parasitic weeds. These weeds have posed tremendous challenges to the farmers as a result it becomes essential to explore remedies for the weeds.

4. Most Common Crop land weeds in India:

The commonly found crop land weeds in India are as follows: *Amaranthus retroflexus*, *Amaranthus hybridus*, *Amaranthus powellii*, *Phalaris minor* Retz., *Echinochloa crus-galli* (L.), *Ageratum conyzoides* L., *Cyperus rotundus* L., *Cyperus compressus* L., *Cynodon dactylon* (L.) Pers., L., *Convolvulus arvensis* L., *Digitaria sanguinalis* L. (Scop.), *Fimbristylis miliacea* (L.) Vahl, *Ipomoea cairica* (L.) Sweet., *Medicago denticulata* Willd., *Oxalis corniculata* L., *Setaria glauca* (L.) P. Beauv., *Parthenium hysterophoru* L., *Chenopodium murale*., *Striga densiflora*, *Striga quphrasioides*, *Striga lutee*, *Striga asiatica*, *Alternanthera caracasana*

5. Available Techniques of Weed Management in India:

Different techniques of weed Management used in India by the farmers are as follows:

5.1. Preventive methods – Application of weed free crop seeds, use of clean seed laws, cleaning farm equipment and produce, cleaning irrigation water, cleaning sand and gravel and reducing the number of weed seeds returned to the soil (Das, 2008), not using fresh or partially decomposed FYM or compost, proper cleaning of farm machinery before sowing and keeping farm bund and irrigation/drainage channel free from weeds (Verma and Singh, 2008)

5.2. Traditional methods – This method is about use of, crop rotation, increase the competitive ability of the crop, time of seeding and irrigation, inclusion of cover crops, and intercropping (Kumar and Rathore, 2014), conscious use of crop interference, use of cropping pattern, and tillage systems (Zimdhal, 2007), inter and mixed cropping, summer ploughing.

5.3. Stale seedbed technique -In stale seedbed technique, after seedbed preparation, the field is irrigated and left unsown to allow weeds to germinate and which are killed either by a non-selective herbicide or by carrying out tillage prior to the sowing (Singh, 2014).

5.4. Mechanical weed control-Most mechanical weed control methods, such as hoeing, tillage, harrowing, torsion weeding, finger weeding and brush weeding, are used at very early weed growth stages (Singh, 2014; Kewat, 2014).

Along with above main four methods Slashing, Mulching, Residue management, Thermal weed control, Flame weeding, Soil solarization, Hand tools, Cutting/mowing, Allelopathy, Biological weed management, Integrated weed management methods are also used worldwide.

6. Common Techniques used by farmers to eradicate weeds in India:

The prominent common methods used by farmers at large scale in India are -pulling out of weeds with the hand, removal of weeds by using the tools like: trowel, small sickle, shovel, ploughing, burning, spraying weedicides, crop rotation, intercropping. etc. These methods have also helped to the farmers to eradicate the weeds and ensure excellent production of the crop leading to profitability.

7. Challenges faced by the farmers and application of Weedicides for Sustainable Agriculture:

Many mechanical control methods become difficult after the cotyledon stage and their

selectivity decreases with increasing crop and weed age. Thus, if the weeds have become too large, an intensive and aggressive adjustment of the implements is necessary to control the weeds, and by doing this one increases the risk of damaging the crop severely (Carter and Ivany, 2006). There is unavailability of man power because of migration, industrialization resulting in increased job opportunities neighboring cities. The best solution to the extermination of this unwanted and undesirable plants is effective application of bio weedicides and contribute in the sustainable development of the agriculture.

8. Need to Use Bio weedicides instead of Chemical Weedicides: In spite of harmful implications involved in the use of synthetic chemicals to control weeds, they are extensively used all over the world. There is necessity of application of eco friendly bio weedicides for the purpose of continuous growth of agriculture products. Bio weedicides is generally extraction of chemicals for eradication of weeds. It is used to express growth inhibition of a plant through the release of chemicals into the environment from another plant.

Conclusion: In this way, an attempt has been made to identify challenges created by the weeds to the farmers and its impact on productivity in agriculture. It also highlights on application of bio weedicide for sustainable agriculture.

Bibliography: -

1. Anderson, R. *An ecological Approach to Strengthen Weed Management in the semiarid Great Plains*. Advances in Agronomy.80: 33-62. 2003.
2. Das, T.K. *Weed Science: basics and application*. Jain Brothers Pub, New Delhi, First edition p.901. 2008.
3. Dubey, R. P. *Integrated Weed Management an in Approach in Training Manual Advance Training in Weed Management*, held at DWS, Jabalpur, India. 2012.
4. Bridges D, Anderson R. *Crop Losses due to Weed in the United States*. The Weed Science Society of America, 1992.
5. *Weed research issues, challenges, and opportunities in India* A.N. Rao, Ravi Gopal Singh, Gulshan Mahajan , S.P. Wani ICRISAT Development Center (IDC) & International Rice Research Institute (IRRI), International Crops Research Institute for Semi-Arid Tropics,

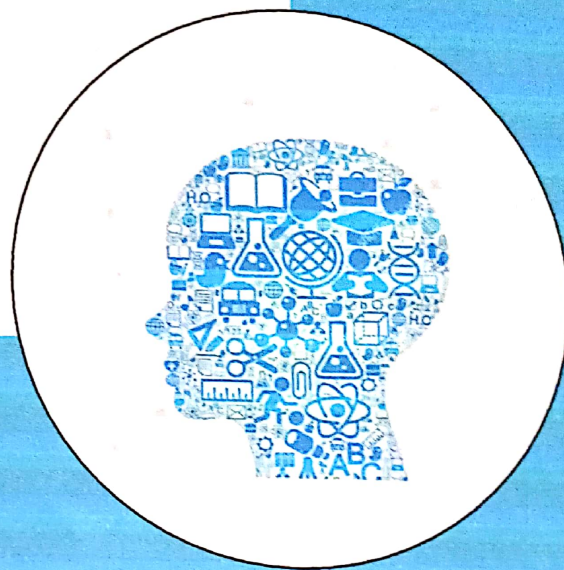
Building # 303, ICRISAT, Patancheru
502324, Hyderabad, India

Webliography: -

1. <https://newsonair.com/2023/03/22/parliament-session>)
2. <https://worldpopulationreview.com/countries/india-population>

ISSN No 2347-7075
Impact Factor- 7.328
Volume-5 Issue-13

**INTERNATIONAL
JOURNAL of
ADVANCE and
APPLIED
RESEARCH**



Publisher: P. R. Talekar
Secretary,
Young Researcher Association
Kolhapur(M.S), India

Young Researcher Association



Sr No	Paper Title	Page No.
1	Ethics and Print Advertisement in Indian Society Prof. Kamran Arbi , Dr. Ashfaq Ahmed Khan	1-5
2	A Comparison Between Mutual Funds & Other Investment Options Mr Ritesh M. Raichana	6-7
3	A Study of Financial Litrecacy and Financial Inclusion Among Households Sarvesh Parab	8-10
4	Embracing Interdisciplinary Approaches For Sustainability And Conservation Dr. Amruta Karlikar	11-13
5	Tribal Dialects Enriching Indian Literature: A Literary Exploration Dipak Shivdas Wakde	14-17
6	Improving health system through communitisation: A case of Maharashtra Sakshi Jeevan Asawale	18-20
7	Study of Various Loan Schemes Applicable to Women Scf Help Groups Dr. Kishor Girish Nawale , Nilesh Sarjerao Salve	21-24
8	A Study on Impact of Government Finance Scheme Awareness, Access and Perception on the MSME's in Mumbai Samiullah Shaikh , Dr. Ashfaq Ahmad Khan	25-31
9	To study the Impact of Lockdown Policies on Unorganized Industrial Labour around Talasari Industrial Area Mahesh Pandurang Malwadkar	32-38
10	Unemployment Among Higher-Educated Persons Is One of The Problems In Building A Aatmanirbhar Bharat Kamble S.S., Kolambikar A.L.	39-43
11	Rural Agro Tourism in Maharashtra – Challenges and Opportunities Mr.Bhaskar R. Khandvi , Mr.Vikram S. Sable	44-47
12	Scientometric Portrait of Dr. Jayant Narlikar: an Indian Astrophysicist N.B. Thakare , Ahirrao M.K.	48-53
13	New Age Financial Services for Msme's In Indian Context Mr. Atul P. Kathare , Dr. Vijay R. Uttarwar	54-57
14	Documentation of some wild fruit and medicinal plants habitually used by tribals of Jawhar Tehsil of Palghar District Maharashtra, India Namdeo Vishnu Mahale	58-63
15	A Comprehensive Study of Financial Literacy Among Muslim Women in Mumbai Prof. (Dr.) Ashfaq Ahmad Khan , Mois A. Patel	64-66
16	Environmental issues and Indian Politics Prof. Dr. Ramesh Gangaram Khairnar	67-68
17	Rainfall and Tempature: The Most Important Components Of Natural Environment With Reference To Indian Climate Nahire Dinesh J. , Sayyed Juned A.	69-71
18	सतत विकास एवं भारत : एक सिंहावलोकन डॉ. विनय कुमार गुप्ता	72-80
19	आदिवासी जमातीच्या चळवळीमागील समस्या व उपाययोजना नारायण यमाजी तुवर , प्रा. डॉ. हरी नारायण जमाले	81-82
20	आदिवासींच्या आरोग्यवर्धक रानभाज्या प्राचार्य डॉ.अंजली मस्करेन्हस , डॉ. शशिकला पोतनीस	83-87
21	आदिवासींच्या विकास योजना – एक अभ्यास अनिल कुंडलिक पठाडे ,डॉ. दीपक पंढरीनाथ सोनटक्के	88-92
22	आपदा , आपदा प्रबंधन और सरकार की भूमिका प्रो. डॉ. संतोष शिवकुमार खत्री	93-96
23	चाव्हाक दर्शनातील सुखवाद संकल्पनेची मिमांसा गोरोबा तुकाराम खुरपे , डॉ. संजय हणमंतराव पाटील	97-101



आदिवासींच्या विकास योजना - एक अभ्यास

अनिल कुंडलिक पठाडे 1 डॉ. दीपक पंढरीनाथ सोनटके 2

1 संशोधक, न्यू आर्ट्स, कॉमर्स, सायन्स कॉलेज, अहमदनगर, (स्वायत्त)

2 संशोधक मार्गदर्शक, न्यू आर्ट्स, कॉमर्स, सायन्स कॉलेजे, अहमदनगर, (स्वायत्त)

Corresponding Author :- अनिल कुंडलिक पठाडे

Email:- profpathade@gmail.com

DOI- 10.5281/zenodo.11259838

प्रस्तावना:

महाराष्ट्र राज्यातील अनुसूचित जमातीच्या लोकांची संस्कृती व त्यांची मुल्ये यांचा आदर राखून त्यांना सक्षम बनवून त्यांचा विकास सुनिश्चित करणे. भारतीय संविधानाच्या मार्गदर्शक तत्वानुसार राज्यातील अनुसूचित जाती व अनुसूचित जमातीच्या लोकांचे शिक्षण व आर्थिक हितसंबंध जपण्यासाठी विशेष काळजी घेणे आणि त्यांचे सामाजिक अन्याय व इतर पिढवणुकीपासून संरक्षण करणे. त्या अनुषंगाने अनुसूचित जमातींचा शैक्षणिक, आर्थिक आणि सामाजिक सुधारणांच्या कार्यक्रमावर भर देण्यात आला आहे. समाज कल्याण विभागाकडून आदिवासी विभागाची निर्मिती सन १९८३ मध्ये करण्यात आली. आदिवासी जनतेच्या विकासासाठी आदिवासी विकास विभाग विविध विकास योजना राबवीत असते.

अनुसूचित जमातींचा लोकांचे शैक्षणिक व आर्थिक हितसंबंध जपण्यासाठी विशेष काळजी घ्यावी आणि त्यांचे सामाजिक अन्याय व इतर शोषणापासून संरक्षण करण्याची जबाबदारी राज्य शासनाची आहे. भारतीय राज्यघटनेतील मार्गदर्शक तत्वानुसार पंचवार्षिक योजनामध्ये मागासवर्गीयांच्या शैक्षणिक, आर्थिक आणि सामाजिक सुधारणांच्या कार्यक्रमावर भर देण्यात आला आहे.

महाराष्ट्र राज्यातील आदिवासी लोकसंख्या:

जनगणना वर्ष	राज्याची एकूण लोकसंख्या (लाखात)	आदिवासी लोकसंख्या (लाखात)	टक्केवारी
१९७१	५०४.१२	३८.४१	७.६२
१९८१	६२७.८४	५७.७२	९.१९
१९९१	७८९.३७	७३.१८	९.२७
२००१	९६८.७९	८५.७७	८.८५
२०११	११२३.७४	१०५.१०	९.३५

महाराष्ट्र राज्यात एकूण ४५ अनुसूचित जमाती आहेत त्यात मुख्यत्वे भिल्ल, गोंड, महादेव कोळी, पावरा, ठाकूर, वारली या प्रमुख आदिवासी जमाती आहेत. कोलाम (यवतमाळ जिल्हा), कातकरी (मुख्यतः रायगड व ठाणे जिल्हा) आणि माडिया गोंड (गडचिरोली जिल्हा) या केंद्र शासनाने आदिम जमाती म्हणून अधिसूचित केलेल्या अशा तीन जमाती आहेत.

राज्यात एकूण ३६ जिल्हे आहेत आणि आदिवासींची संख्या मोठ्या प्रमाणात धुळे, नंदुरबार, जळगाव, नाशिक व ठाणे व नवनिर्मित पालघर (सह्याद्री प्रदेश) चंद्रपूर, गडचिरोली, भंडारा, गोंदिया, नागपूर, अमरावती व यवतमाळ (गोंडवन प्रदेश) या पूर्वेकडील वनाच्छादित जिल्ह्यांमध्ये मुख्यतः अधिक आहे.

१९७५-७६ या वर्षी केंद्र सरकारने निर्देश दिल्याप्रमाणे ज्या गावांतील आदिवासी लोकसंख्या एकूण लोकसंख्येच्या ५० टक्क्याहून अधिक असेल त्या गावांचा समावेश एकात्मिक आदिवासी विकास प्रकल्पामध्ये (आयटीडीपी) करण्यात आला. भारत सरकारने मान्यता देलेले अशा प्रकारे १६ प्रकल्प होते. नंतर ज्या गावांमधील

आदिवासींची लोकसंख्या ५० टक्क्यापेक्षा किंचितसी कमी होती त्या गावांचा समावेशही अशा एकात्मिक आदिवासी विकास प्रकल्प क्षेत्रामध्ये करण्यात आला आणि अशी क्षेत्रे अतिरिक्त आदिवासी उपाययोजना (एसटीएसपी गट/प्रकल्प) म्हणून ओळखण्यात येऊ लागली. राज्य शासनाची मान्यता मिळालेली अशी ४ अतिरिक्त आदिवासी उपाययोजना प्रकल्प क्षेत्रे आहेत. तसेच आदिवासींची लोकसंख्येचे वाढते प्रमाण व मोठे कार्यक्षेत्र पाहता सध्या एकूण प्रकल्प अधिकाऱ्यांची संख्या २९ आहे.

दरम्यानच्या काळात एकात्मिक आदिवासी विकास प्रकल्प क्षेत्रालगतच्या प्रदेशातही काही ठिकाणी आदिवासींची वस्ती असल्याचे भारत सरकारच्या लक्षात आले आहे. म्हणून सुमारे १०,००० लोकवस्तीच्या गावांमध्ये आदिवासींची संख्या ५० टक्क्याहून अधिक असेल तर अशा गावांचा समावेश सुधारित क्षेत्र विकास खंडामध्ये (माडा) करण्यात यावा असे निर्देश देण्यात आले. त्याच प्रमाणे एकूण ५,००० लोकवस्तीच्या दोन किंवा तिन गावांमध्ये ५० टक्क्याहून अधिक आदिवासींची संख्या असेल तर, त्या गावांचा समावेश मिनिमाडा क्षेत्रामध्ये करण्यात

यावा, अशा सूचना आहेत. महाराष्ट्रामध्ये एकूण ४३ माडा क्षेत्रे आणि २४ मिनिमाडा क्षेत्रे आहेत.

आदिवासी विकास विभागाकडे सोपविलेल्या कामकाजामध्ये अधिक उत्तरदायी प्रशासन होण्याच्या दृष्टीने १९९२ मध्ये या विभागाची पुनर्रचना करण्यात आली. राज्यात आयुक्त, आदिवासी विकास, महाराष्ट्र राज्य, नाशिक यांचे अधिपत्याखालील अपर आयुक्त, आदिवासी विकास, नाशिक, ठाणे, अमरावती व नागपूर, प्रकल्प अधिकारी, एकात्मिक आदिवासी विकास प्रकल्प २९ कार्यालय कार्यरत असून त्यांपैकी ११ एकत्मित आदिवासी विकास प्रकल्प अत्यंत संवेदनशील म्हणून घीषित करण्यात आली आहेत. त्यामध्ये नाशिक, कळवण, तळोदा, जव्हार, डहाणू, धारणी, किनवट, पांढरकवडा, गडचिरोली, अहेरी व भामरागड यांचा समावेश आहे.

उद्देश: सदरील शोधनिबंधात महाराष्ट्र राज्यातील आदिवासींच्या विविध विकास योजनांचा आढावा घेऊन अभ्यास करण्याचा प्रयत्न करण्यात आला आहे. तसेच योजनांच्या अंमलबजावणीतील सत्यता पडताळून पाहण्याचा प्रयत्न केला आहे.

आर्थिक उत्पन्नाच्या योजना:

आदिवासी शेतकऱ्यांना वीजपंप/तेलपंप पुरवठा करणे योजनेचा उद्देश व स्वरूप:

अ. आदिवासी शेतकऱ्यांना त्यांचा शेतीविकास किफायतशीरपणे होण्याच्या दृष्टीने उपलब्ध असलेल्या साधनाचा व उर्जेचा पुरेपुर उपयोग करून त्याद्वारे जास्तीत जास्त जमीन ओलिताखाली आणून आदिवासींचा आर्थिक विकास साधण्याच्या हेतुन १०० टक्के अनुदानावर विजपंप/तेलपंप पुरविण्यात येत आहे.

ब. या योजनेखाली सर्वसाधारण पणे ३ किंवा ५ अश्वशक्तीचे विजपंप/तेलपंप मंजूर करण्यात येतात.

क. राज्यातील आदिवासी उपयोजना क्षेत्र व क्षेत्राबाहेरील आदिवासी शेतकऱ्याकडे किमान ६० आर (दीड एकर) आणि कमाल ६ हे. ४० आर (१.६ एकर) इतकी लागवाडीयोग्य जमीन उपलब्ध आहे. अशा शेतकरी या योजनेचा लाभ घेवू शकतात.

पात्रतेचे निकष:

१. आदिवासी शेतकऱ्यांना विजपंप मंजूर करतांना त्यांच्या शेतातील पाण्याचे साधन असलेल्या विहिर/नाल्यास कमीत कमी सहा महिने पाणी उपलब्ध असणे आवश्यक आहे.

२. आदिवासी शेतकरी स्वतः जमीन कसत असला पाहिजे.

३. ६० आरपेक्षा कमी जमीन ज्यांच्या नांवाने असेल अशा किंवा ३ लगतच्या जमीन धारकांना एकत्रित येऊन करार लिहून दिला तर एका पेक्षा अधिक लाभधारक एकत्रितपणे या योजनेचा लाभ घेऊ शकतील. मात्र अशा एकत्रित आलेल्या शेतकऱ्यांची एकूण जमीन ६० आरपेक्षा जास्त असली पाहिजे.

४. या योजनेखाली ज्या गांवात/शेतात विजपुरवठा केला जावू शकतो त्या गावच्या शेतकऱ्यास विजपंप व जेथे वीजपुरवठा केला जात नाही अथवा नजीकच्या ३ वर्षात केली जाण्याची शक्यता नाही अशा ठिकाणी तेलपंप पुरविण्यात येतो.

अनिल कुंडलिक पठाडे, डॉ. दीपक पंढरीनाथ सोनटक्के

संपर्क:

संबंधित प्रकल्प अधिकारी, एकात्मिक आदिवासी विकास प्रकल्प.

प्रादेशिक व्यवस्थापक/उपप्रादेशिक व्यवस्थापक, महाराष्ट्र राज्य सहकारी आदिवासी विकास महामंडळ.

केंद्रवर्ती अर्थसंकल्प (न्युक्लिअस बजेट)

उद्देश व स्वरूप :

ज्या योजनाचा समावेश अर्थसंकल्पात नाही अशा अभिनव स्वरूपाच्या स्थानिक महत्वाच्या कर्जविरहीत योजना तातडीने व प्रभावीपणे कार्यान्वित करून गरजू आदिवासींना प्रत्यक्ष लाभ मिळवून देणे हा योजनेचा मुख्य उद्देश. आदिवासी व्यक्ती/कुटूंब केंद्रविंदु मानून या योजनेतर्गत कर्ज देणे अपेक्षित नाही. योजनेचे स्वरूप खालीलप्रमाणे

१. योजनेतर्गत प्रत्येक आदिवासी व्यक्तीस/कुटूंबाम/मामुद्रिक प्रकल्पात/कार्यक्रमांतर्गत आर्थिक मर्यादा रु. १५०००/- पर्यंत.

२. ४ गट नमूद केले असून

अ) उत्पन्न निर्मितीच्या किंवा वाढीच्या योजना

ब) प्रशिक्षणाच्या योजना

क) मानवी साधनसंपत्तीच्या विकासाच्या योजना

ड) आदिवासी कल्याणात्मक योजना

३. अ या गटात अनुदानाची मर्यादा खालीलप्रमाणे

अ) सर्वसाधारण आदिवासी लाभार्थी - ८५ टक्के व १५ टक्के वैयक्तिक सहभाग

ब) आदिम जमाती लाभार्थी - ९५ टक्के व ५ टक्के वैयक्तिक सहभाग

क) जेथे अर्थसहाय्य रु. २००० असेल तेथे १०० टक्के अर्थसहाय्य.

४. शासन निर्णय दि. ३१ मे २००१ च्या मार्गदर्शक सूचनातील अटी शर्तीनुसार पात्र लाभार्थी व त्यांनी मागणी केल्या नुसार योजना तयार करून प्रकल्प अधिकारी यांनी अपर आयुक्ताकडे निर्देश समितीचे अध्यक्ष या नात्याने मंजुरी घेणे.

५. योजना मंजुरीचे अधिकार रु. ७.५० पर्यंतच्या अपर आयुक्त, आदिवासी विकास रु. ७.५० ते ३०.०० लक्षपर्यंतची योजना आयुक्त, आदिवासी विकास व रु.

३०.०० लक्ष पेक्षा जास्त रकमेच्या योजनेस शासनाची मान्यता अधिकार प्रदान

६. अर्थसंकल्पात तरतूद असलेल्या एखाद्या योजनेवर अत्यावश्यक आणि अपवादात्मक परिस्थितीत पुरक खर्च न्युक्लिअस बजेट मधून करावयाचा असल्यास प्रस्ताव मंजुरीसाठी आयुक्त, आदिवासी विकास यांच्याकडे मादर करणे.

७. शासनाने विहित केलेल्या मार्गदर्शक सूचनानुसार जे कार्यक्रम न्युक्लिअस बजेट अंतर्गत देता येत नाहीत परंतु स्थानिक परिस्थितीनुसार खास कार्यक्रम घेणे आवश्यक आहे



UGC CARE LISTED
ISSN No. 2394-5990

इतिहासाचार्य वि. का. राजवाडे मंडळ, धुळे
या संस्थेचे त्रैमासिक
॥ संशोधक ॥

पुरवणी अंक ४९ - मार्च २०२४ (त्रैमासिक)

- शके १९४५
- वर्ष : ९२
- पुरवणी अंक : ४९

संपादक मंडळ

- प्राचार्य डॉ. सर्जेराव भामरे
- प्रा. डॉ. मृदुला वर्मा
- प्राचार्य डॉ. अनिल माणिक बैसाणे
- प्रा. श्रीपाद नांदेडकर

अतिथी संपादक

- डॉ. मृणालिनी शेखर
- प्रो. (डॉ.) पांडुरंग भोसले
- प्रो. (डॉ.) कामायनी सुर्वे

* प्रकाशक *

श्री. संजय मुंदडा

कार्याध्यक्ष, इ. वि. का. राजवाडे संशोधन मंडळ, धुळे ४२४००१
दूरध्वनी (०२५६२) २३३८४८, ९४२२२८९४७९, ९४०४५७७०२०

Email ID : rajwademandaldhule1@gmail.com

rajwademandaldhule2@gmail.com

कार्यालयीन वेळ

सकाळी ९.३० ते १.००, सायंकाळी ४.३० ते ८.०० (रविवारी सुट्टी)

सदस्यता वर्गणी : रु. २५००/-

विशेष सूचना : संशोधक त्रैमासिकाची वर्गणी चेक/ड्राफ्टने
'संशोधक त्रैमासिक राजवाडे मंडळ, धुळे' या नावाने पाठवावी.

अक्षरजुळणी : सौ. सीमा शिंत्रे, पुणे.

टीप : या नियतकालिकेतील लेखकांच्या विचारांशी मंडळ व शासन सहमत असेलच असे नाही.



INDEX

1. **Indian Classical Theatre: A Colossal Influence on Modern Indian Drama**
- Dr. Anand Uddhav Hipparkar ----- 9
2. **Myth and Realism in Hayavadana by Girish Karnard**
- Dr. Anil Gaman Ahire ----- 15
3. **Intersections of Indian Knowledge Systems, Culture, and Identity in Indian English Literature**
- Ankit Wadatkar ----- 19
4. ***Manache Shloka* by Samarth Ramdas Swami: Guide for Psychological Well-Being**
- Dr. Archana Pandit ----- 24
5. **Gender Disparity: An Ongoing Battle for Equality in India**
- i) Archana Singh, ii) Dr. Rajendra Sarode ----- 28
6. **Indian Knowledge Systems (IKS) and Its Impact on Literary Discourse**
- Dr Sandeep Hanmantrao Patil ----- 33
7. **Indian Knowledge System and its relevance to literature**
- Dr. Anuradha Ghodke ----- 38
8. **English Literary Criticism : 16th to 19th Century Literary Criticism**
- Dr. Kamble Satwa Ramchandra ----- 42
9. **What Makes Us Human: A Multifaceted Investigation**
- Dr. Laxman Arun Kshirsagar ----- 46
10. **Concept of Consciousness: East precedes West**
- Dr. Neelkanth Jagannath Dahale ----- 50



32. **Unrevealed Facts and Facets of Caste and Societal System in India as Depicted in *Sita Warrior of Mithila* (2017)**
 - i) L.Vijayalakshmi, ii) Prof. Dr. Shilpagauri Prasad Ganpule ----- 148
33. **Ecological Crisis in Amitav Ghosh's 'The Hungry Tide'**
 - Ashok Vitthal More ----- 154
34. **Present status and views of Teacher Educators towards Teaching of Phonetics in Training Colleges: A Study**
 - Dr. Vijay Santu Patole ----- 158
35. **Indian Knowledge System: Vedic Period to the Contemporary Indian English Drama**
 - Dr. Ayodhya Kalyan Jadhav ----- 164
36. **Sanskrit Theatre: Milestone in the Indian Drama**
 - Dr. Santosh Dadu Ghangale ----- 168
37. **Toru Datt's Verse : Myths into Poetic Rendering**
 - Dr. Mrunalini Vasant Shekhar ----- 171
38. ***IKS and Indian Folktales***
 - Avinash Bhagwan Shelke ----- 175
39. **The Role of Tradition in Kamala Markandya's *Nectar in a Sieve***
 - Smt. Dipali Sadashiv Suryawanshi ----- 179
40. **A kaleidoscopic survey of Indian Classical Drama (Sanskrit Theatre): Its Historical significance and Development**
 - Dr. Ganesh Chintaman Wagh ----- 183
41. **भारतीय ज्ञान परंपरा आणि गोंदिया जिल्ह्यातील 'बहुरूपी' लोककला**
 - भूमेश्वर शंकर शेंडे ----- 189



ECOLOGICAL CRISIS IN AMITAV GHOSH'S 'THE HUNGRY TIDE'

Ashok Vitthal More

Assistant Professor in English, Department of English
New Arts, Commerce and Science College, Parner

E-mail- postcol2019@gmail.com

Contact: +919011353000

Abstract:

Ecological challenges are critical to national growth. Typically, progress is hampered by the unexpected arrival of humans, which disrupts ecological and unbalanced biodiversity. Amitav Ghosh's literary works addressed environmental issues and highlighted how they affect the ecosystem. Migrants and the underclass suffer as a result of over-settlement, over-urbanisation, and deforestation throughout India. This study aims to investigate the ecological crisis that impedes environmental protection. The Sundarbans, a coastal region between India and Bangladesh, revolves around water. Water swallows and regurgitates land with each tide cycle. The 1970s tiger protection initiative in the Sundarbans leads to the ruthless state-led displacement of Bangladeshi refugees from the islands. In 2000, the government imposed significant portions of the islands on a private business for an ecotourism project. These events are the backdrop for Amitav Ghosh's novel *The Hungry Tide*. The novel recounts the first incident and presents a political critique of the second development. This study investigates the author's use of water as both a metaphor and a material presence in the text to examine how the novelist articulates the rupture of social hierarchies and expresses dissatisfaction with the violation of human rights for conservation.

Keywords: Ecosystem, Environment, Biodiversity, Over-urbanisation, Deforestation

Introduction :

The present study focuses on the ecological crisis in Amitav Ghosh's *The Hungry Tide*. Ecological issues are significant due to humans' undue intrusion into nature and their effects on the environment. It also focuses on how humans and Nature could coexist if they didn't affect each other. It aims to create awareness among people for environmental conservation. It acquaints people with the power of nature and its ecology and environmental concerns. Man and Nature are integral and can not be separated due to their bonding. The lives of men have been dependent on Nature since they started agriculture. Nature can be revealed through ecology- the scientific study of the relationship between humans and nature. The present study limits and focuses on the ecological crisis in Amitav Ghosh's *The Hungry Tide*.

Amitav Ghosh is a well-recognized contemporary Indian English novelist. He was born in Kolkata on July 11, 1956, and grew up in India, Sri Lanka, and Bangladesh. He completed his education at the Doon School in Dehradun. He studied higher education at St. Stephen's College, Delhi University, and the Delhi School of Economics. Ghosh received the Scholarship for a D.Phil. in social anthropology at St. Edmund Hall, Oxford. First, he worked for the Indian Express newspaper in Delhi. He also worked as a faculty member in colleges and universities. The Indian government awarded him the Padma Shri in 2007. His contribution to Indian English literature is noteworthy. His works



can be classified into two parts: fiction and nonfiction. Famous fiction works include *The Shadow Lines*, *Calcutta Chromosome*, *Glass Palace*, *Hungry Tide*, *Ibis Trilogy*, and *Gun Island*. Non-fiction works include *In an Antique Land*, *Dancing in Cambodia and Burma*, *Countdown*, *The Imam and India*, and *The Great Derangement: Climate Change and the Unthinkable*. The

Objectives:

The paper highlights crucial issues, such as examining Ghosh's main environmental storylines and themes. The study recognises how the Sundarbans depict the precarious balance between humans and the environment. The paper evaluates the book's contribution to and effectiveness in raising readers' environmental consciousness.

Literature Review:

The Sundarbans is a large archipelago of islands in the Bay of Bengal, and "The Hungry Tide," written by Amitav Ghosh, is a moving depiction of the intertwining of human lives, socio-cultural realities, and the powerful, unexpected dynamics of nature there. The book is not merely a story of human attempts and aspirations; it also paints a clear picture of environmental difficulties, interspecies connections, and the ongoing struggle between people and nature's unbridled force. (Mukherjee, 2010).

The term "eco-criticism," which derives from the Greek words "oikos," which means "house" or "environment," and "kritikos," which means "discerning judge," refers to an approach to literary and cultural criticism that looks at the complex interaction between people and their environment in literature. While books that express concerns about the natural world and how humans affect it make up environmental literature. This section defines the term "eco-criticism" and recounts the development of ecological literature, emphasising the connections between them. (DeLoughrey, Elizabeth M., 2011)

Discussion and Arguments:

The narrative revolves around the Sundarbans, a vast, mysterious, and unstable delta that crosses

Eastern India and Southern Bangladesh. Major plot points are played by the human characters and the terrain, usually described as a shifting maze of rivers, islands, and tidal waterways. Ghosh paints vivid pictures of the Bengal tigers that lurk in the mangroves, the cyclones that may suddenly change a person's path in life, and the waves that come and go. The novel's characters, Piya, the devoted cetologist, Fokir, and the determined Kanai, all represent different ties to the land and waters of the Sundarbans. While Piya bases her existence on the tide patterns and approaches the mangroves with a scientific eye, Fokir's knowledge is more instinctive and has been passed down through the centuries. On the other hand, Kanai has to tread carefully because he is both an outsider and has family ties to the area. With the help of these people, Ghosh paints a picture of the Sundarbans as a region where culture and environment coexist harmoniously.

In an era when these concerns are of global concern, literature by authors such as Ghosh provides a critical lens through which ecological disasters, sea level rise, and environmental degradation may be analysed. Such books enhance literary traditions and contribute to broader discussions on cohabitation and environmental sustainability by fusing narrative with in-depth ecological understanding. Additionally, the novel offers a case study of the more significant challenges faced by endangered ecosystems worldwide by concentrating on a particular and distinctive site like the Sundarbans.

The river's significance is highlighted since the narrative regularly explores the complex and often perilous relationship between humans and their natural environment. Ghosh illustrates the varied fauna and plants of the Sundarbans, emphasising the region's ecological relevance. The narrative highlights the impacts of climate change by acknowledging the region's increasing frequency of hurricanes. The struggle to preserve the ecosystem and the Bengal tiger serves as a reminder of the conservation efforts made by both domestic and foreign groups. The



novel highlights the intimate connection between tradition, culture, and the land, primarily via the character Piya. Because they depict the complex web of ecological, cultural, and human elements inside the Sundarbans, these topic elements are essential to the novel's ecocritical point of view.

The novel's evocative descriptions and character interactions illustrate the complex and often dangerous links between humans and the natural world. The river, in particular, is a significant metaphor and source of inspiration for these interactions and emphasises the novel's eco-critical point of view. The textual analysis reveals that Amitav Ghosh's storytelling effectively conveys eco-critical subjects and highlights the intricate links between the natural and human worlds in the Sundarbans. Additional research, like theme coding and reader response surveys, will help us better understand the novel's eco-critical impact.

"The Hungry Tide" by Amitav Ghosh eloquently captures the relationship between humans and their surroundings. Throughout the book, the Sundarbans and humankind maintain a delicate equilibrium that demonstrates how living in the delta is more than coexistence—a never-ending dance with survival. This motif keeps coming up because it shows how the people in the area are strongly connected to the environment, even if it can sometimes be hostile. The frequency of this topic's appearances indicates how vital it is to the plot and how understanding the book's larger environmental message is.

The book describes the Sundarbans as a site of frequent tragedy mixed with breathtaking natural beauty. Because the scenery changes due to storms, tides, and other natural events, it is a place of wonder and dread. Environmental disasters like this one draw attention to the ecosystem's fragility and, in turn, to more widespread concerns about climate change and its consequences on a global scale.

Ghosh's detailed descriptions of the Sundarbans' biodiversity—which includes everything from deadly tigers to a wide variety of aquatic creatures—highlight the complexity and richness of the local

ecosystem. By showing the range of species that share the same waterways and the delicate balance they maintain, Ghosh draws attention to the area's biological value and crafts an intriguing tale about the interdependence of species.

One of the book's central themes is the struggle between exploitation and conservation. The unique biodiversity of the Sundarbans is being protected and preserved. However, the local population usually depends on the land and its resources for their livelihood, often leading to overuse. Ghosh tackles this paradox with various characters and subplots, raising thought-provoking issues regarding the ethics and realities of survival and conservation.

Thematic coding in "The Hungry Tide" draws attention to how ecological themes are intricately woven. More than merely describing the Sundarbans, Ghosh's story raises important questions about how humans relate to the environment. This article's questions highlight the novel's literary value in environmental debate and offer new avenues for ecocritical investigation.

"The Hungry Tide" by Amitav Ghosh is a compelling tale that provides deep insights into the intricacies of human-nature connections, especially in the fragile ecology of the Sundarbans. It stands out at the junction of literature and environmental discourse. Rather than being limited to being a vehicle for storytelling, the text becomes a web of narratives about personal, cultural, and ecological resilience. Ghosh imagines a world where the environment is a living thing that is both shaped and shaped by its inhabitants rather than merely a backdrop. The book's eco-critical analysis highlights Ghosh's wide-ranging investigation of environmental issues and his perceptive understanding of how they are changing social and physical environments. The author's layers of environmental commentary are made visible through the thematic coding, and the overt and covert ecological themes are emphasised through the textual analysis. The reader response poll highlights the book's impact even more by demonstrating how literature can encourage



environmental knowledge and advocacy. The novel's sustained appeal and the insights gained from this study show the value of ongoing eco-critical literary inquiry. Future studies might broaden the scope to encompass other South Asian writers who investigate the relationships between culture and environment or go more into analysing Ghosh's other writings in comparison. It's evident in the end that literature could be more than just a tool of escape; it may also work as a catalyst for change by promoting understanding, empathy, and conservation efforts.

Conclusion:

Environmental concerns endanger human life and cause profound climate change. Nature has turned hostile to people searching for justice due to humans' reckless behaviour, ignoring its regenerative and life-giving properties. Eco-catastrophism gives an apocalyptic vision while warning us to take the necessary precautions to prevent catastrophe. In light of the present situation of environmental decline, conservationists and writers worldwide are calling on us to take action and stop the destruction of our environment. The worldwide problem has resulted from the ecosystem's failure to meet our unusual demands. Amitav Ghosh, a well-known Indian writer, talks about social, political, cultural, and environmental themes in a fresh manner. In his work, *The Hungry Tide*, Ghosh investigates nature's annoyance and human suppression, as well as the voices that advocate the need to preserve nature. The novel illustrates the global issue in a local context.

Amitav Ghosh's *The Hungry Tide* promotes awareness among people regarding the importance and need to preserve and maintain our planet for ourselves and future generations.

References:

1. Ghosh, Amitav. (2002) *The Hungry Tide*, India: Harper Collins Harper
2. Abrams, M.H. (2005) *Glossary of Literary Terms*. Banglore: Prism Books
3. Bhabha, K, Homi.(1994) *The Location of Culture*. London: Routledge
4. Beverley, John.(1999) *Subalternity and representation: arguments in cultural theory*. Durham: Duke in University Press
5. Said, Edward W. (1978) *Orientalism*, UK: Pantheon Books
6. Spivak, Gayatri Chakravorty, (1988) *Can the subaltern Speak?*, India: Macmillan
7. Aspea, Kazi. (2019). Voice of the Voiceless: A Subaltern Study of The Hungry Tide.
8. Guha, Ranjit. "Introduction". *Subaltern Studies*. Ed. Ranjit Guha. Vol: 1. Delhi: Oxford University Press, 1982.
9. Sivaramakrishnan K. "Situating the Subaltern: History and Anthropology in the Subaltern Study Project". *Reading Subaltern Studies*. Ed. David Ludden. Delhi: Parmanent Black, 2008.
10. Dhawan, R.K. *The Novels of Amitav Ghosh*. New Delhi: Prestige Books, 1999





Exploring Farm Pond Patterns In Ahmednagar: Enhancing Agriculture Through Protective Irrigation Strategies

Dr. Dattatray Sheshrao Ghungarde

Abstract:

This research delves into Ahmednagar district, a drought-prone region in Maharashtra, to investigate the spatial distribution and impact of farm ponds on agricultural development, water resources, and groundwater dynamics. The primary aim is to assess the role of farm ponds in alleviating water scarcity for horticultural crops and their influence on the net irrigated area. Utilizing field surveys, questionnaires, and interviews, the study gathers primary data on farm pond characteristics. Among approximately 9798 farm ponds constructed from 2005 to 2015, a 10% sample is analyzed to comprehend their role in agricultural development. Statistical analysis reveals that farm ponds serve as vital irrigation tools, ensuring a reliable water source and contributing to increased crop production. Spatial distribution analysis categorizes tehsils into various density levels, with Rahata, Nagar, and Karjat showing notably high densities. This categorization sheds light on the diverse contributions of farm ponds to the irrigation landscape. Exploring the proportion of irrigated area by farm ponds relative to Net Irrigated Area (NIA) at different levels, the study unveils an average proportion of 50.53%, with a standard deviation of 19.33%. These findings underscore the substantial impact of farm ponds on agricultural productivity and water security in the region. The abstract highlights farm ponds as crucial solutions to water scarcity challenges, offering valuable insights for policymakers and agricultural extension workers to implement sustainable water resource management strategies in drought-prone areas. Furthermore, the study considers potential drawbacks of lined farm ponds, such as hindering rainwater percolation and impacting groundwater resources, contributing to a comprehensive understanding of the implications of farm pond adoption in agricultural landscapes.

Keywords: farm ponds, irrigation, water resources, Ahmednagar district, droughts etc.

Introduction:

“Ahmednagar district is one of the drought-prone regions in Maharashtra state.” (IPCC, 2007) [3] The extremity of droughts has its long-term effects on the Agricultural sector as it does not allow the capital formation and hence farmers become a vulnerable community. The modern agricultural farming methods such as horticultural crops contribute significantly in the capacity building of farmers especially in drought prone areas. Shroff S. and Kajale J. stated that, “Horticulture in the country and Maharashtra in particular has tremendous potential while infrastructure bottlenecks, absence of post-harvest management and other logistics can act as major constraints.” [6] Therefore, the water harvesting structures like farm ponds can act as a life saviour of horticultural crops in the state of water scarcity in drought prone areas. “Considering the fast decline of irrigation potential and increased demand for water from different sectors, many initiatives have been introduced to conserve the scarce water resources in India. One of the methods introduced to save water consumption in agriculture was drip method of irrigation (DMI).” [4] The drip irrigation method of modern irrigation techniques requires a source of water. The farm-pond is proving to be a secure water source for growth of Horticultural crops.

According to Pooja Prasad and Milind ohani in their research article, “It is unlikely that a desired state of equilibrium can be achieved without regulation because economic incentives continue to drive farmers to invest in farm-ponds even as groundwater levels fall thereby leading to the tragedy of the commons.” [5] “The role of farm pond density in groundwater recharge” by Green, W. C., et al. (2006) in the journal Hydrogeology Journal evaluates the impact of farm pond density on groundwater recharge rates. The study found that watersheds with higher densities of farm ponds had lower

groundwater recharge rates, due to reduced infiltration of rainwater into the ground. [7] Therefore, the presented study entitled “Exploring farm pond patterns in Ahmednagar: Enhancing agriculture through protective irrigation strategies” is undertaken.

Study Area:

Ahmednagar district is selected as the study area in the state of Maharashtra. The district is spread between 18°10' to 20°00' North Latitude and 73°30' to 75°37' East Longitude. [1] (Figure 1). The total geographical area of the district is 17048 sq. km. having 14 tehsils. [2] The district lies in the rain shadow zone of the western ghat. The distribution of the rainfall is very uneven and average annual rainfall received is 583.5 mm. About 75% of the annual rainfall is received during the southwest monsoon season

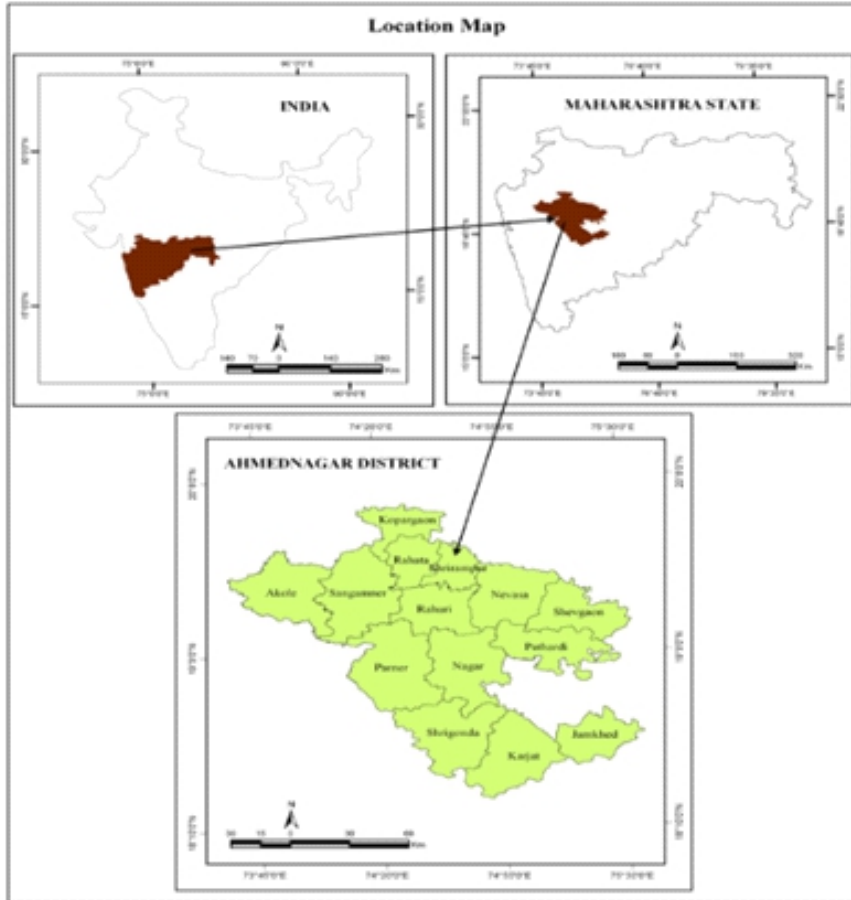


Figure NO. 1: Location Map of Study Area

Objective:

The present study's main objectives are,

1. To investigate the spatial distribution of farm ponds in Ahmednagar district and
2. To assess farm ponds' influence on net irrigated area, enhancing water resources for agriculture in Ahmednagar district.

Database and Methodology:

The present study is based on primary data. The primary data is collected through field-survey using questionnaire and personal interviews. The required data and information about various factors

like number of farm ponds, respective location, shape and sizes, irrigation facilities, land data and other related information etc. is collected. The detailed database and methodology are presented in the flowchart (Figure 2).

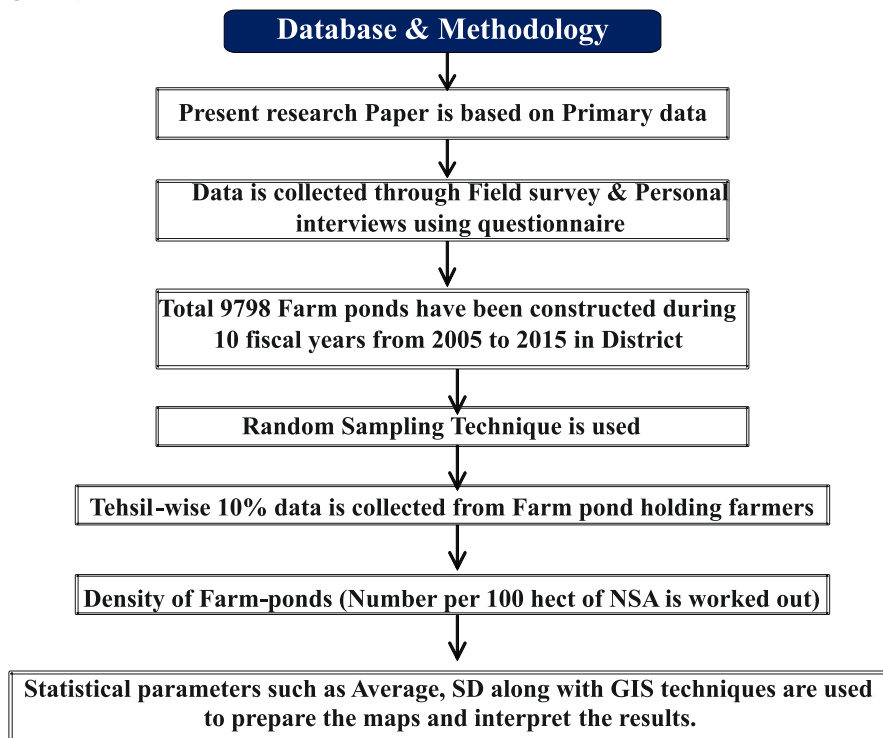


Figure No. 2: Flowchart for database and Methodology

As per available data from the office of agricultural of Ahmednagar district, about 9798 farm-pond have been constructed during ten fiscal years from 2005 to 2015 in the 14 tehsils of the district. The 10% sample of the same has been used to understand agricultural development based on farm-pond.

Results and Discussion:

Farm ponds have become an essential irrigation tool in many regions, providing a reliable source of water during dry spells. By collecting and storing rainwater, farm ponds enable farmers to supplement their irrigation needs, increasing and stabilizing crop production. Research has shown that farm ponds are particularly beneficial in the study region, where water resources are limited. The spatial distribution of farm ponds in Ahmednagar district is shown in the table (Table 1) and the map (Figure 3) in the form of levels of number of constructed farm-ponds per 100 hect of NSA.

Table No. 1: Density of Farm-Ponds (Number per 100 hect of NSA)

Density of Farm Ponds	Scale	Tehsils	% tehsils
Very Low	Below 30	Shrirampur	7
Low	30-35	Akole, Kopargaon, Parner	21
Medium	36-40	Newasa, Shrigonda	14
High	41-45	Sangamner, Shevgaon, Pathardi, Rahuri, Jamkhed	37
Very High	Above 45	Rahata, Nagar, Karjat	21
District		14	100
		Average:41	SD:7

(Source: Compiled by researcher based on primary data)

The average proportion of constructed farm-pond per 100 hecter NSA is 41. Shirrampur, Akole, Kopargaon and Parner tehsils have very low and low (upto 35) level of density of farm-ponds, while Newasa, Shrigonda, Sangamner, Shevgaon, Pathardi, Rahuri, and Jamkhed tehsils have medium to high (36-45) density and Rahata, Nagar and Karjat falls under very high (Above 45) density of farm ponds.

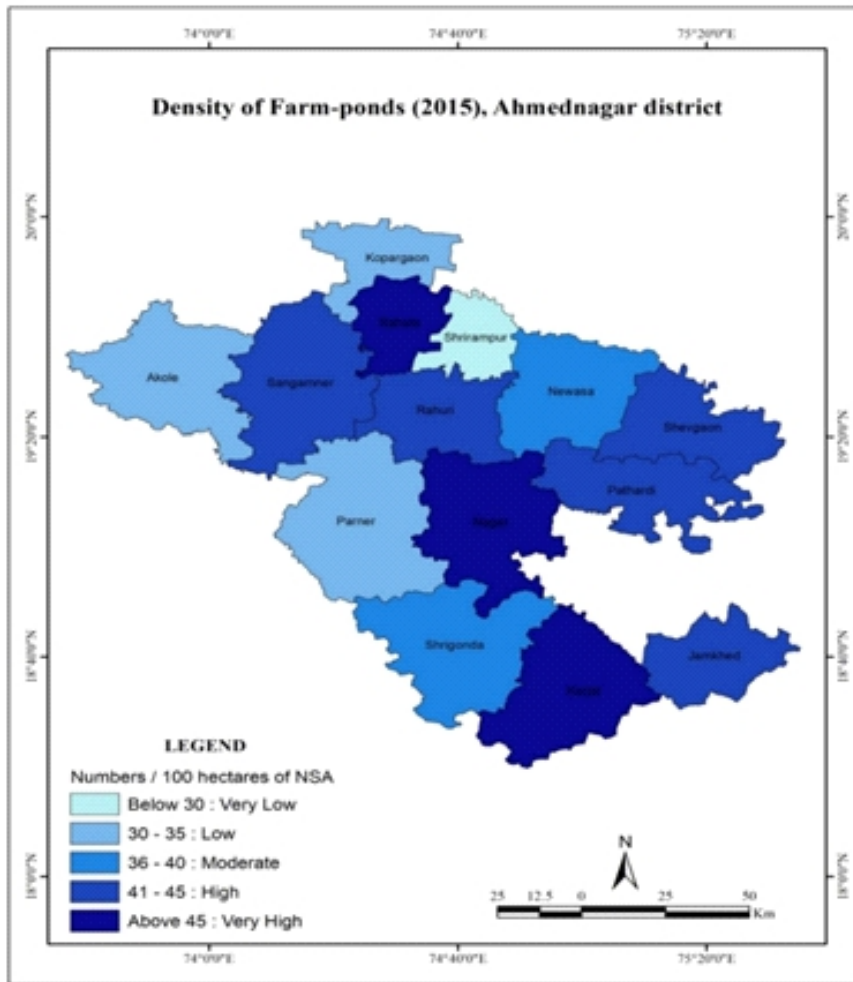


Figure No. 3: Density of Farm-ponds (2015) in Ahmednagar District

In the study region, farm ponds are particularly important in the tehsils of Rahata, Nagar and Karjat, which have a very high density of farm ponds. This suggests that farmers in these tehsils have recognized the benefits of farm ponds and are investing in this technology to improve their crop production.

Half of the tehsils in the study region have a high and very high density of farm ponds. These tehsils have traditionally relied on farming, have fertile land and adequate water resources. However, in some tehsils, such as Newasa, Shevgaon, and Rahuri, there is no guarantee of canal water rotation. Therefore, farmers in these tehsils have built a high number of farm ponds (35 to 45 per 100 hectares) to ensure a reliable supply of water for irrigation.

Farm ponds can play a significant role in improving agricultural productivity and water security in the study region. By promoting the construction and use of farm ponds, policymakers and agricultural extension workers can help farmers to adapt to climate change and produce more food with less water.

Table No. 2: Proportion of Irrigated area by Farm-pond to Net Irrigated Area (NIA)

Level of Irrigated area by Farm-pond	Scale of % to NIA	Irrigated area by Farm-Pond	
		Tehsils	% tehshils
Very Low	below 25.00	Shrirampur	7.14
Low	25.00-40.00	Kopargaon, Rahata, Newasa, Rahuri	28.56
Medium	40.01-55.00	Akole, Sangamner, Shrigonda	21.46
High	55.01-70.00	Shevgaon, Parner	14.28
Very High	above 70.00	Pathardi, Nagar, Karjat, Jamkhed	28.56
District		14	100
		Average:50.53 SD:19.33	

(Source: Compiled by researcher based on primary data)

The table (Table 2) and map (Figure 4) presents a detailed breakdown of the proportion of irrigated area contributed by farm-ponds relative to the Net Irrigated Area (NIA) across different levels. The first column categorizes the levels of irrigated areas by farm-pond, ranging from "Very Low" to "Very High," with corresponding scales of percentage to NIA. The second column identifies the Tehsils (sub-districts) falling within each level, providing a geographical context to the data. For instance, Tehsils like Shirampur fall under the "Very Low" category, with a scale below 25.00%. In contrast, Tehsils such as Pathardi, Nagar, Karjat, and Jamkhed are classified as "Very High," boasting a scale above 70.00%.

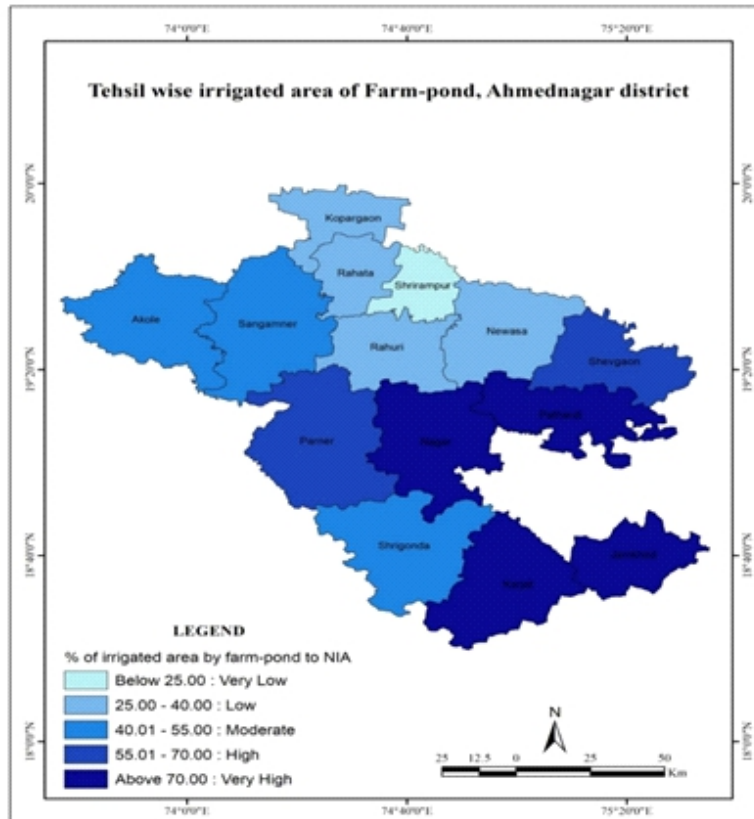


Figure No. 4: Tehsil wise Irrigated area of Farm-pond (2015), Ahmednagar District

The third column showcases the percentage of Tehsils within each level, offering insights into the distribution of farm-pond-based irrigation across the region. Notably, Tehsils in the "Low" category, including Kopargaon, Rahata, Newasa, and Rahuri, collectively contribute 28.56% to the overall irrigated area by farm-ponds. Meanwhile, the "Medium" level Tehsils, such as Akole, Sangamner, and Shrigonda, account for 21.46%. Interestingly, the "Very High" category, represented by Tehsils like Pathardi, Nagar, Karjat, and Jamkhed, also contributes a significant 28.56% to the total irrigated area.

The district-level summary at the bottom of the table consolidates the data, indicating that the overall average proportion of irrigated area by farm-ponds to NIA is 50.53%, with a standard deviation of 19.33%. This district-level overview provides a comprehensive snapshot of the distribution of farm-pond-based irrigation, emphasizing the varying contributions across different Tehsils and levels within the region.

The photo (Figure 4) shows a typical farm pond in the study region. The pond is lined with polyethylene (PE) to prevent water seepage and is fenced with galvanized iron chain link fence to protect it from livestock.

Lined farm ponds, while offering some benefits in terms of water conservation and prevention of soil erosion, can also have certain disadvantages that impact groundwater resources. First, lined ponds prevent rainwater percolation into the ground, which is a crucial process for replenishing groundwater aquifers. By impeding this natural recharge process, lined ponds can contribute to groundwater depletion, especially in areas with limited surface water sources.



Figure No. 4: Farm pond with Poly-ethane (PE) lining and Galvanized Iron chain link fencing
Conclusion:

In conclusion, the research conducted in Ahmednagar district illuminates the pivotal role of farm ponds as a strategic intervention to address water scarcity challenges in drought-prone regions. The study reveals a substantial spatial distribution of farm ponds, particularly evident in tehsils like Rahata, Nagar, and Karjat, underscoring their importance in enhancing agricultural productivity. Statistical results indicate an average density of 41 farm ponds per 100 hectares of Net Sown Area

(NSA). Furthermore, the study delves into the proportion of irrigated area contributed by farm ponds to Net Irrigated Area (NIA), presenting a district-wide average of 50.53%, with a standard deviation of 19.33%. These findings emphasize the positive impact of farm ponds on irrigation practices while acknowledging potential challenges such as groundwater recharge rates and the need for regulated development. Overall, the research underscores the significant potential of farm ponds as a sustainable water management strategy for agricultural development in drought-prone areas like Ahmednagar district.

References:

1. Government of Maharashtra, District Social and Economic Review, Ahmednagar (2005), pp 1-6.
2. Government of Maharashtra, District Social and Economic Review, Ahmednagar (2016), pp 1-6.
3. IPCC, "Special Report on Managing the Risks of Extreme Events and Disasters to Advance Climate Change Adaptation" (2007).
4. Waghmare, M. N., Y. C. Sale and Shendage, P. N., "An Economic Impact of Drip Irrigation in Vegetable Production in Scarcity Region of Western Maharashtra." *Int.J. Curr. Microbiol. App.Sci.*9(07):2259-2265.doi: <https://doi.org/10.20546/ijcmas.2020.907.263>
5. Pooja Prasad, Milind A. Sohoni: A research paper on "Farm-ponds for Horticulture: Boon or Curse? Analysing Impact on Farm Profitability, Resource Sustainability and Social Welfare" Centre for Technology Alternatives for Rural Areas (CTARA), IIT Bombay.
6. Shroff S. and Kajale J.: A research paper on "Government Intervention in Horticulture Development – The Case of Maharashtra" published in *Ind. Jn. of Agri. Econ.* Vol.63, No.3, July-Sept. 2008
7. Green, W. C., et al. (2006): "The role of farm pond density in groundwater recharge" in the journal *Hydrogeology Journal*

Dr. Dattatray Sheshrao Ghungarde

Associate Professor, Department of Geography,
New Arts, Commerce and Science College,
Parner, Dist - Ahmednagar

AKSHARA
MULTIDISCIPLINARY RESEARCH JOURNAL
Peer-Reviewed & Refereed International Research Journal
January 2024 Special Issue 10 Volume II (B)

हिंदी साहित्य की सामाजिक एवं लोकतांत्रिक भूमिका नये संदर्भ



अतिथि संपादक
प्रो.डॉ.पी. एम. डोंगरे
प्राचार्य

लोकनेते डॉ.बालासाहेब विखे पाटील (पद्मभूषण उपाधि से सम्मानित)
प्रवरा ग्रामीण शिक्षण संस्था का कला, वाणिज्य एवं विज्ञान महाविद्यालय, सात्रल
तह.राहुरी, जि. अहमदनगर (महाराष्ट्र)

कार्यकारी संपादक

डॉ. गजानन चव्हाण
प्रधान सचिव

महाराष्ट्र हिंदी परिषद

प्रो.डॉ. जिजावराव पाटील
अध्यक्ष

डॉ. भाऊसाहेब नवले
अध्यक्ष, हिंदी विभाग

कला, वाणिज्य एवं विज्ञान महाविद्यालय, सात्रल

डॉ. अनंत केदारे
सह-आचार्य

Chief Editor :
Dr. Girish S. Koli

55	समकालीन काव्य में चेतना के विविध आशय	डॉ. गिर्जा अनिसा बेग रज्जाक बेग	181
56	धूमिल के काव्य में समाज और लोकतंत्र (संसद से सड़क तक के परिप्रेक्ष्य में)	डॉ. उत्तम ओंकार येवले	184
57	हिन्दी कहानी: सामाजिक एवं लोकतांत्रिक सरोकार	डॉ. झेलम झेंडे	187
58	समकालीन समाज एवं लोकतंत्र के परिप्रेक्ष्य में मीडिया	डॉ. विजयकुमार राऊत	191
59	दुष्यंत कुमार के गजलों में समाज एवं लोकतंत्र	जाधव शितल शंकर	194
60	निर्गुण संत साहित्य में सामाजिक समरसता	धीरेन्द्र कुमार जलवानी	196
61	प्रत्यक्षा सिन्हा के कथा साहित्य में नारी विमर्शोन्मुख सामाजिक एवं लोकतांत्रिक भूमिका	जानकी नामदेव देसाई	199
62	हिंदी आत्मकथाओं में समाज एवं लोकतंत्र की भूमिका	देवहंस राधा लखनलाल प्रो. डॉ. संजीवकुमार नरवाडे	201
63	हिंदी फिल्मों में 'ड्रेग प्रदर्शन' और किन्नर समुदाय की अभिव्यक्ति (विशेष संदर्भ तमन्ना और शबनम मौसी)	अनीता कुमारी	204
64	बदलते सामाजिक परिवेश में 'संचार माध्यम' प्रिंट मीडिया की भूमिका हिंदी के संदर्भ में	डॉ. किरण चौगुले	208
65	समकालीन हिन्दी नाटक में सामाजिक चेतना	डॉ. अंशुमान वल्लभ मिश्र	211
66	समकालीन हिंदी काव्य की सामाजिक भूमिका में सुनीता जैन का योगदान	श्री. सुनीलकुमार विठ्ठल पाटील	215
67	कवि सुदाम पाण्डेय 'धूमिल' के काव्य में लोकतांत्रिक और सामाजिक भूमिका	कवि. प्रा. डॉ. देवीदास क. बामणे 'संघर्ष'	217
68	हिंदी फिल्मी गीतों में विरोध का स्वर (व्यवस्था के संदर्भ में)	डॉ. दादासाहेब नारायण डांगे	222
69	पूर्वोत्तर भारत की लोक नृत्य और समाज व्यवस्था	डॉ. नुरजाहान रहमतुल्लाह	224
70	बादल सरकार का नाटक 'एवम् इंद्रजीत' में सामाजिक चिंतन	डॉ. अविनास अहिरे	227
71	कमलेश्वर की कहानियों में लोकतांत्रिक अवमूल्यन	डॉ. प्रकाश राजाराम मुंज	230
72	हिंदी वेब साहित्य की सामाजिक एवं लोकतांत्रिक भूमिका	डॉ. भाऊसाहेब नवले श्रीमती. यादव माधवी रामचंद्र	233

समकालीन समाज एवं लोकतंत्र के परिप्रेक्ष्य में मीडिया

डॉ. विजयकुमार राजत

अध्यक्ष, पदव्युत्तर हिंदी विभाग एवं अनुसंधान केंद्र,
न्यू आर्ट्स कॉमर्स अँड सायन्स कॉलेज, पारनेर महाराष्ट्र

आज के युग में मीडिया हमारे दैनिक जीवन का एक मुख्य भाग है। शासन में मीडिया की प्रत्यक्ष भूमिका नहीं है लेकिन यह लोगों की राय बनाने में महत्वपूर्ण भूमिका निभाता है। जनता की आवाज बनता है और सार्वजनिक संस्थाओं को सूचना उपलब्ध कराता है। वर्तमान समय में लोक मत के सृजन और दिशा देने में मीडिया महत्वपूर्ण भूमिका निभाता है और इस कारण से समाज के प्रति मीडिया का दायित्व बढ़ गया है। मीडिया के लिए लोकतंत्र एक प्राथमिक आवश्यकता है। और यह भी सच है कि मीडिया के बिना लोकतंत्र वैसे ही है जैसे चक्की बिना गाड़ी। जनता में जागरूकता मीडिया द्वारा लाई जाती है और सामाजिक परिवर्तन के लिए मीडिया महत्वपूर्ण भूमिका निभाती है। लोकतांत्रिक परिदृश्य में मीडिया ही लोकतांत्रिक प्रक्रिया को मजबूती देता है और विकास की प्रक्रिया को रफ्तार प्रदान करता है। लोकतंत्र और सुशासन में मीडिया की तीन प्रमुख भूमिकाएं हैं। प्रथम है, सत्ताधारी पर लगाम रखना, जवाबदेही को बढ़ावा देना, पारदर्शी और सार्वजनिक जांच यह सब मीडिया के महत्वपूर्ण कार्य हैं। मीडिया का दूसरा प्रमुख कार्य है, राजनीतिक बहस के लिए नागरिक मंच उपलब्ध कराना, और तीसरा कार्य है सामाजिक समस्याओं के लिए सरकार की जवाबदेही को बढ़ाना। लोकतंत्र में जनता की सहभागिता आवश्यक है।

मीडिया जनता को सरकार के कार्यक्रमों और कार्यों की जानकारी देकर तथा उन्हें संगठित कर शासन का भाग बनाए रखता है। लोकतंत्र तभी सही रूप में कार्य कर सकता है जब उसमें जनता की सहभागिता अधिकतम होगी। जनता को मुद्दे की जानकारी देना, शासन में वर्तमान में क्या चल रहा है इसकी जानकारी तथा सामाजिक और राजनीतिक मुद्दों को लेकर सजक होना ही उनकी सहभागिता को बढ़ाता है। यह जानकारी जनता तक मीडिया ही पहुंचाता है। इस जानकारी से लोग शासन की प्रशंसा या आलोचना कर सकते हैं और नीतियों का समर्थन या विरोध करते हैं। मीडिया संप्रेषण का भी एक साधन है, जिसके द्वारा जनता आवाज उठाती है। कई बार यह देखा गया है कि जनता द्वारा उठाई गई आवाज के कारण सरकार ने दबाव में आकर अपनी नीति संशोधित या परिवर्तित की है। इस प्रकार से मीडिया सुशासन हेतु आधार बनाता है। उदाहरण के लिए भारत में अन्ना हजारे द्वारा लोकपाल बिल के लिए किए गए आंदोलन को मीडिया ने समर्थन दिया था। इस समाचार और कवरेज ने देश के संपूर्ण जनता को भ्रष्टाचार के खिलाफ एक कर दिया और सरकार पर लोकपाल बिल को संसद में पेश करने हेतु दबाव बना। लगातार यह देखने को मिल रहा है कि विभिन्न मुद्दों पर जनता आंदोलित हो रही है। अतः मीडिया की भूमिका और गंभीर हो गई है। मीडिया प्रत्येक नागरिक को आवाज देता है और साथ ही ऐसे वातावरण तैयार करने में सहयोग देता है। जहां निर्णय प्रक्रिया में आवाज सुनी जा सके। लोकतांत्रिक प्रणाली में जो कमियां हैं वह भी मीडिया उजागर करता है और सरकार को इन कमियों को दूर करने में सहयोग करता है तथा शासन प्रणाली इस कारण से अधिक जवाब दे उत्तरदाई बनता है। स्वस्थ लोकतंत्र को बनाने में मीडिया एक अहम भूमिका निभाता है। मीडिया को जनहित का संरक्षक के रूप में देखा जाता है साथ ही साथ यह न्याय और सरकार कि नीतियों के लाभ को समाज के आंतरिक वर्गों तक पहुंचाने में महत्वपूर्ण भूमिका निभाता है। मीडिया सरकार और जनता के बीच एक शृंखला के रूप में कार्य करता है। लोगोंको मीडिया पर विश्वास है क्योंकि यह दर्शकों पर प्रभाव डालता है।

मीडिया को समाज में उसकी भूमिका को लेकर होने वाली चर्चा में उसे नयी उम्मीद और लोकतंत्र को कायम करने वाला बताया जाता है। इस चौथे खम्भे अर्थात् मीडिया ने पिछली आधी सदी में अजब गजब चोले बदले। और हर चोले के साथ यह बदलता गया। प्रिंट, विजुअल से इलेक्ट्रॉनिक मीडिया तक पहुँचते-पहुँचते जहां इसकी गति में परिवर्तन हुआ वहीं मूल स्वरूप और उद्देश्य कहीं पीछे छूटते गए। संचार-क्रान्ति के बाद मीडिया ने पहला काम यहीं किया है कि हर्दें तोड़ दी हैं और दूसरा काम इसी के बावजूद, वह है हर्दें बनाने का और उसके साथ ही बढ़ाने का। यह तीनों बातें परस्पर विरोधाभासी हैं, मगर आज के दौर में तीनों एक बड़ा सच हैं, जिसे लगभग हर विद्वान् स्वीकारता है। प्रत्येक राज्य चाहे वह उदारवादी हो या समाजवादी या साम्यवादी, यहाँ तक कि सेना के जनरल द्वारा शासित पाकिस्तान का अधिनायकवादी भी अपने को लोकतान्त्रिक कहता है। सच पूछा जाये तो आज के युग में लोकतान्त्रिक होने को दावा करना एक फैशन सा हो गया है।

लोकतन्त्र की पूर्णतः सही और सर्वमान्य परिभाषा देना कठिन है। लोकतन्त्र के सम्बन्ध में अलग-अलग धारणाएँ हैं। 'लोकतन्त्र एक ऐसी राजनीतिक प्रणाली है जो पदाधिकारियों को बदल देने के नियमित सांविधानिक अवसर प्रदान करती है और एक ऐसे रचनातंत्र का प्रावधान करती है जिसके तहत जनसंख्या का एक विशाल हिस्सा राजनीतिक प्रभार प्राप्त करने के इच्छुक प्रतियोगियों में से मनोनुकूल चयन कर महत्त्वपूर्ण निर्णयों को प्रभावित करती है।' मैक्फर्सन ने लोकतन्त्र को परिभाषित करते हुए इसे 'एक मात्र ऐसा रचनातंत्र माना है जिसमें सरकारों को चयनित और प्राधिकृत किया जाता है अथवा किसी अन्य रूप में कानून बनाये और निर्णय लिए जाते हैं।' शूटर के अनुसार, 'लोकतान्त्रिक विधि राजनीतिक निर्णय लेने हेतु ऐसी संस्थागत व्यवस्था है जो जनता की सामान्य इच्छा को क्रियान्वित करने हेतु तत्पर लोगों को चयनित कर सामान्य हित को साधने का कार्य करती है। वास्तव में, लोकतन्त्र मूलतः नागरिक और राजनीतिक स्वतन्त्रता के लिए सहभागी राजनीति से संबद्ध प्रणाली है।

आज का भारतीय मीडिया पुरी तरह से बाजार के चंगुल में फंस गया है। भारतीय मीडिया में फर्जी खबरों कि समस्या मौजूद है, जिसके कारण लोग गलत सूचना प्राप्त करते हैं और बड़े पैमाने पर अफवाह और भ्रम फैलाते हैं। जहाँ लोकतंत्र को बढ़ावा देने में मीडिया की महत्त्वपूर्ण भूमिका है, वहीं नागरिकों की भी यह ज़िम्मेदारी है कि वे आलोचनात्मक तरीके और समझदारी से समाचारों का उपभोग करें। मीडिया साक्षरता कार्यक्रम नागरिकों को यह बेहतर ढंग से समझने में मदद कर सकते हैं कि मीडिया कैसे कार्य करता है, विश्वसनीय एवं अविश्वसनीय स्रोतों के बीच अंतर कैसे करें और सूचना-संपन्न सार्वजनिक संवाद में कैसे शामिल हों। यह महत्त्वपूर्ण है कि मीडिया सच्चाई एवं तथ्यपरकता, पारदर्शिता, स्वतंत्रता, न्यायपरकता एवं निष्पक्षता, उत्तरदायित्व और निष्पक्ष कार्य जैसे मूल सिद्धांतों से संबद्ध रहे। अभिव्यक्ति की स्वतंत्रता को लोकतंत्र की बुनियाद माना जाता है किन्तु लोकतंत्र का मतलब सिर्फ संख्याओं तक सीमित नहीं होता है। लोकतंत्र संस्थाओं के बूते पर चलता है। लोकतांत्रिक मिजाज़ केवल भावनाओं को नहीं विवेक को भी महत्त्व देता है। केवल अपने को नहीं दूसरे के दुःख-सुख के बारे में भी सोचता है। इस लिहाज़ से सोचें तो किसी हद तक सोशल मीडिया ने अभिव्यक्ति की स्वतंत्रता का स्पेस रचा ज़रूर है लेकिन इस स्पेस के भीतर जो हाल है उस पर फिलहाल तो यही पुगनी कहावत लागू होती है- अंधाधुंध के राज में गधा पंजीरी खाए।

मीडिया वह इंजन है जो सत्य, न्याय और समानता की तलाश के साथ लोकतंत्र को आगे बढ़ाता है। आज के डिजिटल युग में, तेज़ी से बदलते मीडिया परिदृश्य से उत्पन्न चुनौतियों से सफलतापूर्वक निपटने के लिये पत्रकारों को अपनी रिपोर्टिंग में सटीकता, निष्पक्षता और उत्तरदायित्व के मानकों को बनाए रखने की आवश्यकता है। मीडिया का काम शिक्षा प्रदान करना भी है और वह यह काम चर्चा के द्वारा राजनीतिक शिक्षा का शिक्षा पर टिप्पणी देकर लोकतांत्रिक संस्कृति को बढ़ावा देता है राजनीतिक वैज्ञानिक कार्य दिवस ने संप्रेषण प्रणाली को राजनीति के तांत्रिक बताया है और किसी भी तांत्रिक में गड़बड़ी होने से राजनीति के कार्य पर प्रभाव पड़ता है और शासन का अक्षय होता है अनभिज्ञ या अज्ञानी जनता को बड़े पैमाने पर शिक्षित करना कठिन है यह कार्य केवल मीडिया द्वारा सफलतापूर्वक किया जा सकता है मीडिया के प्रसार से लोगों के बीच मुद्दों को लेकर चर्चा प्रारंभ होती है तथा उन्हें सही निर्णय लेने में सहायक होता है जागरूक और अवगत नागरिक निर्णय की प्रक्रिया में अधिक सक्रिय रूप से भाग लेते हैं

आज की मीडिया के सामने कुछ चुनौतियां भी दिखाई देती हैं जिसका जिक्र करना बहुत आवश्यक होगा। राजनीतिक दल मीडिया और कॉर्पोरेट संस्थाओं के बीच गठ जोड़ होने से सुशासन में बाधा आ रही है। कई बार यह होता है कि मीडिया सच्चाई को न दिखाते हुए कुछ लोगों के हितों में ध्यान रखते हुए सूचना प्रसारित करता है। जन भागीदारीता को प्रोत्साहन नहीं दिया जाता है। शासन की जवाबदेही को कम करके आंका जाता है और भ्रष्टाचार को बढ़ावा दिया जाता है। इसलिए यह बहुत आवश्यक है कि मीडिया स्वतंत्र और गैर पक्षपाती हो ताकि लोकतंत्र अभिजात वर्गीय में न परिवर्तित हो जाए। भारतीय राजनीति की बदलती गतिशीलता ने मीडिया से लोगों की उम्मीदें बढ़ाई हैं क्योंकि परिवर्तन का यह चरण व्यक्तिगत धारणा के साथ विश्वास करना बहुत आसान हो गया है।

सारांशतः इस समय मीडिया कि आज़ादी जितनी आवश्यक है उतना ही यह भी आवश्यक है कि मीडिया के अधिकारों पर भी नियंत्रण रहे मीडिया द्वारा अपने अधिकारों का गलत प्रयोग भी देखने को मिलता है। उसे अपने सीमाओं का उल्लंघन नहीं करना चाहिए और सरकार की अन्य तीन शाखों के कार्य में हस्तक्षेप नहीं करना चाहिए। तभी मीडिया सुशासन का जरिया बन सकता है। मीडिया आपको उन मुद्दों को लेकर समय संवेदनशील होना चाहिए जो विकास के कारक हैं। जागरूक नागरिक बनने में तकनीक और मीडिया महत्त्वपूर्ण भूमिका निभाते हैं। मीडिया को पेशावर बनाना, स्वतंत्रता नैतिकता को महत्त्व देना, जवाबदेही को बढ़ाना, शासन और मालिकों के हस्तक्षेप को समाप्त करना, मीडिया की पहुंच का लोकतांत्रिक कारण, मीडिया की स्वतंत्रता को सुनिश्चित करना और शुभ शासन हेतु इसे बनाए रखने आदि कम मीडिया के लिए आने वाले समय में करने होंगे। चीन में जिस तरह मीडिया पर निर्वंध है और उसे नियंत्रित करणे के लिए एक विशिष्ट व्यवस्था दिखाई देती है उस व्यवस्था का हमारे यहां अभाव है। चीन में जो

निर्बंध है वह स्वस्थ समाज के लिए अच्छी बात नहीं लेकिन निर्बंध मुक्त मीडिया भी समाज के हित में सौ प्रतिशत काम करेगा ऐसा हम कह नहीं सकते।

संदर्भ ग्रंथ-

- (1) डॉ. पुरुषोत्तम अग्रवाल, अंधाधुंध के राज में, साहित्य वार्षिकी इंडिया टुडे, 2017 सं. अंशुमान तिवारी.
- (2) गुलाब कोठारी, समाचार पत्र प्रबंधन, राजकमल प्रकाशन, नई दिल्ली.
- (3) अखिलेश मिश्रा, पत्रकारिता: मिशन से मीडिया तक, राजकमल प्रकाशन, नई दिल्ली.
- (4) मीडिया और लोकतंत्र, प्रकाश चौबे, निरामय प्रकाशन, कानपुर.
- (5) मीडिया और उसका भविष्य, नीलिमा जैन, प्रतिभा प्रकाशन, नई दिल्ली.



महाराष्ट्र राज्य हिंदी साहित्य अकादमी, मुंबई

संयोजक डॉ. बाळासाहेब विठ्ठल पाटील (सदरमुकाम) अतिथि डॉ. सत्यनारायण (विज्ञान) अतिथि डॉ. बाळासाहेब विठ्ठल पाटील

कला, वाणिज्य एवं विज्ञान महाविद्यालय, सात्रळ तथा महाराष्ट्र हिंदी परिषद

के समुक्त उल्लासघान में आयोजित परिषद का 30 वीं अधिवेशन पर राष्ट्रीय सम्मेली



प्रमाणपत्र



प्रमाणित किया जाता है कि डॉ. / श्री. / श्रीमती / सुदी विजयकुमार शंकर
न्यू ठार्टन, कोमन इंग्लिश सायन्स कॉलेज परनेर ने दिनांक 12 तथा 13
 जनवरी 2024 को महाराष्ट्र राज्य हिंदी साहित्य अकादमी, मुंबई हिंदी विभाग, कला, वाणिज्य एवं विज्ञान महाविद्यालय, सात्रळ तथा महाराष्ट्र हिंदी
 परिषद के समुक्त उल्लासघान में हिंदी साहित्य की सांस्कृतिक एवं औद्योगिक भूमिका एवं समर्थ विषय पर आयोजित राष्ट्रीय सम्मेली में विशेष
 अतिथि / सहायक / विषय-प्रवर्तक / अधिवर्तक प्रस्तोता / प्रतिभागी के रूप में सक्रिय सहभागिता के दायित्व का निर्वहण किया।

डॉ. बाळासाहेब विठ्ठल पाटील

संयोजक

महाराष्ट्र राज्य हिंदी साहित्य अकादमी, मुंबई

डॉ. बाळासाहेब विठ्ठल पाटील

उपसंयोजक

ए. सी. एम. कॉलेज, सात्रळ

डॉ. डॉ. विजयकुमार पाटील

सचिव

महाराष्ट्र हिंदी परिषद

डॉ. बाळासाहेब विठ्ठल पाटील

उपसचिव

महाराष्ट्र हिंदी परिषद

डॉ. बाळासाहेब विठ्ठल पाटील

संयोजक एवं उपसचिव

हिंदी विभाग



हिंदी साहित्य की सामाजिक एवं लोकतांत्रिक भूमिका नये संदर्भ



अतिथि संपादक
प्रो.डॉ.पी. एम. डोंगरे
प्राचार्य

लोकनेते डॉ.बालासाहेब विखे पाटील (पद्मभूषण उपाधि से सम्मानित)
प्रवरा ग्रामीण शिक्षण संस्था का कला, वाणिज्य एवं विज्ञान महाविद्यालय, सात्रल
तह.राहुरी, जि. अहमदनगर (महाराष्ट्र)

कार्यकारी संपादक

डॉ. गजानन चव्हाण
प्रधान सचिव

महाराष्ट्र हिंदी परिषद

प्रो.डॉ. जिजाबराव पाटील
अध्यक्ष

डॉ. भाऊसाहेब नवले
अध्यक्ष, हिंदी विभाग

कला, वाणिज्य एवं विज्ञान महाविद्यालय, सात्रल

डॉ. अनंत केदारे
सह-आचार्य

Chief Editor :
Dr. Girish S. Koli

32	इक्कीसवीं सदी के प्रथम दशक की आंबेडकरवादी कविताओं में लोकतांत्रिक मूल्यों का नव स्वर	डॉ. रगडे परसराम रामजी	123
33	कबीर की सामाजिक एवं लोकतांत्रिक भूमिका पर बुद्ध का प्रभाव	डॉ. संतोष रघुनाथराव रायबोले	126
34	हिन्दी साहित्य में स्त्री - विमर्श	डॉ. नवनाथ रघुनाथ जगताप	129
35	सामाजिक एवं लोकतांत्रिक सरोकार और समकालीन हिन्दी कहानी	प्रा.दिपाली दत्तात्रय तांबे	132
36	समकालीन हिन्दी कविता में व्यंग्य	प्रा.संतोष नागरे	135
37	हिन्दी साहित्य का सामाजिक एवं लोकतांत्रिक सरोकार	डॉ. तौंडाकुर एल.पी.	139
38	हिन्दी कथा साहित्य में सामाजिक एवं लोकतांत्रिक भूमिका	प्रा.डॉ.जी.बी.उपमवार	142
39	जयशंकर प्रसाद के 'स्कंदगुप्त' नाटक में सामाजिक एवं लोकतांत्रिक भूमिका	डॉ. मधुकर लक्ष्मण डोंगरे	145
40	समकालीन हिन्दी कविता की सामाजिक एवं लोकतांत्रिक भूमिका	डॉ.पठान खातून बेगम अकबर खान	148
41	स्वतंत्र भारत के बदलते परिप्रेक्ष्य में सामाजिक एवं लोकतांत्रिक भूमिका	डॉ. आशा दत्तात्रय कांबळे	152
42	हिन्दी काव्य की सामाजिक एवं लोकतांत्रिक भूमिका: नये संदर्भ	प्रा. पूर्णिमा उमेश झेंडे	155
43	जनजातीय समाज में विनिमय प्रथा	करुणा पाटगिरी	157
44	आजादी के बाद के हिन्दी साहित्य की स्थिति	संजय वसंत निंबाळकर	159
45	हिन्दी फिल्में और देशभक्ति	प्रा. सिद्धाराम पाटील	161
46	डॉ. सुशीला टाकभरि के 'संघर्ष' कहानीसंग्रह में अभिव्यक्त लोकतांत्रिक मूल्य	डॉ.माधव राजप्पा मुंडकर	164
47	हिन्दी आत्मकथाओं में समाज एवं लोकतंत्र की भूमिका (आत्मकथा, मेरा जीवन और संतम के संदर्भ में)	प्रा.डॉ.दत्तात्रय सिताराम खिलारी	167
48	हिन्दी साहित्य में वैश्वीकरण के दौर में मूल्य विघटन	डॉ. सविता व्ही. रुक्के	170
49	समकालीन हिन्दी साहित्य में समाज एवं लोक-जीवन	प्रा. डॉ. हनुमंत येदु गायकवाड	173
50	समकालीन कविता में अभिव्यक्त लोकतंत्र की विसंगतियाँ	विक्रम बाळकृष्ण वारंग	175
51	जेनेद्र कुमार की कहानी 'पढाई' में शैक्षिक-सामाजिक यथार्थ	प्रा. डॉ. दिग्विजय टेंगसे	178
52	साठोत्तरी हिन्दी व्यंग्य नाटककारों के नाटकों में व्यक्त राजनैतिक एवं समाज व्यवस्था	राहुल गोपाल गुरुखुदे प्रोफेसर डॉ. बाबासाहेब कोकाटे	180
53	हिन्दी कथा साहित्य की सामाजिक एवम लोकतांत्रिक भूमिका	प्रा.पल्लवी भूपेंद्र पाटील	183
54	ममता कालिया की कथा साहित्य में सामाजिक संघर्ष	शुभांगी श्रीधर भागवत	185
55	कुँवर नारायण की कविताओं में लोकतंत्र	प्रतिक्षा शिवाजी तनपुरे	188
56	डॉ. सादिका नवाब 'सहर' के उपन्यास "जिस दिन से" में स्थित भाषा शैली	येवले सविता महादेव	191
57	जयप्रकाश कर्दम की कहानियों में सामाजिक बोध	प्रा. संदीप दामू तपासे	194
58	हिन्दी काव्य की सामाजिक एवं लोकतांत्रिक भूमिका : उमाकांत खुबालकर के साहित्य के परिप्रेक्ष्य में	सुनिता देविदास अकोलकर	200
59	हिन्दी कथा-साहित्य के सामाजिक संदर्भ के रूपमें 'वृद्ध-विमर्श'	अविनाश मारुती कोल्हे प्रो.डॉ.अनिल काले	203
60	हिन्दी बाल साहित्य का सामाजिक एवं लोकतांत्रिक पक्ष	लोभान वर्मा	206
61	लोकतंत्र को आईना दिखाती 'धूमिल' की कविता	डॉ. रमेश बाळासो खबाले	209
62	प्रभाकर श्रांत्रिय के नाटक 'फिर से जहाँपनाह' में लोकतंत्र एवं समाज	प्रा. डॉ. हंबीरराव चौगले	215
63	हिन्दी काव्य की सामाजिक एवं लोकतांत्रिक भूमिका : नये संदर्भ	प्रो.(डॉ) संजीवकुमार नरवाडे	218
64	दामोदर खडसे के कथासाहित्य में निहित सामाजिक मूल्य	प्रो. बालकवि सुरंजे वृषाली पराडकर	222
65	हिन्दी बालसाहित्य का सामाजिक और लोकतांत्रिक पक्ष	प्रकाश बलभीम गांगर्डे डॉ. विशाला शर्मा	225

समकालीन हिंदी साहित्य में समाज एवं लोक-जीवन

प्रा. डॉ. हनुमंत येदु गायकवाड

न्यू आर्ट्स, कॉमर्स एंड सायंस कॉलेज, पारनेर, जिला-अहमदनगर

समकालीन कहानीकारों ने सामाजिक एवं लोकतांत्रिक सरोकारों के सवाल को बखूबी पड़ा है और उसे अपनी कहानियों का रूप बनाया है। इन कहानियों को मानवीय दिशा और सकारात्मक चिंतन की पृष्ठभूमि बन सकता है। समकालीन गद्य की विभिन्न विधाओं में कहानी एक अत्यंत सशक्त एवं समाज के लोकप्रिय विधाओं में से एक है। बदले हुए परिवेश एवं समाज के साथ यह निरंतर अपने को नए रूप में ढलती रही है। स्वतंत्र उत्तर दशकों में सामाजिक आर्थिक राजनीतिक परिवर्तनों के मध्य नजर कहानी विधा अत्यंत सशक्त रही है। इन कहानियों में आने का अनेक आंदोलन दृष्टिगत हुए। इसमें नई कहानी सहज कहानी समानांतर कहानी सचेतन कहानी जनवादी कहानी आदि। समकालीन कहानीकारों ने अपने कहानियों में बदलते हुए जीवन मूल्यों को विभिन्न कोनों से देखा परखा और अपनी अनुभूति के धरातल पर उसे नए विचारों को अभिव्यक्त करने का प्रयास किया समकालीन कहानी जीवन के यथार्थ से सीधे टकराती है। वह जीवन के भोगे हुए सत्य को ईमानदारी और प्रखरता के साथ अभिव्यक्त करती हुई आगे बढ़ती है। समकालीन कहानी में जो कुछ है वह मनुष्य ही है मनुष्य के इतर और कोई भेद नहीं।

समकालीन हिंदी कहानी अपने को समकालीन होने का अर्थ बोध कराती है। इस संदर्भ में डॉ. मधुरेश लिखते हैं कि " समकालीन होने का अर्थ सिर्फ समय के बीच होने से नहीं है। समकालीन होने का अर्थ है। समय के वैचारिक और रचनात्मक दबावों को झेलते हुए, उनसे उत्पन्न तनावों और टकराहटों के बीच अपनी सर्जनशीलता द्वारा अपने होने को प्रमाणित करना " १ हिंदी साहित्य या रचना या रचनाकार अपने केवल प्रासंगिक, यथार्थ और सत्य कहता है। जब वह अपने सामाजिक परिवेश ' जीवन - पद्धति एवं समस्याओं के प्रति पाठक की संवेदनाओं को जागृत करने की मानिषा रखता है। इससे व्यक्ति परिवार और समाज इन तीनों इकाइयों के मध्य होने वाली आपसी अन्तः क्रियाओं से सामाजिक सरोकारों की सृष्टि होती है। इस संबंध में विश्वनाथ तिवारी का वक्तव्य है कि " लेखक का रचना दायित्व दोनों एक - दूसरे में घुले - मिले होते हैं। वह अपनी रचना के प्रति जितना प्रतिबद्ध होता है उतना ही अपने चारों ओर की जिंदगी के प्रति भी। अंदर एवं बाहर के दोनों ही संसार उसके भीतर एक हो जाते हैं " २ हमारे समाज की विडंबना पूर्ण त्रासदी है कि एक वर्ग के पास अधिक धन संपदा है, दूसरे वर्ग के पास दो जून की रोटी मय्यसर नहीं हो पाती। वे दिन - हीन, शोषित, दलित, आंसू व पीड़ा से बेकल जीवन की बुनियादी जरूरतों से वंचित है। औद्योगिकीकरण के कारण समाज में आने का अनेक समस्याएं यथा घनी और गंदी बस्तियों का निर्माण, वर्ग संघर्ष में अभिवृद्धि, बेकरी औद्योगिक झगडे, अपराध और अनैतिकता में वृद्धि, श्रमिक समस्याएं इत्यादि का प्रसार हुआ है। सहज स्वाभाविक जीवन - शैली से दूर सर्वत्र कृत्रिम जीवन का खोखलापन हावी है। डॉ. धीरजभाई वणकर लिखते हैं - " मूल्य समाज के आधार बिंदु है। जिसके द्वारा किसी समाज या देश की संस्कृति व सभ्यता निर्मित होती रहती है। आज भिन्न परिस्थितियों ने जीवन मूल्यों को विशेष रूप में परिवर्तित किया है मुख्यतः शिक्षा, आबादी, वैज्ञानिक प्रगति, भौतिकवादी अवधारणा, नगरीकरण, औद्योगिकीकरण, राजनीति, व्यक्तिवाद तथा व्यक्तिक चेतना व पाश्चात सभ्यता ने प्रभावित किया जिसके कारण भारतीय जीवन मूल्यों के संक्रमण की जो स्थिति आई वह पिछले दशकों में नहीं थी। इन प्रवृत्तियों के कारण हमारे अचार - विचार, आदर्श व व्यवहार में अंतर आने लगा " 3

समकालीन कहानियों में समाज जीवन महत्वपूर्ण रहा है। समकालीन कहानी सत्य की खोज करती है। इन कहानियों में अर्थ प्रधान सामाजिक व्यवस्था के कारण वैयक्तिक स्वार्थों में निरंतर अभिवृद्धि हुई है। डॉ. पुष्पपाल सिंह लिखते हैं - " आज सामाजिक जीवन का एक महत्वपूर्ण अंग यह है कि आज हमारी सामाजिक संबंधों और पारिवारिक रिश्तों पर अर्थतंत्र हावी हो गया है। आत्मीय रिश्तों की पहचान और परख तथा उन संबंधों के निर्वाह में अर्थ प्रधान दृष्टि प्रमुख हो जाने से आज संबंध निभाएं नहीं जाते हैं। " 4 समकालीन हिंदी कथा साहित्य में स्त्री समस्या को ऐतिहासिक एवं सामाजिक परिप्रेक्ष्य में उठाया है। चित्रा मुगदल, उषा प्रियवंदा, मन्नु भण्डारी, अनामिका, मैत्रेयी पुष्पा, ममता कालिया इत्यादि अनेक कथाकारों ने समाज - रचना के वर्ग तथा वर्ग की विसंगतियों स्त्री के संत्रास, उसके अमानवीय शोषण का मार्मिक चित्रण कर, समतावादी सोच को आगे बढ़ाया है। ममता कालिया की कहानी ' जाँच अभी जारी है ' में अपर्णा बैंक से मिले स्पष्टीकरण को बहाल कराते - कराते, दुनिया की नजरों में गुनहगार हो जाती है। सच्ची एवं ईमानदार कार्मिक होने के बावजूद समाज की नजर में भ्रष्ट बन जाती है। प्रत्येक व्यक्ति की नजर उसके प्रति टेढ़ी हो जाती

है। ममता कालिया 'जाँच अभी जारी है' इस कहानी में लिखती है कि - " अब उसे उसका कुछ कुछ अंदाजा था कि इसका नतीजा क्या होगा? उसके निर्दोष साबित होने के पूरे आसार थे , पर इस सम्भावना के बावजूद अपर्णा के चेहरे की मनहूसियत घट नहीं बढ़ रही थी। उसे लग रहा था कि असली सजा तो वह पा चुकी है। दुनिया की नजरों में गुनहगार की हैसियत से जी लेना उसके लिए एक भयंकर अनुभव रहा था , जिसे जांच अधिकारी के दिलासे भी कम नहीं कर सके थे।"⁵

समकालीन कहानीकारों ने आज के सवालियों को गंभीरता के साथ पकड़ा और विचार किया है। आम आदमी के सवालियों और नयी सामाजिक आर्थिक व्यवस्था में बदलते मध्यवर्गीय समाज की चिंताओं को अभिव्यक्त किया है। नौकरी पेशा महिलाओं की हर महीने मिलने वाली आया का मोह उनके पति एवं परिवारजन नहीं छोड़ पाते। चित्रा मुग्दल की कहानी 'स्टेपनी' में यह यथार्थ चित्रित हुआ है- नौकरी कर रही आभा जब गर्भावस्था के दौरान नौकरी छोड़ने की सोच रहीं होती है तभी उसका पति विनोद ऐसा करने से मना करता है। गर्भावस्था के आखिरी महीनों में उसने सोचा था। " बच्चा पालना और नौकरी करना साथ- साथ संभव नहीं। नौकरी छोड़ देगी। बच्चा जब स्कूल जाने लगेगा , तब पुनः विचार करेगी नौकरी के विषय में। लेकिन निश्चय दृढ़ होने से पूर्व ही आर्थिक दबाव और आत्मनिर्भरता की कचोट के चलते विवश हो उठा। तभी पति विनोद ने कहा " नौकरी आसानी से नहीं मिलती , संभल जाएगा सब। दीदी आ रही है। जचगी के लिए , आगे - पीछे नौकरानी भी ढंग की मिल जायेगी। पूरे समय के लिए न सही। अभी तो तुम्हारे हाथ में दो - दो आय आ रही हैं , खुलकर खर्च कर पाती हो , फिर पैसे - पैसे के लिए सोचना होगा।"⁶

सारांश :-

हिन्दी गद्य की विभिन्न विधाओं में कहानी एक अत्यंत सशक्त एवं लोकप्रिय विधाओं में एक है बदले हुए परिवेश एवं समाज के साथ यह निरन्तर अपने को नये रूप में ढालती रही है। स्वतंत्रयोत्तर दशकों में सामाजिक आर्थिक , राजनीतिक परिवर्तनों के मध्यनजर कहानी विधा में अनेकानेक आन्दोलन दृष्टिगत हुए यथा - नयी कहानी, सहज कहानी , समान्तर कहानी, सचेतन कहानी , जनवादी कहानी आदि - आदि। समकालीन कहानीकारों ने वर्तमान जटिल यथार्थ , पल - पल परिवर्तित होते परिवेश , बदलते हुए जीवन मूल्यों को विभिन्न कोणों से देखा, परखा और अपनी अनुभूति के धरातल पर उस नये स्वर को अभिव्यक्त करने का प्रयास किया। समकालीन कहानी जीवन के यथार्थ से सीधे टकराती है। वह जीवन के भोगे हुए सत्यों को ईमानदारी व प्रखरता के साथ अभिव्यक्त करती हुई आगे बढ़ती है। समकालीन कहानी में जो कुछ है , वह मनुष्य ही है , मनुष्य के इतर और कोई भेद नहीं।

संदर्भ :-

- १) गंगा प्रसाद विमल , समकालीन कहानी दशा और दृष्टी, पृष्ठ - १६६
- २) विश्वनाथ तिवारी , रचना के सरोकार , पृष्ठ - ३२
- ३) डॉ. धीरज भाई वणकार , कमलेश्वर की कहानीयों में यथार्थ, पृष्ठ - १७८
- ४) डॉ. पुष्पाल सिंह , समकालीन कहानी , युगबोध का संदर्भ, पृष्ठ - १२४
- ५) ममता कालिया , जाँच अभी जारी है, पृष्ठ - ४०
- ६) चित्रा मुग्दल , आदि अनादि (भाग - तीन) पृष्ठ - ६०

हिंदी साहित्य की सामाजिक एवं लोकतांत्रिक भूमिका नये संदर्भ



अतिथि संपादक
प्रो.डॉ.पी. एम. डोंगरे
प्राचार्य

लोकनेते डॉ.बालासाहेब विखे पाटील (पद्मभूषण उपाधि से सम्मानित)
प्रवरा ग्रामीण शिक्षण संस्था का कला, वाणिज्य एवं विज्ञान महाविद्यालय, सात्रल
तह.राहरी, जि. अहमदनगर (महाराष्ट्र)

कार्यकारी संपादक

डॉ. गजानन चव्हाण
प्रधान सचिव
महाराष्ट्र हिंदी परिषद

प्रो.डॉ. जिजाबराय पाटील
अध्यक्ष

डॉ. भाऊसाहेब नयले
अध्यक्ष, हिंदी विभाग

डॉ. अनंत केदारे
सह-आचार्य

कला, वाणिज्य एवं विज्ञान महाविद्यालय, सात्रल

Chief Editor :
Dr. Girish S. Koli

29	मनु शर्मा के कथाओं में सामाजिक भूमिका के नए आयाम	डॉ. क्रान्ति नासुदेव सोनवणे	106
30	अमरकांत के कथासाहित्य में सामाजिक यथार्थ	डॉ. नारायण बागुल	109
31	सुदामा पांडे का प्रजातन्त्र के परिप्रेक्ष्य में लोकतंत्र	प्रा महेश नाना भोपले	111
32	ज्ञानप्रकाश विवेक की गज़लों में सामाजिक भूमिका के नए आयाम	डॉ. अनिल बाबुलाल सूर्यवंशी	115
33	हिंदी कथा में वैश्वीकरण और लोकतांत्रिक मूल्य अभिव्यक्ति	स.प्रा.प्रकाश लहाने	118
34	'शकुंतला की अंगूठी' नाटक का मनोवैज्ञानिक पक्ष	प्रा. दशरथ काशिनाथ खेमनर	122
35	इक्कीसवीं सदी के हिन्दी उपन्यासों की सामाजिक तथा लोकतांत्रिक भूमिका	सुश्री. टेकाळे रागिनी पुरुषोत्तम डॉ. भाऊसाहेब नवले	125
36	नासिरा शर्मा के 'कागज की नाव' उपन्यास में व्यक्त नारी विमर्श	योजना रामकिशन नाकाडे डॉ. रमेश शिंदे	128
37	ज्ञानप्रकाश विवेक के उपन्यासों में सामाजिक भूमिका के नये संदर्भ	प्रा. वैशाली प्रमोद अहिरे	130
38	हिंदी मीडिया में समाज और लोकतंत्र	शुभदा शिवाजी आर्डे	133
39	हिंदी काव्य की सामाजिक एवं लोकतांत्रिक भूमिका : नये संदर्भ	समृद्धि संजय सुर्वे / डॉ. अनिल काळे	135
40	हिंदी कथा साहित्य में दलित चेतना	सुमेध जालिंदर इंगले	137
41	हिंदी काव्य की सामाजिक एवं लोकतांत्रिक भूमिका - नये संदर्भ	श्रीमती प्राजक्ता नानासाहेब देशमुख डॉ. ललिता राठोड	140
42	'दोहरा अभिशाप' दलित आत्मकथा में समाज और लोकतंत्र	प्रा.डॉ. गडाख दिपाश्री कैलास	143
43	यतीन्द्र मिश्र के साक्षात्कारों में लोकतांत्रिकता	सारिका मूंदड़ा / डॉ. मधुकर राठोड़	148
44	अस्तित्व - स्त्री अस्मिता की नई पहचान	वैशाली दत्तात्रय शिंदे / डॉ.सचिन कदम	151
45	लोकतांत्रिक जीवन की असफल दास्तां 'जमीन अपनी तो थी'	डॉ.स्वाति सुधाकर ठुबे	154
46	अखिलेश के कथा साहित्य में सामाजिक एवं लोकतांत्रिक भूमिका	शर्मा संतोष कुमार कमला प्रसाद प्रोफेसर बालकवि सुरंजे	156
47	दुष्यंत कुमार के गज़ल साहित्य में लोकतंत्र की भूमिका (साथ में धूप -विशेष संदर्भ में)	डॉ. प्रवीण तुलशीराम तुपे	158
48	दुष्यंत कुमार की गज़लों में सामाजिक भूमिका	प्रा. सुषमा बाळाराम खोत	161
49	हिंदी साहित्य की सामाजिक भूमिका में इन्बे मरियम	प्रा.डॉ.पिरू आर. गवळी	164
50	चंद्रसेन विराट की गज़लों में अभिव्यक्त सामाजिक भूमिका	डॉ. जगदीश बन्सीलाल चव्हाण	166
51	गांधीवाद और हिंदी काव्य में सामाजिक चेतना	डॉ. कृष्णा प्रल्हाद पाटील	169
52	डॉ श्रीराम परिहार के ललित निबंधों में अभिव्यक्त सामाजिक एवं लोकतांत्रिक भूमिका	प्रा. डॉ. जितेंद्र पीतांबर पाटिल	172
53	हिंदी कविता में सामाजिक, साहित्यिक तथा लोकतंत्र की भूमिका	डॉ. युवराज राजाराम मुळये	174
54	हिंदी कथा-साहित्य की सामाजिक एवं लोकतांत्रिक भूमिका पंकज सुबीर के उपन्यास 'अकाल में उत्सव' में किसान विमर्श	सविता एकनाथ मुंडे	177

हिंदी मीडिया में समाज और लोकतंत्र

शुभदा शिवाजी आर्डे
शोधार्थी, हिंदी विभाग
न्यू आर्ट्स, कॉमर्स एंड सायन्स कॉलेज पारनेर

एक वस्तु को एक व्यक्ति से दूसरे व्यक्ति तक या एक स्थान से दूसरे स्थान तक ले जाने के लिए एक माध्यम की आवश्यकता होती है। समाचार और विचारों को फैलाने के लिए इस्तेमाल किए जाने वाले माध्यम को मीडिया कहा जाता है। भारत में समाचार प्रकाशन का इतिहास मुद्रण के आविष्कार से होता है। अंग्रेजी शासन के होने के कारण पत्रिका और पत्रिकाओं का उद्देश्य उस समय की स्वतंत्रता को जगाना था। यही कारण है उस समय सैकड़ों पत्रकारों ने काम किया, जिससे जीवन और जेल का जोखिम उठा। भारत के संचार माध्यम के अंतर्गत टेलीविजन, सिनेमा समाचार, पत्रिकाएँ तथा आंतजातीय पृष्ठ आदि हैं। अधिकांश मीडिया निजी हाथों में है और बड़ी-बड़ी कंपनियों द्वारा नियंत्रित है। भारत में ७०००० से अधिक समाचार पत्र और ६९० उपग्रह चैनल हैं। आज भारत विश्व का सबसे बड़ा समाचार पत्र का बाजार है।

भारत में मीडिया का विकास तीन चरणों में हुआ। पहले दौर की नींव उन्नीसवीं सदी में उस समय पड़ी जब औपनिवेशिक हुकूमत के खिलाफ असंतोष की अंतर्विरोधी छाया में हमारे सार्वजनिक जीवन की रूपरेखा बन रही थी। १८२६ में कलकत्ता से जुगल किशोर सुकुल ने उदंत मार्तण्ड नामक पहला हिंदी समाचार पत्र प्रकाशित किया था।

दूसरा दौर आजादी मिलने के साथ प्रारंभ हुआ और ८० के दशक तक चला। इस लंबी अवधि में मीडिया के प्रसार और गुणवत्ता में जबरदस्त बढ़ोतरी हुई। ९० के दशक में भूमंडलीकरण के आगमन के साथ तीसरे दौर की शुरुआत हुई, जो आज तक जारी है। निजी क्षेत्र में २४ घंटे चलने वाले उपग्रह, टीवी चैनलों और एफ.एम. रेडियो चैनलों का बहुत तेजी से प्रसार हुआ।

मीडिया को लोकतंत्र का चौथा स्तंभ माना जाता है। अगर लोकतंत्र के तीन स्तंभ विधायिका, कार्यपालिका एवं न्यायपालिका उचित तरीके से अपने-अपने निर्वाह नहीं कर पाए तो मीडिया के द्वारा ही उनके उत्तरदायित्व का बोध करा कर लोकतंत्र को मजबूत किया जाता है। मीडिया एक लोकतंत्र का ऐसा स्तंभ है जहां आम आदमी अपनी बातों को रख सकता है। देश की सामान्य जनता की खबर पूरे देश में पहुंचाने का महान काम मीडिया के माध्यम से ही होता है।

आज विश्व की घटित घटनाओं को हम घर में बैठकर या कहीं पर भी देख सकते हैं। इतना ही नहीं तो उन पर अपनी राय भी दे सकते हैं। इन सब का श्रेय केवल जनसंचार माध्यम को दिया जा सकता है जो, सामाजिक, सांस्कृतिक परंपराओं को निस्तारण करते हुए एक नए समाज की स्थापना कर रहा है। नैतिक मूल्यों के साथ वर्तमान में जिस परिवर्तन का दर्शन कर रहे हैं उसमें सबसे अधिक श्रेय मीडिया को जाता है।

आज सामान्य से सामान्य आदमी भी अपनी राय दे रहा है। लोगों की जीवन शैली में परिवर्तन आया है। सामाजिक, राजनीतिक समस्याओं के प्रति लोक जागरूक हो गए हैं। यह सब मीडिया का ही प्रभाव है। मीडिया समाज को दशा व दिशा देने का महत्वपूर्ण काम कर रहा है। मीडिया मानव चेतना के विकास में महत्वपूर्ण भूमिका निभा रहा है। मीडिया के प्रभाव के कारण समाज में विभिन्न क्षेत्रों में होने वाले परिवर्तन महत्वपूर्ण हैं।

सामाजिक विकास में मीडिया प्रिंट एवं टी.वी. की महत्वपूर्ण भूमिका है। मीडिया का मुख्य दायित्व लोगों के अधिकारों एवं कर्तव्यों के प्रति जागरूक करना जनहित की सूचनाओं को शीघ्र एवं सही तरीके से लोगों तक पहुंचाना और सरकार पर लोक कल्याणकारी दायित्व हेतु दबाव बनाना है। इंटरनेट के इस युग में मीडिया समाज के निम्नतम जड़ों तक भी पहुंच गया है। हम कह सकते हैं कि - 'जहाँ न पहुँचे शासन, वहाँ पहुँचे मीडिया'

समाज में चल रहे अन्य अत्याचार, गैर तरीके से चल रहे कामों को मीडिया के माध्यम से लोगों एवं सरकार तक प्रभावीशाली पहुंचा जा रहा है। इसका ही एक उदाहरण 'निर्भया' को ले सकते हैं। जहां मीडिया द्वारा कवरेज के कारण ही अंततः दोषी को फांसी की सजा हुई। लगातार कवरेज से बने जनमत के कारण ही सरकार को सुधारात्मक उपाय करने पड़े। पंचविभूषण अन्ना हजारे जी का जन आंदोलन मीडिया के द्वारा ही घर-घर में पहुंच चुका। उससे बहुत अच्छे नतीजे हमारे सामने आए हैं। देश में पड़े अकाल, सांप्रदायिक घटनाओं को लोगों तक पहुंचाने का महत्वपूर्ण कार्य मीडिया के माध्यम से ही हो रहा है। किसानों की खुदकुशी, आरक्षण पर चल रहे आंदोलन उचित-अनुचित प्रकारों को समाज के सामने लाने का महत्वपूर्ण काम मीडिया ही कर रहा है।

यद्यपि मीडिया के अन्वेषण तो सराहनीय है किंतु वर्तमान में मीडिया अपनी व्यापक पहुंच एवं प्रभावशालिता का अनुचित लाभ भी उठा रहा है। जिससे इस स्तंभ की पवित्रता पर आंच आई है। उसी प्रकार मीडिया खबरों टीआरपी बढ़ाने के लिए चलता है। छोटी-छोटी बातों को सनसनी खबर ब्रेकिंग न्यूज का नाम देकर लोगों को अपनी ओर आकर्षित करने की कोशिश करता है। मीडिया का महत्वपूर्ण कार्य समाज हित होता है लेकिन अपना टीआरपी बढ़ाने के लिए और लोगों का सिर्फ मनोरंजन करने के लिए बॉलिवूड हरिनयां, राजनीतिक नेता और क्रिकेटर की निजी जीवन की खबरे दिनभर दिखाता रहता है। हैरानी की बात तो यह है कि ब्रेकिंग न्यूज का नाम देकर हिरो - हिरोईन की ब्रेकअप की खबरों, उनका खान - पान, वेशभूषा आदि की चर्चाएं दिनभर की जाती है। मगर अफसोस की बात यह है कि जिस देश को कृषिप्रधान देश कहा जाता है वहाँ किसानों की खबरों को समय और स्थान नहीं होता। अखबार के पहले पन्ने पर खबरें कम और विज्ञापन जादा होते हैं। विज्ञापनों के बीच खबर दूँढनी पड़ती है।

मीडिया ने पूरी दुनिया में लोकतंत्र की स्थापना में महत्वपूर्ण भूमिका निभाई है। भारतीय लोकतंत्र में मीडिया की महत्वपूर्ण भूमिका एक स्वस्थ लोकतंत्र को आकार देने में एक महत्वपूर्ण भूमिका निभाता है। यह दुनिया भर में चल रहे विभिन्न सामाजिक, राजनीतिक गतिविधियों के बारे में हमें जागरूक करता है। यह एक दर्पण की तरह जीवन की वास्तविकताओं को प्रतिबिम्बित करता है। मीडिया लोकतंत्र प्रणाली की कमियों को उजागर करता है और प्रणाली को और अधिक उत्तरदायी बनाने में मदद करता है। 1990 के दशक में मीडिया घरानों, निवेश भारतीय अर्थव्यवस्था के उदारीकरण से प्रभावित हुआ था। क्योंकि बड़े कॉर्पोरेट घरानों, व्यवसायियों, राजनीति कुलीनों और उद्योगपतियों ने इसे अपनी ब्रांड छवि को सुधारने के लिए एक सुविधा के रूप में इस्तेमाल किया है। भारतीय मीडिया की विश्वसनीयता तेजी से मिट रही है क्योंकि, राष्ट्र की मीडिया द्वारा समय-समय पर विश्व दर्शकों द्वारा सनसनी फैलाने वाली खबरों की आलोचना की जाती है। भारतीय मीडिया जिस तरह से जानकारी घूमाता है इसलिए मीडिया का स्तर लगातार गिर रहा है। लोगों का उस पर से भरोसा घट रहा है। और लोकतंत्र तथा सार्वजनिक सुरक्षा के परीक्षण पर हो रहे भूमिका संदेह के घेरे में है।

वस्तुतः मीडिया को लोकतंत्र का चतुर्थ और सबसे मजबूत स्तंभ कहा जाता है। 'पहले अखबार छपकर बिकते थे अब बिक के अखबार छपते हैं' की छाया से बाहर आना होगा। मीडिया का लोकतंत्र में योगदान का वर्तमान उदाहरण वर्तमान परिवेश में चुनाव के समय देखा जाता है। जहां फिजिकल रैली पर प्रबंधक के बाद सभी पार्टियों डिजिटल रैली करके अपनी बातों को जनता तक पहुंच रही है। विभिन्न चैनलों, समाचार पत्रों में उनके नेताओं के साक्षात्कार आदि से प्रभावि प्रचार कर रहे हैं। संवाददाताओं द्वारा क्षेत्र में जाकर जनता से संवाद, उनकी समस्याओं को व्यापक कवरेज आदि से विभिन्न पार्टियों पर नैतिक दबाव का निर्माण करते हैं। कि वह अपनी घोषणा पत्रों में जनहित के मुद्दों का समावेश करें। मीडिया के आचरण एवं मुद्दों की संवेदनशीलता और प्रसारण छपने से पूर्व विश्लेषण में थोड़ा सुधार अपेक्षित है क्योंकि, अगर मीडिया की विश्वसनीयता पर संदेह हुआ तो जनता की आवाज सरकार के समक्ष कैसे पहुंचेगी। मीडिया लोकतंत्र प्रणाली की कमियों को उजागर करता है और प्रणाली को और अधिक जवाबदेही, उत्तरदाई और नागरिकों के अनुकूल बनाने में मदद करता है। लोकतंत्र में मीडिया की तीन जिम्मेदारियां हैं। पहला सत्तारूढ लोगों पर कड़ी नजर रखना। दूसरा समाज को पूरे दिन की महत्वपूर्ण सामाजिक और राजनीतिक मुद्दों पर विश्वसनीय जानकारी प्रदान करना और तीसरा केवल निष्पक्ष तथ्यों को उजागर करना।

दुर्भाग्यवश बढ़ते व्यवसायीकरण के कारण मीडिया में एक दूसरे के प्रति कड़ी प्रतिस्पर्धा पैदा हो गई है। मीडिया जिम्मेदार पत्रकारिता पर ध्यान केंद्रित न करके खुले तौर से पेड न्यूज और घटिया पत्रकारिता को बढ़ावा दे रही है। यह और भी ज्यादा दुखद है कि भारतीय मीडिया और कुछ व्यापारियों और राजनीतिक हितों के नियंत्रण में आ गया है। इसलिए सामाजिक हितों को राजनीतिक हितों के नीचे दबाया जा रहा है। वर्तमान में मीडिया राजनीति को ध्रुवीकरण का केंद्र बन गया है। समय की मांग यह है कि मीडिया की विश्वसनीयता बढ़ाई जाए। एक लोकतांत्रिक संस्था के रूप में मीडिया की विश्वसनीयता तभी बढ़ेगी जब वह जनता की ओर जवाबदेह होगी। अपनी गलतियां स्वीकार करेगी और नैतिकता का पालन करेगी। अतः मीडिया कोभी अपनी नैतिक दायित्व का ध्यान रखते हुए उसे अपने सिमा के अंतर्गत रिपोर्टिंग करनी चाहिए। जिससे समाज में तार्किक ज्ञान का प्रसारण ही लोग वास्तविक मुद्दों एवं घटनाओं की सत्यता को जाने।

संदर्भ :-

1. मीडिया और भाषा - वर्तिका नंदा
2. मीडिया और राजनीति - महेंद्र अल्होत्रा
3. जनसंचार और पत्रकारिता के विविध आयाम - डॉ.ओमप्रकाश शर्मा



महाराष्ट्र राज्य हिंदी साहित्य अकादमी, मुंबई

एवं

लोकनेते डॉ. बाळासाहेब विखे पाटील (पद्मभूषण उपाधि से सम्मानित) प्रवरा ग्रामीण शिक्षण संस्था का

कला, वाणिज्य एवं विज्ञान महाविद्यालय, सात्रळ तथा महाराष्ट्र हिंदी परिषद

के संयुक्त तत्त्वावधान में आयोजित परिषद का 30 वाँ अधिवेशन एवं राष्ट्रीय संगोष्ठी



प्रमाणपत्र



प्रमाणित किया जाता है कि डॉ./श्री./श्रीमती/सुश्री प्रा. शुभदा आरखे, न्यू आर्ट्स, कॉमर्स
अॅंड सायन्स कॉलेज पार्श्वे ने दिनांक 12 तथा 13

जनवरी 2024 को महाराष्ट्र राज्य हिंदी साहित्य अकादमी, मुंबई, हिंदी विभाग, कला, वाणिज्य एवं विज्ञान महाविद्यालय, सात्रळ तथा महाराष्ट्र हिंदी परिषद के संयुक्त तत्त्वावधान में हिंदी साहित्य की सामाजिक एवं लोकतांत्रिक भूमिका : नये संदर्भ विषय पर आयोजित राष्ट्रीय संगोष्ठी में विशेष अतिथि/सत्राध्यक्ष/विषय-प्रवर्तक/अभिपत्र प्रस्तोता/प्रतिभागी के रूप में सक्रिय सहभागिता के दायित्व का निर्वाह किया.

डॉ. शीतला प्रसाद दुबे

कार्याध्यक्ष

महाराष्ट्र राज्य हिंदी साहित्य अकादमी, मुंबई

डॉ. प्रभाकर डोंगरे

प्राचार्य

ए.सी.एस. कॉलेज, सात्रळ

प्रो. डॉ. जिजाबराव पाटील

अध्यक्ष

महाराष्ट्र हिंदी परिषद

डॉ. गजानन चव्हाण

प्रधान सचिव

महाराष्ट्र हिंदी परिषद

डॉ. भाऊसाहेब नवले

संयोजक एवं अध्यक्ष

हिंदी विभाग



AKSHARA
MULTIDISCIPLINARY RESEARCH JOURNAL
Peer-Reviewed & Refereed International Research Journal
January 2024 Special Issue 10 Volume II (A)

हिंदी साहित्य की सामाजिक एवं लोकतांत्रिक भूमिका नये संदर्भ



अतिथि संपादक
प्रो.डॉ.पी. एम. डोंगरे
प्राचार्य

लोकनेते डॉ.बालासाहेब विखे पाटील (पद्मभूषण उपाधि से सम्मानित)
प्रवरा ग्रामीण शिक्षण संस्था का कला, वाणिज्य एवं विज्ञान महाविद्यालय, सात्रल
तह.राहुरी, जि. अहमदनगर (महाराष्ट्र)

कार्यकारी संपादक

डॉ. गजानन चव्हाण
प्रधान सचिव

महाराष्ट्र हिंदी परिषद

प्रो.डॉ. जिजाबराव पाटील
अध्यक्ष

डॉ. भाऊसाहेब नवले
अध्यक्ष, हिंदी विभाग

कला, वाणिज्य एवं विज्ञान महाविद्यालय, सात्रल

डॉ. अनंत केदारे
सह-आचार्य

Chief Editor :
Dr. Girish S. Koli

32	इबकीसवी सदी के प्रथम दशक की आंबेडकरवादी कविताओं में लोकतांत्रिक मूल्यों का नव स्वर	डॉ. रगडे परसराम रामजी	121
33	कबीर की सामाजिक एवं लोकतांत्रिक भूमिका पर बुद्ध का प्रभाव	डॉ. संतोष रघुनाथराव रायबोले	126
34	हिन्दी साहित्य में स्त्री - विमर्श	डॉ. नवनाथ रघुनाथ जगताप	129
35	सामाजिक एवं लोकतांत्रिक सरोकार और समकालीन हिन्दी कहानी	प्रा.दिपाली दत्तात्रय तांबे	132
36	समकालीन हिन्दी कविता में व्यंग्य	प्रा.संतोष नागरे	135
37	हिन्दी साहित्य का सामाजिक एवं लोकतांत्रिक सरोकार	डॉ. तोंडाकुर एल.पी.	139
38	हिन्दी कथा साहित्य में सामाजिक एवं लोकतांत्रिक भूमिका	प्रा.डॉ.जी.बी.उषमवार	142
39	जयशंकर प्रसाद के 'स्कंदगुप्त' नाटक में सामाजिक एवं लोकतांत्रिक भूमिका	डॉ. मधुकर लक्ष्मण डोंगरे	145
40	समकालीन हिन्दी कविता की सामाजिक एवं लोकतांत्रिक भूमिका	डॉ.पठाण खातून बेगम अकबर खान	148
41	स्वतंत्र भारत के बदलते परिप्रेक्ष्य में सामाजिक एवं लोकतांत्रिक भूमिका	डॉ. आशा दत्तात्रय कांबळे	152
42	हिन्दी काव्य की सामाजिक एवं लोकतांत्रिक भूमिका: नये संदर्भ	प्रा. पूर्णिमा अमेश झेंडे	155
43	जनजातीय समाज में विनियम प्रथा	करुणा पाटगिरी	157
44	आजादी के बाद के हिन्दी साहित्य की स्थिति	संजय वसंत निंबाळकर	159
45	हिन्दी फिल्मों और देशभक्ति	प्रा. सिद्धाराम पाटील	161
46	डॉ. सुशीला टाकभौर के 'संघर्ष' कहानीसंग्रह में अभिव्यक्त लोकतांत्रिक मूल्य	डॉ.माधव राजप्पा मुंडकर	164
47	हिन्दी आत्मकथाओं में समाज एवं लोकतंत्र की भूमिका (आत्मकथा, मेरा जीवन और संतम के संदर्भ में)	प्रा.डॉ.दत्तात्रय सिताराम खिलारी	167
48	हिन्दी साहित्य में वैश्वीकरण के दौर में मूल्य विघटन	डॉ. सविता व्ही. रुक्के	170
49	समकालीन हिन्दी साहित्य में समाज एवं लोक-जीवन	प्रा. डॉ. हनुमंत येदु गायकवाड	173
50	समकालीन कविता में अभिव्यक्त लोकतंत्र की विसंगतियाँ	विक्रम बाळकृष्ण वारंग	175
51	जेनेद्र कुमार की कहानी 'पढाई' में शैक्षिक-सामाजिक रथार्थ	प्रा. डॉ. दिग्विजय टेंगसे	178
52	साठोत्तरी हिन्दी व्यंग्य नाटककारों के नाटकों में व्यक्त राजनैतिक एवं समाज व्यवस्था	राहुल गोपाल गुरखुदे प्रोफेसर डॉ. बाबासाहेब कोकाटे	180
53	हिन्दी कथा साहित्य की सामाजिक एवम लोकतांत्रिक भूमिका	प्रा.पल्लवी भूपेंद्र पाटील	183
54	ममता कालिया की कथा साहित्य में सामाजिक संघर्ष	शुभांगी श्रीधर भागवत	185
55	कुँवर नारायण की कविताओं में लोकतंत्र	प्रतिक्षा शिवाजी तनपुरे	188
56	डॉ. सादिका नवाब 'सहर' के उपन्यास "जिस दिन से" में स्थित भाषा शैली	येवले सविता महादेव	191
57	जयप्रकाश कर्दम की कहानियों में सामाजिक बोध	प्रा. संदीप दामू तपासे	194
58	हिन्दी काव्य की सामाजिक एवं लोकतांत्रिक भूमिका : उमाकांत खुवालकर के साहित्य के परिप्रेक्ष्य में	सुनिता देविदास अकोलकर	200
59	हिन्दी कथा-साहित्य के सामाजिक संदर्भ के रूपमें 'वृद्ध-विमर्श'	अविनाश मास्ती कोल्हे प्रो.डॉ.अनिल काले	203
60	हिन्दी बाल साहित्य का सामाजिक एवं लोकतांत्रिक पक्ष	लोभान वर्मा	206
61	लोकतंत्र को आईना दिखाती 'धूमिल' की कविता	डॉ. रमेश बाळासो खबाले	209
62	प्रभाकर श्रोत्रिय के नाटक 'फिर से जहाँपनाह' में लोकतंत्र एवं समाज	प्रा. डॉ. हंबीरराव चौगले	215
63	हिन्दी काव्य की सामाजिक एवं लोकतांत्रिक भूमिका : नये संदर्भ	प्रो.(डॉ.) संजीवकुमार नरवाडे	218
64	दामोदर खडसे के कथासाहित्य में निहित सामाजिक मूल्य	प्रो. बालकवि सुरंजे वृषाली पराडकर	222
65	हिन्दी बालसाहित्य का सामाजिक और लोकतांत्रिक पक्ष	प्रकाश बलभीम गांगर्डे डॉ. विशाला शर्मा	225

कुँवर नारायण की कविताओं में लोकतंत्र

प्रतिक्षा शिवाजी तनपुरे

पीएच.डी शोधार्थी, हिंदी विभाग,
सावित्रीबाई फुले पुणे विश्वविद्यालय, पुणे

चिंतन के केंद्र में व्यक्ति और समाज के आने से आधुनिकता की शुरुआत मानी जाती है। इनके अंततः संबंध से आधुनिक काल के अधिकांश विचार प्रणालियाँ और शासन व्यवस्थाएँ प्रकाश में आईं। व्यक्ति और समाज के संबंध सदैव एक से नहीं रहे। ये संबंध कभी विरोध पूर्ण तो कभी सहयोगी रहे हैं। लोकतंत्र व्यक्ति और समाज के सहयोगपूर्ण संबंध का लक्ष्य लेकर प्रकाश में आया। लोकतंत्र को सामान्यतः राजतंत्र की विलोम शासन प्रणाली के रूप में जाना जाता है। शासन प्रणाली के अतिरिक्त यह एक जीवन दर्शन और विचार प्रणाली भी है। लोकतंत्र को परिभाषित करने के क्रम में सबसे पहले जो विचार आता है वह है अब्राहम लिंकन का यह वाक्य - लोकतंत्र जनता का जनता के द्वारा और जनता के लिए शासन प्रणाली है।¹ इसका मतलब हुआ वह शासन व्यवस्था जो जनता के लिए हो, जनता ने खुद जिसका निर्माण किया हो और जो पूर्णतः जनता की हितों के लिए हो, लोकतंत्र कहलाती है। लोकतंत्र के प्रमुख लोक है और लोग का अर्थ है - जनसामान्य।² इसलिए लोकतंत्र का सामान्य और अनिवार्य अर्थ हुआ वह शासन तंत्र जिसमें जन सामान्य की भागीदारी हो और जो जनता की ओर उन्मुक्त शासन प्रणाली हो। वही आम आदमी लोकतंत्र का अर्थ एक ऐसे राजनीतिक व्यवस्था से समझता है जिसमें हर व्यक्ति को एक निश्चित उम्र के बाद वोट डालने का समान अधिकार हो, जहां ईमानदारी से नियमित चुनाव हो।³ इससे स्पष्ट होता है कि, लोकतंत्र किसी वर्ग विशेष की सरकार न होकर एक लोग सरकार है। शासन का वह रूप जिसमें अपने शासकों का चुनाव जनता करती है।

1950 में संविधान की स्थापना के साथ भारत में लोकतंत्र आ गया। जिसके तहत मताधिकार दिया गया। साथ ही सामाजिक, आर्थिक, राजनीतिक न्याय विचार की अभिव्यक्ति, धर्म की स्वतंत्रता देने के साथ-साथ प्रतिष्ठा और अवसर की सामानता भी प्रदान करने का संकल्प लिया गया। स्वतंत्रता, समानता और बंधुत्व इन तीन संकल्पनाओं को लेकर लोकतंत्र भारत में आया। ऐसी शासन प्रणाली की इच्छा व्यक्त हुई जो अपनी कार्य पद्धति से गरीबी, भुखमरी, बेरोजगारी, अशिक्षा, जाति, लिंग और भाषा के आधार पर व्याप्त सामाजिक भेदभाव, समाज में व्याप्त रूप में फैले भ्रष्टाचार, आर्थिक असमानताओं को दूर करने के साथ-साथ न्याय आधारित समाज की स्थापना करें। लेकिन यह बात वर्तमान परिदृश्य में कई साकार होती नहीं दिखती। लोकतंत्र के आते ही मानों सभी विषमताएँ और दुख तुरंत ही दूर हो जाएंगे। लेकिन यह देखा गया कि यह शब्द केवल नारा बनकर रह गया।

प्रत्येक रचनाकार अपने समय को और उसके यथार्थ को सामान्य व्यक्ति की अपेक्षा अधिक गहराई से देखता और पकड़ता है। स्वतंत्रता के पश्चात भारतीय लोकतंत्र की दशा कैसी रही उसका कुँवर नारायण ने खुले रूप में चित्रण किया। उनकी कविताएँ भारतीय लोकतंत्र से जुड़े आम आदमी की आशाओं, आकांक्षाओं और सपनों से बनी गई है। आजादी के बाद लगभग दो दशक आशावाद में डूबे दिखाई देते हैं। भारत का बुद्धिजीवी वर्ग इसी आशावादिता के कारण एक नए भारत, नए समाज और एक नई राजनीति का सपना देख रहा था। परंतु यह

आशावाद अधिक समय तक ना रह सका। इन सब परिस्थिति में शासन व्यवस्था ही जिम्मेदार है। यह लोगों की धारणा बनी। कहीं ना कहीं यह सच भी है कि हमने देश की बागडोर इन सबको बढ़ावा देने के लिए राजनेताओं को सौंपी थी। आज के शासक के करनी और कथनी में अंतर आया है। चुनाव के समय अलग-अलग हथकण्डे अपनाते हैं। चुनाव जीतने के बाद जनता को भूल जाते हैं। कवि ने महाभारत के प्रसंग द्वारा महाभारत नामक कविता में आधुनिक राजनीति का चित्रण किया है।

धृतराष्ट्र अन्धे / विदुर नीति हुई फेल / धर्मराज धूर्तराज दोनों जुआड़ी/पाँसे खनखनाते हुए/राजनीति में शुकुनी का प्रवेश।⁴

राजनीति में भ्रष्टाचार का बोलबाला है। शुकुनी जैसे स्वार्थी इसमें सम्मान पाते हैं। लोकतांत्रिक शासन व्यवस्था में जनता और शासन मिलकर शासन व्यवस्था चलाते हैं किंतु दोनों के बीच प्रत्यक्ष संवाद होते हैं। परंतु शासन और सत्ता के पक्ष के लोग मात्रा चुनाव के दौरान जनता के संपर्क में आते हैं। चुनाव के बाद उनका जनता के से कोई सरोकार नहीं होता। जनता और सरकार के बीच बढ़ती दूरी का चित्रण कुँवर नारायण ने एक यात्रा के दौरान कविता में राजनीतिक व्यवस्था का चित्र किया है -

याद आने लगता कुछ बढ़ते फासले/जैसे जनता और सरकार के बीच/ जैसे उसूलों और व्यवहार के बीच/जैसे संपत्ति और विपत्ति के बीच/जैसे गति और प्रगति के बीच।⁵

कुंवर नारायण लोकतांत्रिक व्यवस्था वाले एक आदर्श राज्य के पक्षधर रहे हैं। उन्होंने 'आत्मजयी' प्रबंधकाव्य में मिथक प्रयोग कर किया है। इसमें नचिकेता का पौराणिक व्यक्तित्व नहीं उभरता वह कवि के आधुनिक लोकतांत्रिक चिंतन का प्रतीक बन गया है। इस रचना में राजा वाजश्रवा राजतंत्र का प्रतीक है। राजा वाजश्रवा महान यज्ञ का आयोजन करता है इसमें यज्ञ कर्म संपन्न करनेवाले शताधिक ऋत्विजों को दुग्धविहीन, कृशकाय, अधमरी बूढ़ी गौएँ दक्षिणा के रूप में प्रदान करना चाहते हैं। नचिकेता अपने पिता की इस कार्य को जनहित में नहीं उसका विरोध करता है। नचिकेता के पिता राजा वाजश्रवा है। नचिकेता उन्हें राजा के पद के गरिमा और वास्तविकता का एहसास कराता हुए कार्यों से परिचित कराता है। नचिकेता मानता है कि राजा अथवा शासक एक साधारण प्राणी है जिसे सिंहासन एक भूमिका देता है और मुकुट एक शीर्षक देता है। किंतु सिंहासन, मुकुट, सेना, सभासद सभी राजा को इस तरह हर लेते हैं कि उसे पहचानना कठिन हो जाता है।

तुम भी एक प्राणी हो / सब की तरह समय के बने / जिसे सिंहासन एक भूमिका देता है/ मुकुट एक शीर्षक/ सेना एक कर्तव्य / स्वरक्षा एक धर्म / सभासद दायित्व/ पर ये सब तुम्हें इस तरह हर लेते हैं/ कि तुम्हें पहचान कठिन हो जाता है। 16 लोकहित में कार्य करना ही राजा का कर्तव्य और दायित्व है। प्रजा अथवा जनता के लिए समर्पित होना ही राजा का धर्म है। इस प्रकार वर्तमान संदर्भ में भी शासन व्यवस्था को लोकहित में विवेकपूर्ण कार्य करना चाहिए। राजा अथवा शासन को स्वहित को त्यागकर जनहित को प्रमुख मानना चाहिए। नचिकेता राजा के लिए कहता है - पिता तुम भविष्य के अधिकारी नहीं/ क्योंकि तुम 'अपने' हित के आगे नहीं सो पा रहे / न अपने 'हित' को ही अपने सुख के आगे। 17

राजनीति के माध्यम से स्वहित साधनेवाला राजा अधिक समय तक सत्ता में बना नहीं रह सकता। कुंवर नारायण की कविता आठवीं दशक के भारतीय राजनीति अधपतन को दिखाती है। यह कविता शासको द्वारा किए गए शोषण, राजनीतिक, हिंसा, भ्रष्टाचार के विरुद्ध तमाचा है। कुंवर नारायण की कविता स्वतंत्रता के बाद की परिस्थितियों को उजागर करती है। देश का स्वतंत्रता के बाद जो विकास होना चाहिए था वह नहीं हुआ। इसका प्रमुख कारण है नेताओं की स्वार्थपरकता है। स्वतंत्रता के बाद राजनेता वर्ग विलासी, स्वार्थी तथा सुविधा होगी बन गया। जनता के विकास के लिए जो सरकारी नीतियों या योजनाएं बनाई गई उनका कार्यान्वयन जिस तरह होना चाहिए था वह नहीं हुआ। पारित की गई योजनाओं का फायदा राजनेताओं के रिश्तेदार और करीबियों ने उठाया। राजनेता अपने हितों एवं स्वार्थों की पूर्ति में लग रहे उन्हें राष्ट्रहित कोई चिंता नहीं थी। इसी नेताओं के चरित्र पतन के संदर्भ में डॉक्टर लक्ष्मी सागर वर्षिण्य लिखते हैं कि "दुख केवल इस बात का है कि सामंतवादी व्यवस्था तो खत्म हो गई किंतु सामंतवादी प्रवृत्ति का अंत ही नहीं हुआ अंतर केवल इतना है कि जो प्रवृत्ति पहले राजा महाराजाओं और जागीरदारों में थी वह अब नेताओं और मंत्रियों में आ गई। 18

कुंवर नारायण ने राजनीति के हर एक पक्ष का चित्रण अपनी कविता में किया है। कवि कुंवर नारायण ने अयोध्या नामक कविता में राजनेता किस प्रकार अपने हित और स्वार्थ की पूर्ति में लग रहे हैं। जनता से उनका कोई लेना-देना नहीं। कवि राजनेता पर करारा व्यंग्य करते हुए लिखते हैं - हे राम कहाँ यह समय / कहा तुम्हारा त्रेता / कहाँ तुम मर्यादा पुरुषोत्तम / और कहाँ यह नेता - युग / सविनय निवेदन है प्रभु की लौटा जाओ/ किसी - किसी धर्म ग्रंथ / सकुशल सपत्नीक / अबके जंगल वो जंगल नहीं। जिनमें घूमा करते थे वाल्मीकि। 9

नेता नेतृत्व करता है। समाज को दिशा देता है। राष्ट्रहित ही उसके लिए सर्वोपरि होता है। किंतु वर्तमान राजनेता अवसरवादी बन गया। दलबदल की रा राजनेता में राजनेता को जिस दल लाभ मिलता है उसी दल में चला जाता है। 'पहला सवाल' कविता में इसी दलबदल राजनीति का चित्रण कवि ने किया है - संगठन कर्ताओं ने घोषित किया है वे जो/ हमारी तरफ थे/ अब दूसरी तरफ है/ अब दूसरी तरफ के इतिहासों के/ सबसे ऊँचे दरजों में दाखिला खोजते हुए... 110

लोकतांत्रिक व्यवस्था का चुनाव महत्वपूर्ण आधार होता है। संसद का भारतीय लोकतांत्रिक व्यवस्था में महत्वपूर्ण स्थान है। जो चुनाव के आधार पर ही बनती है। लोकतांत्रिक व्यवस्था में भले ही चुनाव का महत्वपूर्ण स्थान रहा है। चुनाव की वर्तमान स्थिति को देखकर कवि को चुनाव की अर्थवत्ता खत्म हो गई है ऐसा प्रतीत होता है। इसी कारण उसकी वास्तविकता से कवि पाठक को अवगत कराता है। कवि कुंवर नारायण चुनाव की वास्तविकता से बेहद नाखुश है। उनका मानना है कि राष्ट्रीय, क्षेत्रीय राजकीय पार्टियाँ तथा उनका नेतृत्व न चाहते हुए सामान्य जनता का इस्तेमाल करते हैं। चुनाव के नाटक में धकेलता है। चुनाव जीतने के लिए लोग सामान्य जनता का इस्तेमाल करते हैं। चुनाव जीतने के बाद वे जनता को पहचानने से इनकार करते हैं। ये लोग भाषा, जाति आदि संकुचित विचारों को सहारा लेकर वोट की मांग करते हैं। इसलिए कवि कहते हैं कि अब कोई धर्मक्षेत्र या कुरुक्षेत्र नहीं है चुनाव क्षेत्र है। जिसके लिए देश के आठों धर्म और अठराह भाषाओं को जूझना पड़ता है। महाभारत नामक कविता में कवि कुंवर

नारायण ने चुनाव के वास्तविक स्थिति का वर्णन किया है- न धर्मक्षेत्र न कुरुक्षेत्र / सीधे-सीधे चुनाव क्षेत्र/ जीत की प्रबल इच्छा से/ इकट्ठा हुए महारथियों के/ युद्ध का श्री गणेश/ दलों के दल से जूझ रहे/ आठ धर्म अद्वारह भाएँ अद्वैत प्रदेश 111

आजादी के बाद आम जनता का मोहभंग हुआ है। उसी मोह भंग को कवि कुंवर नारायण ने अपनी कविता के माध्यम से चित्रित किया है। आजादी के बाद आम जनता ने जो व्यवस्था तय की थी उससे संबंधित सभी आशाएँ, इच्छाएँ, आकांक्षाएँ, धूमिल हुई थी। देश की स्थिति में स्वतंत्रता के बाद भी विशेष परिवर्तन नहीं हुआ। जिस खुशहाल भारत की कल्पना की थी वह मात्र कल्पना ही रही। आजादी का जो सपना जनता को दिखाया था वह मात्र सपना बनकर रह गया। वर्तमान समय इतना भयावक हो चुका है कि आम जन का एक खुशहाली भी बड़ी मुश्किल से नसीब हो रही है। स्वतंत्र भारत के आम जनता की जो तकलीफ और दर्द को कवि ने दिखाया है। भारत के ग्रामीण भागों या गांव में आज भी लोग अव्यवस्था के शिकार हैं। आधी से ज्यादा जनसंख्या गरीबी, भुखमरी जैसे समस्याओं से जूझ रही है। आम आदमी का आज भी पुरतैनी कर्ज में डूबा है। सरकार की जो कल्याणकारी नीतियां बनाई जा रही हैं। उससे वह आम आदमी कोसो दूर है। ग्रामीण जनसंख्या आजादी के इतने वर्ष बीतने पर भी नंगी फतेहाल स्थिति में अपना जीवन व्यतीत कर रही है। पालकी नामक कविता में कवि ने हमारे ग्रामीण समाज के विकास की सही प्रस्तुति की है- काँधे धरी पालकी / है किस कन्हैयालाल की ? इस गाँव से उस गाँव तक नंगे बदन, फेटा कसे/ बारात किसकी ढो रहे ?/ किसकी कहारी में फँसे ?/ यह कर्ज पुरतैनी अभी किरते हजारो साल की/ काँधे धरी यह पालकी है किस कन्हैयालाल की?12

कवि कुंवर नारायण ने अपने तत्कालीन परिवेश में जो कुछ भी यथार्थ रूप से देखा उसे प्रत्यक्ष उतारने की कोशिश की है। स्वतंत्रता के पश्चात भारत की जो स्थिति है उसे देखकर कभी उदास होते हैं। कवि को लगता था कि स्वतंत्रता के बाद दिन बदलेंगे बुरे दिन खत्म होकर अच्छे दिन आएंगे। किंतु स्वतंत्रता के बाद भी राजनीतिक व्यवस्था सुधार न सकी। कवि की आशाओं पर पानी फिर गया। जनता पर स्वयं शासकोद्वारा भ्रष्टाचार किया जाने लगा। तो कवि का समकालीन व्यवस्था से मोहभंग हो गया। आजादी के बाद हमने जो प्रजातंत्र व्यवस्था स्थापित की उसकी जड़े अब शोषण रूपी पानी पीकर मजबूत होने लगी। हमारी व्यवस्था भी शोषण करने वालों के हाथों से चलती है। हमारी व्यवस्था इतनी भयावक हो गई है कि कई को लगता है कि यहां अगर एक दिन भी चैन से गुजर जाए तो यहाँ के भयभीत लोगों को हैरानी होती है।

आज सारे दिन बाहर घूमता रहा / और कोई दुर्घटना नहीं हुई / आज सारे दिन लोगों से मिलता रहा / और कई अपमानित नहीं हुआ / आज सारे दिन सच बोलता रहा / और किसी ने बुरा न माना / आज सब का यकीन किया / और कहीं धोखा नहीं खाया / और सबसे बड़ा चमत्कार तो यह / की घर लौटकर मैं किसी और को नहीं अपने को लौटा हुआ पाया 113

निष्कर्ष के तौर पर कह सकते हैं कि कुंवर नारायण की कविता में लोकतंत्र की विडम्बना हर स्तर पर प्रकट हुई है। कुंवर नारायण का लोकतंत्र कोई प्रसंत संसार नहीं है। उन्होंने अपने समाज और राजनीति से पाया की तत्कालीन परिस्थितियों में लोकतंत्र मात्र संजा बनकर रह गया।

संदर्भ :

1. राजनीतिक सिद्धांत की रूपरेखा ओम प्रकाश गाबा, पृ .221
2. हिंदी साहित्य कोश, भाग -1 - ज्ञान मंडल लिमिटेड, पृ .591
3. आधुनिक राजनीति के सिद्धांत भाग 2 - एम पी , .150
4. कुंवर नारायण : संसार भाग1 - सं . यतीन्द्र मिश्र पृ.136
5. कुंवर नारायण, कोई दुसरा नहीं पृ 27
6. कुंवर नारायण : संसार भाग1 - सं . यतीन्द्र मिश्र पृ.68
7. कुंवर नारायण : संसार भाग1 - सं . यतीन्द्र मिश्र पृ.69
8. उपन्यास और राजनीति - सुषमा शर्मा पृ .26
9. कुंवर नारायण : संसार भाग1 - सं . यतीन्द्र मिश्र पृ.137
10. कुंवर नारायण : संसार भाग1 - सं . यतीन्द्र मिश्र पृ.136
11. कुंवर नारायण : संसार भाग1 - सं . यतीन्द्र मिश्र पृ.136
12. कुंवर नारायण : संसार भाग1 - सं . यतीन्द्र मिश्र पृ.122
13. कुंवर नारायण : संसार भाग1 - सं . यतीन्द्र मिश्र पृ.100



महाराष्ट्र राज्य हिंदी साहित्य अकादमी, मुंबई

एवं

लोकनेते डॉ. बाळासाहेब विखे पाटील (पद्मभूषण उपाधि से सम्मानित) प्रवरा ग्रामीण शिक्षण संस्था का

कला, वाणिज्य एवं विज्ञान महाविद्यालय, सात्रळ तथा महाराष्ट्र हिंदी परिषद

के संयुक्त तत्त्वावधान में आयोजित परिषद का 30 वाँ अधिवेशन एवं राष्ट्रीय संगोष्ठी



प्रमाणपत्र



प्रमाणित किया जाता है कि डॉ./श्री./श्रीमती/सुश्री प्रा. प्रतिक्षा तनपुरे, न्यु आईस कॉमर्स
ऑड सायन्स कॉलेज पार्नेर ने दिनांक 12 तथा 13

जनवरी 2024 को महाराष्ट्र राज्य हिंदी साहित्य अकादमी, मुंबई, हिंदी विभाग, कला, वाणिज्य एवं विज्ञान महाविद्यालय, सात्रळ तथा महाराष्ट्र हिंदी परिषद के संयुक्त तत्त्वावधान में हिंदी साहित्य की सामाजिक एवं लोकतांत्रिक भूमिका : नये संदर्भ विषय पर आयोजित राष्ट्रीय संगोष्ठी में विशेष अतिथि/सत्राध्यक्ष/विषय- प्रवर्तक/अभिपत्र प्रस्तोता/ प्रतिभागी के रूप में सक्रिय सहभागिता के दायित्व का निर्वाह किया.

डॉ. शीतला प्रसाद दुबे

कार्याध्यक्ष

महाराष्ट्र राज्य हिंदी साहित्य अकादमी, मुंबई

डॉ. प्रभाकर डोंगरे

प्राचार्य

ए.सी.एस. कॉलेज, सात्रळ

प्रो. डॉ. जिजाबराव पाटील

अध्यक्ष

महाराष्ट्र हिंदी परिषद

डॉ. गजानन चव्हाण

प्रधान सचिव

महाराष्ट्र हिंदी परिषद

डॉ. बाळसाहेब नवले

संयोजक एवं अध्यक्ष

हिंदी विभाग





PAPER

Microstructural, optical, and morphological investigations of SnO₂ nanomaterials grown by microwave assisted sol gel methodRECEIVED
30 September 2023REVISED
27 December 2023ACCEPTED FOR PUBLICATION
31 January 2024PUBLISHED
12 February 2024Lalita Deshmukh^{1,*}  and S L Kadam²¹ Department of Physics, Ahmednagar College, Ahmednagar, Maharashtra, India² New Art's, Commerce and Science College, Parner, Ahmednagar, Maharashtra, India

* Author to whom any correspondence should be addressed.

E-mail: lalita.deshmukh@aca.edu.in

Keywords: tin oxide nanomaterials, XRD, W-H plots, stress, strain, UV-Vis, SEM etc

Abstract

Tin Oxide (SnO₂) nanomaterials were grown using the microwave-assisted sol–gel method at different concentrations of tin precursor (namely 0.05, 0.1, 0.2, and 0.3 M). Stannous chloride is used as a Sn precursor. Liquid ammonia was used to maintain the pH in the range of 12–13. Synthesis was carried out in an aqueous medium using a Teflon container in a microwave oven for 1 hour. Precipitate was annealed in ambient air for 600°C. Structural, optical, and morphological investigations were done. XRD reveals the growth of the tetragonal phase of SnO₂. The prominent presence of (110), (101), and (211) reflections was noticed at 26.6, 33.7, and 52 two-theta values. Tin oxide is transparent in the visible region of the electromagnetic spectrum. However, several attempts have been made to decrease the visible blindness of tin oxide. The band gap is a property of nanomaterials that can tailor their application in the optoelectronic field. Band gap and crystallite size show a prominent relationship in the nano-domain. Strain was not considered while calculating crystallite size using the Scherrer formula. In this investigation, we have measured the crystallite size and other structural features such as strain, stress, deformation energy, dislocation density, etc using the W-H plot method. All modified models of the W-H method have been utilized for this measurement. A comparative and comprehensive study of structural features was carried out using the Scherrer method, the Williamson–Hall method, and all its modified models. The crystallite size measured by the Scherrer method and various models of the W-H method shows a peak at 0.2 M concentration. Crystallite size plots of various modified W-H methods show similar trends, followed by the Scherrer plot. Strain calculated by Bragg's theory as well as all modified W-H depicts similar behaviour upon changing the concentration. Globular agglomerated morphology was revealed by scanning electron microscopy (SEM). The presence of tin (Sn) and oxygen (O) was confirmed by energy dispersive x-ray spectroscopy. The band gap was obtained using the Tauc theory, which portrays variation in the range of 3.4 to 3.6 eV.

1. Introduction

Metal oxide nanomaterials claim promising candidature in various fields of applications. Sensors, optoelectronics, photovoltaics, etc fields heavily depend on the use of metal oxide nanoparticles. Semiconducting metal oxide nanomaterials show attractive features such as surface area, band gap, non-toxicity, and chemical stability [1]. It is a wide-band gap semiconductor with a band gap of nearly 3.6 eV. It has a rutile tetragonal crystal structure. Tin oxide is present in two forms: stannous and stannic oxide [2]. Due to its multiple oxidation states, it has multiple applications. SnO₂ is a versatile material due to its attractive features. Conducting oxide is used to make the transparent conductor. It has stability, large optical transparency, and small electrical resistance [2]. SnO₂ is a multifunctional metal oxide, as it is used in photovoltaics [3],

optoelectronics [4], gas sensing [5], spintronics [6], transparent conducting electrodes [7], antioxidant activities [8], antimicrobial activities [8], batteries [9] and many more.

Different synthesis methods were used to synthesize SnO₂. Co-precipitation, precipitation, mechanochemical, microwave irradiation, electrochemical reduction, hydrolysis method, sol-gel method, electrochemical method, microwave assisted method, vacuum evaporation, chemical vapor deposition, biosynthesis, etc techniques were used to grow SnO₂ nanomaterials.

The co-precipitation method was used to synthesize and dope SnO₂ nanoparticles. Ni and Cu were used as dopants. The tetragonal rutile structure has been revealed. Ni-doped SnO₂ nanoparticles show a higher value of saturation magnetization. Enhanced electrical and magnetic properties were detected in Ni-doped SnO₂ nanoparticles [10].

SnO₂-graphene nanocomposites were synthesized by the one-pot hydrothermal method. An excellent specific capacity was shown by grown nanocomposites even at low temperatures. A detailed storage mechanism for Na was revealed. This work triggers the use of SnO₂ as an anode in Na-ion batteries [11]. Ultrafast SnO₂-graphene nanoplates were synthesized using the rapid microwave irradiation method. CV reveals the excellent alloying-dealloying mechanism of Sn. Three-fold charging-discharging capacity was observed as that of conventional electrolytes. It demonstrates the role of material as an anode in a lithium-ion battery [12]. SnO₂ nanoparticles were grown on carbon cloth using the facile hydrothermal method. The SnO₂/Sn Mott-Schottky junction causes CO₂R electrolysis. Reduction in the energy barrier during CO₂R formation. SnO₂/Sn heterojunction plays a vital role in this work [13]. Tin oxide nanoparticles show enhanced features such as large specific capacitance. The electrode of SnO₂ synthesized by the electrolysis method shows significant cycling stability up to 150 cycles. The performance of Li and Ni-doped and un-doped tin oxide electrodes was examined and compared [14].

Microwave-assisted green synthesis was carried out for the synthesis of SnO₂ nanoparticles. The photocatalytic and antibacterial activities of synthesized nanoparticles were investigated thoroughly. Plant-based synthesized nanoparticles show excellent photocatalytic and antibacterial behavior [15].

The SnO₂ electron transport nanolayer in a solar cell was deposited using the vapor deposition method. Devices fabricated using multilayer have shown 27% the same power conversion efficiency as those fabricated with a single SnO₂ nanolayer [16]. SnO₂/graphene monolayer was grown via the chemical vapour deposition technique. These layers were tested for the sensing of NO₂ gas. An enhancement in sensitivity of a SnO₂-based sensor was observed compared to a graphene-based sensor. Recovery time shows a significant decrease upon UV irradiation. UV irradiation contributed to the fast response and recovery time of the gas sensor [17].

Zhan *et al* have explored the photocatalysis activity and growth mechanism of SnO₂ nanocrystals using the Sol-gel method. In this work, Ostwald's Ripening Mode (OR) and Oriented Attachment (OA) Mode were used to study the growth mechanism. This work successfully demonstrates the dependence of photocatalysis activity on growth mechanisms [18].

The sol-gel method was used to grow the SnO₂ nanoparticle for the application of humidity sensors. A synthesized nanoparticle shows enhanced detection of humidity. Good relative humidity detection was reported in this work [19].

A facile microwave-assisted method was developed to synthesize large-scale SnSe_{1-x}Te_x nanoplates. An enhanced thermoelectric performance was observed in this work. They have achieved the tailoring of electronic band structure using Density Functional Theory (DFT) [20].

SnO₂ nanostructures were synthesized using the co-precipitation method. The tetragonal rutile structure was confirmed using XRD. Structural data was obtained and compared using the Nelson-Riley, Williamson-Hall plot, and Debye-Scherrer methods [21].

Iron oxide and Europium oxide-doped SnO₂ nanomaterials were prepared by the solid-state reaction method. Dislocation density and strain were calculated using the Williamson-Hall method. Confirmation of incremental grain boundaries due to doping was reported from structural analysis. An increase in resistance was reported due to these grain boundaries [22, 23]. Bare and sulfur-doped SnO₂ nanoparticles were prepared using the hydrothermal method. The Scherrer method, Williamson-Hall method, and size-strain plot method were used to obtain the structural parameters, such as crystallite size and microstrain. The values reported in this work show good agreement with each other. Further, these prepared nanomaterials were used in energy storage applications [24].

In this investigation, we have synthesized SnO₂ nanomaterials using the novel microwave-assisted Sol-gel method.

Grown nanomaterials will be used for optoelectronic applications such as photo detection. Crystallite size and strain are interdependent features of crystallite materials. Defect/dislocation free crystallites result in minimal-strain nanostructures. The Scherrer formula is widely used to obtain the crystallite size; however, strain broadening is ignored while calculating the crystallite size. In Williamson-Hall and its modified equations, the strain and isotropy of material were considered. This gives a meticulous idea of the crystalline aspects of grown

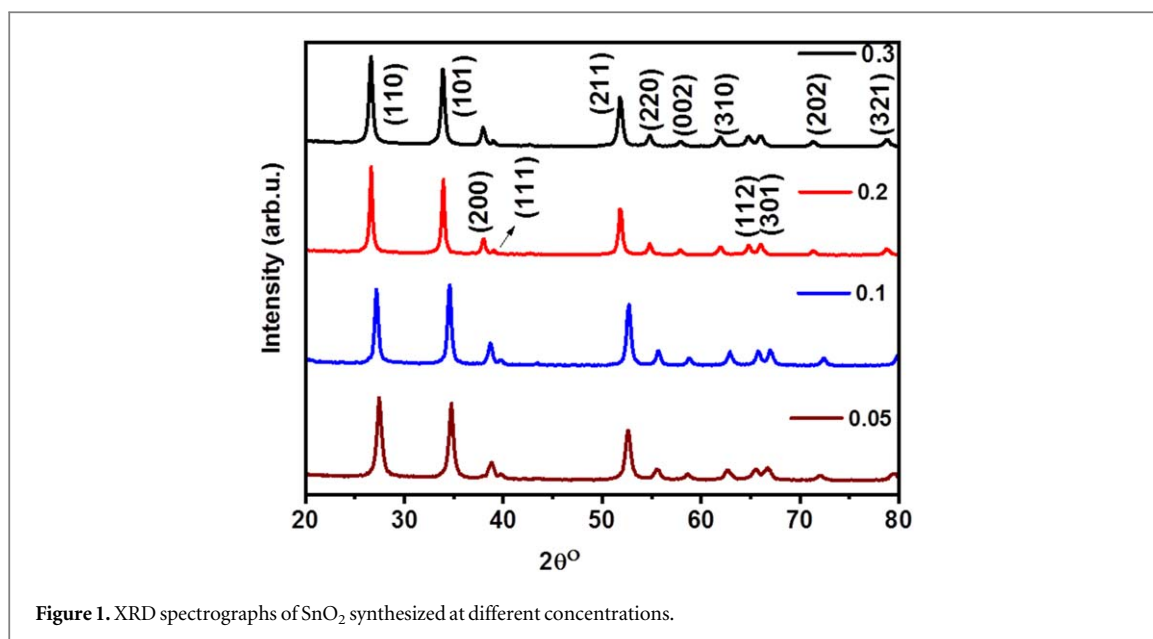


Figure 1. XRD spectrographs of SnO₂ synthesized at different concentrations.

nanostructures. Surface features such as shape, size, surface area, and nature of the surface affect the detection mechanism. These comprehensive morphological measurements are complementary to the synthesis of nanomaterials for optoelectronic applications. Optical probing is helpful in measuring optical aspects such as the band gap of the grown nanostructure that affect the detection range in photodetection.

An airtight Teflon container was used to maintain the temperature and pressure during the microwave treatment. These syntheses were carried out at different concentrations of Tin precursor. The effect of concentration on the structural, optical, morphological, and elemental features of Tin oxide nanoparticles was studied in this work. Especially, structural parameters such as crystallite size, dislocation density, microstrain, stress, and deformation energy density were obtained using the Scherrer method and Williamson–Hall plot method.

2. Experimental

Microwave assisted Sol gel method was used to synthesize Tin Oxide (SnO₂) nanomaterials. Stannous Chloride (SnCl₂·2H₂O) and ammonia solution (NH₃) (Molychem A.R. grade) used as starting precursors. Stannous chloride was used as Sn source. pH of solution was maintained at 12–13 using drop-wise addition of Ammonia solution in continuously stirring solution. Four different concentrations (0.05, 0.1, 0.2, and 0.3 M) were synthesized in an aqueous medium. The solution with a white precipitate suspension was transferred to an airtight Teflon container. Further, microwave heating was carried out for 1 h. Precipitate was collected using filtering, followed by natural cooling. Precipitate was dried using an IR lamp for 2 h. Air ambient annealing was carried out in a furnace at 600 °C for 5 h.

The annealed precipitate was investigated structurally, optically, and morphologically using XRD, UV–vis, and SEM techniques. Structural studies were performed using an x-ray diffractometer, model D8 Advanced Bruker, with a CuK α (radiation wavelength, =0.154 nm) anode. The optical features of the grown nanomaterial were examined using a JASCO V-750 UV–vis spectrometer. Surface morphology and elemental composition were investigated using the Scanning Electron Microscope (SEM) JSM IT50.

3. Result and discussion

3.1. Structural analysis

Figure 1 reveals the x-ray diffractograms of SnO₂ synthesized at different concentrations. (110), (101) and (211) reflections show their prominent presence. XRD reveals the formation of the tetragonal phase of Tin Oxide which is in agreement with standard data (JCPDS-72–1147). The average crystallite size was obtained using the Scherrer [25] formula.

Table 1. Crystallite size, microstrain, dislocation density, and band gap dependence on concentration.

Concentration (M)	Crystallite size (nm)	Dislocation Density (nm^{-2}) ($\times 10^{-3}$)	microstrain ($\times 10^{-3}$)	Band gap (eV)
0.05	12.68	6.42	6.637	3.57
0.1	16.01	3.93	5.33	3.5
0.2	18.39	3.07	4.446	3.42
0.3	15.84	4.06	5.205	3.61

Table 2. Structural parameters using williamson–hall method.

Conc.(M)	Williamson–hall method								
	UDM		USDM			UEDDM			
	d (nm)	ϵ ($\times 10^{-3}$)	d (nm)	ϵ ($\times 10^{-3}$)	σ (MPa)	d (nm)	ϵ ($\times 10^{-3}$)	σ (MPa)	u (KJm^{-3})
0.05	16.55	1.45	13.81	0.3131	1700	14.57	0.6551	655.5	1166
0.1	18.95	0.5969	18.08	0.3923	2130	18.88	0.6069	606.9	1000
0.2	26.04	1.13	23.25	0.8068	4380	27.27	1.3899	1389.9	5244
0.3	18.91	0.6265	18.33	0.5121	2780	19.70	0.9225	922.5	2310

$$d = \frac{0.9\lambda}{\beta \cos \theta} \quad (1)$$

Where d is the average crystallite size, β is the full width at half maximum, λ is the diffraction wavelength of the Cu anode (0.154 nm), and θ is the angle of diffraction. Dislocation density was calculated using the dislocation density equation [26] given by

$$\delta = \frac{1}{d^2} \quad (2)$$

Scherrer theory gives an estimate of particle size; however, it completely neglects the contribution due to microstrain in peak broadening. Microstrain is given by,

$$2\epsilon = \frac{\Delta d}{d} \quad (3)$$

Contribution to peak broadening due to microstrain [27] is given by,

$$\beta = 4\epsilon \tan \theta \quad (4)$$

$$\epsilon = \frac{\beta}{4 \tan \theta} \quad (5)$$

Table 1 displays the values of crystallite size, dislocation density, microstrain, and band gap.

Upon an increase in the concentration of Sn precursor, average crystallite size shows a rise up to 0.2 M concentration; further increase in concentration result in a decrease in crystallite size. This is attributed to the fact that an increase in concentration results in a rise in nucleation. This trend continues from 0.05 M to 0.2 M, further increase in concentration result in a reduction in crystallite size; this may be due to the presence of an excessive number of nuclei. The chemical reaction rate is directly influenced by the concentration of the solution. This causes the evolution of the density of nuclei in solution, which governs the growth of crystallite size. Dislocation density and microstrain exhibit the same inverse trend as that of average crystallite size. Larger the crystallite, the fewer the boundaries, resulting in a decrease in imperfections and a more compact structure. This could be the reason for the inverse trend of dislocation density and microstrain with crystallite size. These parameters are obtained using the Scherrer theory; however, this theory has its own limitations. Crystallite size consists of broadening due to stress, strain, crystalline imperfections, faults, voids, etc present in the crystallite. This limitation can be overcome using the Williamson–Hall method, which considers broadening of the peak due to crystallite size as well as microstrain. A Williamson–Hall plot was used to measure crystallite size, dislocation density, strain, stress, and deformation energy. In the W-H plot method, three modified models: Uniform Deformation Model (UDM), Uniform Deformation Stress Model (USDM), and Uniform Deformation Energy Density Model (UEDDM) were used. Table 2 shows concentration-dependent structural features obtained by the W-H method.

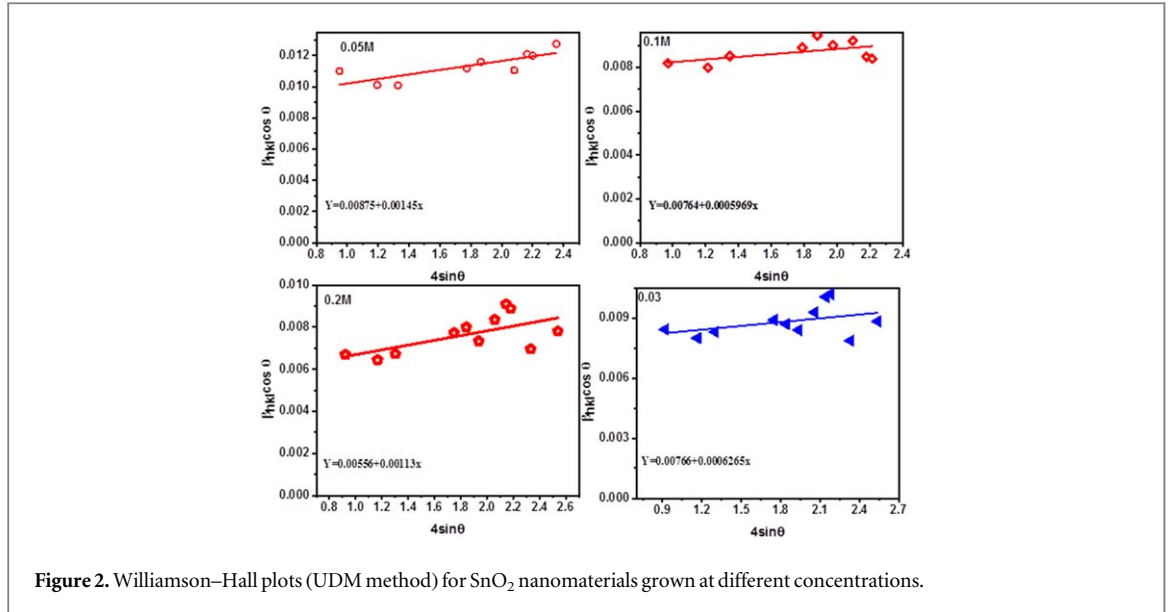


Figure 2. Williamson–Hall plots (UDM method) for SnO₂ nanomaterials grown at different concentrations.

3.1.1. Uniform deformation model

Williamson–Hall equation for Uniform deformation model is given [28] by

$$\beta_{hkl} \cos \theta = \frac{k\lambda}{d} + 4\epsilon \sin \theta \quad (6)$$

Where, β_{hkl} is the full width at half maxima of a particular reflection, θ is the angle of diffraction, k is the shape factor, d is the crystallite size, ϵ intrinsic strain present in crystallite due to imperfections, defects or dislocations. Intercept and slope of linearly fitted data of plot of $\beta_{hkl} \cos \theta$ versus $4\epsilon \sin \theta$ gives crystallite size and microstrain present. Figure 2 shows Williamson–Hall plots (UDM method) of synthesized samples.

Crystallite size and microstrain obtained using the W–H method and the Scherer method are close to each other. Microstrain and crystallite size obtained in the W–H method show similar behaviour to that of the Scherer method. Crystallite size shows a rise with an increase in concentration from 0.05 to 0.2 M; further increase in concentration result in a decrease in crystallite size.

3.1.2. Uniform stress deformation model (USDM)

Hook's law exhibits proportional relationship between stress and strain which is given by,

$$\sigma = Y\epsilon$$

Where, σ , is stress, ϵ is strain and Y , is constant of proportionality or Young's modulus. This equation is valid for small strain. However, for lattice strain, it is considered that strain and stress are uniform. This gives rise to modification in second term of UDM equation, ϵ is replaced by $\frac{\sigma}{Y}$. Modified equation due to uniform stress consideration is given by USDM model [29, 30] as,

$$\beta_{hkl} \cos \theta = \frac{k\lambda}{d} + \frac{4\sigma \sin \theta}{Y_{hkl}} \quad (7)$$

Where, β_{hkl} is full width at half maxima of a particular reflection, θ is angle of diffraction, k is shape factor, d is crystallite size, σ intrinsic stress and Y_{hkl} Young's modulus along the particular (hkl) plane. Crystallite size can be determined from the Y axis intercept and microstrain is obtained by slope of linear fitted plot of $\beta_{hkl} \cos \theta$ versus $\frac{4 \sin \theta}{Y_{hkl}}$. Figure 3 shows the plots USDM method.

Young's modulus Y_{hkl} for tetragonal crystal structure [31] is given by formula,

$$\frac{1}{Y_{hkl}} = \frac{S_{11}(h^2 + k^2) + l^2(2S_{13} + S_{44})}{(h^2 + k^2 + l^2)} + \frac{l^4(S_{33} - 2S_{13} - S_{44}) + h^2k^2(2S_{12} + S_{66})}{(h^2 + k^2 + l^2)^2} \quad (8)$$

Where, S_{11} , S_{12} , S_{13} , S_{33} , S_{44} and S_{66} are elastic compliances of tetragonal phase [30] of SnO₂, the values of S_{11} , S_{12} , S_{13} , S_{33} , S_{44} and S_{66} are 7.4262, -4.4081 , -1.0438 , 2.9462, 9.6432, and $4.8216(TPa)^{-1}$ respectively [32]. The values of Young's modulus were determined for all lattice planes. Crystallite size and microstrain obtained using the USDM model are in agreement with the Scherer method and the UDM method.

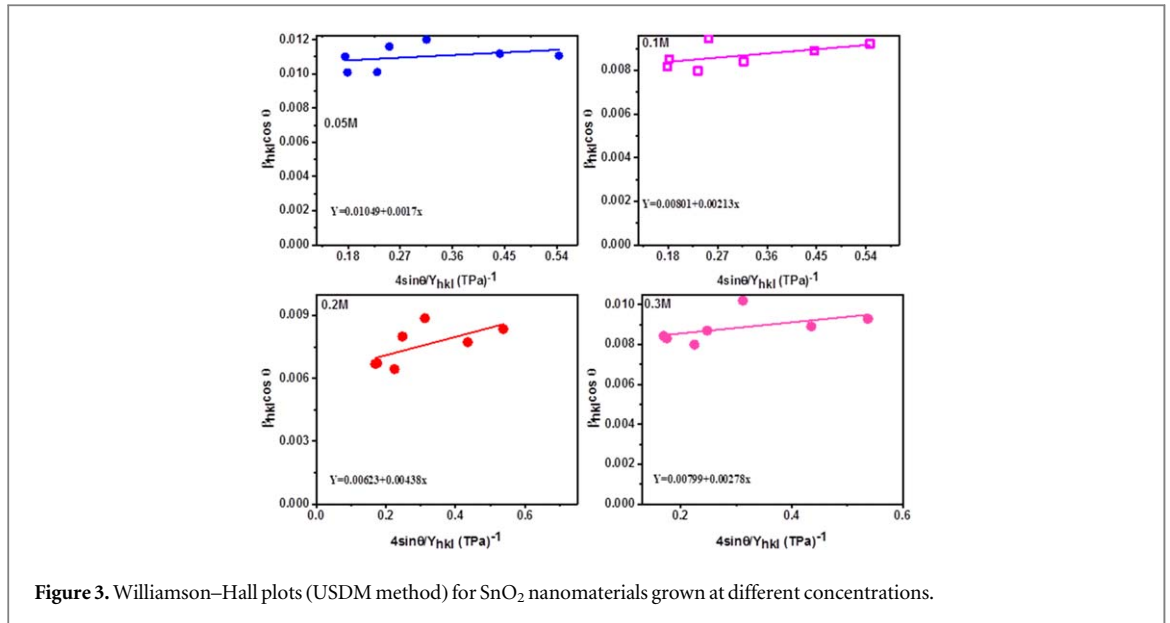


Figure 3. Williamson–Hall plots (USDM method) for SnO₂ nanomaterials grown at different concentrations.

3.1.3. Uniform deformation energy density model (UDEDM)

As per the UDM model, crystals are isotropic and have homogeneity; however, in reality, such a crystal system is no longer in existence. Therefore, it is required to modify the UDM equation by considering the anisotropic nature of a realistic crystal system.

Along with this linear relation between stress and strain cannot be considered due to defects, imperfections present in the crystal. In UDEDM, deformation energy density is denoted by u and given by

$$u = \frac{1}{2} \epsilon^2 Y_{hkl} = \frac{\sigma^2}{2Y_{hkl}}$$

Intrinsic strain can be written as a function of deformation energy density as,

$$\epsilon = \sigma \sqrt{\frac{2u}{Y_{hkl}}}$$

Using above in UDM formula, we get the modified equation [32] as given by

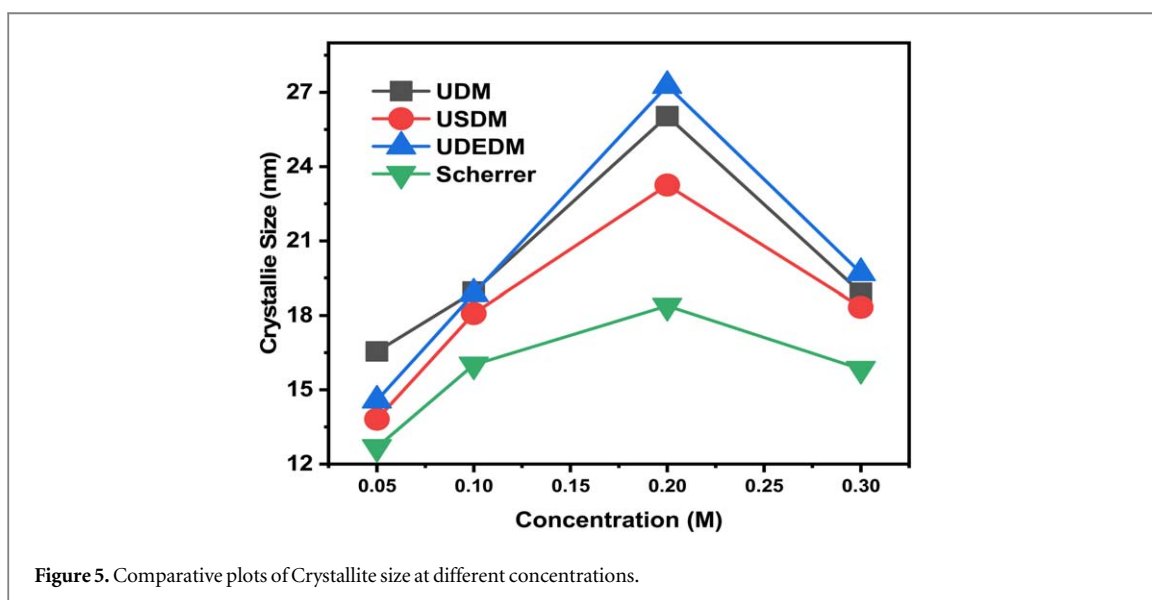
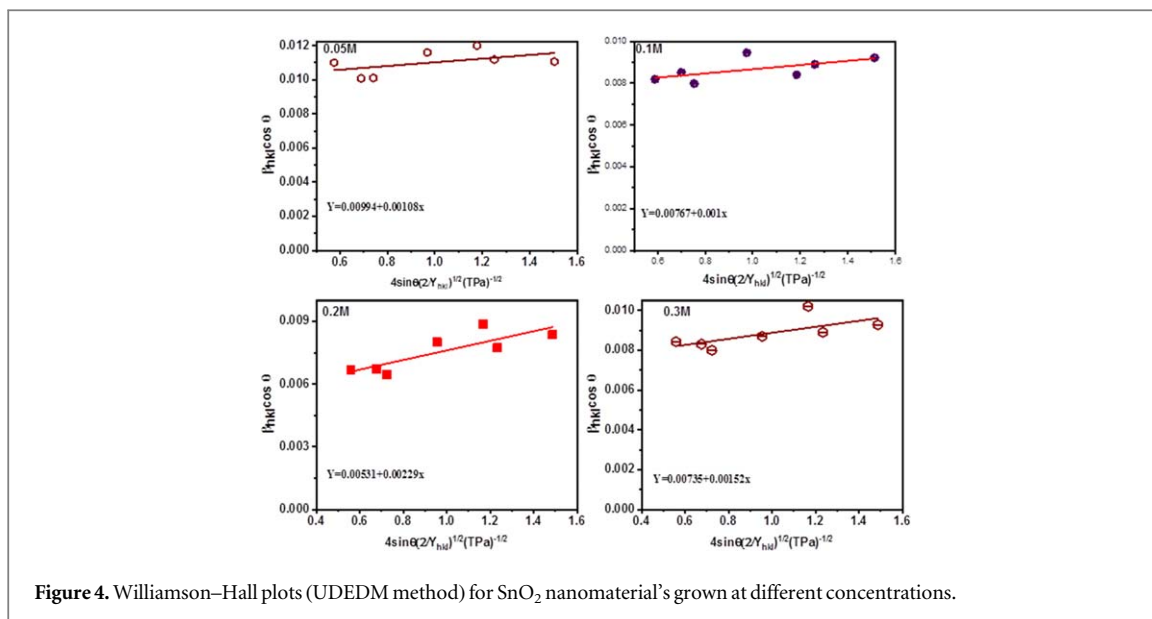
$$\beta_{hkl} \cos \theta = \frac{k\lambda}{d} + 4 \sin \theta \sqrt{\frac{2u}{Y_{hkl}}} \quad (9)$$

Figure 4 shows the plot of UDEDM, $\beta_{hkl} \cos \theta$ Vs $4 \sin \theta \sqrt{\frac{2u}{Y_{hkl}}}$. Y axis intercept gives the value of crystallite size. Slope of linearly fitted data yield the value of energy. Further energy strain and uniform deformation stress is obtained.

Figure 5 reveals that the crystallite size obtained by using the Scherrer method, UDM, USDM, and UDEDM shows agreement. Average crystallite size for 0.2 M concentration shows a peak; further increase in concentration result in a decrease. Similar trends were observed in the crystallite size obtained by using different methods. It is well known that, Scherrer equation considers broadening completely due to crystallite size; it neglects the broadening due to strain. This results in small crystallite size as that of W-H method. Figure 5 depicts, crystallite size obtained by UDEDM shows larger values as that of USDM and UDM as UDEDM follows more realistic anisotropic model of crystallite system.

Figure 6 shows comparative plots of strain measured by Bragg's and different models of the W-H plot method. Strain measured by Bragg's theory exhibits higher values than those of different models of the W-H plot method. This is attributed to the fact that W-H plot counts contribution in peak broadening due to crystallite size as well as strain. However, UDEDM has higher strain values compared to UDM and USDM.

This is due to consideration of the anisotropic picture of the crystal, which yields an increase in strain compared USDM. Synthesized nanomaterials will be deployed for the purpose of photodetection applications. Larger the crystallite size, lesser the microstrain, dislocation density, and grain boundaries. This reduces the losses during photo detection.



4. Optical study

The Tauc theory was used to obtain the band gap of synthesized nanoparticles. Figure 7 reveals the Tauc plots of SnO₂ nanomaterials grown at different concentrations.

The band gap values obtained using these Tauc plots vary from 3.42 eV to 3.61 eV. Upon an increase in concentration, the band gap shows a decrease up to 0.2 M; however, with a further increase in concentration, the 0.3 M band gap value increases. This could be due to the fact that an increase in molarity from 0.05 to 0.2 M causes increases in crystallinity. A decrease in crystallinity was witnessed at 0.3 M. Variation in band gap with concentration could be linked to variation in crystallite size. This is attributed to the quantum confinement effect. Tin oxide is a visible-blind material. 3.42 eV is the band gap obtained for a 0.2 M concentration of Tin precursor. Further optimization in concentration, temperature, and reaction time may result in a reduction in the band gap. This may lead to detection within a higher threshold of the visible range.

4.1. Morphological study

Figure 8 shows the morphological features of SnO₂. The inset shows the distribution of the average length of particle distribution obtained by using Image-J software.

This average length also shows a similar kind of trend with concentration. Agglomeration of the globular type of morphology is clearly seen. Figure 9 reveals the EDS spectra for different concentrations. The EDS spectra confirm the presence of Sn and O.

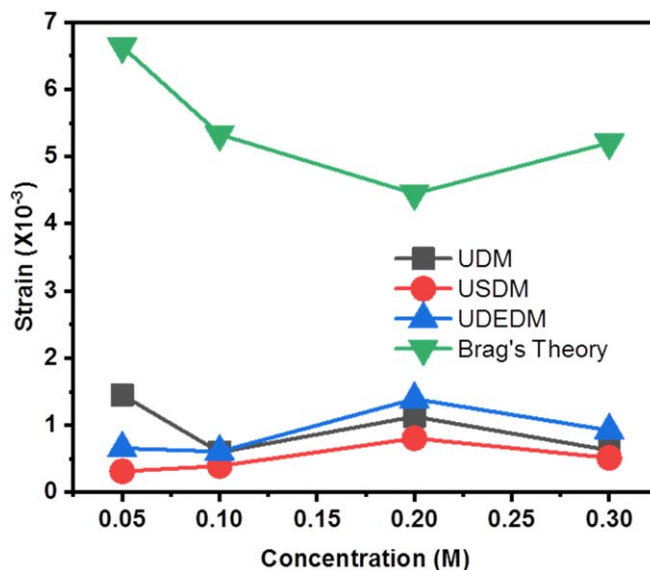


Figure 6. Comparative plots of strain calculated for different concentrations.

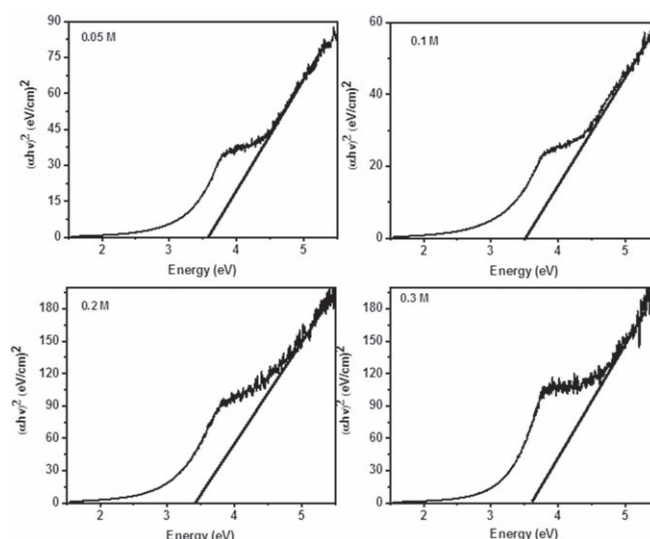


Figure 7. Tauc plots for SnO₂ nanomaterial's synthesized at different concentrations.

There is no specific trend in elemental composition or concentration observed.

Tuning of the energy band gap could be possible using process control parameters such as concentration, power, reaction time, etc. Crystallite size and energy gap are interrelated. The quantum confinement effect is observable in the microworld. Determination of crystallite size can be done using various formulas, such as the Scherrer formula, the Williamson–Hall method, and its various models. The Scherrer formula does not consider the microstrain present in the crystal lattice, which is obvious in crystalline materials as crystal with zero entropy do not exist. However, the Williamson–Hall method is more precise as it considers microstrain while obtaining the crystallite size. Modified W-H models even consider the isotropy of the crystal.

This ensures a more precise measurement of crystallite size and can be interlinked with the energy gap. Tuning of the energy gap could result in variation in the detection range. These results will be utilized for further optimization of the band gap so that the resultant SnO₂ nanomaterial may work in the upper threshold region of the visible spectrum. Surface features such as shape, size, surface area, and nature of the surface affect the detection mechanism. These comprehensive morphological measurements are complementary to the synthesis of nanomaterials for optoelectronic applications.

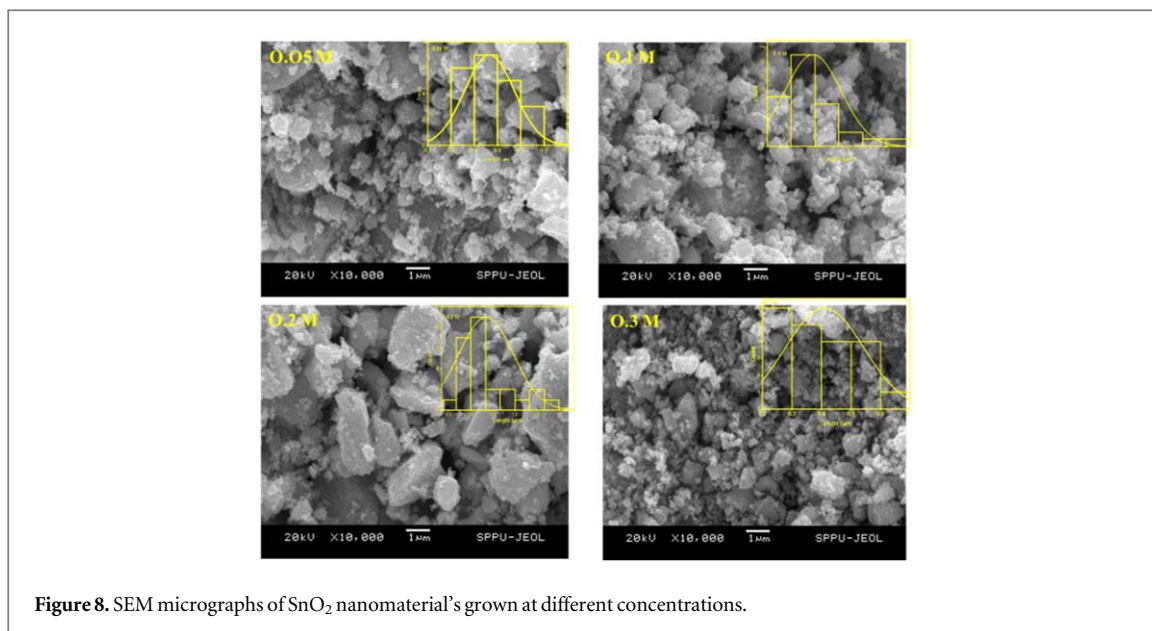


Figure 8. SEM micrographs of SnO₂ nanomaterial's grown at different concentrations.

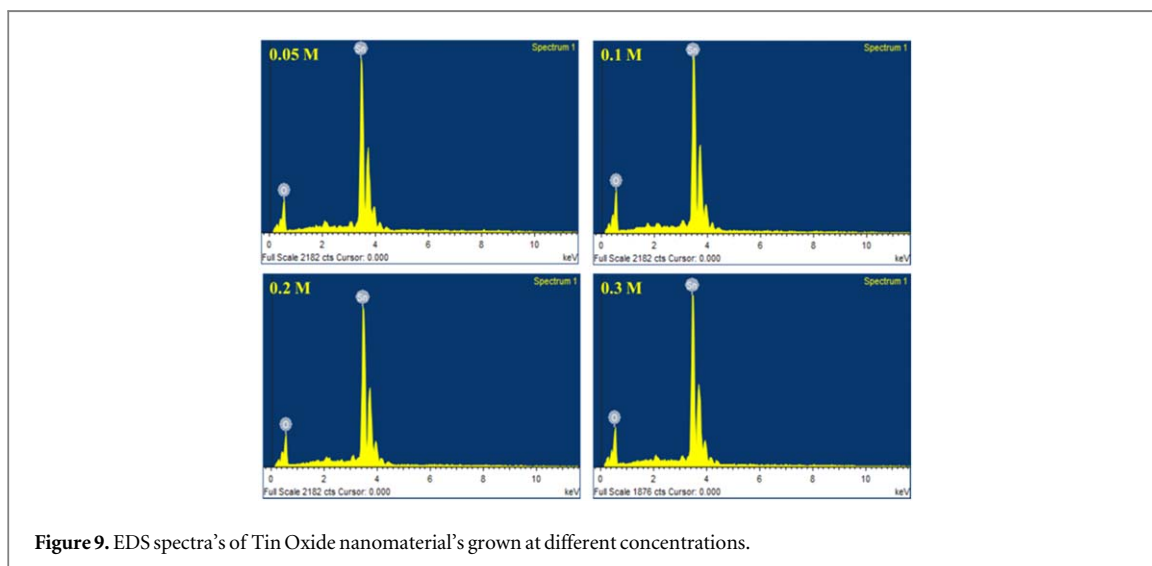


Figure 9. EDS spectra's of Tin Oxide nanomaterial's grown at different concentrations.

5. Conclusion

In this investigation, the effects of the concentration of Sn precursor on structural, morphological, elemental, and optical properties were studied. XRD reveals the formation of a tetragonal structure with an increase in crystallite size upon an increase in concentration. (110), (101) and (211) reflections show their prominent presence in diffractograms. The average crystallite size obtained using the Scherer formula shows an increment with an increase in concentration. Dislocation density and microstrain exhibit an inverse relationship with crystallite size. The Williamson–Hall method was used to obtain the crystallite size, stress, strain, and deformation energy density. UDM, USDM and UDEDM these three models were used. Crystallite size and strain obtained using the W-H method show good agreement with the Scherer method. The band gap obtained using the Tauc method varies from 3.42 eV to 3.57 eV. Agglomerated globular morphology was seen in SEM imagery. EDS confirms the presence of Sn and O in synthesized nanomaterial.

Data availability statement

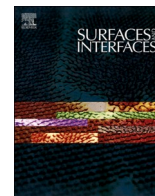
The data cannot be made publicly available upon publication because no suitable repository exists for hosting data in this field of study. The data that support the findings of this study are available upon reasonable request from the authors.

ORCID iDs

Lalita Deshmukh  <https://orcid.org/0009-0007-1593-2280>

References

- [1] Medhi R, Marquez M D and Lee T R 2020 *ACS Appl. Nano Mater.* **3** 6156–85
- [2] Dheyab M A, Aziz A A, Jameel M S and Oladzadabbasabadi N 2022 *Surfaces and Interfaces* **28** 101677
- [3] Li Z *et al* 2019 *J. Am. Chem. Soc.* **141** 17610–6
- [4] Huang Z, Zhu J, Hu Y, Zhu Y, Zhu G, Hu L, Zi Y and Huang W 2022 *Nanomaterials* **12** 632
- [5] Chiu H C and Yeh C S 2007 *J. Phys. Chem. C* **111** 7256–9
- [6] Afify N, Abbady G, Hamad D, Abdelbaki R F, Yousef E S, Shaaban E R and Abd-el Salam M N 2021 *Sensors Actuators A Phys.* **331** 112984
- [7] Hwang M S, Jeong B Y, Moon J, Chun S K and Kim J 2011 *Mater. Sci. Eng. B* **176** 1128–31
- [8] Giridasappa A, Shareef M I, Gopinath S M, Rangappa D, Shivaramu P D and Sabbanahalli C 2023 *Proc. Natl. Acad. Sci. India Sect. B Biol. Sci.* 2023, 1–12
- [9] Xin Y, Pan S, Hu X, Miao C, Nie S, Mou H and Xiao W 2023 *J. Colloid Interface Sci.* **639** 133–44
- [10] Divya J, Pramothkumar A, Joshua Gnanamuthu S, Bernice Victoria D C and Jobe prabakar P C 2020 *Phys. B Condens. Matter* **588** 412169
- [11] Meng J K, Wang W W, Wang Q C, Cao M H, Fu Z W, Wu X J and Zhou Y N 2019 *Electrochim. Acta* **303** 32–9
- [12] Palanisamy M, Jamison C, Sun X, Qi Z, Wang H and Pol V G 2021 *Carbon N. Y.* **185** 608–18
- [13] Ning S, Wang J, Xiang D, Huang S, Chen W, Chen S and Kang X 2021 *J. Catal.* **399** 67–74
- [14] Vázquez-López A, Maestre D, Ramírez-Castellanos J, González-Calbet J M, Piš I, Nappini S, Yuca N and Cremades A 2020 *J. Phys. Chem. C* **124** 18490–501
- [15] Manimaran M, Muthuvel A and Said N M 2022 *Nanotechnol. Environ. Eng.* **8** 1–11
- [16] Ullah S *et al* 2022 *ACS Appl. Nano Mater.* **5** 7822–30
- [17] Zhang Z, Gao Z, Fang R, Li H, He Wei and Du C 2020 *Ceramic Interanational* **46** 2255–60
- [18] Zhang Z, Gao Z, Fang R, Li H, He W and Du C 2020 *Ceram. Int.* **46** 2255–60
- [19] Kumar P, Khadtare S, Park J and Yadav B C 2020 *Mater. Lett.* **278** 128451
- [20] Hong M, Chen Z G, Yang L, Chasapis T C, Kang S D, Zou Y, Auchterlonie G J, Kanatzidis M G, Snyder G J and Zou J 2017 *J. Mater. Chem. A* **5** 10713–21
- [21] Amutha T, Rameshbabu M, Muthupandi S and Prabha K 2022 *Mater. Today Proc.* **49** 2624–7
- [22] Ahmed A, Siddique M N, Ali T and Tripathi P 2019 *Appl. Surf. Sci.* **483** 463–71
- [23] Rehani D, Saxena M, Solanki P R and Sharma S N 2022 *J. Supercond. Nov. Magn.* **35** 2573–81
- [24] Dar M A, Mala N A, Bhat M Y, Ahamed S R, Reshi B A, Ashok M and Rather A A 2023 *Appl. Surf. Sci. Adv.* **13** 100360
- [25] Cullity B D 1956 *Elements Of X Ray Diffraction* (United States of America: PEARSON)
- [26] Habte A G, Hone F G and Dejene F B 2020 *Phys. B Condens. Matter* **580** 411832
- [27] Gonçalves N S, Carvalho J A, Lima Z M and Sasaki J M 2012 *Mater. Lett.* **72** 36–8
- [28] Yogamalar R, Srinivasan R, Vinu A, Ariga K and Bose A C 2009 *Solid State Commun.* **149** 1919–23
- [29] Nath D, Singh F and Das R 2020 *Mater. Chem. Phys.* **239** 122021
- [30] Cazzani A and Rovati M 2005 *Int. J. Solids Struct.* **42** 5057–96
- [31] Nye J F 1957 *Physical Properties of Crystals: Their Representation by Tensors and Matrices* (Oxford University Press London)
- [32] Gürakar S and Serin T 2019 *Mater. Sci. Eng. B Solid-State Mater. Adv. Technol.* **251** 114445



Bimetallic $\text{Co}_3\text{V}_2\text{O}_8$ microstructure: A versatile bifunctional electrode for supercapacitor and electrocatalysis applications

R.A. Kadam^{a,1}, M.A. Yewale^{b,1}, A.M. Teli^c, Annu^b, U.T. Nakate^{d,*}, V. Kumar^b, S.L. Kadam^{a,*}, D.K. Shin^{b,*}

^a Department of Physics, Ahmednagar college, Ahmednagar 414001, India

^b School of Mechanical Engineering, Yeungnam University, Gyeongsan 38541, South Korea

^c Division of Electronics and Electrical Engineering, Dongguk University, Seoul 04620, South Korea

^d Department of Polymer Nano Science and Technology, Jeonbuk National University, 567 Baekjeaero, Deokjin-gu, Jeonju-si, Jeollabuk do 54896, South Korea

ARTICLE INFO

Keywords:

$\text{Co}_3\text{V}_2\text{O}_8$ nanoparticles
Hydrothermal
Supercapacitor
HER
OER
XPS
HRTEM

ABSTRACT

Our research focuses on hydrothermally synthesizing a bimetallic cobalt vanadium oxide $\text{Co}_3\text{V}_2\text{O}_8$ (CVO) microstructure, tailoring it for use in both bifunctional supercapacitor and electrolysis applications. We carefully optimized the molar ratio of Co and V to achieve a hexagonal microstructure for $\text{Co}_3\text{V}_2\text{O}_8$, confirming it through field emission scanning electron microscopy (FESEM) and High resolution transmission electron microscopy (HRTEM) studies. The optimized electrode exhibited exceptional electrochemical characteristics when utilized in a supercapacitor application. It demonstrated a superior areal capacitance of 3.76 F/cm^2 at a current density of 1 mA/cm^2 . Subsequently, we utilized the optimized electrode in an asymmetric supercapacitor configuration with activated carbon (AC), resulting in an areal capacitance of 126.1 mF/cm^2 and an energy density of 29.6 mWh/cm^2 at a power density of 2.6 W/cm^2 . To assess the stability of this configuration, we conducted 5000 cycles at 5 mA/cm^2 and observed a retention rate of 87%. Additionally, we investigated the effectiveness of the optimized electrode as an electrocatalyst for water oxidation in a 1 M KOH electrolyte. In this setup, the CVO-4 electrode exhibited a lower overpotential of 226 mV for the hydrogen evolution reaction (HER) and a Tafel slope of 178 mV/dec for HER. Overall, our findings indicate that the as-prepared optimized electrode operates highly efficiently in bifunctional applications, positioning it as a promising candidate for energy conversion and storage operations.

1. Introduction

Increasing industrialization and the use of fossil fuel-powered vehicles have given rise to the most severe issues of global warming and energy crises. The usage of hybrid vehicles equipped with low-cost energy storage devices and energy sources can alleviate these issues. Various electrochemical devices with different functionalities can be built by combining electrodes with active materials and electrolytes containing diverse components. Examples of these technologies include solar cells, sensors, batteries, photo electrochemical cells, and supercapacitors [1,2]. Supercapacitors, also known as ultracapacitors, possess unique properties that make them a viable long-term alternative energy storage solution. In the future, supercapacitors (SCs) and hydrogen energy will emerge as excellent choices for energy storage and

consumption. Hydrogen, which is ecologically acceptable and has high density, can be regarded as a green energy source, and it can be generated through the process of water electrolysis via the hydrogen evolution reaction (HER). Therefore, synthesizing nanomaterial electrodes with high output for SCs and HER assumes importance [3]. The researchers directed their focus toward developing a bifunctional material for energy strategies that encompass both supercapacitors and hydrogen generation through electrocatalysis. Water electrolysis is the process through which hydrogen, regarded as a clean energy source, is obtained. In this process, water splitting occurs through two half-cell reactions, transpiring at the cathode and anode, respectively, resulting in the production of hydrogen and oxygen. Theoretically, full water splitting takes place at 1.23 V with a current density of 10 mA/cm^2 . Up to this point, platinum has demonstrated exceptional electrocatalytic

* Corresponding authors.

E-mail addresses: umesh.nakate@gmail.com (U.T. Nakate), mr.sukadeo@rediffmail.com (S.L. Kadam), dkshin@yu.ac.kr (D.K. Shin).

¹ These authors contributed equally to this work.

activity for the hydrogen evolution reaction (HER), but its high cost poses a hindrance to commercial production [4,5]. Rechargeable batteries, with their high energy density, have been widely adopted as common energy storage technologies in recent decades, alongside supercapacitors (SCs). SCs are gaining popularity as an alternative to rechargeable batteries due to their quick charging time and high power density. Currently, achieving high energy density, stability, and a reasonable price is the primary requirement for commercial energy storage SCs. Researchers are extensively exploring novel electrode materials to enhance energy density. Nanomaterial-based efficient electrodes play a crucial role as catalysts for the hydrogen evolution reaction (HER) and oxygen evolution reaction (OER) processes [6]. There are two types of SCs based on their capacitive behavior: pseudocapacitors (PCs) and electric double-layer supercapacitors (EDLCs). PCs involve a redox reaction as their charge storage mechanism, which can be further divided into two subparts: the bulk process and the surface process. The charging mechanism of PCs consists of three components: monolayer ion adsorption at the electrode surface, surface redox reaction, and ion intercalation [7]. The transition metal oxides, such as CuO [6], Co₃O₄ [8], Mn₃O₄ [9], NiO [10], NiCo₂O₄ [11,12] and similar materials, have captured the attention of researchers in the field of pseudocapacitors (PCs). In the case of electric double-layer supercapacitors (EDLCs), the electrical double-layer capacitance is generated at the electrode-electrolyte interface through fast ion adsorption and desorption. Electrode materials with high surface areas exhibit superior charge storage capacities [13]. Carbon-based electrode materials, such as graphene, graphene oxide, reduced graphene oxide, carbon nanotubes, and various metal oxides, shows their charge storage mechanism in EDLCs. Currently, the focus of research is on studying bimetallic metal oxides instead of single metal oxide nanoparticles. This shift in focus is driven by the fact that bimetallic metal oxides exhibit different oxidation states and enhanced conductivity, leading to the generation of extraordinary energy storage capacities through their synergetic effects. Several research articles [1,14–18] have reported on the utilization of bimetallic metal oxides in the field of energy storage, such as NiCo₂O₄ [19], MnCo₂O₄ [20], MoMn-oxide [21], BiMnO₃ [22], Ni₂V₃O₈ [23], MoVMnAg-oxide [24], MnCo-LDH [25], S-NiCo-LDH [26], NiCo₂O₄/NiMoO₄ [27,28] nickel cobalt molybdenum copper oxide [29] electrodes for asymmetric supercapacitors demonstrate excellent energy storage capacity. In recent studies, the attention has shifted towards higher metal oxide or tri-metal oxide materials because of their intriguing properties. It has been found that higher-order metal oxides can introduce defects, which enhance the redox reactions and result in increased electrical conductivity of the electrode material. This increased electrical conductivity plays a significant role in enhancing the energy storage capacity [30,31]. Cobalt vanadium oxide (CVO) has been used for energy storage applications due to its excellent capacitance compared to other metal oxides. Additionally, CVO maintains a non-zero oxidation state for vanadium and demonstrates a strong binding between vanadium and oxygen. Furthermore, cobalt-based oxide exhibits high capacitance, environmentally friendly properties, excellent redox chemistry, and stable chemical properties, and is abundantly available. Therefore, CVO is considered an appropriate material for energy storage applications [32]. Several articles reported the different microstructures cobalt vanadium oxide (CVO) nanorose [33], CVO multilayer nano sheet [34], CVO microsphere [35], CVO nanosheets [36], CVO-mesoporous nanoparticles [37], are reported for energy storage application.

S. Chandra Sekhar has reported the development of a multifunctional binder-free electrode, Co₃V₂O₈, for a hybrid supercapacitor and Li-ion battery. The researchers grafted nano hexagonal Co₃V₂O₈ prisms onto copper vanadium oxide nanorod arrays that were grown on copper foam through solution processing. The hybrid Co₃V₂O₈ supercapacitor exhibits excellent electrochemical properties, demonstrating a good areal capacitance of 0.464 F/cm² and excellent cyclic stability. Furthermore, the hybrid supercapacitor delivers a remarkable energy density of 0.092

mAh/cm² at a power density of 24.40 mW/cm² [2]. Z. Fahimi et al. used the hydrothermal method to prepare a sphere with mesoporous walls containing Co₃V₂O₈ nanoparticles. They fabricated the hybrid supercapacitor using the optimum electrode and activated carbon electrode. The hybrid supercapacitor demonstrated an energy density of 59.2 Wh/kg and a power density of 36.6 kW/kg, while also exhibiting excellent electrochemical stability over 10,000 cycles [32]. W. Fang reported on the very effective catalysis of the hydrogen evolution process (HER) by a vanadium cobalt bimetallic metal oxide framework [5]. and, Z. Lue et colleagues prepared cobalt vanadium oxide nanosheets for total water splitting using the hydrothermal technique [38]. The aim of this article is to investigate how different cobalt-to-vanadium ratios affect the electrochemical performance and hydrogen evolution reaction (HER) in the context of electrochemical storage and electrocatalytic activity.

In this study, we utilize the hydrothermal technique with urea to prepare the electrode material, employing four different Co/V ratios. We analyze the electrode material using techniques such as X-ray diffraction (XRD), Field emission scanning electron microscopy (FE-SEM), energy dispersive X-ray spectroscopy (EDS), High resolution transmission electron microscopy (HRTEM), and X-ray photoelectron spectroscopy (XPS). To evaluate the electrochemical properties of the electrode material, we employ cyclic voltammetry (CV), galvanometric charge and discharge (GCD), and electrochemical impedance spectroscopy (EIS). The power law and duns approach are used to investigate the charge contribution and surface and diffusion current contributions, respectively. Additionally, we assess the HER/OER performance of the electrode material in a 1 M KOH electrolyte using linear sweep voltammetry (LSV). The results highlight the significant impact of the cobalt-to-vanadium ratio on the electrochemical performance of the electrode material. This study offers valuable insights for future research in this field.

2. Materials and methods

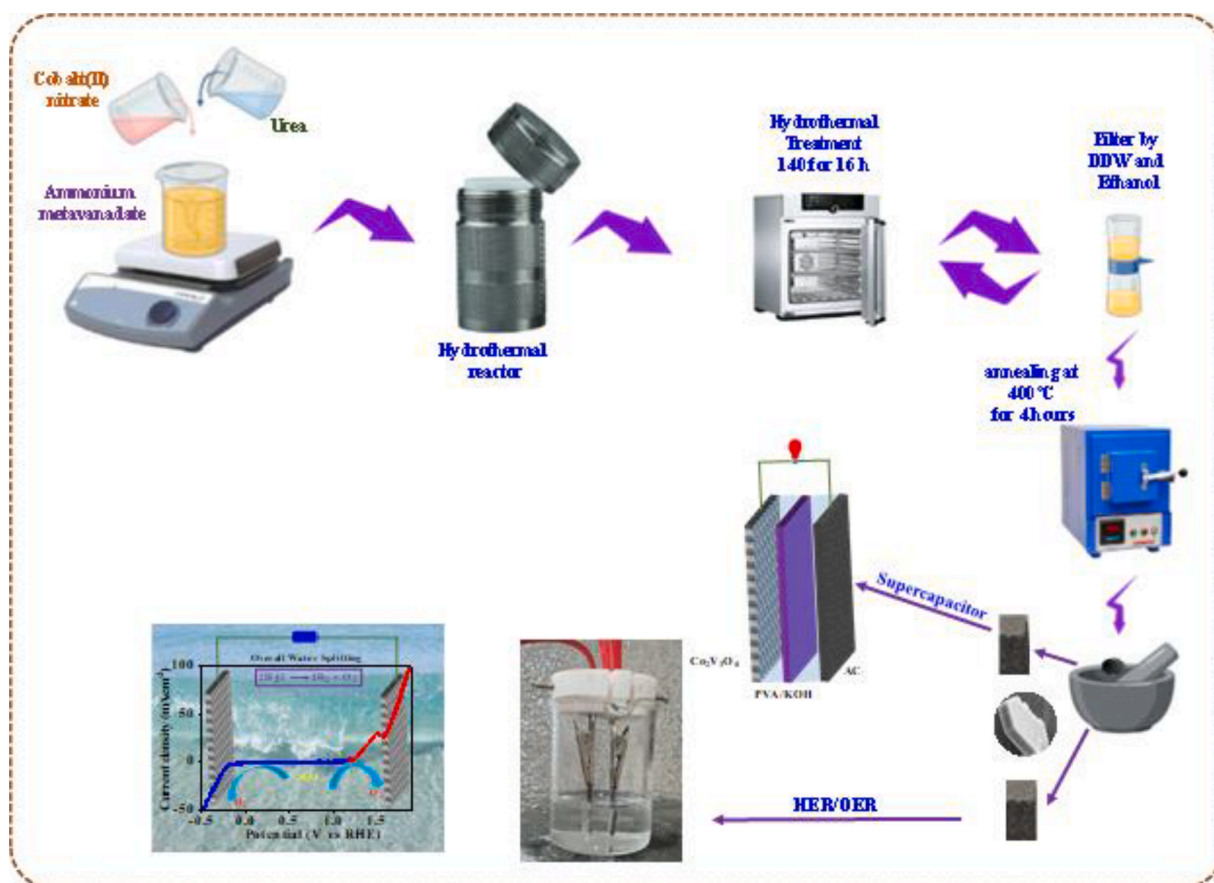
2.1. Materials

All chemicals, particularly cobalt nitrate hexahydrate (Co(NO₃)₂·6H₂O (98%), urea (CO(NH₂)₂) (99%), ammonium metavanadate (NH₄VO₃) (99%), acetone (CH₃CO) (99%), ethanol (C₂H₆O) (99.5%), polyvinylidene fluoride (PVDF), N-Methyl-2-pyrrolidone (NMP) and potassium hydroxide (KOH) (85%), has sourced from Sigma-Aldrich and used without extra purification processing, purchased from Daejung Chemical in the Republic of Korea supplied hydrochloric acid (HCL).

2.2. Sample preparation

2.2.1. Synthesis of the Co₃V₂O₈

The Co₃V₂O₈ samples were synthesized through a simple hydrothermal method. Firstly, a homogeneous solution was prepared by dissolving 0.12 M cobalt nitrate hexahydrate (Co(NO₃)₂ · 6H₂O), 0.06 M ammonium metavanadate (NH₄VO₃), and 0.560 M urea (CO(NH₂)₂) in 50 ml of deionized (DI) water at room temperature (300 K) with constant stirring. The solution was then transferred into a Teflon-lined steel mold (100 ml) and subjected to a hydrothermal reaction in an oven at 140 °C for 16 h. The hydrothermal reactor was allowed to cool gradually to room temperature. Afterward, the product was extracted using filter paper and meticulously washed with DI water and ethanol several times, resulting in a refined material. The collected samples were subsequently annealed at 400 °C for 4 h and designated as CVO-1. Furthermore, other microparticle variants, including CVO-2, CVO-3, and CVO-4, were synthesized using a similar approach, but with different concentrations of ammonium metavanadate (NH₄VO₃) of 0.12 M, 0.180 M, and 0.24 M, respectively, each exhibiting distinctive characteristics. The same nomenclature was adopted throughout the manuscript for easy identification. [Scheme 1](#) provides a schematic representation of the



Scheme 1. Schematic of the hydrothermal synthesis of $\text{Co}_3\text{V}_2\text{O}_8$ nanoparticles.

hydrothermal synthesis of $\text{Co}_3\text{V}_2\text{O}_8$ microparticles.

2.3. Material characterization

The crystal structure and phase development of the microparticles were examined using X-ray diffraction (XRD; PANalytical) with CuK radiation. Field-emission scanning electron microscopy was used to analyze the surface morphology and elemental mapping of the nanoparticles (FE-SEM; S-4800 HITACHI, Ltd., Japan). The surface chemical composition was examined using X-ray photoelectron spectroscopy (XPS; K-alpha, Thermo Scientific, UK). High-resolution transmission electron microscopy was used to examine element mapping and surface morphology further (HRTEM; Tecnai F21, FEI Company), Nitrogen adsorption-desorption was performed at 77.2 K to obtain the Brunauer-Emmett-Teller (BET) specific surface area (Micromeritics; 3-flex analyzer). Electrochemical measurements such as cyclic voltammetry (CV), electrochemical impedance spectroscopy (EIS), galvanostatic charge/discharge (GCD), linear sweep voltammetry (LSV), and cyclic stability measurements were performed on a ZIVE SP5 electrochemical workstation. These measurements were carried out in a conventional three-electrode arrangement consisting of a platinum counter electrode, the active material as a working electrode, and an Ag/AgCl reference electrode (WonAtech).

2.4. Electrode preparation

The fabrication of the working electrode was undertaken with utmost precision and care to enable a thorough analysis of the active material's electrochemical performance. A slurry of the active material (CVO), PVDF, and carbon black (CB) in an 80:10:10 ratio was prepared using an NMP solution and used to construct the electrode. To ensure a

pristine electrode surface, the $2 \times 1 \text{ cm}^2$ area of Ni-foam was thoroughly cleaned with hydrochloric acid to eliminate any impurities. The dried Ni-foam substrate was then used for the final electrode preparation. The active material slurry was drop-cast onto the Ni substrate's $1 \times 1 \text{ cm}^2$ active area and subjected to an overnight drying process at 60°C prior to electrochemical analysis. The mass loaded on the Ni foam was 8.3 mg for CVO-1, 11.6 mg for CVO-2, 9.8 mg for CVO-3, and 6.46 mg for CVO-4 electrodes. For the two-electrode system, KOH and PVA electrolytes were utilized. The electrolyte was prepared by dissolving 2 g of PVA in 20 ml of water for 1 hour at 80°C . Afterward, 5 ml of a 2 g KOH solution was added to the above solution, and the mixture was heated for an additional hour. Two electrode devices were fabricated, consisting of the positive electrode, the negative electrode, and the PVA-KOH electrolyte. The two terminals were retained as positive and negative terminals for the electrochemical evaluation of the device. The fabricated device was then used for the electrochemical study, ensuring optimal electrode fabrication for reliable and accurate results.

2.5. Equations

The areal capacitance of the electrode and ASC device were calculated from the following equation from CV profile [32,39,40].

$$\text{Areal capacitance} = \frac{\int idV}{2 \times v \times A \times \Delta V} \quad (1)$$

The areal capacitance, energy density and power density of the electrode and ASC of device were calculated from the following equation

$$\text{Areal capacitance} = \frac{2 \times T_d \times i}{V \times A} \quad (2)$$

$$\text{Energy Density } (ED_a) = \frac{V^2 \times C_{areal}}{7.2} \quad (3)$$

$$\text{Power Density } (PD_a) = \frac{3600 \times ED_a}{T_d} \quad (4)$$

Where 'i' is the current, m is the mass loaded on electrode, ΔV is the potential window of the CV profile, ν is the scan rate of the, A is area of the electrode, T_d is the discharge time, V is the potential window of GCD profile.

3. Result and discussion

3.1. XRD analysis

The phase evolution of the prepared sample was evaluated using XRD analysis. Fig. 1 shows the XRD pattern of all CVO microparticles. The XRD spectrum indicates that the molar concentration of ammonium metavanadate has an influence on the crystal structure. The XRD pattern reveals all CVO microparticles have a polycrystalline nature. The XRD spectra of CVO-1, CVO-2, and CVO-3 show diffraction peaks at 30.49, 35.83, 43.42, and 63.62°, which are attributed to the planes (220), (311), (400), and (440). The XRD spectra of CVO-1, CVO-2, and CVO-3 are in good agreement with JCPDS card 0160–675 [31], confirming the cubic phase of $\text{Co}_3\text{V}_2\text{O}_8$. In the CVO-4 XRD spectra, exhibited diffraction peaks at 26.34, 27.57, 29.55, 30.99, 32.84, 35.09, 35.87, 43.61, 57.67, 63.67, and 77.67°. These peaks correspond to the planes of $\text{Co}_2\text{V}_3\text{O}_8$ (220), (211), (002), (140), (231), (320), (400), (520), (024), and (622), respectively, as identified by the JCPDS card No 01–074–1486 with an orthorhombic crystal structure [41]. While observing the CVO microparticles at different concentrations (CVO-1, CVO-2, and CVO-3), no significant changes were observed. However, in CVO-4, an additional peak was observed at 26.46, 27.61, 29.61, 32.94, and 35.14°. The increase in the vanadium concentration results in intensity growth and a little bit of peak shift. Moreover, a phase change from cubic to orthorhombic were noticed with an increase in vanadium concentration. The increased peak intensity of the (220), (211), (002), (040), and (140) planes confirms the enhanced crystallinity of the $\text{Co}_3\text{V}_2\text{O}_8$ microparticles with increasing molar concentration. M Akram reported a similar impact of molar concentration on crystallinity [42]. The concentration had an influence on the surface microstructure and crystalline structure. The XRD analysis demonstrates that CVO-4 possesses an orthorhombic crystal structure and CVO-1, CVO-2, and CVO-3 have a cubic crystal

structure which influences the electrochemical performance.

3.2. XPS analysis

XPS analysis was conducted to investigate the nanocrystal involvement and electronic state. Fig. 2a presents the survey spectra of CVO-4 microparticles. The survey spectra exhibited peaks at 517.81 eV, 530.26 eV, 779.24 eV, and 284.16 eV, indicating the presence of V2p, O1s, Co2p, and C1s, respectively. Fig. 2b shows the spin-orbit splitting of the V2p, The V2p_{3/2} with two peaks observed at 515.63 eV and 516.67 eV, representing the V⁴⁺ and V⁵⁺ oxidation states, respectively. The V2p_{1/2} two peaks were observed at 522.85 eV and 523.99 eV representing the V⁴⁺ and V⁵⁺ oxidation states, respectively [43,44]. In Fig. 2c, the spin-orbit splitting spectra of Co2p are depicted. The two peaks observed at 795.64 eV and 779.68 eV, with a peak separation of 16.07 eV, correspond to the Co2p_{1/2} and Co2p_{3/2} states, respectively. Additionally, peaks were observed at 795.54 eV and 779.43 eV, confirming the presence of the Co²⁺ state, while peaks at 797.07 eV and 781.14 eV indicate the presence of the Co³⁺ state. The two shake-up satellite peaks observed at 802.38 eV and 785.99 eV align well with the reported results, confirming the existence of the Co²⁺ oxidation state [43]. A Co³⁺/Co²⁺ ratio of over 1.09 for Co2p_{3/2} and 1.04 for Co2p_{1/2} suggests the presence of an oxygen surface [45]. Fig. 2d illustrates the deconvolution spectrum of O1s. The prominent peaks in the O1s spectra are observed at 529.0 eV, 529.54 eV, and 531.21 eV. The peak at 531.21 eV (O_{III}) indicates the presence of hydrated species on the nanoparticle surface. The peak at 529.54 eV (O_{II}) represents adsorbed oxygen species, while the peak at 529.0 eV (O_I) corresponds to lattice oxygen [43].

3.3. Surface morphology

Field electron Scanning Electron Microscopy (FESEM) was used to examine the surface morphology and particle size of the nanoparticles. The surface FESEM microstructure of all CVO microparticles is depicted in Figure S1 (Supporting Information S.I.). The synthesized microparticles exhibited a hexagonal shape with varying thicknesses. Changes in the Co/V concentration ratio led to modest tailoring of the surface microstructure. The structure and uniformity of particle dispersion varied with the Co/V ratio ranging from 2 to 0.5. At a Co/V ratio of 2, a nonuniform hexagonal microstructure with tiny surface overgrowth was observed, having an average thickness of 514 nm. When the Co/V ratio was changed to 1 and 0.66, the growth on the discs increased, resulting in thicknesses of 547 nm and 830 nm, respectively. As the Co/V ratio approached 0.5, a complete hexagonal microstructure of CVO nanoparticles with an average thickness of 1.232 micrometers and an average length of 4.07 micrometers was observed, as shown in Figure S1 and Fig. 3a. The average crystallite structure increased with the concentration of ammonium metavanadate. Fig. 3 (a-e) illustrates the FESEM of CVO-4 nanoparticles. J. Rajesh observed an increase in crystallite structure size as the precursor's concentration increased [46]. The volume of the disk increased with the thickness, providing a greater surface area and active site for electrolyte and electrode interaction. This effect was reflected in the electrochemical performance of the electrode material. The elemental composition of the electrode was examined using EDS measurements. Fig. 3f illustrates the EDS spectra showing the elemental content of the CVO-4 nanoparticles. The sharp peaks of Co, V, and O are also visible in the EDS spectra, indicating the presence of all CVO nanoparticles and their variation with the precursor concentration. Figure S2 depicts the EDS spectra of CVO-1, CVO-2, CVO-3, and CVO-4.

High resolution Transmission Electron Microscopy (HRTEM) was employed to examine the structural and surface differences of the hexagonal microstructure of CVO-4 nanoparticles, along with their elemental composition. Figure 3(g-n) illustrates a HRTEM micrograph of CVO-4 nanoparticles at various magnifications. Fig. 3g shows the edge of the hexagonal microstructure. Figs. 3h and 3k reveal a compact arrangement of nanoparticles within the hexagonal microstructure, with

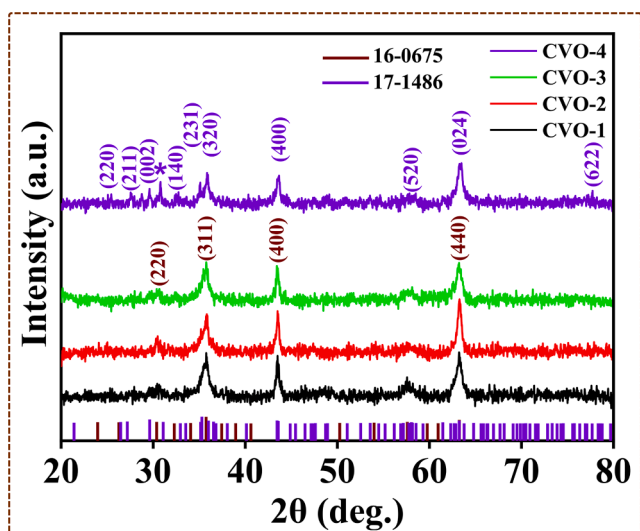


Fig. 1. XRD spectra of CVO-1, CVO-2, CVO-3 and CVO-4 nanoparticle for different Co/V molar ration.

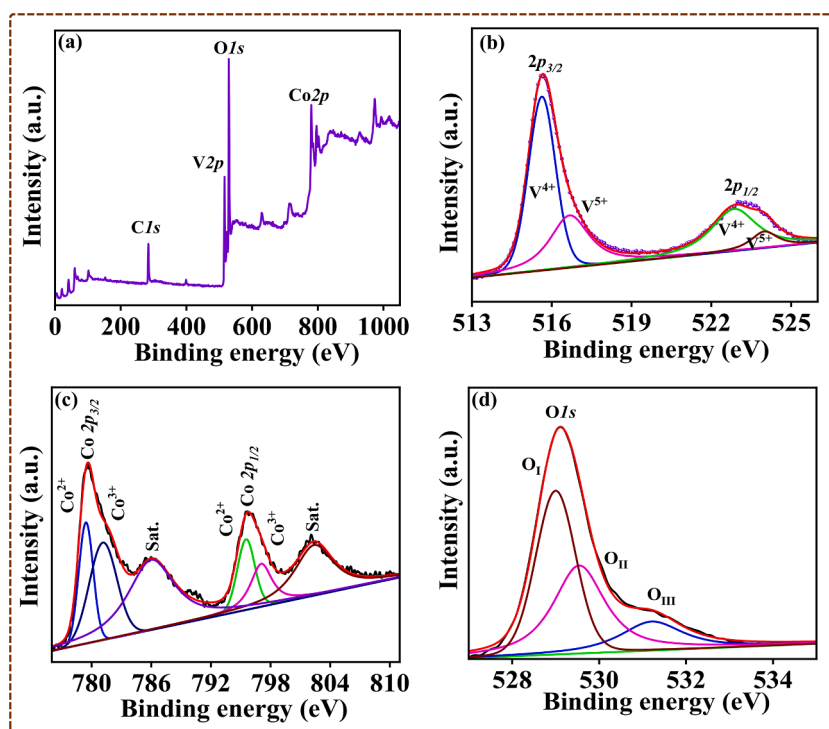


Figure.2

Fig. 2. (a) The high resolution XPS Survey spectra (b) V2p spectra, (c) Co2p spectra (d) O1s XPS core level spectra of CVO-4 nanoparticle.

small gaps between them. The presence of small surface pores provides areas for ion intercalation and charge storage, thereby increasing the storage capacity of the CVO-4 electrode material compared to other electrodes in the electrochemical study. Fig. 3i presents the Selected Area Electron Diffraction (SEAD) pattern of the CVO-4 microparticles. The SEAD pattern confirms the crystalline nature of the CVO-4 microparticles. These results align with the findings from XRD analysis, which also indicated the crystalline nature of the CVO microparticles. High-Resolution TEM (HRTEM) measurements of CVO-4 microparticles were conducted to illustrate the lattice spacing of the two layers, as depicted in Fig. 3m and 3n. The HRTEM images reveal a lattice spacing of 0.52 nm corresponding to the (220) plane of the CVO-4 microparticles. The elemental composition of the CVO-4 microparticles was investigated using EDS spectra, shown in Fig 3 l. The presence of Co, V, and O peaks in the spectra confirms the existence of these elements in the CVO-4 microparticles. The EDS spectra align with the elemental composition of CVO-4, demonstrating near-stoichiometry with the chemical composition of $\text{Co}_3\text{V}_2\text{O}_8$. Furthermore, the surface area of the CVO-4 active material was calculated using the Brunauer-Emmett-Teller (BET) method. Figure S4 illustrates the N_2 adsorption-desorption isotherms of CVO-4 micro particles, which reveal a surface area of $13.10 \text{ m}^2/\text{g}$. The hexagonal disk-shaped microstructure, with its appropriate thickness, provides a substantial surface area that enhances electrochemical and electrocatalytic activities. The presence of large surfaces with hexagonal microstructures favors ion conduction, thereby improving the electrochemical and electrocatalytic performance.

3.4. Supercapacitance analysis

An electrochemical analysis of the electrode material was performed using a three-electrode configuration. The working electrode consisted of active materials, platinum served as the counter electrode, and Ag (AgCl) was used as the reference electrode. The purpose of this analysis was to examine the energy storage capacity of the electrode material. Figure S3 illustrates the cyclic voltammetry (CV) profile of the CVO

electrode in a 2 M KOH aqueous electrolyte, with scan rates ranging from 5 mV/s to 50 mV/s within a potential window of 0.0–0.5 V. All CV profiles of the electrodes exhibit visible oxidation and reduction peaks, indicating the occurrence of faradic reactions. The electrode material demonstrates pseudocapacitive properties, as evidenced by the non-rectangular shape of the CV curves. The CV profile shows a pair of redox peaks, which correspond to the redox reaction of $\text{Co}_3\text{V}_2\text{O}_8$ at the electrolyte interface. The equation representing the redox reaction at the electrode interface is as follows [32]. $\text{Co}_3\text{V}_2\text{O}_8 + 6\text{OH}^- \rightarrow 3\text{CoOOH} + \text{H}_3\text{V}_2\text{O}_8^{3-} + 3\text{e}^-$. The CV profile exhibits the same shape for all scan rates. Furthermore, the area beneath the CV profile expands monotonically with the scan rate, indicating strong electrochemical reversibility of the electrode. The comparative cyclic voltammetry (CV) profiles of the CVO electrodes are depicted in Fig. 4a. The CVO-4 electrode has a greater integral area under the CV profile than other CVO electrodes, indicating that it has superior redox activity and a higher energy storage capacity. The CVO-4 electrode may have a high energy storage capacity due to the synergistic impact of Co and V. The relationship between the peak current and the square root of the scan rate demonstrates a reasonable linear relationship, indicating the contribution of diffusion-controlled processes and the battery-type nature of the CVO electrode to the electrochemical current at a constant potential. Figure S4 illustrates that as the scan rate increases, the area under the curve expands, and the reduction and oxidation peaks shift towards lower or higher potential values. This behavior suggests that the redox reaction of the CVO electrode is quasi-reversible. The observed phenomena can be attributed to the high scan rate, which leads to charge polarization and ohmic resistance within the electrode material [47–50].

The galvanostatic charge-discharge (GCD) investigation was also conducted to examine the rate capability and areal capacitance of the CVO electrode. Fig. 4b illustrates the comparative GCD profiles of the CVO electrode. Among all the electrodes, the CVO-4 electrode exhibits a longer charge-discharge time. This can be attributed to its longer charging time and greater electrode surface area, which provide a larger active site for the electrochemical reaction [39]. The extended discharge

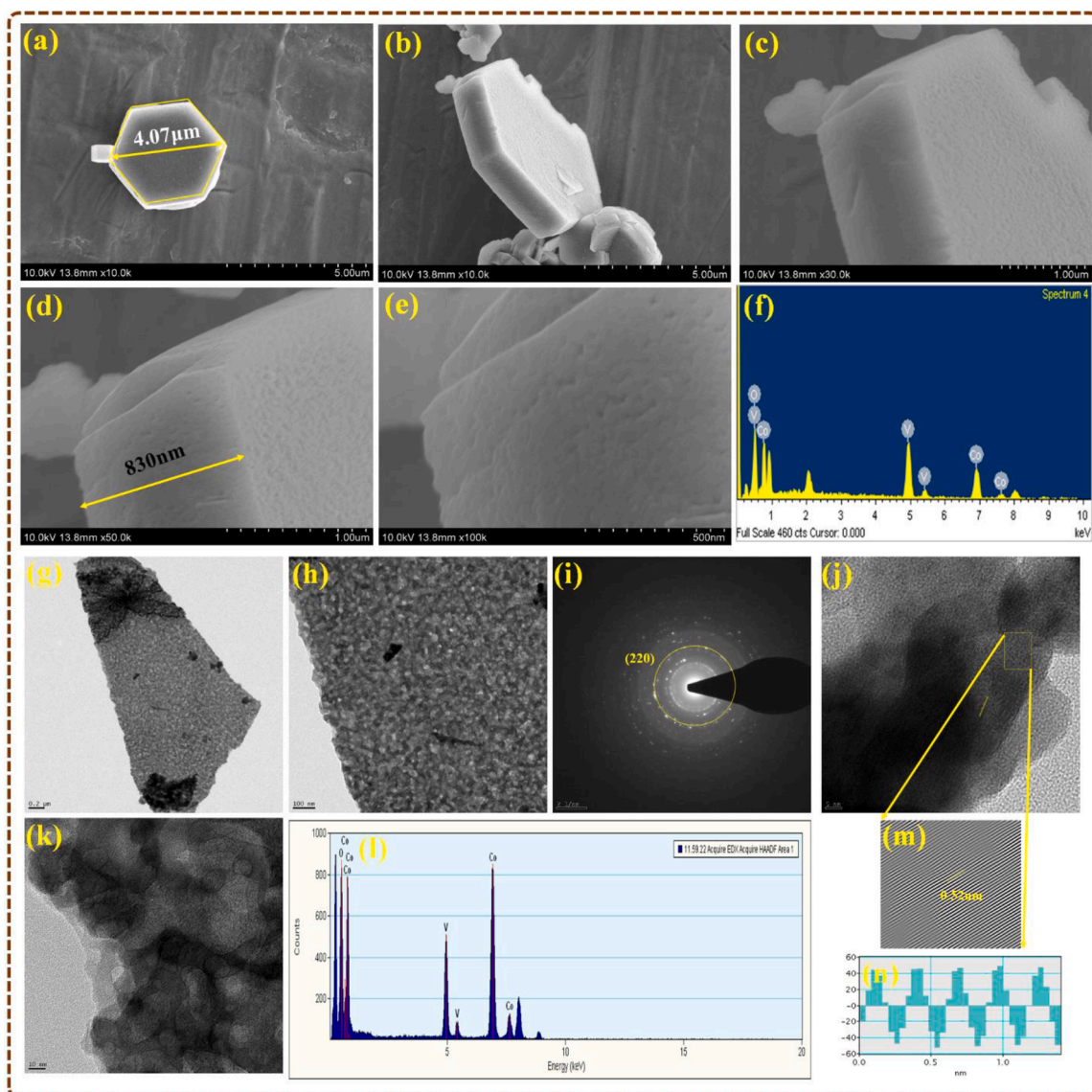


Fig. 3. (a-e) FESEM micrographs of CVO-4 nanoparticles at different magnifications, and (f) EDS spectra of CVO-4 nanoparticles, (g,h,k,j) HRTEM image of at different magnification, (i) SEAD pattern, (m,n) d spacing, (l) EDS spectra of CVO-4 nanoparticles.

time of the CVO-4 electrode may be attributed to the synergistic effect of Co and V, as well as the electro conductivity of $\text{Co}_2\text{V}_3\text{O}_8$. **Figure S5** presents the GCD profiles of all electrodes, which are nearly symmetrical, indicating a high energy storage capacity of the electrode material. The areal capacitance of the electrode material was estimated using Eq. (2). **Figs. 4c** and **4d** represent the comparative areal capacitance of the electrode at various scan rates and current densities. The specific capacitance of all electrode were listed in table 1, as the scan rate and current density increase, the areal capacitance of the electrode decreases. This is because the higher current density makes electrolyte diffusion and penetration more challenging. The table provides the capacitance values of the electrodes. **Figure S5** illustrates the GCD profiles of all electrodes at current densities ranging from 1 to 20 mA/cm^2 . The areal capacitance of the CVO-4 electrode is found to be greater than that of the other electrodes, as indicated by the analysis results. The porous surface structure of the CVO-4 electrode could account for this difference [51]. The electrochemical performance of the electrode material primarily relies on the ingress and egress of OH^- ions from the electrolyte through the porous electrode surface. SEM and TEM investigations reveal that the hexagonal surface of the CVO-4 electrode contains tiny pores that facilitate ion insertion and extraction. The

charge storage mechanism is capacitive with a diffusive contribution, which was explored by analyzing the peak current and scan rate of the CV profile. The charge distribution is quantified by the 'b' value, computed using the following equation, where 'b' represents the slope of the logarithm of peak current and the logarithm of the scan rate.

$$i = av^b \quad (5)$$

$$\log(i) = a + \log(v) \quad (6)$$

The 'b' value ranges between 0.5 and 1.0, representing the current distribution as diffusive, capacitive, or a combination of both. A 'b' value of 0.5 describes the charging and discharging process primarily driven by diffusion, while a 'b' value of 1.0 indicates a pseudocapacitive charging and discharging mechanism. In **Fig. 4e** and **4f**, the logarithm of peak current is plotted against the logarithm of the scan rate to determine the 'b' value. **Table 1** shows that the 'b' value ranges from 0.5 to 0.56. For the CVO-4 electrode, the 'b' value is 0.51, indicating that ion diffusion is the dominant process during charging and discharging. The porous hexagonal microstructure of CVO-4 is advantageous for ion diffusion and charge storage. The $b = 0.5$ value of the CVO electrode suggests that it undergoes charging primarily through diffusion. By

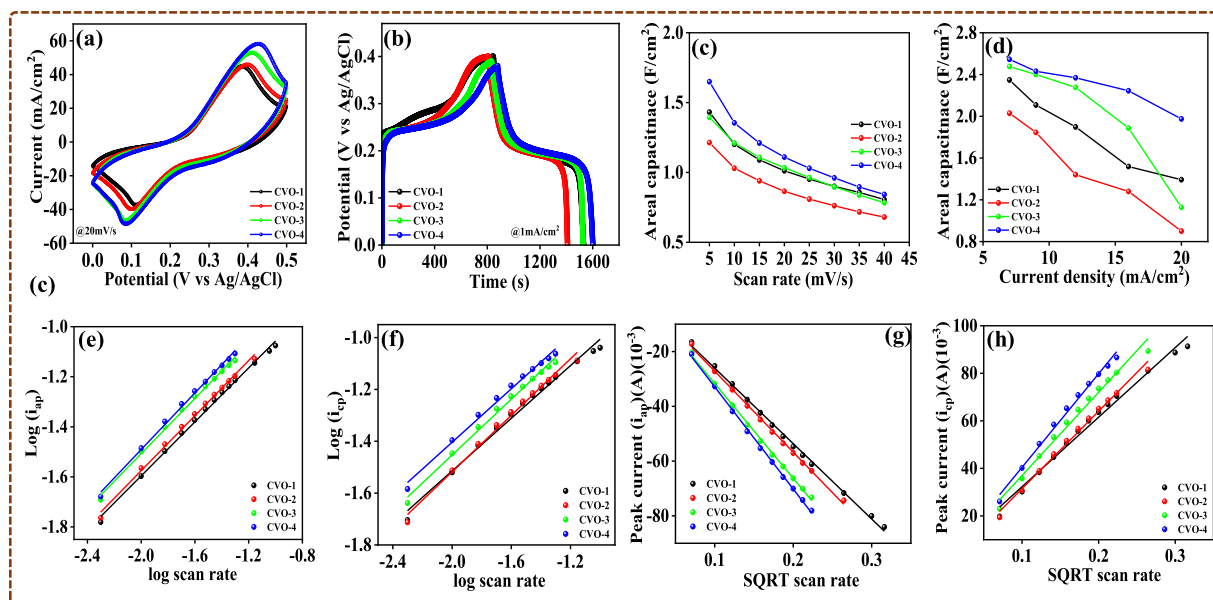


Fig. 4. (a) Comparative CV profile, (b) comparative GCD profile, (c) Comparative areal capacitance from CV, and (d) Comparative areal capacitance from GCD, (e,f) $\log(i_p)$ vs \log scan rate cathodic and anodic, (g,h) peak current(i_p) vs \sqrt{v} cathodic and anodic of CVO-1, CVO-2 CVO-3 and CVO-4 nanoparticles.

Table 1

Areal capacitance (GCD), b value, standard rate constant (K^0), diffusion coefficient (D), series resistance of CVO-1, CVO-2, CVO-3, and CVO-4.

Sample Code	Areal Capacitance F/cm ²	Specific capacitance F/g	b value	Standard rate constant (K^0) cm/S	Diffusion coefficient 10^{-4} cm ² /S	Series resistance Ω
CVO-1	1.24	150	0.53	2.43	5.46	2.14
CVO-2	1.51	130	0.54	2.18	6.07	2.31
CVO-3	1.75	182	0.53	2.41	6.53	2.19
CVO-4	1.92	195	0.51	2.64	7.28	2.11

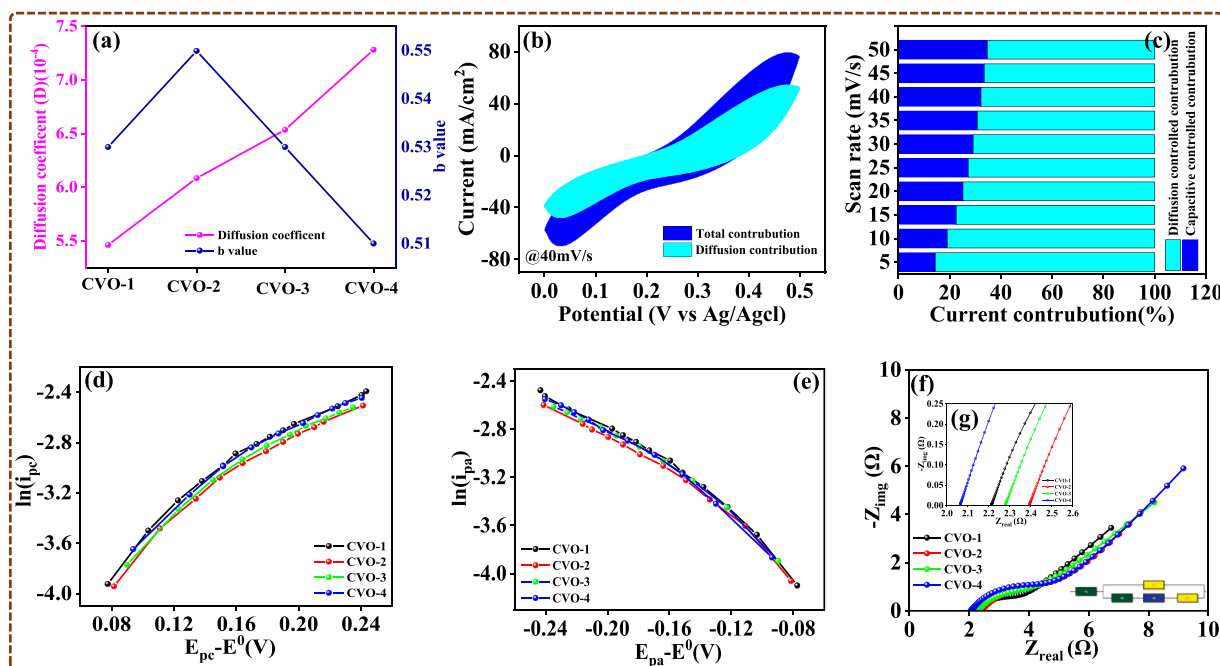


Fig. 5. (a) Diffusion coefficient and b value of CVO-1, CVO-2 CVO-3 and CVO-4 nanoparticles (b) Diffusive contribution at 40 mV/s (c) capacitive and diffusion-controlled charge at different scan rates of CVO-4 electrode, (d,e) $\ln(i_p)$ vs $E_{pc}-E^0$ plot for cathodic and anodic, (f) EIS spectra of CVO-1, CVO-2 CVO-3 and CVO-4 nanoparticles.

varying the scan rate of the CV profile, the diffusion coefficient of the electrode material can be determined, which reflects its charge transfer kinetics. The diffusion coefficient of the electrode can be calculated using the following equation: The diffusion coefficient represents the movement of K^+ ions into the electrode.

$$i_p = 0.4463 \times A \times C \times F \times n \times \sqrt{\frac{nFvD}{RT}} \quad (7)$$

Where D is the diffusion coefficient, i_p is the peak current, A is the electrode area, C is the electrolyte concentration, F is the faraday constant, R is the universal gas constant, v is the scan rate, T is the temperature, and n is the available number of electrons for redox processes. To compute the diffusion coefficient acquired from the slope of the i_p vs \sqrt{v} plot and slope were obtained from Fig. 4g,h, the diffusion coefficient of the electrode was enhanced with a reduction in the b value, noting that a b value around 0.5 indicates a greater diffusion coefficient value [22]. The hexagonal, porous surface area of the electrode is more suitable for diffusing the K^+ ion into the CVO-4 electrode. The Fig. 5a illustrates the diffusion coefficients and b values for all electrodes. The overall charge contribution of the electrode at constant potential is the sum of the capacitive and diffusion controlled contributions, as expressed by the following equation:

$$i(v) = i_{\text{capacitive}} + i_{\text{Diffusive}} \quad (8)$$

$$i(v) = k_1v + k_2v^{0.5} \quad (9)$$

The capacitive charge contribution and the diffusive controlled contribution are expressed by the coefficients k_1 and k_2 , respectively. The CV profile provides values for k_1 and k_2 , representing the rate constants of the electrochemical reaction. The graph illustrates the charge storage contribution at different scan rates. The analysis indicates that as the scan rate increases, the contribution from diffusion decreases. This is because at higher scan rates, the time available for ion diffusion to the electrode surface is shorter. The CVO-4 electrode exhibits a higher 'b' value, indicating a greater contribution from the diffusion process. Fig. 5b shows the quantification of charge contribution at a scan rate of 40 mV/s for the CVO-4 electrode. The diffusion-controlled contribution accounts for 68% of the total charge, while the capacitive charge contribution is 32%. In Fig. 5c, the charge quantification at a scan rate of CVO-4 electrode is depicted. The standard rate constant (K^0) and charge transfer constant were utilized to study the kinetics of the electrochemical reaction. These parameters provide insights into the detailed study of the electrochemical reaction's kinetics.

The quasi reversible, reversible, irreversible and electrochemical reaction of the electrode were identified by the K^0 value, $10^{-1} > K^0 > 10^{-5}$ represents the quasireversible electrochemical reaction. The $K^0 > 10^{-1}$ represents the reversible reaction and $K^0 < 10^{-5}$ represent the irreversible electrochemical reaction. The value of the K^0 were calculated from the following equation.

$$i_p = 0.227 \times n \times C \times A \times F \times K^0 \times \exp \left[- \left(\frac{\alpha n F}{RT} \right) (E_p - E^0) \right] \quad (10)$$

Where α is the charge transfer coefficient, K^0 standard rate constant, i_p is the peak current, A is the electrode area, C is the electrolyte concentration, F is the faraday constant, R is the universal gas constant, v is the scan rate, T is the temperature, and n is the available number of electrons for redox processes, E^0 and E_p is the formal and peak potential. The K^0 value of the CVO electrode ranges from 1.8 to 2.0×10^{-4} , indicating a quasi-reversible electrode chemical reaction. The K^0 values are listed in Table 1, obtained from Eq. (10). The charge transfer coefficient is calculated from the intercept of the $\ln(i_p)$ vs $E_p - E^0$ plot shown in Fig. 5d,e. The charge transfer coefficient ranges from 0.20 to 0.22, indicating that the electrochemical reactions are quasi-reversible. The values of the charge transfer coefficient are also listed in Table 1. The electrochemical impedance spectra (EIS) of the electrode were utilized

to investigate the electrical conductivity of the electrode material [52]. Fig. 5f displays the comparative EIS spectra of the CVO electrode. The EIS results show that the series resistance of the CVO-4 electrode is smaller than that of the other electrodes, illustrating the remarkable conductivity of CVO-4 and its effect on the electrochemical performance of the electrode. The R_s values for CVO-1, CVO-2, CVO-3, and CVO-4 electrodes are 2.21 Ω , 2.39 Ω , 2.28 Ω , and 2.06 Ω , respectively. The frequency-dependent real and imaginary capacitances of the CVO electrode were estimated using EIS spectra. Compared to the other electrodes, the CVO-4 electrode exhibits the highest C values, which align with the CV and GCD research conducted on the CVO electrode. The real and imaginary capacitance vs. frequency graph of all electrodes is depicted in Fig. S6. The porous surface of CVO-4 may contribute to its high-performance rate by shortening the diffusion paths of electrolyte ions and reducing series resistance. The practical utility of the prepared CVO-4 electrode was examined by combining CVO-4 electrodes as the positive electrode and activated carbon (AC) as the negative electrode in a two-electrode configuration. The CVO-4//AC combination was used to fabricate asymmetric supercapacitors (ASC) with 2 M KOH, PVA, and electrolyte, and the entire design was wrapped in paraffin paper. Fig. 6a illustrates the CV profile of the ASC CVO-4//AC at varying potentials ranging from 0.8 V to 1.3 V. The CV profile of the ASC device shows a redox peak primarily attributed to CVO-4, confirming its pseudocapacitive behavior, as depicted in Fig. 6b. Based on the CV profile study, the acceptable potentials for the ASC were found to be at 1.3 V. Fig. 6c and 6d depict the GCD evaluation of the CVO-4//AC ASC at various current densities and potentials. In accordance with Eq. (2), the areal capacitance of the CVO-4//AC ASC is 126 mF/cm² at a current density of 4 mA/cm². Eqs. (3) and (4) were employed to calculate the energy density and power density of the CVO-4//AC ASC, which resulted in an energy density of 29 mWh/cm² and a power density of 2.6 W/cm² at a current density of 4 mA/cm². These findings suggest that the CVO-4//AC ASC could serve as electrode material for energy storage devices in supercapacitors. The comparative study of the ASC were listed in Table 2. The cyclic stability of the CVO-4//AC ASC device was examined over 5000 cycles at a current density of 5 mA/cm². The CVO-4//AC ASC device retains 87% of its charge, demonstrating remarkable cyclic stability, as illustrated in Fig. S7a. Fig. S7b displays the EIS assessment of the CVO-4//AC ASC device, revealing stability over the cyclic tests. The series resistance of the CVO-4//AC ASC was measured to be 6.32 Ω throughout the cyclic stability evaluation. Thus, the electrochemical evaluation of the CVO-4//AC ASC devices indicates that the CVO-4 active material holds promising potential for energy storage applications.

3.5. HER and OER studies

The CVO-4 electrode was electrocatalytically evaluated for the hydrogen evolution reaction (HER), oxygen evolution reaction (OER), and overall water splitting to assess its multifunctional catalytic activity. Fig. 7a presents the linear sweep voltammetry (LSV) curve of the CVO-4 electrode measured in a 1 M KOH electrolyte at a scan rate of 1 mV/s. The LSV plot indicates an overpotential of 226 mV at a current density of 10 mA/cm². To perform a comprehensive kinetic analysis of the HER investigation, the Tafel plot was employed, as depicted in the Fig. 7b. In Fig. 7b, the exceptional Tafel slope of the CVO-4 electrode is shown to be 178 mV/dec. The observed modest overpotential and Tafel slope could be attributed to the hexagonal surface microstructure. Fig. 7c illustrates the recorded EIS spectra at the overpotential, which demonstrate a small series resistance of 3.32 Ω and a charge transfer resistance of 12.2 Ω . The presence of small pinholes in the hexagonal microstructure might contribute to the low series resistance by providing accessible pathways for charge transfer. For the evaluation of the OER catalytic activity, the CVO-4 electrode underwent linear sweep voltammetry (LSV) at a scan rate of 1 mV/s, as shown in Fig. 7d, along with the Tafel plot for kinetic analysis in Fig. 7e. At a current density of 10 mA/cm², the OER

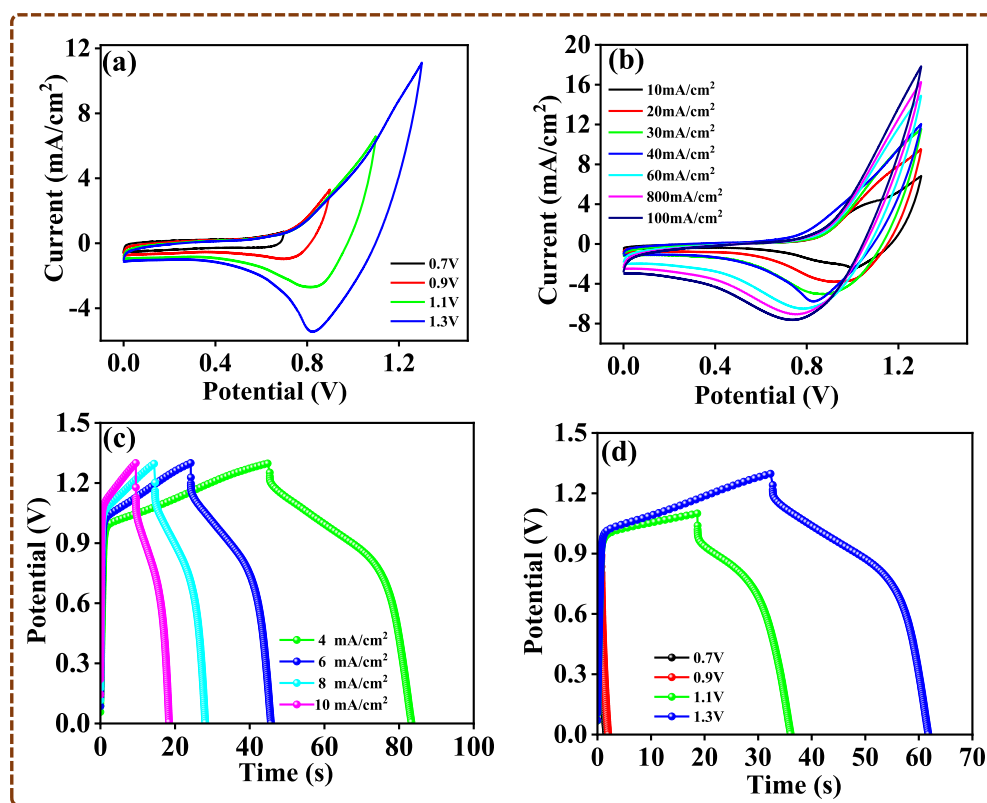


Fig. 6. (a) CV profile at different potential window (b) CV profile at different scan rate (c) GCD profile at different current density and (d) GCD profile at different potential of ASC.

Table 2
Comparison of asymmetric supercapacitor.

Asymmetric supercapacitor	Capacitance	Energy density	Power density	Reference
NiMoO ₄ @Co ₃ V ₂ O ₈ //AC	131 F/g (at 1 A/g)	48.5 (Wh/Kg)	0.839 (kW/Kg)	[53]
Ni ₂ P/Co ₃ V ₂ O ₈ //AC	147.5 F/g (at 0.5 A/g)	40.2 (Wh/Kg)	0.353 (kW/Kg)	[54]
Co ₃ V ₂ O ₈ //AC	F/g (at 1 A/g)	22.39 (Wh/Kg)	0.649 (kW/Kg)	[55]
Co ₃ V ₂ O ₈ -Ni ₃ V ₂ O ₈ @PCNF//PCNF	191 F/g (at 5 A/g)	59.7 (Wh/Kg)	1.97 (kW/Kg)	[56]
Ni ₃ V ₂ O ₈ /Co ₃ V ₂ O ₈	105 F/g (at 5 A/g)	37 (Wh/Kg)	0.13 (kW/Kg)	[57]
Co ₃ V ₂ O ₈ //AC	165.3 F/g (at 1 A/g)	59.2 (Wh/Kg)	0.25 (kW/Kg)	[32]
Co ₃ V ₂ O ₈ //AC	126 mF/cm ² (at 4 mA/cm ²)	29.61 (mWh/cm ²)	2.6 (W/cm ²)	Present work

overpotential of the CVO-4 electrode is 489 mV, as depicted in the Fig. 7d. The corresponding Tafel slope for the CVO-4 electrode at the same current density is 184 mV/dec illustrated in Fig. 7e. Fig. 7f displays the EIS spectra recorded at an overpotential. According to the EIS analysis, the CVO-4 electrode exhibits a series resistance of 3.05 Ω and a charge transfer resistance of 3.15 Ω . The low overpotential and Tafel slope can be attributed to the hexagonal microstructure, and the similar charge transfer resistance between OER and HER with little variation in series resistance suggests the availability of pathways in the hexagonal

microstructure in all directions. In 1 M KOH electrolyte, the CVO-4 electrode demonstrates excellent electrocatalytic activity for both HER and OER. Furthermore, the CVO-4 electrode was used in a simple two-electrode design, with the cathode and anode both composed of CVO-4 electrodes, to evaluate its performance in overall water splitting. Fig. 7g shows the LSV plot of overall water splitting. In Fig. 7h inset, the two electrode setups are displayed, illustrating the overall water-splitting cell. The cell voltage of the overall water-splitting cell is measured to be 1.81 V at a current density of 10 mA/cm². These results highlight the effectiveness of the CVO-4 electrode, as shown in Fig. 7h. Among the electrodes tested, the CVO-4 electrode exhibits the highest catalytic activity, and the generation of air bubbles at both electrodes is observed throughout the entire water-splitting process, as depicted in the inset of Fig. 7h. The comparative overpotential and Tafel for HER and OER were listed in Table 3. The stability of the overall water-splitting cell is evaluated over a period of 9 h at a current density of 10 mA/cm². The LSV plot of the CVO-4 electrode before and after stabilization is presented in Fig. 7h. After stabilization, a slight increase in the cell voltage is observed. The stability of the CVO-4 electrode for overall water splitting is depicted in Fig. 7i. Furthermore, inset Fig. 7i provides schematic representations of the HER, OER, and overall water-splitting processes.

4. Conclusions

We have presented a groundbreaking synthesis of Co₃V₂O₈ micro-particles through hydrothermal means, utilizing urea, at various Co-to-V molar ratios. Our aim was to investigate the potential of these nanoparticles in supercapacitor and electrocatalysis applications within an alkaline medium. The resulting CVO-4 nanoparticles showcase a stunning hexagonal microstructure with pinholes, as confirmed by both FESEM and HRTEM analyses. Through our thorough evaluation of electrochemical performance in 2 M KOH, we discovered that the CVO-4

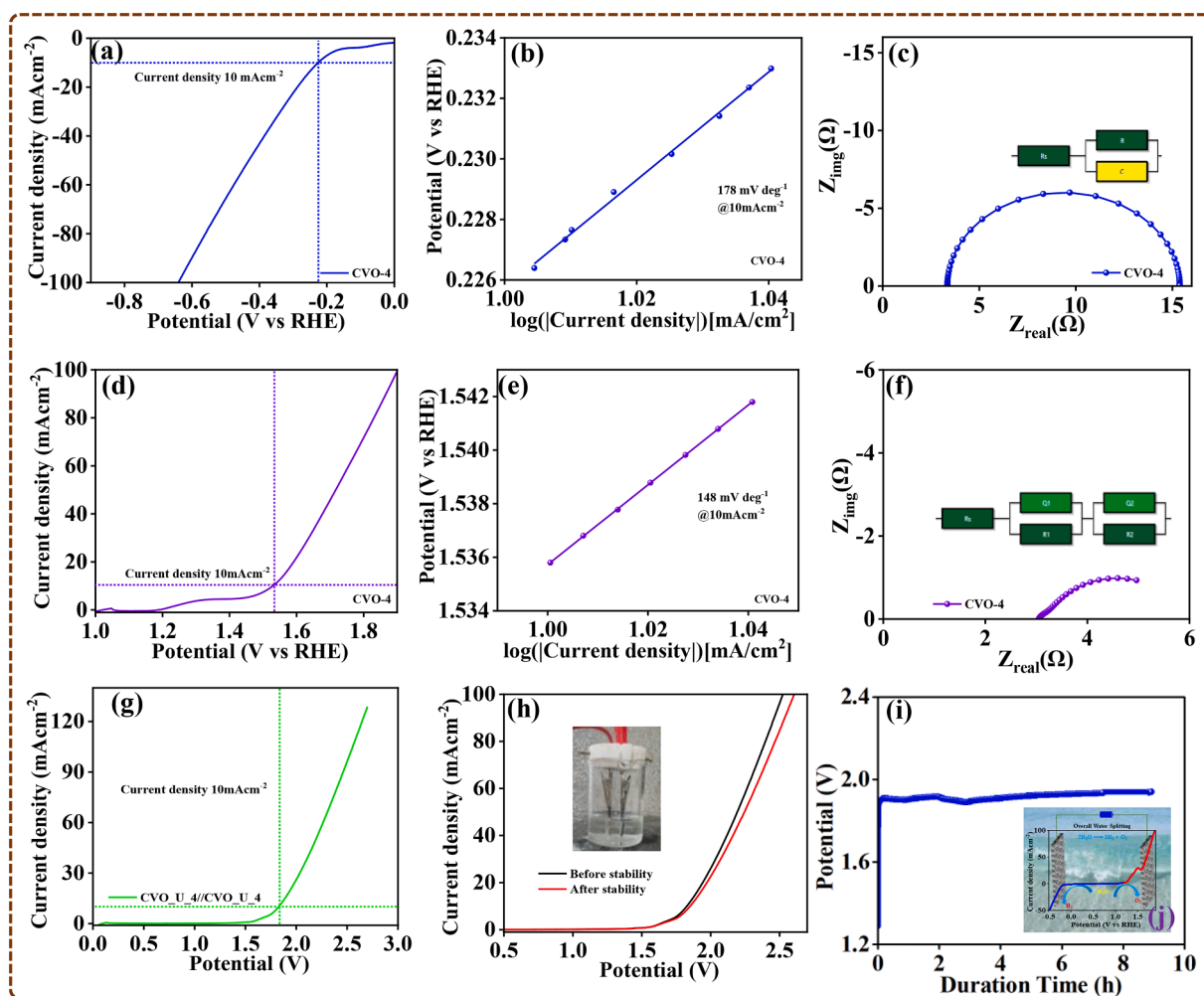


Fig. 7. CVO-4 nanoparticles; (a and d) LSV plots, (b and e) Tafel plots, and (c and f) EIS plots of OER and HER, respectively, (g) LSV plot overall water splitting (h) LSV plot before and after stability and two electrode configuration of overall water splitting, (i) stability plot at 10 mA/cm² and schematic of overall water splitting of CVO-4 electrode.

Table 3
Comparison of overpotential, Tafel for HER and OER.

Electrode	Overpotential mV (HER)	Tafel mV/ dec (HER)	Overpotential mV (OER)	Tafel mV/ dec (OER)	Reference
Co ₃ V ₂ O ₈	–	–	190	85	[58]
CoO- V ₂ O ₅	297	159	429	175	[59]
V _{8.3} -Co- MOF	293	156	435	78	[5]
Co ₃ V ₂ O ₈	278	180	318	130	[59]
Co ₃ V ₂ O ₈	–	–	359	65	[60]
V _{16.7} -Co- MOF	271	146	413	77	[5]
Co ₃ V ₂ O ₈	226	178	487	148	Present work

electrode exhibits remarkable electrochemical capabilities, boasting an areal capacitance of 3.79 F/cm² at a current density of 1 mA/cm². The CVO-4 electrode reveals itself to be diffusion-controlled, displaying a higher diffusion coefficient than its counterpart. When we pair it with activated carbon in a two-electrode configuration, the asymmetric supercapacitor displays an areal capacitance of 126 F/cm², an energy density of 29 mWh/cm², and a power density of 2.6 W/cm² showing promising potential for practical applications. Remarkably, even after

5000 cycles at 5 mA/cm², the asymmetric supercapacitor maintains 87% of its charge. Moreover, the CVO-4 electrode demonstrates excellent over-potential for HER and OER, with a Tafel slope of 178 mV/dec and 148 mV/dec, respectively. We attribute this impressive performance to the unique nanostructured shape of the hexagonal microstructure with pinholes, low charge-transfer resistance, and a high number of active sites, all of which provide enhanced electrochemical and electrocatalytic capabilities. In conclusion, our findings suggest that hydrothermally synthesized Co₃V₂O₈ nanoparticles exhibit exceptional potential for use in supercapacitor and electrocatalysis applications, making them a promising avenue for further research and development.

CRedit authorship contribution statement

R.A. Kadam: Conceptualization, Investigation, Writing – original draft. **M.A. Yewale:** Investigation, Writing – original draft. **A.M. Teli:** Formal analysis, Methodology. **V. Kumar:** Investigation, Writing – original draft. **U.T. Nakate:** Conceptualization. **S.L. Kadam:** Supervision, Writing – review & editing. **D.K. Shin:** Supervision.

Declaration of Competing Interest

The authors declare that they have no known competing financial interests or personal relationships that could have appeared to influence the work reported in this paper.

Data availability

Data will be made available on request.

Acknowledgement

This work was supported by the Technology Innovation Program (#20010170) funded By the Ministry of Trade, Industry & Energy (MOTIE, Korea).

Supplementary materials

Supplementary material associated with this article can be found, in the online version, at [doi:10.1016/j.surfin.2023.103267](https://doi.org/10.1016/j.surfin.2023.103267).

References

- [1] K.L. Chiu, L.Y. Lin, Applied potential-dependent performance of the nickel cobalt oxy sulfide nanotube/nickel molybdenum oxide nanosheet core-shell structure in energy storage and oxygen evolution, *J. Mater. Chem. A*. 7 (2019) 4626–4639.
- [2] S.C. Sekhar, B. Ramulu, D. Narsimulu, S.J. Arbaz, J.S. Yu, Metal-Organic Framework-Derived $\text{Co}_3\text{V}_2\text{O}_8/\text{CuV}_2\text{O}_6$ Hybrid Architecture as a Multifunctional Binder-Free Electrode for Li-Ion Batteries and Hybrid Supercapacitors, *Small* 16 (2020) 1–15.
- [3] C. Wang, G. Sui, D. Guo, J. Li, X. Ma, Y. Zhuang, D.F. Chai, Oxygen vacancies-rich NiCo_2O_4 - x nanowires assembled on porous carbon derived from cigarette ash: a competitive candidate for hydrogen evolution reaction and supercapacitor, *J. Energy Storage*. 50 (2022), 104280.
- [4] A. Jiang, Z. Wang, Q. Li, M. Dong, Ionic Liquid-Assisted Synthesis of Hierarchical One-Dimensional MoP/NPC for High-Performance Supercapacitor and Electrocatalysis, *ACS Sustain. Chem. Eng.* 8 (2020) 6343–6351.
- [5] W. Fang, J. Dang, Y. Hu, Y. Wu, S. Xin, B. Chen, H. Zhao, Z. Li, Electronic distribution tuning of vanadium-cobalt bimetallic MOFs for highly efficient hydrazine-assisted energy-saving hydrogen production, *Electrochim. Acta.* (2023) 439.
- [6] H. Chen, Y. Liu, J. Sun, C. Xu, High-performance hybrid supercapacitor based on the porous copper cobaltite/cupric oxide nanosheets as a battery-type positive electrode material, *Int. J. Hydrogen Energy*. 46 (2021) 28144–28155.
- [7] V. Lady, I.E. Quispe-Garrido, E.O. Monje, J.M. López, C.S. Gonçalves, G.Á. Martins, J.G. Planes, A.M. Ruiz-Montoya, Baena-Moncada, Influence of the Molar Ratio of Co and V in Bimetallic Oxides on Their Pseudocapacitive Properties, *ACS Omega* 7 (2022) 43522–43530.
- [8] D.M. Alqahtani, C. Zequine, C.K. Ranaweera, K. Siam, P.K. Kahol, T.P. Poudel, S. R. Mishra, R.K. Gupta, Effect of metal ion substitution on electrochemical properties of cobalt oxide, *J. Alloys Compd.* 771 (2019) 951–959.
- [9] M.A. Yewale, A.A. Jadhavar, R.A. Kadam, N.B. Velhal, U.T. Nakate, A.M. Teli, J. C. Shin, L.N. Nguyen, D.K. Shin, N.K. Kaushik, Hydrothermal synthesis of manganese oxide (Mn_3O_4) with granule-like morphology for supercapacitor application, *Ceram. Int.* (2022) 1–9.
- [10] S.I. Kim, J.S. Lee, H.J. Ahn, H.K. Song, J.H. Jang, Facile route to an efficient niO supercapacitor with a three-dimensional nanonetwork morphology, *ACS Appl. Mater. Interfaces*. 5 (2013) 1596–1603.
- [11] M.A. Yewale, R.A. Kadam, N.K. Kaushik, N.N. Linh, A.M. Teli, J.C. Shin, L. P. Lingamdinne, J.R. Koduru, D.K. Shin, Mesoporous hexagonal nanorods of NiCo_2O_4 nanoparticles via hydrothermal route for supercapacitor application, *Chem. Phys. Lett.* 800 (2022), 139654.
- [12] M.A. Yewale, R.A. Kadam, N.K. Kaushik, L.N. Nguyen, U.T. Nakate, L. P. Lingamdinne, J.R. Koduru, P.S. Auti, S.V.P. Vattikuti, D.K. Shin, Electrochemical supercapacitor performance of NiCo_2O_4 nanoballs structured electrodes prepared via hydrothermal route with varying reaction time, *Colloids Surfaces A Physicochem. Eng. Asp.* 653 (2022), 129901.
- [13] S. Patrice, Y. Gogotsi, *Materials For Electrochemical Capacitors*, Springer Handbooks, 2017, pp. 495–561.
- [14] P.Y. Lee, L.Y. Lin, S. Yougbaré, Sulfurization of nickel-cobalt fluoride decorating ammonia ions as efficient active material of supercapacitor, *J. Solid State Chem.* 313 (2022).
- [15] S.H. Chou, L.Y. Lin, Y.H. Chiu, Pulse reverse electrodeposited nickel cobalt sulfide nanosheets on Ni foam as battery-type electrode for battery supercapacitor hybrids, *J. Energy Storage*. 25 (2019), 100903.
- [16] E. Biyik, A. Kahraman, A predictive control strategy for optimal management of peak load, thermal comfort, energy storage and renewables in multi-zone buildings, *J. Build. Eng.* 25 (2019), 100826.
- [17] K.H. Lin, L.Y. Lin, W.L. Hong, Incorporating redox additives in sodium hydroxide electrolyte for energy storage device with the nickel cobalt molybdenum oxide active material, *J. Energy Storage*. 25 (2019), 100823.
- [18] S.C. Kulkarni, K.D. Bhalerao, S. Shirse, Y.T. Nakate, U.T. Nakate, B. Pandit, M. A. Yewale, Screen printed Zn-doped nanostructured In_2O_3 thick films, characterizations, and enhanced NO_2 gas sensing at low temperature, *Ceram. Int.* (2022).
- [19] M.A. Yewale, R.A. Kadam, N.K. Kaushik, J.R. Koduru, N.B. Velhal, U.T. Nakate, A. A. Jadhavar, N.D. Sali, D.K. Shin, Materials Science & Engineering B Interconnected plate-like NiCo_2O_4 microstructures for supercapacitor application, *Mater. Sci. Eng. B*. 287 (2023), 116072.
- [20] T. Pettong, P. Iamprasertkun, A. Krittayavathananon, P. Sukha, P. Sirisindudomkit, A. Seubsai, M. Chareonpanich, P. Kongkachuichay, J. Limtrakul, M. Sawangphruk, High-Performance Asymmetric Supercapacitors of MnCo_2O_4 Nanofibers and N-Doped Reduced Graphene Oxide Aerogel, *ACS Appl. Mater. Interfaces*. 8 (2016) 34045–34053.
- [21] A.M. Teli, S.A. Beknalkar, T.S. Bhat, S.M. Mane, J.C. Shin, Molybdenum-Manganese hydroxide microcubes based electrode via hydrothermal method for asymmetric supercapacitor, *Ceram. Int.* 48 (2022) 29386–29393.
- [22] A.M. Teli, T.S. Bhat, S.A. Beknalkar, S.M. Mane, L.S. Chaudhary, D.S. Patil, S. A. Pawar, H. Efstathiadis, J. Cheol Shin, Bismuth manganese oxide based electrodes for asymmetric coin cell supercapacitor, *Chem. Eng. J.* 430 (2022), 133138.
- [23] M.A. Yewale, A.A. Jadhvar, R.B. Kharade, R.A. Kadam, V. Kumar, U.T. Nakate, P. B. Shelke, D.H. Bobade, A.M. Teli, S.D. Dhas, D.K. Shin, Hydrothermally synthesized $\text{Ni}_3\text{V}_2\text{O}_8$ nanoparticles with horny surfaces for HER and supercapacitor application, *Mater. Lett.* 338 (2023), 134033.
- [24] A.M. Teli, S.A. Beknalkar, Y.R. Lee, J.C. Shin, Novel one-step synthesis for 3-D four-pointed micro-star of quaternary metal (Mo–V–Mn–Ag) oxide electrode for asymmetric supercapacitor, *Ceram. Int.* (2022).
- [25] Y.C. Hsiao, C.H. Liao, C.S. Hsu, S. Yougbaré, L.Y. Lin, Y.F. Wu, Novel synthesis of manganese cobalt layered double hydroxide and sulfur-doped nickel cobalt layered double hydroxide composite as efficient active material of battery supercapacitor hybrids, *J. Energy Storage*. 57 (2023).
- [26] Y.F. Wu, Y.C. Hsiao, C.H. Liao, C.S. Hsu, S. Yougbaré, L.Y. Lin, Novel design of Sulfur-doped nickel cobalt layered double hydroxide and polypyrrole nanotube composites from zeolitic imidazolate Framework-67 as efficient active material of battery supercapacitor hybrids, *J. Colloid Interface Sci.* 628 (2022) 540–552.
- [27] W.L. Hong, L.Y. Lin, Design of nickel cobalt oxide and nickel cobalt oxide@nickel molybdenum oxide battery-type materials for flexible solid-state battery supercapacitor hybrids, *J. Power Sources*. 435 (2019), 226797.
- [28] W.L. Hong, L.Y. Lin, Studying the substrate effects on energy storage abilities of flexible battery supercapacitor hybrids based on nickel cobalt oxide and nickel cobalt oxide@nickel molybdenum oxide, *Electrochim. Acta.* 308 (2019) 83–90.
- [29] T.Y. Chen, L.Y. Lin, Morphology variation for the nickel cobalt molybdenum copper oxide with different metal ratios and their application on energy storage, *Electrochim. Acta.* 298 (2019) 745–755.
- [30] Q. Li, S. Jing, Z. Yong, Q. Zhang, C. Liu, K. Zhu, Y. Feng, W. Gong, Y. Yao, Towards ultrahigh-energy-density flexible aqueous rechargeable Ni//Bi batteries: free-standing hierarchical nanowire arrays core-shell heterostructures system, *Energy Storage Mater* 42 (2021) 815–825.
- [31] Y. Zhang, Y. Liu, J. Chen, Q. Guo, T. Wang, H. Pang, Cobalt vanadium oxide thin nanoplates: primary electrochemical capacitor application, *Sci. Rep.* 4 (2014) 2–6.
- [32] Z. Fahimi, O. Moradlou, A. Sabbah, K.H. Chen, L.C. Chen, M. Qorbani, $\text{Co}_3\text{V}_2\text{O}_8$ hollow spheres with mesoporous walls as high-capacitance electrode for hybrid supercapacitor device, *Chem. Eng. J.* (2022) 436.
- [33] J. Zhang, B. Yuan, S. Cui, N. Zhang, J. Wei, X. Wang, D. Zhang, R. Zhang, Q. Huo, Facile synthesis of 3D porous $\text{Co}_3\text{V}_2\text{O}_8$ nanoroses and 2D $\text{NiCo}_2\text{V}_2\text{O}_8$ nanoplates for high performance supercapacitors and their electrocatalytic oxygen evolution reaction properties, *Dalt. Trans.* 46 (2017) 3295–3302.
- [34] S. Gongzheng Yang, Hao Cui, Guowei Yang, Chengxin Wang, Self-Assembly of $\text{Co}_3\text{V}_2\text{O}_8$ Multilayered Nanosheets: controllable Synthesis, Excellent Li-Storage Properties, and Investigation of Electrochemical Mechanism, *Acta Crystallogr. Sect. B Struct. Crystallogr. Cryst. Chem.* 29 (1973) 2304–2306.
- [35] H. Chai, Y. Wang, Y. Fang, Y. Lv, H. Dong, D. Jia, W. Zhou, Low-cost synthesis of hierarchical $\text{Co}_3\text{V}_2\text{O}_8$ microspheres as high-performance anode materials for lithium-ion batteries, *Chem. Eng. J.* 326 (2017) 587–593.
- [36] Q. Zhang, J. Pei, G. Chen, C. Bie, J. Sun, J. Liu, Porous $\text{Co}_3\text{V}_2\text{O}_8$ Nanosheets with Ultrahigh Performance as Anode Materials for Lithium Ion Batteries, *Adv. Mater. Interfaces*. 4 (2017) 1–7.
- [37] Y. Li, L. Bin Kong, M.C. Liu, W. Bin Zhang, L. Kang, Facile synthesis of $\text{Co}_3\text{V}_2\text{O}_8$ nanoparticle arrays on Ni foam as binder-free electrode with improved lithium storage properties, *Ceram. Int.* 43 (2017) 1166–1173.
- [38] Z. Luo, Q. Peng, Z. Huang, L. Wang, Y. Yang, J. Dong, T.T. Isimjan, X. Yang, Fine-tune π -band center of cobalt vanadium oxide nanosheets by N-doping as a robust overall water splitting electrocatalyst, *J. Colloid Interface Sci.* 629 (2023) 111–120.
- [39] A.M. Patil, J. Wang, S. Li, X. Hao, X. Du, Z. Wang, X. Hao, A. Abudula, G. Guan, Bilateral growth of monoclinic WO_3 and 2D $\text{Ti}_3\text{C}_2\text{Tx}$ on 3D free-standing hollow graphene foam for all-solid-state supercapacitor, *Chem. Eng. J.* 421 (2021), 127883.
- [40] M. Qorbani, O. Khajehdehi, A. Sabbah, N. Naseri, Ti-rich TiO_2 Tubular Nanolettices by Electrochemical Anodization for All-Solid-State High-Rate Supercapacitor Devices, *ChemSusChem* 12 (2019) 4064–4073.
- [41] Y. Lu, J. Nai, X.W.D. Lou, Formation of $\text{NiCo}_2\text{V}_2\text{O}_8$ Yolk-Double Shell Spheres with Enhanced Lithium Storage Properties, *Angew. Chemie.* 130 (2018) 2949–2953.
- [42] M. Akram, A.T. Saleh, W.A.W. Ibrahim, A.S. Awan, R. Hussain, Continuous microwave flow synthesis (CMFS) of nano-sized tin oxide: effect of precursor concentration, *Ceram. Int.* 42 (2016) 8613–8619.
- [43] A. Maitra, A.K. Das, S.K. Karan, S. Paria, R. Bera, B.B. Khatua, A mesoporous high-performance supercapacitor electrode based on polypyrrole wrapped iron oxide decorated nanostructured cobalt vanadium oxide hydrate with enhanced electrochemical capacitance, *Ind. Eng. Chem. Res.* 56 (2017) 2444–2457.

- [44] H. Wang, L. Lei, Z. Li, L. Huang, T. Wei, C. Wang, X. Wei, Surface defect modulation with intercalation ion doping vanadium oxide to enhance zinc storage performance, *Energy Fuels* 36 (2022) 2872–2879.
- [45] C. Alex, S.C. Sarma, S.C. Peter, N.S. John, Competing Effect of Co³⁺-reducibility and oxygen-deficient defects toward high oxygen evolution activity in Co₃O₄ systems in alkaline medium, *ACS Appl. Energy Mater.* 3 (2020) 5439–5447.
- [46] J.A. Rajesh, J.Y. Park, S.H. Kang, K.S. Ahn, Effect of molar concentration on the crystallite structures and electrochemical properties of cobalt fluoride hydroxide for hybrid supercapacitors, *Electrochim. Acta.* 414 (2022).
- [47] Y. Wang, Y. Song, Y. Xia, Electrochemical capacitors: mechanism, materials, systems, characterization and applications, *Chem. Soc. Rev.* 45 (2016) 5925–5950.
- [48] X. He, R. Li, J. Liu, Q. Liu, R.R. chen, D. Song, J. Wang, Hierarchical FeCo₂O₄@NiCo layered double hydroxide core/shell nanowires for high performance flexible all-solid-state asymmetric supercapacitors, *Chem. Eng. J.* 334 (2018) 1573–1583.
- [49] T. Pu, J. Li, Y. Jiang, B. Huang, W. Wang, C. Zhao, L. Xie, L. Chen, Size and crystallinity control of two-dimensional porous cobalt oxalate thin sheets: tuning surface structure with enhanced performance for aqueous asymmetric supercapacitors, *Dalt. Trans.* 47 (2018) 9241–9249.
- [50] B. Huang, W. Wang, T. Pu, J. Li, C. Zhao, L. Xie, L. Chen, Rational design and facile synthesis of two-dimensional hierarchical porous M₃V₂O₈ (M = Co, Ni and Co–Ni) thin sheets assembled by ultrathin nanosheets as positive electrode materials for high-performance hybrid supercapacitors, *Chem. Eng. J.* 375 (2019), 121969.
- [51] J. Zhang, F. Liu, J.P. Cheng, X.B. Zhang, Binary Nickel-Cobalt oxides electrode materials for high-performance supercapacitors: influence of its composition and porous nature, *ACS Appl. Mater. Interfaces.* 7 (2015) 17630–17640.
- [52] Z. Shi, Y. Liu, Y. Zhang, J. Sun, J. Zheng, C. Wei, W. Du, L. Liu, C. Cheng, Designed synthesis of yolk-shelled NiCo₂O₄/MnCo₂O₄ hollow sphere with boosted performance for supercapacitors, *Appl. Surf. Sci.* 611 (2023) 1–10.
- [53] B. Hu, Y. Cen, C. Xu, Q. Xiang, M.K. Aslam, L. Liu, S. Li, Y. Liu, D. Yu, C. Chen, Hierarchical NiMoO₄@Co₃V₂O₈ hybrid nanorod/nanosphere clusters as advanced electrodes for high-performance electrochemical energy storage, *Nanoscale* 12 (2020) 3763–3776.
- [54] Y.M. Hu, M.C. Liu, Y.X. Hu, Q.Q. Yang, L. Bin Kong, W. Han, J.J. Li, L. Kang, Design and synthesis of Ni₂P/Co₃V₂O₈ nanocomposite with enhanced electrochemical capacitive properties, *Electrochim. Acta.* 190 (2016) 1041–1049.
- [55] Y. Teng, Y. Li, D. Yu, Y. Meng, Y. Wu, X. Zhao, X. Liu, The microwave-assisted hydrothermal synthesis of CoV₂O₆ and Co₃V₂O₈ with morphology tuning by pH adjustments for supercapacitor applications, *ChemistrySelect* 4 (2019) 956–962.
- [56] H. Hosseini, S. Shahrokhian, Advanced binder-free electrode based on core – shell nanostructures of mesoporous Co₃V₂O₈-Ni₃V₂O₈ thin layers @ porous carbon nano fibers for high-performance and flexible all-solid-state supercapacitors, 341 (2018) 10–26.
- [57] M.C. Liu, L. Bin Kong, L. Kang, X. Li, F.C. Walsh, M. Xing, C. Lu, X.J. Ma, Y.C. Luo, Synthesis and characterization of M₃V₂O₈ (M = Ni or Co) based nanostructures: a new family of high performance pseudocapacitive materials, *J. Mater. Chem. A.* 2 (2014) 4919–4926.
- [58] M. Gyanprakash D, P.K. Gupta, G.P. Sharma, R.G.S. Pala, Surface-enhanced OER activity in Co₃V₂O₈ using cyclic charge-discharge to balance electrocatalytic active site generation and degradation, *Electrochim. Acta.* (2021) 367.
- [59] Z. Yang, H. Chen, M. Xiang, C. Yu, J. Hui, S. Dong, Coral reef structured cobalt-doped vanadate oxometalate nanoparticle for a high-performance electrocatalyst in water splitting, *Int. J. Hydrogen Energy.* 47 (2022) 31566–31574.
- [60] M. Xing, L. Bin Kong, M.C. Liu, L.Y. Liu, L. Kang, Y.C. Luo, Cobalt vanadate as highly active, stable, noble metal-free oxygen evolution electrocatalyst, *J. Mater. Chem. A.* 2 (2014) 18435–18443.



Sphere-shaped CuCo_2O_4 nanostructures battery type electrode for supercapacitor via hydrothermal synthesis approach

M.A. Yewale^a, R.A. Kadam^b, Umesh T. Nakate^{c,d,*}, A.M. Teli^e, V. Kumar^a, S.A. Beknalkar^e, A.A. Jadhavar^f, S.L. Kadam^g, Nitin T. Shelke^h, D.K. Shin^{a,**}

^a School of Mechanical Engineering, Yeungnam University, Gyeongsan 38541, Republic of Korea

^b Department of Physics, Ahmednagar College, Ahmednagar 414001, India

^c Department of Polymer Nano Science and Technology, Jeonbuk National University, 567 Baekjedaero, Deokjin-gu, Jeonju-si, Jeollabuk do 54896, Republic of Korea

^d Department of Chemical Engineering, Hanyang University, Seoul 04763, Republic of Korea

^e Division of Electronics and Electrical Engineering, Dongguk University-Seoul, Seoul 04620, Republic of Korea

^f Department of Physics, New Arts, Commerce and Science College, Ahmednagar 414001, India

^g Department of Physics, New Arts Commerce and Science College, Parner, Ahmednagar, Maharashtra 414302, India

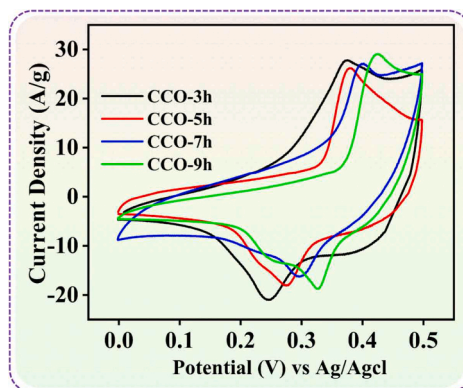
^h Vidya Pratishthan's Kamalnayan Bajaj Institute of Engineering & Technology, Vidyanagari, Baramati 413133 Maharashtra, India

HIGHLIGHTS

- Spherical balls having the nanostructure of CuCo_2O_4 have been created using a hydrothermal technique.
- The effect of hydrothermal reaction timeframe on an electrode's electrochemical performance has been observed.
- Overgrowth of CuCo_2O_4 nanoparticles on the knobby surface improves electrode's electrochemical performance at 7 h of reaction time and shows a specific capacitance of 432 F/g.

GRAPHICAL ABSTRACT

Cyclic Voltammetry curve of CCO-3h, CCO-5h, CCO-7h, and CCO-9h electrode.



ARTICLE INFO

Keywords:

Hydrothermal method
Knobby surface spherical balls
XPS
FE-SEM
TEM
Battery type electrode, supercapacitor

ABSTRACT

Transition metal oxide (TMO) is expected to be a highly competitive electrode material for energy storage applications based on its superior electrical and theoretical capacity in supercapacitors. However, a larger surface area and higher porosity are required to improve the electrode's electrochemical performance for practical applications. The nanostructured CuCo_2O_4 nanoparticles were prepared via a simple hydrothermal process with increased surface area and favorable active site to promote electrolyte penetration. The optimal hydrothermal reaction time was investigated to allow nanoparticle overgrowth, which will be critical in determining the

* Corresponding author at: Department of Polymer Nano Science and Technology, Jeonbuk National University, 567 Baekjedaero, Deokjin-gu, Jeonju-si, Jeollabuk do 54896, Republic of Korea.

** Corresponding author.

E-mail addresses: umesh.nakate@gmail.com (U.T. Nakate), dkshin@yu.ac.kr (D.K. Shin).

<https://doi.org/10.1016/j.colsurfa.2023.132541>

Received 23 August 2023; Received in revised form 28 September 2023; Accepted 8 October 2023

Available online 11 October 2023

0927-7757/© 2023 Elsevier B.V. All rights reserved.

specific surface area of the electrode material. The CuCo_2O_4 prepared at 7 h hydrothermal reaction period, (i.e. CCO-7 h) battery type electrode revealed a capacity of 193 F/g (96.5 C/g) at $3 \text{ mA}/\text{cm}^2$ and capacity retention of 85.9% over 6000 cycles at $15 \text{ mA}/\text{cm}^2$. Furthermore, the activated carbon and CCO-7 h (CCO//AC) asymmetric supercapacitor (ASC) exhibited energy and power densities of 2.120 Wh/kg and 277 W/kg, respectively with a capacity retention of 64% after 2000 cycles. The binary metal oxide CuCo_2O_4 with unique morphology could be a promising battery type electrode for supercapacitor device application.

1. Introduction

Industries are increasingly adopting electronic technology. Energy storage devices, crucial for many modern electronics, are on the rise. Supercapacitors are being explored as alternatives to traditional batteries [1]. They can function as both components and backup energy sources for high-power devices. Engineers and scientists are studying electrochemical devices for energy storage solutions. Supercapacitors are gaining attention due to their unique features [2]. Their properties include high power density, fast charging, and long life cycles, making them attractive in the current market. [3,4]. A supercapacitor's charging and discharging processes are incredibly fast. While this signifies that it has a lower energy density than a battery, it's able to deliver a higher power density in a shorter duration [5]. Owing to their noteworthy characteristics, such as high power density and long life cycles, supercapacitors are being evaluated as potential battery replacements. Electric double-layer capacitors (EDLCs) and pseudocapacitors (PCs) are the two different kinds of supercapacitors that differ in their energy way of storing energy. Charges accumulate at the electrode/electrolyte interaction in EDLC electrodes due to a non-faradaic process. Graphene [6], graphene oxide, reduced graphene oxide, and carbon nanotubes [7,8] are examples of carbon-based materials with high surface area electrodes that exhibit EDLC-type storage. The metal oxides [9–16], metal chalcogenide [17–20], and polymers [21] exhibit PCs behavior where the charge is stored both via redox reaction and non-faradic redox reaction. The third type under consideration is the battery-type electrode. This type of electrode material exhibits a redox peak at a distinct potential in its CV profile, and a clear plateau in its nonlinear GCD profile. This behavior sets it apart from EDLC-based or pseudocapacitive materials. As a result, should express charge storage in battery-type electrodes at a specific capacity (mAh g^{-1} or C g^{-1}) rather than specific capacitance [13,22]. EDLCs are widely used in commercial applications. Their energy density, however, is lower than that of batteries. This limitations their wide-ranging use.

Transition metal oxide is a valuable supercapacitor material for the electrode. It possesses a high capacitance and varied oxidation states. Moreover, its distinct surface structure enhances redox reactions. Metal sulfides suffer conductivity and stability concerns. Conducting polymers, on the other hand, are unreliable over a period of time. A feasible alternative is transition metal oxide. Metal oxide composites and bimetallic oxides are gaining importance. In electrochemical testing, they surpass single metal oxides. Cobalt-based bimetallic oxides stand out among them. They outperform Co_3O_4 in terms of conductivity and capacitance [23–25]. CuCo_2O_4 has received great attention due to its inexpensive cost, low toxicity, and high theoretical capacitance [26–28]. The copper cation reduces the activation energy of electron transport and the cobalt cation increases electrochemical activity in the faradic reaction. Hence, CuCo_2O_4 is expected to improve the electrochemical performance of the device when compared to cobalt oxide and copper oxide [29,30]. Alqahtani et al., described the hydrothermal synthesis of CuCo_2O_4 for energy storage applications with a specific capacitance of 478 F/g, the electrode has the largest specific capacitance [31]. Kambale et al. used a simple hydrothermal technique to produce an Urchin-like microstructure of CuCo_2O_4 nanomaterial and reported a specific capacitance of 443 F/g. The Urchin-like microstructure architecture is then utilized to adorn metal oxide nanoparticles in order to improve the device's electrochemical performance [32]. Silambarasan et al.

measured the 290 F/g specific capacitance of CuCo_2O_4 nanoparticles produced by chemical precipitation without the use of a surfactant [33]. CuCo_2O_4 , with its multiple valence states that enable rich redox reactions, has been extensively studied as a battery-type material.

The electrochemical performance of electrode materials can be influenced by the surface microstructure of nanomaterials. The surface microstructure of the electrode influences the electrochemical performance of the electrode materials. Many researchers have reported different microstructures of CuCo_2O_4 , including dendrite structures [34], nanoneedle arrays, nanosheet arrays, nanorod arrays [35], and hexagonal nanoparticles [36]. Each has a distinct electrochemical performance. We focused on the growth of tiny nanogranules on CuCo_2O_4 nanoparticles due to the importance of surface microstructure on the electrochemical performance of the electrode. The tiny nanogranules have been produced at 7 h of hydrothermal reaction time by tweaking the hydrothermal reaction duration. When compared to CuCo_2O_4 nanoparticles synthesized utilizing different hydrothermal reaction durations, the CVO-7 h electrode demonstrated superior electrochemical performance. Nanostructured CuCo_2O_4 and an activated carbon electrode were used to fabricate the supercapacitor device. The two-electrode device exhibited high cycle stability and good charge storage specific capacitance. The CuCo_2O_4 nanoparticles may be used battery type electrode for energy storage applications, the right hydrothermal reaction time gave the highest electrochemical characteristics.

2. Experimental

2.1. Chemicals

All chemicals were used for the experiment without further purification. Cobalt acetate ($\text{C}_4\text{H}_6\text{CoO}_4$), copper acetate ($\text{C}_4\text{H}_6\text{CuO}_4$), and sodium hydroxide (NaOH) were purchased from the Loba chemicals from Mumbai, India. Potassium hydroxide (KOH), NMP, PVDF, carbon black (CB), and activated carbon (AC) were purchased from sigma Aldrich, Nickel electrodes 1.6 mm thickness were purchased from the MTI Corporation.

2.2. Synthesis of materials

A hydrothermal approach was used for the preparation of cobalt-copper oxide nanostructures: 2 M cobalt acetate ($\text{C}_4\text{H}_6\text{CoO}_4$) was dissolved in 40 mL of double-distilled water and homogenized for 10 min before adding 1 M copper acetate ($\text{C}_4\text{H}_6\text{CuO}_4$) and stirring for another 10 min. A 0.3 mM sodium hydroxide solution was then added gradually to the precursor mixture, followed by 10 min of continuous stirring. The solution was transferred to a 100 mL Teflon liner, sealed in a stainless steel autoclave, and exposed to 3 h of hydrothermal treatment. To get the sample CCO-3 h, the product was cleaned with water and ethanol alternately, the nanoparticles were dried under infrared light for 5 h, then annealed at 400°C for 5 h. similar to the above procedure has been utilized with longer hydrothermal durations of 5 h, 7 h, and 9 h, for the synthesis of samples CCO-5 h, CCO-7 h, and CCO-9 h. These materials were then characterized and used to make electrodes to evaluate their electrochemical characteristics.

2.3. Characterization

X-ray Diffraction (XRD; PAN analytical, Cu-K radiation) and X-ray Photoelectron Spectroscopy (XPS; K-alpha, Thermo Scientific, UK) were used to investigate the structural and chemical surface states of a CCO sample. Purity and phase formation were studied using Raman spectroscopy (Xplora micro-Raman spectrometer, Horiba, Kyoto, Japan), and surface area measurements were obtained using the Brunauer-Emmett-Teller (BET) method with a Micromeritics 3-Flex analyzer. The Field Emission Scanning Electron Microscope (FESEM, S-4800 HITACHI, Ltd., Japan) and Transmission Electron Microscope (TEM) were used to investigate surface morphology, element mapping, and element composition (energy dispersive spectroscopy, (EDS)) (HRTEM; Tecnai F21, FEI Company).

2.4. Electrochemical measurements

Electrochemical investigations were carried out using a three-electrode configuration that includes graphite as the counter electrode, Ag/AgCl as the reference electrode, and a CCO nanoparticles working electrode. This composite, which included Cobaltite (CCO) active material, Polyvinylidene Fluoride (PVDF), and carbon black, was disseminated in N-Methyl-2-pyrrolidone (NMP) at an 80:10:10 wt ratio and ultrasonicated for 30 min. The resultant slurry was drop-cast over Ni foam and allowed to cure overnight at 60 °C. On Ni foam, the active material loadings were 1.11 mg for CCO-3 h, 1.06 mg for CCO-5 h, 0.8 mg for CCO-7 h, and 1.12 mg for CCO-9 h. The electrodes that were created were then used for further electrochemical characterizations. At the time of electrode preparation, Ni foam was ultrasonically cleaned for 10 min each in acetone, ethanol, and water. The CCO composite served as the working electrode in the asymmetric supercapacitor, with activated carbon (AC) serving as the counter electrode, both of which were manufactured using a similar technique. The CCO working electrode, AC counter electrode, and a separator made of 2 M KOH-saturated filter paper were all encased in paraffin paper in the device arrangement. These built asymmetric supercapacitors (ASC) were then characterized to determine their electrochemical properties.

3. Results and discussion

XRD was used to examine the crystal structure and purity of CCO nanoparticles. The XRD spectra of all CCO nanoparticles synthesized via varying hydrothermal reaction times are shown in Fig. 1. All XRD peaks are seen at 2θ values of 31.01, 36.78, 38.74, 48.99, 59.24, 65.10, and

68.49, which are indexed with the planes (220), (311), (222), (400), (331), (511), (440), (531), and (620) of CuCo_2O_4 nanoparticles with cubic crystal phase and polycrystalline nature. The XRD spectra revealed the mixed phase of $\text{Cu}_x\text{Co}_{2-x}\text{O}_4$. The phase fluctuation was detected when the hydrothermal reaction time changes. At a hydrothermal reaction of 3 h, the peak intensity and splitting were not detected. The peak intensity increases as the hydrothermal reaction duration increases, up to a 7 h hydrothermal reaction period. At 7 h reaction time, a broad XRD peak at 36.7 was detected, and no mixed phase of $\text{Cu}_x\text{Co}_{2-x}\text{O}_4$ was noticed. Peak intensity increases for 9 h prepared sample, and crystal development and mixed crystal phase were detected along the different plane directions. According to the XRD results, single crystal development was seen for up to 7 h of hydrothermal reaction time for $\text{Cu}_x\text{Co}_{2-x}\text{O}_4$. The mixed crystal phase of $\text{Cu}_x\text{Co}_{2-x}\text{O}_4$ was observed for CCO-9 h sample. Mixed $\text{Cu}_x\text{Co}_{2-x}\text{O}_4$ phases were found as a result of the extended hydrothermal process. The mixed phase has an influence on the electrochemical performance of the CCO electrode.

The chemical valence states and elemental composition of $\text{Cu}_x\text{Co}_{2-x}\text{O}_4$ were determined using X-ray photoelectron spectroscopy (XPS). All XPS data were examined using the C1s as a reference. The CCO survey spectrum is depicted in Fig. 2 (a), with prominent peaks appearing at 529.29 eV, 779.46 eV, and 933.37 eV, indicating the presence of O, Co, and Cu in the sample. Fig. 2 (b) depicts the Co2p's core-level spectrum. With an energy separation of 14.92 eV, the strong peak was observed at 779.41 eV and 794.33 eV, reflecting the $\text{Co}2p_{3/2}$ and $\text{Co}2p_{1/2}$, respectively [37]. The peak $\text{Co}2p_{3/2}$ was fitted into two peaks at 779.27 eV and 780.7 eV, respectively, indicating the existence of Co^{+3} and Co^{2+} [37]. The peak $\text{Co}2p_{1/2}$ was fitted into two peaks at 793.93 eV and 796.19 eV, indicating the presence of Co^{+3} and Co^{2+} [38]. Furthermore, the presence of CCO's spinal structure was verified by two large peaks at 786.10 eV and 804.7 eV [39]. The Fig. 2 (c) indicates that two spin-orbit peaks arise in the core level spectra of Cu2p at 953.49 eV and 933.15 eV with an energy difference of 22.24 eV, indicating the presence of $\text{Cu}2p_{3/2}$ and $\text{Cu}2p_{1/2}$. The peak present at binding energy 961.71 eV and 941.51 eV shows the characteristic peak of Cu^{2+} [40,41]. The presence of oxygen is depicted in Fig. 2 (d) by high-resolution O1s spectra. The deconvoluted peaks in the O1s spectrum are 529.56 eV, 531.22 eV, and 533.13 eV. The 533.13 eV peak corresponds to lattice oxygen (Co-O), the 531.22 eV peak corresponds to H_2O oxygen, and the 529.56 eV peak indicates lattice oxygen [42-44]. Cu^{2+} and $\text{Co}^{2+}/\text{Co}^{3+}$ were confirmed in CuCo_2O_4 molecules, according to the XPS data. The Raman study measurement was used to study the structural properties of the CCO-7 h nanoparticle, and the Raman spectra of the CCO-7 h nanoparticles were shown in the Fig. S1 (S.I). The

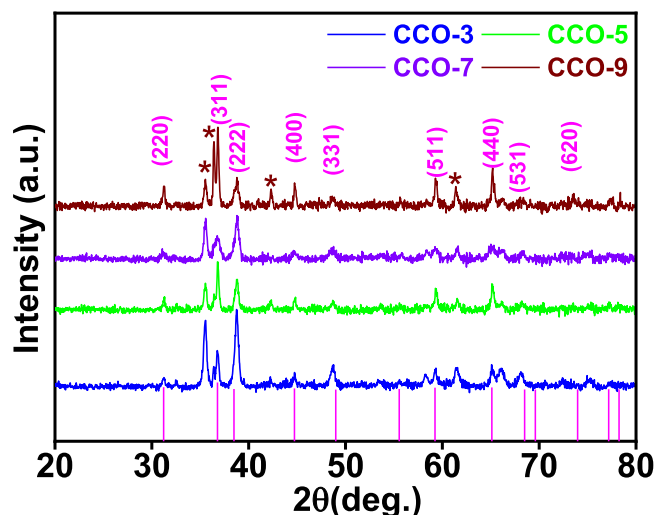


Fig. 1. (a) XRD spectra for CCO-3h, CCO-5h, CCO-7h, CCO-9h samples.

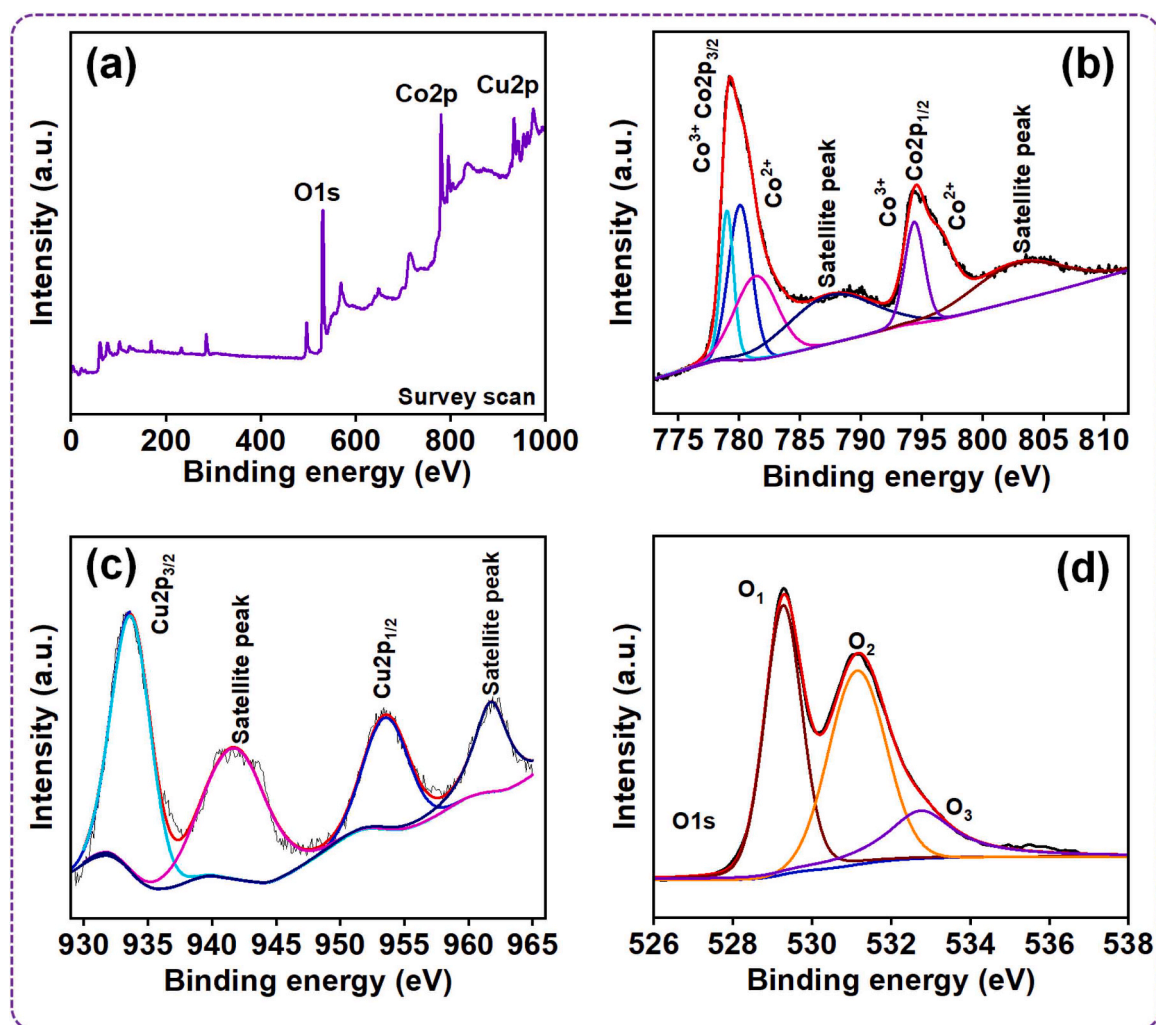


Fig. 2. (a) XPS survey for CCO-7 h, (b) XPS peaks for Co2p species, (c) XPS peaks for Cu2p species, (d) XPS peaks for O1s species.

F_{2g} , E_g , E_{2g} , and A_{1g} modes of the CuCo_2O_4 signals were detected in the CCO-7 h Raman spectra at 197, 470, 513, and 672 cm^{-1} , respectively, which indicated the formation of the CuCo_2O_4 nanoparticle at 7 h hydrothermal reaction time [30].

Field electron scanning electron microscopy (FE-SEM) was used to examine the surface microstructure of all the CCO samples. Fig. 3 illustrates the FE-SEM of CCO-3, CCO-5, CCO-7, and CCO-9 samples. The FESEM picture depicts the reaction time-dependent progressive surface alteration of all nanoparticles. Fig. 3(a, b, c) depicts a CCO-3 sample prepared at 3 h of hydrothermal reaction time. The particles resemble non-uniform spherical particles, and the nanoparticle's development is only beginning. There is less porosity observed for the nanoparticles since they are tightly packed together. It might be because of the short hydrothermal reaction time. As the hydrothermal reaction time was increased to 5 h, nanoparticles growth was observed and the nanoparticles begin to exhibit a different microstructure than CCO-3, as seen in the Fig. 3(e, f, g). Tiny overgrowth was discovered in sample CCO-5, and the small overgrowth particles form a rough surface. The rough surface of the nanoparticle influences the electrode material's electrochemical performance. At 7 h of hydrothermal reaction time, these tiny nanoparticles began to acquire the small granular form of the nanoparticle and are separated from each other, creating space between them. The effect of the small growth of the nano granules has been observed in its electrochemical performance. Small granules were clumped together over the nanoparticle with an increase in the size of the nanoparticles for the entire 9 h reaction period. The surface area of

the nanoparticle was decreased due to the clumping of the nanoparticles into each other, affecting the electrochemical performance. The size of the nanoparticles grew as the hydrothermal reaction duration increased. The average particle size of the CCO-3 nanoparticle is ~ 71 nm, while the CCO-5 particle size was significantly enhanced up to ~ 76 nm for the sample. The nanogranules are around ~ 23 nm in size. The nanogranules over the nanoparticles confirmed the highest surface-to-volume ratio, which improves the electrode's electrochemical performance. The clumping of the nanogranules increased the particle size of the sample by up to ~ 138 nm, minimizing space between the nanogranules.

Surface microstructure modification was detected while reaction time was varied. EDS measurements were used to determine the elemental makeup of all samples. Fig. 3(d,h,l,p) depicts the EDS spectra for all samples. The sharp peak that occurs in EDS spectra indicates the presence of Co, Cu, and O in all samples, and the peak intensity of the elements varied with the hydrothermal reaction time. The atomic composition of the element changes with the hydrothermal reaction time in each EDS spectrum. With reaction time, the Cu/Co proportion dropped down to 0.40. The Cu/Co ration was closely matched with XRD data for the 7 h hydrothermal reaction time, confirming the phase development of $\text{Cu}_x\text{Co}_{2-x}\text{O}_4$, and the Cu/Co ration increased, perhaps owing to the mixed phase of CCO. The sample CCO-7 h performed the best in terms of CV and GCD. It might be attributable to the sample's elemental makeup and phase development. An inductive coupled plasma emission spectrometer (ICP) was used for additional elemental

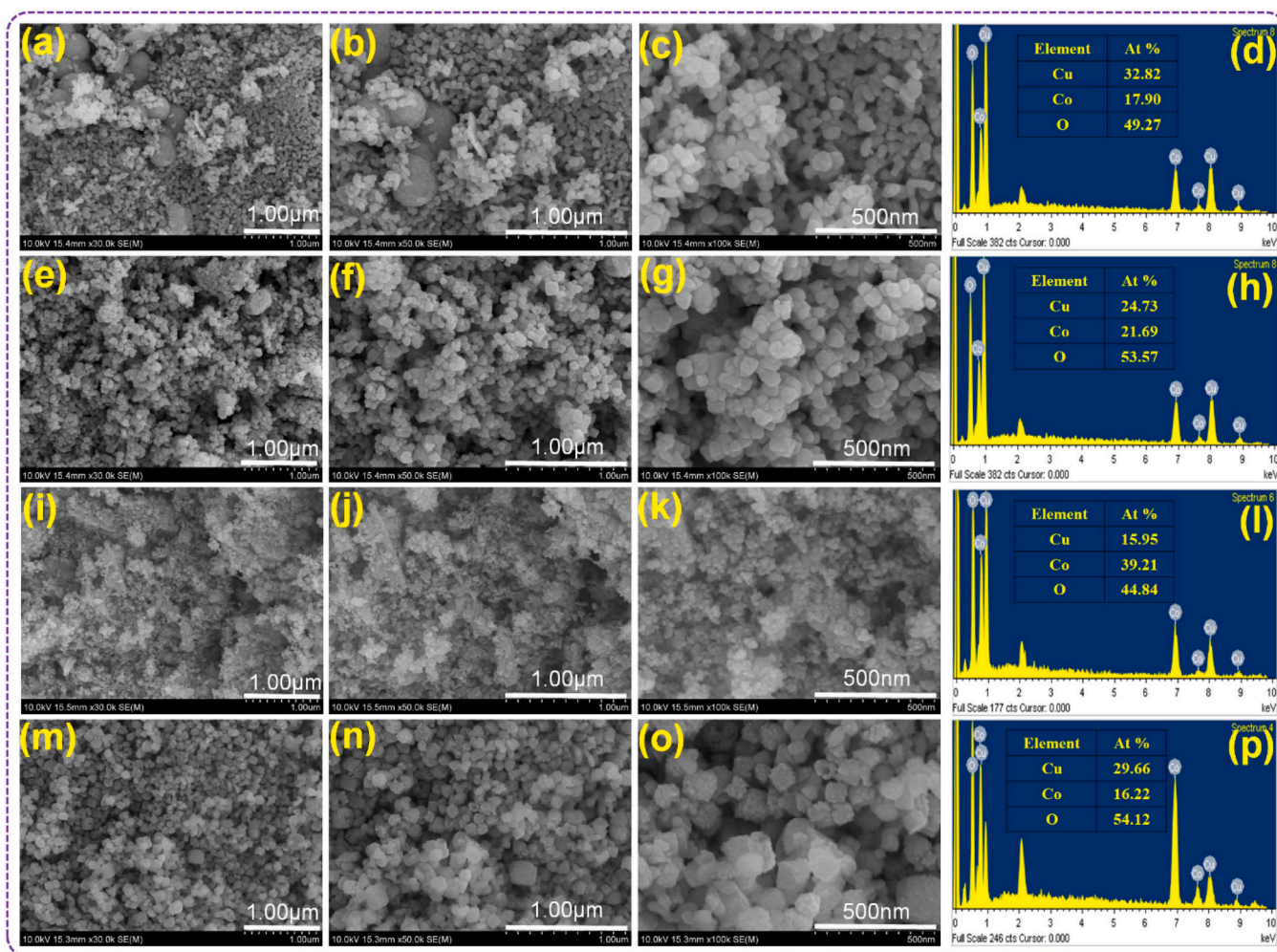


Fig. 3. Scanning Electron Micrographs of CCO-3 h (a-c), CCO-5 h (e-g), CCO-7 h (i-k), CCO-9 h (m-o) at different magnification, corresponding EDS spectra (d, h, i, p).

analysis investigation. CCO-7 nanoparticles were studied at three concentrations: 0.1 ppm, 1 ppm, and 5 ppm. The estimated average elemental composition showed that the Co and Cu concentrations were 50.51% and 30.91%, respectively. The results of this study are consistent with those of XPS and EDS, revealing that the CCO-7 electrode appears to be stoichiometric. A transmission electron microscopy (TEM) was also performed for the CCO-7 h sample to resolve microstructure at higher magnification. The TEM images of CCO-7 h nanoparticles are shown in Fig. 4. A small overgrowth of nanoparticles was observed for the CCO-7 h nanoparticles. The particle overgrowth offers maximal surface area and an electroactive site, allowing the essay electrolyte ions transportation and improving the electrochemical performance of the electrode. Fig. 4 (a, b, and d) depicts the overgrowth of tiny nanoparticles in CCO-7 h sample. The SAED pattern of the CCO-7 h particles is shown in Fig. 4c. SAED observation demonstrates that the CCO-7 h nanoparticles are highly crystalline. The interplanar spacing was determined to be 0.274 nm, as illustrated in Fig. 4 (e,f) 'd' spacing. Fig. 4 (g, h, i, j) shows the elemental mapping and EDS spectrum of the CCO-7 h nanoparticles. The elemental mapping shows that all elements were uniformly distributed i.e. Co, Cu, and O, in the sample and the EDS spectrum confirms the stoichiometry of the CCO-7 h nanoparticle, which is well matched with XRD and XPS results.

Using a Cyclic Voltammetry curve, the influence of the hydrothermal reaction time on the electrochemical performance of the electrode was investigated. Fig. 6 depicts the Cyclic Voltammetry of all CCO electrodes measured in 2 M KOH electrolytes obtained at different scan rates of 10,

20, 40, 60, 80, and 100 mV/s within the potential range of 0.0–0.5 V. The existence of a pair of redox peaks in all CV curves caused by the faradic reaction of Cu^{2+} - Cu^+ and Co^{4+} - Co^{3+} suggests that the electrode material is a battery type electrode [45]. All the CV profile shows the pair of redox peak which originated from the reversible faradic reaction associated with OH^- anion [46]. As the scan rate increases, the peaks shift. This shift correlates to an increase in internal resistance to ion and electron transport at higher scan rates, resulting in a modest drop in electrochemical performance [47]. The faradic reactions are represented by the following Eqs. (1–3)[34,35].

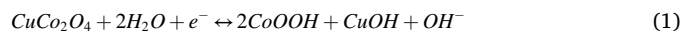


Fig. 5 (a) illustrates the CV of CVO-3 electrode at various scan speeds. The CV profile illustrates different oxidation and reduction peaks that rise with scan rate. Fig. 5(b) shows sharp oxidation and reduction peaks for the CCO-5 electrode, as well as an increase in the plateau region. Fig. 5(c) shows a reduction in the plateau region for the CVO-7 electrode, presumably due to the formation of tiny nanogranules on the nanoparticle. In Fig. 5(d), the sharpness of the peak and the plateau both diminish for CVO-9. This might be attributable to nanogranules overgrowth, which lowers surface area and ion diffusion, lowering the electrode's electrochemical performance. In Fig. S2 (SI) the CV

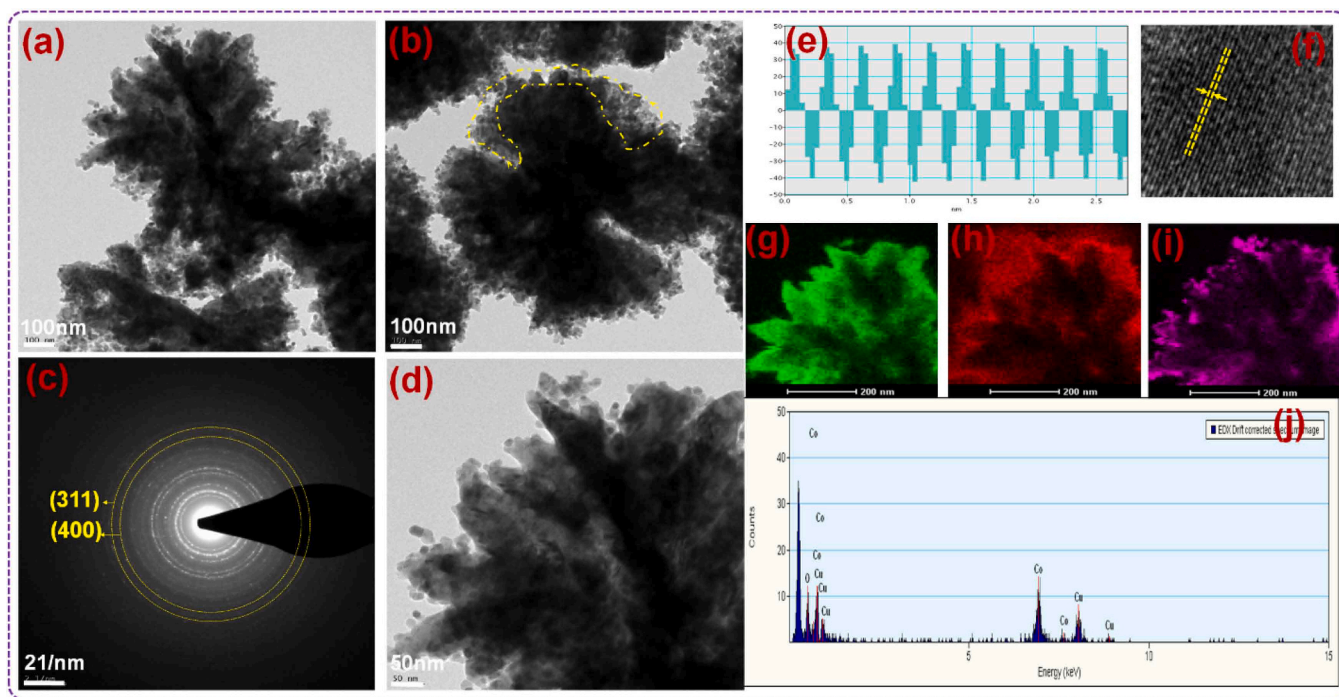


Fig. 4. (a, b, d) The TEM images, (c) SAED pattern, (e-f) 'd' spacing, (g-i) Elemental mapping, and (j) EDS spectrum of CCO-7 h.

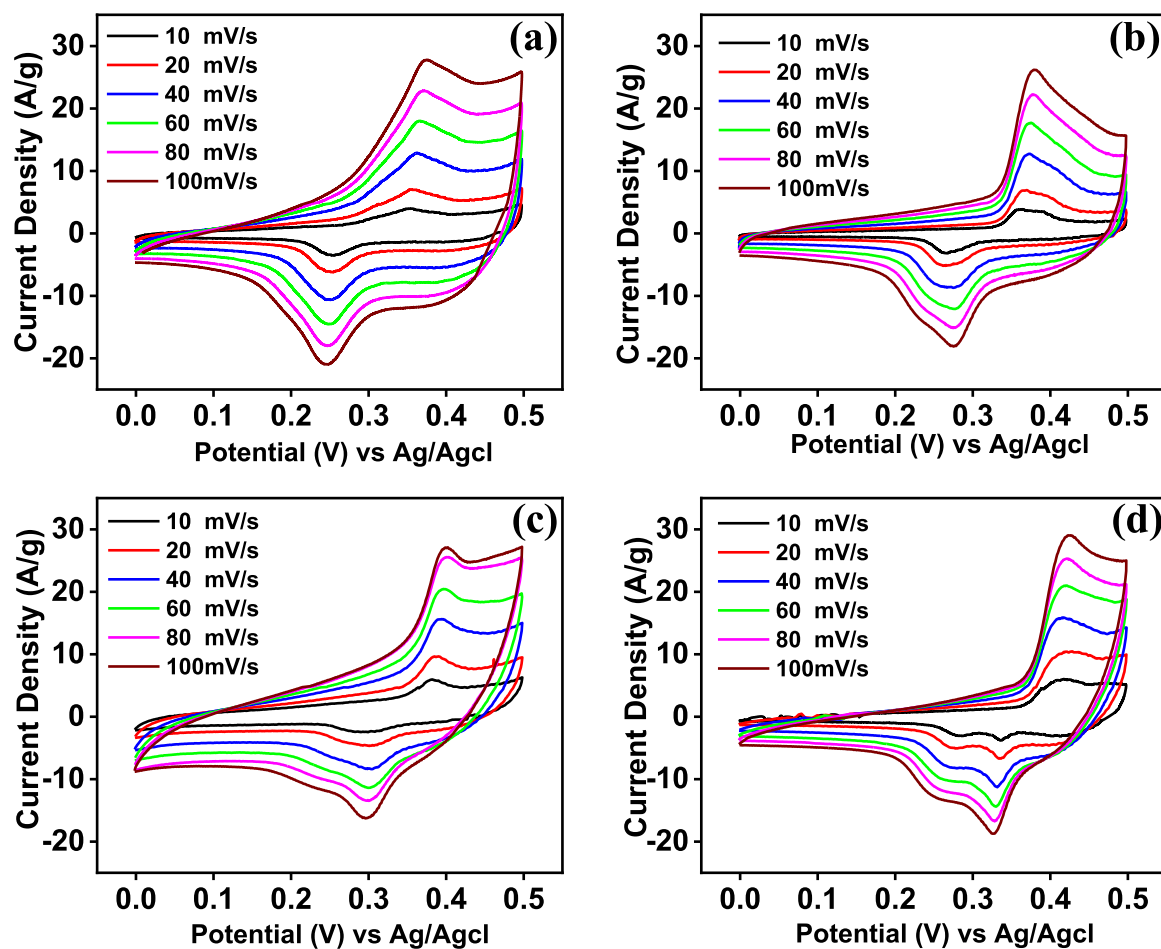


Fig. 5. Cyclic Voltammetry curve of (a) CCO-3 h, (b) CCO-5 h, (c) CCO-7 h, (d) CCO-9 h.

demonstrates that as the hydrothermal reaction time was varied, changes were observed in the shape of the CV curve and the area under the curve also changed. The variation of the cathodic and anodic peaks was noticed when the hydrothermal reaction time changed. The elemental composition and phase formation of the electrode material may account for the change in area under the curve and peak shift. The Cu/Co ratio changes with the hydrothermal reaction period, according to the EDS results. The Cu/Co ratio reduced as the hydrothermal reaction time increased up to 7 h and then increased again for 9 h of reaction time. The electrode's specific capacity changes with reaction time as well. The Cu/Co ratio from the XRD analysis is 0.33, while the EDS Cu/Co ratio is 0.4. It has the potential to improve the electrochemical performance of the CCO-7 h electrode. The electrochemical performance of the CCO-9 h was reduced once again. It might be because of the mixed phase detected in the XRD data.

The charge storage mechanism could be due to a capacitive-controlled mechanism on the outer surface and a diffusion-controlled mechanism on the inner surface. The following equation was used to determine the charge storage contribution using an empirical power law: The peak current in the CV profile is the sum of the capacitive (surface) and diffusion (inner surface) contributions, which are given by the formulae below.

$$i = i_{\text{surface}} + i_{\text{diffusion}} \quad (4)$$

$$i = av^b \quad (5)$$

After rearranging the above equation

$$\log(i) = \log(a) + b \cdot \log(v) \quad (6)$$

Where, 'I' represent the peak current in CV profile, 'v' is the scan rate of the CV profile and the 'b' is the slope of the $\log(i)$ vs $\log(v)$ and 'a' is the intercept of the same plot.

Charge storage in an electrochemical system involves interactions between the electrolytic ions and the active material. This storage mechanism can be explained by both faradaic and non-faradaic processes. In the non-faradaic process, charge storage occurs through the Electric Double Layer Capacitor (EDLC) mechanism, where charges accumulate at the interface between the electrolyte and the electrode.

Faradaic processes, on the other hand, employ two approaches for charge storage. The first is the pseudocapacitive approach, where charge is stored through a redox reaction occurring at the interface between the electrode and the electrolyte. The second is the battery-type approach, where charge storage occurs through the faradaic reactions involving electrolyte ions within the matrix of the active material. [48]. According to the slope of $\log(i)$ vs $\log(v)$, the material's charge storage contribution were determined as either a diffusion contribution from the faradic redox activity or a capacitive contribution from the non-faradic activity. The $b = 1.0$ indicates charge storage from non-faradic activity with a capacitive charge storage contribution, whereas $b = 0.5$ represents charge storage from faradic activity with a diffusion contribution [11, 49]. The 'b' value of the electrode material lies between 0.66 and 0.83 as shown in Fig. 6(a-b). The 'b' value was observed to be lowered for

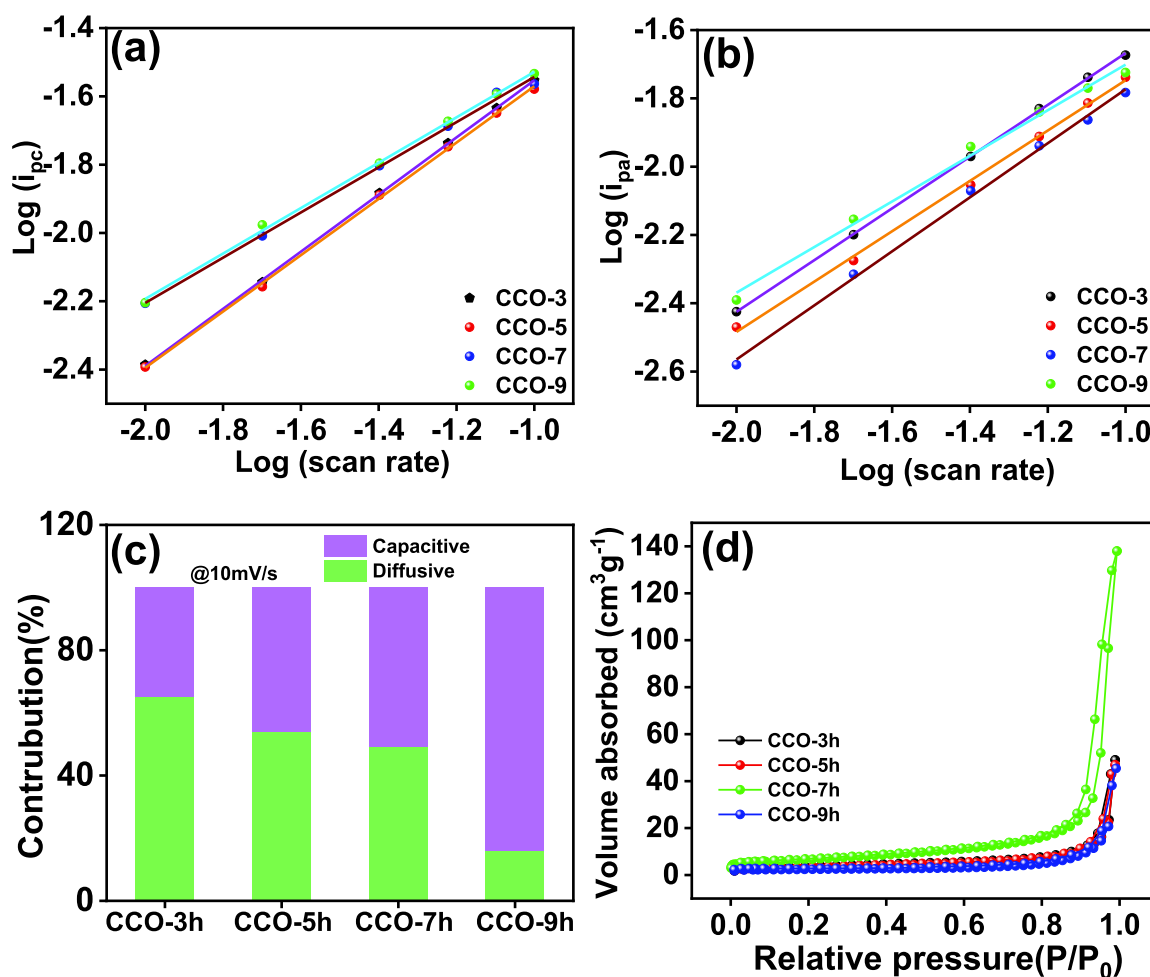


Fig. 6. (a) log current vs log scan rate for b value for all electrodes (cathodic), (b) log current vs log scan rate for b value for all electrodes (Anodic), (c) Comparative diffusion controlled and capacitive contribution for different scan rates of all electrodes, (d) Nitrogen adsorption-desorption isotherm of CCO-3 h, CCO-5 h, CCO-7 h, CCO-9 h.

increasing hydrothermal reaction time from 3 h to 9 h. As 'b' value decreases with increasing hydrothermal reaction, the contribution of diffusion charge storage decreases. Fig. 6(c) depicts the comparative charge storage contribution of all electrodes at 10 mV/s. The 'b' value for CCO-7 h is 0.66, which explains the diffusion contribution charge storage was dominated over capacitive contribution. The diffusion-controlled contribution in CCO-7 h electrode material may be attributed to the nanoparticle's tiny growth, which provides a greater surface for diffusion contribution. BET were used to compute the specific surface area of the nanoparticles. Fig. 6(d) depicts the N_2 absorption and desorption isotherms of all samples. The CCO-3 h CCO-5 h CCO-7 h CCO-9 h electrode has an absolute surface area of 10.53, 10.61, 23.40 and 8.96 m^2/g , the CCO-7 h electrode has higher surface it might be due to the overgrowth of the nanoparticles which increases the energy storage capacity of the CCO-7 h electrode. The increased surface area impact may benefit ion diffusion and increase the specific capacity of the CCO-7 h electrode [50]. The CV profile was used to estimate the diffusion controlled and capacitive controlled percentages to total charge storage. The capacitive and diffusion-controlled contributions to total current are depicted in the equation below.

$$i = k_1 v + k_2 \sqrt{v} \quad (7)$$

$$\frac{i}{\sqrt{v}} = k_1 \sqrt{v} + k_2 \quad (8)$$

Where $k_1 v$ signifies the capacitive controlled contribution and $k_2 \sqrt{v}$ indicates the diffusion contribution. Fig. 7(b) depicts the capacitive and diffusion-controlled contributions of CCO-7 h at varying scan rates, in addition to the quantitative charge storage distribution at 100 mV/s as shown in Fig. 7(a). The diffusion-controlled contribution dropped as

scan rates go up, confirming that surface-limited charge storage prevails at high scan speeds. To compute the diffusion coefficient and explain the charge storage kinetics, the Randles-Sevcik relation was employed. The diffusion constant is approximately the same, at $0.000198 \text{ cm}^2 \text{ s}^{-1}$. The hydrothermal reaction period does not influence the diffusion coefficient. The diffusion coefficient D was calculated from i_p vs \sqrt{v} plot as shown in Fig. 7(c-d) using equation [49]. As The D decreases with an increase in scan rate. At a high scan rate, the detection of redox species is small, which affects the diffusion contribution, and at a small scan rate, the detection of redox species is greater, which increases the diffusion contribution [49]. The GCD profile was utilized to calculate the electrode's specific capacity(C/g), specific capacitance(F/g), energy density, and power density using the equation.

$$\text{Mass capacity}(C_m) = I \times T_d / M \quad (9)$$

$$\text{Specific capacitance}(C_s) = I \times T_d / M \times V \quad (10)$$

$$\text{Energy density}(ED) = (C_s V^2) / 7.2 \quad (11)$$

$$\text{Power density}(PD) = (ED \times 3600) / T_d \quad (12)$$

where C_m is the specific capacity, C_s is the specific capacitance of the sample, M is the mass of the active material on Ni foam in g, V is the voltage window, T_d is the discharge time in s. Fig. 8(a) depicts the GCD cure of all electrodes at 3 mA/cm² and the GCD profile of the CCO-7 h electrode at the various current densities as shown in Fig. 8 (b). Fig. S2 depicts the GCD profiles of CCO-3 h, CCO-5 h, CCO-7 h, and CCO-9 h. Fig. 8 (a) depicts the nonlinear character of the GCD profile, which demonstrates the faradic behavior of the battery type electrode material, and the results were comparable to the CV profile. When all of the

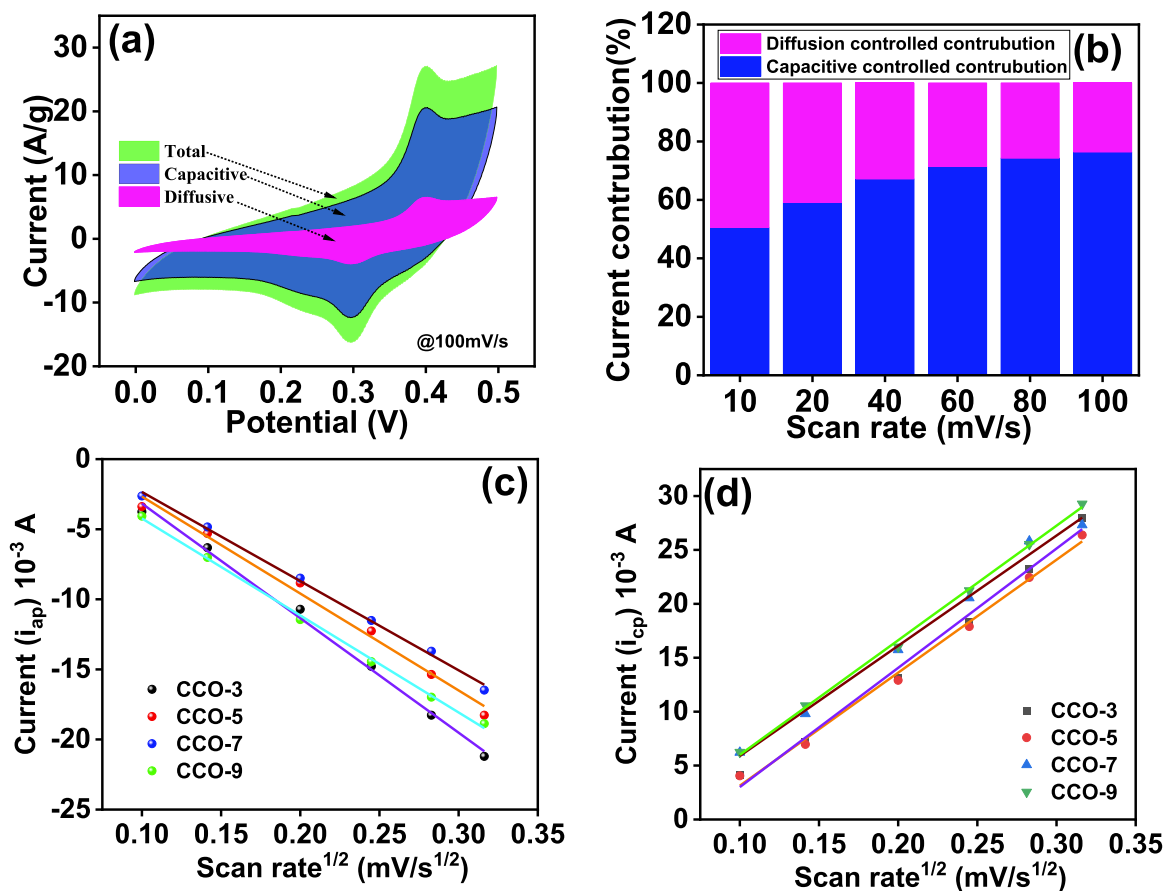


Fig. 7. (a) Diffusion-controlled and capacitive contribution of CCO-7 h at 100 mV/s, (b) Comparative diffusion controlled and capacitive contribution for different scan rates of all electrodes, (c-d) Peak current vs scan rate^{1/2} for diffusion coefficient oxidation and reduction for all electrodes.

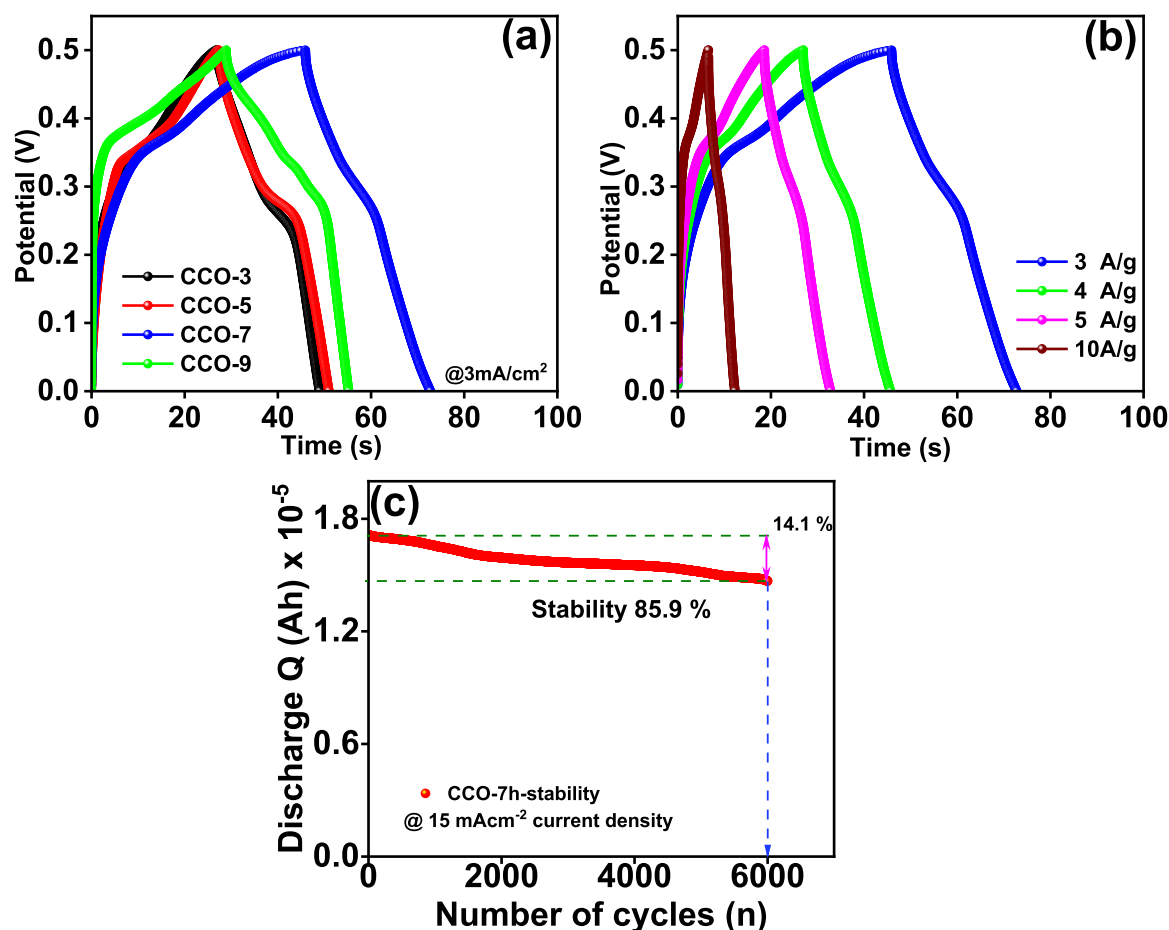


Fig. 8. (a) Comparative Galvanostatic charge-discharge curve of CCO-3 h, CCO-5 h, CCO-7 h, CCO-9 h at 1 mAcm^{-2} , (b) Galvanostatic charge-discharge curve of CCO-7 h at different current densities, (c) Cyclic stability of CCO-7 h at 15 mAcm^{-2} .

electrodes are compared, the CCO-7 h electrode has the longest charge and discharge profile, showing its high specific capacity. CuCo_2O_4 electrode material has specific capacitance (specific capacity) of 121 F/g (60 C/g), 82 F/g (41 C/g), 193 F/g (96.5 C/g), and 143 F/g (71.5 C/g) at 3 mA/cm^2 current density. The influence of the hydrothermal reaction duration on the specific capacity of the electrode was detected due to variations in the surface microstructure of the electrode material. Nanoballs-like structures were observed at 3 h hydrothermal reaction time, and their size was marginally enhanced up to 5 h hydrothermal reaction time. A little overgrowth on the nanoparticle was found after 7 h of the hydrothermal reaction period, providing the porous surface area and increasing the specific capacity of the CCO-7 h electrode. Instead of a single metallic oxide, the synergistic impact of Cu and Co increases the specific capacity of the bimetallic oxide. The Eqs. (11–12) was used to compute the electrode's energy density and power density. The power density and energy density were obtained as 7.09 Wh/kg and 312.5 W/kg, respectively for CCO-7 h electrode material.

The long-term endurance of the electrode material is critical in practical applications. Fig. 8(c) demonstrates the CCO-7 h electrode cyclic stability over 6000 cycles at constant current density 15 mAcm^{-2} . The capacity retention of the CCO-7 h electrode after 6000 cycles was studied. The CCO-7 h electrode material offers improved long-life stability, high rate capability, and superior specific capacity due to the ideal hydrothermal reaction duration of 7 h for CuCo_2O_4 electrode material. The kinematic electrochemical reaction that happens in a cell at the electrode-electrolyte interface was explained by the EIS spectra of the electrode material in the 2 M KOH electrolyte. Fig. 9 (a) depicts the EIS spectra of all electrodes. At high frequencies, the x-axis intercept shows the specifics of the equivalent series resistance (R_s) for all

electrodes, with almost the same intercept, at 0.44Ω , corresponding to the system's bulk resistance. The charge transfer resistance has given by the tiny semicircle diameter in the high-frequency zone (R_{ct}). The charge transfer resistance of a CuCo_2O_4 electrode is 2.24Ω , 5.24Ω , 1.81Ω , and 2.74Ω at 3 h, 5 h, 7 h, and 9 h. The small R_s and R_{ct} values of the CCO-7 h electrode may provide higher specific capacitance. The low R_{ct} value might be due to nanoparticle overgrowth and the wide surface area, which provides a larger active surface area for diffusion into the electrode material without obstructions. The ionic conductivity of the electrode is represented by the straight line in the low-frequency region. The phase angle frequency plot was used to evaluate the electrode's optimum capacitive behavior. The curve of phase angle versus frequency is shown in Fig. 9(b). For the CCO electrode, the frequency that crosses the phase angle at 45° is 3.08 Hz, 2.05 Hz, 0.1 Hz, and 1.14 Hz for the 3 h, 5 h, 7 h, and 9 h hydrothermal reaction periods, respectively. CCO-7 h electrode offers the best capacitive nature and quick frequency response, with a phase angle of 45° at 0.1 Hz. The influence of the surface microstructure on frequency variation was detected, which was reduced to 0.1 from 3.08, implying that tiny overgrowth of nanoparticles gives superior capacitive behavior [51]. Fig. 9 (c) reveals the lowest value of frequency-dependent impedance for CCO-7 h revealing that it has a higher conductivity than other. It might be due to nanoparticle overgrowth [52,53]. The capacitive nature of the active electrode material is demonstrated by the frequency-dependent impedance as shown in Fig. 9 (d). The Eqs. (13–15) were used to compute the frequency-dependent capacitance of the electrode material. Fig. 9(d) depicts the frequency dependence electrode's real and imaginary capacitances of the CCO-7 h, which is roughly 4.22 mF.

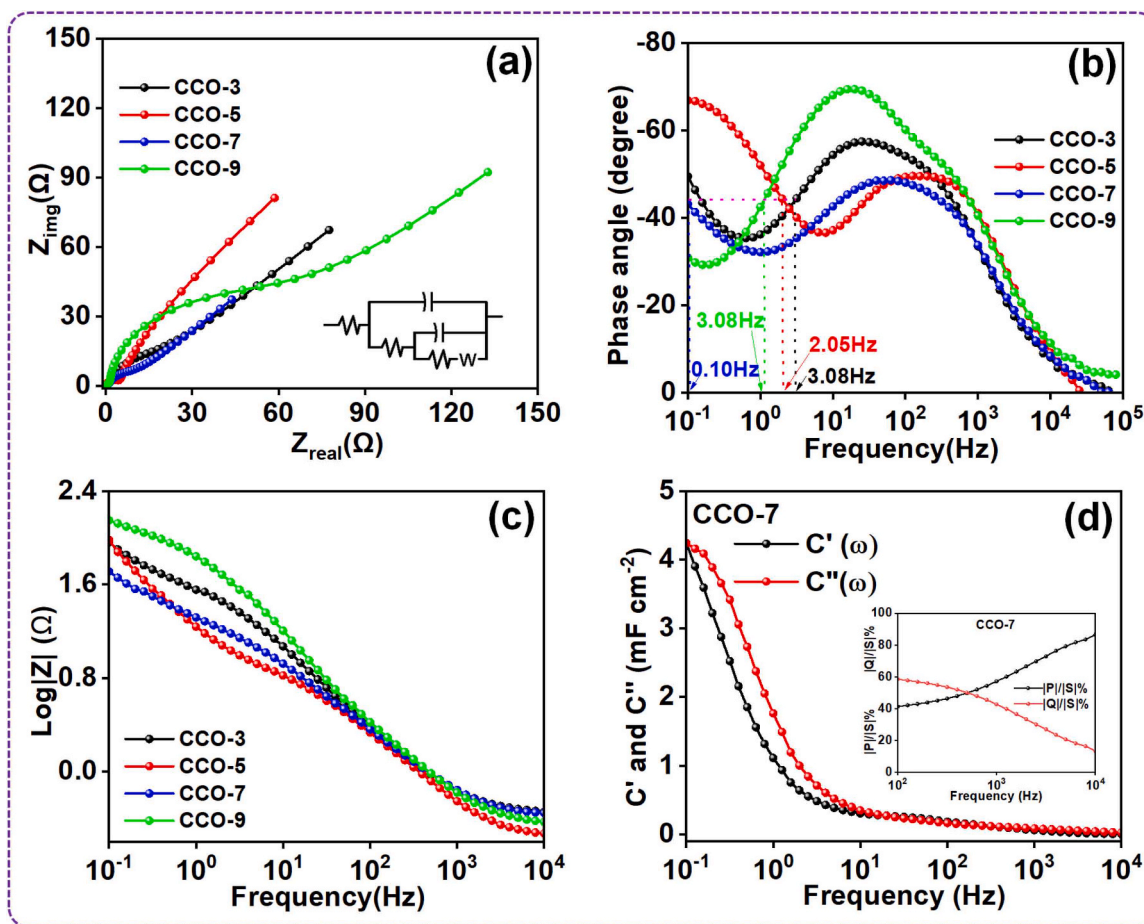


Fig. 9. (a) Electrochemical impedance spectroscopy spectra, (b) Phase angle vs. frequency, (c) $\log |Z|$ vs Frequency of CCO-3 h, CCO-5 h, CCO-7 h, CCO-9 h, and (d) Real capacitance (C') and imaginary capacitance (C'') versus frequency (inset plot of normalized active power and normalized reactive power vs frequency of CCO-7 h).

$$C(\omega) = C'(\omega) - jC''(\omega) \quad (13)$$

$$C'(\omega) = \frac{Z'(\omega)}{[\omega|Z(\omega)|]^2} \quad (14)$$

$$C''(\omega) = \frac{Z''(\omega)}{[\omega|Z(\omega)|]^2} \quad (15)$$

where Z' and Z'' are imaginary and real parts of the Nyquist plot. $Z(\omega)$ is the complex impedance represented by $Z(\omega) = Z'(\omega) + jZ''(\omega)$, $\omega = 2\pi f$, f is the frequency. $C'(\omega)$, and $C''(\omega)$ are the energy loss due to irreversible processes and accessible capacitance of the electrode. The Eqs. (16–18) were used to compute the complex power, normalized active power, and normalized reactive power of the electrode material. The image depicts the two power crosses at frequency f_0 , which corresponds to the relaxation period $\tau_0 = 1/f_0$. The relaxing time yields a discharge time with an efficiency greater than 50%. The CCO-7 h electrode has a relaxation time of 1.9 ms [52,54].

$$S(\omega) = P(\omega) - jQ(\omega) \quad (16)$$

$$P(\omega) = [\omega C'(\omega)] \times [|\Delta V_{rms}|]^2 \quad (17)$$

$$Q(\omega) = [\omega C''(\omega)] \times [|\Delta V_{rms}|]^2 \quad (18)$$

where $|\Delta V_{rms}|^2 = \frac{\Delta V_{max}^2}{2}$, ΔV_{max} is the maximum amplitude of A.C. signal the electrode.

To explore the practicability of the CCO-7 h electrode for energy storage, an asymmetric supercapacitor was fabricated using activated carbon and CCO-7 h electrodes as anode and cathode, respectively, with a separator between the two electrodes and is denoted by CCO//AC. The CV analysis of the CCO-7 h and AC electrodes in the 2 M KOH electrolyte was used to figure out the total voltage of the CCO//AC ASC device. Fig. S4(a)(SI) represents the CV profile of CCO//AC ASC and Fig. 10 (a-b) shows the CV and GCD profile of the device at different scan rates and current density at the potential. Based on the CV studies, the voltage of the CCO-7 h electrode was 0.0–0.5 V and the voltage of the AC carbon electrode is –1.0–0.00 V. Fig. S4(b)(SI) represents the CV profile of the CCO//AC electrode with a range of 0.6–1.0 V at 100 mV/s scan rate showing a rectangular shape with a redox peak. The CV profile's form stayed constant. The form of the CV profile stayed unchanged but the area under the curve enlarged as the scan rate increased, confirming its outstanding rate property up to 1.0 V. Further expansion of the CV profile's potential window beyond 1 V was observed, as a stretched CV profile, presumably due to an undesired peak of oxygen emission [55, 56]. Fig. S4(c) (SI) shows the GCD profile of CCO//AC ASC, which was accomplished to examine the further capacitive property at a current density of 1 mA/cm². The almost symmetric nature of CCO//AC ASC's GCD exhibits enhanced electrical reversibility. The specific capacitance of the CCO//AC ASC is 35 F/g and specific capacity of 35 C/g, illustrating the capability derived from the overgrowth structure and the high conductivity of the CCO-7 h electrode. The Eqs. (11–12) were used to compute the energy density and power density of the CCO//AC ASC. The galvanostatic charge-discharge (GCD) measurements of the CCO//AC asymmetric supercapacitor (ASC) showed energy and power

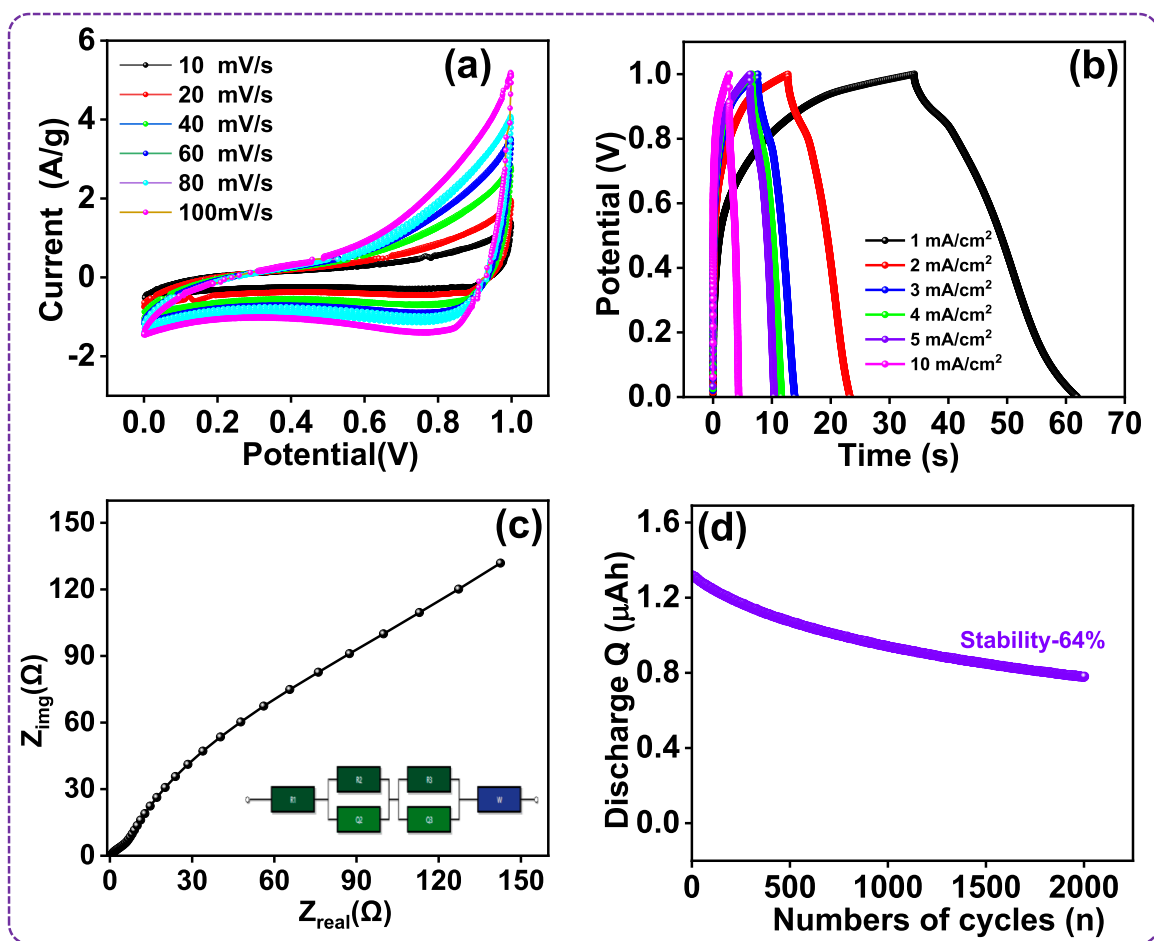


Fig. 10. Electrochemical performance of CCO-7 h (CCO//AC) asymmetric device. (a) Cyclic voltammetry at different scan rates (10–100 mVs⁻¹), (b) Galvanostatic charge-discharge at different current densities (1–10 mAcm⁻²), (c) Nyquist plot. (d) Cyclic stability of CCO-7 h (CCO//AC) asymmetric device based on discharge Q, up to 2000 cycles.

densities of 2.12 Wh/kg and 277 W/kg, respectively. These results are represented in the Ragone plot shown in Fig. S4d. The cyclic performance of the ASC during 2000 cycles of 1 A/g was used to investigate the stability of the CCO//AC ASC. Over 2000 GCD cycles, the ASC retains 64% of its capacity as shown in Fig. 10 (d). Fig. 10 (c) depicts the EIS spectrum of CCO//AC ASC following stabilization. R_s and R_{ct} have values of 1.14 and 24.96 Ω , respectively. Table 1.

Table 1
Comparison of specific capacitance for different microstructure reported in the literature.

Sr. No.	Surface microstructure	Synthesis Method	Specific capacitance (F/g)	Reference
1.	Spheroidal	Chemical Method	210	[57]
2.	Rose-Like	Hydrothermal	235	[58]
3.	Spherical	Co-Precipitation	290	[33]
4.	Needleshaped Nanorods	Hydrothermal	335	[58]
5.	Cauliflower-	Precipitation	338	[59]
6.	Nanoneedle	Hydrothermal	390	[60]
7.	Hexagonal	Precipitation	24	[36]
8.	Nanowire	Electrospinning	0.423	[61]
9.	Spherical	Hydrothermal	432	Present work

4. Conclusions

CuCo₂O₄ battery-type electrode material has been efficiently synthesized with uniform overgrowth at sub-ambient temperatures using a hydrothermal approach. Optimal hydrothermal reaction durations resulted in a porous morphology with finely dispersed nanoparticles, which boosted the electrode-electrolyte interface area and hence electrochemical efficacy. Under a current density of 3 mA/cm², the CCO-7 h electrode achieved specific capacity and capacitance of 96.5 C/g and 193 F/g, respectively. Concurrently, the CCO//AC ASC device exhibited an energy density of 2.12 Wh/kg and a power density of 277 W/kg, while retaining 64% of its initial capacity after 2000 cycles, indicating excellent cycle durability. This study highlights the critical importance of hydrothermal reaction duration in fine-tuning the microstructural properties of CuCo₂O₄, making it suitable for high-performance supercapacitor applications.

CRediT authorship contribution statement

M. A. Yewale: Conceptualization, Investigation, Writing – original draft, **R. A. Kadam:** Investigation, Writing – original draft, **A. A. Jadhavar,** **A. M. Teli:** Characterizations, **Nitin T. Shelke,** **V. Kumar,;** Formal analysis **S. A. Beknalkar,** **S. L. Kadam:** Methodology: Data analysis, **U. T. Nakate:** Supervision, Writing – review & editing, **D. K. Shin:** Supervision.

Declaration of Competing Interest

The authors declare that they have no known competing financial interests or personal relationships that could have appeared to influence the work reported in this paper.

Data Availability

Data will be made available on request.

Acknowledgments

This work was supported by the Technology Innovation Program (#20010170) funded by the Ministry of Trade, Industry & Energy (MOTIE, Korea).

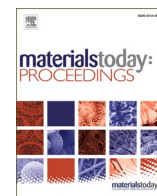
Appendix A. Supporting information

Supplementary data associated with this article can be found in the online version at [doi:10.1016/j.colsurfa.2023.132541](https://doi.org/10.1016/j.colsurfa.2023.132541).

References

- [1] D.P. Dubal, O. Ayyad, V. Ruiz, P. Gómez-Romero, Hybrid energy storage: the merging of battery and supercapacitor chemistries, *Chem. Soc. Rev.* 44 (2015) 1777–1790, <https://doi.org/10.1039/c4cs00266k>.
- [2] A.M. Patil, S. Moon, A.A. Jadhav, J. Hong, K. Kang, S.C. Jun, Modifying electronic structure of cation-exchanged bimetallic sulfide/metal oxide heterostructure through in situ inclusion of silver (Ag) nanoparticles for extrinsic pseudocapacitor, *Adv. Funct. Mater.* (2023), <https://doi.org/10.1002/adfm.202305264>.
- [3] C. Long, M. Zheng, Y. Xiao, B. Lei, H. Dong, H. Zhang, H. Hu, Y. Liu, Amorphous Ni-Co binary oxide with hierarchical porous structure for electrochemical capacitors, *ACS Appl. Mater. Interfaces* 7 (2015) 24419–24429, <https://doi.org/10.1021/acsami.5b03036>.
- [4] I. Shakir, M. Sarfraz, U.A. Rana, M. Nadeem, M.A. Al-Shaikh, Synthesis of hierarchical porous spinel nickel cobaltite nanoflakes for high performance electrochemical energy storage supercapacitors, *RSC Adv.* 3 (2013) 21386–21389, <https://doi.org/10.1039/c3ra43973a>.
- [5] S.A. Beknalkar, A.M. Teli, A.C. Khot, T.D. Dongale, M.A. Yewale, K.A. Nirmal, J. C. Shin, A new path to high-performance supercapacitors: Utilizing Ag-embedded CoFe-phosphate and Ti3C2 MXene as hybrid electrodes, *J. Energy Storage* 72 (2023), 108272, <https://doi.org/10.1016/j.est.2023.108272>.
- [6] W. Ge, Q. Ma, Z. Ai, W. Wang, F. Jia, S. Song, Three-dimensional reduced graphene oxide/montmorillonite nanosheet aerogels as electrode material for supercapacitor application, *Appl. Clay Sci.* 206 (2021), 106022, <https://doi.org/10.1016/j.clay.2021.106022>.
- [7] C. Portet, P.L. Taberna, P. Simon, E. Flahaut, Influence of carbon nanotubes addition on carbon-carbon supercapacitor performances in organic electrolyte, *J. Power Sources* 139 (2005) 371–378, <https://doi.org/10.1016/j.jpowsour.2004.07.015>.
- [8] Y. Zhang, E. Xie, Functionalized and tip-open carbon nanotubes for high-performance symmetric supercapacitors, *Dalt. Trans.* 50 (2021) 12982–12989, <https://doi.org/10.1039/d1dt02055b>.
- [9] Y. Gao, Y. Xia, H. Wan, X. Xu, S. Jiang, Enhanced cycle performance of hierarchical porous sphere MnCo₂O₄ for asymmetric supercapacitors, *Electrochim. Acta* 301 (2019) 294–303, <https://doi.org/10.1016/j.electacta.2019.01.173>.
- [10] M.A. Yewale, A.A. Jadhav, R.A. Kadam, N.B. Velhal, U.T. Nakate, A.M. Teli, J. C. Shin, L.N. Nguyen, D.K. Shin, N.K. Kaushik, Hydrothermal synthesis of manganese oxide (Mn₃O₄) with granule-like morphology for supercapacitor application, *Ceram. Int.* 48 (2022) 29429–29437, <https://doi.org/10.1016/j.ceramint.2022.06.144>.
- [11] M.A. Yewale, R.A. Kadam, N.K. Kaushik, S.V.P. Vattikuti, L.P. Lingamdinne, J. R. Koduru, D.K. Shin, Hydrothermally synthesized microrods and microballs of NiCo₂O₄ for supercapacitor application, *Ceram. Int.* 48 (2022) 22037–22046, <https://doi.org/10.1016/j.ceramint.2022.04.190>.
- [12] A.M. Teli, S.A. Beknalkar, S.M. Mane, M.A. Yewale, T.D. Dongale, J. Cheol, Synergetic effect of ternary MnVMO-oxide electrode by hydrothermal method for high-performance asymmetric supercapacitor, *J. Energy Storage* 65 (2023), 107289, <https://doi.org/10.1016/j.est.2023.107289>.
- [13] C.D. Lokhande, D.P. Dubal, O.S. Joo, Metal oxide thin film based supercapacitors, *Curr. Appl. Phys.* 11 (2011) 255–270, <https://doi.org/10.1016/j.cap.2010.12.001>.
- [14] S.D. Dhas, P.N. Thonge, S.D. Waghmare, G.K. Kulkarni, S.K. Shinde, D.Y. Kim, T. M. Patil, M.A. Yewale, A.V. Moholkar, D. Kim, Hierarchical spinel NiMn₂O₄ nanostructures anchored on 3-D nickel foam as stable and high-performance supercapacitor electrode material, *J. Energy Storage* 71 (2023), 108168, <https://doi.org/10.1016/j.est.2023.108168>.
- [15] R.A. Kadam, M.A. Yewale, A.M. Teli, Annu, U.T. Nakate, V. Kumar, S.L. Kadam, D. K. Shin, Bimetallic Co₃V₂O₈ microstructure: a versatile bifunctional electrode for supercapacitor and electrocatalysis applications, *Surf. Interfaces* 41 (2023), 103267, <https://doi.org/10.1016/j.surfint.2023.103267>.
- [16] M.A. Yewale, V. Kumar, R.A. Kadam, R.B. Kharade, A.M. Teli, S.A. Beknalkar, S. D. Dhas, U.T. Nakate, D.K. Shin, Wrapped nanochain microstructures of Ni₃V₂O₈ nanoparticles for supercapacitor applications using the hydrothermal method, *J. Energy Storage* 73 (2023), 109005, <https://doi.org/10.1016/j.est.2023.109005>.
- [17] R. Pothu, R. Bolagam, Q.H. Wang, W. Ni, J.F. Cai, X.X. Peng, Y.Z. Feng, J.M. Ma, Nickel sulfide-based energy storage materials for high-performance electrochemical capacitors, *Rare Met* 40 (2021) 353–373, <https://doi.org/10.1007/s12598-020-01470-w>.
- [18] M.A. Yewale, A.K. Sharma, D.B. Kamble, C.A. Pawar, S.S. Potdar, S.C. Karle, Electrochemical synthesis of Cu₂S_{1-x} thin film for supercapacitor application, *J. Alloy. Compd.* 754 (2018) 56–63, <https://doi.org/10.1016/j.jallcom.2018.04.208>.
- [19] V.K. Mariappan, K. Krishnamoorthy, P. Pazhamalai, S. Sahoo, S.S. Nardekar, S. J. Kim, Nanostructured ternary metal chalcogenide-based binder-free electrodes for high energy density asymmetric supercapacitors, *Nano Energy* 57 (2019) 307–316, <https://doi.org/10.1016/j.nanoen.2018.12.031>.
- [20] S.L. Kadam, R.N. Bulakhe, R.A. Kadam, M.A. Yewale, Electrochemical synthesis of CuS thin film for supercapacitor application, *Macromol. Symp.* 392 (2020) 5–9, <https://doi.org/10.1002/masy.201900209>.
- [21] G. Wang, L. Zhang, J. Zhang, A review of electrode materials for electrochemical supercapacitors, *Chem. Soc. Rev.* 41 (2012) 797–828, <https://doi.org/10.1039/c1cs15060j>.
- [22] D.P. Dubal, N.R. Chodankar, D.H. Kim, P. Gomez-Romero, Towards flexible solid-state supercapacitors for smart and wearable electronics, *Chem. Soc. Rev.* 47 (2018) 2065–2129, <https://doi.org/10.1039/c7cs00505a>.
- [23] Y. Zhu, X. Ji, Z. Wu, W. Song, H. Hou, Z. Wu, X. He, Q. Chen, C.E. Banks, Spinel NiCo₂O₄ for use as a high-performance supercapacitor electrode material: Understanding of its electrochemical properties, *J. Power Sources* 267 (2014) 888–900, <https://doi.org/10.1016/j.jpowsour.2014.05.134>.
- [24] Y. Chen, T. Liu, L. Zhang, J. Yu, N-doped graphene framework supported nickel cobalt oxide as supercapacitor electrode with enhanced performance, *Appl. Surf. Sci.* 484 (2019) 135–143, <https://doi.org/10.1016/j.apsusc.2019.04.074>.
- [25] M.A. Yewale, R.A. Kadam, N.K. Kaushik, N.N. Linh, A.M. Teli, J.C. Shin, L. P. Lingamdinne, J.R. Koduru, D.K. Shin, Mesoporous hexagonal nanorods of NiCo₂O₄ nanoparticles via hydrothermal route for supercapacitor application, *Chem. Phys. Lett.* 800 (2022), 139654, <https://doi.org/10.1016/j.cplett.2022.139654>.
- [26] D. Liu, Y. Liu, X. Liu, C. Xu, J. Zhu, H. Chen, Growth of uniform CuCo₂O₄ porous nanosheets and nanowires for high-performance hybrid supercapacitors, *J. Energy Storage* 52 (2022), 105048, <https://doi.org/10.1016/j.est.2022.105048>.
- [27] C. Sun, X. Su, F. Xiao, C. Niu, J. Wang, Synthesis of nearly monodisperse Co₃O₄ nanocubes via a microwave-assisted solvothermal process and their gas sensing properties, *Sens. Actuators, B Chem.* 157 (2011) 681–685, <https://doi.org/10.1016/j.snb.2011.05.039>.
- [28] A.K. Das, N.H. Kim, S.H. Lee, Y. Sohn, J.H. Lee, Facile synthesis of CuCo₂O₄ composite octahedrons for high performance supercapacitor application, *Compos. Part B Eng.* 150 (2018) 269–276, <https://doi.org/10.1016/j.compositesb.2018.07.021>.
- [29] J. Sun, C. Xu, H. Chen, A review on the synthesis of CuCo₂O₄-based electrode materials and their applications in supercapacitors, *J. Mater.* 7 (2021) 98–126, <https://doi.org/10.1016/j.jmat.2020.07.013>.
- [30] A.K. Das, N.H. Kim, S.H. Lee, Y. Sohn, J.H. Lee, Facile synthesis of porous CuCo₂O₄ composite sheets and their supercapacitive performance, *Compos. Part B Eng.* 150 (2018) 234–241, <https://doi.org/10.1016/j.compositesb.2018.05.028>.
- [31] D.M. Alqahtani, C. Zequine, C.K. Ranaweera, K. Siam, P.K. Kahol, T.P. Poudel, S. R. Mishra, R.K. Gupta, Effect of metal ion substitution on electrochemical properties of cobalt oxide, *J. Alloy. Compd.* 771 (2019) 951–959, <https://doi.org/10.1016/j.jallcom.2018.09.014>.
- [32] G.P. Kamble, A.S. Rasal, S.B. Gaikwad, V.S. Gurav, J.Y. Chang, S.S. Kolekar, Y. C. Ling, A.V. Ghule, CuCo₂O₄ nanorods coated with CuO nanoneedles for supercapacitor applications, *ACS Appl. Nano Mater.* 4 (2021) 12702–12711, <https://doi.org/10.1021/acsnm.1c03284>.
- [33] M. Silambarasan, N. Padmanathan, P.S. Ramesh, D. Geetha, Spinel CuCo₂O₄ nanoparticles: facile one-step synthesis, optical, and electrochemical properties spinel CuCo₂O₄ Nanoparticles: facile one-step synthesis, optical, and electrochemical properties, *Mater. Res. Express* 3 (2016), 095021 <https://iopscience.iop.org/article/10.1088/2053-1591/3/9/095021>.
- [34] A. George, M. Kundu, Construction of self-supported hierarchical CuCo₂O₄ dendrites as faradaic electrode material for redox-based supercapacitor applications, *Electrochim. Acta* 433 (2022), <https://doi.org/10.1016/j.electacta.2022.141204>.
- [35] Q. Gao, J. Wang, J. Wang, Morphology-controllable synthesis of CuCo₂O₄ arrays on Ni foam as advanced electrodes for supercapacitors, *J. Alloy. Compd.* 789 (2019) 193–200, <https://doi.org/10.1016/j.jallcom.2019.03.041>.
- [36] J. Bosco Franklin, S. Sachin, S. John Sundaram, G. Theophil Anand, A. Dhayal Raj, K. Kaviyarasu, Investigation on copper cobaltite (CuCo₂O₄) and its composite with activated carbon (AC) for supercapacitor applications, *Mater. Sci. Energy Technol.* 7 (2024) 91–98, <https://doi.org/10.1016/j.mset.2023.07.006>.
- [37] J. Sun, Y. Wang, Y. Zhang, C. Xu, H. Chen, Egg albumin-assisted hydrothermal synthesis of Co₃O₄ quasi-cubes as superior electrode material for supercapacitors with excellent performances, *Nanoscale Res. Lett.* 14 (2019), <https://doi.org/10.1186/s11671-019-3172-y>.
- [38] H. Chen, J. Wang, F. Liao, X. Han, C. Xu, Y. Zhang, Facile synthesis of porous Mn-doped Co₃O₄ oblique prisms as an electrode material with remarkable

- pseudocapacitance, *Ceram. Int.* 45 (2019) 8008–8016, <https://doi.org/10.1016/j.ceramint.2019.02.010>.
- [39] H. Wu, W. Sun, J. Shen, D.W. Rooney, Z. Wang, K. Sun, Role of flower-like ultrathin Co₃O₄ nanosheets in water splitting and non-aqueous Li-O₂ batteries, *Nanoscale* 10 (2018) 10221–10231, <https://doi.org/10.1039/c8nr02376j>.
- [40] S. Kamari Kaverlavani, S.E. Moosavifard, A. Bakouei, Self-templated synthesis of uniform nanoporous CuCo₂O₄ double-shelled hollow microspheres for high-performance asymmetric supercapacitors, *Chem. Commun.* 53 (2017) 1052–1055, <https://doi.org/10.1039/c6cc08888k>.
- [41] S.M. Pawar, B.S. Pawar, P.T. Babar, A.T.A. Ahmed, H.S. Chavan, Y. Jo, S. Cho, J. Kim, B. Hou, A.I. Inamdar, S.N. Cha, J.H. Kim, T.G. Kim, H. Kim, H. Im, Nanoporous CuCo₂O₄ nanosheets as a highly efficient bifunctional electrode for supercapacitors and water oxidation catalysis, *Appl. Surf. Sci.* 470 (2019) 360–367, <https://doi.org/10.1016/j.apsusc.2018.11.151>.
- [42] L.F. Chen, Z.Y. Yu, J.J. Wang, Q.X. Li, Z.Q. Tan, Y.W. Zhu, S.H. Yu, Metal-like fluorine-doped β -FeOOH nanorods grown on carbon cloth for scalable high-performance supercapacitors, *Nano Energy* 11 (2015) 119–128, <https://doi.org/10.1016/j.nanoen.2014.10.005>.
- [43] C. Zhang, T. Kuila, N.H. Kim, S.H. Lee, J.H. Lee, Facile preparation of flower-like NiCo₂O₄/three dimensional graphene foam hybrid for high performance supercapacitor electrodes, *Carbon N. Y* 89 (2015) 328–339, <https://doi.org/10.1016/j.carbon.2015.03.051>.
- [44] M. Lan, B. Liu, R. Zhao, M. Dong, X. Wang, L. Fang, L. Wang, Dandelion-like CuCo₂O₄ arrays on Ni foam as advanced positive electrode material for high-performance hybrid supercapacitors, *J. Colloid Interface Sci.* 566 (2020) 79–89, <https://doi.org/10.1016/j.jcis.2020.01.077>.
- [45] J. Sun, X. Tian, C. Xu, H. Chen, Porous CuCo₂O₄ microtubes as a promising battery-type electrode material for high-performance hybrid supercapacitors, *J. Mater.* 7 (2021) 1358–1368, <https://doi.org/10.1016/j.jmat.2021.03.011>.
- [46] J. Lin, H. Wang, Y. Yan, X. Zheng, H. Jia, J. Qi, J. Cao, J. Tu, W. Fei, J. Feng, Core-branched CoSe₂/Ni_{0.85}Se nanotube arrays on Ni foam with remarkable electrochemical performance for hybrid supercapacitors, *J. Mater. Chem. A* 6 (2018) 19151–19158, <https://doi.org/10.1039/c8ta08263d>.
- [47] D. Cai, S. Xiao, D. Wang, B. Liu, L. Wang, Y. Liu, H. Li, Y. Wang, Q. Li, T. Wang, Morphology controlled synthesis of NiCo₂O₄ nanosheet array nanostructures on nickel foam and their application for pseudocapacitors, *Electrochim. Acta* 142 (2014) 118–124, <https://doi.org/10.1016/j.electacta.2014.06.119>.
- [48] S.M. Mane, A.M. Teli, J.C. Shin, 3D self-supported hierarchical lettuce-like Ni₃S₂ super architecture with an internal nanowire network for high-performance supercapacitors, *J. Alloy. Compd.* 925 (2022), 166626, <https://doi.org/10.1016/j.jallcom.2022.166626>.
- [49] A.M. Teli, T.S. Bhat, S.A. Beknalkar, S.M. Mane, L.S. Chaudhary, D.S. Patil, S. A. Pawar, H. Efstathiadis, J. Cheol Shin, Bismuth manganese oxide based electrodes for asymmetric coin cell supercapacitor, *Chem. Eng. J.* 430 (2022), 133138, <https://doi.org/10.1016/j.cej.2021.133138>.
- [50] J. Yu, N. Fu, J. Zhao, R. Liu, F. Li, Y. Du, Z. Yang, High specific capacitance electrode material for supercapacitors based on resin-derived nitrogen-doped porous carbons, *ACS Omega* 4 (2019) 15904–15911, <https://doi.org/10.1021/acsomega.9b01916>.
- [51] D.P. Dubal, N.R. Chodankar, R. Holze, D.H. Kim, P. Gomez-Romero, Ultrathin mesoporous RuCo₂O₄ nanoflakes: an advanced electrode for high-performance asymmetric supercapacitors, *ChemSusChem* 10 (2017) 1771–1782, <https://doi.org/10.1002/cssc.201700001>.
- [52] D. Jain, J. Kanungo, S.K. Tripathi, Synergistic approach with redox additive for the development of environment benign hybrid supercapacitor, *J. Electrochem. Soc.* 166 (2019) A3168–A3181, <https://doi.org/10.1149/2.0321914jes>.
- [53] M.A. Yewale, R.A. Kadam, N.K. Kaushik, L.N. Nguyen, U.T. Nakate, L. P. Lingamdinne, J.R. Koduru, P.S. Auti, S.V.P. Vattikuti, D.K. Shin, Electrochemical supercapacitor performance of NiCo₂O₄ nanoballs structured electrodes prepared via hydrothermal route with varying reaction time, *Colloids Surf. A Physicochem. Eng. Asp.* 653 (2022), 129901, <https://doi.org/10.1016/j.colsurfa.2022.129901>.
- [54] A. Adan-Mas, L. Alcaraz, P. Arévalo-Cid, F.A. López-Gómez, F. Montemor, Coffee-derived activated carbon from second biowaste for supercapacitor applications, *Waste Manag* 120 (2021) 280–289, <https://doi.org/10.1016/j.wasman.2020.11.043>.
- [55] Y. Wang, D. Yang, J. Lian, J. Pan, T. Wei, Y. Sun, Cedar leaf-like CuCo₂O₄ directly grow on nickel foam by a hydrothermal/annealing process as an electrode for a high-performance symmetric supercapacitor, *J. Alloy. Compd.* 735 (2018) 2046–2052, <https://doi.org/10.1016/j.jallcom.2017.12.005>.
- [56] Y. Wang, D. Yang, J. Lian, T. Wei, Y. Sun, Ordered corn-like CuCo₂O₄ nanoforests covering Ni foam for a high-performance all-solid-state supercapacitor, *J. Alloy. Compd.* 741 (2018) 527–531, <https://doi.org/10.1016/j.jallcom.2018.01.168>.
- [57] S.G. Krishnan, M.V. Reddy, M. Harilal, B. Vidyadharan, I.I. Misnon, M.H.A. Rahim, J. Ismail, R. Jose, Characterization of MgCo₂O₄ as an electrode for high performance supercapacitors, *Electrochim. Acta* 161 (2015) 312–321, <https://doi.org/10.1016/j.electacta.2015.02.081>.
- [58] Y.Q. Zhao, Y. Zhang, K.Z. Xu, Effect of precursor on the morphology and supercapacitor performance of CuCo₂O₄, *Int. J. Electrochem. Sci.* 14 (2019) 3885–3896, <https://doi.org/10.20964/2019.04.62>.
- [59] A. Pendashteh, M.S. Rahmanifar, R.B. Kaner, M.F. Mousavi, Facile synthesis of nanostructured CuCo₂O₄ as a novel electrode material for high-rate supercapacitors, *Chem. Commun.* 50 (2014) 1972–1975, <https://doi.org/10.1039/c3cc48773c>.
- [60] J. Qi, D. Chen, W. Wang, Y. Sui, Y. He, Q. Meng, F. Wei, Y. Ren, J. Liu, Y. Jin, Facile synthesis of N-doped activated carbon derived from cotton and CuCo₂O₄ nanoneedle arrays electrodes for all-solid-state asymmetric supercapacitor, *J. Mater. Sci. Mater. Electron.* 30 (2019) 9877–9887, <https://doi.org/10.1007/s10854-019-01325-w>.
- [61] Q. Wang, D. Chen, D. Zhang, Electrospun porous CuCo₂O₄ nanowire network electrode for asymmetric supercapacitors, *RSC Adv.* 5 (2015) 96448–96454, <https://doi.org/10.1039/c5ra21170k>.



Effect of microwave annealing on Tin Oxide nanomaterials

Lalita Deshmukh^{a,*}, S.L. Kadam^b

^a Department of Physics, Ahmednagar College, Ahmednagar 414001, India

^b New Art's, Commerce and Science College, Parner, Ahmednagar 414302, India

ARTICLE INFO

Keywords:

Tin Oxide nanoparticles (NPs)
XRD
UV-Vis
FTIR
Etc

ABSTRACT

We herein reported SnO₂ (Tin Oxide) nanoparticles (NPs) synthesis using microwave assisted method. Stannous Chloride is used as a source of Sn, pH level 8 was maintained throughout the reaction for one hour using liquid ammonia. Domestic microwave oven with frequency of 2.54 GHz was used to treat the precipitate. Microwave treatment with different power modes (High power, low power, and direct heating mode) was given to collected dried synthesized samples for 30 min duration. Synthesized nanoparticles were investigated using UV-Vis, XRD, and FTIR spectroscopy. Crystallite size obtained using Scherrer formula. Tetragonal Rutile crystal structure has been obtained in XRD investigation. Prominent existence of (110) and (101) reflection has been revealed in X ray diffractogram. Microstrain and dislocation density shows dependence on microwave power. Optical features are investigated using UV-Vis spectroscopy. Band gap shows variation upon increase in microwave power. Stretching band modes were investigated using FTIR spectroscopy. There are multiple advantages of microwave assisted method. Microwave assisted method is fast, cost effective as well as scalable method. Domestic Microwave was deployed for the purpose of nanoparticle synthesis. Various power modes available were used innovatively for reported synthesis.

1. Introduction

Tin Oxide is a versatile material due to its striking features. It is a wide band gap (3.6 eV to 3.8 eV) n type compound semiconductor. This material has excellent thermal stability. Its high optical transparency and low electrical conductivity makes this material a promising candidate for different optoelectronic applications [1]. There are different phases exists in this nanomaterial. SnO₂ is cheaper and non-toxic hence eco-friendly nanomaterial. It is a better option in energy applications as it has attractive specific capacitance. Tin Oxide has shown potential candidature in various fields such as catalysis, medicine, optoelectronics, sensing and energy storage devices [2,3]. Various synthesis techniques were used to synthesize SnO₂ NPs. These NPs can be synthesized using solvothermal method, gel-combustion method, spray pyrolysis method, physical vapour deposition method, sol-gel method, hydrothermal method, microwave assisted method etc [4-8].

Microwave assisted technique is unique with regards to its properties. It is possible to tune microwave energy instantaneously. This reduces reaction time, reaction cost etc. This technique leads to uniform heating and hence improves reaction yield [4,9-14]. It is possible to synthesize nanomaterials mainly metal oxides, without using traditional

annealing method. Krishnakumar *et.al.* have used microwave synthesis method to synthesize Tin Oxide NPs [11]. They have confirmed the formation of single crystalline Tin Oxide using this technique. TEM confirms formation of crystalline Tin Oxide nanomaterial. Electrical resistivity measurements were carried out showing an inverse trend upon increase in temperature. Karthik *et.al.* have synthesized Tin Oxide NPs using microwave assisted method [12]. XRD reveals formation of crystalline nanoparticles. SEM images show nano-spherical morphological features of grown Tin Oxide NPs. Desired elemental composition has been revealed in EDS study. In this synthesis method traditional annealing method was not used. Xu *et.al.* have used microwave assisted method to grow the Tin Oxide Quantum dots. They have used these NPs in thin film solar cells. They have reported enhancement in parameters of solar devices [12].

Microwave assisted synthesis method has been used to synthesize Tin Oxide NPs. Microwave treatment with different power levels were used to treat the synthesized samples. Annealing via microwave treatment is innovative method as it requires less power so it is cost effective, provides instantaneous and uniform heat transfer through the sample. Sample heating takes place via ionic conduction mechanism and dipole rotations in sample.

* Corresponding author.

E-mail address: lalita.deshmukh@aca.edu.in (L. Deshmukh).

<https://doi.org/10.1016/j.matpr.2023.08.359>

Received 16 June 2023; Received in revised form 27 August 2023; Accepted 29 August 2023

2214-7853/Copyright © 2024 Elsevier Ltd. All rights reserved. Selection and peer-review under responsibility of the scientific committee of the International Conference on Advances in Materials, Mechanics, Mechatronics and Manufacturing.

Synthesized samples were dried using microwave treatment for 20 min. Further these samples were treated in the microwave at different microwave power levels.

2. Experimental

Tin Oxide NPs were synthesized using microwave assisted method. For this synthesis Stannous Chloride ($\text{SnCl}_2 \cdot 2\text{H}_2\text{O}$ (99%)), Ammonia solution (NH_4OH 28%) from Thermo Fisher Scientific were used as starting precursors. 0.1 M solution of Stannous chloride was prepared in 500 ml deionised water. pH of solution is maintained at value 8 using drop wise addition of liquid ammonia. Reaction time for this mixture was kept for 1 h. Precipitation was formed and kept 24 h to settle down. This precipitate was filtered out and chloride contents are removed using distilled water rinsing. Prepared precipitate was grinded followed by 20 min microwave (Model-IFB20SC2) drying. These samples were treated using microwave at different power levels for 30 min. Microwave treated samples were investigated structurally using XRD, Model D8 Advanced Bruker with $\text{CuK}\alpha$ anode having radiation wavelength, $\lambda = 0.154$ nm. Optical feature was examined using JASCO V-750 UV-Vis spectrometer. 5DX FTIR spectrometer is used to obtain the Fourier Transformed infrared spectra (FT-IR).

3. Results and discussion

3.1. Structural analysis

Fig. 1 portrays XRD patterns of SnO_2 nanoparticles synthesized at different microwave power levels. XRD confirms formation of tetragonal rutile crystal structure with space group P42/mnm . The reflections observed in XRD shows good agreement with standard JCPDS data (01-072-1147). (110), (101), (200), (211) and (301) reflections associated with 26.65° , 34° , 37.89° , 51.78° , and 65.93° two theta values. Weak presence of secondary phase SnO (06-0395) appears in pattern for as prepared (A). These secondary phases get removed due to microwave treatment at different powers. Strong reflection associated with (110) plane shows increment in intensity upon increase in microwave power. This may be attributed to fact that, upon increase in power, increase in energy gives rise to boost significant growth along this plane. Average crystallite size has been calculated using Scherrer formula [14].

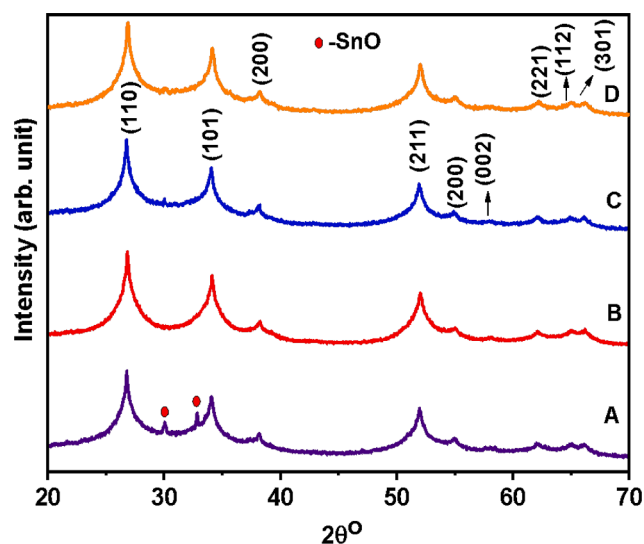


Fig. 1. XRD of Tin Oxide nanoparticle grown at different Microwave power levels. (A) as prepared, (B) Low power (c) High Power (d) Direct Heating mode.

$$D = \frac{0.9\lambda}{\beta \cos\theta} \quad (1)$$

Where, D , β , λ , and θ represents average crystallite size, full width at half maximum, diffraction wavelength (0.154 nm) and the angle of diffraction respectively.

Dislocation density was obtained using [8],

$$\delta = \frac{1}{D^2} \quad (2)$$

Microstrain is obtained using Wilson's equation given by [15],

$$\epsilon = \frac{\beta}{4 \tan\theta} \quad (3)$$

Where, ϵ is micro-strain, this depends Gaussian profile broadening.

Samples A is as prepared and B, C, and D are the samples treated at increasing microwave power level using domestic purpose microwave oven. As prepared Tin Oxide sample depicts small crystallite size, increasing trend in crystallite size upon increasing microwave power levels was observed. This could be due to increase in power causes rise in energy which is required to crystallite growth. Power triggers the initiation of reaction; required reaction temperature could be attained using microwave power level. Activation energy enhancement for molecule formation could be done using microwave power level. Similar results were reported by Gerbec *et.al.* have discussed microwave enhanced reaction rates for NPs synthesis [16]. Dislocation density and microstrain shows inverse nature with respect to crystallite size. Rise in crystallite size leads to reduction in voids, defects this could be attributed to reverse trend in dislocation density and microstrain of grown nanoparticle.

3.2. Optical analysis

UV-Vis spectroscopy was used to investigate the optical features of grown Tin Oxide NPs. Band gap was obtained by using Tauc Theory.

Fig. 2 shows Tauc plots of Tin Oxide samples treated at different microwave power levels. Band gap valued are tabulated in Table 1. Band gap shows systematic decrement upon increase in microwave power. This result is attributed indirectly to fact that increases in microwave power results in larger crystallite growth. This could be responsible for quantum confinement effect.

3.3. FTIR analysis

Presence of Sn-O-Sn stretching has been displayed in Fig. 3. This shows the FTIR spectra taken in the range from 4000 to 500 cm^{-1} . This spectrum depicts the Sn-O-Sn stretching around 600 cm^{-1} for the Tin Oxide samples treated with different microwave powers. The characteristic Sn-O-Sn bond is identified at 640 cm^{-1} , similar results were reported in earlier work [10,12].

Near about 540 cm^{-1} was attributed to terminal oxygen vibration for microwave dried precipitate. Peaks around 1400 cm^{-1} are associated with NH^- stretching vibration [17-19]. For higher microwave power, these peaks were almost vanishes, this is attributed to microwave treatment at increasing microwave power. At higher power, -OH group could be removed which disappears the corresponding vibration peaks from the FTIR spectra.

4. Conclusions

In conclusion, Instead of traditional annealing method we have adapted microwave assisted method for Tin Oxide NP synthesis. Appearance of SnO phase has been observed in as prepared sample. After microwave annealing at different microwave power levels these phases get removed. Synthesized samples were treated at different increasing microwave power levels. Tetragonal rutile structural growth

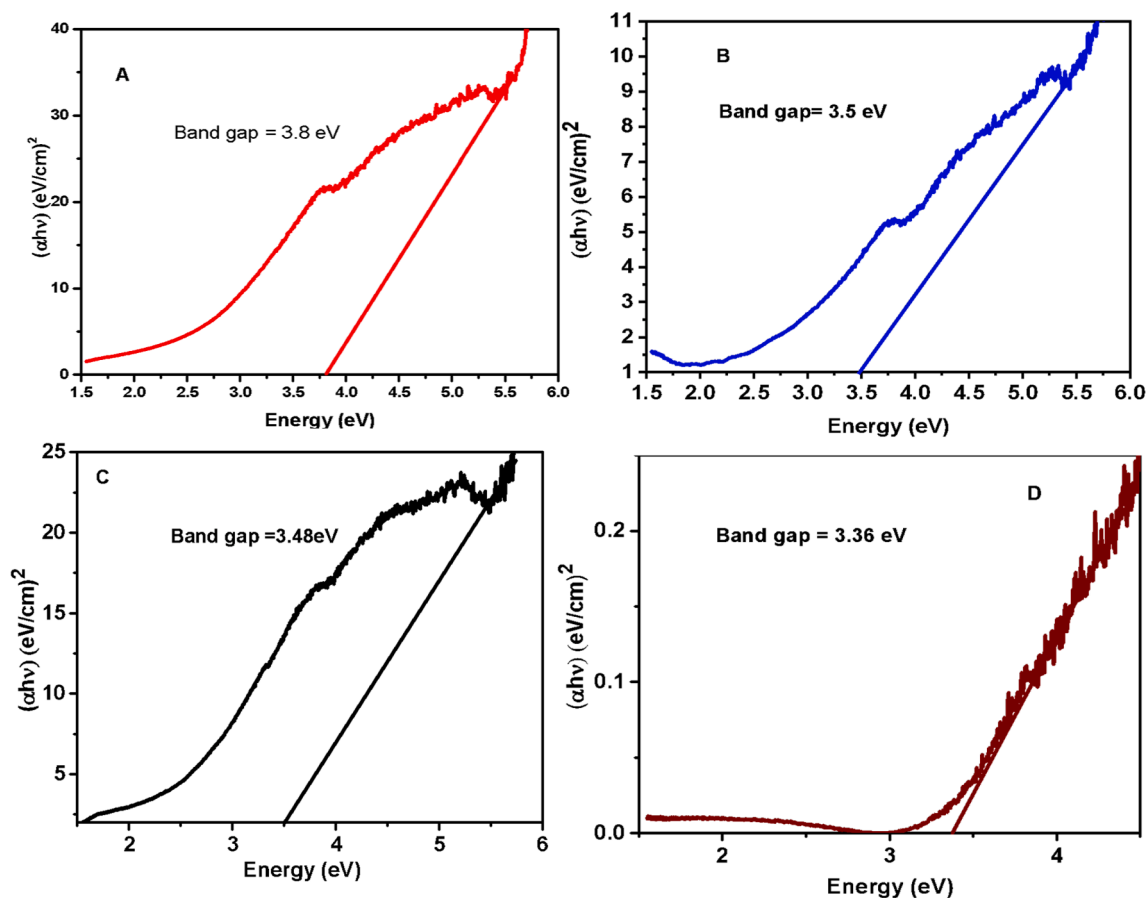


Fig. 2. Tauc Plots of Tin Oxide samples treated at different microwave power levels: (A) as prepared, (B) Low power (c) High Power (d) Direct Heating mode.

Table 1

Values of average crystallite size, microstrain, dislocation density and band gap.

Sample Designation	Average Crystallite size (nm)	Dislocation density (nm^{-2})	Microstrain (Radians)	Band gap (eV)
A (As prepared)	6.52	0.024	0.0187	3.8
B (10% power)	6.99	0.020	0.0168	3.5
C (100% Power)	8.46	0.014	0.0143	3.4
D (Direct Heating mode)	8.91	0.013	0.0133	3.36

has been observed in structural study. Upon increase in microwave power, increment in crystallite size was noticed. Dislocation density, microstrain and band gap displays reduction with increase in microwave power. FTIR spectra portrays, Sn-O-Sn stretching at different signature peaks. Peaks associated with $-OH$ group disappear with increase in microwave power levels.

CRedit authorship contribution statement

Lalita Deshmukh: . S.L. Kadam: Writing – review & editing.

Declaration of Competing Interest

The authors declare that they have no known competing financial interests or personal relationships that could have appeared to influence the work reported in this paper.

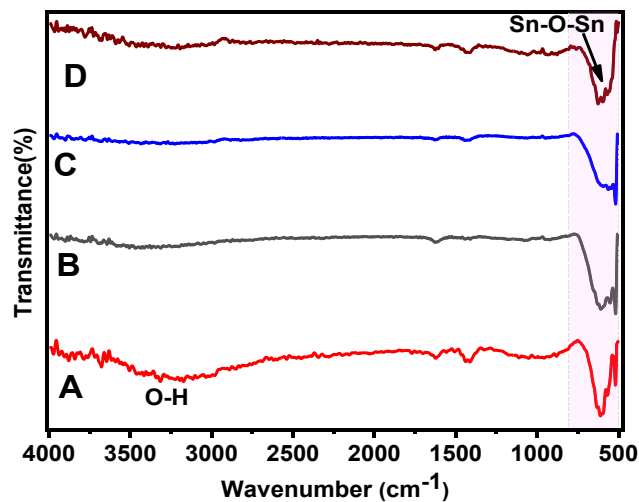


Fig. 3. FTIR Spectra of Tin Oxide samples treated at different Microwave power levels: (A) as prepared, (B) Low power (c) High Power (d) Direct Heating mode.

Data availability

Data will be made available on request.

Acknowledgement

Authors are grateful to Principal Dr. R. J. Barnabas, Ahmednagar College, for his support in this work.

References:

- [1] G.K. Dalapati, et al., Tin oxide for optoelectronic, photovoltaic and energy storage devices: A review, *J. Mater. Chem. A* 9 (2021) 16621–16684.
- [2] A. Klein, et al., Transparent conducting oxides for photovoltaics: Manipulation of fermi level, work function and energy band alignment, *Materials (Basel)* 3 (2010) 4892–4914.
- [3] J. Celina Selvakumari, S.T. Nishanthi, J. Dhanalakshmi, M. Ahila, D. Pathinettam Padiyan, Bio-active synthesis of tin oxide nanoparticles using eggshell membrane for energy storage application, *Appl. Surf. Sci.* 441 (2018) 530–537.
- [4] F.M. Borges de Oliveira, J.A. Varela, M.O. Orlandi, Influence of pH in obtaining indium tin oxide nanoparticles by microwave assisted solvothermal method, *Mater. Res.* 21 (2018) 2.
- [5] Q. Lin, Y. Li, M. Yang, Tin oxide/graphene composite fabricated via a hydrothermal method for gas sensors working at room temperature, *Sensors Actuators, B Chem.* 173 (2012) 139–147.
- [6] M. Mariikkannan, V. Vishnukanthan, A. Vijayshankar, J. Mayandi, J.M. Pearce, A novel synthesis of tin oxide thin films by the sol-gel process for optoelectronic applications, *AIP Adv.* 5 (2) (2015).
- [7] M. Sathishkumar, S. Geethalakshmi, Enhanced photocatalytic and antibacterial activity of Cu:SnO₂ nanoparticles synthesized by microwave assisted method, *Mater. Today.. Proc.* 20 (2020) 54–63.
- [8] R. Thomas, et al., Investigation of erbium co-doping on fluorine doped tin oxide via nebulizer spray pyrolysis for optoelectronic applications, *Opt. Quant. Electron.* 52 (5) (2020) 1–15.
- [9] Z. Xu, et al., Rapid microwave-assisted synthesis of SnO₂ quantum dots for efficient planar perovskite solar cells, *ACS Appl. Energy Mater.* 4 (2) (2021) 1887–1893.
- [10] C. Aydın, Synthesis of SnO₂:rGO nanocomposites by the microwave-assisted hydrothermal method and change of the morphology, structural, optical and electrical properties, *J. Alloy. Compd.* 771 (2019) 964–972.
- [11] T. Krishnakumar, R. Jayaprakash, M. Parthivarman, A.R. Phani, V.N. Singh, B. R. Mehta, Microwave-assisted synthesis and investigation of SnO₂ nanoparticles, *Mater. Lett.* 63 (11) (2009) 896–898.
- [12] K. Karthik, V. Revathi, T. Tatarchuk, Microwave-assisted green synthesis of SnO₂ nanoparticles and their optical and photocatalytic properties, *Mol. Cryst. Liq. Cryst.* 671 (1) (2018) 17–23.
- [13] M. Krishna, S. Komarneni, Conventional- vs microwave-hydrothermal synthesis of tin oxide, SnO₂ nanoparticles, *Ceram. Int.* 35 (8) (2009) 3375–3379.
- [14] B.D.Cullity, Addison-Wesley Publishing Company, 3, (1957).
- [15] S. Sivakumar, E. Manikandan, B. Mahalakshmi, N. Ahmad mala, and L. Nelson prabu, "Synthesis and characterization of optical, magnetic and electrochemical behavior of manganese–zinc co-doped tin oxide nanoparticles," *Vacuum*, 173, p. 109116, 2020.
- [16] J.A. Gerbec, D. Magana, A. Washington, G.F. Strouse, Microwave-enhanced reaction rates for nanoparticle synthesis, *J. Am. Chem. Soc.* 127 (45) (2005) 15791–15800.
- [17] M.A. Farrukh, P. Tan, R. Adnan, Influence of reaction parameters on the synthesis of surfactant-assisted tin oxide nanoparticles, *Turkish J. Chem.* 36 (2) (2012) 303–314.
- [18] M. Vidhya, P. Raja Pandi, R. Archana, K. Sadyandi, S. Suresh Sagadevan, J. P. Gunasekaran, F. Mohammad, H.A. Al-Lohedan, O.h. Won Chun, Comparison of sunlight-driven photocatalytic activity of semiconductor metal oxides of tin oxide and cadmium oxide nanoparticles, *Optik* 217 (2020), 164878.
- [19] M. Das, S. Roy, Preparation, characterization and properties of newly synthesized SnO₂-polycarbazole nanocomposite via room temperature solution phase synthesis process, *Mat. Today Proc.* 18 (2019) 5438–5446.

RESEARCH ARTICLE

Synthesis and Characterization of V₂O₅ Nanorods Using Hydrothermal Method for Energy Application

Rupin Ranu^{1,*}, Kalyan B. Chavan², Sachin V. Desarada³, V.K. Gade⁴ and S.L. Kadam⁵

¹Department of Physics, New Arts, Commerce and Science College, Ahmednagar, Maharashtra, India; ²Department of Physics, Ahmednagar College, Ahmednagar, Maharashtra, India; ³Department of Physics, Savitribai Phule Pune University, Pune, India; ⁴Department of Physics, Ahmednagar College, Ahmednagar, Maharashtra, India; ⁵Department of Physics, New Arts, Commerce and Science College, Parner, Maharashtra, India

Abstract: Background: Nanomaterials are very useful in energy harvesting and energy storage devices. Morphological features play a vital role in energy storage devices. Supercapacitors and batteries are examples of energy storage devices. The working of a supercapacitor is decided by the nature of the microstructure and other features of the electrode material. Vanadium Pentoxide (V₂O₅) is one of the promising materials due to its attractive features, such as band gap, multiple oxidation state, and large conductivity transition from semiconducting to conducting domain.

ARTICLE HISTORY

Received: July 15, 2023
Revised: September 18, 2023
Accepted: October 23, 2023

DOI:
10.2174/0118764029265057231121094206

Objective: This study aimed to perform the tuning of structural, optical and morphological properties of V₂O₅ nanomaterials using the hydrothermal method.

Methods: A low-cost hydrothermal method was used in this work. Hydrothermal synthesis was carried out at different concentrations of Ammonium Metavanadate (NH₄VO₃), varying from 0.06 M, 0.08 M, and 0.1 M in the aqueous medium. Moreover, the pH of the solution was maintained at 4 using drop-wise addition of H₂SO₄. Hydrothermal synthesis was carried out at 160 °C for 24 hours. The synthesized precipitate was annealed at 700 °C for 7 hours in ambient air. Structural, optical, morphological, and elemental probing was carried out.

Result: XRD revealed the formation of monoclinic crystalline phase formation of V₂O₅. Crystallite size increased with an increase in the concentration of vanadium precursor. The band gap obtained using UV-Vis spectroscopy decreased upon an increase in concentration. SEM micrographs displayed nanosheet and nanorod-like distorted morphology. The presence of vanadium and oxygen was noticed in the EDS study.

Conclusion: Nanoparticles with attractive features are very useful as an electrode material for supercapacitors. Upon changing concentration, we can change the band gap of the material, adding an extra edge in the use of these materials.

Keywords: V₂O₅ nanoparticle, hydrothermal synthesis, XRD, SEM.

1. INTRODUCTION

Vanadium pentoxide (V₂O₅) shows promising candidature due to its versatile features. It has multiple oxidation states (V²⁺, V³⁺, V⁴⁺, and V⁵⁺). Due to elemental abundance, this metal oxide is cost-effective [1, 2]. It is more eco-friendly due to the low toxicity of the constituents of this metal oxide. Its band gap lies at 2.2 eV to 2.6 eV, making this material more photoactive [3]. It has diverse crystal structures, rutile, monoclinic and orthorhombic. Crystal

structure transition gives rise to a large variation in conductivity. V₂O₅ has the capability to host different ions and molecules. V₂O₅ is used as electrode material in lithium-ion batteries due to its attractive electrochemical features.

Different synthesis methods have been used to develop V₂O₅ nanomaterials. Hydrothermal, sol-gel, simple precipitation, microwave-assisted method, etc., are the different methodologies adapted to synthesize V₂O₅ nanomaterials. Ayyaru *et al.* used the hydrothermal method to synthesize V₂O₅ nanorods [4]. These nanorods were used as an alternate cathode catalyst for microbial fuel cell applications. Codoped V₂O₅ nanoparticles were synthesized by Yazadi *et al.* using sol-gel method [5]. They found that upon an increase

*Address correspondence to this author at the Department of Physics, New Arts, Commerce and Science College, Ahmednagar, Maharashtra, India; E-mail: rupinranu@gmail.com

in Co doping, lattice constant and particle size also increased. Taylor *et al.* used a liquid laser ablation technique to develop the naked vanadium pentaoxide nanostructures [6]. Sol-gel and hydrothermal methods were used by Sajid *et al.* to synthesize V_2O_5 nanomaterials [7]. They studied the photoresponse of V_2O_5 nanomaterials developed by these two methods. Comparative photocatalytic activity of V_2O_5 nanomaterials developed by hydrothermal and sol-gel methods was evaluated in this investigation. The wet chemical method was utilized to develop V_2O_5 nanomaterial by Tahir and coworkers [8]. Nanocomposites with GO and Mxene were synthesized for advanced supercapacitor electrodes, and some extraordinary electrochemical results were obtained. Tang *et al.* demonstrated the laser synthesis of vanadium oxide bonded graphene for energy application [9]. A significant increase in the electrochemical properties was found in this work. Velpula *et al.* performed comparative measurements on V_2O_5 nanostructures developed by green and chemical synthesis methods [3]. Aerosol synthesis of V_2O_5 – carbon nanostructures has been carried out successfully by Chung *et al.* [10]. They demonstrated Lithium extraction using the electrochemical deionization technique. Hien V_2O_5 nanosheets were prepared using vanadium powder with the help of the hydrothermal synthesis method [11]. Prepared nanosheets display efficient ethanol sensing properties. Rasheed *et al.* used a novel colorimetric method to synthesize V_2O_5 nanoparticles. Synthesized V_2O_5 nanoparticles exhibited catalase mimetic activity; further increase in annealing temperature showed an increase in mimetic activity [1]. In a study, palladium decoration on vanadium pentaoxide was carried out using the hydrothermal synthesis method [12].

In this investigation, we demonstrated the synthesis of V_2O_5 nanorods using the hydrothermal synthesis method. The hydrothermal synthesis method has attractive features, such as grain size control, crystalline phase, morphology, etc., *via* controlling the concentrations of reactants, solution composition, reaction temperature, reaction time, etc.

2. MATERIALS AND METHODS

Ammonium metavanadate (NH_4VO_3 99%) and sulfuric acid (H_2SO_4 98%) were purchased from Molychem. In this work, all reagents were used without further purification.

Vanadium pentaoxide nanomaterials were synthesized using the hydrothermal method at different concentrations of vanadium precursor. Synthesized nanomaterials were investigated using several probing techniques.

Structural studies were performed by using an X-ray diffractometer, Model D8 Advanced Bruker, with $Cu K\alpha$ (0.154 nm) radiation. The optical feature of the Mo layer was examined using a JASCO V-750 UV-Vis spectrometer. Surface morphology was imaged using SEM Joel model JSM-IT 100.

3. EXPERIMENTAL SECTION

Aqueous solution of ammonium metavanadate was prepared with 0.06 M, 0.08 M, and 0.1 M concentration in 40

ml double distilled water. Sulfuric acid was diluted using double distilled water in a 1:4 ratio (H_2SO_4/H_2O : 1/4). Moreover, the pH of the vanadium precursor solution was kept at 4 using drop-wise addition of diluted sulfuric acid. The orange color solution was stirred at room temperature for 30 minutes and transferred to a 50 ml Teflon container. Hydrothermal reaction was carried out in a stainless steel autoclave at 160°C for 24 hours. The precipitate was filtered out and rinsed using double distilled water several times, followed by 24 hours of natural cooling. The precipitate was annealed in the furnace at 700°C for six hours.

3. RESULTS AND DISCUSSION

3.1. Structural Analysis

Fig. (1) shows the XRD spectrographs of V_2O_5 (Vanadium Pentaoxide) nanomaterial with different concentrations of vanadium precursor. XRD revealed the formation of an orthorhombic crystal structure. All XRD reflections of synthesized V_2O_5 were indexed using a JCPDS card (41-1426). The dominance of the (001) plane is clearly seen in XRD spectrographs of all the samples. Nanomaterials synthesized with a molarity of 0.08 M showed highly intense (001) reflection. Dominating signature peaks of V_2O_5 were observed at 2θ equal to 20.26°, 26.12°, and 31.05° corresponding to (001), (110) and (301) reflection, respectively. The average crystallite size was obtained using the Scherrer formula [13]:

$$D = \frac{0.9\lambda}{\beta \cos\theta} \quad (1)$$

Where, λ , β , and θ are the wavelength of X-rays used for diffraction ($CuK\alpha = 0.154 \text{ nm}$), full width at half maxima, and angle of diffraction, respectively.

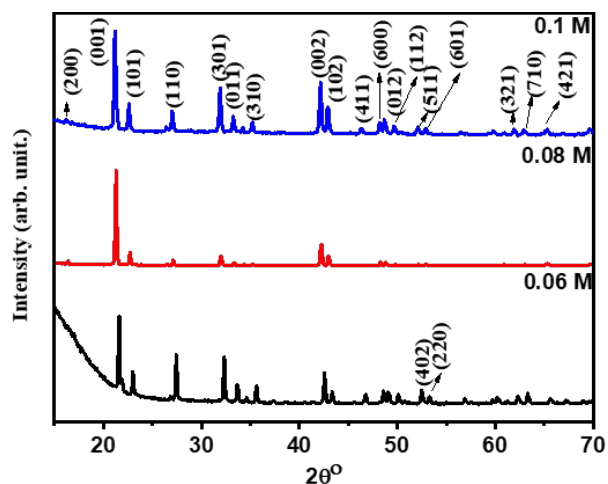


Fig. (1). XRD diffractograms of V_2O_5 nanomaterials synthesized at different concentrations. (A higher resolution / colour version of this figure is available in the electronic copy of the article).

In Fig. (1), the intensity of (001) reflection is much higher than other peaks. This is due to the highly preferential growth of nanomaterial along the (001) plane. This could be

Table 1. Structural and Optical Aspects of V2O5 Nanomaterials Developed by the Hydrothermal Method.

Concentration of Vanadium Precursor (M)	Crystallite Size (nm)	Dislocation Density (X 10 ⁻³) (nm ⁻²)	Band Gap (eV)	Cutoff Wavelength (nm)
0.1	46.2	4.7	2.29	672
0.08	38.4	6.8	2.57	660
0.06	31.8	9.9	2.66	651

due to the relationships between synthesis conditions and reaction kinematics of the hydrothermal method.

Table 1 presents the values of the average crystallite size obtained. This reveals an increase in crystallite size with an increase in the concentration of vanadium precursor. This is attributed to the fact that an increase in concentration results in an increase in the number of nuclei, which can nucleate and may cause a rise in crystallite size. The concentration of precursor may affect the rates of reaction as well as nucleation; this could be the reason for the rise in crystallite size.

Dislocation density is obtained using the formula [14]:

$$\delta = \frac{1}{D^2}$$

Where, D is the crystallite size.

Dislocation density shows a decrease with an increase in concentration. It is the parameter that indicates the defects in crystalline solids. It is also a measure of number of dislocation lines per unit volume of the crystal. This could be due to the fact that an increase in crystallite size with concentration results in a decrease in movements and generation of dislocation density. Neupane *et al.* [15] reported similar trends in association with capping agents.

3.2. Optical Analysis

Fig. (2) shows the absorbance plots of vanadium pentoxide nanomaterials prepared at different concentrations. This could be due to an increase in crystallite size. Crystallite size variation results in a change in the band gap.

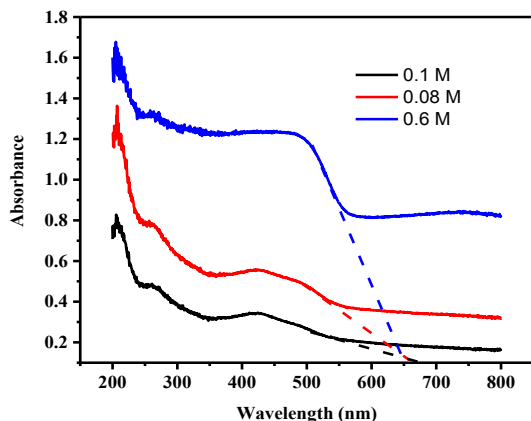


Fig. (2). UV-Vis Absorbance Plots of V₂O₅ Nanomaterials Synthesized at Different Concentrations. (A higher resolution / colour version of this figure is available in the electronic copy of the article).

Change in the band gap may reflect a shift in the cut-off wavelength in the absorbance plot. Band gaps were obtained using the Tauc theory. Fig. (3) presents Tauc plots of vanadium pentoxide nanoparticles synthesized at different concentrations.

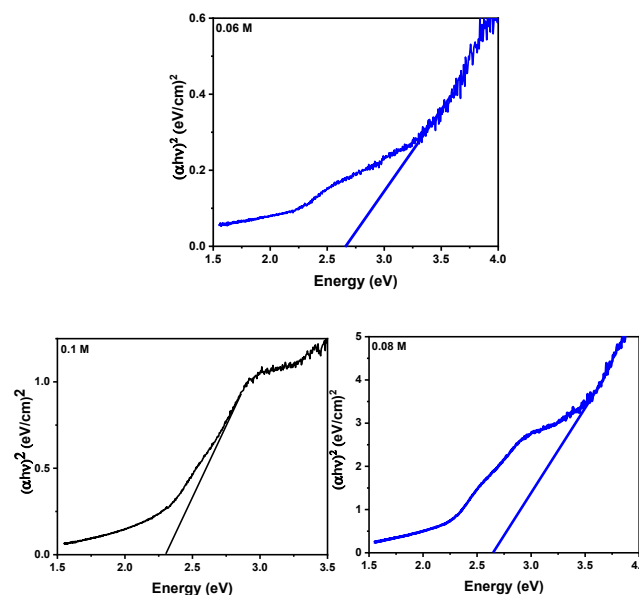


Fig. (3). Tauc Plots of V₂O₅ Nanomaterials Synthesized at Different Concentrations. (A higher resolution / colour version of this figure is available in the electronic copy of the article).

Band gap values are tabulated in Table 1. The band gap shows a decrease with an increase in concentration. These results are in good agreement with the crystallite size obtained from XRD. This could be due to the quantum confinement effect.

3.3. Morphological Analysis

Scanning electron microscopy was used to study the morphological features of developed nanomaterials. Figure 4 illustrates the nanorod-like shapes. Image j software was used to obtain the average length of developed nanorods.

The average length shows an increase with an increase in the concentration of precursor. Furthermore, 1.2, 0.8, and 0.55 μm are the values of average length measured by Image J software of samples developed at 1, 0.08, and 0.06 M concentrations. This could be due to the fact that the higher the

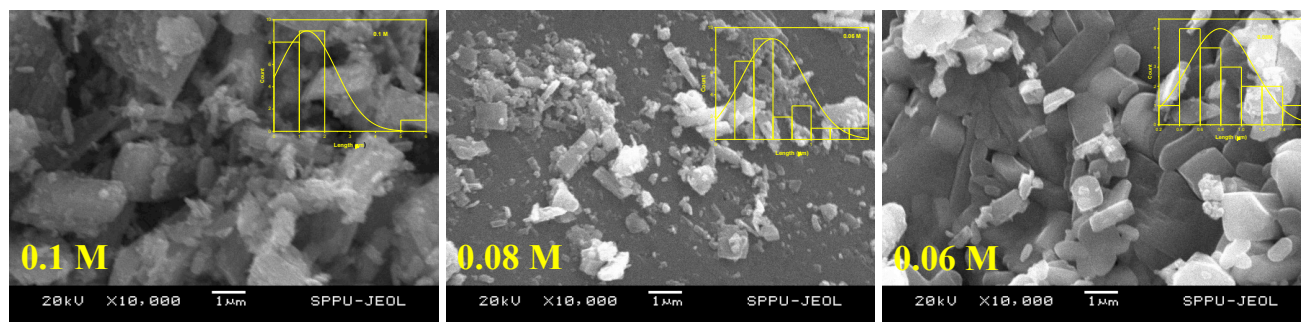


Fig. (4). SEM Micrographs of V_2O_5 Nanomaterials Synthesized at Different Concentrations (Inset: Average length).

Table 2. Elemental composition.

Concentration of Vanadium Precursor (M)	Vanadium (At%)	Oxygen (At%)
0.1	46.42	53.56
0.08	46.95	53.05
0.06	42.03	57.97

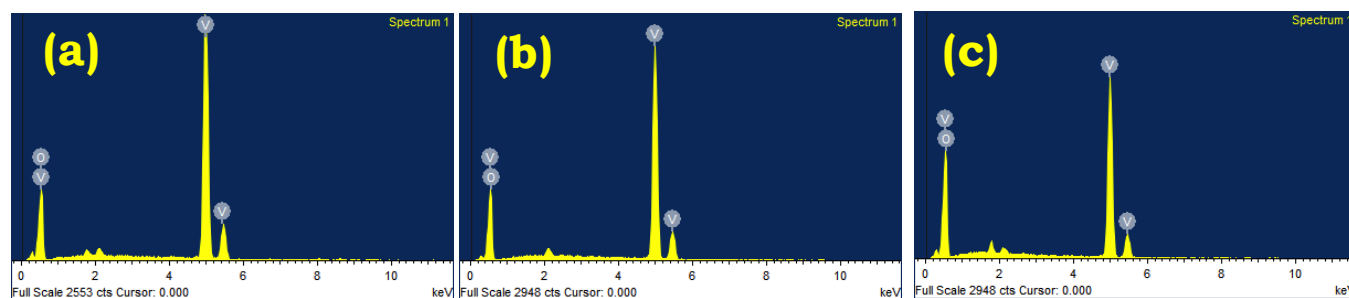


Fig. (5). Presents the presence of vanadium and oxygen. (A higher resolution / colour version of this figure is available in the electronic copy of the article).

concentration, the more the nucleation centers and the growth.

Elemental analysis was carried out using energy-dispersive X-ray spectroscopy. Fig. (5) shows the elemental content in synthesized nanomaterials.

Fig. (5) EDS Spectrographs of Vanadium Pentaoxide Nanomaterials Synthesized at Different Concentrations.

The concentrations of vanadium and oxygen in atomic percentages are tabulated in Table 2.

No significant change was observed in atomic percentages of vanadium and oxygen upon changing concentrations of vanadium precursor.

CONCLUSION

This investigation demonstrated the synthesis of V_2O_5 nanomaterials using the hydrothermal method. The effect of the concentration of vanadium precursor on structural, optical, and morphological features has been studied. XRD confirmed the formation of phase pure vanadium pentaoxide.

Crystallite size showed an increment upon an increase in concentration. Dislocation density portrayed an inverse trend as that of crystallite size with concentration. Absorption plots showed an increase in cutoff wavelength with a rise in concentration. The band gap decreased with an increase in concentration. Optical results were found to be in good agreement with concentration. SEM images revealed the formation of rod-shaped morphological features. EDS confirmed the presence of vanadium as well as oxygen in synthesized nanomaterials.

CONSENT FOR PUBLICATION

Not applicable.

AVAILABILITY OF DATA AND MATERIALS

All of the findings and results are based on the data and materials as figures and tables, which have been given in the manuscript.

FUNDING

None.

CONFLICT OF INTEREST

The authors declare no conflict of interest, financial or otherwise.

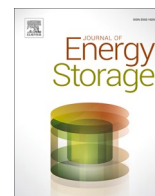
ACKNOWLEDGEMENTS

The authors are very much thankful to principal Dr. B. H. Zaware for his extensive support and motivation during this work.

REFERENCES

- [1] Rasheed, R.T.; Mansoor, H.S.; Abdullah, T.A.; Juzsakova, T.; Al-Jammal, N.; Salman, A.D.; Al-Shaikhly, R.R.; Le, P.C.; Domokos, E.; Abdulla, T.A. Synthesis, characterization of V₂O₅ nanoparticles and determination of catalase mimetic activity by new colorimetric method. *J. Therm. Anal. Calorim.*, **2021**, *145*(2), 297-307. <http://dx.doi.org/10.1007/s10973-020-09725-5>
- [2] Liu, X.; Zeng, J.; Yang, H.; Zhou, K.; Pan, D. V₂O₅-Based nanomaterials: Synthesis and their applications. *RSC Advances*, **2018**, *8*(8), 4014-4031. <http://dx.doi.org/10.1039/C7RA12523B>
- [3] Velpula, D.; Konda, S.; Vasukula, S.; Chidurala, S.C. Microwave radiated comparative growths of vanadium pentoxide nanostructures by green and chemical routes for energy storage applications. *Mater. Today Proc.*, **2021**, *47*, 1760-1766. <http://dx.doi.org/10.1016/j.matpr.2021.02.599>
- [4] Ayyaru, S.; Mahalingam, S.; Ahn, Y.H. A non-noble V₂O₅ nanorods as an alternative cathode catalyst for microbial fuel cell applications. *Int. J. Hydrogen Energy*, **2019**, *44*(10), 4974-4984. <http://dx.doi.org/10.1016/j.ijhydene.2019.01.021>
- [5] Tabatabai Yazdi, S.; Mousavi, M.; Khorrami, G.H. Effect of Co-doping in V₂O₅ nanoparticles synthesized via a gelatin-based sol-gel method. *Mater. Today Commun.*, **2021**, *26*, 101955. <http://dx.doi.org/10.1016/j.mtcomm.2020.101955>
- [6] Taylor, P. Synthesis of naked vanadium pentoxide nanoparticles. *Nanoscale Adv.*, **2021**, *3*(7), 1954-1961.
- [7] Sajid, M.M.; Shad, N.A.; Javed, Y.; Khan, S.B.; Zhang, Z.; Amin, N.; Zhai, H. Preparation and characterization of Vanadium pentoxide (V₂O₅) for photocatalytic degradation of monoazo and diazo dyes. *Surf. Interfaces*, **2020**, *19*, 100502. <http://dx.doi.org/10.1016/j.surfin.2020.100502> PMID: 36133079
- [8] Tahir, T.; Alhashmialameer, D.; Zulfiqar, S.; Atia, A.M.E.; Warsi, M.F.; Chaudhary, K.; El Refay, H.M. Wet chemical synthesis of Gd³⁺ doped vanadium Oxide/MXene based mesoporous hierarchical architectures as advanced supercapacitor material. *Ceram. Int.*, **2022**, *48*(17), 24840-24849. <http://dx.doi.org/10.1016/j.ceramint.2022.05.135>
- [9] Tang, J.; Zhang, L.; Zhong, X.; Wang, X.; Pan, F.; Xu, B. A laser synthesis of vanadium oxide bonded graphene for high-rate supercapacitors. *J. Energy Chem.*, **2020**, *49*, 174-178. <http://dx.doi.org/10.1016/j.jechem.2020.02.015>
- [10] Chung, S.T.; Chiang, M.T.; Chin, Y.X.; Hu, C.C.; Tsai, D.H. Controlled aerosol-based synthesis of vanadium oxides nanoparticle for supercapacitor applications. *J. Taiwan Inst. Chem. Eng.*, **2021**, *128*, 220-226. <http://dx.doi.org/10.1016/j.jtice.2021.08.030>
- [11] Hien, V.X.; Nhat, D.D.; Nghi, N.T.; Phuoc, L.H.; Khoa, C.T.; Vuong, D.D.; Chien, N.D. From vanadium powder to vanadium pentoxide rolled-up nanosheets: Hydrothermal synthesis and its ethanol sensing properties. *Mater. Sci. Semicond. Process.*, **2021**, *126*, 105670. <http://dx.doi.org/10.1016/j.mssp.2021.105670>
- [12] Birajdar, S.N.; Adhyapak, P.V. Palladium-decorated vanadium pentoxide as NO_x gas sensor. *Ceram. Int.*, **2020**, *46*(17), 27381-27393. <http://dx.doi.org/10.1016/j.ceramint.2020.07.223>
- [13] Cullity, B.D.; Cullity, B.D. *The Elements of X-Ray Diffraction*; Addison-Wesley Publishing Company, Inc., **1956**.
- [14] Isacfranklin, M.; Deepika, C.; Ravi, G.; Yuvakkumar, R.; Velauthapillai, D.; Saravanakumar, B. Nickel, bismuth, and cobalt vanadium oxides for supercapacitor applications. *Ceram. Int.*, **2020**, *46*(18), 28206-28210. <http://dx.doi.org/10.1016/j.ceramint.2020.07.320>
- [15] Neupane, G.R.; Hari, P. Role of Polyvinylpyrrolidone (PVP) on Controlling the Structural, optical, and Electrical Properties of Vanadium Pentoxide (V₂O₅) Nanoparticles. *ChemistrySelect*, **2020**, *5*(37), 11596-11607. <http://dx.doi.org/10.1002/slct.202002916>

DISCLAIMER: The above article has been published, as is, ahead-of-print, to provide early visibility but is not the final version. Major publication processes like copyediting, proofing, typesetting and further review are still to be done and may lead to changes in the final published version, if it is eventually published. All legal disclaimers that apply to the final published article also apply to this ahead-of-print version.



Research papers

Wrapped nanochain microstructures of Ni₃V₂O₈ nanoparticles for supercapacitor applications using the hydrothermal method

M.A. Yewale^{a,*}, V. Kumar^a, R.A. Kadam^b, R.B. Kharade^b, A.M. Teli^{c,*}, S.A. Bknalkar^c, S.D. Dhas^{d,1}, U.T. Nakate^{e,f}, D.K. Shin^{a,*}

^a School of Mechanical Engineering, Yeungnam University, Gyeongsan 38541, Republic of Korea

^b Department of Physics, Ahmednagar College, Ahmednagar 414001, India

^c Future Semiconductor Device Lab, Division of Electronics and Electrical Engineering, Dongguk University-Seoul, Seoul 04620, Republic of Korea

^d Department of Electronic Engineering, Institute for Wearable Convergence Electronics, Kyung Hee University, 1732 Deogyong-daero, Giheung-gu, Yongin 17104, Republic of Korea

^e Department of Polymer Nano Science and Technology, Jeonbuk National University, 567 Baekje-daero, Deokjin-gu, Jeonju-si, Jeollabuk-do 54896, Republic of Korea

^f Department of Chemical Engineering, Hanyang University, Seoul 04763, Republic of Korea



ARTICLE INFO

Keywords:

Ni₃V₂O₈ nanoparticles

FESEM

TEM

Supercapacitor

ABSTRACT

With the improved microstructure, porosity, and surface area, bimetal oxides make excellent electrode materials for supercapacitor applications. Here, the hydrothermal method for different molar concentration ratios of Nickel and Vanadium sources was successfully used to synthesize the Ni₃V₂O₈ microballs with a porous microstructure. At a current density of 3 mA/cm², the electrode prepared at a Ni:V molar ratio of 1:0.5 exhibits excellent areal capacitance of 1.56 F/cm². The Ni₃V₂O₈//AC device is an asymmetrical one, delivering 6.6 mWh/cm² energy density at 2.2 W/cm² power densities while exhibiting an area capacitance of 39 mF/cm² at 8 mA/cm² current density. With a retention of 72 % for the most recent 5 K GCD cycles, the device exhibits excellent stability for use in practical applications over 5 k GCD cycles at 12 mA/cm². This research offers a Ni₃V₂O₈ microstructure that offers excellent areal capacitance for energy storage applications.

1. Introduction

Energy crises result from the fact that human everyday activities do not meet the need for energy sources, despite the necessity and availability of such sources. The current energy used to power all sectors comes primarily from natural fossil fuels such as coal, oil, natural gas, and nuclear energy, which are being depleted rapidly. Although batteries and fuel cells can be used as alternative energy sources to solve the energy storage problem, they are limited by their large size and short lifespan. Supercapacitors, on the other hand, are the best alternative for energy storage since they can address all of the critical concerns mentioned above. Supercapacitors have higher power density and energy density than conventional capacitors and batteries. They have a longer lifespan, faster charging and discharging periods, smaller size, less weight, high power and energy density, and ease of assembly [1–3]. Based on the charge storage mechanism, supercapacitors are divided into two subclasses: pseudocapacitors (PCs) and electric double-layered

capacitors (EDLCr) [4]. Metal oxides [5–7], and metal chalcogenides [8,9] exhibit the charge storage PCs nature through redox reaction, producing high power and energy density over an extended period of time. Transition metal oxides have a porous structure, numerous active sites, a large surface area, and multiple oxidation states, making them better suited for ion insertion and extraction for charge storage, increasing the electrode material's capacity for energy storage. Bimetal oxide can be more advantageous for redox reactions that significantly increase energy capacity compared to mono-metal oxide, which has one metal [10,11].

Solid state stretchable micro supercapacitor [12], Zinc ion micro-supercapacitor [13], CoFe-phosphate [14], ternary oxide MnVMO oxide [15], Bimetallic oxides, such as NbMn oxide [16], NiMnO₄ [17], NiCo₂O₄ [18], CuCo₂O₄ [19], Ni₃V₂O₈ [20–23] and Co₃V₂O₈ [24], have been studied for energy storage applications due to their various oxidation states, synergetic effects, and excellent electronic conductivity [25]. Among them, Ni₃V₂O₈ has garnered more attention because of its

* Corresponding authors.

E-mail addresses: maneshphd@yu.ac.kr (M.A. Yewale), avteli.teli@gmail.com (A.M. Teli), dkshin@yu.ac.kr (D.K. Shin).

¹ Shows equal contribution.

diverse oxygen states. There are a few reports where researchers have synthesized $\text{Ni}_3\text{V}_2\text{O}_8$ in the form of nanospheres and nanorods using various methods such as solvothermal, hydrothermal, and co-precipitation [20,26]. These methods have been used to create electrodes with excellent energy storage capacity. W. H. Low reported, a Solvothermal method was used to prepare an electrode with a capacitance of 319 F/g at 0.5 A/g current density, while a hydrothermal method produced nickel-vanadium oxide Nano spheres with an energy storage capacity of 562.5 F/g at 1 A/g current density [27]. An asymmetric device was then constructed using the active electrode material and acetylene black, demonstrating a remarkable capacity for energy and power density, as well as long-term stability with a retention of 74 % over 3000 cycles reported by Li et al. [28]. In addition S. E. Arasi reported, a co-precipitation method was used to create nanorods of nickel-vanadium oxide nanoparticles, resulting in an electrode with a capacitance of 894 F/g at 0.4 mA/cm² and a performance retention of 94.1 % over 3000 cycles. These findings suggest that by creating a porous microstructure for $\text{Ni}_3\text{V}_2\text{O}_8$, it is possible to further increase its energy storage capacity [29].

$\text{Ni}_3\text{V}_2\text{O}_8$ is a bimetal oxide that exhibits excellent energy storage capacity for supercapacitor applications [20]. In this report, we present an electrochemical study of $\text{Ni}_3\text{V}_2\text{O}_8$, by tuning the molar concentration of vanadium source. $\text{Ni}_3\text{V}_2\text{O}_8$ nanoparticles were synthesized using a simple hydrothermal method. We thoroughly investigated the effect of modifying the molar concentration on both the stoichiometry of the electrode material and the electrochemical performance of the electrode. An electrode synthesized at a 1:0.5 M ratio of nickel and vanadium shows excellent areal capacitance of 1.56 F/cm² at 3 mA/cm² current density in a 2 M KOH electrolyte. With a power density of 2.2 W/cm², a constructed asymmetric supercapacitor (ASC) has an excellent areal energy density of 6.6 mWh/cm². Throughout 5 K cycles, ASC has outstanding cyclic stability. The excellent electrochemical performances of $\text{Ni}_3\text{V}_2\text{O}_8$ indicate that it is a viable candidate electrode material for energy storage applications.

2. Experimental section

2.1. Synthesis of $\text{Ni}_3\text{V}_2\text{O}_8$ and electrode preparation

In the synthesis of $\text{Ni}_3\text{V}_2\text{O}_8$ nanoparticles, initially prepared 150 mM of nickel nitrate hexahydrate, 37 mM of ammonium metavanadate, and 700 mM urea solution in 40 mL of double distilled water. Stirred the solutions for 30 min at 350 RPM using a magnetic stirrer until we achieved a homogeneous solution, then transferred the homogenous solution to a stemless steel hydrothermal reaction vessel, tightly sealed it, and placed it in a fan-forced oven. The reaction was carried out the reaction at 120 °C for 18 h. After completion of the reaction, the reactor allowed the mixture to cool down to room temperature naturally. Remove the resulting product from the reaction vessel and washed it with ethanol and water through filter paper and dried the prepared product at 60 °C overnight and then anneal it at 400 °C for 4 h. The final product was named NVO-1 and used for further study. We used a similar procedure to prepare other electrode materials with different molar ratios of Ni:V named the product NVO-2 for the 75 mM concentration of ammonium vanadate, NVO-3 for the 150 mM concentration of ammonium vanadate sample and NVO-4 for the 225 mM concentration of ammonium vanadate sample. A similar nomenclature was used in the manuscript throughout. The prepared nanoparticles for further characterization. The electrodes were prepared for studying the electrochemical performance of the electrode material by using $\text{Ni}_3\text{V}_2\text{O}_8$ nanoparticles, carbon black, and NMP solution. Similarly, procedures were used to prepare activated carbon electrodes using activated carbon, carbon black, and NMO solution [30].

3. Result and discussion

3.1. X-ray diffraction (XRD)

X-ray diffraction was used to look into the crystal structure and phase formation of $\text{Ni}_3\text{V}_2\text{O}_8$ nanoparticles. A $\text{Ni}_3\text{V}_2\text{O}_8$ nanoparticle's XRD pattern is shown in the Fig. 1. The XRD spectra demonstrate that the peak intensity rises until a vanadium precursor concentration of 150 mM. Peak intensity decreases while the number of peaks increases at a vanadium precursor concentration of 225 mM. The phase formation of $\text{Ni}_3\text{V}_2\text{O}_8$ was seen at a concentration of 150 mM vanadium precursor concentration. The excess peak has been observed at higher molar concentrations. $\text{Ni}_3\text{V}_2\text{O}_8$ and V_2O_5 were found in a mixed phase at high vanadium precursor concentrations. As the concentration rises, the growth rate increases according to the XRD analysis [31]. The XRD spectra of NVO-2 nanoparticles at 75 mM concentrations were observed at (20), 35.87°, 43.95°, 58.34°, and 63.84°, with oriental miller indices of (211), (151), (022), (023), and (244). An orthorhombic structure with lattice constants of 5.93 Å, 11.42 Å, and 8.24 Å is seen in the XRD spectra of the NVO-2 nanoparticle. This JCPDS card 10-70-1394's XRD spectra are an exact match. Peak intensity increased as vanadium precursor concentration increased due to the nanoparticles' increased growth rate with concentration [31], but the identical JCPDS cards were well matched for NVO-3 peak data. The oriental miller indices for NVO-4 are (010), (110), (101), (010), (310), (011), (301), (411), (600), (002), and (701), and the NVO-3 spectrum shows additional peaks at 20.31°, 21.14°, 26.16°, 31.05°, 32.39°, 34.32°, 45.49°, 47.35°, and 51.23°. $\text{Ni}_3\text{V}_2\text{O}_8$ and V_2O_5 have been found to coexist in a mixed phase. Because of the higher vanadium concentration, the mixed-phase formation in the NVO-4 electrode may be formed.

The elemental valence of $\text{Ni}_3\text{V}_2\text{O}_8$ nanoparticles studied through an XPS study. The Fig. 2(a) shows survey spectra of $\text{Ni}_3\text{V}_2\text{O}_8$ nanoparticles display sharp peaks at 854.75 eV, 515.76 eV, and 529.25 eV, indicating the presence of nickel, vanadium, and oxygen in the sample, respectively. The high-resolution spectra of Ni 2p shown in Fig. 2(b) shows peaks at 872.22 eV and 856.34 eV, which correspond to Ni 2p_{1/2} and Ni 2p_{3/2}. These peaks suggest the sample contains Ni(II). The observed satellite peaks associated with Ni 2p_{1/2} and Ni 2p_{3/2} at 879.22 eV and 860.96 eV, indicate the presence of highly oxidized or bivalent Ni. The deconvoluted Ni 2p_{1/2} and Ni 2p_{3/2} peaks into four spin-orbit doublets. Peaks at 856.30 eV and 874.43 eV suggest the presence of Ni³⁺, while peaks at 854.57 eV and 872.18 eV point to Ni²⁺ [32]. The Fig. 2(c) shows XPS spectra of V split the spin-orbit doublets of V into four peaks at 516.2 eV, 517.4 eV, 523.6 eV, and 524.8 eV. These peaks correspond

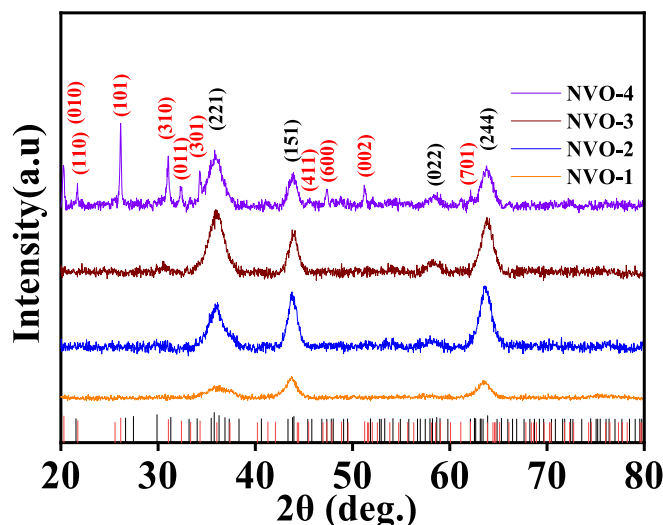


Fig. 1. XRD spectra of $\text{Ni}_3\text{V}_2\text{O}_8$ nanoparticles.

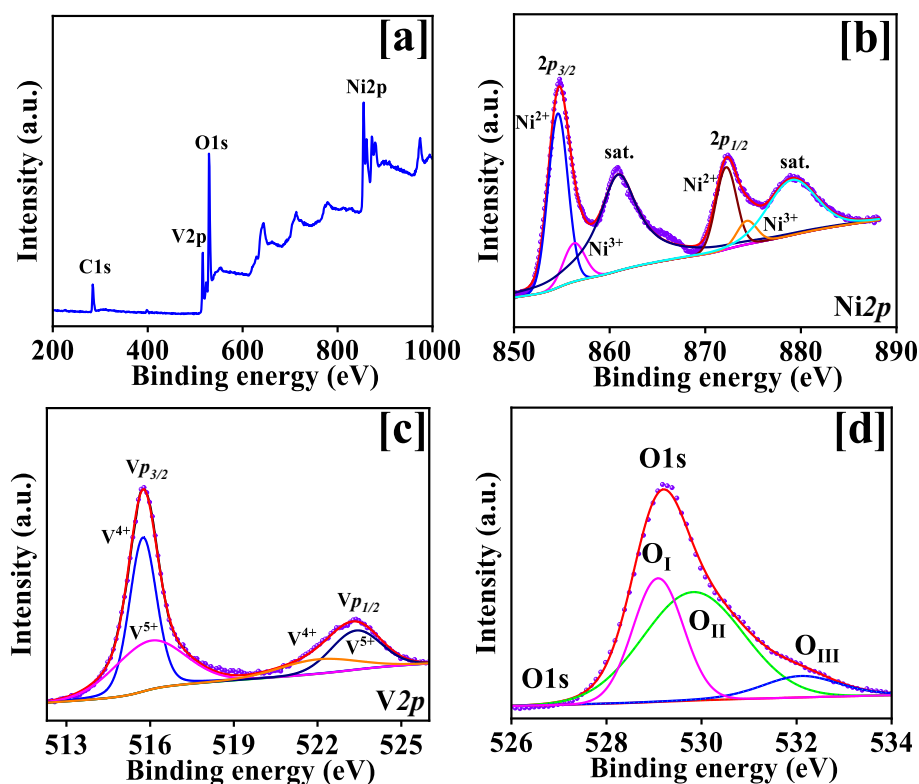


Fig. 2. X-ray photoelectron spectra (a) survey scan, (b) Ni 2p, (c) V 2p, (d) O 1s spectra of NVO-2.

to $V^{4+} 2p_{3/2}$, $V^{5+} 2p_{3/2}$, $V^{4+} 2p_{1/2}$, and $V^{5+} 2p_{1/2}$, confirming the presence of vanadium [33]. Fig. 2(d) shows the O1s spectra, show three deconvoluted peaks at 529.10 eV (O_I), 529.84 eV (O_{II}), and 532.15 eV (O_{III}). The peaks at 529.10 eV and 529.84 eV represent lattice oxygen and H_2O water vacancy, respectively, while researchers attribute the peak at 532.15 eV to lattice oxygen ($V-O$ & $Ni-O$) [34].

3.2. Field emission scanning electron microscope (FE-SEM) and transmission electron microscope (TEM)

$Ni_3V_2O_8$ nanoparticle surface morphology and elemental composition were investigated using a field emission scanning electron microscope (FESEM). Fig. 3 displays a magnified FESEM micrograph of the NVO-1, NVO-2, NVO-3, and NVO-4 samples. The impact of the ammonium metavanadate's molar concentration was seen in the surface microstructures. Fig. 3(a1–a3) displays the FESEM micrographs of the NVO-1 sample at different magnifications, prepared at a 37 mM concentration of ammonium metavanadate. The FESEM reveals the beginning of $Ni_3V_2O_8$ nanoparticle growth. The NVO-2 sample prepared at a 75 mM ammonium metavanadate concentration is shown in the Fig. 3 (b1–b3) using FESEM. The surface microstructure resembled an irregular sponge nanoball. These nanoballs are connected to one another *via* links. All of the nanoballs have a porous appearance and offer an interaction pathway to the electrolyte in the essay. The surface microstructure of the nanoparticle was tuned to spherical nanoball-like nanostructures as shown in Fig. 3(c1–c3) as the ammonium metavanadium concentration increased to 150 mM. Instead of creating a nanochain and wrapping it in NVO-2, nanoballs are wrapped one over the other to form a Nano sphere-like structure. As the nanoballs grow, they are wrapped over each other once more, completely filling the space between them. This decreases the porosity of the nanoballs, which has an impact on how the electrolyte interacts with them. The ammonium metavanadate concentration may be the cause of the nanoball's growth. The more compact and dense nanosphere were seen at 225 mM molar concentration of the NVO-4 nanoparticle, as shown in the Fig. 2(d1–d3).

These surface microstructure almost resemble NVO-3 with nanosphere beginning to link together *via* overgrowth minimizes the porous nanostructure; this could be due to an excess concentration of ammonium metavanadate. The electrochemical performance of the electrode in the supercapacitor was also affected by the molar concentration that was observed on the surface microstructure. The EDS analysis was used to determine the elemental compositions of each sample. The Fig. 4 below displays the $Ni_3V_2O_8$ EDS spectra. The EDS spectrum reveals that all of the spectra had a sharp, intense peak of nickel, vanadium, and oxygen, but the peak's intensity varied depending on the molar concentration of ammonium vanadate. Inside the Fig. 4 displayed the $Ni_3V_2O_8$ atomic percentage. The surface microstructure of the $Ni_3V_2O_8$ showing porous nanostructure and demonstrates NVO-2 nanoparticles exhibit nearly close stoichiometry to the chemical structure. The study using transmission electron microscopy (TEM) provided additional information about the surface morphology and the elemental makeup of the $Ni_3V_2O_8$ nanoparticle. Fig. 5 displays a TEM micrograph of NVO-2 nanoparticles at various magnifications. The $Ni_3V_2O_8$ nanoparticles were composed of the tiny $Ni_3V_2O_8$ nanoparticles, as shown in the Fig. 5(a–d). The porous nanoparticle sphere were created by uniformly wrapping nanoparticles one on top of the other, starting from the center of the particle, as some of the nanoparticles were initially linearly linked together up to a certain length. Unwrapped nanoparticles were seen at the loosely bound outer shells of the nanoparticles, which offer the simplest pathway for the electrolyte insertion. The average particle size of the minuscule nanoparticles is nm, but they are not uniformly distributed. The smaller molar concentration of ammonium metavanadate may prevent the excessive growth of the minute nanoparticles that maintain the void spacing between two or more nanoparticles and increase the porosity of the nanoparticles. This effect was seen in the electrochemical performance of the electrode. Fig. 5(e) shows the SEAD pattern with crystal plane. The TEM analysis was used to determine the $Ni_3V_2O_8$ nanoparticle's d-spacing. As seen in the Fig. 5(c (magnified) and h), the $Ni_3V_2O_8$ electrode has a d-spacing of 0.21 nm. The EDS spectra were used to analyze the elemental makeup of the $Ni_3V_2O_8$ nanoparticles. As

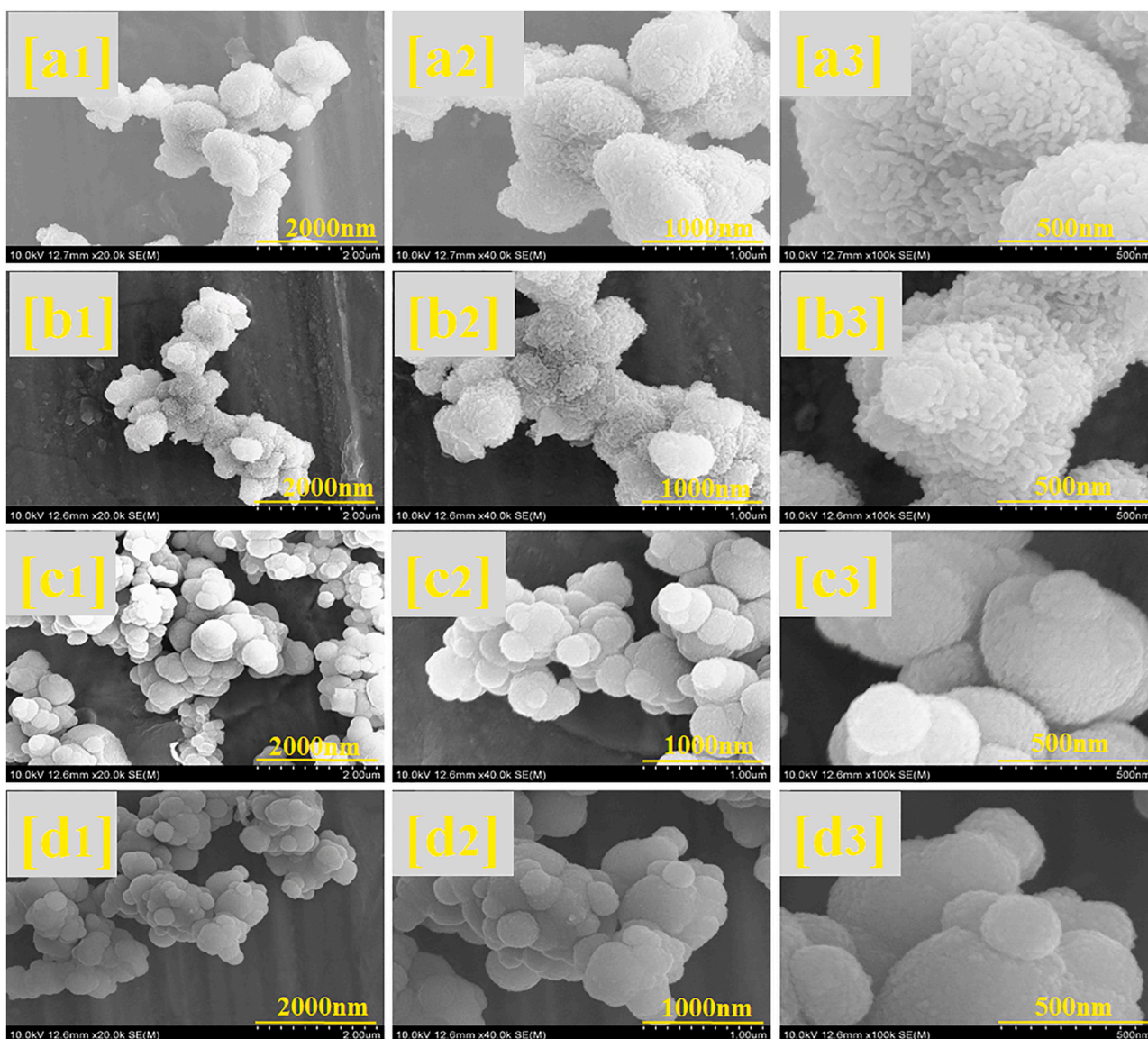


Fig. 3. FESEM micrograph of $\text{Ni}_3\text{V}_2\text{O}_8$ nanoparticles-NVO-1 (a1–a3), NVO-2 (b1–b3) and NVO-3 (c1–c3), and NVO-4 (d1–d3).

depicted in the Fig. 5g, the presence of a sharp peak confirms the presence of Ni, V, and O elements. The $\text{Ni}_3\text{V}_2\text{O}_8$ nanoparticle's elemental mapping is shown in Fig. 5f (i - iii). Elemental mapping of the $\text{Ni}_3\text{V}_2\text{O}_8$ nanoparticle reveals that the Ni, V, and O are distributed uniformly throughout the entire nanoparticle. The elemental composition of the NVO-2 nanoparticle was studied using inductively coupled plasma-atomic emission spectroscopy (ICP-AES). ICP analysis of the NVO-2 nanoparticle was performed at three different concentrations: 0.1 ppm, 1 ppm, and 5 ppm. The average atomic percentages of Ni and V were 48.38 % and 20.68 %, respectively. The results from transmission electron microscopy EDS and ICS studies showed nearly identical elemental matches. The surface area of the NVO-2 nanoparticle was studied using the Brunauer–Emmett–Teller (BET) analysis. Fig. 6a displays the BET plot, which shows that the surface area of the NVO-2 electrode is $79.77 \text{ m}^2/\text{g}$. A higher surface area of the material is more beneficial for ion diffusion and for interactions between ions, the electrode, and the electrolyte. This enhances the electrochemical performance, which is why NVO-2 electrode exhibits excellent areal capacitance.

3.3. Electrochemical study

Through the use of cyclic voltammetry (CV), galvanostatic charge and discharge (GCD), and electrochemical impedance spectroscopy (EIS) measurement, the electrochemical analysis of the prepared electrode were investigated. The Fig. 7a shows the compared CV profiles of the NVO-1, NVO-2, NVO-3, and NVO-4 electrodes measured at a $5 \text{ mV}/\text{s}$ scan rate over the potential range of 0.0 to 0.5 V. All electrodes' CV profiles exhibit a pair of redox peaks, indicating that the electrode material and electrolyte are undergoing faradic reactions, which are the mechanism for storing energy. The NVO-2 electrode's larger surface area than the other electrode reveals that it has a greater capacity for energy storage than the other electrode. The CV profile showed a strong couple redox peak at 0.19 V and 0.38 V, indicating the presence of a reversible faradic redox reaction between Ni and V with OH and demonstrating the pseudocapacitor's ability to store energy. The NVO-2 electrode's surface morphology may be the reason why the area under its CV profile is larger. The NVO-2 electrode's surface microstructure resembles a wrapping of nanochains, one on top of the other, with void spaces in between. For the redox reaction of the electrode material with the electrolyte, the void space may serve as both an easy pathway and a

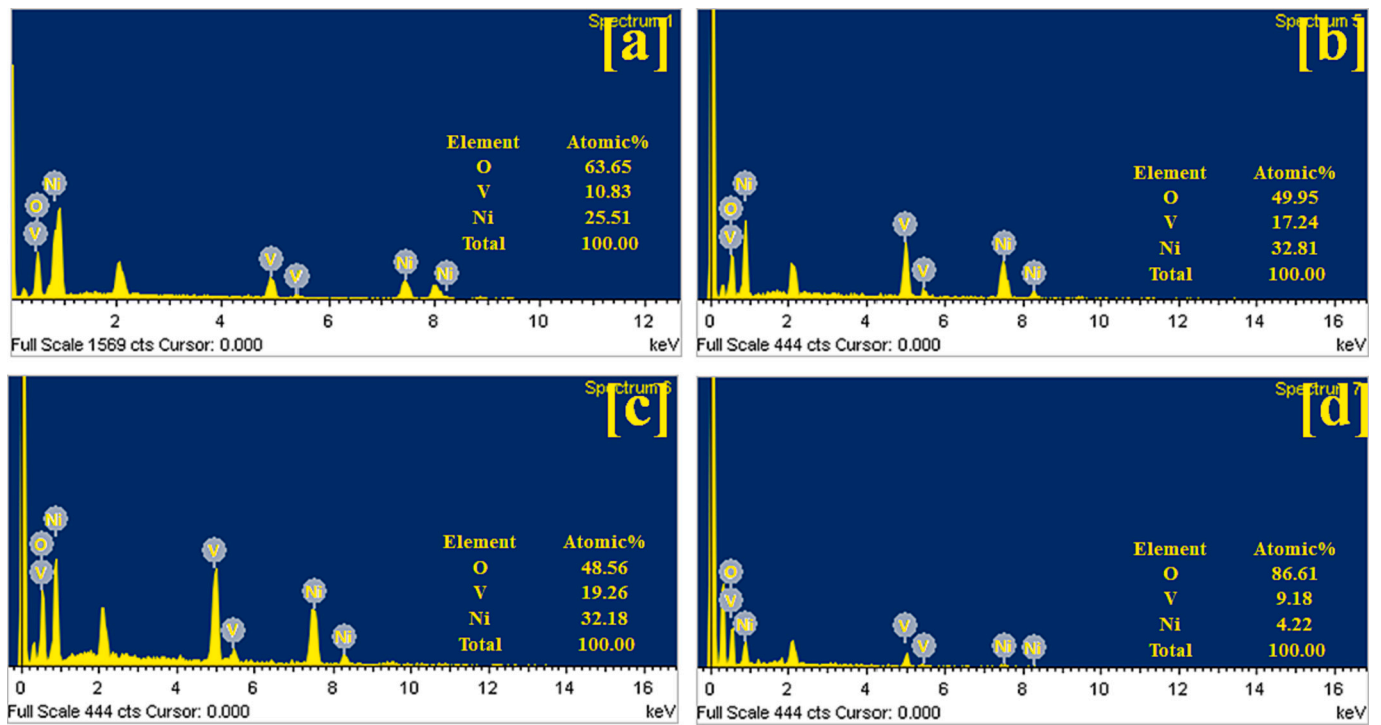


Fig. 4. EDS spectra of Ni₃V₂O₈ nanoparticles-NVO-1 (a), NVO-2 (b), NVO-3 (c) and NVO-4 (d).

more active site. As the nanochain density increased and the surface microstructure started to become more compact, the pathway for the faradic reaction and the synergistic effect of the Ni and V became more difficult. This made it easier for the electrolyte to access and react with the more active site on the NVO-2 electrode compared to the other electrodes. The CV profiles of all electrodes, which range from 5 to 100 mV/s scan rates, are shown in the Fig. S1(a–d). The electrode's CV profile showed that the faradic reaction responsible for the valence change of the Ni and V in measurements is what causes the redox peak's strong intensity of pair. According to the CV profile, the electrode polarization caused by the redox reaction causes the CV curve to shift monotonically and increase peak separation as the scan rate rises from 5 to 100 mV/s as shown in Fig. 7c. The NVO-2 electrode exhibits excellent electrochemical performance, which is thought to be a result of its porous structure and the synergetic effect of Ni and V, which may help to precisely regulate the electronic structure and facilitate charge transport at the electrode-electrolyte interface. The electrode's GCD profile was used to study the electrochemical performance of each electrode. The Fig. 7b displays the comparative GCD profiles for each electrode at a current density of 3 mA/cm². The graph demonstrates that the NVO-2 electrode requires more time to charge and discharge than the other electrode. At a scan rate of 3 mA/cm², the NVO-2 electrode displays an areal capacitance of 1.56 F/cm². The porous structure, microstructure, and accessibility of the void space and active site for the electrode and electrolyte interaction may all contribute to the large areal capacitance of the NVO-2 electrode. The Fig. 7d shows the GCD profile of NVO-2 electrode at different current density and GCD profile of all electrode were shown in Fig. S2(a–d). The Eqs. (6), (7), (8) were used to calculate the areal capacitance, areal energy density and power density of each electrode, and the results for the NVO-2 electrode show that it is an effective electrode material for energy storage applications with an energy density of 34 mWh/cm² and a power density of 600 mW/cm².

The CV profile were carefully examined to learn more about the specifics of the capacitance contribution and charge storage mechanism, as shown in the Fig. 8(a, b). To investigate the details, the peak current was used [35–37]. The following equation was used to represent the peak current of the CV profile.

$$i = av^b \quad (1)$$

where 'i' is the maximum current in the CV, v is the rate at which the CV scans, and 'a' and 'b' are the constant parameters. Whether charge storage is controlled by capacitive, diffusion, or both, the value of the b represents the contribution of the charge. If b = 0.5 represents the current is controlled by the diffusion-controlled behavior, if b = 1.0 represents the current is capacitive controlled behavior, and if b = 0.5 > b > 1 represents the total current is capacitive and diffusion-controlled behavior [35,36]. Eq. (1) is used with the following modifications to determine the value of the variable b.

$$\log(i) = \log(a) + b \log(v) \quad (2)$$

The slope of log(i) vs. log(v) provides the value of 'b'. The Fig. 8(a, b) displays the log(i) vs log(v) plot for anodic and cathodic current for all electrodes. Table 1 contained a list of the 'b' values for each electrode. The porous design of the NVO-2 electrode and the presence of an active site for charge carrier diffusion to the active electrode material may be the cause of the NVO-2 electrode's low 'b' values. The electrode material had a further capacitive charge distribution, and the following equation provided diffusion-controlled current at a constant potential [38–40].

$$i(V) = k_1v + k_2v^{1/2} \quad (3)$$

$$\frac{i_p}{\sqrt{v}} = 2.69 \times A \times C \times \sqrt{D} \times \sqrt{n} \quad (4)$$

$$i_p = 0.227ACFnk^0 \exp \left[-\frac{anF}{RT} (E_p - E^0) \right] \quad (5)$$

$$C_a = \frac{I \times \Delta t}{\Delta V \times A} \quad (6)$$

$$E_a = \frac{1}{7.2} C_a \times \Delta V^2 \quad (7)$$

$$P_a = \frac{E_a}{\Delta t} \times 3600 \quad (8)$$

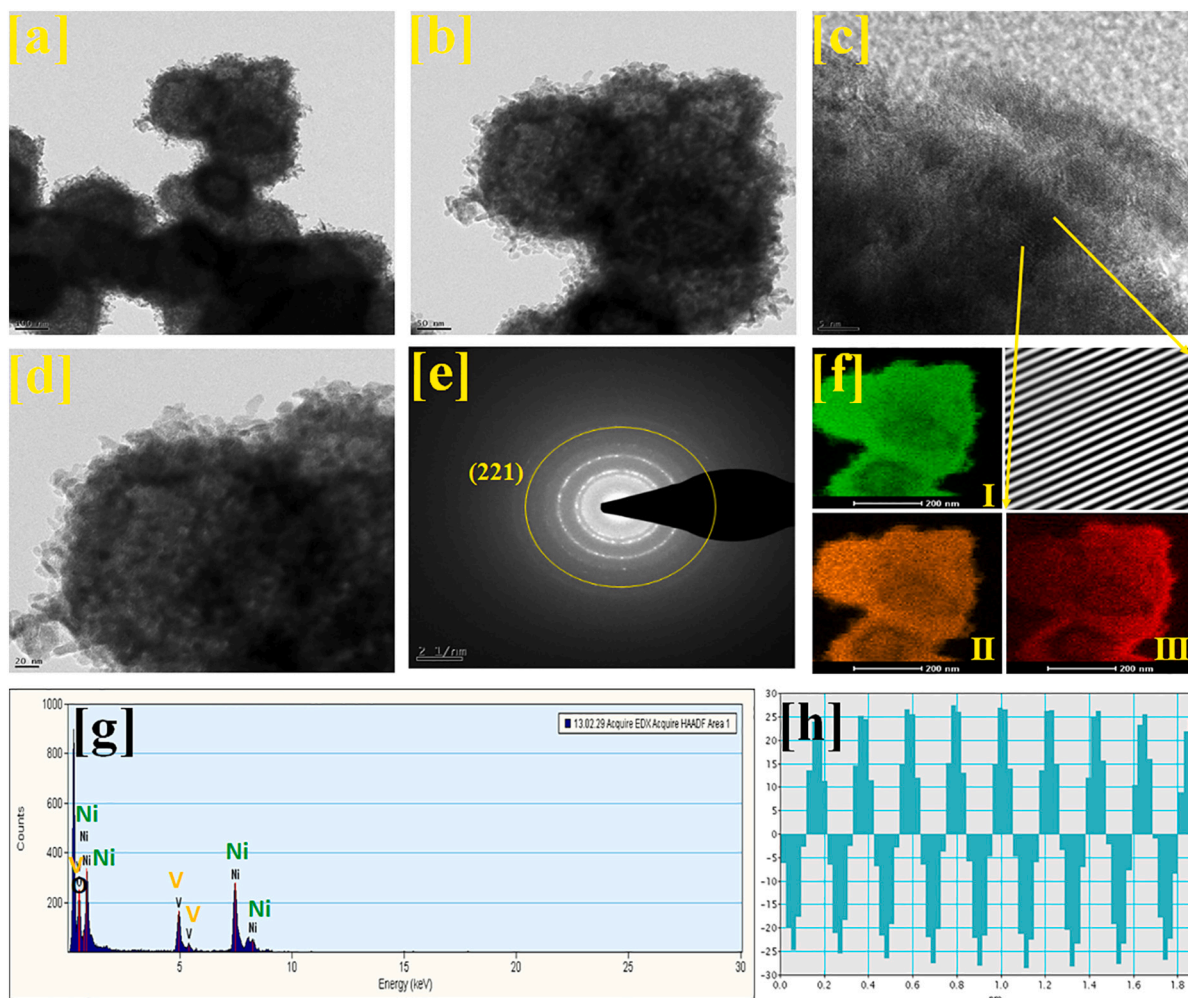


Fig. 5. FE-TEM of $\text{Ni}_3\text{V}_2\text{O}_8$ (NVO-2) nanoparticles at different magnification (a-d), (e) SAED pattern, (f) elemental mapping and 'd' spacing, (g) EDS spectra from FE-TEM, (h) FFT 'd' spacing.

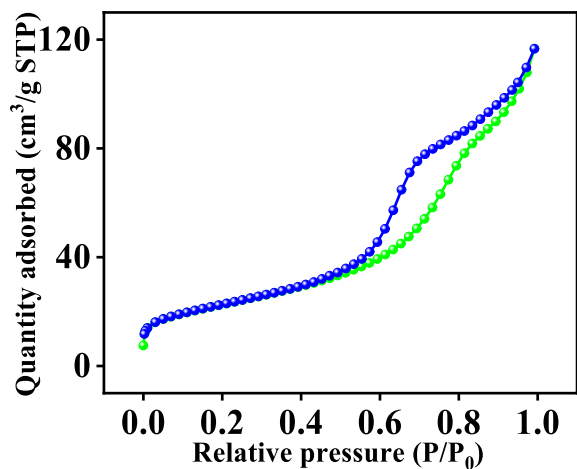


Fig. 6a. Brunauer–Emmett–Teller (BET) surface area analysis of $\text{Ni}_3\text{V}_2\text{O}_8$ (NVO-2) sample.

where ' ν ' is scan rate, ' A ' is the area, ' C ' concentration of the solution, ' D ' is diffusion coefficient, ' F ' faraday constant, ' Δt ' discharge time, ' R ' is universal gas constant, ' k^0 ' is standard rate constant, ' I ' current density, ' ΔV ' potential window, ' C_a ' areal capacitance, ' E_a ' areal energy density,

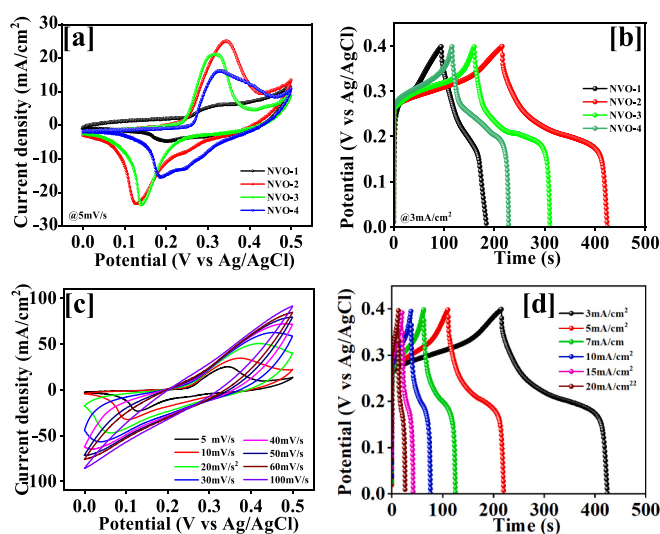


Fig. 7. Comparative CV (a) GCD (b) of NVO-1, NVO-2, NVO-3, and NVO-4, CV (c), GCD (d) of NVO-2.

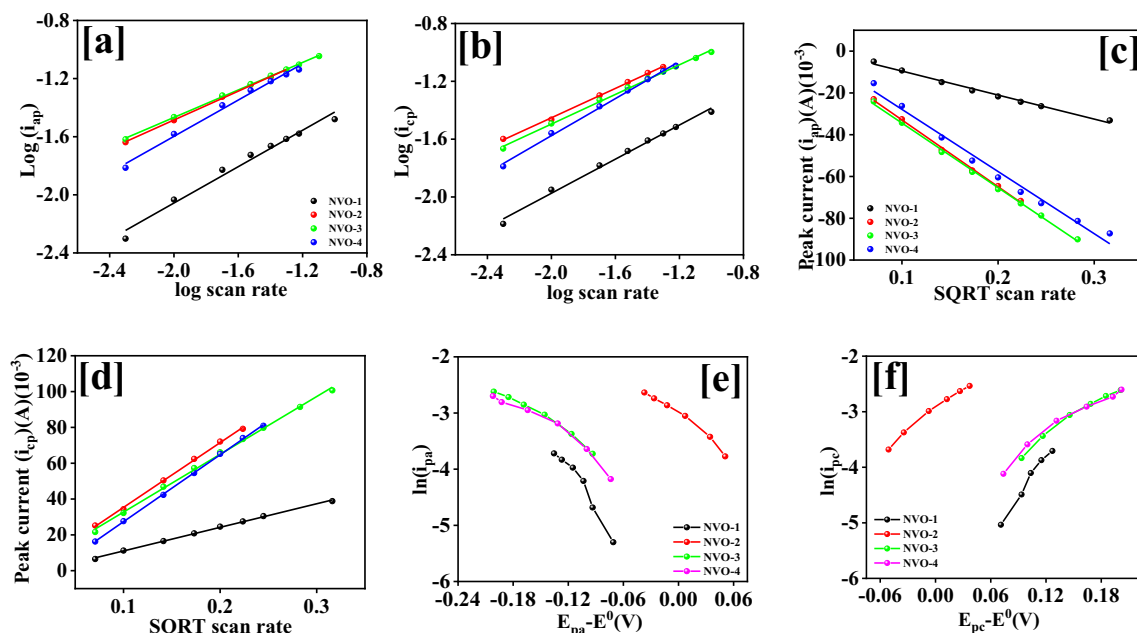


Fig. 8. $\log i_p$ vs $\log v$ plot for b value (a,b), peak current vs \sqrt{v} rate plot for diffusion coefficient (c,d) and $\ln i_p$ vs $E_{pa}-E^0$ plot for standard rate constant k^0 and transfer coefficient (e,f) for NVO-1, NVO-2, NVO-3 and NVO-4 electrode.

Table 1

Comparison of b value, diffusion coefficient, transfer coefficient, and standard rate constant of NVO-1, NVO-2, NVO-3 and NVO-4 electrode.

Sr. no	b value	Diffusion coefficient $\text{cm}^2/\text{s} \times 10^{-7}$	Transfer coefficient (α)	Standard rate constant (k^0) $\text{cm}/\text{s} \times 10^{-4}$
1	0.58	0.46	0.49	0.37
2	0.50	3.4	0.33	9.6
3	0.51	3.1	0.080	5.5
4	0.64	3.0	0.27	1.6

P_a' areal power density. Where the diffusion-controlled current is represented by the other term in the equation above and the capacitive-controlled current is represented by the first term at a constant potential. The k_1' and k_2' values were determined from the $i(V)$ vs \sqrt{v} plot at constant potential and represented in the charge contribution at 10 mV/s and the charge contribution at various scan rates in the Fig. 9(a, b). The NVO-2 electrode's 'b' value demonstrates that the diffusion charge contribution outweighs the capacitive charge distribution. The ion

diffusion for the capacity to store charges is provided by the diffusion coefficient. The CV profile was used to calculate the diffusion coefficient for every electrode. From the Eq. (4) and Fig. 8(c, d), the diffusion coefficient for each electrode were determined. The NVO-2 electrode has a higher diffusion coefficient value than the other electrode. Table 1 shows the values for all electrodes' diffusion coefficients. In comparison to the other electrode, the micro ball's porous structure and the presence of void space may have contributed to the higher diffusion coefficient. Additionally, the standard rate constant (k^0) and the charge transfer coefficient (α) study was done on the redox process. The α values of all electrodes are listed in Table 1 and range from 0.081 to 0.49, with alpha representing the quasi-reversible process. From the standard rate constant (k^0), additional kinematics of the redox process were investigated. The value of k^0 in the range of 10^{-1} to 10^{-5} cm/s represented a quasi-reversible process [30,36,41], and the range of k^0 for all electrodes, which ranges from 0.37 to 9.6×10^{-4} cm/s, demonstrates that all electrodes exhibit this reaction. The higher k^0 value of the NVO-2 may be

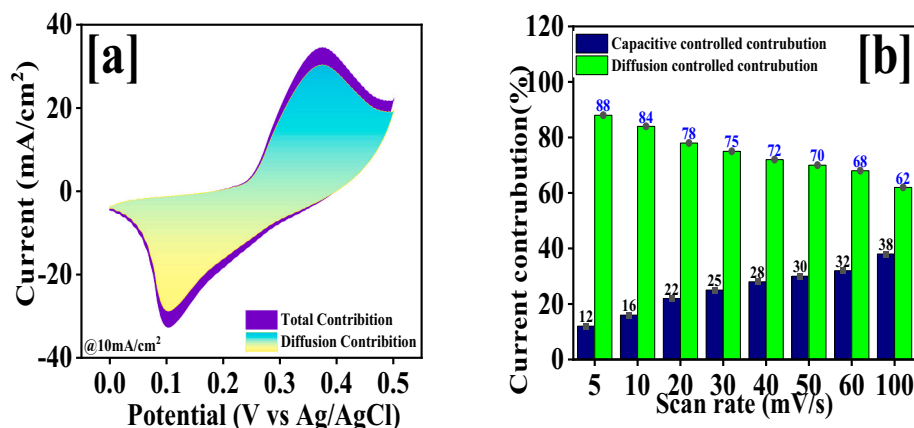


Fig. 9. Capacitive and diffusion controlled contribution at 10 mA/cm² current density (a) and at different scan rate (b) of NVO-2 electrode.

because its porous structure allows for a greater number of active sites for the quasi-reversible redox reaction. Table 1 provided a list of all electrodes' k^0 values. Through the use of electrochemical impedance spectroscopy (EIS), the NVO electrode's electrochemical characteristics were assessed. The frequency range of 0.1 Hz–100 kHz was used to run the EIS spectra. In the Fig. 10a, the Nyquist plots of all NVO electrodes are depicted. The Nyquist plot is divided into two regions: the lower frequency region and the higher frequency region. The curve's intercept on the x-axis at the high-frequency region denotes the series resistance (R_s), which is the sum of the resistances to contact between the active material and the electrolyte, the electrolyte, and the active material [42]. The NVO electrode's R_s value for NVO-1, NVO-2, and NVO-3, respectively, is 2.12 Ω , 2.01 Ω , 2.42 Ω , and 2.26 Ω . Since the NVO-2 electrode's R_s value is lower than that of other electrodes, it indicates that the electrode and electrolyte are more accessible to ions for energy storage. The porous microstructures of the micro balls, which offer an active site for the interaction of the ion with the electrode and increase the capacity of the NVO-2 electrode to store energy, may be the cause of the NVO-2 electrode's low R_s value. The NVO-2 electrode has the highest areal capacitance compared to other electrode materials, demonstrating that it is a superior electrode material for energy storage. The Bode plot is used to illustrate the relationship between the phase angle and the frequency. The electrode's bode plot for NVO-2 is shown in Fig. 10b. For the capacitor, the phase angle should ideally be 90° or less. It is at 45° for the pseudocapacitor as well. The pseudocapacitor nature of the NVO-2 electrode is represented by a phase angle close to 45° [43,44]. The NVO-2 electrode's capacitive properties are depicted by the Fig. 10b log (Z) vs Frequency plot. The porous structure of the $\text{Ni}_3\text{V}_2\text{O}_8$ microsphere may be the cause of the frequency-dependent impedance that the NVO-2 electrode exhibits over a wide frequency range. The capacitance $C(\omega)$, real capacitance $C_{\text{real}}(\omega)$, and imaginary capacitance $C_{\text{img}}(\omega)$ were calculated from the equation [30,44–46] reported in the previous article using the EIS profile of the NVO-2 electrode. The Fig. 10c shows accessible capacitance, $C_{\text{real}}(\omega)$, and imaginary capacitance, $C_{\text{img}}(\omega)$, represent the energy dispersion of the electrode material through an irreversible process. The area around the NVO-2 electrode exhibits a higher capacitance value at low frequencies. NVO-2 electrodes' complex power $S(\omega)$, active $P(\omega)$, and reactive $Q(\omega)$ powers were calculated using the equation [30,46,47]. Calculations were made to determine the normalized active power and reactive power, which are shown in the Fig. 10d. At a point known as the transition point, where behavior

switches from capacitive to resistive and is denoted by the relaxation time (τ_0), the active power and reactive power were crossed [48]. The relaxation time (τ_0), which also exhibits the electrode material's response to discharge, served as a representation of the duration of discharge with >50 % efficiency. Because of the porous microstructure of the electrode material, the NVO-2 electrode exhibits a relaxation time (τ_0) of 0.91 s. This implies that the majority of the time is needed for ion diffusion into porous electrode material that engages the active site.

3.4. Asymmetric supercapacitor (ASC)

Activated carbon (AC) was used as the counter electrode and NVO-2 served as the working electrode in an asymmetric supercapacitor (ASC) to study the practical applicability of the NVO-2 electrode. Activated carbon and NVO-2 electrode material prepared with polyvinyl alcohol (PVDF), carbon black (CB), and N-Methyl-2-pyrrolidone (NMP) solution were used to make the counter and working electrodes. With the aid of paraffin paper and a separator between the counter electrode and working electrode, the counter electrode and working electrode were wrapped together in 2 M KOH electrolyte. The Wonatech SP5 electrochemical workstation was used to analyze the devices electrochemical study. The CV and GCD profiles were tested over the range of 0.8–1.1 V in order to obtain the best potential window, and they confirmed the potential window of 1.1 V for NVO-2//AC as shown in the Fig. 11a. The NVO-2//AC's CV profile, with potential windows of 0.0 to 1.1 V, is depicted in the Fig. 11a. Fig. 11c displays the area of the CV profile increases with an increase in scan rate. This result reveals that the NVO-2//AC ASC has the good rate capability and the reversibility of the NVO-2//AC ASC. The Fig. 11(b, d), depicts the GCD profile of the NVO-2//AC, which has an approximately triangular shape for all current densities. The Regon plot in the Fig. 12b illustrates the area capacitance, energy density, and power density of the NVO-2//AC ACS, which exhibits excellent areal capacitance of 39 mF/cm^2 at current densities of 8 mA/cm^2 and 6.6 mWh/cm^2 energy density at power densities of 2.2 W/cm^2 . For excellent areal capacitance, the NVO-2's porous structures might be advantageous. The long-term stability for 5 k cycles at a scan rate of 12 mA/cm^2 , as depicted in the Fig. 12a in the form of discharge Q, was used to study the practical stability of the NVO-2//AC ASC. The device shows the maximum capacitance over 1 K cycles, and again the capacitance decreases up to 72 % retention till 5 k cycles, which may be due to the change in the structure of the electrode material [49]. The EIS measurement was used to analyze the electrochemical impedance of the NVO-2//AC ASC. The EIS spectra of the NVO-2//AC ASC are depicted in the Fig. 12c. According to the EIS study, the NVO-1//AC ASC has an R_s value of 4.93 Ω before stability R_s value of 6.42 Ω after stability R_s value were increase after stability due to the change in the structure of the electrode material [49]. The results of the overall investigation and the analysis of the NVO-2 and NVO-2//AC ASC show that the $\text{Ni}_3\text{V}_2\text{O}_8$ nanomaterial prepared at Ni:V molar ratio of 1:0.5 makes an excellent electrode material for the application in energy storage.

4. Conclusions

In this work, we used the hydrothermal method to prepare $\text{Ni}_3\text{V}_2\text{O}_8$ nanoparticles with various Ni:V molar ratios. We prepared a porous microstructure of $\text{Ni}_3\text{V}_2\text{O}_8$ nanoparticles at a Ni:V molar ratio of 1:0.5, which provided high active sites for electrolyte and electrode interaction. The large diffusion coefficient and b-value indicated a significant contribution to charge storage. An electrode with a 1:0.5 M ratio of Ni:V demonstrated an excellent areal capacitance of 1.56 F/cm^2 at 3 mA/cm^2 current density. At a current density of 8 mA/cm^2 , the asymmetric device exhibited an areal capacitance of 39 mF/cm^2 . The device delivered an energy density of 6.6 mWh/cm^2 at power densities of 2.2 W/cm^2 . The device showed excellent stability over 5 k GCD cycles, retaining 72 % of its capacity in the most recent 5 k GCD cycles. The optimized Ni:V molar ratio made the unique microstructure of $\text{Ni}_3\text{V}_2\text{O}_8$ possible, and this

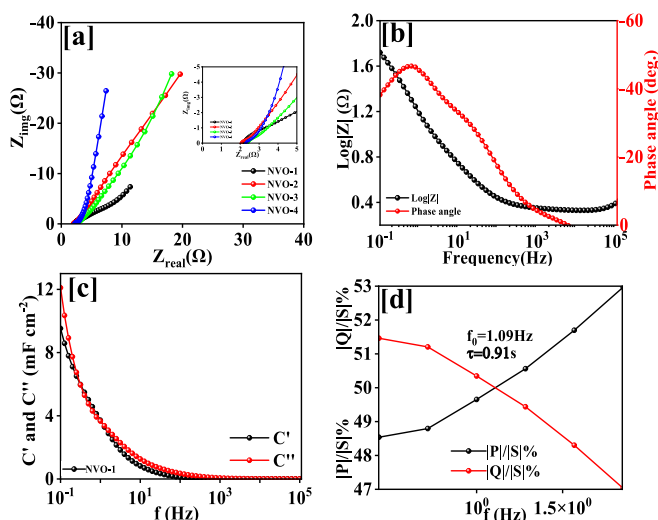


Fig. 10. EIS spectra of for NVO-1, NVO-2, NVO-3, and NVO-4 electrode (a), $\log|Z|$ vs Frequency and phase angle vs frequency plot of (b), C_{real} and C_{img} vs frequency plot of NVO-2 electrode and active and reactive power for τ_0 for NVO-2 electrode (d).

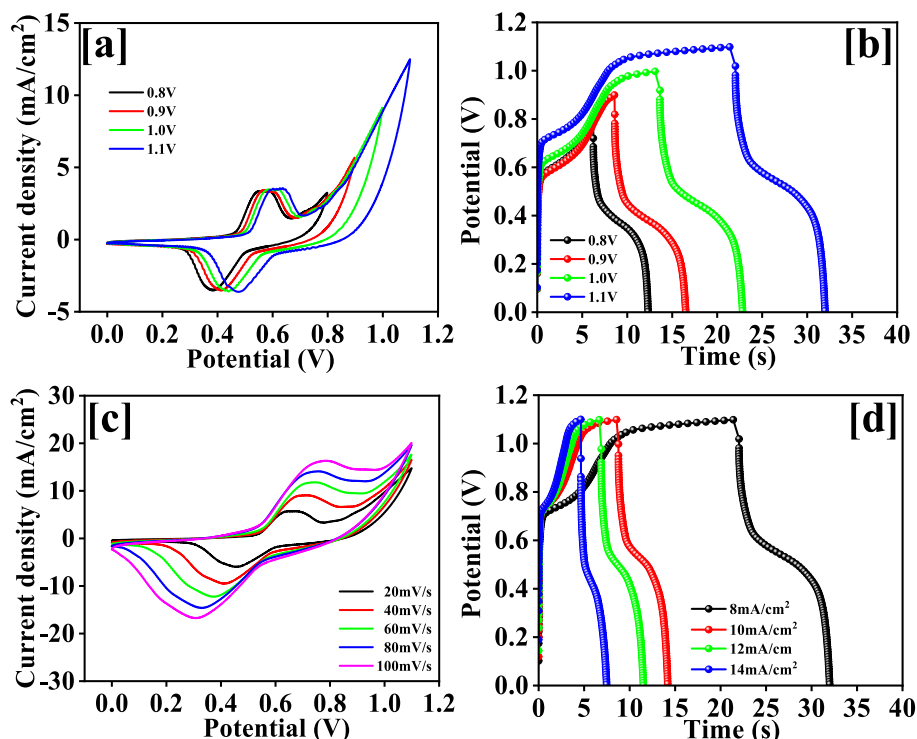


Fig. 11. Cyclic voltammetry for different potential at 10 mV/s scan rate (a), Galvanostatic charge discharge (GCD) for different potential at 8 mA/cm² current density (b), cyclic voltammetry for different scan rate (c), and Galvanostatic charge discharge (GCD) at different density of NVO-2//AC asymmetric supercapacitor.

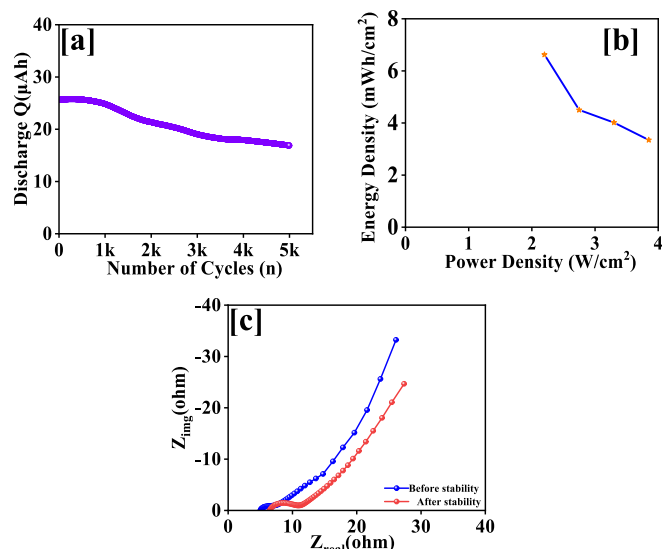


Fig. 12. Cyclic stability over 5 K cycles (a), Regon plot (b) and EIS spectra of NVO-2//AC asymmetric supercapacitor.

material shows potential for energy storage applications.

CRediT authorship contribution statement

Manesh A. Yewale: Conceptualization, Investigation
R. B. Kharade: Writing - original draft
R. A. Kadam: formal analysis
U. T. Nakate: Characterizations
A. M. Teli, S. A. Beknalkar: Data Curation, software
S. D. Dhas: Methodology
V. Kumar: Data analysis

D. K. Shin: Supervision.

Declaration of competing interest

The authors declare that they have no known competing financial interests or personal relationships that could have appeared to influence the work reported in this paper.

Data availability

Data will be made available on request.

Acknowledgement

This work was supported by the Technology Innovation Program (#20010170) funded By the Ministry of Trade, Industry & Energy (MOTIE, Korea).

Appendix A. Supplementary data

Supplementary data to this article can be found online at <https://doi.org/10.1016/j.est.2023.109005>.

References

- [1] S. Patrice, Y. Gogotsi, *Materials for Electrochemical Capacitors*, Springer Handbooks, 2017, pp. 495–561, https://doi.org/10.1007/978-3-662-46657-5_16.
- [2] Y. Lan, H. Zhao, Y. Zong, X. Li, Y. Sun, J. Feng, Y. Wang, X. Zheng, Y. Du, Phosphorization boosts the capacitance of mixed metal nanosheet arrays for high performance supercapacitor electrodes, *Nanoscale*. 10 (2018) 11775–11781, <https://doi.org/10.1039/c8nr01229f>.
- [3] G. Wang, L. Zhang, J. Zhang, A review of electrode materials for electrochemical supercapacitors, *Chem. Soc. Rev.* 41 (2012) 797–828, <https://doi.org/10.1039/c1cs15060j>.
- [4] T. Chen, L. Dai, Carbon nanomaterials for high-performance supercapacitors, *Mater. Today* 16 (2013) 272–280, <https://doi.org/10.1016/j.mattod.2013.07.002>.
- [5] K. Xu, S. Ma, Y. Shen, Q. Ren, J. Yang, X. Chen, J. Hu, CuCo2O4 nanowire arrays wrapped in metal oxide nanosheets as hierarchical multicomponent electrodes for

- supercapacitors, *Chem. Eng. J.* 369 (2019) 363–369, <https://doi.org/10.1016/j.cej.2019.03.079>.
- [6] T. Panja, N. Diez, R. Mysyk, D. Bhattacharjya, E. Goikolea, D. Carriazo, Robust NiCo₂O₄/superactivated carbon aqueous supercapacitor with high power density and stable cyclability, *ChemElectroChem.* 6 (2019) 2536–2545, <https://doi.org/10.1002/celec.201900130>.
- [7] M.A. Yewale, R.A. Kadam, N.K. Kaushik, J.R. Koduru, N.B. Velhal, U.T. Nakate, A. A. Jadhavar, N.D. Sali, D.K. Shin, Materials Science & Engineering B Interconnected plate-like NiCo₂O₄ microstructures for supercapacitor application, *Mater. Sci. Eng. B* 287 (2023) 116072, <https://doi.org/10.1016/j.mseb.2022.116072>.
- [8] S. Ghosh, P. Samanta, P. Samanta, N.C. Murmu, T. Kuila, Investigation of electrochemical charge storage efficiency of NiCo₂Se₄/RGO composites derived at varied duration and its asymmetric supercapacitor device, *Energy Fuels* 34 (2020) 13056–13066, <https://doi.org/10.1021/acs.energyfuels.0c02152>.
- [9] Y. Dahiya, M. Hariram, M. Kumar, A. Jain, D. Sarkar, Modified transition metal chalcogenides for high performance supercapacitors: current trends and emerging opportunities, *Coord. Chem. Rev.* 451 (2022) 214265, <https://doi.org/10.1016/j.ccr.2021.214265>.
- [10] T. Brousse, D. Bélanger, J.W. Long, To be or not to be pseudocapacitive? *J. Electrochem. Soc.* 162 (2015) A5185–A5189, <https://doi.org/10.1149/2.0201505jes>.
- [11] D.P. Dubal, N.R. Chodankar, D.H. Kim, P. Gomez-Romero, Towards flexible solid-state supercapacitors for smart and wearable electronics, *Chem. Soc. Rev.* 47 (2018) 2065–2129, <https://doi.org/10.1039/c7cs00505a>.
- [12] S. Jiao, A. Zhou, M. Wu, H. Hu, Kirigami patterning of MXene/bacterial cellulose composite paper for all-solid-state stretchable micro-supercapacitor arrays, *Adv. Sci.* 6 (2019), <https://doi.org/10.1002/adv.201900529>.
- [13] Z. Cao, J. Fu, M. Wu, T. Hua, H. Hu, Synchronously manipulating Zn²⁺ transfer and hydrogen/oxygen evolution kinetics in MXene host electrodes toward symmetric Zn-ions micro-supercapacitor with enhanced areal energy density, *Energy Storage Mater.* 40 (2021) 10–21, <https://doi.org/10.1016/j.ensm.2021.04.047>.
- [14] S.A. Beknalkar, A.M. Teli, A.C. Khot, T.D. Dongale, M.A. Yewale, K.A. Nirmal, J. C. Shin, A new path to high-performance supercapacitors: utilizing Ag-embedded CoFe-phosphate and Ti₃C₂ MXene as hybrid electrodes, *J. Energy Storage.* 72 (2023) 108272, <https://doi.org/10.1016/j.est.2023.108272>.
- [15] A.M. Teli, S.A. Beknalkar, S.M. Mane, M.A. Yewale, T.D. Dongale, J. Cheol, Synergetic effect of ternary MnVMO-oxide electrode by hydrothermal method for high-performance asymmetric supercapacitor, *J. Energy Storage.* 65 (2023) 107289, <https://doi.org/10.1016/j.est.2023.107289>.
- [16] A.M. Teli, S.A. Beknalkar, R.U. Amte, P.J. Morankar, M.A. Yewale, V.V. Burungale, C.W. Jeon, H. Efstathiadis, J.C. Shin, Investigating into the intricacies of charge storage kinetics in NbMn-oxide composite electrodes for asymmetric supercapacitor and HER applications, *J. Alloys Compd.* 965 (2023) 171305, <https://doi.org/10.1016/j.jallcom.2023.171305>.
- [17] S.D. Dhas, P.N. Thonge, S.D. Waghmare, G.K. Kulkarni, S.K. Shinde, D.Y. Kim, T. M. Patil, M.A. Yewale, A.V. Moholkar, D. Kim, Hierarchical spinel NiMn₂O₄ nanostructures anchored on 3-D nickel foam as stable and high-performance supercapacitor electrode material, *J. Energy Storage.* 71 (2023) 108168, <https://doi.org/10.1016/j.est.2023.108168>.
- [18] M.A. Yewale, R.A. Kadam, N.K. Kaushik, S.V.P. Vattikuti, L.P. Lingamdinne, J. R. Koduru, D.K. Shin, Hydrothermally synthesized microrods and microballs of NiCo₂O₄ for supercapacitor application, *Ceram. Int.* 48 (2022) 22037–22046, <https://doi.org/10.1016/j.ceramint.2022.04.190>.
- [19] H. Chen, Y. Liu, J. Sun, C. Xu, High-performance hybrid supercapacitor based on the porous copper cobaltite/cupric oxide nanosheets as a battery-type positive electrode material, *Int. J. Hydrogen Energy* 46 (2021) 28144–28155, <https://doi.org/10.1016/j.ijhydene.2021.06.056>.
- [20] D. Merum, R.R. Nallapureddy, M.R. Pallavolu, T.K. Mandal, R.R. Guttururu, N. Parvin, A.N. Banerjee, S.W. Joo, Pseudocapacitive performance of freestanding Ni₃V₂O₈Nanosheets for high energy and power density asymmetric supercapacitors, *ACS Appl. Energy Mater.* (2022), <https://doi.org/10.1021/acsaem.1c03754>.
- [21] M.A. Yewale, A.A. Jadhvar, R.B. Kharade, R.A. Kadam, V. Kumar, U.T. Nakate, P. B. Shelke, D.H. Bobade, A.M. Teli, S.D. Dhas, D.K. Shin, Hydrothermally synthesized Ni₃V₂O₈ nanoparticles with horny surfaces for HER and supercapacitor application, *Mater. Lett.* 338 (2023) 134033, <https://doi.org/10.1016/j.matlet.2023.134033>.
- [22] B. Huang, W. Wang, T. Pu, J. Li, C. Zhao, L. Xie, L. Chen, Rational design and facile synthesis of two-dimensional hierarchical porous M₃V₂O₈ (M = Co, Ni and Co-Ni) thin sheets assembled by ultrathin nanosheets as positive electrode materials for high-performance hybrid supercapacitors, *Chem. Eng. J.* 375 (2019) 121969, <https://doi.org/10.1016/j.cej.2019.121969>.
- [23] Y. Zhang, X. Xu, Y. Gao, D. Gao, Z. Wei, H. Wu, In-situ synthesis of three-dimensionally flower-like Ni₃V₂O₈@carbon nanotubes composite through self-assembling for high performance asymmetric supercapacitors, *J. Power Sources* 455 (2020) 227985, <https://doi.org/10.1016/j.jpowsour.2020.227985>.
- [24] R.A. Kadam, M.A. Yewale, A.M. Teli, Annu, U.T. Nakate, V. Kumar, S.L. Kadam, D. K. Shin, Bimetallic Co₃V₂O₈ microstructure: a versatile bifunctional electrode for supercapacitor and electrocatalysis applications, *Surfaces and Interfaces* 41 (2023), 103267, <https://doi.org/10.1016/j.surfin.2023.103267>.
- [25] A. Tyagi, M.C. Joshi, A. Shah, V.K. Thakur, R.K. Gupta, Hydrothermally tailored three-dimensional Ni-V layered double hydroxide nanosheets as high-performance hybrid supercapacitor applications, *ACS Omega* 4 (2019) 3257–3267, <https://doi.org/10.1021/acsomega.8b03618>.
- [26] M. Guo, J. Balamurugan, N.H. Kim, J.H. Lee, High-energy solid-state asymmetric supercapacitor based on nickel vanadium oxide/NG and iron vanadium oxide/NG electrodes, *Appl. Catal. Environ.* 239 (2018) 290–299, <https://doi.org/10.1016/j.apcatb.2018.08.026>.
- [27] W.H. Low, P.S. Khiew, S.S. Lim, C.W. Siong, E.R. Ezeigwe, Facile solvothermal designing of graphene/Ni₃V₂O₈ nanocomposite as electrode for high performance symmetric supercapacitor, *J. Alloys Compd.* 768 (2018) 995–1005, <https://doi.org/10.1016/j.jallcom.2018.07.139>.
- [28] Y. Li, H. Sun, Y. Yang, Y. Cao, W. Zhou, H. Chai, Controllable fabrication of NiV₂O₆ nanosphere as a high-performance flexible all-solid-state electrode material for supercapacitors, *J. Colloid Interface Sci.* 580 (2020) 298–307, <https://doi.org/10.1016/j.jcis.2020.03.097>.
- [29] S. Ezhil Arasi, R. Ranjithkumar, P. Devendran, M. Krishnakumar, A. Arivarasan, Electrochemical evaluation of binary Ni₂V₂O₇ nanorods as pseudocapacitor electrode material, *Ceram. Int.* 46 (2020) 22709–22717, <https://doi.org/10.1016/j.ceramint.2020.06.034>.
- [30] M.A. Yewale, R.A. Kadam, N.K. Kaushik, L.N. Nguyen, U.T. Nakate, L. P. Lingamdinne, J.R. Koduru, P.S. Auti, S.V.P. Vattikuti, D.K. Shin, Electrochemical supercapacitor performance of NiCo₂O₄ nanoballs structured electrodes prepared via hydrothermal route with varying reaction time, *Colloids Surfaces A Physicochem. Eng. Asp.* 653 (2022) 129901, <https://doi.org/10.1016/j.colsurfa.2022.129901>.
- [31] B.Y. Fugare, B.J. Lokhande, The influence of concentration on the morphology of TiO₂ thin films prepared by spray pyrolysis for electrochemical study, *Appl. Phys. A Mater. Sci. Process.* 123 (2017), <https://doi.org/10.1007/s00339-017-1008-0>.
- [32] Q. Zhang, Y. Xu, C. Li, W. Chen, W. Zhu, L. Wang, Staggered nickel-vanadium layered double hydroxide nanosheets on reduced graphene oxide via in-situ growth for enhanced supercapacitor performance, *J. Alloys Compd.* 935 (2023) 168048, <https://doi.org/10.1016/j.jallcom.2022.168048>.
- [33] J.F. Hou, J.F. Gao, L. Bin Kong, A crystalline nickel vanadium oxide@amorphous cobalt boride nanocomposites with enhanced specific capacity for hybrid supercapacitors, *Electrochim. Acta* 377 (2021) 138086, <https://doi.org/10.1016/j.electacta.2021.138086>.
- [34] M.A. Yewale, R.A. Kadam, N.K. Kaushik, N.N. Linh, A.M. Teli, J.C. Shin, L. P. Lingamdinne, J.R. Koduru, D.K. Shin, Mesoporous hexagonal nanorods of NiCo₂O₄ nanoparticles via hydrothermal route for supercapacitor application, *Chem. Phys. Lett.* 800 (2022) 139654, <https://doi.org/10.1016/j.cplett.2022.139654>.
- [35] P. Delahay, *New instrumental methods in electrochemistry*, *Intersci. Publ.* 12 (1955) 499–500.
- [36] N. Frenzel, J. Hartley, G. Frisch, Voltammetric and spectroscopic study of ferrocene and hexacyanoferrate and the suitability of their redox couples as internal standards in ionic liquids, *Phys. Chem. Chem. Phys.* 19 (2017) 28841–28852, <https://doi.org/10.1039/c7cp05483a>.
- [37] H. Lindström, S. Södergren, A. Solbrand, H. Rensmo, J. Hjelm, A. Hagfeldt, S. E. Lindquist, Li⁺ ion insertion in TiO₂ (anatase). 1. Chronoamperometry on CVD films and nanoporous films, *J. Phys. Chem. B* 101 (1997) 7710–7716, <https://doi.org/10.1021/jp970489r>.
- [38] T.-C. Liu, W.G. Pell, B.E. Conway, S.L. Roberson, Behavior of molybdenum nitrides as materials for electrochemical capacitors: comparison with ruthenium oxide, *J. Electrochem. Soc.* 145 (1998) 1882–1888, <https://doi.org/10.1149/1.1838571>.
- [39] H. Zhang, L. Wang, X. Xing, S. Zhao, K. Wang, S. Liu, High-energy-density supercapacitors based on high-areal-specific-capacity Ti₃C₂T_x and a redox-active organic-molecule hybrid electrode, *Adv. Funct. Mater.* 32 (2022), <https://doi.org/10.1002/adfm.202208403>.
- [40] A.M. Patil, J. Wang, S. Li, X. Hao, X. Du, Z. Wang, X. Hao, A. Abudula, G. Guan, Bilateral growth of monoclinic WO₃ and 2D Ti₃C₂T_x on 3D free-standing hollow graphene foam for all-solid-state supercapacitor, *Chem. Eng. J.* 421 (2021) 127883, <https://doi.org/10.1016/j.cej.2020.127883>.
- [41] A.M. Teli, T.S. Bhat, S.A. Beknalkar, S.M. Mane, L.S. Chaudhary, D.S. Patil, S. A. Pawar, H. Efstathiadis, J. Cheol Shin, Bismuth manganese oxide based electrodes for asymmetric coin cell supercapacitor, *Chem. Eng. J.* 430 (2022) 133138, <https://doi.org/10.1016/j.cej.2021.133138>.
- [42] D. Qu, The study of the proton diffusion process in the porous MnO₂ electrode, *Electrochim. Acta* 49 (2004) 657–665, <https://doi.org/10.1016/j.electacta.2003.08.030>.
- [43] L. Yuan, X.H. Lu, X. Xiao, T. Zhai, J. Dai, F. Zhang, B. Hu, X. Wang, L. Gong, J. Chen, C. Hu, Y. Tong, J. Zhou, Z.L. Wang, Flexible solid-state supercapacitors based on carbon nanoparticles/MnO₂ nanorods hybrid structure, *ACS Nano* 6 (2012) 656–661, <https://doi.org/10.1021/nn2041279>.
- [44] D.P. Dubal, N.R. Chodankar, R. Holze, D.H. Kim, P. Gomez-Romero, Ultrathin mesoporous RuCo₂O₄ nanoflakes: an advanced electrode for high-performance asymmetric supercapacitors, *ChemSusChem.* 10 (2017) 1771–1782, <https://doi.org/10.1002/cssc.201700001>.
- [45] D. Yuan, J. Zeng, N. Kristian, Y. Wang, X. Wang, Bi₂O₃ deposited on highly ordered mesoporous carbon for supercapacitors, *Electrochem. Commun.* 11 (2009) 313–317, <https://doi.org/10.1016/j.elecom.2008.11.041>.
- [46] C. Portet, P.L. Taberna, P. Simon, E. Flahaut, Influence of carbon nanotubes addition on carbon-carbon supercapacitor performances in organic electrolyte, *J. Power Sources* 139 (2005) 371–378, <https://doi.org/10.1016/j.jpowsour.2004.07.015>.
- [47] N.C. Maile, M. Moztahida, A.A. Ghani, M. Hussain, K. Tahir, B. Kim, S.K. Shinde, V. J. Fulari, D.S. Lee, Electrochemical synthesis of binder-free interconnected nanosheets of Mn-doped Co₃O₄ on Ni foam for high-performance electrochemical

- energy storage application, Chem. Eng. J. 421 (2021) 129767, <https://doi.org/10.1016/j.cej.2021.129767>.
- [48] A. Adan-Mas, L. Alcaraz, P. Arévalo-Cid, F.A. López-Gómez, F. Montemor, Coffee-derived activated carbon from second biowaste for supercapacitor applications, Waste Manag. 120 (2021) 280–289, <https://doi.org/10.1016/j.wasman.2020.11.043>.
- [49] A.M. Teli, S.A. Bknalkar, T.S. Bhat, S.M. Mane, J.C. Shin, Molybdenum–manganese hydroxide microcubes based electrode via hydrothermal method for asymmetric supercapacitor, Ceram. Int. 48 (2022) 29386–29393, <https://doi.org/10.1016/j.ceramint.2022.06.002>.

Design and Development of Feedback Controller for Scanning Probe Microscopy Applications

Gaikwad S. B.¹, Dr. S. L. Kadam², Dr. S. B. Iyer³

Department of Physics, Shri Dhokeshwar College, Takali Dhokeshwar, Ahmednagar, Maharashtra¹

Department of Physics, New Arts, Commerce and Science College, Parner, Ahmednagar, Maharashtra²

Department of Physics, Ahmednagar College, Ahmednagar, Maharashtra³

Abstract: *The Scanning Probe Microscopy (SPM) techniques, mainly Scanning tunneling microscopy (STM) and atomic force microscopy (AFM) instruments have great important in surface science laboratories due to its high potential to achieve image at atomic scale resolution. SPM has revolutionized our ability to explore the nanoscale world enabling the imaging, manipulation and characterization of materials at the atomic and molecular level. The experimental designing and its analysis of feedback network system has proposed for scanning tunneling microscopy. Instability in feedback network could affect the measurements and accuracy in surface topology of material. Feedback network circuit controls the necessary arrangement for proper functioning of STM. It Controls the STM operation like a regulator circuit in sealing fan even if input voltage changes, the output has controlled by the regulator. The working of each element of feedback network is well discussed and analysed. The interconnection between the different elements of feedback control network is analysed with mathematical equations. STM has the outstanding advantage from the biological perspective of allowing measurements has made with a resolution of nanometers in aqueous media. Hence, living cells, working enzyme systems etc. can be examined. [4] SEM also investigates 'Trichomes' which is present on both surfaces of leaf. [5].*

Keywords: Scanning Probe Microscopy

I. INTRODUCTION

Scanning probe microscopy (SPM) includes STM, AFM, and chemical force microscopy that have extensively applied in nanostructure characterization. Scanning Probe Microscopy (SPM) is device based on a new technique to investigate the structures at the atomic or molecular level.

Scanning Tunnelling Microscopy was first developed by Gerd Binnig and Heinrich Rohrer in 1981 and earned its inventors the Nobel Prize in Physics in 1986. STM has considered the godfather of all the other tip-based microscopy methods, including atomic force microscopy (AFM). It creates powerful surface images and characterization method, which have developed of our understanding of material, condensed matter and device operation at nanoscale. A key future of SPM is the nano sized probe, which interacts with the surface and produce the information used to create an image of the surface topography. [9]

After high success in providing high-resolution imaging, some limitation are still at the centre of researchers interests like low speed of imaging, limit of processes in real time, interpretation of complex data, issues related to tip-surface interaction. The sensing principle has remained unchanged since the development of SPM. This influences careful piezoelectric actuation for a raster scan of the sample surface while a feedback system senses the tip - surface interaction in one of the many modes such as contact or contactless. It providing high-resolution imaging and information required for spectroscopy. Machine learning introduced some new technology to enhance performance data collection to improve traditional limitation and enhanced the quality of SPM. [9]

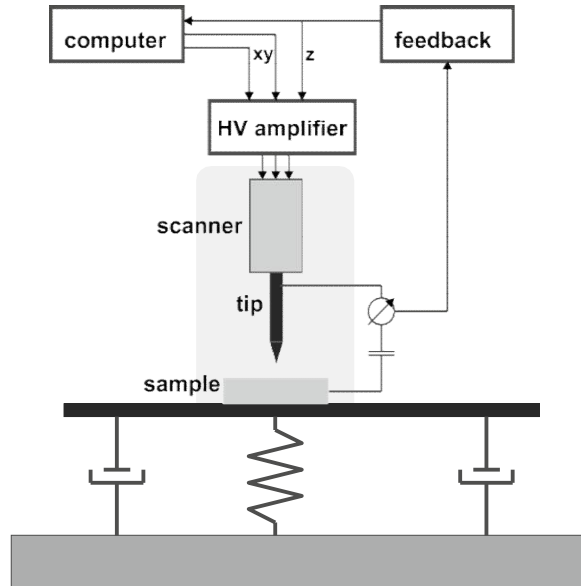


Figure 1.1: Schematic diagram of the scanning tunneling microscope

Scanning Tunnelling Microscopy (STM) is applicable to the conductive sample or the surface operating under different environment. STM operation has invented based on the mechanism of the quantum tunnelling effect. [3]

After building this microscope with increasing accuracy and complexity, we look towards to design a simple, cheap system that has to be useful for students and our research laboratory. An analogue control proportional feedback controller with sample and sharp conducting tip which has used to control the STM operation. The STM consists of a sharp metal tip, often made of Pt-Rh or tungsten and a conducting or semiconducting planer sample surface. When sample is clean and flat, even atoms can imaged. The distance between tip and sample control during data collection is change by synchronising the parameter of feedback loop. Instead of tip position, D- A convertor maintained velocity of tip to reduce generated noise. This will provide time delay for the collection of data. [2,18]

In scanning tunnelling microscopy (STM), where a small tunnelling current has measured between probing tip and sample. Various operation modes such as constant tunnelling and constant height modes as well as tunnelling spectroscopy had described and application are given. [10] By using combination of a coarse approach and piezoelectric transducers, a sharp, metallic probing tip has brought into close proximity with the sample. The surface contact between tip and sample is only a few angstrom units, which implies that the electron wave functions of tip and sample start to overlap. [16,17]

II. BACKGROUND AND DESIGNING OF PREAMPLIFIER

There are three major part of STM device. It contains head stainless steel with differential screw and piezo tube for scanning. [2] Scan area has limited by the choice of the piezoelectric scanner and the maximum output voltage V_{max} of the high voltage amplifier. In the driver amplifier of piezo, we can use op-amps. The scan tube sensitivity is 30nm/V for X and Y and 5 nm/V for Z. The tunnel current converted in to a voltage for feedback system by using pre amplifier with a $10^8 \Omega$ and OPA 128. The signal is amplified 10 times to get a 1 V/nA. Preamplifier has mounted at base of head to reduce mechanical noise. Since the current is exponential dependence tip-sample distance. The current has linearized with logarithmic amplifier. This voltage has apply to feedback controller, which is the difference amplifier. The output voltage of the log amplifier has compared with set reference, which decides the value of the tunnel current desired. Feedback circuit generated proportional voltage depending on error signal. [1,14]

To achieve constant tunnel current, this proportional signal has applied to the Z electrode of the piezo, which is in corresponding to reference voltage. For this rules and condition, we assume that tunnel current locked by applying voltage to the XY electrode of the piezo, the surface has scanned in a raster pattern. At the same time, output of the

feedback controller is gain by the data acquisition system. The software produced then a grey scale image, which is image of the sample topography.[16]

The preamplifier circuit converts small current through the high impedance tunnel junction into low impedance voltage signal. It has two stages, Op amp 1 has used as current to voltage converter. The tunnel current is of the order of 1 nA with an impedance of a few MΩ range. Here, the Op amp OPA 128 has used, which has high input impedance ($10^{12}\Omega$). The tunnel signal has amplified by the instrumentation amplifier AD 524 with variable gain. The proper selection of feedback resistor is necessary since the increase in R_f will increase signal to noise ratio but will decrease band-width the system. Infrequency response, gain picking has observed at a particular frequency. Here no drift has observed in the output.[14]

III. FEEDBACK CONTROLLER NETWORK

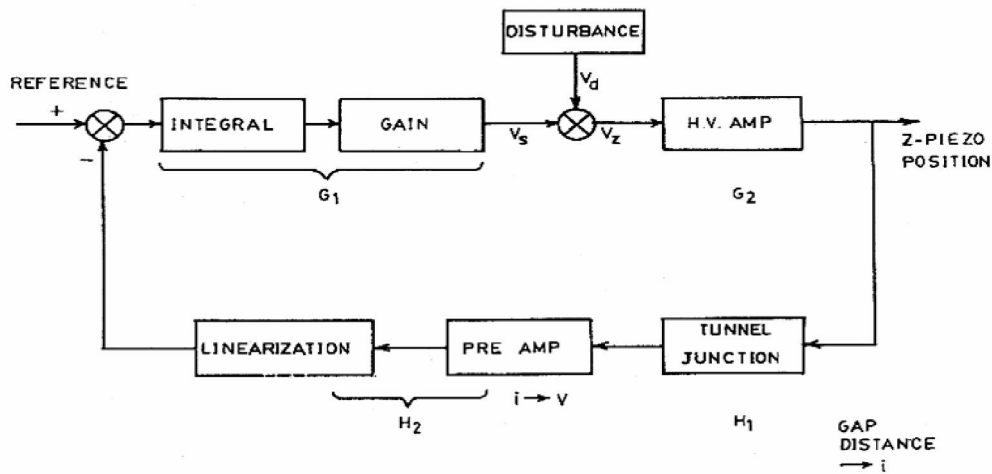


Figure 3.1: Block diagram of feedback controller network

The important and central part of a scanning tunneling microscope electronic system is the feedback controller network. For every system should be controlled system. In STM system, it is necessary that the Z piezo-electric element and tip-sample is in contact. The tunneling current is exponential function of tip-sample separation. The logarithmic amplifier is used to linearized the tunneling current. [1,5,13]

In figure 3.1, block diagram shows the control system in constant current scan the gap separation has set by comparing the tunneling current to the demanded current and has compensated by a negative feedback loop. Before designing feedback circuit, it is necessary to analyze it.[4,11,12].

The feedback circuit uses integrator. If V_i and V_o are the input and output of the integrator, R is the input variable resistance 500KΩ and C is the capacitance, 0.22 μf across the integrator, then the output of an integrator is given as

$$V_o = - \frac{1}{R C} \int V_i d t$$

The amplifier is adjusting the gain of the feedback circuit to match with piezo electric devices. The next circuit is summing amplifier, which allow the addition of external voltage to the control signal. The output of it has connected to high voltage amplifier, which is necessary in order to get larger movable range for the Z tip. The problem of perfect tuning of the controller to match to the system is common. Initially system has locked for required tunneling current. Therefore, error signal from differential amplifier is zero; which indicates Z control signal V_z is set. [15,19]

At time $t=0$ sec, the Z piezo is raised up or lowered by step input V_d , which simulates the disturbances created by scanning the STM tip laterally. The changing the tip-sample distance produces finite the error signal that makes the feedback operation to recover the initial V_z .

After the feedback loop stabilizes, all outputs from each stage have returned to the initial values before disturbances except V_s to the summing amplifier. [12] By simply monitoring the response of V_s to the disturbances V_d on an oscilloscope, we can easily adjust the loop gain.

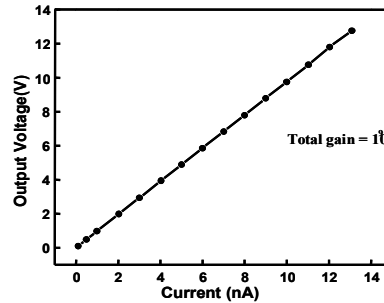


Figure-3.2 Graph of pre-amplifier

For Op-Amp, IC1, 3140, if $V_{in} < V_{ref}$, the negative feedback will move the tip in upward direction. It acts as buffer circuit. When V_{in} increases the output of IC1 is negative and if V_{in} decreases of IC1 is the output is positive. IC2 is integrator when $V_{in} < V_{ref}$, then output is positive. The output of integrator is negative. It is gain amplifier and no phase change in it. For IC3 output is negative. It has feed to IC4 and now its output is positive. IC5 is unity gain amplifier of gain 2. It is inverting amplifier and output is negative. [11]

IC6 removes the noise and output is negative. V_z is negative and tip moves in downward direction. Tunnel current increasing and now $V_{ref} = V_{in}$. Feedback controller is tested by changing V_{in} for fixed value of V_{ref} and Output is monitored.

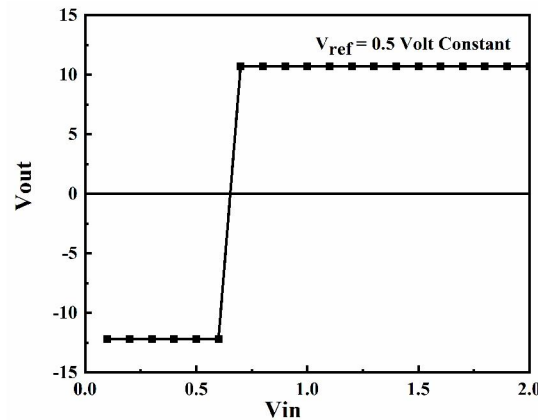


Figure- 3.2 Graph of V_{in} against $V_{o/p}$, for $V_{ref} = 0.5$ Volt Constant.

We have been able to obtain the stability region of an STM analytically using the all the possible element in feedback loop. We have use theoretical and mathematical model for each element of feedback loop and we have solve the problems by using logical and technical way. It is possible to achieve real condition of stability of loop. The parameter permits us to achieve the highly accurate and stable condition for imaging.

ACKNOWLEDGMENTS

This work was possible by the support of institutes like research center of Department of physics, Ahmednagar College, Ahmednagar and research center, Department of physics, New Arts, Commerce and science college, Parner, Ahmednagar. The author wants to thank for helpful discussion for this project.

REFERENCES

- [1]. Guoliang Ping and Michael A. Player, Meas. Sci. Technol. 4, 677(1993).

- [2]. Design of simple high –resolution scanning tunneling microscope with analogue scan Generator.- J.W. Gerritsen, E.J.C. Boon, G. Janssens, H. van Kempen. Research institute for materials, University of Nijmegen, Toernooiveld, 6525 ED Nijmegen, The Netherlands Received 25 July 1997.
- [3]. Zhixiong Cai, Xiaoru Wang, in Novel Nanomaterials for Biomedical, Environmental and Energy Applications, 2019
- [4]. D. Jeon and R.F. Willis, Rev.Sci.Instrument,62(6), 1650(1991).
- [5]. SCANNING ELECTRON MICROSCOPY ANALYSIS OF THE *CYATHOCLINE MANILALIANA* Jayesh T. Salve*1, Ashok R. Tuwar2, Sarala C. Tadavi3
- [6]. An STM Study of Metal Nanoclusters and Molecular Fragments on Graphene/Cu(111) ByEsin Soy, Ph.D Thesis, University of Illinois at Chicago, 2018
- [7]. Data acquisition and control system for molecule and atom-resolved tunneling spectroscopy ByE.I. Altman, D.P. Dilella, J.Ibe, K.Lee and R.j. Colton
- [8]. Optimal condition for imaging in scanning tunneling microscopy: Theory E. Anguiano, A.I. olive and M. Anuilar, instituto de Ciencia de Materiales, Campus UniversidadAutonoma, Madrid, Spain
- [9]. Scanning probe microscopy inthe age of machine learning- Md Ashiqur Rahman Laskar and Umberto Celano, School of Electrical, Computer and Energy Engineering, Arizona State University, Tempe, Arizona 85287, USA
- [10]. Scanning probe microscopyErnst Meyer, Roland Bennewitz, Hans J. Hug. ISSN 1868-4513
- [11]. Y. Kuk, P. J. Silvermn, Rev. Sci. Instrum. 60, 165 (1989)
- [12]. D.P. Dilella, J.H.Wandass, R.J. Colton and C.R.K. Marrian, Rev.Sci.Instrum.,60,997(1989).
- [13]. Dieter W.Pohl, IBM. J.Res. Develop. 30, 417 (1986).
- [14]. Grame, Jerald G, Design with operational Amplifiers-Applications Alternatives, McGraw-Hill, Pg. 14(18\997)
- [15]. D.Jeon and R.F.Willis, Rev. Sci.Instrum.,62(6),1650 (1991)
- [16]. Analysis of Scanning tunneling microscopy feedback system- A.I. Oliva,^{a)} E Anguiano, N. Denisenko, and M.Agullar, Institute de Clencia de materiales del C.S.I.C., campus de Universidad de madrid, C-III, 28049 Madrid, Spain. J.L. Pena, Centro de Investigacion y de Evanzadas del IPN, Unidad, A.P. 73-Cardemex, 97310, Merida(Yucatan), Mexico.
- [17]. A Data Acquisition and image Processing for Scaning Tunneling Microscopy H. FUCHS, W EUSTACHI, R. SEIFERT,BASFAktiengesellschaft, Kunststofflaboratorium, D-6700 Ludwigshafen, Federal, Federal Republic of Germany.
- [18]. Scanning Tunneling Microscopy- JIN-FENGJIA, WEI-SHENG YANG, AND QI-KUN XUE
- [19]. Scanning Tunneling microscope Computer Automation- IBM T.J. Watson Research Center, P.O. Box 218, Yorktown heights, N Y 10598, USA.

Design and Simulation of 4 bit- Successive Approximation ADC

Suraj P. Gaikwad

Assistant Professor, Department of Computer Science, New Arts Commerce and Science

College Parner 414302, Ahmednagar, Maharashtra, India

Abstract: The digital signal is easy to process than the analog circuits. The design of digital circuits is less complex than the analog circuit. The digital circuit is cheap, robust, stable, less affected by noise and more accurate than analog circuit. The analog to digital converter is bridge between digital and analog. The biomedical and industrial sensor requires powerful analog to digital converter which consume less energy and high speed of operation.

In this paper, the four-bit successive approximation ADC is designed which consumes less power with high precision. The converter consists of SAR (Successive Approximation Register), Weighted Register Digital to analog converter and comparator. The simulation of the circuit is implemented and tested into proteus software.

Keywords: Analog to Digital Converter, Successive Approximation Register, simulation.

I. INTRODUCTION

Successive Approximation type ADC is the most widely used and popular ADC method. The successive approximation ADC used in biomedical, industrial circuits, Voltmeters, ammeters, multimeter etc.

The successive approximation ADC is used to approximate the given analog input with higher accuracy, low power and in less time. ADC plays an important role where there is need of increasing digital components these demand increases in industrial equipment's, biomedical and sensors which demand low power consumption, accurate and more life. The technologies like VLSI make the device compact. The ADC is used where the accuracy is needed. The accuracy of the ADC depends upon the resolution. While the error of the ADC varies on its linearity. ADC plays in important role where accuracy is needed. The most popular ADC is the flash ADC but it consumes much power because of the many comparators.

II. LITERATURE REVIEW

ADC plays an important role in many processing circuits. In all the different types the Successive Approximation ADC is used where the low power, high resolution is required. The recent development in the field of CMOS ADC decreases the power consumption and increase the efficiency. The ADC have accurate for low to medium resolution. In some research time complexity is decreased based on the design. The capacitance plays important role for deciding the time complexity and power consumption. The number of capacitance decrease switching and power consumption.

In this proposed paper the time and power consumption by the design so it can solve the problem based on the need of the biomedical devices.

Architecture:

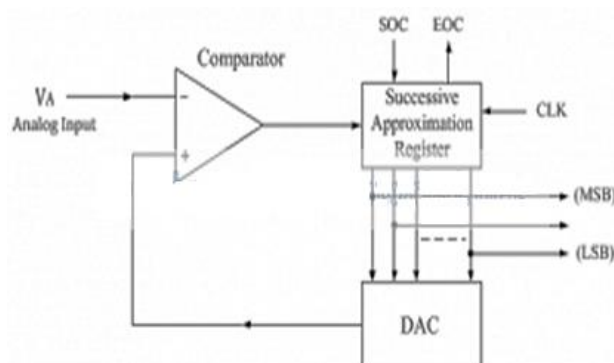
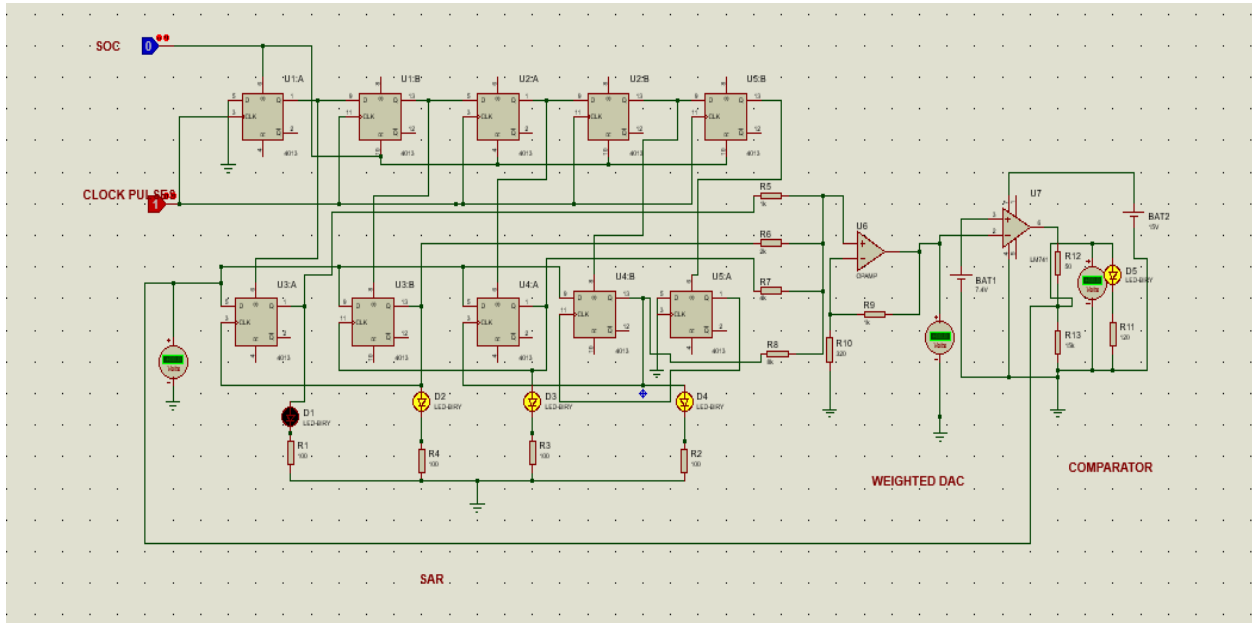


Fig: Typical Block of DAC



When the start command is applied, the SAR sets the MSB to logic 1 and other bits are made logic 0, so that the trial code becomes 1000.

This type of ADC operates by successively dividing the voltage range by half, as explained in the following steps.

- (1) The MSB is initially set to 1 with the remaining three bits set as 0000. The digital equivalent voltage is compared with the unknown analog input voltage.
- (2) If the analog input voltage is higher than the digital equivalent voltage, the MSB is retained as 1 and the second MSB is set to 1. Otherwise, the MSB is set to 0 and the second MSB is set to 1. Comparison is made as given in step (1) to decide whether to retain or reset the second MSB.

The above steps are more accurately illustrated with the help of an example.

Let us assume that the 4-bit ADC is used and the analog input voltage is $V_A = 11\text{ V}$. when the conversion starts, the MSB bit is set to 1.

$$\text{Now } V_A = 11\text{V} > V_D = 8\text{V} = [1000]_2$$

Since the unknown analog input voltage V_A is higher than the equivalent digital voltage V_D , as discussed in step (2), the MSB is retained as 1 and the next MSB bit is set to 1 as follows

$$V_D = 12\text{V} = [1100]_2$$

$$\text{Now } V_A = 11\text{V} < V_D = 12\text{V} = [1100]_2$$

Here now, the unknown analog input voltage V_A is lower than the equivalent digital voltage V_D . As discussed in step (2), the second MSB is set to 0 and next MSB set to 1 as

$$V_D = 10\text{V} = [1010]_2$$

$$\text{Now again } V_A = 11\text{V} > V_D = 10\text{V} = [1010]_2$$

Again, as discussed in step (2) $V_A > V_D$, hence the third MSB is retained to 1 and the last bit is set to 1. The new code word is

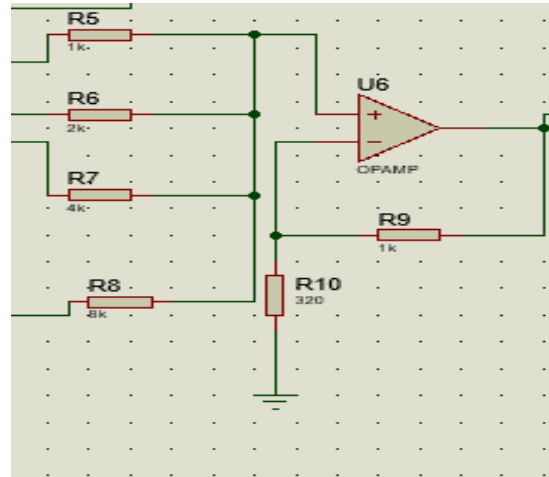
$$V_D = 11\text{V} = [1011]_2$$

$$\text{Now finally } V_A = V_D, \text{ and the conversion stops.}$$

Hardware

1) WEIGHTED DAC:

A weighted DAC produces an analog output, which is almost equal to the digital input by using binary weighted resistor in non-inverting adder circuit. The resistor 1k, 2k, 4k and 8k is given to the non-inverting input of the op-amp whereas the feedback resistor is connected to the inverting input.



Since the number of inputs is four in the binary input, we will get sixteen possible value of output voltage by varying the binary input 0000 to 1111 for a fixed reference voltage V_R . Output of DAC is applied to the inverting input of the comparator.

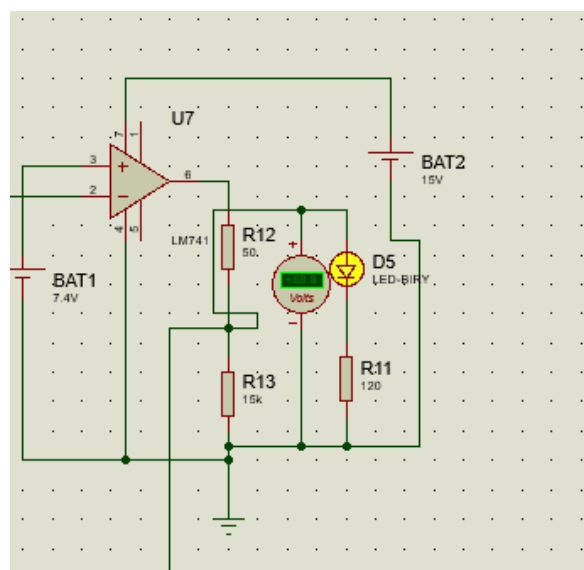
2) Comparator:

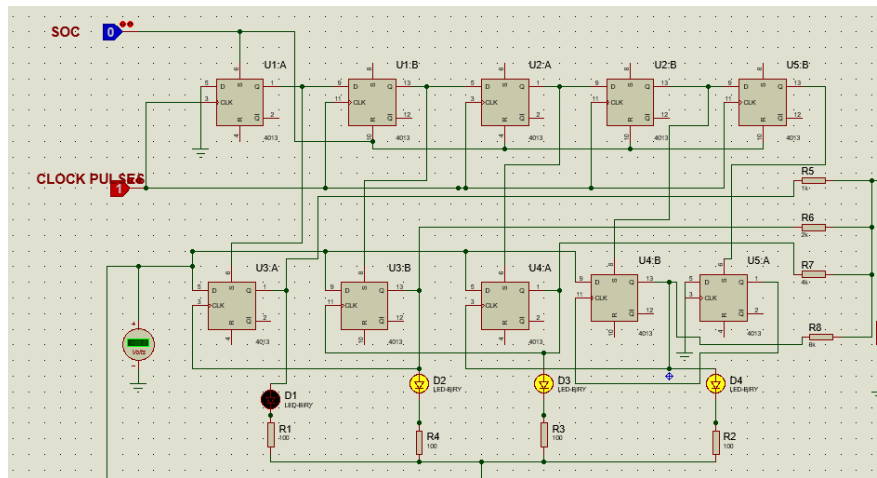
Comparator compare the the two inputs voltage and output a binary signal indicating which is larger.

If the non-inverting input is grater than the inverting input, the output goes high. If the inverting input is grater than the non-inverting the output goes low.

Due to high open loop gain, the output of the comparator is +Vcc or -Vcc.

The voltage comparator is 1 bit analog to digital converter as the input signal is analogue but the output behaves digitally. The output of the comparator is connected to the SAR.



3) SAR (Successive approximation ADC)

SAR consist of ring counter which is divided into control logic and comparator. The SAR consists of D flip flops. Control logic is depended upon the output from the comparator. According to the output of the comparator, the shift register decides whether to shift the output of the ring counter. The SAR works on asynchronous clock. As the output from the previous flip flop act clock input to the next flip flop. This method was proposed by Anderson. The SAR starts by the SOC (start of the conversion). The output of the SAR is given to the input of DAC. The circuit is reset by the reset input. The circuit works like binary search. One can add more shift register to the circuit and extend the circuit to implement the algorithm. The increase in shift register increases the power consumption and propagation delay. The clock is given manually but it can be processed using the clock generator.

III. CONCLUSION

SAR ADC is the most efficient ADC, this is because of its Power Efficiency, Complexity, Conversion rate which is better than the flash ADC, single and dual slope ADC. This paper gives architecture of the ADC which is Comparator, DAC and SAR. Along with the binary search algorithm, the parameter like offset error, gain error, parasitic effect, jitter and management all these considered while designing the circuit. It is observed that the ADC have conversion time of less than 100 micro sec with less power consumption.

REFERENCES

- [1] C. Liu, S. Chang, G. Huang and Y. Lin, "A 10-bit 50-MS/s SAR ADC With a Monotonic Capacitor Switching Procedure," in *IEEE Journal of Solid-State Circuits*, vol. 45, no. 4, pp. 731-740, April 2010, doi: 10.1109/JSSC.2010.2042254.
- [2] V. Hariprasath, J. Guerber, S. -. Lee and U. -. Moon, "Merged capacitor switching based SAR ADC with highest switching energy-efficiency," in *Electronics Letters*, vol. 46, no. 9, pp. 620-621, 29 April 2010, doi: 10.1049/el.2010.0706.
- [3] S. Mortezaipoor and E. K. F. Lee, "A 1-V, 8-bit successive approximation ADC in standard CMOS process," in *IEEE Journal of Solid-State Circuits*, vol. 35, no. 4, pp. 642-646, April 2000, doi: 10.1109/4.839925.
- [4] H. Sepehrian, M. Saberi and R. Lotfi, "A signal-specific successive-approximation analog-to-digital converter," 2011 *IEEE International Symposium of Circuits and Systems (ISCAS)*, Rio de Janeiro, 2011, pp. 1624-1627, doi: 10.1109/ISCAS.2011.5937890.
- [5] J. Yang, T. L. Naing and R. W. Brodersen, "A 1 GS/s 6 Bit 6.7 mW Successive Approximation ADC Using Asynchronous Processing," in *IEEE Journal of Solid-State Circuits*, vol. 45, no. 8, pp. 1469-1478, Aug. 2010, doi: 10.1109/JSSC.2010.2048139.

Secure Home Door Bell using Python and Raspberry Pi

S. P. Gaikwad

Assistant Professor, Department of Computer Science, New Arts Commerce and Science College, Parner (MH)

Abstract:

Security is the main concern in the current world. Recently there are many security systems are developed for securing Home, offices and Personal Properties. The security system includes camera, fingerprint identification, RFID and sensors. In all this security system camera face recognition system is most common, it takes less time for implementation and installation.

In this work, a system is implemented that recognise the family members of the home by face recognition and rang a simple bell. Whereas when the unknown person detected by the system then the system rang a different bell and shows the face in the system display. The system also send email to the home owner. The process is performed automatically without human help. In this system, the raspberry microcontroller installed with Open CV & Face recognition library, the raspberry pi camera module is connected for face recognition and bell is connected to Raspberry microcontroller. The data of the persons is stored in the memory card which is connected to the Raspberry Pi. The result shows that it feels secure while opening the door for the persons and alerts home owner.

Keyword: face recognition, Open CV, Bell, E-mail

Date of Submission: 12-03-2023

Date of Acceptance: 26-03-2023

I. Introduction:

The current system rang different bell works on face detection and identification. Generally, the door is opened by looking through door hole but it is quite risky. Hence it is necessary to develop such system that identify the difference between the family members and the unknown person. This system also sends the email to the home owner so any accidental situation happened then it helps for investigation. The Raspberry Pi uses Open command Visualization (Open-CV) and the Face recognition library in used in which Source code is open and which is used for image processing. The main aim of this system is to feel free and secure for the door Opener.

II. Literature Survey:

Many Companies providing the home security system that includes various sensor network, network devices and it automatically increases the cost and Power requirement. These system takes more time for installation.

The face detection has been implemented using a method called Histogram of Oriented Gradients.

The Existing system using smart doorbell using raspberry pi send SMS and Email notification to the person in the home.

The existing system of IOT based smart doorbell send video call when someone presses the door bell as well as send an SMS.

In above systems the internet to be continuously on but current system works well without internet.

Hardware Description

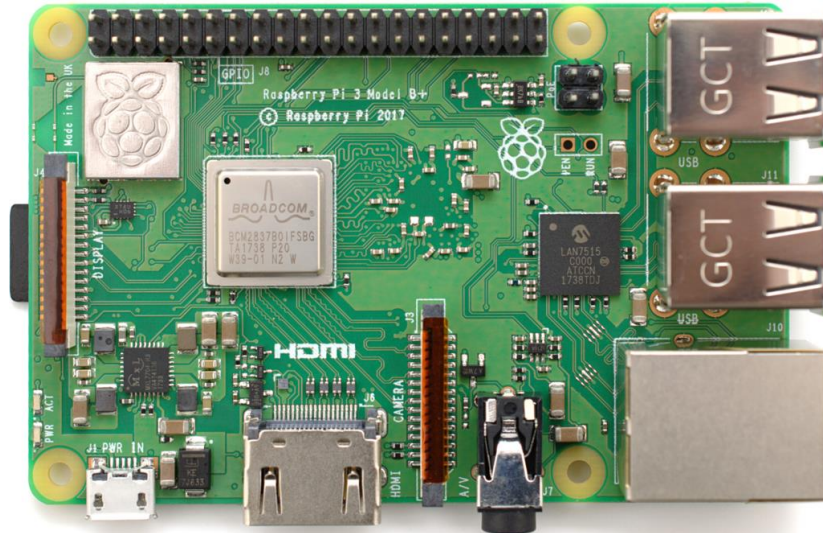
The hardware of the current system is basically consisting of Raspberry pi, Camera module, bell, network device (switch).

Raspberry pi board:

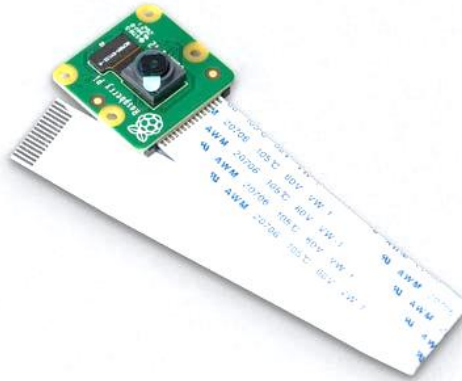
The raspberry pi 3 accept the input from the camera, then raspberry pi identifies the person and sending the signal to bell and send the email to the home owner through the switch.

Specification of Raspberry Pi:

- 1) Broadcom BCM2837 64bit Quad Core Processor 1.2 GHz
- 2) RAM: 1Gbytes DDR2
- 3) Bluetooth: 4.1 LE
- 4) WIFI



Camera Module:



face detected by using of the camera module. It is Raspberry Pi Camera Module with Automatic IR-Cut Night Vision Camera 5MP 1080p HD Webcam for Raspberry Pi 3 Model. It's easily affordable to any inventor for camera projects.

Software Description:

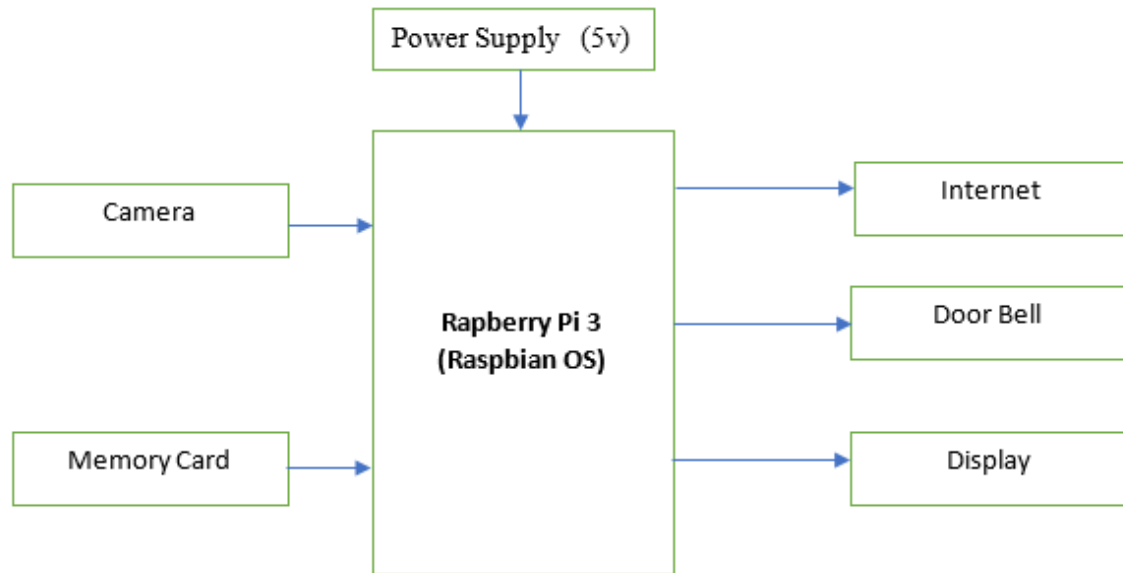
Write the code for the hardware it's required a Linux terminal.

The capture image, its recognition all command written in the Linux terminal. Linux command is:

- Sudo apt-get update = to update the raspberry pi 4.
- Cd /home/pi/Desktop = To use the open file its located on the desktop.
- Sudo apt-get install rpi.gpio = To install a require library for the GPIO pin.
- sudo apt install python3-opencv
- pip3 install face_recognition
- Python face.py = To run the source code.

Proposed Model

The Proposed system is used for home security by using face detection and bell. The system block diagram consists of Camera module attached to the raspberry pi3 and it is placed at the entry of the home. Camera is used to detect the face of the person next to the door.

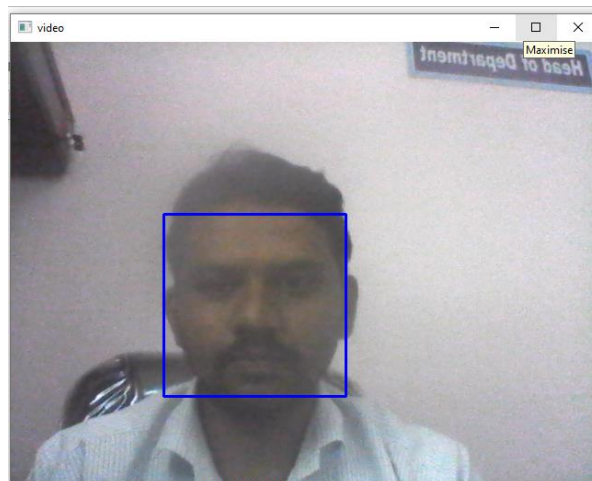


The face of the person is recognized and compare with the face of the family which is stored in the databases through library file present in the Open CV and face recognition. Face recognition is simple and effective method.

The process of face recognition and bell as follows

1) Image from Camera:

The camera is installed in the area where people enter through door. The camera collects the images as well as video from the camera. The collected images is used for face recognition.



2) Creating and verifying the image in the databases:

The image of family member with name is stored in the databases. The database contains the five to six sample of images of each family members with different lightning situation.

3) Detecting faces:

There is different algorithm is present in the Open CV library Here we have to detect the face in real time so Haar cascade Algorithm is used because it is Robust.

4) Face Recognition:

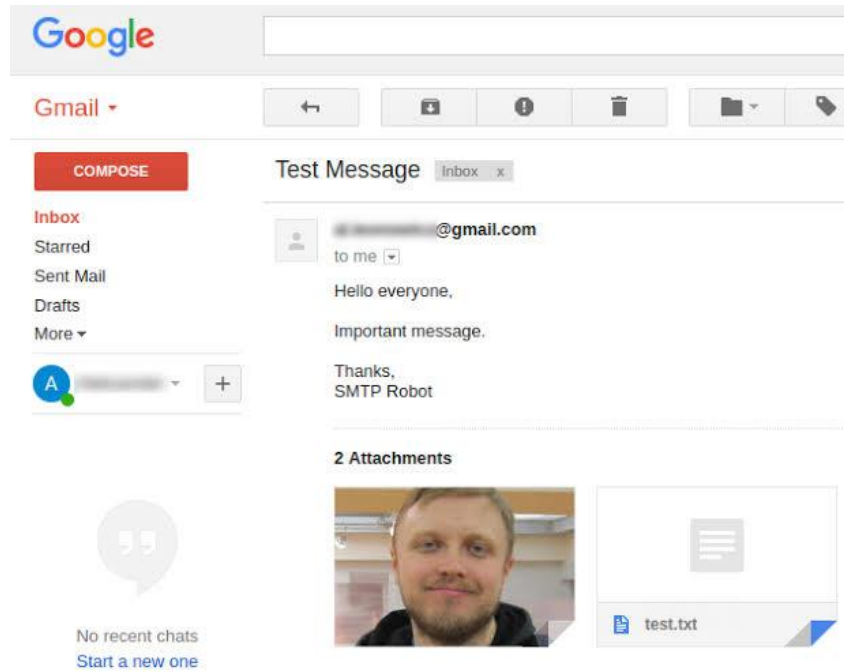
The detected face is compared with the images stored in the databases. The accuracy of image detection is increased by comparing with 30-40 images. The distance from camera to face is also critical while recognition and it is found that ideal distance is 2-6 meters.

5) Bell:

After the face is detected if the person is family member, then Raspberry Pi send the signal to the bell to sound for simple bell and if the person detected is unknown then bell rang differently to indicate new person.

6) Email:

If the identified person is unknown then Raspberry pi send the email to the house owner which helps for security and in accidental situation.



III. Conclusion:

Secure Home Bell system proves the system is robust, safe, cheap, accurate and easy to install. In real time Scenario, the haar cascade algorithm is suitable for work.

Raspberry Pi improves the mobility of the setup and debugging. The work can be improved by night vision camera and HD camera.

References:

- [1]. Ruian Liu Mimi Zhang Shengtao Ma, "Design of Face Detection and Tracking System", 2010 IEEE 3rd International Congress on Image and Signal Processing.
- [2]. Rafael C. Gonzalez. 2009. Digital Image Processing. Pearson Education India.
- [3]. Yi-Qing Wang. 2014. An Analysis of the Viola-Jones Face Detection Algorithm. Image Processing on Line. 4: 128-148.
- [4]. Harshal V. Khodaskar, Shashank Mane "Human Face Detection & Recognition Using Raspberry Pi" International Journal of Advanced Engineering, Management and Science ISSN: 2454-1311.
- [5]. Shrutika V. Deshmukh, Prof Dr. U. A. Kshirsagar "Face Detection and Face Recognition Using Raspberry Pi", International Journal of Advanced Research in Computer and Communication Engineering, Vol. 6, Issue 4, April 2017



Sol-gel assisted β -cyclodextrin coated $\text{MoO}_3\text{-Fe}_2\text{O}_3$ nanocomposite for photodegradation of methylene blue dye

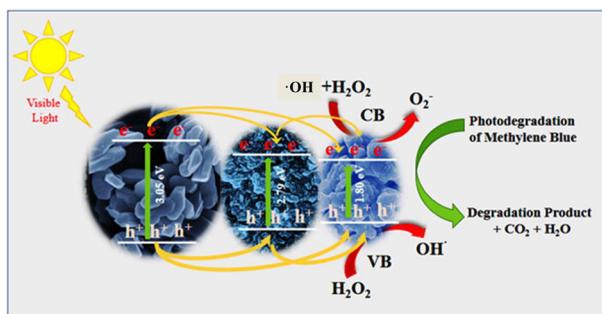
Akash Nagare¹ · Amol Dhadage¹ · Mallesham Baithy² · Priyanga Manjuri Bhuyan³ · Parikshit Gogoi³ · Anil Athare¹ · Madhukar Navgire⁴

Received: 2 January 2024 / Accepted: 28 February 2024 / Published online: 11 March 2024
© The Author(s), under exclusive licence to Springer Science+Business Media, LLC, part of Springer Nature 2024

Abstract

In this work, a series of β -Cyclodextrin coated $\text{MoO}_3\text{-Fe}_2\text{O}_3$ nanocomposites were synthesized by the sol-gel technique for degradation of methylene blue in presence of light from aqueous solutions. The prepared materials were analyzed by using powder XRD, FT-IR, UV-DRS, FE-SEM, HR-TEM, RAMAN, BET, and XPS techniques. The X-ray diffraction spectra of β -CD coated MoO_3 -doped Fe_2O_3 confirms the orthorhombic phase of the $\text{Fe}_2(\text{MoO}_4)_3$ nanocomposite. The allowed indirect transition optical energy band gap of nanocomposites lies between 2.67 and 1.71 eV. The FE-SEM study revealed that nanoflakes change in the morphology of the nanocomposites sample, and it gives an estimated size below 30 nm. The 10 mg L^{-1} methylene dye degrades efficiently around 91.62% within 1 h. with reaction condition of 15 mg 5% β -Cyclodextrin coated $\text{MoO}_3\text{-Fe}_2\text{O}_3$ catalyst, 6 pH, 10 mM concentration of H_2O_2 , at room temperature under sunlight. The pure MoO_3 and Fe_2O_3 gives 38.21% and 77.10%, shows less activity compare with 5 β MF catalyst. This study provides newer catalytic system which shows better photocatalytic degradation of dyes from industrial waste water.

Graphical Abstract



Keywords β -Cyclodextrin · Methylene Blue · Nanocomposites · Oxidation · Photodegradation

✉ Madhukar Navgire
navgireme@gmail.com

¹ New Arts, Commerce and Science College,
Ahmednagar, Maharashtra 414001, India

² Department of Chemistry, School of Science, Gandhi Institute of
Technology and Management (GITAM) University,

Hyderabad, Telangana 502329, India

³ Department of Chemistry, Nowgong College (Autonomous),
Nagaon, Assam 782001, India

⁴ Jijamata College of Science and Arts, Bhende Bk., Maharashtra
414605, India

Highlight

- The β -Cyclodextrin coated $\text{MoO}_3\text{-Fe}_2\text{O}_3$ nanocomposites was successfully prepared by using the cost effective sol-gel technique.
- The efficiency of nanocomposites was improve using β -Cyclodextrin which gives more active sites and fast charge carrier separation.
- The reaction successfully carried outstanding efficiency of 5 β MF for the degradation of methylene blue.
- Its result gives 91.62% degradation of MB in short reaction time as compare to the other nanocomposites samples.
- It concludes that, efficiency of photocatalyst increases with the loading of MoO_3 on Fe_2O_3 . This 5 β MF catalyst shows better activities within short duration, use of less quantity of catalyst and in works in visible light region.

1 Introduction

William Henry Perkin discovered dye mauveine in the 19th century. After that, as rapid industrialization increases, the use of dyes also increases. All over the world, up to 800,000 tons of dyes are produced and used each year [1]. There are many industries like cloths, paints, carpets, leather, food, printing, and paper that release hazardous dyes directly into the environment [2, 3]. These releases of pollutants into water bodies affect human health. Dyes cause so many hazardous effects on the human body, like skin damage, hypertension, anemia, and vomiting [4]. Methylene blue, a cationic dye with carcinogenic properties, also causes nausea and hyperhidrosis due to direct contact and is used in many industries. Therefore, the removal of this organic pollutant from waste water is a major issue worldwide [5–7].

There are many techniques used to degrade these organic pollutants in wastewater treatment: adsorption techniques, advanced oxidation processes (AOP), ion exchange, coagulation, and membrane processes are some of them [8]. Adsorption and coagulation techniques have some limitations, such as the use of much more amounts of chemicals. Also, the membrane process has an expensive technique that requires a high cost [9, 10]. Photodegradation is one of the advanced oxidation processes (AOP's) that is useful for the removal of organic pollutants from wastewater because it is a simple, easy, and non-toxic technique. The availability of sunlight also makes this technique clean and requires a low cost [11–13].

Transition metal oxide, like MoO_3 , is a n-type of semi-conducting material that attracts researchers because of its properties like being highly stable, cost-efficient, and non-toxic [14]. MoO_3 has a large band gap range of 2.5–3.2 eV. MoO_3 is used in various applications as a catalyst, superconductor, gas sensor, energy storage, solid lubricant, and photocatalyst. It has the exclusive property to act as a photocatalyst in a wide range of ultraviolet to visible light [15]. Molybdenum oxide has some polymorphs, which are orthorhombic (α - MoO_3), monoclinic (β - MoO_3), and hexagonal (β - MoO_3) [16]. Also, it has some boundaries: limited electrical conductivity, low quantum yield, low visible light absorptivity, and low reduction capacity. Therefore, it was less active in the

ultraviolet and visible regions as a photocatalyst, so the reconstruction of the photocatalyst is a must [17].

Iron oxide nanoparticles are applied in many areas, like catalysts, sensors, biodiagnosis, biomedication, and also as photocatalysts [18]. Iron oxide has three main types, which are as follows: hematite (α - Fe_2O_3), maghemite (γ - Fe_2O_3), and magnetite (Fe_3O_4) [19, 20]. Due to their properties such as chemical and biological stability, large surface area, non-toxicity, low cost, and paramagnetic nature, iron oxide nanoparticles are efficient to use [21, 22]. But, due to the various types of limitations of a single iron oxide, including its low light absorption coefficient, higher band gap, and fast recombination (e-h) pair rate, it is not suitable for photocatalytic activity under visible light [23].

Further, the properties of a single metal oxide material are effectively influenced by the various types of doping, coating, substituting, and composites of nanoparticles. Doping refers to the addition of impurities to a material's structure in order to modify its properties and improve its activity for a particular application [24, 25]. It is the new way to enhance photocatalytic performance to degrade harmful organic pollutants. Thakur et al. [26] modify polyvinylpyrrolidone and *Tinospora Cordifolia* in dual (Co-Cu) doped TiO_2 nanoparticles to remove organic water pollutants methyl orange and methylene blue under ultraviolet irradiation.

Many researchers show that the doping of other metal oxides increases defects like O_2 vacancy, which improves the efficiency of nanocomposite as compared with pure Fe_2O_3 under visible light irradiation [27–29]. Literature study gives information about work reported on degradation of dyes from industrial waste water, but some catalyst were active in UV light, or time required is more. Recently our research group was reported similar work on Fe-oxide framework using β -cyclodextrin and its application as a Fenton catalyst for degradation of some pollutant [30–35]. But there is very less or no work reported on doping of MoO_3 on Fe_2O_3 which may works as a photocatalyst under sunlight.

Here we first time reported the removal of organic pollutants from industrial waste water using MoO_3 doped on Fe_2O_3 under sunlight irradiation. In this work, we synthesized a series of mesoporous nanocomposite β -cyclodextrin coated $\text{MoO}_3\text{-Fe}_2\text{O}_3$ by varying molybdenum contents. The

photodegradation of methylene blue (MB) under direct sunlight has been successfully tested by using prepared nanocomposites. The impact on the photodegradation reaction of various parameters like the effect of various photocatalyst, the initial amount of photocatalyst, the concentration of H_2O_2 , the initial amount of dye concentration, and the effect of pH are also studied. It provides an efficient and environmentally friendly way to degrade organic dyes pollutant from waste water.

2 Experimental section

2.1 Chemicals and reagents

The chemicals used for the synthesis of pure MoO_3 , pure Fe_2O_3 , and β -cyclodextrin coated $\text{MoO}_3\text{-Fe}_2\text{O}_3$ nanocomposite, including specifications and grades stated by Chemo Equip Corporation, Sangamner, Maharashtra, India (Supplementary Table S1). All chemicals purchased were analytical grade and used without further purification; the solutions were made by dissolving in double-distilled water (DDW).

2.2 Synthesis of pure Fe_2O_3 and pure MoO_3

The pure Fe_2O_3 nanocomposite was synthesized with precursor amounts of ferrous (II) sulfate heptahydrate (1.20 g) and ferric (III) sulfate hexahydrate (1.72 g), respectively. After dissolving all of the above precursors in 120 mL of double-distilled water, CTAB (0.2 g) and PVA (0.2 g) were added to the mixture until a sol was produced. Aqueous ammonia solution (10 mL) was added dropwise while being constantly stirred to produce the gel. After three time washings with DDW the resultant precipitate and mother liquors were analyzed for presence of ammonium and sulfate ions. Subsequently, it was then heated at 70–80 °C to evaporate any remaining water with constant stirring for 3 h. After that, it was oven-dried at 110 °C for 2 h. The solid product was crushed finely and then calcined at 500 °C for 3 h in an open-air muffle furnace. Finally it gives 5.8 gm (95%) pure Fe_2O_3 nanocomposite. By using the similar path, we prepared pure MoO_3 nanocomposites where starting material ammonium heptamolybdate tetrahydrate (8.58 g) was taken as precursor. Finally we were obtaining 3.33 gm of pure MoO_3 nanocomposite material.

2.3 Synthesis of β -cyclodextrin coated $\text{MoO}_3\text{-Fe}_2\text{O}_3$ nanocomposite

We synthesized a series of β -Cyclodextrin coated 1% $\text{MoO}_3\text{-Fe}_2\text{O}_3$, 5% $\text{MoO}_3\text{-Fe}_2\text{O}_3$, 10% $\text{MoO}_3\text{-Fe}_2\text{O}_3$, 15% $\text{MoO}_3\text{-Fe}_2\text{O}_3$, and 20% $\text{MoO}_3\text{-Fe}_2\text{O}_3$ nanocomposites catalysts with the help of the conventional standard sol-gel method, which is

named as 1 β MF, 5 β MF, 10 β MF, 15 β MF, and 20 β MF, respectively. Typically, in the synthesis of 1 β MF, the requisite quantities of ammonium heptamolybdate tetrahydrate (0.4293 g), ferrous (II) sulfate heptahydrate (5.9429 g), and ferric (III) sulfate hexahydrate (8.5475 g) precursors were dissolving in 120 mL of DDW under constant stirring conditions. Further, β -CD (0.2 g), CTAB (0.2 g), and PVA (0.2 g) were added to the following mixture until a viscous sol was formed. It was then immersed in water, and a dropwise addition of aqueous ammonia solution (10 mL) with continuous stirring to form gel. The obtained precipitate was washed with DDW several times and mother liquors were tested for presence of sulfate ions as well as ammonium ions. The gel is subsequently heated at 70–80 °C to eliminate excess water with constant stirring for 3 h then oven-dried at 110 °C for 2 h. Finally, the resulting solid product was finely crushed and calcined at 500 °C for 3 h in an open-air atmosphere in muffle furnace. The same procedures were followed for the synthesis of series of 5, 10, 15, and 20 wt% by changing the requisite amount of ammonium heptamolybdate tetrahydrate. The practical % yield was varies from 5.79 to 5.31 gm (91 to 95%) for series of nanocomposite respectively. Furthermore, Supplementary Fig. S1 provides a schematic representation of the nanocomposite formation process.

2.4 Characterization techniques

By using various analytical techniques, the synthesized materials were characterized to find out some important information, such as crystalline size, surface structure, morphology, particle size, etc.

The X-Ray Diffraction (XRD) analysis of the synthesized nanocomposites is recorded on a powder X-ray diffractometer (Rigacu MiniFlex 600) using the radiation source Cu $K\alpha$ with $\lambda = 0.154$ nm and a scanning range between angle 2θ (°) = 20–80. Fourier Transform Infra-red Spectroscopy (FT-IR) of the prepared nanocomposite was analyzed by PerkinElmer (Spectrum 2) using a diamond ATR in the region between 4000 to 450 cm^{-1} . The UV-Visible Diffused Reflectance Spectra (UV-DRS) of the nanocomposites were measured using a Lab India UV-Vis spectrophotometer (UV 3092) in the wavelength range of 200–800 nm. Raman spectral analysis of the photocatalyst was done by a Renishaw Raman analyzer with a scanning wavelength of 1500–100 cm^{-1} . The morphological study of the prepared nanocomposite was done by High Resolution Transmission Electron Microscopy and Field Emission Scanning Electron Microscopy (FE-SEM), supported by FEI Nova (Nano SEM 450) with ultra-high resolution. The surface area of the nanocomposites was measured by Brunauer-Emmett-Teller (BET) using the Microtrac MRB BELSORP MAX II instrument. X-ray Photoelectron Spectrum (XPS) was recorded by the Thermo Scientific NEXA Surface Analyzer

using a monochromatic Al K α X-ray source. Similarly, photocatalytic activity applications of synthesized catalytic material were carried out in a dye degradation experiment monitored through a Systronics UV-Vis spectrophotometer (Double Beam UV-VIS Spectrophotometer AU 2790).

2.5 Photocatalytic activity study

The catalytic activity of prepared β MF nanocomposites materials was examined by photodegradation of Methylene blue (MB) dyes in the presence of sunlight at room temperature. The activity performed in between 11.00 am to 3.00 pm day time. The dye degradation experiment was performed using a series of catalysts (15–35 mg) dispersed in 50 ml of MB dye solution (10–20 mgL⁻¹). To achieve an adsorption-desorption equilibrium, these mixtures were vigorously stirred for 30 min in a dark environment. After completing 30 minutes in the above solution, the addition of H₂O₂ (5–15 mM) took place. The pH of solutions was adjusted by adding dilute hydrochloric acid or a diluted sodium hydroxide solution. During the experiment, the various reaction parameters, including catalyst amount, concentration of MB dye solution, H₂O₂ concentration, and the impact of pH were optimized.

For the monitoring of the photodegradation reaction process, 3 ml of the reaction mixture were taken off during a 10 min time interval. The catalysts were removed by centrifuging the solution and then using an external magnet. The resultant clear dye solution was then examined using a UV-Vis spectrophotometer at $\lambda_{\text{max}} = 660$ nm for MB. The percent dye degradation efficiency of the catalyst is expressed by the equation...

$$\text{Degradation efficiency of catalyst(\%)} = \frac{C_0 - C_t}{C_0} \times 100 \quad (1)$$

Where C₀ stands the initial concentration of dye (mgL⁻¹) and C_t stands the concentration of dye remaining at time (t) (mgL⁻¹).

2.6 Turnover number (TON) and turnover frequency (TOF)

In catalysis, the turnover number and turnover frequency are states that describe a catalyst's efficiency and activity. The turnover number represents the number of substrate molecules that can be transformed into products by a single catalyst molecule during its lifetime. TON indicates the catalytic efficiency of a catalyst and how many times it can facilitate a reaction before becoming deactivated or consumed.

$$\text{Turnover number (TON)} = \frac{\text{No. of moles of MB degraded}}{\text{No. of moles of catalyst taken}}$$

Turnover frequency represents the number of catalytic cycles that go through via a single active site per unit time in the catalyst. It is a measure of the catalytic activity of the catalyst and describes how quickly it can convert substrates into products.

$$\text{Turnover frequency(TOF)} = \frac{\text{Turnover number}}{\text{Time (min)}}$$

TOF is usually expressed in units of moles of substrate converted per minute. It indicates the rate at which the catalyst can perform the catalytic reaction.

Both TON and TOF are essential parameters in evaluating and comparing different catalysts. A catalyst with a higher TON and TOF is more efficient and active. It indicates the ability to convert more substrate molecules into products in a shorter time. Here we check TON and TOF of our synthesized catalyst.

3 Results and discussion

3.1 X-ray diffraction spectroscopy (XRD) analysis

XRD of pure MoO₃ shows a very sharp peak was observed at 2 θ (°) values of 23.3, 25.8, 27.3, 33.7, 38.9, 46.3, 49.2, 52.7, which is corresponding to (110), (120), (021), (111), (060), (061), (002), (080). All planes of the MoO₃ exactly match the orthorhombic crystal structure of the JCPDS card no. 76-1003 [36] as shown in Fig. 1a. Similarly, Fig. 1b shows that the XRD pattern of pure Fe₂O₃ gives peaks at 2 θ (°) values of 20.7, 21.5, 24.8, 29.8, 32.5, 36.9, 37.5, 50.6, 53.6, 63.0 that are attributed to the planes of (114), (201), (212), (215), (118), (305), (1 0 10), (2 2 11), (2 1 13), (4 0 12), which indicate the tetragonal phase (Fe₂O₃) of all species exactly match with JCPDS card 76-1470 [37]. Figure 1c–f shows the XRD peaks of a series of β -CD coated MoO₃-doped Fe₂O₃ nanocomposite materials. It shows an intense peak at 2 θ (°) values of 22.3, 23.5, 28.0, 34.7, and 53.7, corresponding to the planes (112), (202), (122), (023), and (152) that match the orthorhombic structure of Fe₂(MoO₄)₃ with JCPDS card 85-2287 [38].

Figure 1c–f, it was observed that the peak at a 2 θ (°) value of 23.50 for the (110) plane is mainly due to the presence of MoO₃ in all of the prepared samples. It indicates the gradual increases in peak intensity with increasing Mo-loading. It was observed that proper MoO₃ was doped into the Fe oxide, which exhibited the crystalline nature of the composite material. However, the intensity of the peaks at 24.8 and 32.5 (°) for Fe₂O₃ also decreases as it clearly shifts to the lower angle with the addition of MoO₃. It indicates occupying the vacant space, which is available in Fe₂O₃ material by MoO₃.

The crystallite sizes of nanocomposite samples have been estimated using the Debye-Scherrer equation, and the

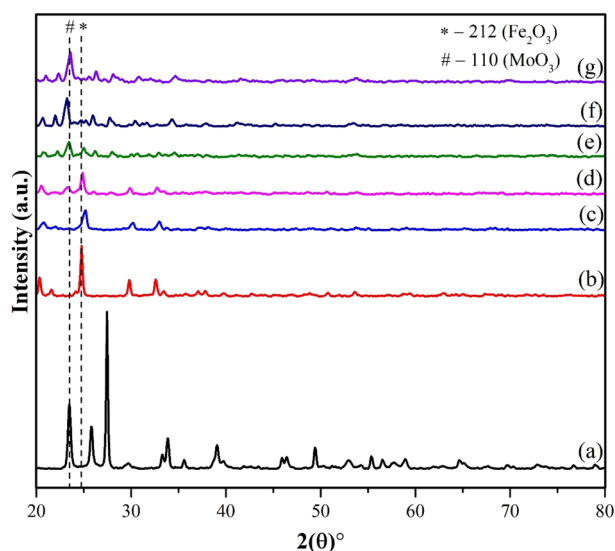


Fig. 1 XRD of **a** Pure MoO₃, **b** Pure Fe₂O₃, **c** 1βMF, **d** 5βMF, **e** 10βMF, **f** 15βMF, **g** 20βMF

Table 1 The various physicochemical properties of β-CD coated MoO₃ doped Fe₂O₃ material

Entry	Sample	2 Theta (°)	Crystallite size (nm)
1	MoO ₃	27.3	39.44
2	Fe ₂ O ₃	24.8	32.98
3	1βMF	23.5	11.35
4	5βMF	23.5	11.78
5	10βMF	23.5	14.93
6	15βMF	23.5	17.33
7	20βMF	23.5	15.72

results are shown in Table 1 [39, 40].

$$D = \frac{0.9\lambda}{\beta \cos \theta} \quad (2)$$

Where λ is the wavelength (λ) of Cu α radiation (0.1514 nm), θ is the angular position of the peak, and β is the FWHM in radians of the more intense diffraction peak. The increase in MoO₃ concentration from 1βMF to 20βMF sample is correlated with an increase in the intensity peak at the 23.5°, which implies that the nanocomposites crystallinity has increased from 11.35 to 17.33 nm. This was revealed as a result of the strong interactions between the incorporated MoO₃ and Fe₂O₃ species.

3.2 FE-SEM analysis

The investigation morphology of the prepared catalysts surface nature was studied by scanning electron microscopy. The Fig. 2a shows the FE-SEM morphology of pure MoO₃, which represents a nano-flakes-like material. Figure 2b–f shows gradual changes in morphology from

flakes to the nanocomposites sample, and it gives an estimated size of ranges below 30 nm. The addition of β-CD to the MoO₃/Fe₂O₃ shows the dispersion of MoO₃ particles on the surface of Fe₂O₃. Similarly, the presence of β-CD was also observed in the FE-SEM images [35].

3.3 HR-TEM EDS analysis

Figure 3a–e gives the HR-TEM image of 15βMF that indicates a spherical shape with a uniform crystallite size range of 20 ± 2 nm. This value closely matches the XRD data of 17.33 nm. The Fig. 3f shows selected area electron diffraction (SAED) pattern that is closely matched to the tetragonal structure of Fe₂O₃. According to the SAED pattern, the distance between the center of the ring and the diffraction spots is 0.28 nm for the (111) planes of MoO₃ and 0.26 nm for the (305) planes of Fe₂O₃ [41].

The EDS images were shown in Fig. 3g as well as EDS spectra shown in Supplementary Fig. S2 and in Supplementary Table S2. It was indicating that the stoichiometric ratio of the synthesized nanocomposite contains iron (13.03%), molybdenum (5.43%), oxygen (47.29%), and carbon (34.25%) for 15βMF material. The peaks between 0–1 keV are associated with oxygen and carbon that exist in β-Cyclodextrin, CTAB and PVA. The EDS and XRD results demonstrate that the synthesized nanocomposite is very pure and has not presented any impurity.

3.4 UV-Diffuse Reflectance Spectrum (UV-DRS)

The UV-DRS is typically used to designate highly scattering and absorbed nanoparticles in all material matrixes. As discussed earlier, the investigated change in optical properties of pure MoO₃ and Fe₂O₃ and their various percentages of molar concentrations of MoO₃ and its Fe₂O₃ nanocomposites was studied using UV-visible spectroscopy (UV-DRS) [42]. The reflectance spectra measured can be converted to the equivalent absorbance spectra, as shown in Fig. 4a.

The optical absorption coefficient (α), which is calculated by using the Kubelka–Munk equation [43].

$$F(R_{\infty}) = \frac{K}{S} = \frac{(1 - R_{\infty})^n}{2R_{\infty}}$$

Where ‘ α ’ absorption coefficient is equivalent to the $F(R_{\infty})$, K and S were absorption and scattering coefficient, subsequently, $R_{\infty} = \frac{R_{\text{sample}}}{R_{\text{standard}}}$ was the diffused reflectance (%) of an infinity specimen, and the optical band gap was directly related to the Kubelka–Munk function [44].

$$[F(R) \cdot hv]^n = A(hv - (E_g)_{\text{eff}})$$

Fig. 2 FE-SEM images of **a** Pure MoO_3 , **b** $1\beta\text{MF}$, **c** $5\beta\text{MF}$, **d** $10\beta\text{MF}$, **e** $15\beta\text{MF}$, **f** $20\beta\text{MF}$ nanocomposite

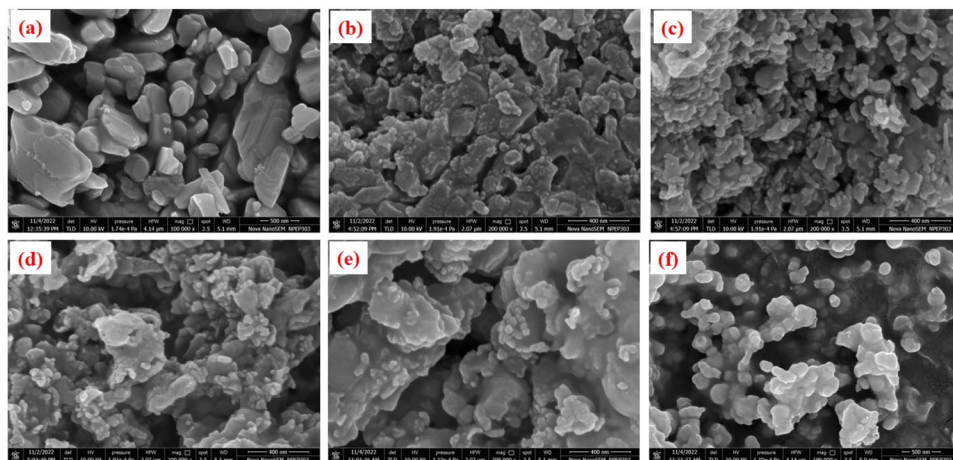
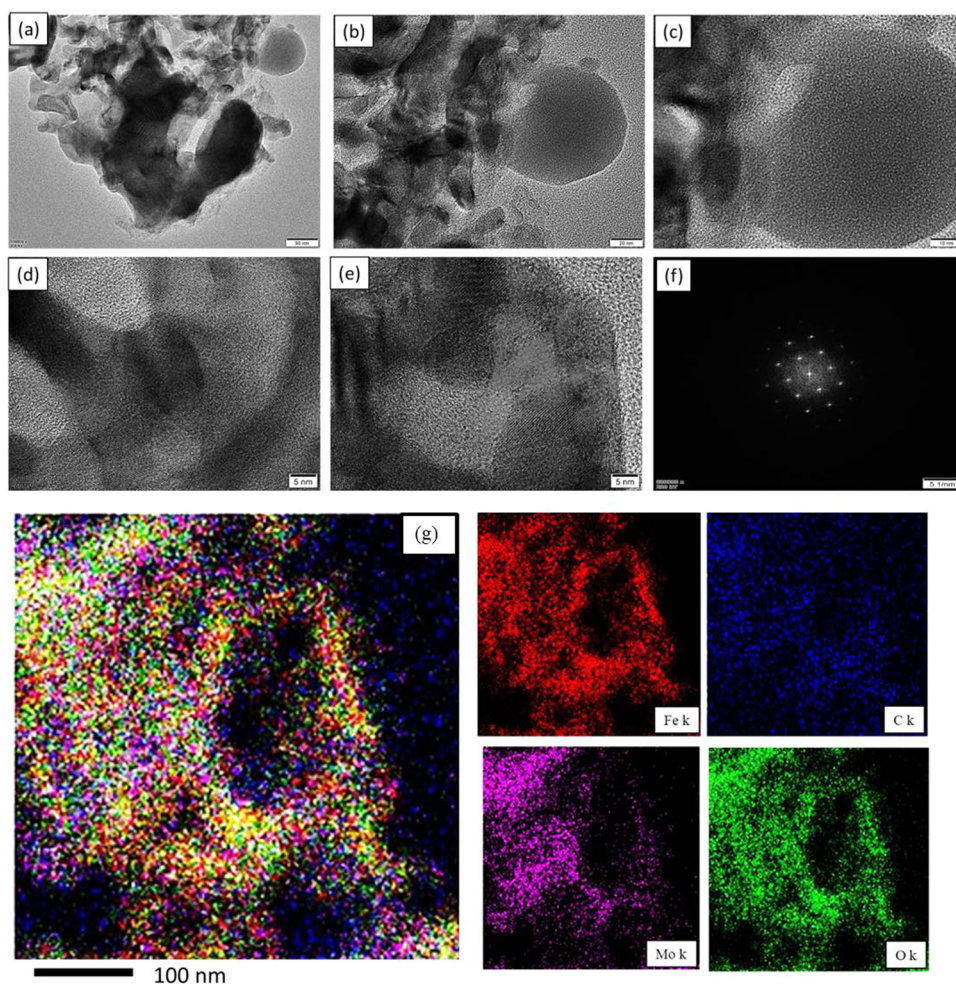


Fig. 3 **a–e** HR-TEM images of $15\beta\text{MF}$ catalyst with different resolution and **f** SAED pattern, **g** EDS image



Here, A is a constant dependent through the transition (direct and indirect) possibility. $(E_g)_{\text{eff}}$ was the effective optical band gap energy, and n was an order magnitude level known as the transition power factor ($n = 1/2, 3/2, 2, 4$), respectively [45, 46]. As discussed, the indirect band gap energy was calculated via a graph that included the y-axis, incident energy of photon ($h\nu$), and the x-axis, $[F(R)h\nu]^{1/2}$,

as well as a straight line on the y-intercept $(E_g)_{\text{eff}}$, which is well-known as effectively optical band gap energy [47].

Figure 4b shows the plot $[F(R)h\nu]^{1/2}$ versus $(h\nu)$ for a $5\beta\text{MF}$ sample having a band gap energy of 1.80 eV. The analysis of the effective optical band gap is shown in Fig. 4c [48]. The MoO_3 percentage level ratio increased in nanocomposites, which showed that the optical band gap

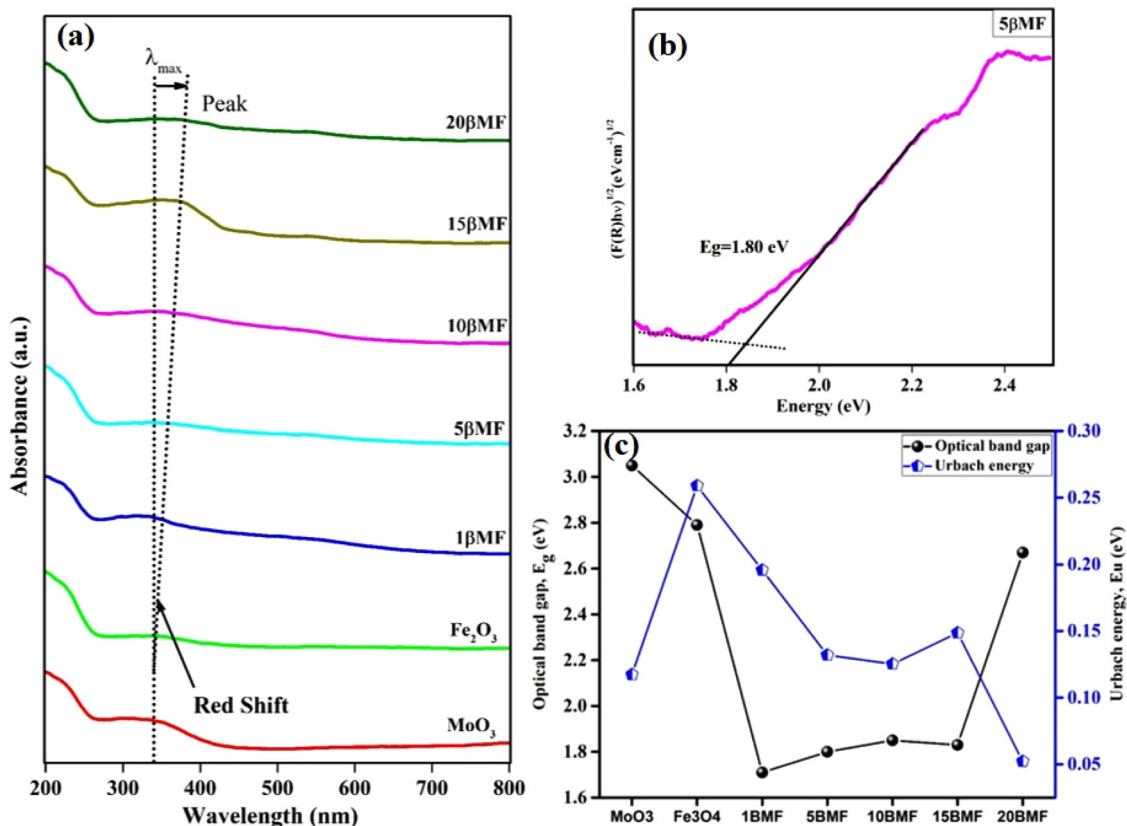


Fig. 4 **a** UV-DRS Absorption spectra of catalyst, **b** Optical band gap energy 5βMF, **c** Optical band gap energy and Urbach energy plots of $[F(R)hv]^{1/2}$ versus (hv) for all series of catalyst

energy was significantly lower as compared to the pure samples. It was absolutely due to the localized defect sites and absorption edge point towards the visible region (400–650 nm). The absorption peaks were shifted towards the higher wavelength (red shift) [49]. In addition to the point of tail of the width of localized defect states through the band gap, this is said to be Urbach energy. The Urbach energy equation was calculated via the following equation:

$$\alpha = \alpha_0 \exp\left(\frac{(E - E_g)}{E_U}\right)$$

Where α_0 is a constant as a dependent-material coefficient as a function of E_g . The optical absorption coefficient was associated with the incident energy of photons, and E_g was compared to the optical band gap energy of pure and nanocomposites samples investigated at room temperature (25 °C) [50, 51].

$$E_U = \Delta E_g - \Delta E'_g$$

Where ΔE_g was the energy gap between conduction band and valence band and also $\Delta E'_g$ was the energy gap between

valence band tail and conduction band tail [52, 53].

$$\ln(\alpha) = \ln(\alpha_0) \exp\left(\frac{(E - E_g)}{E_U}\right)$$

Now, Urbach energy (E_U) was investigated by fitting a graph plotted $\ln(\alpha)$ vs Photon energy ($E = hv$), which is seen in Fig. 4c for all series samples. The fitted linear exponential function that gives the inverse slope of values is known as Urbach energy, and the value of Urbach energy is seen in Fig. 4c [54]. Urbach energy was found below the absorption edge or tails in the series nanocomposites than the pure samples. More specifically, the current case's higher oxygen vacancies produce a variety of defect states that disturb the material's band structure and significantly narrow the optical band gap [55].

3.5 FT-IR analysis

The functional group and chemical structure of nanocomposites were determined by using the FT-IR spectrum. Figure 5a of pure MoO_3 shows a broad peak around 860 cm^{-1} . Four strong vibrational peaks were detected at 543 , 814 , 860 , and 990 cm^{-1} , which are assigned to the oxygen linking of three atoms in the stretching modes. These stretching modes assign oxygen to the Mo-O-Mo

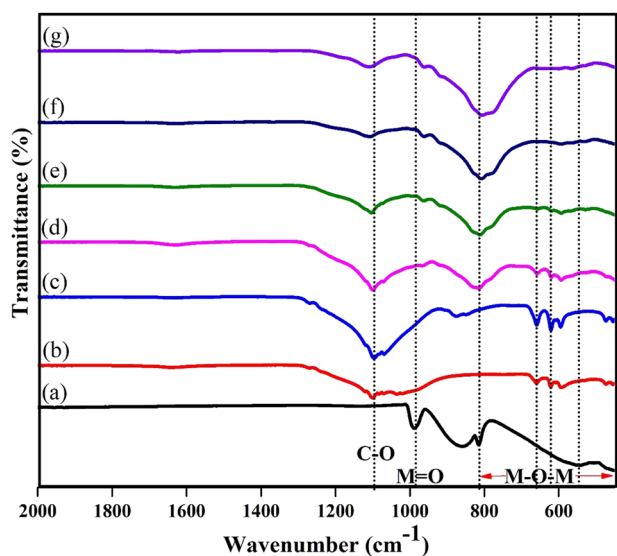


Fig. 5 FT-IR spectrum of (a) MoO₃, (b) Fe₂O₃, (c) 1βMF, (d) 5βMF, (e) 10βMF, (f) 15βMF, (g) 20βMF

units, and the Mo=O stretching mode associates with orthorhombic MoO₃ [56, 57].

The spectrum of Fig. 5b Fe₂O₃ shows sharp peaks at 430, 453, 473, 592, 621, 661, 1020, 1034, 1100, and 1642 cm⁻¹. The absorption peaks at 500–700 cm⁻¹ correspond to the characteristic vibration of the Fe-O bonds of magnetite nanoparticles [58]. The peaks at 950–1100 cm⁻¹ indicate Fe-O-Fe stretching vibration, and the adsorbed water has a peak at 1642 cm⁻¹. Also Fig. 5c–g βMF shows absorption peaks at 430, 591, 620, 659, 807, and 1099 cm⁻¹ for stretching and bending vibration modes for M-O-M, M-M, and M-O bonds. A peak of 1631 cm⁻¹ informs the bending vibrations of H-O-H bonds [59].

3.6 RAMAN analysis

The spectra of pure MoO₃ in Fig. 6a exhibit strong absorption bands at 818 cm⁻¹ (A_g, B_{1g}) and weak absorption bands at 993 cm⁻¹ (A_g, B_{1g}) due to Mo-O-Mo symmetric stretching and Mo=O terminal asymmetric stretching, respectively [60]. Similarly, the spectra of nanocomposites bands shown at 781, 785, and 787 cm⁻¹ were associated with the ν₃ (MoO₄)²⁻ asymmetric stretching vibrations for Fig. 6d–g. The Infrared band at 968, 970, 971, and 972 cm⁻¹ was given to the ν₁ (MoO₄)²⁻ symmetric stretching vibrations. The ferrimolybdate Raman spectrum in the 100–500 cm⁻¹ spectral range is exhibited in Fig. 6c. 466 cm⁻¹ was given to the doubly degenerate ν₂ (δ) (MoO₄)²⁻ bending vibrations. These bands are mostly related to the ν₃ Fe-(O) stretching vibrations in the Fe-(O)₆ octahedra. The Raman band at 347, 349, and 351 cm⁻¹ was assigned to ν₄ (δ) triply degenerate (MoO₄)²⁻ bending vibrations. It was observed that the Raman spectra of the studied ferrimolybdate sample demonstrate that structurally

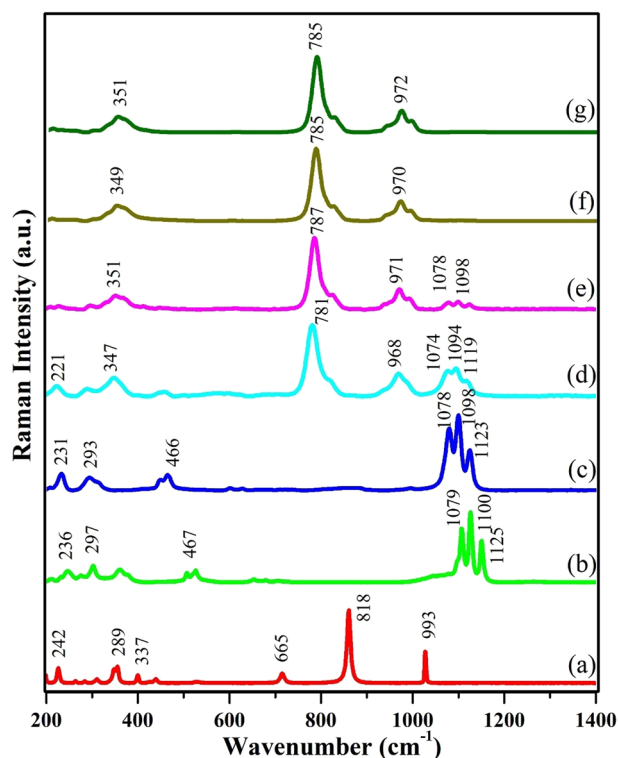


Fig. 6 Raman spectrum of (a) MoO₃, (b) Fe₂O₃, (c) 1βMF, (d) 5βMF, (e) 10βMF, (f) 15βMF, (g) 20βMF

distinct (MoO₄)²⁻ units are represented in the crystal structure of ferrimolybdate [61, 62].

Due to stretching vibrations, MoO₃ composite shows new bands at 781–787 and 968–972 cm⁻¹, which are shifted towards the blue shift and represent the bridging and terminal stretching, which confirms the formation of the composite and signs the new phase Fe₂(MoO₄)₃ [63, 64].

3.7 BET analysis

Brunauer-Emmette-Teller N₂ adsorption-desorption isotherm of 5βMF nanocomposite is presented in Fig. 7a, which informs about the pore volume, pore size, and pore area of nanocomposites. The average pore area of a 5βMF catalyst is 1.947 m²g⁻¹ and the average pore volume is 0.0226 cm³g⁻¹. Also, the pore size of nanocomposites calculated by the Barrett-Joyner-Halenda (BJH) plot, which is 28.98 nm, specifies the mesoporous nature of nanocomposites.

3.8 XPS analysis

The XPS analysis primarily provides information about the surface composition and chemical composition of the surface and the inferior surface of the sample. The XPS survey spectra of 15βMF clearly display distinct signals corresponding to iron (Fe 2p peaks), molybdenum (Mo 3d peaks), oxygen (O 1s peak), and carbon (C 1s peak), as

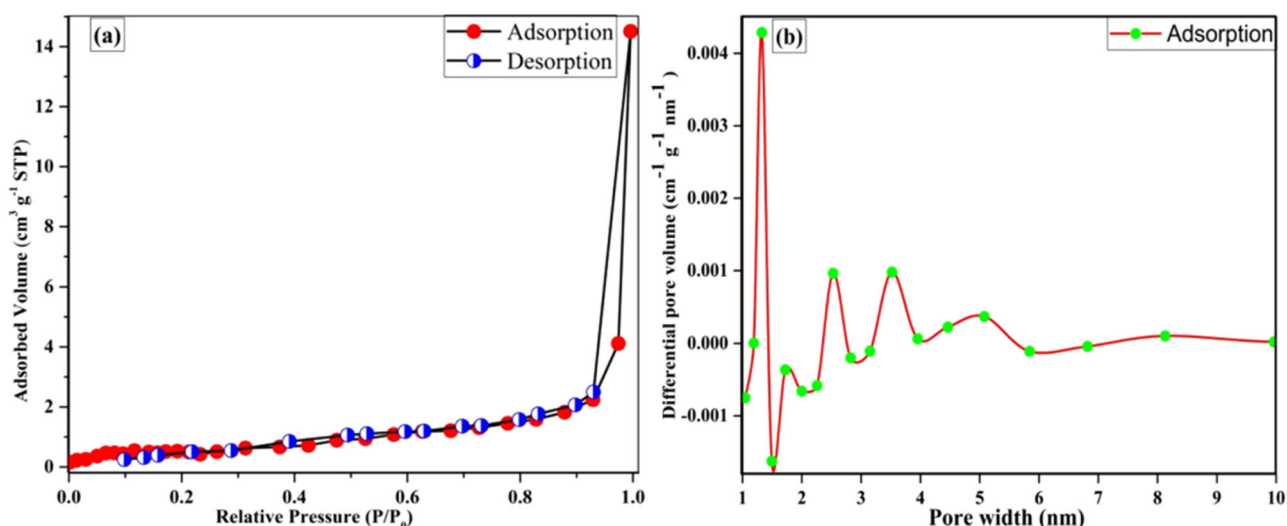


Fig. 7 BET images of **a** N_2 adsorption-desorption isotherm, **b** (BJH plot) pore size distribution of 5β MF catalyst

shown in Fig. 8a. High resolution spectra of Fe 2p show two main peaks at around 711.4 eV and 725.3 eV, which are assigned to the binding energies of Fe $2p_{3/2}$ and Fe $2p_{1/2}$. The Fe 2p peak was deconvoluted to four peaks (Fig. 8b) at 724.70 eV for $Fe^{2+} 2p_{1/2}$, 711.15 eV for $Fe^{2+} 2p_{3/2}$, 727.13 eV for $Fe^{3+} 2p_{1/2}$, and 713.38 eV for $Fe^{3+} 2p_{3/2}$. For these four peaks, two satellite peaks are consigned to binding energies of 733.30 and 718.53 eV, respectively [65, 66]. The XPS spectrum for Mo 3d (Fig. 8c) of 15β MF clearly displayed two distinct peaks at around 235.6 eV (Mo $3d_{3/2}$) and 232.5 eV (Mo $3d_{5/2}$), signifying well-defined spin-orbit components. This observation suggests that the Mo element predominantly exists in the chemical state of Mo^{6+} on the composite [67]. These values are in accordance with the MoO_3 binding energy. The result further proved the presence of MoO_3 in the β MF catalyst [68, 69]. High resolution O 1s spectra (Fig. 8d) showed peaks at 530.3 eV, 531.6 eV, and 532.8 eV assigned to the lattice oxygen (Fe-O), lattice hydroxyl groups (Fe-OH), and peroxide groups ($-O_2^{2-}$) [70]. The most intense peaks at 711.4 eV (Fe $2p_{3/2}$), 232.5 eV (Mo $3d_{5/2}$), and 530.5 eV (O 1s) confirm the presence of $Fe_2(MoO_4)_3$ in nanocomposite [71]. High resolution C 1s spectra (Fig. 8e) showed three peaks derived from C-C/C=C in graphite carbon (284.6 eV), C-O (285.6 eV), and C=O (288.8 eV) [72, 73].

3.9 Photodegradation of methylene blue

The study of photocatalytic activity nanocomposites was performed by photodegradation of MB dye in the presence of H_2O_2 under sunlight. Figure 9 shows the typical visible spectrum of results obtained from the photodegradation of MB dye. Reactions with controlled experimental conditions show that without catalyst or without H_2O_2 , reaction was

not proceeds. The 5β MF material shows 91.62% photodegradation of MB in 1 h, while the pure Fe_2O_3 and pure MoO_3 showed 77.10% and 38.21%, respectively. Similarly, 1β MF (84.09%), 10β MF (79.25%), 15β MF (59.44%) and 20β MF (46.64%) showed gradual decreases in degradation efficiency, respectively mentioned in Fig. 10. It is mainly due to the more active sites provided by β -CD gives higher degradation efficiency of nanocomposites.

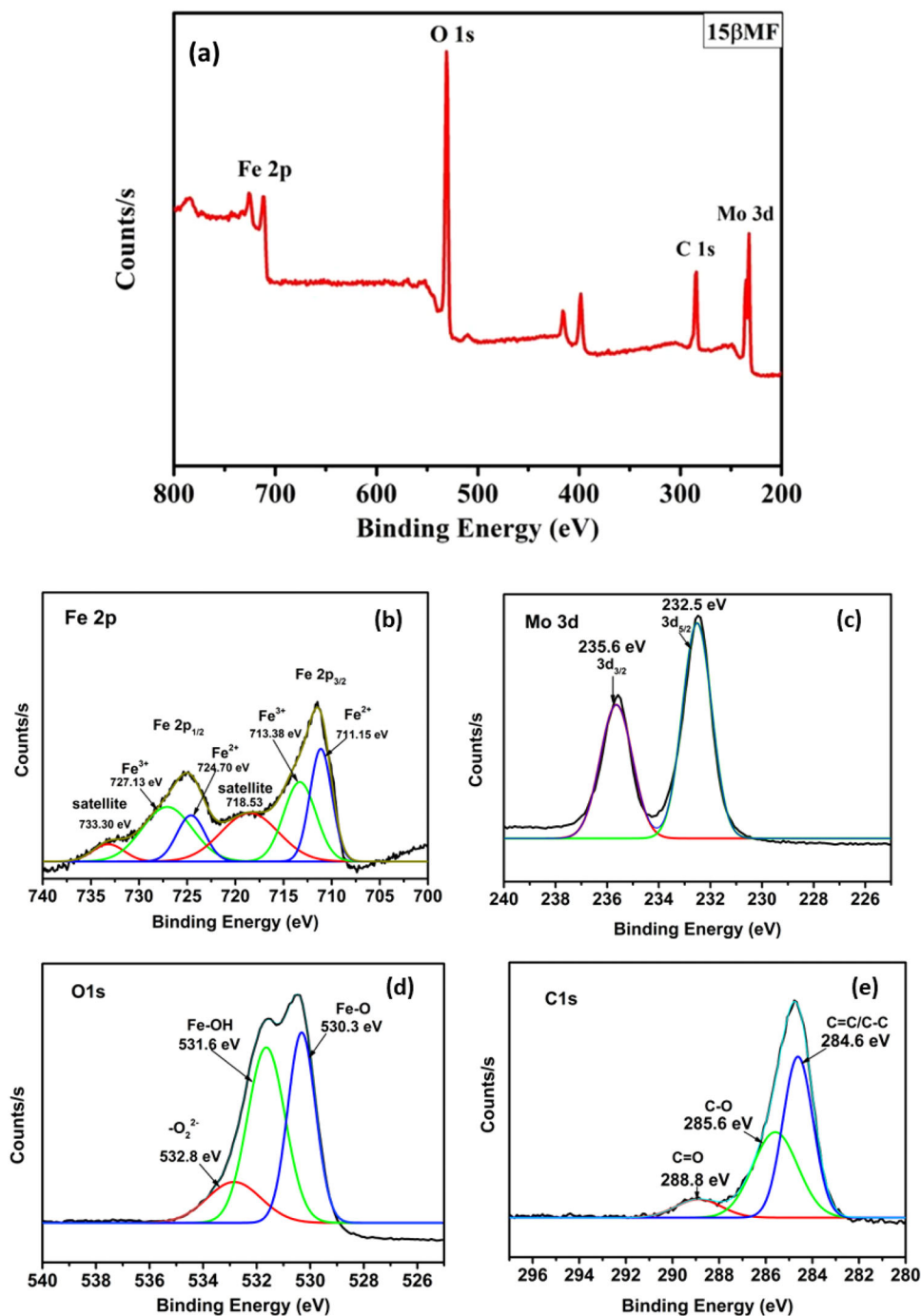
3.10 Impact of concentration of H_2O_2 on photodegradation

To on reaction the effect of the H_2O_2 was studied. The reaction was performed by varying amounts of H_2O_2 concentrations (5 mM, 10 mM, and 15 mM). By increasing the amount of H_2O_2 from 5 mM to 15 mM, the photodegradation of MB was also enhanced from 81.81, 91.62, and 82.03%, respectively. As shown in Fig. 11, the significant degradation efficiency of 10 mg/L of MB dye at 10 mM H_2O_2 indicates that it is directly dependent on the concentration of hydroxyl radicals produced by the H_2O_2 . When the concentration of H_2O_2 increases, the rate of photodegradation of dye is also increased up to a certain limit, but when the concentration of H_2O_2 passes this limit, it acts as a scavenger, which decreases the rate of photodegradation of dye [74, 75]. It was concluded that increased H_2O_2 concentration decreases the rate of photodegradation due to the scavenger effect of H_2O_2 .

3.11 Impact of photocatalyst amount on photodegradation

The photodegradation process of methylene blue is affected by the initial amount of catalyst shown in Fig. 12. An

Fig. 8 XPS of **a** full scan spectrum of 15 β MF catalyst, **b** Fe 2p, **c** Mo3d, **d** O 1s, **e** C 1s spectra



increasing amount of 5 β MF catalyst ranging between 15, 25, and 35 mg was tested, and the results shows that 91.62, 81.08, and 83.64% photodegradation of MB dye, respectively. Thus, the 15 mg catalyst shows better degradation efficiency at room temperature under sunlight. When the concentration of catalyst increases, the production of \cdot OH radicals on the catalytic surface were also increases. This phenomenon raises the degradation percentage at a certain limit, and after that, it decreases due to reduced light intensity because of the excess loading of the catalyst [76].

3.12 Impact of initial dye concentration on photodegradation

Similarly, Fig. 13 shows the impact of a variation in the concentration of dye solution from 10 to 20 mg/L by keeping reaction parameters the same at room temperature on the degradation reaction. It was found that the 10, 15, and 20 mg/L concentrations of MB solution give 91.62, 75.68, and 25.51% photodegradation, respectively. The result shows that increasing the concentration of dye decreases the rate of

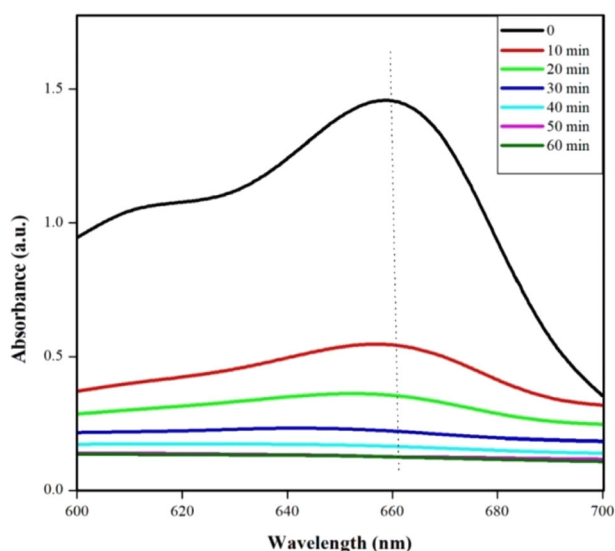


Fig. 9 Typical visible spectrums of photodegradation of MB dye, reaction condition : $\lambda_{\max} = 660$ nm, catalyst - $5\beta\text{MF}$, catalyst amount - 15 mg, concentration of H_2O_2 - 10 mM, pH -6, concentration of methylene blue dye - 10 mgL $^{-1}$, temperature - room temperature

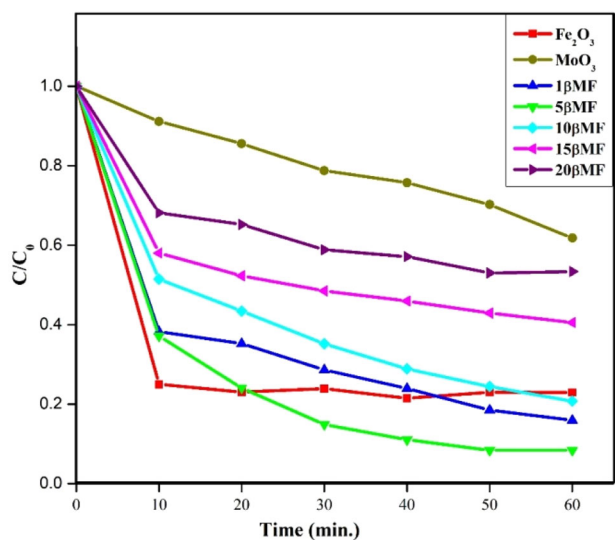


Fig. 10 Effect of various catalyst on photodegradation of MB dye Reaction condition: $\lambda_{\max} = 660$ nm; catalyst - (a) pure Fe_2O_3 , (b) pure MoO_3 , (c) $1\beta\text{MF}$, (d) $5\beta\text{MF}$, (e) $10\beta\text{MF}$, (f) $15\beta\text{MF}$, (g) $20\beta\text{MF}$, catalyst amount - 15 mg, concentration of H_2O_2 - 10 mM, pH -6, concentration of methylene blue dye - 10 mgL $^{-1}$, temperature - room temperature

reaction. It is due to the occupation of active sites of the βMF catalyst, which reduces the generation of photons from the βMF surface, as well as the formation of $\cdot\text{OH}$ radicals, which decreases the photodegradation [77, 78].

3.13 Impact of solution pH on photodegradation

The pH of the solution, which is an essential factor in the efficiency of the photodegradation reaction, affects the

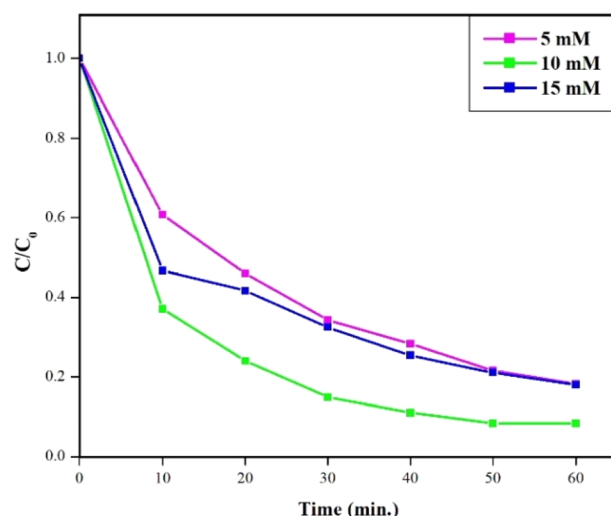


Fig. 11 Impact of concentration of H_2O_2 on photodegradation of MB, Reaction condition: $\lambda_{\max} = 660$ nm, catalyst - $5\beta\text{MF}$, catalyst amount - 15 mg, concentration of H_2O_2 - 10 mM, pH -6, concentration of methylene blue dye - 10 mgL $^{-1}$, temperature - room temperature

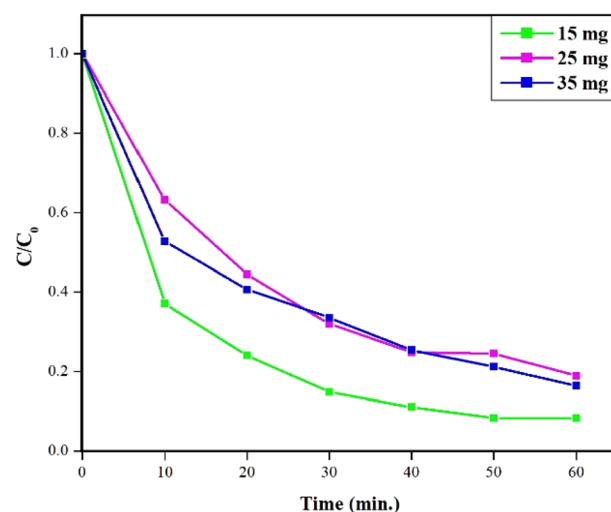


Fig. 12 Impact of catalyst amount on photodegradation of MB, Reaction condition: $\lambda_{\max} = 660$ nm, catalyst - $5\beta\text{MF}$, concentration of H_2O_2 - 10 mM, pH -6, concentration of methylene blue dye - 10 mgL $^{-1}$, temperature - room temperature

surface characteristics of the catalyst [79]. So, in this study, the effect of pH varying at (2–11) was studied by adjusting pH by using dilutions of HCl (0.1 M) and NaOH (0.1 M) solutions. Figure 14 shows that photodegradation of MB gives the highest 91.62% degradation at pH 6, which is a natural pH of MB dye solution. In an acidic medium of pH 2 and 4, the efficiency of the catalyst decreases up to 61.82 and 87.28%, while in a basic medium of pH 9 and 11, the efficiency of the catalyst also decreases to 86.20 and 83.19%, respectively. As a result, the results show that the rate of dye degradation is more efficient at pH 6.

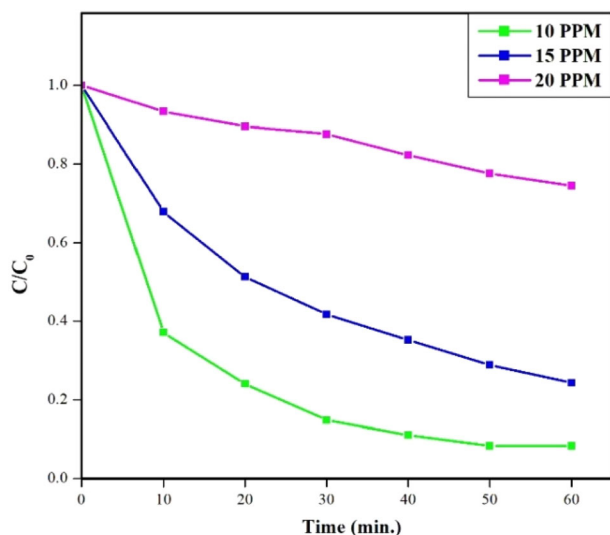


Fig. 13 Impact of concentration of MB dye solution on photodegradation, Reaction condition: $\lambda_{\max} = 660$ nm), catalyst - $5\beta\text{MF}$, catalyst amount - 15 mg, concentration of H_2O_2 - 10 mM, pH -6, temperature - room temperature

The turnover number (TON) and turnover frequency (TOF) are calculated for all series of catalysts shown in Table 2. It was interestingly shown that the values of TON (7.3782–14.4953) as well as TOF (0.1229–0.2415) increase with increasing from $1\beta\text{MF}$ to $20\beta\text{MF}$. Further increases in doping of MoO_3 from 5 to 20%; values were decreasing consistently. It indicates that $5\beta\text{MF}$ catalytic material shows maximum activity, which is full supportive evidence as shown in Fig. 10.

3.14 Photodegradation process on the $\beta\text{-CD}$ Coated $\text{MoO}_3\text{-Fe}_2\text{O}_3$ Catalyst

Figure 15 show the photocatalytic process in presence prepared nanocomposites ($\beta\text{-CD}$ Coated $\text{MoO}_3\text{-Fe}_2\text{O}_3$) catalysts and hydrogen peroxide in presence of sunlight. When incident sunlight emits photon energy, it is greater than optical band gap energy in pure and nanocomposites, and it forms an electron (e^- - h^+) pair after the transition of electrons transporting from the valence band to the conduction band [80]. The Fe^{2+} reacts with H_2O_2 to produces $\cdot\text{OH}$ radicals and Fe^{3+} ion. It was observed that the modified surface drastically improved photocatalytic activity due to the smaller crystallite size and reduced optical band gap energy as compared to the pure surface. As a result of the formation of Fe^+ ions on the surface, there is a rapid migration of charge carriers to the catalyst/dye interface. Additionally, these species are very reactive and can quickly convert hazardous dye into nontoxic dye, as well as water and carbon dioxide as side products [81].

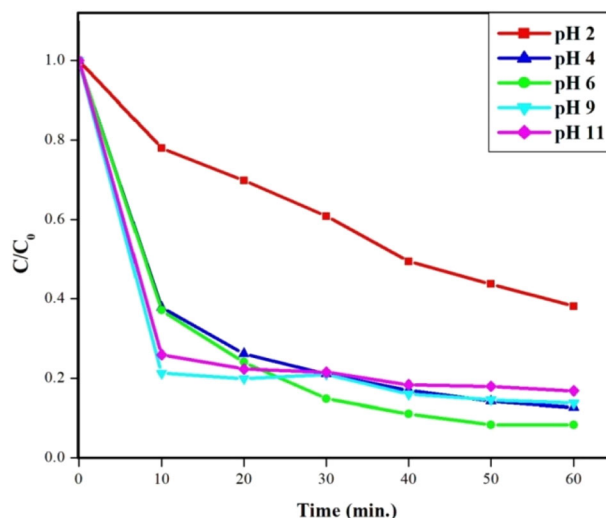
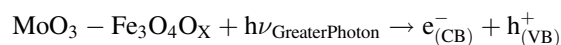


Fig. 14 Impact of pH on photodegradation of MB, Reaction condition: $\lambda_{\max} = 660$ nm, catalyst - $5\beta\text{MF}$, catalyst amount - 15 mg, concentration of H_2O_2 - 10 mM, concentration of methylene blue dye - 10 mgL^{-1} , temperature - room temperature

Table 2 Turnover number and turnover frequency of various $\beta\text{-CD}$ Coated $\text{MoO}_3\text{-Fe}_2\text{O}_3$ material

Entry	Sample	TON	TOF (min^{-1})
1	MoO_3	5.7314	0.0955
2	Fe_2O_3	12.830	0.2138
3	$1\beta\text{MF}$	13.300	0.2216
4	$5\beta\text{MF}$	14.4953	0.2415
5	$10\beta\text{MF}$	12.5329	0.2088
6	$15\beta\text{MF}$	9.4028	0.1567
7	$20\beta\text{MF}$	7.3782	0.1229

Bold: maximum activity catalytic material ($5\beta\text{MF}$).

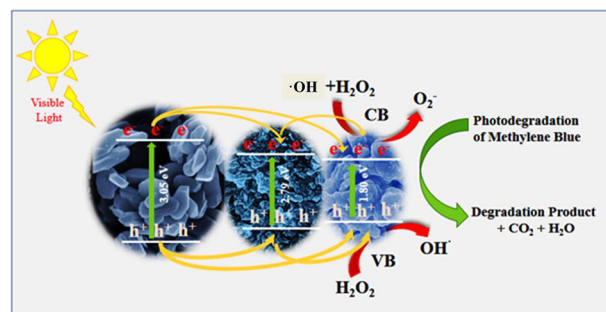


Fig. 15 Photocatalytic process behind the reaction mechanism of prepared nanocomposites ($\beta\text{-CD}$ Coated $\text{MoO}_3\text{-Fe}_2\text{O}_3$) catalyst

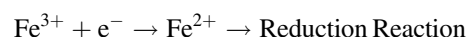
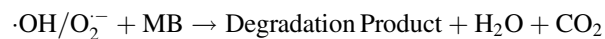
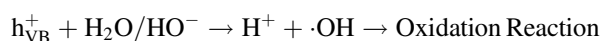
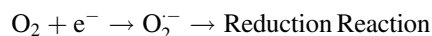


Table 3 Comparison of photodegradation of methylene blue with other catalyst

Photocatalyst	Light source	Concentration (ppm)	Solution (ml)	Catalyst amount (mg)	Time (Min.)	Degradation (%)	Reference
ZnO/Au/rGO	Sunlight	10	10	5	120	95	[82]
Fe ₃ O ₄ @C@Ru	Visible Light	10 ⁻⁴ M	30	10	140	92.70	[83]
NiO/α-MoO ₃	Simulated Solar Light	10	100	10	120	96.5	[84]
MoO ₃ /TiO ₂	UV-visible Light	20	25	600	20	99	[85]
Fe ₃ O ₄ -MWCNT	Visible Light pH = 11 Temp 50 °C	10	100	40	60	98.49	[86]
α-Fe ₂ O ₃	Sunlight/U.V. Light pH = 12	10	70	50	90	96	[87]
γ Fe ₂ O ₃ / Fe ₃ O ₄ / SiO ₂	U. V. Light	50	200	100	120	87.5	[88]
γ Fe ₂ O ₃ / Fe ₃ O ₄ / SiO ₂	Visible Light	50	200	100	180	79.6	[88]
Co-Ox-Ac	U. V. Light	100	500	100	60	98	[89]
Ni-Ox-Ac	U. V. Light	100	500	100	60	91	[89]
ZnO	U. V. Light	10	50	200	70	100	[90]
Co _x Zn _{1-x} Fe ₂ O ₄	Visible Light	10	100	5	60	77	[91]
Bi ₂ MoO ₆ /ZIF-8	Visible Light	20	80	20	100	66.88	[92]
GO/Fe ₃ O ₄ /BiOI	Visible Light	3.19	100	100	170	91.4	[93]
rGO/Fe ₃ O ₄	U. V. Light	12.5	20	2	60	74	[94]
β-CD Coated MoO ₃ -Fe ₂ O ₃	Sunlight	10	50	15	60	91.62	Present Work

Bold: maximum activity catalytic material (5βMF).



3.15 Comparison of photodegradation of methylene blue with other catalyst

We compared our results with literature as shown in Table 3. The ZnO/Au/rGO material gives 95% degradation, but the reaction was completed within 120 min. The MoO₃/TiO₂ shows a 99% degradation result within only 20 min, but the amount of catalyst required is about 600 mg. Similarly, ZnO shows excellent results up to 100% within 70 min, but it works in the UV light region. When we compared our catalytic material with previously reported works, our present catalyst shows better activities within a short duration, with a smaller quantity of catalyst, and it works in the visible light region.

4 Conclusion

The present study reveals the enhancement of the photodegradation activity of MoO₃-Fe₂O₃ nanocomposites with the coating of β-Cyclodextrin. The XRD and Raman spectra confirm the change in the tetragonal phase of Fe₂O₃ to the orthorhombic phase (Fe₂(MoO₄)₃) after the addition of MoO₃ via the sol-gel method. Furthermore, the crystalline size varies

with the changes in a phase. FE-SEM shows the nanoflakes like surface morphology, where the particle size observed below 30 nm. The efficiency of nanocomposites was improved using β-Cyclodextrin, which gives more active sites and fast charge carrier separation. The reaction shows a better efficiency of 5βMF for the degradation of MB dye. This material gives 91.62% degradation MB within a short reaction time as compared to the Fe₂O₃ and MoO₃. The synthesized catalytic material shows maximum degradation efficiency within short time, under acidic medium using H₂O₂. The catalyst could be easily recovered using magnetic separation. It can be recycled and reused many time. This study may provide useful in the application of photocatalyst for dye degradation of waste water of dye industries. Tailoring the nanocomposite materials properties for specific applications such as biomedical, gas sensor, etc. can leads to breakthroughs in environmental protection and clean energy technologies.

Supplementary information The online version contains supplementary material available at <https://doi.org/10.1007/s10971-024-06357-1>.

Acknowledgements The authors are grateful to the Principal of New Arts Commerce and Science College, Ahmednagar, and Jijamata College of Science and Arts, Bhende, Maharashtra, India, as well as to the Principal of Nowgong College (Autonomous), Nagaon, Assam, India, for providing all the required facilities to carry out this work. Also, thanks to the Department of Chemistry, School of Science, Gandhi Institute of Technology and Management (GITAM) University, Hyderabad, Telangana, India.

Author contributions The first author (AN) performed all laboratory and experimental work. The authors AD, MB, and PMB help in the analysis and processing of characterization data and the preparation of manuscripts. The PG, AA, and MN (corresponding author) were

supervised during all processes. Thus, all authors have made equal contributions to this manuscript.

Compliance with ethical standards

Conflict of interest The authors declare no competing interests.

References

- De I, Pahuja M, ud din Wani HM et al. (2022) *Ecotoxicol. Environ. Saf.* 243:113985. <https://doi.org/10.1016/j.ecoenv.2022.113985>
- Honarmand M, Golmohammadi M, Naeimi A (2019) *Adv. Powder Technol.* 30:1551. <https://doi.org/10.1016/j.apt.2019.04.033>
- Li, X-F, Li RX, Qiang Feng X (2023) *Russ. J. Inorg. Chem.* <https://doi.org/10.1134/S0036023623601307>
- Balu P, Asharani IV, Thirumalai D (2020) *J. Mater. Sci. Mater. Electron.* 31:10669. <https://doi.org/10.1007/s10854-020-03616-z>
- Tichapondwa SM, Newman JP, Kubheka O (2020) *Phys. Chem. Earth* 118–119:102900. <https://doi.org/10.1016/j.pce.2020.102900>
- Yan S, Liang X, Liu S et al. (2023) *J. Sol-Gel Sci. Technol.* <https://doi.org/10.1007/s10971-023-06253-0>
- Thakur N, Kumar A, Thakur N (2023) *Hybrid Adv* 4:100086. <https://doi.org/10.1016/j.hybadv.2023.100086>
- Din MI, Khalid R, Najeeb J, Hussain Z (2021) *J. Clean. Prod.* 298:126567. <https://doi.org/10.1016/j.jclepro.2021.126567>
- Binsabt M, Sagar V, Singh J, Rawat M, Shaban M (2022) *Polymers* 14:2677. <https://doi.org/10.3390/polym14132677>
- Rani M, Singh K, Panwar N (2023) *J. Sol-Gel Sci. Technol.* <https://doi.org/10.1007/s10971-023-06249-w>
- Balcha A, Yadav OP, Dey T (2016) *Environ. Sci. Pollut. Res.* 23:25485. <https://doi.org/10.1007/s11356-016-7750-6>
- Thakur N, Kumar P, Thakur N et al. (2022) *Biomater. Polym. Horiz.* 1. <https://doi.org/10.37819/bph.1.331>
- Thakur N, Thakur N, Kumar K et al. (2022) *Biomater. Polym. Horiz.* 1. <https://doi.org/10.37819/bph.1.330>
- Thomas P, Lai CW, Johan MR (2022) *Environ. Res.* 212:113417. <https://doi.org/10.1016/j.envres.2022.113417>
- Nagabhushana GP, Samrat D, Chandrappa GT (2014) *RSC Adv* 4:56784. <https://doi.org/10.1039/C4RA05135A>
- Chithambararaj A, Rajeswari Yogamalar N, Bose AC (2016) *Cryst. Growth Des.* 16:1984. <https://doi.org/10.1021/acs.cgd.5b01571>
- Rani V, Malhotra M, Patial S et al. (2023) *Mater. Chem. Phys.* 299:127454. <https://doi.org/10.1016/j.matchemphys.2023.127454>
- Roy SD, Das KC, Dhar SS (2021) *Inorg. Chem. Commun.* 134:109050. <https://doi.org/10.1016/j.inoche.2021.109050>
- Selvaraj R, Pai S, Vinayagam R et al. (2022) *Chemosphere* 308:136331. <https://doi.org/10.1016/j.chemosphere.2022.136331>
- Batool T, Shah ZH, Ashraf H et al. (2023) *J. Sol-Gel Sci. Technol.* 108:655. <https://doi.org/10.1007/s10971-023-06210-x>
- Suppiah DD, Julkapli NM, Sagadevan S, Johan MR (2023) *Inorg. Chem. Commun.* 152:110700. <https://doi.org/10.1016/j.inoche.2023.110700>
- Kumar P, Kumar S, Thakur N (2023) *Inorg. Chem. Commun.* 155:111084. <https://doi.org/10.1016/j.inoche.2023.111084>
- Harikumar B, Kokilavani S, Sudheer Khan S (2022) *Chem. Eng. J.* 446:137273. <https://doi.org/10.1016/j.cej.2022.137273>
- Thakur N, Thakur N (2024) *J. Mater. Sci. Mater. Electron.* 35:134. <https://doi.org/10.1007/s10854-023-11851-3>
- Thakur N, Thakur N, Kumar A et al. (2024) *Sci. Total Environ.* 914:169815. <https://doi.org/10.1016/j.scitotenv.2023.169815>
- Thakur N, Thakur N (2023) *Environ. Pollut.* 335:122229. <https://doi.org/10.1016/j.envpol.2023.122229>
- Ma D, Yang L, Sheng Z, Chen Y (2021) *Chem. Eng. J.* 405:126538. <https://doi.org/10.1016/j.cej.2020.126538>
- Gheorghita S, Bogatu C, Duta A (2023) *J. Sol-Gel Sci. Technol.* <https://doi.org/10.1007/s10971-023-06263-y>
- Thakur N, Arya V, Kumar A, Thakur N (2023) *Int. J. Environ. Anal. Chem.* 1. <https://doi.org/10.1080/03067319.2023.2246012>
- Gogoi A, Baithy M, Navgire M et al. (2023) *ChemistrySelect* 8, <https://doi.org/10.1002/slct.202302553>
- Baithy M, Gogoi A, Borgohain C et al. (2023) *Bull. Mater. Sci.* 46:137. <https://doi.org/10.1007/s12034-023-02971-x>
- Gogoi A, Navgire M, Sarma KC, Gogoi P (2019) *Mater. Chem. Phys.* 231:233. <https://doi.org/10.1016/j.matchemphys.2019.04.013>
- Gogoi A, Navgire M, Sarma KC, Gogoi P (2017) *RSC Adv* 7:40371. <https://doi.org/10.1039/C7RA06447K>
- Gogoi A, Navgire M, Sarma KC, Gogoi P (2017) *Chem. Eng. J.* 311:153. <https://doi.org/10.1016/j.cej.2016.11.086>
- Navgire ME, Gogoi P, Mallesham B et al. (2016) *RSC Adv* 6:28679. <https://doi.org/10.1039/C5RA25966E>
- Kihlborg L (1963) *Ark. Kemi* 21:357
- Greaves C (1983) *J. Solid State Chem.* 49:325. [https://doi.org/10.1016/S0022-4596\(83\)80010-3](https://doi.org/10.1016/S0022-4596(83)80010-3)
- Harrison WTA (1995) *Mater. Res. Bull.* 30:1325. [https://doi.org/10.1016/0025-5408\(95\)00157-3](https://doi.org/10.1016/0025-5408(95)00157-3)
- Mallesham B, Sudarsanam P, Venkata Shiva Reddy B, Govinda Rao B, Reddy BM (2018) *ACS Omega* 3:16839. <https://doi.org/10.1021/acsomega.8b02008>
- Intaphong P, Phuruangrat A, Yeebu H et al. (2021) *Russ. J. Inorg. Chem.* 66:2123. <https://doi.org/10.1134/S0036023621140047>
- Navgire ME, Nagare A, Kale G, Bhitre S (2019) *J. Met. Mater. Res.* 2. <https://doi.org/10.30564/jmmr.v2i2.1124>
- Aher R, Punde A, Shinde P et al. (2022) *ACS Omega* 7:31877. <https://doi.org/10.1021/acsomega.2c02666>
- Kumari P, Lather V, Khatri S et al. (2022) *RSC Adv* 12:35827. <https://doi.org/10.1039/d2ra05796d>
- Dukstiene N, Sinkeviciute D, Guobiene A (2012) *Cent. Eur. J. Chem.* 10:1106. <https://doi.org/10.2478/s11532-012-0012-7>
- Tiwari S, Khatun N, Rajput P et al. (2018) *Appl. Phys. A Mater. Sci. Process.* 124:0. <https://doi.org/10.1007/s00339-018-2036-0>
- Tauc J (1968) *Mater. Res. Bull.* 3:37. [https://doi.org/10.1016/0025-5408\(68\)90023-8](https://doi.org/10.1016/0025-5408(68)90023-8)
- Mayabadi AH, Waman VS, Kamble MM et al. (2014) *J. Phys. Chem. Solids* 75:182. <https://doi.org/10.1016/j.jpcs.2013.09.008>
- ASLAN N (2022) *Türk Doğa ve Fen Derg* 11:95. <https://doi.org/10.46810/tdfd.1011220>
- Choudhury B, Choudhury A (2014) *Phys. E Low Dimensional Syst. Nanostructures* 56:364. <https://doi.org/10.1016/j.physe.2013.10.014>
- Adewinbi SA, Taleatu BA, Busari RA et al. (2021) *Mater. Chem. Phys.* 264:124468. <https://doi.org/10.1016/j.matchemphys.2021.124468>
- Norouzzadeh P, Mabhouti K, Golzan MM, Naderali R (2020) *Optik* 204:164227. <https://doi.org/10.1016/j.ijleo.2020.164227>
- Moualkia H, Hariech S, Aida MS (2009) *Thin Solid Films* 518:1259. <https://doi.org/10.1016/j.tsf.2009.04.067>
- Khan M, Alam MS, Saha B, Ahmed SF (2021) *Mater. Today Proc.* 47:2351. <https://doi.org/10.1016/j.matpr.2021.04.316>
- Sadat ME, Kaveh Baghbador M, Dunn AW et al. (2014) *Appl. Phys. Lett.* 105:1. <https://doi.org/10.1063/1.4895133>
- Sharma N, Prabakar K, Ilango S, Dash S, Tyagi AK (2021) *Adv. Mater. Proc.* 2:342. <https://doi.org/10.5185/amp.2017/511>
- He T, Wu Y, Jiang C et al. (2020) *PLoS One* 15:1. <https://doi.org/10.1371/journal.pone.0237389>
- Xia T, Li Q, Liu X, Meng J, Cao X (2006) *J. Phys. Chem.* 110:2006–2012. <https://doi.org/10.1021/jp055945n>
- Asnan HHM, Soh SKC, Wan Nor WFK et al. (2019) *Malaysian J. Anal. Sci* 23:781. <https://doi.org/10.17576/mjas-2019-2305-03>

59. Gogoi A, Navgire M, Sarma KC, Gogoi P (2017) *Indian J. Chem. Technol.* 24:498
60. Windom BC, Sawyer WG, Hahn DW (2011) *Tribol. Lett.* 42:301. <https://doi.org/10.1007/s11249-011-9774-x>
61. Sejkora J, Čejka J, Malíková R et al. (2014) *Spectrochim. Acta - Part A Mol. Biomol. Spectrosc* 130:83. <https://doi.org/10.1016/j.saa.2014.03.112>
62. Li D, Xue J, Ma J, Tang J (2016) *New J. Chem.* 40:3330. <https://doi.org/10.1039/c5nj03227j>
63. Bowker M, Brookes C, Carley AF et al. (2013) *Phys. Chem. Chem. Phys.* 15:11988. <https://doi.org/10.1039/c3cp50399b>
64. Brookes C, Bowker M, Gibson EK et al. (2016) *Catal. Sci. Technol.* 6:722. <https://doi.org/10.1039/c5cy01175b>
65. Liu CG, Wu XT, Li XF, Zhang XG (2014) *RSC Adv* 4:62492. <https://doi.org/10.1039/C4RA10616D>
66. Gan Q, Hou H, Liang S et al. (2020) *Sci. Total Environ.* 725:138299. <https://doi.org/10.1016/j.scitotenv.2020.138299>
67. Li W, Zhao S, Qi B et al. (2009) *Appl. Catal. B Environ.* 92:333. <https://doi.org/10.1016/j.apcatb.2009.08.012>
68. He T, Wu Y, Jiang C et al. (2020) *PLoS One* 15:E0237389. <https://doi.org/10.1371/journal.pone.0237389>
69. Thomas T, Jayababu N, Shruthi J et al. (2021) *Thin Solid Films* 722:138575. <https://doi.org/10.1016/j.tsf.2021.138575>
70. Tao S, Yang J, Hou H et al. (2019) *Chem. Eng. J.* 372:966. <https://doi.org/10.1016/j.cej.2019.05.002>
71. Zhou Q, Fu S, Zou M et al. (2015) *RSC Adv* 5:69388. <https://doi.org/10.1039/C5RA11028A>
72. Dai XH, Fan HX, Yi CY, Dong B, Yuan SJ (2019) *J. Mater. Chem. A* 7:6849. <https://doi.org/10.1039/c8ta11661j>
73. Liu G, Zhang Y, Yu H, Jin R, Zhou J (2020) *J. Hazard. Mater.* 397:122783. <https://doi.org/10.1016/j.jhazmat.2020.122783>
74. Badvi K, Javanbakht V (2021) *J. Clean. Prod.* 280:124518. <https://doi.org/10.1016/j.jclepro.2020.124518>
75. Kozlov DA, Artamonov KA, Revenko AO et al. (2022) *Russ. J. Inorg. Chem.* 67:715. <https://doi.org/10.1134/S0036023622050102>
76. Kumar AP, Ahmed F, Kumar S et al. (2022) *J. Clust. Sci.* 33:853. <https://doi.org/10.1007/s10876-021-02149-7>
77. Vasiljevic ZZ, Dojcinovic MP, Vujancevic JD, et al. (2020) *R. Soc. Open Sci.* 7. <https://doi.org/10.1098/rsos.200708>
78. Li X-F, Feng XQ, Li RX, Liu W (2022) *Russ. J. Inorg. Chem.* 67:S98. <https://doi.org/10.1134/S0036023622602124>
79. Gharbani P, Mehrizad A, Mosavi SA (2022) *npj Clean Water* 5. <https://doi.org/10.1038/s41545-022-00178-x>
80. Khan F, Khan MS, Kamal S et al. (2020) *J. Mater. Chem. C* 8:15940. <https://doi.org/10.1039/D0TC03684F>
81. Ranjitha R, Meghana KN, Kumar VGD et al. (2021) *New J. Chem.* 45:796. <https://doi.org/10.1039/D0NJ05268J>
82. Naik SS, Lee SJ, Begildayeva T et al. (2020) *Environ. Pollut.* 266:115247. <https://doi.org/10.1016/j.envpol.2020.115247>
83. Q Zhang, L Yu, C Xu et al. (2019) Preparation of highly efficient and magnetically recyclable Fe 3 O 4 @C@Ru nanocomposite for the photocatalytic degradation of methylene blue in visible light, <https://doi.org/10.1016/j.apsusc.2019.03.225>
84. Li J, Liu H, Liu Z et al. (2022) *Arab. J. Chem.* 15:103513. <https://doi.org/10.1016/j.arabjc.2021.103513>
85. Jada N, Sankaran KJ, Sakthivel R, Sethi D, Mohapatra P (2021) *Bull. Mater. Sci.* 44. <https://doi.org/10.1007/s12034-021-02436-z>
86. Hussain S, Mottahir Alam M, Imran M et al. (2022) *Alexandria Eng. J.* 61:9107. <https://doi.org/10.1016/j.aej.2022.02.050>
87. Weldegebrerial GK, Sibhatu AK (2021) *Optik (Stuttg)* 241:1. <https://doi.org/10.1016/j.ijleo.2021.167226>
88. Sanad MMS, Farahat MM, El-Hout SI, El-Sheikh SM (2021) *J. Environ. Chem. Eng.* 9:105127. <https://doi.org/10.1016/j.jece.2021.105127>
89. Murugesan A, Loganathan M, Senthil Kumar P, Vo DVN (2021) *Sustain. Chem. Pharm.* 21:100406. <https://doi.org/10.1016/j.scp.2021.100406>
90. Almezahia AA, Al-Omar MA, Naglah AM, Bhat MA, Al-Shakliah NS (2022) *Alexandria Eng. J.* 61:2386. <https://doi.org/10.1016/j.aej.2021.06.102>
91. Chahar D, Taneja S, Bisht S et al. (2021) *J. Alloys Compd.* 851:156878. <https://doi.org/10.1016/j.jallcom.2020.156878>
92. Xia Y, Shang SK, Zeng XR, Zhou J, Li YY (2019) *Nanomaterials* 9. <https://doi.org/10.3390/nano9040545>
93. Xia YM, Zhang JH, Xia M et al. (2020) *J. Mater. Sci. Mater. Electron.* 31:1996. <https://doi.org/10.1007/s10854-019-02719-6>
94. Vinodhkumar G, Wilson J, Inbanathan, SSR et al. (2020) *Phys. B Condens. Matter* 580. <https://doi.org/10.1016/j.physb.2019.411752>

Publisher's note Springer Nature remains neutral with regard to jurisdictional claims in published maps and institutional affiliations.

Springer Nature or its licensor (e.g. a society or other partner) holds exclusive rights to this article under a publishing agreement with the author(s) or other rightsholder(s); author self-archiving of the accepted manuscript version of this article is solely governed by the terms of such publishing agreement and applicable law.



Ultrasonic wave-assisted synthesis of CeO₂-MoO₃ nanocomposite for photo-Fenton degradation of Rhodamine-B dye

Amol Dhadage¹ · Akash Nagare¹ · Pravin Ghare³ · Anil Athare¹ · Parikshit Gogoi² · Madhukar Navgire³ 

Received: 18 February 2024 / Accepted: 19 April 2024

© The Author(s), under exclusive licence to the Institute of Chemistry, Slovak Academy of Sciences 2024

Abstract

The highly crystalline mesoporous series of various percentages such as 1, 3 and 5% of CeO₂-doped MoO₃ nanocomposite were synthesized successfully by using ultrasonic wave-assisted sol-gel synthesis procedure and calcined at 873 K for 3 h. The synthesized CeO₂-MoO₃ nanocomposite material characterized by different techniques like XRD, Raman, FT-IR, FE-SEM, HR-TEM, BET, XPS and UV-DRS measurements to find crystallinity, surface morphology, surface area, structural and optical properties. Among these, 5% CeO₂-MoO₃ nanocomposite shows excellent photo-Fenton dye degradation activity of Rhodamine-B (Rh-B) dye in visible light irradiation using direct sunlight. Maximum degradation was observed (95.36% in 120 min) with optimum condition of pH, catalyst amount and H₂O₂ concentration. These nanocomposite material was recovered, recycle and its reusability also gives excellent results up to the 4th cycle. Similarly, turn over number, turn over frequency, kinetic study and scavenger study of photo-Fenton degradation reaction were also discussed.

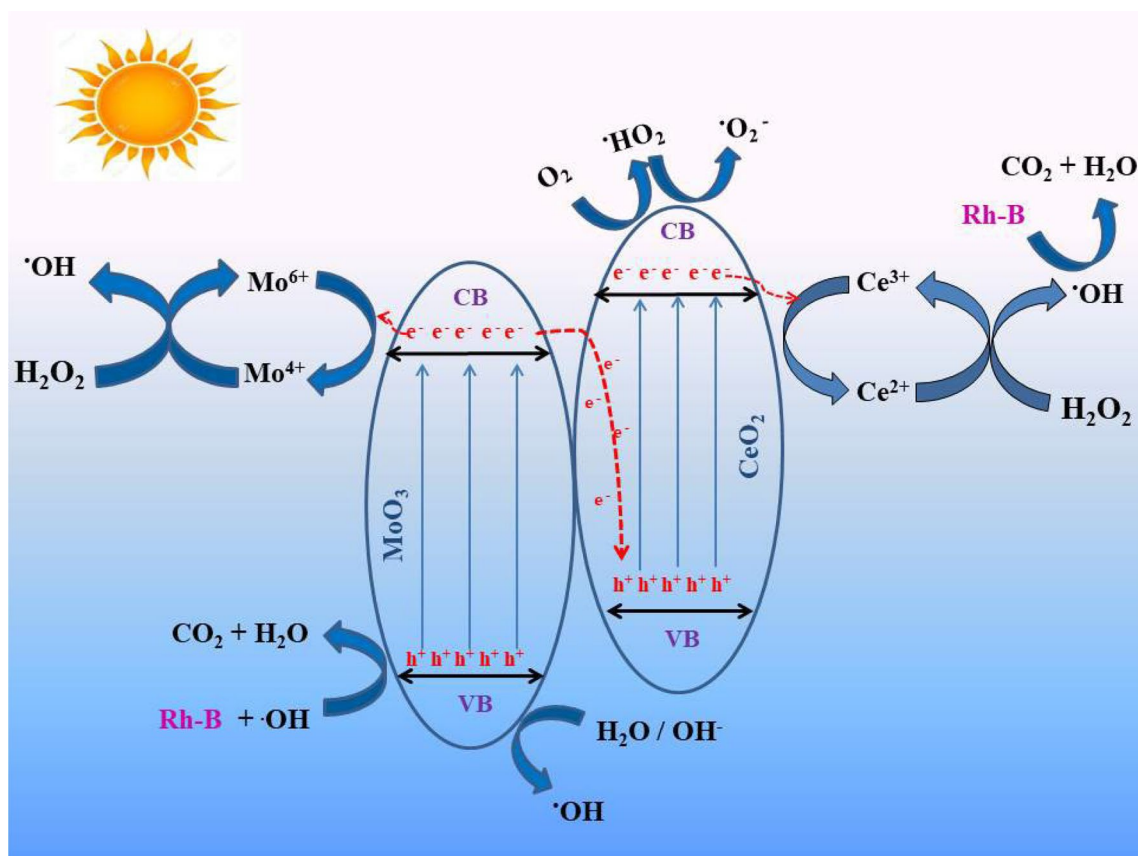
✉ Madhukar Navgire
navgireme@gmail.com

¹ New Arts, Commerce and Science College, (Autonomous),
Ahmednagar, Maharashtra PIN-414001, India

² Department of Chemistry, Nowgong College (Autonomous),
Nagaon, Assam 782001, India

³ Jijamata College of Science and Arts, Bhende,
Dnyaneshwarnagar, Ahmednagar, Maharashtra PIN-414605,
India

Graphical abstract



Keywords CeO₂-MoO₃ · Nanocomposite · Photo-Fenton · Rhodamine-B · Sol-gel · Ultrasonic

Introduction

In the last few decades, we have witnessed rapid changes in the world we live in, including increased urbanization and human population growth. Consequently, ever-increasing scarcity of clean water and environmental contamination has become a fundamental problem worldwide. (Yang et al. 2013), (Getahun 2022), (Gogoi et al. 2017). One reason for this contrast is the increasing number of textile industries, which have become an ingrained part of the industry's effluent, releasing contaminants directly into water resources. The consumption of this contaminated dyestuff-laden water has adverse health effects such as skin and eye infections, breathing problems, allergic reactions and central nervous system disorders. (Singha et al. 2021), (Rauf and Ashraf 2009), (Karri, Ravindran and Dehghani 2021). With regard to, photo-Fenton catalyst has been proposed as an eco-friendly approach and a challenging

technique for researchers to boot pollutants from water and air via the possible oxidation of organic pollutants into non-toxic CO₂ and H₂O (Jo and Tayade 2014).

Photo irradiation of the synthesized semiconductor photo catalytic material ejects electron from valence band to the conduction band and this ejected mobile electrons are used for various catalytic reactions like dye degradation and organic transformation reactions. And this ejected photons having the energy in between 1.8 and 3.1 eV in visible region (Lu et al. 2021), (Navgire and Lande 2017). So fabrication of nanocomposite material which is operating in visible light is the innovative idea for researchers.

The molybdenum oxide is the earlier investigated photocatalyst ergo of its not only high photocatalytic activity but also of its low cost, low toxicity and good thermal and chemical stability. It shows band gap energy of 3.1 eV which is very high and limits its applications in

UV region only which is of only 5% in solar radiations (Kamoun et al. 2016). To surmount this problem doping of some impurities may leads to reduce its band gap energy and overcoming its limitations in visible region (95% of solar radiations) also. For that purpose, some metal oxides from lanthanide series will be doped on MoO_3 material which has unique applications in visible light region for photo-Fenton degradation reactions and similarly it shows luminescent properties due to f-f transitions of electrons in their partially filled f orbitals and fully filled $5s^2$ and $5p^6$ shells (López-Pacheco et al. 2022), (Cerrato et al. 2022).

Inner transition metal oxides like cerium oxide (ceria) material consist of high concentration of oxygen vacancies and these acts as a source for oxidation reactions due to variable stable + II, + III and + IV oxidation states, it takes place on the surface which is helpful for its catalytic activities (Lawrence et al. 2011), (Li et al. 2009). This nanocomposite material not only shows high oxygen storage capacity but also oxygen mobility and strong interaction with the supported metal shows synergistic applications to degrade the organic pollutants (Saranya et al. 2014), (Bui et al. 2021). Recent literature work reported on ceria-supported metal oxides shows application in various fields such as catalyst in organic reactions, photocatalysts as well as Fenton catalyst in the degradation of toxic waste, electrocatalyst, etc. (Sudarsanam, Singh, and Kalbande 2022), (Qamar et al. 2023), (Abdulwahab, Khan, and Jennings 2023), (Ravula et al. 2024), (Gogoi et al. 2023), (Bandalla et al. 2022), (Sudarsanam et al. 2015). The compounds containing MoO_3 and CeO_2 has great promising and challenging nanocomposite material which shows an exciting applications in various fields such as for catalytic activities for hydrocarbon oxidation, hydro-desulphurization, sensing applications and photocatalytic applications also (Allam et al. 2021), (Liu et al. 2018), (Li et al. 2009), (Shadidi et al. 2022), (Navgire et al. 2016).

To overcome this problem, here we reported the fabrication of desired cerium oxide doped molybdenum oxide nanocomposite material by using ultrasonic wave-assisted sol–gel synthetic route. The effect of doping of inner transition metal oxide modifies the properties of molybdenum trioxide and shows better photo-Fenton efficiency towards the degradation of pollutants in textile wastewater as well as in the degradation of organic dyes.

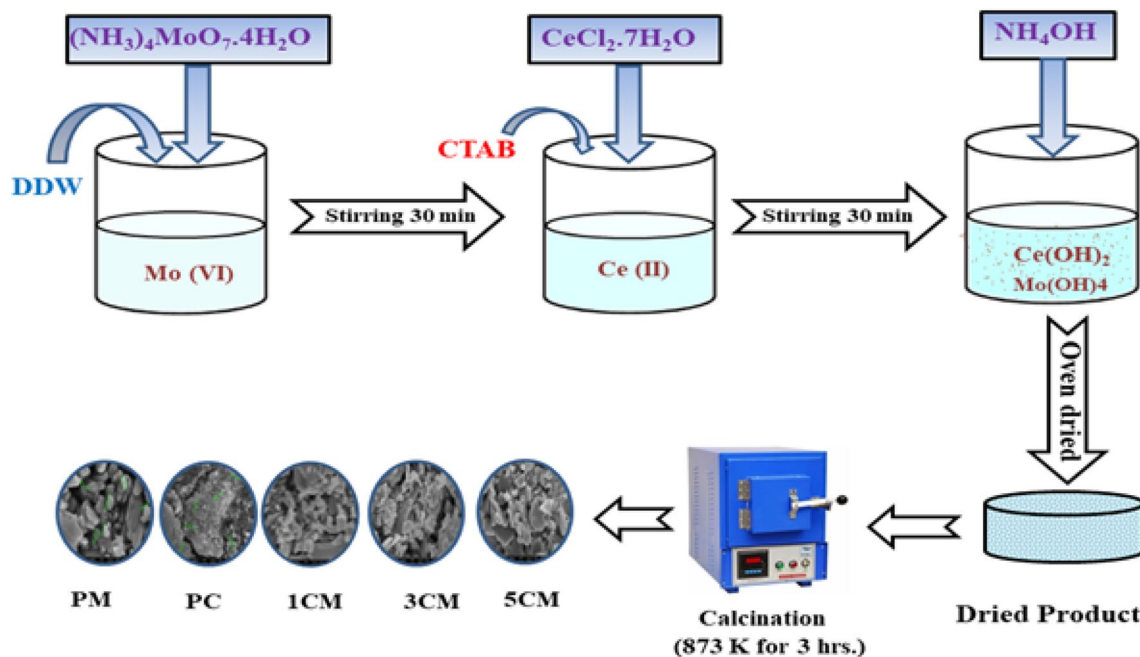
Experimental section

Materials

Precursor materials used for the synthesis of MoO_3 are AR grade Ammonium molybdate tetrahydrate $(\text{NH}_3)_4\text{MoO}_7 \cdot 4\text{H}_2\text{O}$ (99.3%) as well as dopant material AR grade cerous chloride heptahydrate $\text{CeCl}_2 \cdot 7\text{H}_2\text{O}$ (98.5%) was obtained from Loba chemie pvt. Ltd., surfactant AR grade cetyltrimethyl ammonium bromide ($\text{C}_{19}\text{H}_{42}\text{BrN}$), Rhodamine-B ($\text{C}_{28}\text{H}_{31}\text{ClN}_2\text{O}_3$), hydrogen peroxide (H_2O_2) was obtained from Research Lab fine industries and used as it is. Similarly, the solvents ammonia solution (NH_4OH) and double distilled water were used. The information regarding the grade, purity and source company of each chemical used are reported in tabular form, and it was included it in the supplementary material (Table S1).

Synthesis of CeO_2 -doped MoO_3 nanocomposite

The ultrasonic wave-assisted sol–gel method was used for synthesis of MoO_3 nanocomposite with varying percentages of CeO_2 doping (1, 3 and 5%). The calculated mole % of cerous chloride heptahydrate was added to an aqueous solution made by dissolving 8.53 g of ammonium molybdate tetrahydrate in 60 ml of double distilled water (DDW). And after that, 0.1 g of CTAB was added to enhance the surface morphology of nanocomposites. This aqueous solution was kept near about 30 min at the speed of 350 rpm at room temperature with continuous magnetic stirring. The resultant clear solution was then ultra-sonicated with sonicator (Ultrasonics Labline 6.5 L) for 30 min to obtain sol. In the sol, 15 ml NH_4OH has been added drop by drop to get gel of molybdenum hydroxide. With continuous stirring for 4 h, the clear solution converted into milky precipitate of molybdenum hydroxide. The precipitate obtained was filtered and dry it in an oven for 6 h at 353 K. The dried powder material were grinded in mortar and pestle then kept it in a muffle furnace for 873 K for 3 h for complete oxide formation. The obtained nanocomposite was named as 1CM, 3CM and 5CM, respectively. By using same method, we synthesized MoO_3 and CeO_2 . The schematics of detailed procedure are as follows...



Schematic Representation of the nanocomposite formation process.

Photo-Fenton activity experiment

The Fenton activities of the prepared catalysts (CeO_2 , MoO_3 , 1CM, 3CM and 5CM) were tested for the degradation of RhB in visible light, i.e. under direct sunlight. In this photo-Fenton activity, Rhodamine-B (1 ppm, 40 ml) dye was firstly placed in dark for 30–35 min to obtain adsorption–desorption equilibrium. Then, dye solution (under different conditions of catalyst concentration, pH and H_2O_2 concentration) were placed in direct sunlight for 2 h. During experimental trial, after every 15 min absorbance of dye solution was monitored using a double beam AU-2701 UV–Visible spectrophotometer. The following steps are used to select the optimal nanocomposite catalyst that yields the best outcomes with a minimum amount of economy:

- (1) Selection of better nanocomposite catalyst,
- (2) Nanocomposite catalyst amount variation for selected catalyst (15, 25, 35 mg/1 ppm/40 ml),
- (3) Effect of concentration of oxidizing agent (H_2O_2 : 5 mM, 10 mM and 15 mM),
- (4) Effect of pH variation (pH: 3, 5, 7, 9 and 11),
- (5) Reuse and Recycle of the selected nanocomposite photocatalyst.

Nanocomposite photocatalyst was recycled and reused to determine its successive reusability runs with slight decrease in degradation efficiency was observed. And lastly photo-Fenton percentage was calculated by using following equation:

$$\% \text{ Degradation} = \left[\frac{(A_0 - A_t)}{A_0} \right] \times 100\% \text{ where, } A_0: \text{ absorbance at time 'zero', } A_t: \text{ absorbance at time 't'.$$

Results and discussion

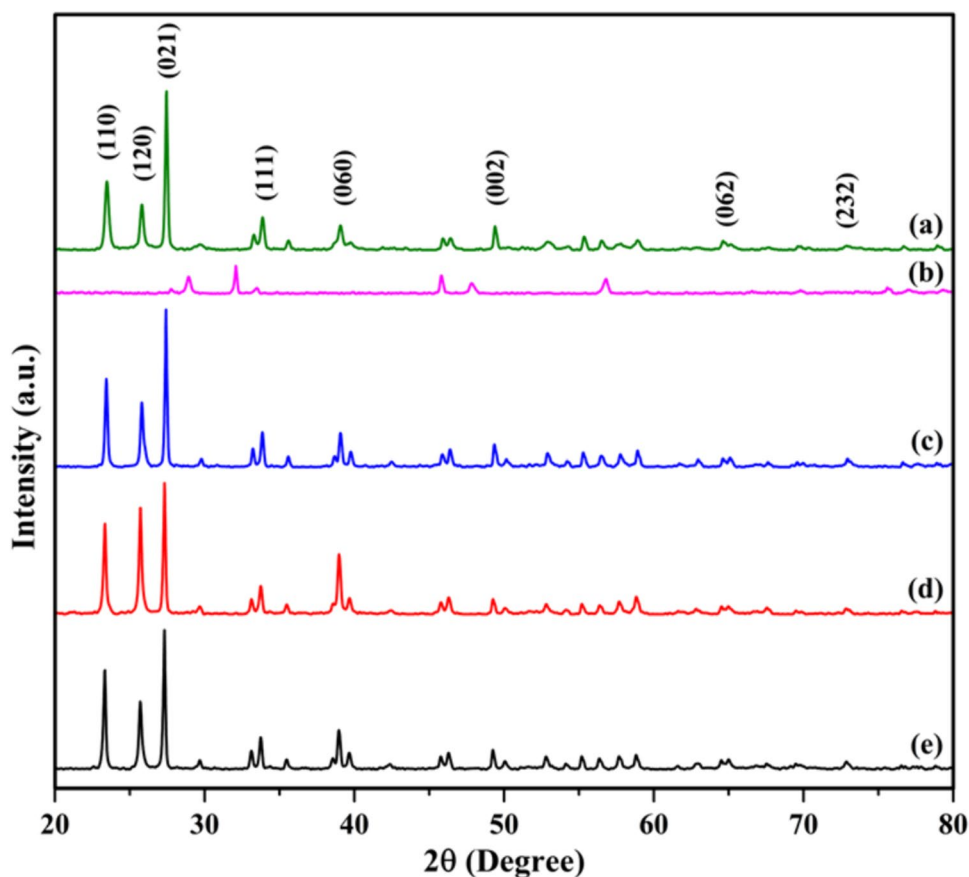
Characterization of synthesized nanocomposite

Prepared nanocomposite material were analysed with the help of XRD, Raman, FT-IR FE-SEM, EDAX, HR-TEM, BET, XPS and UV-DRS measurements to obtained crystalline size, surface morphology, surface area, particle size, structural and optical properties, etc. of synthesized nanocomposite material.

X-ray diffraction spectroscopy (XRD) analysis

The crystallite size and phase of the synthesized nanocomposite were analysed by powder XRD diffractometer (Rigaku MiniFlex 600) using $\text{Cu K}\alpha$ ($\lambda = 0.15418 \text{ nm}$) radiations at 40 kV and 15 mA. For all the sample nanocomposite X-ray diffraction measured in the 2θ range between 10 and 80° with a scan rate of 0.12 per second and a step size of 0.02.

Fig. 1 XRD analysis of **a** MoO₃, **b** CeO₂, **c** 1CM, **d** 3CM and **e** 5CM



XRD study gives the phase symmetry and crystallinity of the calcined nanocomposite material which is shown in Fig. 1.

The peaks shown at $2(\theta)^\circ = 23.4, 25.8, 27.4, 33.8, 39.07, 49.3, 64.6$ and 72.9 designates hkl values to the plane (110), (120), (021), (111), (060), (002), (062) and (232). All the XRD peaks confirm the orthorhombic structure of MoO₃ (JCPDS 76–1003) which is shown in Fig. 1a (Kihlberg, L. 1963). The sharp and highly intense peaks suggest that the as-prepared nanocomposite material is highly crystalline in nature. Figure 1b shows highly intense peaks of CeO₂, at $2(\theta)^\circ = 28.93, 32.08, 45.80, 47.82$ and 56.81 which corresponds to $(-221), (-234), (-117), (210)$ and (-443) crystal planes, respectively with monoclinic structure of crystalline CeO₂ (JCPDS 32–0196) (Sørensen 1976).

Similarly, the Fig. 1c–e shows diffraction peaks for 1CM, 3CM and 5CM, respectively. Addition of CeO₂ in MoO₃ causes only slight shifting of 2θ diffraction peaks and no separate peaks were observed for CeO₂ in nanocomposite. The average crystal size (D) of the synthesized nanocomposite material can be calculated by Debye–Scherrer equation (B. Cullity 1978):

$$D = k\lambda / (\beta \cos \theta).$$

Where, λ = wavelength (0.154 nm), β = FWHM (Full Width at Half Maximum of more intense peak), $K = 0.89$ and θ = diffraction angle. The observed crystallite size for CeO₂, MoO₃ and CeO₂-doped MoO₃ is in the range of 45–52 nm which is shown in Table (S2).

Raman spectroscopy analysis

Figure 2 represents the Raman spectra of MoO₃, CeO₂ and 5CM nanocomposite material characterized by using Invia Raman microscope (Renishaw make). According to group theory, the optical vibrational modes of MoO₃ with D_{2h} symmetry were predicted as follows. $\Gamma = 8A_g + 8B_{1g} + 4B_{2g} + 4B_{3g} + 4A_u + 3B_{1u} + 7B_{2u} + 7B_{3u}$. Raman active modes are A_g, B_{1g}, B_{2g} and B_{3g} while A_u is an inactive mode. The B_{1u}, B_{2u} and B_{3u} are only infrared-active. The Raman modes of A_g, B_{1g}, B_{2g}, B_{3g} and A_u shows peaks at 83, 95, 115, 126 and 151 cm⁻¹. $\delta O1 = M = O1$ wagging shows B_{3g} mode at 286 cm⁻¹. Raman mode for CeO₂ shows peak at 463.21 cm⁻¹ which gives the symmetric bending vibration of the O atoms around each cation of CeO₂ with F_{2g} symmetry (Gogoi and Sarma 2017), (Y. Lee et al. 2011) CeO₂-doped MoO₃ nanocomposite has little shifted to 468 cm⁻¹.

Fig. 2 Raman analysis of **a** MoO₃, **b** CeO₂ and **c** 5CM

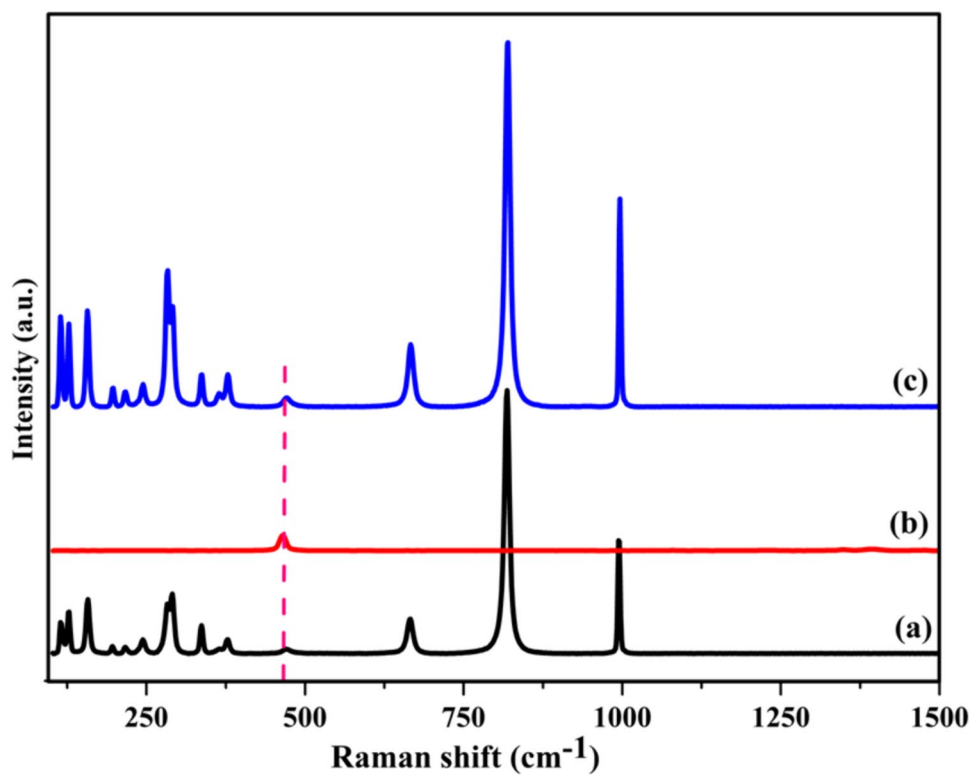
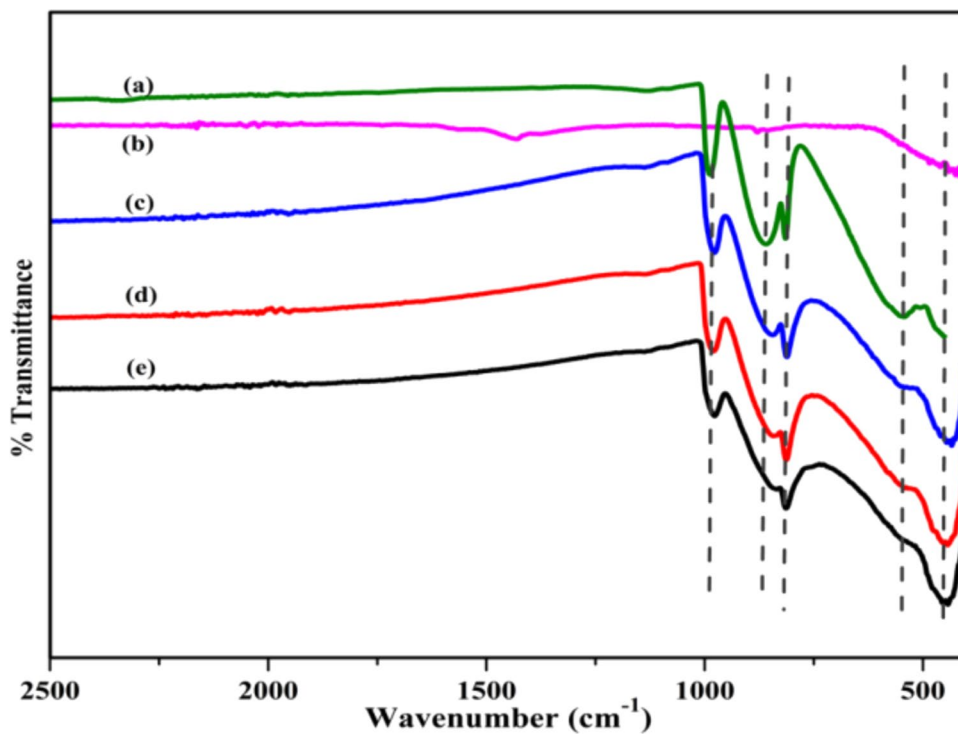


Fig. 3 FT-IR analysis of **a** MoO₃, **b** CeO₂, **c** 1CM, **d** 3CM and **e** 5CM



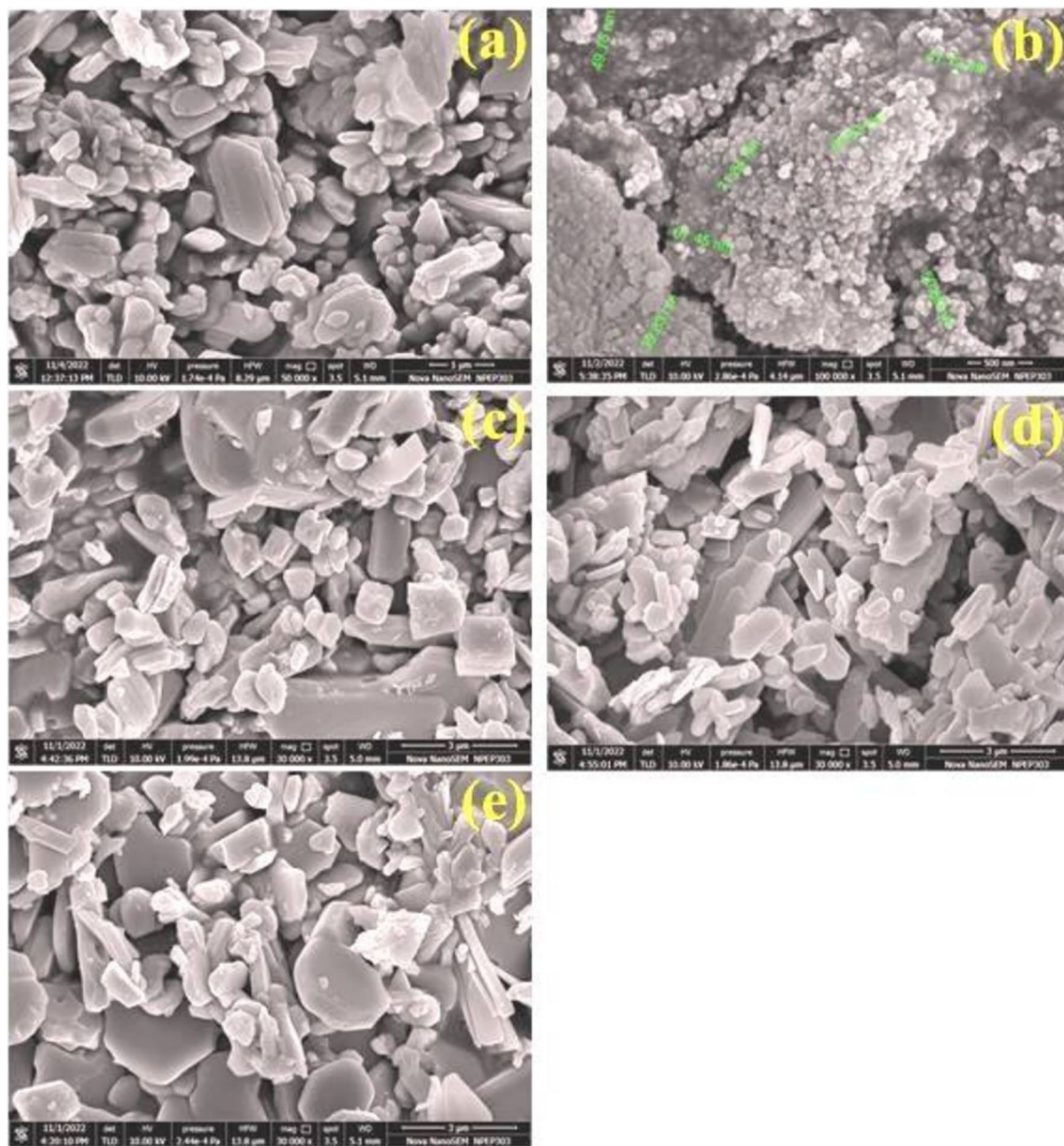


Fig. 4 FE-SEM images of **a** MoO₃, **b** CeO₂ and **c** 1CM, **d** 3CM and **e** 5CM nanocomposite material

Fourier-transform infrared (FT-IR) study

The Fourier-transform infrared (FT-IR) analysis was performed on Perkin Elmer spectrum two instruments in the range of 400–4000 cm⁻¹ wavenumber which is shown in Fig. 3. Peaks observed at 549, 813, 862, 990 cm⁻¹ which indicates Mo–O vibration, Mo–O bending, Mo–O–Mo stretching and Mo=O stretching vibrations respectively for MoO₃ nanomaterial shown in Fig. 3a (Tariq et al. 2020), (Zhao et al. 2010). While due to increases in per cent doping of CeO₂ causes gradual decrease in intensity of peak at

862 cm⁻¹ mainly due to breaking of Mo–O–Mo bond and formation of Mo–O–Ce bond (Li et al. 2009).

Field emission scanning electron microscopy (FE-SEM) images and EDS analysis

Surface morphology of prepared nanocomposite was analysed by FE-SEM (FEI Nova NanoSEM 450) instrument. Figure 4a, b indicates the images of highly crystalline nano flakes of the MoO₃ sheets whereas spherical-shaped morphology for CeO₂, respectively (NAVGIRE et al. 2011),

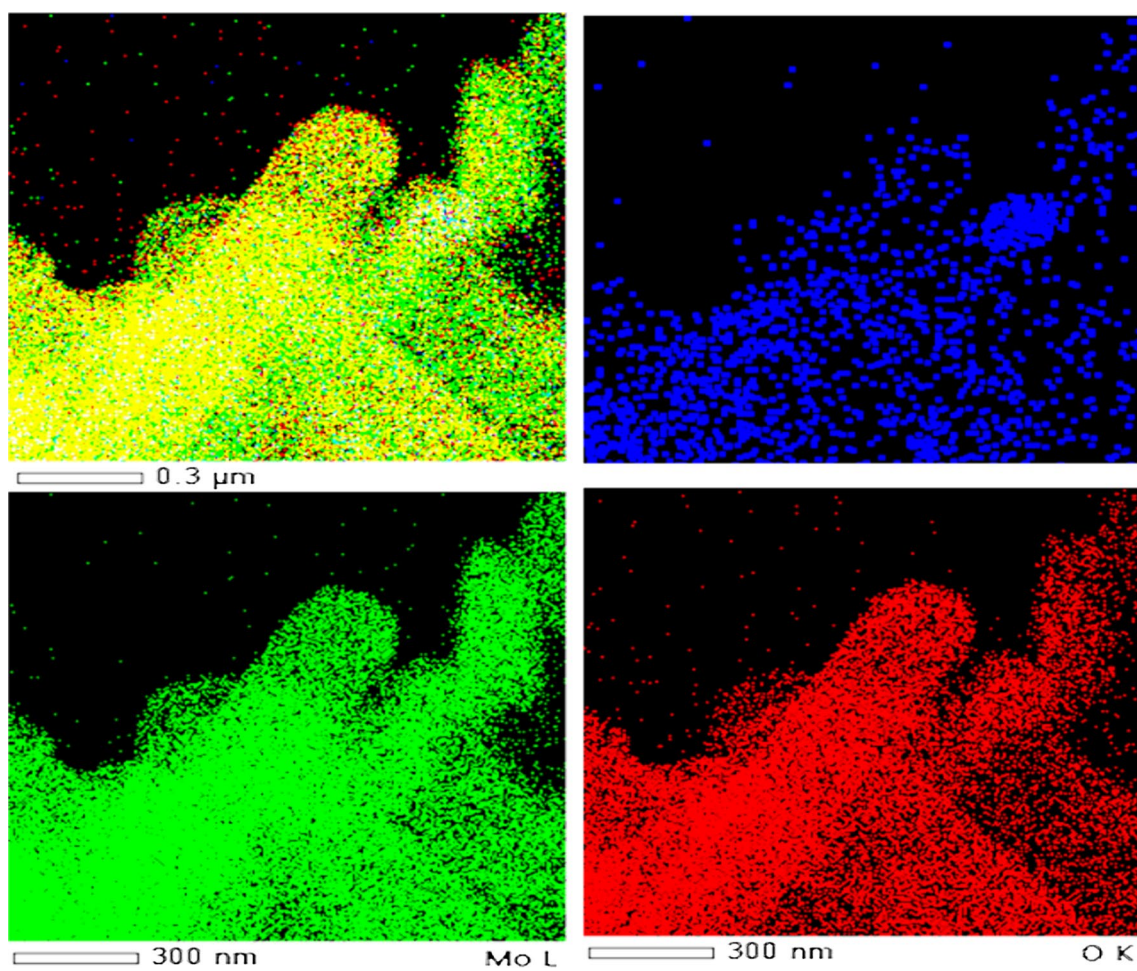


Fig. 5 EDAX mapping of $\text{CeO}_2\text{-MoO}_3$ nanocomposite material

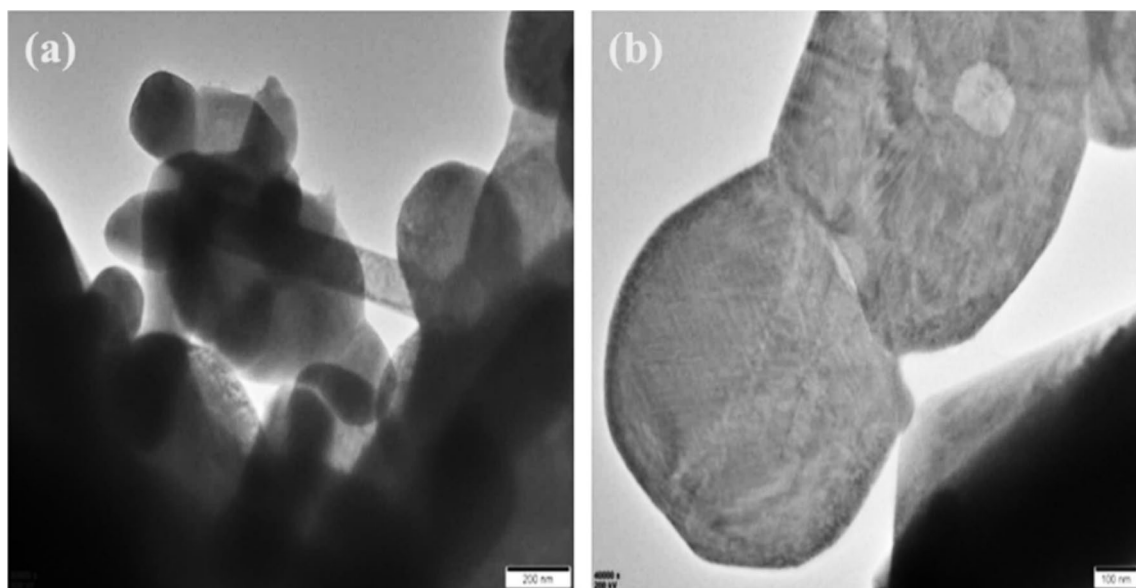


Fig. 6 HR-TEM Images of $\text{CeO}_2\text{-MoO}_3$ nanocomposite material

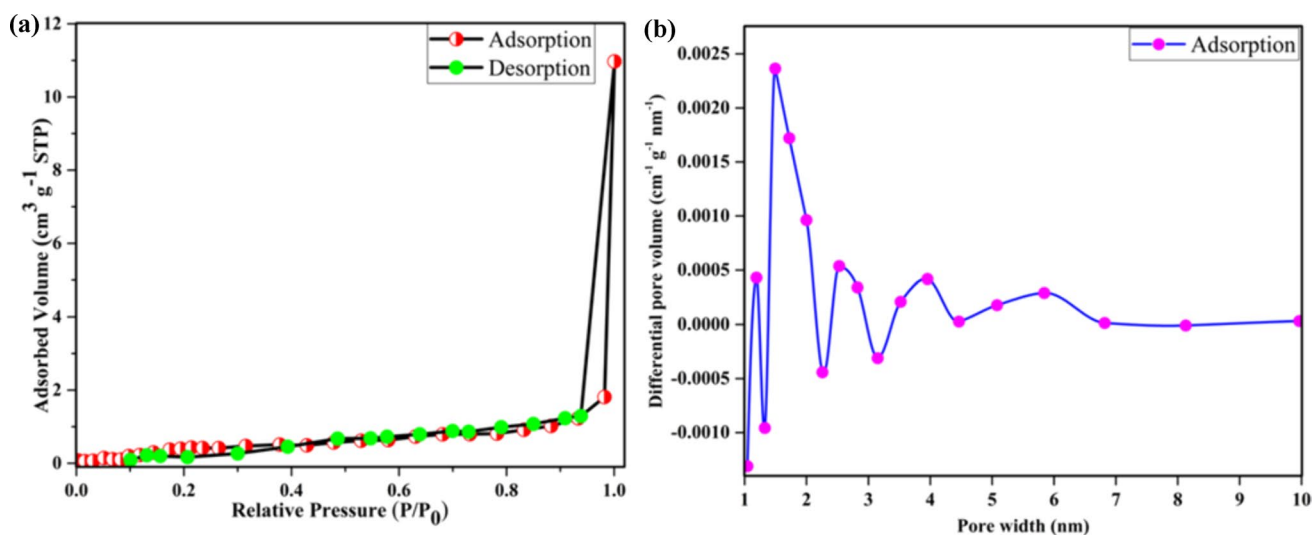


Fig. 7 BET Plot of a N_2 adsorption–desorption isotherm and b Pore size distribution of 5CM composites

(Suresh, Ponnuswamy, and Mariappan 2014). The addition of CeO_2 on MoO_3 results a change in crystallite size and the deposition of Ce on the surface of MoO_3 nanosheets which is shown Fig. 4c–e. These premise that the calcined material is made up of mixed metal oxides is well-supported by the above results.

Chemical composition of the synthesized nanocomposite was investigated by using elemental mapping EDAX analysis and further distribution of dopant elements in the nanocomposite materials was shown in Fig. 5. Results shows that well distinct peaks of Ce, Mo and O, which confirms the formation of CeO_2 - MoO_3 nanocomposite which is in good agreement with the results obtained from XPS analysis.

High-resolution transmission electron microscopy

The internal morphology of the synthesized nanocomposite were analysed with the help of the HR-TEM analysis carried out on a FEI make FEG T20 instrument which is shown in Fig. 6. HR-TEM analysis proves the formation of highly crystalline nanosheets of CeO_2 - MoO_3 nanocomposite and it clearly shows that incorporation of ceria onto the MoO_3 surface which corresponds to SEM results.

Brunauer–Emmett–Teller (BET) analysis

The specific surface area and pore diameter of the synthesized nanocomposite material was successfully calculated with the help of the Brunauer–Emmett–Teller (BET) measurements (BELSORP MAX II). Figure 7a shows that N_2 adsorption–desorption isotherm and observed specific surface area for 5CM nanocomposite material was 2.1201

m^2g^{-1} and BJH (Barrett–Joyner–Halenda) plot shown in Fig. 7b with average pore diameter is 16.503 nm so it concludes that synthesized nanocomposite material is in mesoporous in nature.

X-ray Photoelectron spectroscopy (XPS) analysis

The XPS spectrum of synthesized CeO_2 - MoO_3 nanocomposite were analysed on ThermoScientific NEXA Surface analyser instrument and it shows Mo 3d, Ce 3d and O 1s deconvoluted spectra as shown in Fig. 8a–d. Figure 8a will be exhibits full scan of XPS of synthesized material. The peaks of Fig. 8b for the Ce 3d were asymmetric and broad. The binding energies at 900.3, 904.25 eV belongs to Ce $3d_{3/2}$ and 886 and 882.1 eV belong to Ce $3d_{5/2}$ of Ce^{3+} ions (Li et al. 2009). Thus, Ce^{3+} ions were homogeneously incorporated in the MoO_3 lattice. XPS spectrum for Mo $3d_{3/2}$ and Mo $3d_{5/2}$ exhibits doublet peaks at 235.7 and 232.6 eV, respectively. It was indicated that Mo element existed mainly as the chemical state of Mo^{6+} and after reaction, the XPS spectrum of Mo 3d (Fig. 8c) kept intact compared to that before the reaction, which shows that Mo element existed mainly as the chemical state of Mo^{6+} and was remains same during the reaction. The O 1s peaks (Fig. 8d) appeared at approximately 530.5 eV, due to the O bond present in MoO_3 , Ce–O bond, Mo–O–Ce bond and surface-attached OH^- group (Y. Z. Wang et al. 2017).

UV–visible diffused reflectance spectra (UV-DRS) analysis

The band gap energy studies were done with the help UV-DRS analysis (UV 3092 LABINDIA Analyticals) on UV/VIS

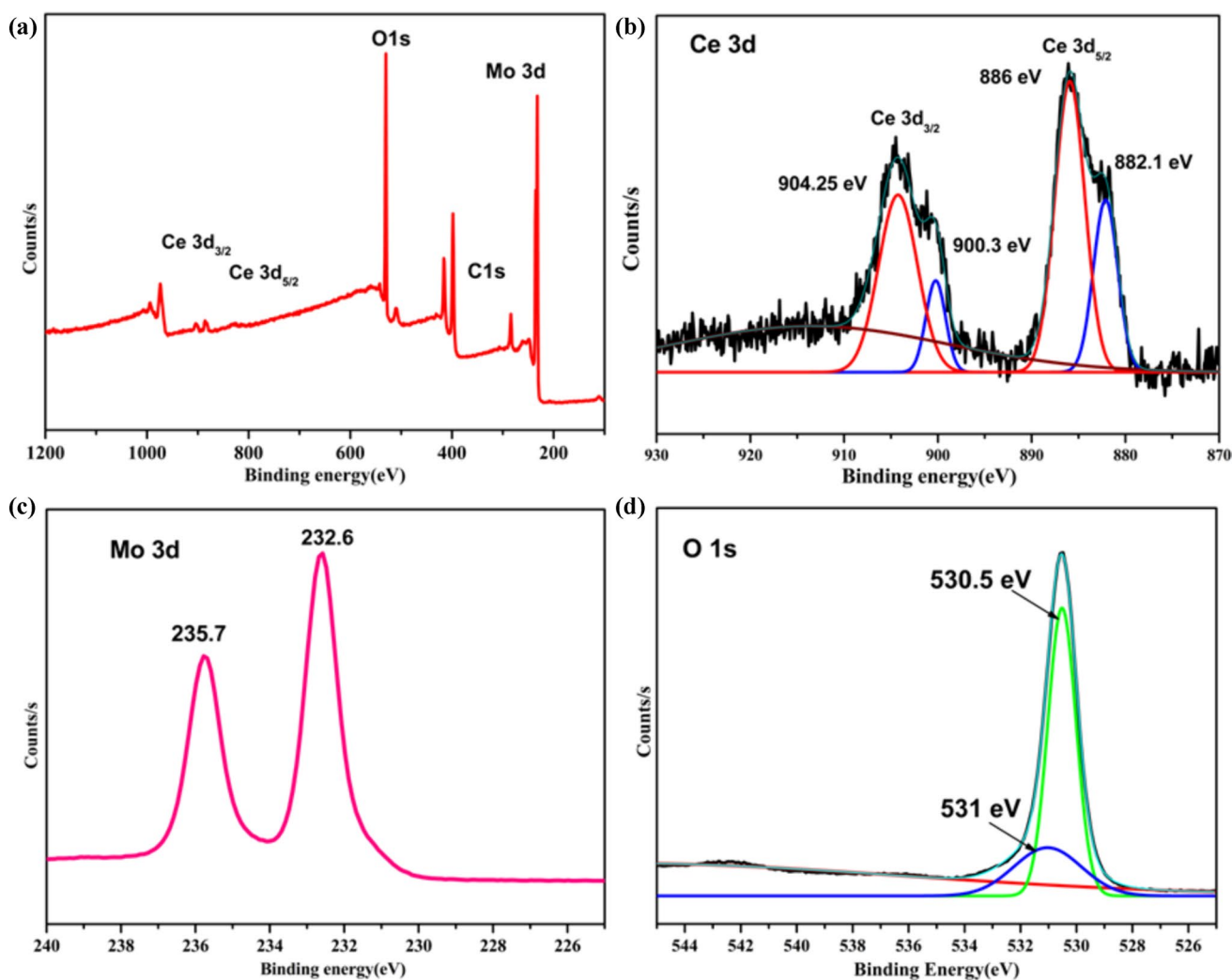


Fig. 8 XPS Spectra of $\text{CeO}_2\text{-MoO}_3$ nanocomposite material, a Overlay, b Ce 3d, c Mo 3d, d O 1 s

spectrophotometer. The band gap energy was calculated with the help of the plot of $(F(R)h\nu)^{1/2}(\text{eV}(\text{cm}^{-1}))^{1/2}$ versus Energy ($h\nu$) and it shows band gap energy of 3.05 eV for MoO_3 which is shown in Figure S1a and Figure S1b shows, interestingly reduce in band gap energy to 2.47 eV for 5CM nanocomposite material which promising its photocatalytic applications in visible region (Makuła, Pacia and Macyk 2018), (Chithambararaj et al. 2015).

Activity study

Selection of nanocomposite catalyst

The photocatalytic dye degradation experiment were carried out for various nanocomposite like CeO_2 , MoO_3 , 1CM, 3CM and 5CM with 25 mg catalyst with 40 ml/1 ppm Rh-B dye solution and 10 mM/ 2 ml H_2O_2 for 120 min. And absorbance was recorded for all above-mentioned nanocomposite catalyst for every 15 min and % degradation was calculated

which is shown in Fig. 9. From that figure 45.32%, 41.87%, 83.03%, 94.68% and 95.36% degradation is observed for MoO_3 , CeO_2 , 1CM, 3CM and 5CM, respectively in 120 min. It concludes that maximum photo-Fenton degradation of Rh-B dye is observed for 5CM nanocomposite material, and this catalyst is selected for further analysis.

Effect of amount of nanocomposite photo-Fenton catalyst

At various amounts (15 mg, 25 mg and 35 mg) of selected 5CM nanocomposite catalyst, photo-Fenton degradation was monitored and Fig. 10; which shows that 86.66%, 95.36% and 91.36% degradation is observed for 15 mg, 25 mg and 35 mg, respectively for 5CM nanocomposite catalytic materials. It summarizes that by increasing the photocatalyst amount from 15 to 25 mg degradation per cent increases because of more active sites are created on catalyst surface and enhances the increase in absorption of light (i.e. photons) and after specific

Fig. 9 Effects of different photo-Fenton catalyst for degradation of Rh-B at $\lambda_{\max} = 550$ nm (Reaction conditions: $[\text{H}_2\text{O}_2] = 10$ mM, $[\text{Rh-B}] = 1$ ppm, $[\text{Catalyst}] = 25$ mg, $\text{pH} = 7$ at room temperature)

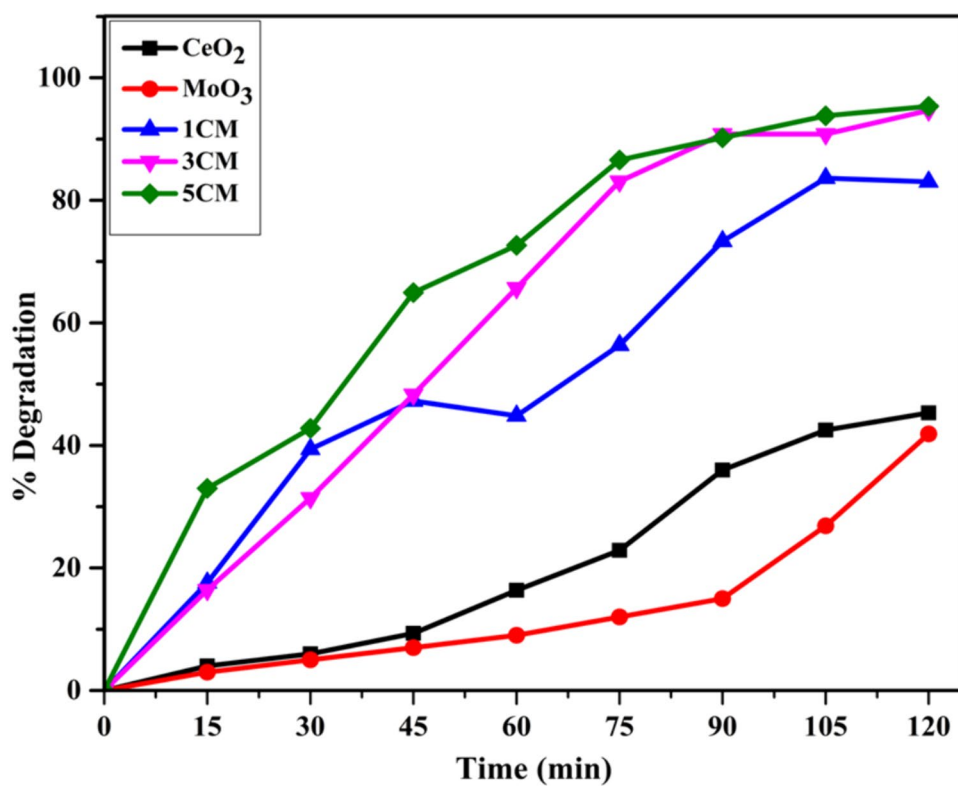


Fig. 10 Effects of 5CM catalyst concentration (15 mg, 25 mg and 35 mg) for photo-Fenton degradation of Rh-B at $\lambda_{\max} = 550$ nm (Reaction conditions: $[\text{H}_2\text{O}_2] = 10$ mM, $[\text{Rh-B}] = 1$ ppm, $\text{pH} = 7$ at room temperature)

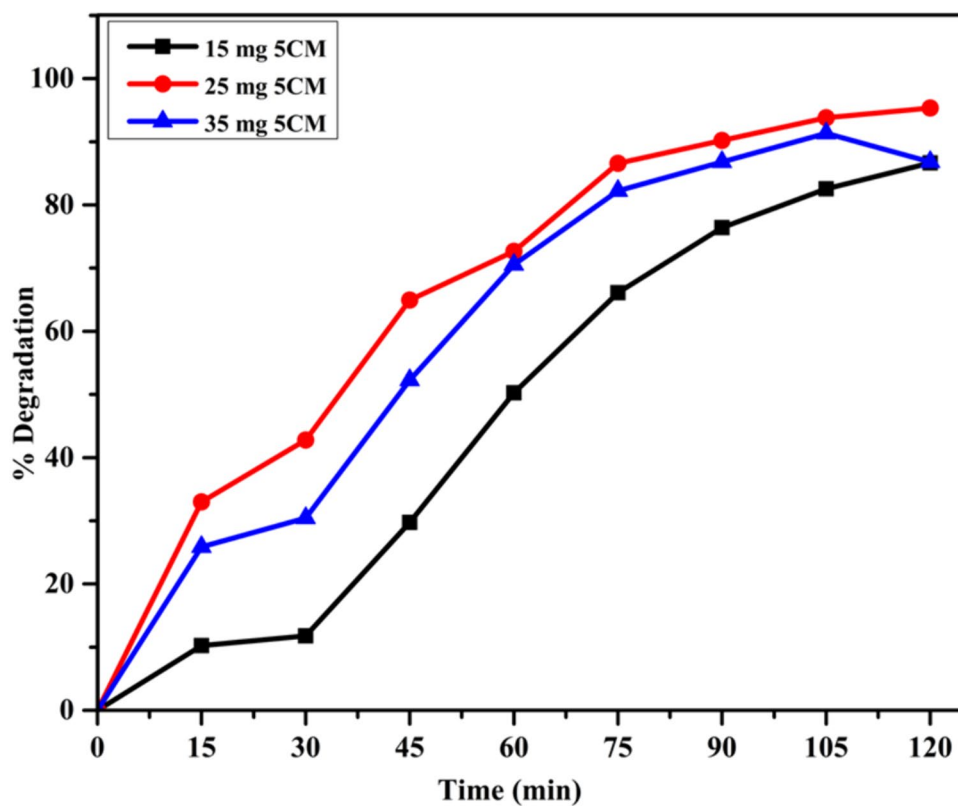


Fig. 11 Effects of H_2O_2 doses for degradation of Rh-B at $\lambda_{\text{max}} = 550 \text{ nm}$ (Reaction conditions: $[\text{Rh-B}] = 1 \text{ ppm}$, $[\text{Catalyst: 5CM}] = 25 \text{ mg}$, $\text{pH} = 7$ at room temperature)

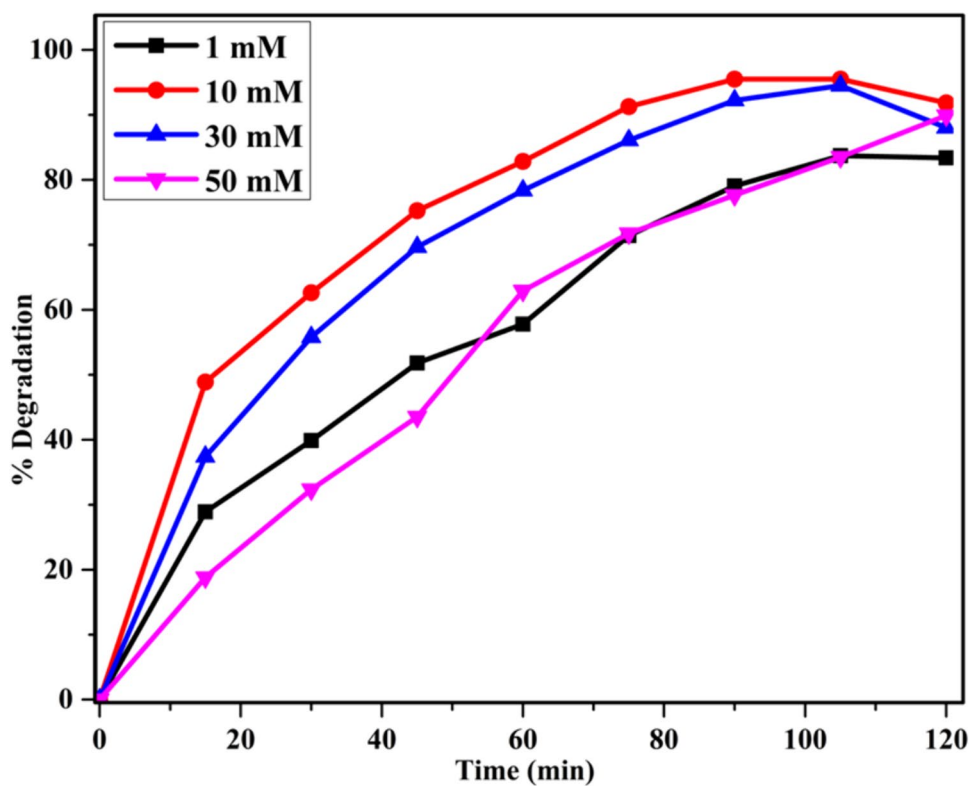
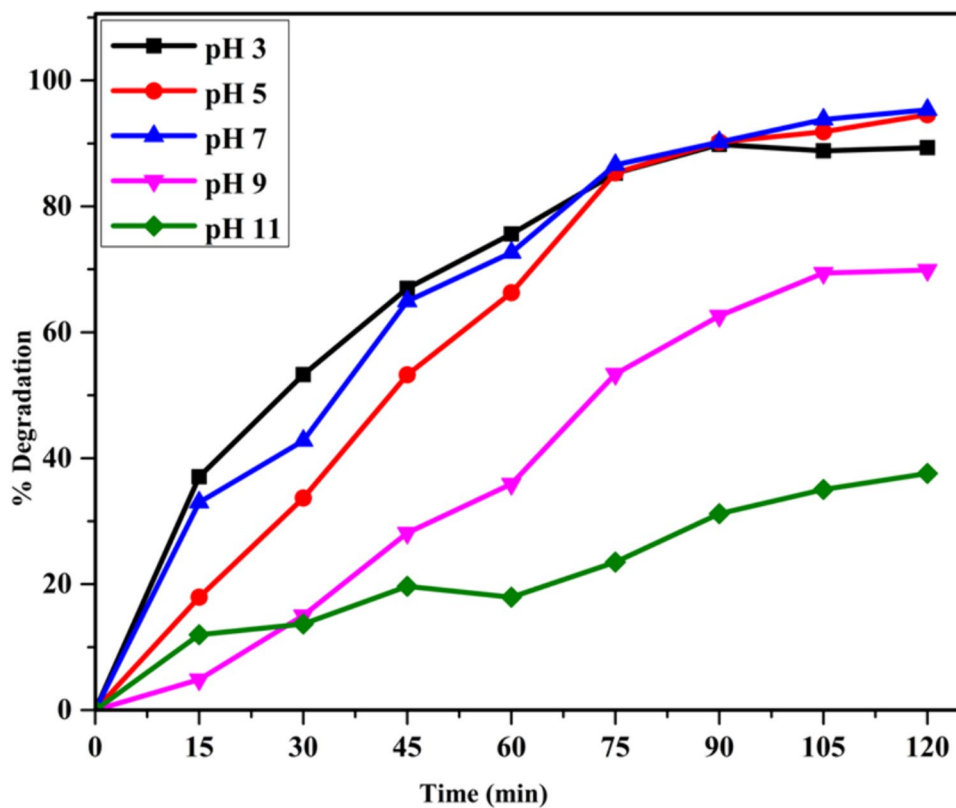


Fig. 12 Effects of pH for degradation of Rh-B at $\lambda_{\text{max}} = 550 \text{ nm}$ (Reaction conditions: $[\text{H}_2\text{O}_2] = 10 \text{ mM}$, $[\text{Rh-B}] = 1 \text{ ppm}$, $[\text{Catalyst: 5CM}] = 25 \text{ mg}$, at room temperature)



amount of catalyst (i.e. from 25 to 35 mg) degradation percentage decreases gradually due to scattering of light to catalytic surface (Kuriechen et al. 2011), (Ahmad Rafaie et al. 2021). Hence it concludes that 25 mg is an effective amount of nanocomposite catalyst for maximum photo-Fenton degradation.

Effect of concentration of H_2O_2

Concentration of H_2O_2 is varied, i.e. 2 ml of 1 mM, 10 mM, 30 mM and 50 mM for optimization of good amount of oxidant for Rh-B dye degradation. Figure 11 shows that by increasing the H_2O_2 concentration, the % degradation increases to a certain amount and then it again decreases. The increase in degradation rate is observed because catalyst is reducing the electron-hole pair recombination rate (W. H. Lee et al. 2015), (Haji, Benstaali, and Al-Bastaki 2011). So it concludes that better degradation is observed at 10 mM H_2O_2 concentration for 5CM nanocomposite catalyst.

Effect of pH variation

Photocatalytic dye degradation activity of Rh-B dye was studied at various pH values (3–11). Selection of optimum pH is necessary to avoid the loss of excess amount of nanocomposite photocatalyst and it is also important to enhance photo-Fenton by absorbing visible light. Figure 12 shows that effect of various pH range with percentage degradation of 89.34, 94.56, 95.36, 69.9 and 37.6% for pH 3, 5,

Table 1 Turn over number and turnover frequency of different nanocomposite materials

Sr. No.	Catalyst	Active sites (moles)	TON	TOF(min^{-1})
1	MoO ₃	1.7407×10^{-4}	20.08	0.17
2	CeO ₂	1.4525×10^{-4}	26.05	0.22
3	1CM	1.7339×10^{-4}	39.98	0.33
4	3CM	1.7283×10^{-4}	40.11	0.34
5	5CM	1.7226×10^{-4}	46.22	0.38

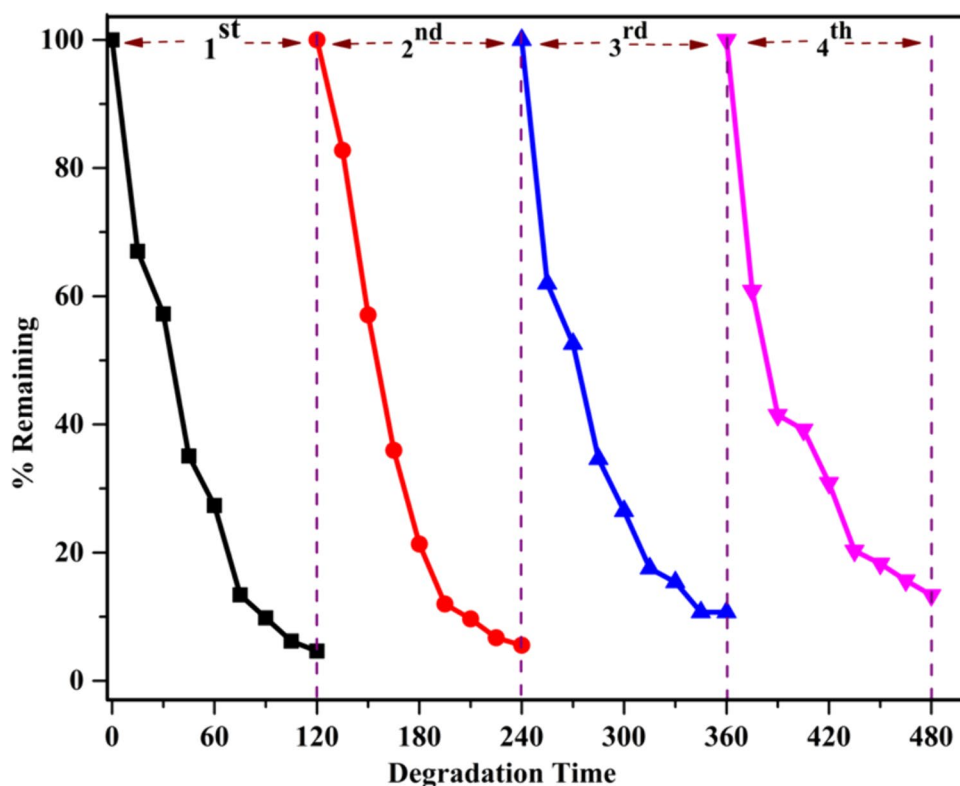
Bold indicates 5CM nanocomposite shows superior catalytic performance as well as shows higher TOF and TON

7, 9 and 11, respectively, and it shows that by increasing pH, degradation efficiency increases up to neutral pH 7 and then decreases in basic condition at pH 9 and pH 11 due to change in structure of Rh-B in basic condition (Guo et al. 2021), (Nguyen Thi Thu et al. 2016). Maximum degradation was done at neutral (pH-7) condition by increasing the active sites on catalytic surface (Xue et al. 2019).

Recycle and reuse of the selected nanocomposite catalyst

Stability of catalyst was performed via recycle and reusability of the catalytic materials. For reuse of the 5CM; photo-Fenton degradation experiment were repeated with several times with Rh-B dye and at the end of the each cycle the nanocomposite material was washed with double distilled water and

Fig. 13 Recycle and reuse of 5CM catalyst for degradation of Rh-B at $\lambda_{\text{max}} = 550 \text{ nm}$ (Reaction conditions: $[H_2O_2] = 10 \text{ mM}$, $[Rh-B] = 1 \text{ ppm}$, [Catalyst: 5CM] = 25 mg, pH = 7 at room temperature)

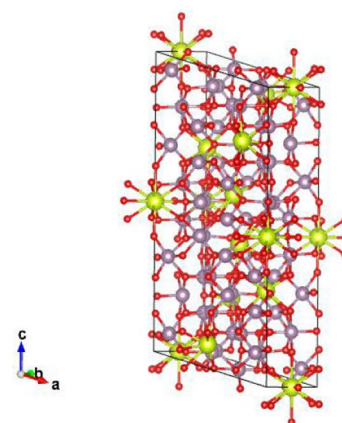
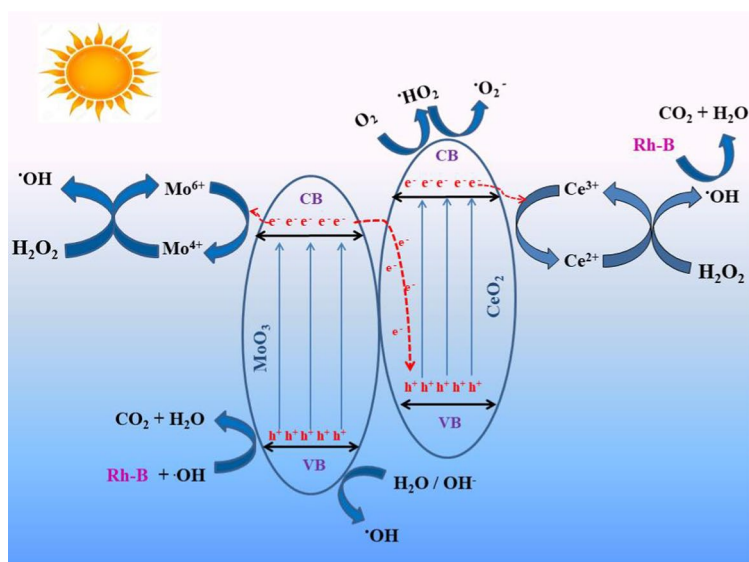


recovered with help of centrifuge machine and further used for next run. Figure 13 concludes that photo-Fenton activity for Rh-B dye degradation in first run is 95.36% and slightly decreases to 94.44, 89.31 and 86.63% for 2nd, 3rd and 4th run, respectively, and it shows that 5CM nanocomposite material is stable during photo-Fenton experiment.

Turnover number (TON) and turnover frequency (TOF)

Active sites present on catalyst are effective sites for especial heterogeneous catalytic reaction. The turnover number and turnover frequency apprise the catalytic performance of synthesized nanocomposite photocatalyst (Gomathi Devi and Shyamala 2018), (Nick Serpone et al. 1993), (N. Serpone et al. 2000).

Plausible mechanism of photo-Fenton reaction



Crystal structure of $\text{CeO}_2\text{-MoO}_3$ nanocomposite

The photo-Fenton degradation activity for Rh-B dye were performed with visible light, i.e. in direct sunlight ($\lambda > 400$ nm), 10 mM H_2O_2 and simultaneous incorporation of 5CM catalyst. Continuous generation of OH radicals takes place by reacting H_2O_2 with catalyst surface and in this step Ce (III) is converted into Ce (IV) and Mo (IV) to Mo (VI) (Zhu et al. 2021), (Xing et al. 2020). These generated OH radicals reacts with Rh-B dye and further decomposes into CO_2 and H_2O which were analysed by decrease in intensity of absorbance peak at $\lambda_{\text{max}} = 550$ nm in 120 min was observed.

Calculation of turnover number

$\text{TON} = \text{Number of moles of Rh-B degraded} / \text{Number of moles of catalyst taken.}$

Calculation of turnover frequency

$\text{TOF} = \text{TON} / \text{time (min)}$

Calculated active sites, turnover number and turnover frequency of synthesized nanocomposite catalyst is summarized in Table 1:

The MoO_3 , 1CM and 3CM shows higher active sites; these active sites are acts as electron-hole recombination centres so it shows lower TOF and TON reflecting its lower catalytic performance. While, 5CM nanocomposite is also shows higher turnover frequency, i.e. 0.38 and 46.22 turnover number which attributing its superior catalytic performance.

Kinetic study

Kinetic study of photo-Fenton degradation of Rh-B dye was done. The experimental data fitted well to the pseudo-first-order kinetics which is shown in Fig. 14 and rate constant (k) was calculated by using following formula.

$$\ln(C/C_0) = -kt \text{ where, 'k' is rate constant (min}^{-1}\text{).}$$

'C' are concentration of Rh-B dye at time 't'

' C_0 ' is initial concentration of Rh-B dye, i.e. (adsorption-desorption equilibrium time).

Fig. 14 Kinetic study of photo-Fenton degradation of Rh-B at $\lambda_{\max} = 550$ nm (Reaction conditions: $[H_2O_2] = 10$ mM, $[Rh-B] = 1$ ppm, $[Catalyst: 5CM] = 25$ mg, $pH = 7$ at room temperature)

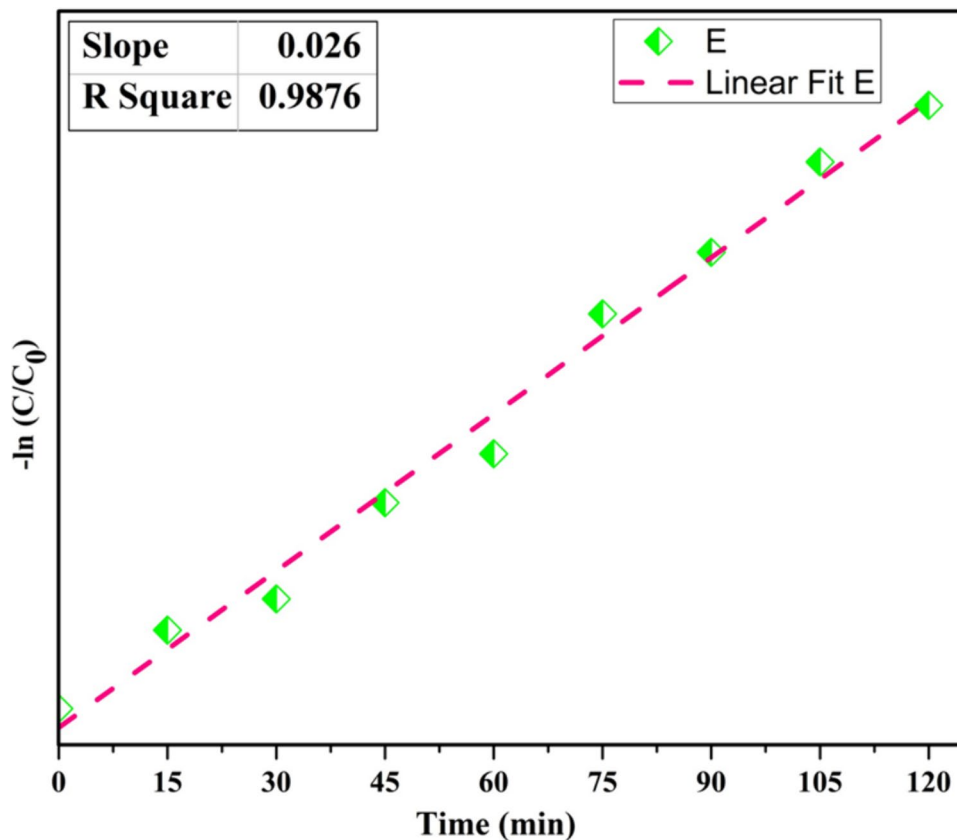
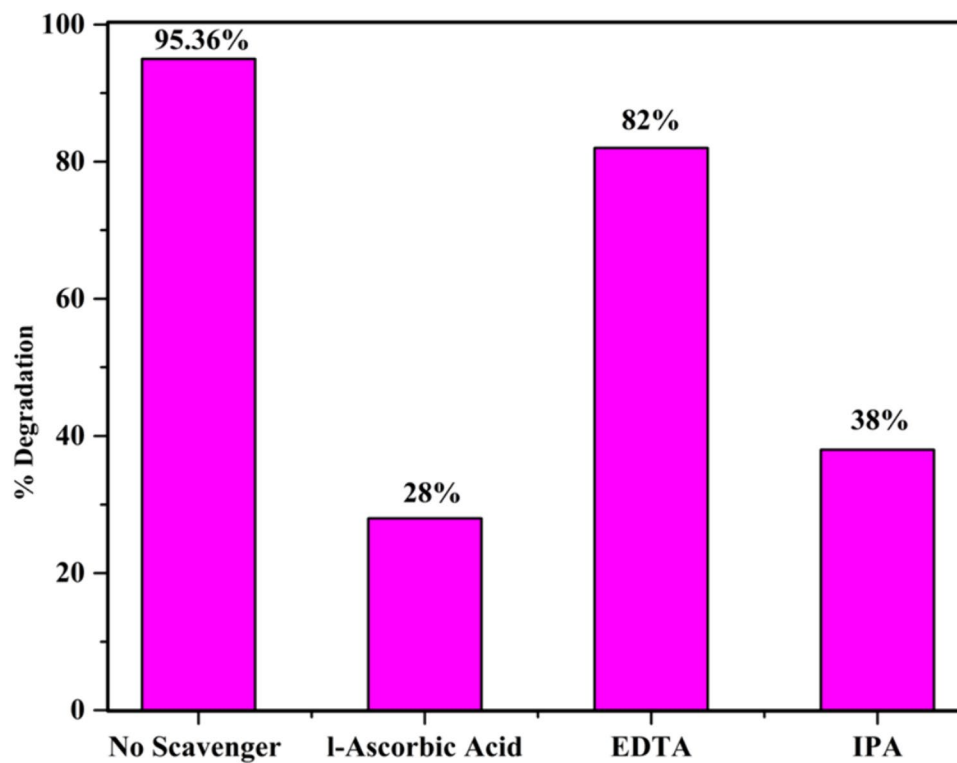


Fig. 15 Effects of scavengers (isopropyl alcohol, EDTA and l-Ascorbic acid) on degradation of Rh-B at $\lambda_{\max} = 550$ nm (Reaction conditions: $[H_2O_2] = 10$ mM, $[Rh-B] = 1$ ppm, $[Catalyst] = 25$ mg, $pH = 7$ at room temperature)



and calculated rate constant value was $2.85 \times 10^{-2} \text{ min}^{-1}$. The correlation coefficient (R^2) indicates that the experimental data could be a fitted linearly and adequately.

Scavenger study

To study the mechanism of CeO₂ doped MoO₃ nanocomposite material, radicals and holes trapping experiments was carried out for determination of which reactive species plays the active role for photo-Fenton degradation mechanism of 5CM nanocomposite catalyst for Rh-B dye. For study of scavenger activity, L-ascorbic acid, Ethylene diamine tetraacetic acid (Na₂-EDTA) and Isopropyl alcohol (IPA) are used for quenching the O²⁻, holes and OH, respectively. The scavengers (10 mM) were added into Rh-B dye solution prior to addition of nanocomposite photocatalyst. After two hours of degradation experiment the results shows that, photocatalytic degradation was observed to be only 28% after addition of L-Ascorbic acid and 38% for IPA and in case of EDTA it is only slightly decreased to 82% this whole part concludes that O²⁻ and OH plays the crucial role in photo-Fenton degradation of Rh-B and holes plays the subsidiary role which is shown in Fig. 15 (Van Doorslaer et al. 2012), (Naraginti et al. 2016).

Table (S3) gives the comparison of synthesis method and photocatalytic performance of the 5CM nanocomposite material (Selvakumar and Palanivel 2022), (Zhang et al. 2019), (Tariq et al. 2020), (Chen et al. 2020), (Pascariu et al. 2020), (Rahman et al. 2021), (Magdalane et al. 2019), (Kuźniarska-Biernacka et al. 2021), (B.-Y. Wang et al. 2022). The majority of work that has been reported has numerous limitations, including the synthesis method, high precursor costs, Rh-B degradation limited to the UV region, a specific pH, the maximum amount of photocatalyst and degradation time. However, this 5CM nanocomposite photocatalyst, which was synthesized using a simple sol-gel method with less economy and exhibits maximum photo-Fenton degradation, i.e. 95.36% in the direct sunlight with only 25 mg of photocatalyst at different pH range.

Conclusion

In this report the synthesis of CeO₂-MoO₃ nanocomposite material is synthesized with help of ultrasonic wave assisted sol-gel synthesis technique. Nanocomposite materials were characterized by different analytical techniques and photo-Fenton degradation for Rh-B for various percentages CeO₂-MoO₃ were performed with variation study on amount of catalyst, H₂O₂ concentration, pH range were investigated. TOF and TON and scavenger study were performed. Finally

it concludes that 5CM is an excellent photo-Fenton catalyst (95.36% in 120 min) for degradation of Rh-B in visible (direct sunlight) region at neutral (pH-7) condition because of high crystallinity, surface morphology, less band gap energy, mesoporous nature and greater surface area of the photocatalyst and also shows best results for recovery and reuse of nanocomposite photocatalyst up to the 4th cycle.

Supplementary Information The online version contains supplementary material available at <https://doi.org/10.1007/s11696-024-03479-2>.

Acknowledgements The authors AD [Fellowship/2021-22/1042(227)] & AN [Fellowship/2021-22/1042(431)] are gratefully acknowledged to Mahatma Jyotiba Phule Research & Training Institute, Nagpur for awarding research fellowship. Authors are also thankful to Principals of New Arts, Commerce and Science College, Ahmednagar, Maharashtra, India; Nowgong College (Autonomous), Nagaon, Assam, India; Jijamata College of Science and Arts, Bhende, Maharashtra, India, for providing all the required facilities to carry out this work.

Declarations

Conflict of interest All authors hereby declared that, we have no conflicts of interest.

References

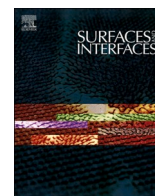
- Abdulwahab KO, Khan MM, Jennings JR (2023) Doped ceria nanomaterials: preparation, properties, and uses. *ACS Omega* 8(34):30802–30823. <https://doi.org/10.1021/acsomega.3c01199>
- Allam EA, El-Sharkawy RM, Gizawy MA, Mahmoud ME (2021) Assembly of CeO₂-MoO₃-SiO₂(CH₂)₃-(Alginate)₂ as a novel nanocomposite for removal of MnII/CrVI and 56Mn/51Cr radionuclides from water. *Mater Chem Phys* 262:124278
- Bandalla S et al (2022) Highly efficient solvent-free oxidation of cyclohexanol to cyclohexanone over nanocrystalline CaO-MgO binary metal-oxide catalysts. *Mol Catal* 533:112759
- Bui HT et al (2021) Oxygen vacancy engineering of cerium oxide for the selective photocatalytic oxidation of aromatic pollutants. *J Hazardous Mater* 404:123976
- Cerrato E, Gaggero E, Calza P, Paganini MC (2022) The role of cerium, europium and erbium doped TiO₂ photocatalysts in water treatment: a mini-review. *Chem Eng J Adv* 10:100268
- Chen J et al (2020) A high performance MoO₃@MoS₂ porous nanorods for adsorption and photodegradation of dye. *J Solid State Chem* 291:121652
- Chithambararaj A et al (2015) Band gap tuning of H-MoO₃ nanocrystals for efficient visible light photocatalytic activity against methylene blue dye. *J Nanosci Nanotechnol* 15(7):4913–4919
- Cullity B (1978) "No Title." *Elements of X-Ray Diffraction, 2nd edn.*
- Getahun YW et al (2022) Green synthesized superparamagnetic iron oxide nanoparticles for water treatment with alternative recyclability. *J Mol Liquids* 356:118983
- Gogoi A, Sarma KC (2017) Synthesis of the novel β-Cyclodextrin supported CeO₂ nanoparticles for the catalytic degradation of methylene blue in aqueous suspension. *Mater Chem Phys* 194:327–336. <https://doi.org/10.1016/j.matchemphys.2017.04.003>
- Gogoi A, Navgire M, Sarma KC, Gogoi P (2017) Novel highly stable β-cyclodextrin fullerene mixed valent Fe-metal framework for quick Fenton degradation of alizarin. *RSC Adv* 7(64):40371–40382. <https://doi.org/10.1039/C7RA06447K>

- Gogoi A et al (2023) Development of highly efficient heterogeneous Fe 3 O 4 -biochar nanocomposite as Fenton-like catalysts for degradation of fast green. *ChemistrySelect*. <https://doi.org/10.1002/slct.202302553>
- Gomathi Devi L, Shyamala R (2018) Photocatalytic activity of SnO 2 - α -Fe 2 O 3 composite mixtures: exploration of number of active sites, turnover number and turnover frequency. *Mater Chem Front* 2(4):796–806
- Guo Y et al (2021) Effect of PH on the catalytic degradation of rhodamine B by synthesized CDs/g-C 3 N 4 /Cu x O composites. *ACS Omega* 6(12):8119–8130. <https://doi.org/10.1021/acsomega.0c05915>
- Haji S, Benstaali B, Al-Bastaki N (2011) Degradation of methyl orange by UV/H₂O₂ advanced oxidation process. *Chem Eng J* 168(1):134–139
- Jo WK, Tayade RJ (2014) Recent developments in photocatalytic dye degradation upon irradiation with energy-efficient light emitting diodes. *Chin J Catal* 35(11):1781–1792
- Kamoun O, Boukhachem A, Amlouk M, Ammar S (2016) Physical study of Eu doped MoO₃ thin films. *J Alloy Compd* 687:595–603
- Karri RR, Ravindran G, Dehghani MH (2021) Wastewater—Sources, Toxicity, and Their Consequences to Human Health. In *Soft Computing Techniques in Solid Waste and Wastewater Management*, Elsevier, Amsterdam, pp 3–33
- Kihlborg L (1963) Least squares refinement of crystal structure of molybdenum trioxide. *Ark Kemi* 21:357–364
- Kuriechen SK, Murugesan S, Raj SP, Maruthamuthu P (2011) Visible light assisted photocatalytic mineralization of reactive red 180 using colloidal TiO₂ and oxone. *Chem Eng J* 174(2–3):530–538. <https://doi.org/10.1016/j.cej.2011.09.024>
- Kuźniarska-Biernacka I et al (2021) Evaluation of rhodamine B photocatalytic degradation over BaTiO₃-MnO₂ ceramic materials. *Materials* 14(12):3152
- Lawrence NJ et al (2011) Defect engineering in cubic cerium oxide nanostructures for catalytic oxidation. *Nano Lett* 11(7):2666–2671. <https://doi.org/10.1021/nl200722z>
- Lee Y et al (2011) Raman analysis of mode softening in nanoparticle CeO 2- δ and Au-CeO 2- δ during CO oxidation. *J Am Chem Soc* 133(33):12952–12955. <https://doi.org/10.1021/ja204479j>
- Lee WH, Lai CW, Hamid SBA (2015) One-step formation of WO₃-loaded TiO₂ nanotubes composite film for high photocatalytic performance. *Materials* 8(5):2139–2153
- Li W et al (2009) Fast catalytic degradation of organic dye with air and MoO₃: Ce nanofibers under room condition. *Appl Catal B* 92(3–4):333–340
- Liu C et al (2018) A high-performance flexible gas sensor based on self-assembled PANI-CeO₂ nanocomposite thin film for trace-level NH₃ detection at room temperature. *Sens Actuators b: Chem* 261:587–597
- López-Pacheco G et al (2022) Insight into the optical absorption and luminescent properties due to the presence of Pr⁴⁺ in Pr-Doped Y₂O₃. *J Lumin* 242:118596
- Lu C et al (2021) photocatalytic reduction of nitroaromatics into anilines using CeO₂-TiO₂ nanocomposite. *Mol Cat* 513:111775
- Magdalane CM et al (2019) Improved photocatalytic decomposition of aqueous rhodamine-B by solar light illuminated hierarchical yttria nanosphere decorated ceria nanorods. *J Mater Res Technol* 8(3):2898–2909
- Małak P, Pacia M, Macyk W (2018) How to correctly determine the band gap energy of modified semiconductor photocatalysts based on UV–Vis spectra. *J Phys Chem Lett* 9(23):6814–6817. <https://doi.org/10.1021/acs.jpcclett.8b02892>
- Naraginti S et al (2016) Mechanistic study of visible light driven photocatalytic degradation of EDC 17 α -ethinyl estradiol and azo dye acid black-52: phytotoxicity assessment of intermediates. *RSC Adv* 6(90):87246–87257
- Navgire ME, Lande MK (2017) Effect of nanocrystalline composite fullerene-doped MoO 3-TiO 2 material on photoassisted degradation of alizarin red S dye. *Inorg Nano-Metal Chem* 47(3):320–327. <https://doi.org/10.1080/15533174.2016.1186055>
- Navgire ME et al (2011) Effect of poly(ethylene glycol) surfactant on carbon-doped MoO 3 nanocomposite materials and its photocatalytic activity. *Bull Mater Sci* 34(3):535–541. <https://doi.org/10.1007/s12034-011-0108-2>
- Navgire ME et al (2016) β -cyclodextrin supported MoO 3 -CeO 2 nanocomposite material as an efficient heterogeneous catalyst for degradation of phenol. *RSC Adv* 6(34):28679–28687
- Nguyen Thi Thu T et al (2016) Synthesis, Characterisation, and Effect of PH on Degradation of Dyes of Copper-Doped TiO 2. *J Exp Nanosci* 11(3):226–238. <https://doi.org/10.1080/17458080.2015.1053541>
- Pascariu P et al (2020) New electrospun ZnO:MoO₃ nanostructures: preparation, characterization and photocatalytic performance. *Nanomaterials* 10(8):1476
- Qamar MT et al (2023) Transition metal doped CeO₂ for photocatalytic removal of 2-chlorophenol in the exposure of indoor white light and antifungal activity. *Front Chem*. <https://doi.org/10.3389/fchem.2023.1126171/full>
- Rafaie HA et al (2021) Photocatalytic Degradation of Methylene Blue Dye Solution Using Different Amount of ZnO as a Photocatalyst. *Science Letters* 15(1):1
- Rahman A et al (2021) Superior photodegradation and antibacterial activity of R-GO supported ternary nanocomposite of doped transition metal compounds. *Ceram Int* 47(10):14569–14578
- Rauf MA, Salman Ashraf S (2009) Fundamental principles and application of heterogeneous photocatalytic degradation of dyes in solution. *Chem Eng J* 151(1–3):10–18
- Ravula M et al (2024) Development of molybdenum oxide promoted CeO 2 -SiO 2 mixed-oxide catalyst for efficient catalytic oxidation of benzylamine to N-benzylidenebenzylamine. *ChemistrySelect*. <https://doi.org/10.1002/slct.202304534>
- Saranya J et al (2014) Cobalt-doped cerium oxide nanoparticles: enhanced photocatalytic activity under UV and visible light irradiation. *Mater Sci Semicond Proc* 26:218–224
- Selvakumar G, Palanivel C (2022) A study on synthesis, characterization and catalytic applications of MoO₃-ZnO nanocompositematerial. *Mater Sci Energy Technol* 5:36–44
- Serpone N et al (1993) On the usage of turnover numbers and quantum yields in heterogeneous photocatalysis. *J Photochem Photobiol a: Chem* 73(1):11–16
- Serpone N, Salinaro A, Emeline A, Ryabchuk V (2000) Turnovers and photocatalysis. *J Photochem Photobiol a: Chem* 130(2–3):83–94
- Shadidi B, Alizade HHA, Najafi G (2022) Performance and exergy analysis of a diesel engine run on petrodiesel and biodiesel blends containing mixed CeO₂ and MoO₃ nanocatalyst. *Biofuels* 13(1):1–7. <https://doi.org/10.1080/17597269.2020.1779976>
- Singha K, Pandit P, Maity S, Sharma SR (2021) Harmful Environmental Effects for Textile Chemical Dyeing Practice. *Green Chemistry for Sustainable Textiles*. Elsevier, Amsterdam, pp 153–164
- Sørensen OT (1976) Thermodynamic studies of the phase relationships of nonstoichiometric cerium oxides at higher temperatures. *J Solid State Chem* 18(3):217–233. [https://doi.org/10.1016/0022-4596\(76\)90099-2](https://doi.org/10.1016/0022-4596(76)90099-2)
- Sudarsanam P et al (2015) highly efficient cerium dioxide nanocubebased catalysts for low temperature diesel soot oxidation: the cooperative effect of cerium- and cobalt-oxides. *Catal Sci Technol* 5(7):3496–3500

- Sudarsanam P, Singh N, Kalbande PN (2022) Shape-controlled nanostructured MoO₃/CeO₂ catalysts for selective cyclohexene epoxidation. *Catal Commun* 164:106433
- Suresh R, Ponnuswamy V, Mariappan R (2014) The role of oxidizing agents in the structural and morphological properties of CeO₂ nanoparticles. *Mater Sci Semicond Proc* 21:45–51
- Tariq N et al (2020) Synthesis and characterization of MoO₃/CoFe₂O₄ nanocomposite for photocatalytic applications. *Ceram Int* 46(13):21596–21603
- Van Doorslaer X et al (2012) TiO₂ Mediated heterogeneous photocatalytic degradation of moxifloxacin: operational variables and scavenger study. *Appl Catal b: Environ* 111–112:150–156
- Wang BY et al (2022) Fabricating hollow, multishell CeO₂ microspheres for enhanced photocatalytic degradation of RhB under visible light. *J Mater Res* 37(5):1070–1082. <https://doi.org/10.1557/s43578-022-00513-5>
- Wang YZ et al (2017) Effect of Calcination Temperature on the Microstructure and Antimicrobial Activity of Boron and Cerium Co-Doped Titania Nanomaterials. 7857 (November).
- Xing W et al (2020) A-FeOOH–MoO₃ nanorod for effective photo-Fenton degradation of dyes and antibiotics at a wide range of pH. *Chem Asian J* 15(17):2749–2753. <https://doi.org/10.1002/asia.202000668>
- Xue S et al (2019) Direct Z-scheme charge transfer in heterostructured MoO₃/g-C₃N₄ photocatalysts and the generation of active radicals in photocatalytic dye degradations. *Environ Pollut* 250:338–345
- Yang Y, Zhang C, Hu Z (2013) Impact of metallic and metal oxide nanoparticles on wastewater treatment and anaerobic digestion. *Environ. Sci: Proc Impacts* 15(1):39–48
- Zhang X et al (2019) Construction of a few-layer g-C₃N₄/α-MoO₃ nanoneedles all-solid-state z-scheme photocatalytic system for photocatalytic degradation. *J Energy Chem* 29:65–71
- Zhao S, Li J, Wang L, Wang X (2010) Degradation of rhodamine B and safranin-T by MoO₃:CeO₂ nanofibers and air using a continuous mode. *CLEAN—Soil, Air, Water* 38(3):268–274. <https://doi.org/10.1002/clen.200900249>
- Zhu Y et al (2021) Direct Z-scheme Fe₂(MoO₄)₃/MoO₃ heterojunction: photo-Fenton reaction and mechanism comprehension. *J Alloy Compd* 873:159830

Publisher's Note Springer Nature remains neutral with regard to jurisdictional claims in published maps and institutional affiliations.

Springer Nature or its licensor (e.g. a society or other partner) holds exclusive rights to this article under a publishing agreement with the author(s) or other rightsholder(s); author self-archiving of the accepted manuscript version of this article is solely governed by the terms of such publishing agreement and applicable law.



Room temperature acetone sensing activity of β -Cyclodextrin coated $\text{MoO}_3\text{-ZrO}_2$ nanocomposite

Akash Nagare^a, Amol Dhadage^a, Pravin Ghare^d, Ramesh Naval^d, Anil Athare^a, Parikshit Gogoi^b, Ashok Datir^c, Madhukar Navgire^{d,*}

^a New Arts, Commerce and Science College (Autonomous), Ahmednagar, Maharashtra, 414001, India

^b Department of Chemistry, Nowgong College (Autonomous), Nagaon, Assam, 782001, India

^c Agasti Arts, Commerce and Dadasaheb Rupwate Science College, Akole, Maharashtra, 422601, India

^d Jijamata College of Science and Arts, Bhende Bk, Maharashtra, 414605, India

ARTICLE INFO

Keywords:

β -Cyclodextrin
Gas sensor
Hexagonal
Room temperature
 $\text{Zr}(\text{MoO}_4)_2$
VOC detection

ABSTRACT

Globalization and industrialization have significantly exacerbated air pollution, particularly through the increase of volatile organic compounds (VOCs), posing severe health risks and environmental challenges. The need for effective VOC detection at room temperature has become critical. In this study, a novel β -Cyclodextrin coated $\text{MoO}_3\text{-ZrO}_2$ nanocomposite was synthesized via a cost-effective simple sol-gel method, aiming to enhance gas sensing properties. Comprehensive characterization techniques confirmed the formation of a mesoporous $\text{Zr}(\text{MoO}_4)_2$ structure with smooth surface morphology in the β -CD coated nanocomposites. The gas sensing performance of the synthesized nanocomposites was rigorously evaluated, with results indicating significantly improved activity towards VOCs at room temperature (30 °C). Among the various compositions, the 10 % β -CD coated $\text{MoO}_3\text{-ZrO}_2$ nanocomposite exhibited the highest response to acetone vapors, with a remarkable sensing response of 1.97, a fast response time of 30 s, and a recovery time of 39 s at a concentration of 100 ppm. This enhanced performance is attributed to the increased specific surface area, the porous structure of the composite, and the unique interaction between acetone and the active sites on the nanocomposite. Comparative analysis with literature-reported materials highlights the superior room-temperature performance of the 10 β MZ nanocomposite, positioning it as a promising material for VOC detection in environmental monitoring and industrial safety. This study not only advances the understanding of composite gas sensors but also introduces a novel catalytic system with enhanced gas sensing activity, selectivity, and reusability.

1. Introduction

The contemporary human population is dealing with a serious problem of air pollution, primarily attributed to volatile organic compounds (VOCs), which exert harmful effects on their health. Environmental air pollution is a primary factor contributing to respiratory diseases. Volatile organic compounds (VOCs) are organic compounds that readily evaporate at room temperature. The compounds acetone, ethanol, methanol, toluene, and n-butanol find widespread use in several applications such as varnishes, cleaning products, cosmetics, air fresheners, printers, and chemical synthesis [1]. Acetone, a colourless, highly volatile, combustible, and hazardous chemical, is used in numerous industries and laboratories. Exposure to it in the environment presents several hazards to human health, including as respiratory

diseases, nasal irritation, and skin burn [2,3]. Hence, it is crucial to carefully check the concentration of acetone at room temperature.

A range of gases have been identified using chemiresistive gas sensors based on metal oxide semiconductors (MOS), including SnO_2 , MoO_3 , ZnO , ZrO_2 , and TiO_2 . The desirability of these metal oxides derives from their high sensing activity, cost-effectiveness, exceptional stability, and remarkable sensitivity to a wide range of target gases [4]. Gas sensors play a crucial role in the identification of hazardous, toxic, and explosive gases that have the potential to cause severe accidents or present health hazards. This study focuses on zirconium oxide (ZrO_2), a commonly used substance in ceramic materials, photocatalysts, catalysts, and p-type semiconductors [4,5]. Moreover, ZrO_2 finds application in the field of medicine owing to its anti-cancer, anti-microbial, and antioxidant characteristics [6]. Zirconium oxide (ZrO_2) exists in three

* Corresponding author.

E-mail address: navgireme@gmail.com (M. Navgire).

<https://doi.org/10.1016/j.surfin.2024.105068>

Received 8 July 2024; Received in revised form 1 September 2024; Accepted 4 September 2024

Available online 6 September 2024

2468-0230/© 2024 Elsevier B.V. All rights are reserved, including those for text and data mining, AI training, and similar technologies.

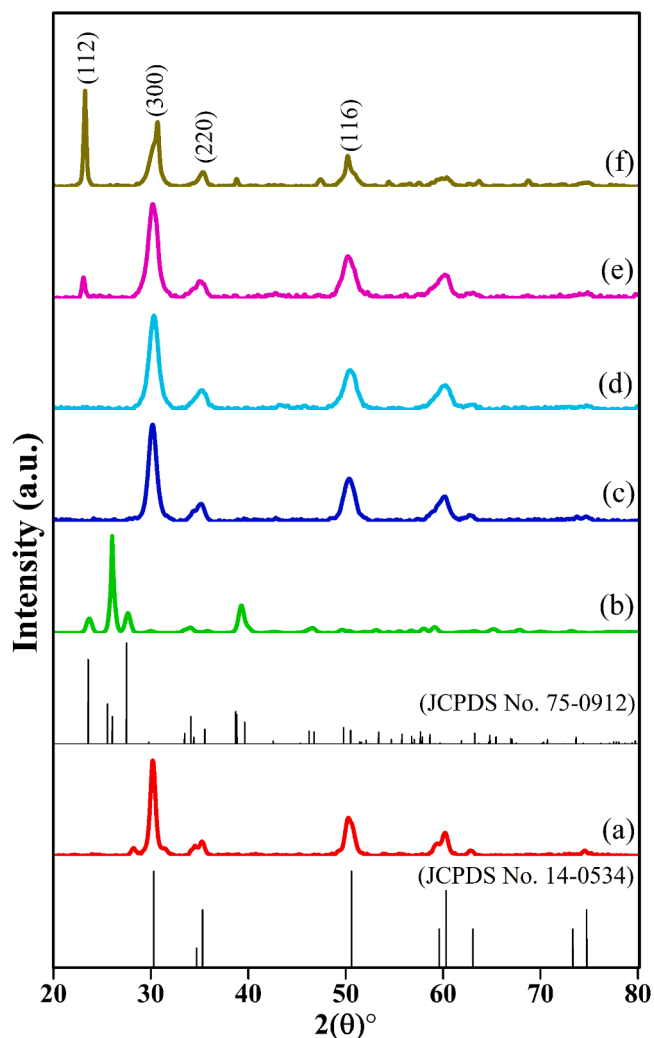


Fig. 1. XRD pattern of (a) Pristine ZrO₂, (b) Pristine MoO₃, (c) 1βMZ, (d) 2βMZ, (e) 5βMZ, and (f) 10βMZ.

distinctly identifiable phases: tetragonal, monoclinic, and cubic. Furthermore, it possesses unique features such as cost-effectiveness, ecological compatibility, and oxidizing and reducing active sites. Furthermore, the material has a wide band gap range of 3.25–5.1 eV [7]. Nevertheless, due to its exceptional stability, ZrO₂ necessitates a greater amount of energy to function at elevated temperatures and exhibits reduced sensitivity to various gases [4,8]. Hence, in order to enhance the gas sensing properties of the ZrO₂ material, it is necessary to dope or coat it with an alternate material.

Molybdenum trioxide (MoO₃) is a semiconducting material exhibiting a band gap ranging from 2.5 to 3.2 (eV). The material has a wide range of applications including photocatalysis, catalysis, gas sensing, and energy storage [9]. The catalytic and photocatalytic applications of mixed metal oxides doped with molybdenum have been comprehensively investigated and documented by our research team. Owing to its acidic sites, it was employed as a catalyst in several organic transformation processes. Furthermore, it was employed as a photocatalyst in the process of degrading pesticides, dyes, and toxic organic contaminants [10–15]. Due to its exceptional stability and surface catalytic activity, MoO₃ is employed for the detection of volatile organic compounds (VOCs). However, pristine MoO₃ has specific limitations such as a high operating temperature, poor selectivity, and a weak sensing response [16,17]. Consequently, there is a lack of published research on the gas sensing capabilities of MoO₃ nanocomposite materials at room temperature.

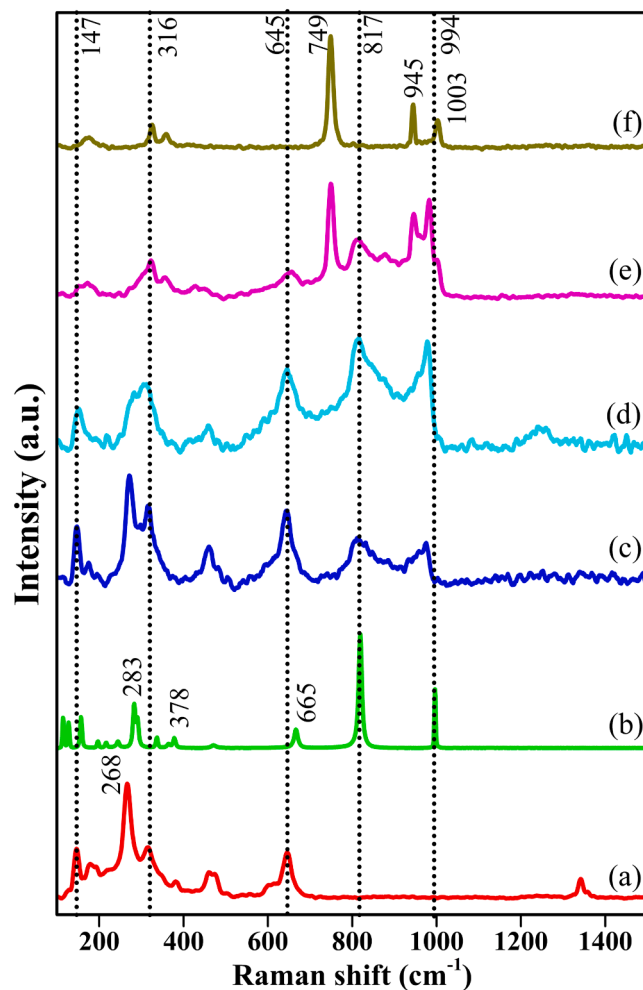


Fig. 2. Raman spectrum of (a) Pristine ZrO₂, (b) Pristine MoO₃, (c) 1βMZ, (d) 2βMZ, (e) 5βMZ, and (f) 10βMZ.

An oligosaccharide polymer with seven glucopyranose units is called β-cyclodextrin. It is used to synthesize porous structures having molecular recognition and solid phase extraction properties [18]. Liu et al. prepared porous carbon for herbicide adsorption by using β-Cyclodextrin MOF [19]. Al. Palaniappan et al. synthesized β-CD functionalized mesoporous silica film for ethanol and benzene detection. They reveal that the mesoporous structure, stability, and chemical bonding of β-CD immobilization on the matrix contribute to the increased sensitivity [20].

In response to the limitations of single metal oxide gas sensors, such as high operating temperatures and poor selectivity, researchers have employed various strategies, including doping, coatings, heterojunction formation, and the development of highly porous nanostructures like nanorods, nanotubes, and nanowires [21]. Among these approaches, doping with metal oxides has proven particularly an effective in enhancing gas sensing properties. For instance, J. Zhang et al. synthesized a porous GO/ZnO heterostructure with responses of 42.9 for 50 ppm acetone at 200 °C, providing more active sites for gas adsorption [22]. L. Qiu et al. developed a three-dimensional ordered Macroporous NiO/ZrO₂ nanocomposite that responded 25.6 to 100 ppm xylene vapours at 330 °C, ten times better than pure NiO [23]. S. Xu et al. created a sea urchin-like SnO₂/α-Fe₂O₃ heterostructure, achieving 18.7 ppm acetone reactivity at 300 °C and faster recovery than pristine SnO₂ [24].

As per the gas sensing mechanism, oxygen adsorbed on the sensor surface reacts with the target gas. Researchers dope, coat, and create heterojunction on nanocomposite surfaces to improve gas sensing.

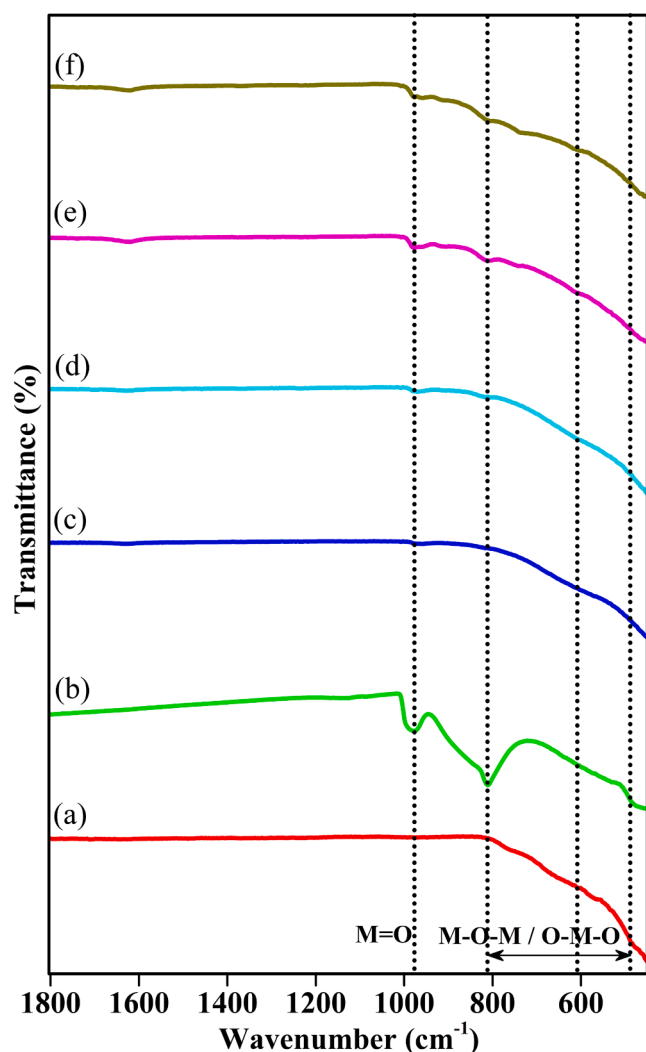


Fig. 3. FT-IR spectrum of (a) Pristine ZrO_2 , (b) Pristine MoO_3 , (c) 1 β MZ, (d) 2 β MZ, (e) 5 β MZ, and (f) 10 β MZ.

need a highly porous nanocomposite material with a more active gas-detecting surface [25]. We made a composite of pristine MoO_3 and ZrO_2 to overcome their limits. To improve gas sensing capability and surface quality, we added β -Cyclodextrin to the composite. ZrO_2 's stability enhances MoO_3 's electrical characteristics, improving gas sensing. Mesoporous $Zr(MoO_4)_2$ has more gas adsorption sites and an increased surface area. These composite materials are important because they lower working temperatures, are chemically stable, and last a long time. This article focuses on mesoporous $Zr(MoO_4)_2$ because it can overcome the constraints of ZrO_2 and MoO_3 . However, no research has reported using MoO_3 -doped ZrO_2 to detect VOCs at room temperature. Building on these findings, this study aims to develop a novel β -Cyclodextrin-coated MoO_3 - ZrO_2 nanocomposite, designed to operate effectively at room temperature (30 °C). By synthesizing this composite using a simple and cost-effective sol-gel method, we aim to address the challenges of traditional metal oxide sensors. The incorporation of β -Cyclodextrin is expected to improve the gas sensing capabilities of the composite by enhancing surface morphology, increasing porosity, and providing more active sites for gas adsorption.

Present a chemiresistive gas sensor, utilizing MoO_3 and ZrO_2 nanocomposite, capable of detecting volatile organic compounds (VOCs) at room temperature. We created β -Cyclodextrin-coated MoO_3 - ZrO_2 nanocomposite with molybdenum concentrations of 1, 2, 5, and 10 %. We synthesized the composite material using the inexpensive sol-gel

method. The prepared material was characterized by various techniques. At 30 °C, purified and nanocomposites samples successfully detected a variety of VOCs. Nanocomposite material has outstanding response time (30 s) and recovery time (39 s) for 100 ppm acetone. The rapid interaction between acetone vapors and nanocomposite active areas shortened recovery time.

The resulting nanocomposite material is anticipated to demonstrate superior sensing performance, with particular emphasis on acetone detection. The mesoporous structure of $Zr(MoO_4)_2$, coupled with the catalytic activity of MoO_3 and the stabilizing effect of ZrO_2 , should contribute to lower operating temperatures, improved sensitivity, and faster response and recovery times. This research, therefore, not only advances the understanding of composite gas sensors but also introduces a promising material for efficient VOC detection in environmental monitoring and industrial safety applications.

2. Experimental section

For this experiment, zirconium oxychloride octahydrate ($ZrOCl_2 \cdot 8H_2O$), ammonium heptamolybdate tetrahydrate ($(NH_4)_6Mo_7O_{24} \cdot 4H_2O$), and β -Cyclodextrin (β -Cd: $C_{42}H_{70}O_{35}$) were purchased from LOBA Chemicals. Cetyl Trimethyl Ammonium Bromide ($C_{19}H_{42}N.Br$) and ammonia solution (NH_4OH) were obtained from SD Fine Chemicals. All chemicals used were A.R. grade and utilized without further purification. Double-distilled water (DDW) was used throughout the experiment.

3. Synthesis of β -Cyclodextrin coated MoO_3 - ZrO_2 nanocomposites

Pristine and β -Cyclodextrin coated MoO_3 - ZrO_2 nanocomposites were synthesized using the cost-effective Sol-Gel method. A series of β Cyclodextrin coated MoO_3 - ZrO_2 nanocomposites with 1, 2, 5, and 10 % MoO_3 were synthesized and named as 1 β MZ, 2 β MZ, 5 β MZ, and 10 β MZ, respectively. For the synthesis of 1 β MZ, zirconium oxychloride octahydrate (2.589 g) and ammonium heptamolybdate tetrahydrate (0.085 g) precursors were dissolved in 100 mL of DDW with constant stirring. After obtaining a clear solution, β -Cd (0.2 g) and CTAB (0.5 g) were added to form viscous Sol. To form the gel, aqueous ammonia solution (10 mL) was added dropwise while stirring continuously. The gel was heated with constant stirring for 3 h to remove excess water, and then dried in an oven at 110 °C for 2 h. The dried gel was crushed with a mortar pestle and calcined in an open-air muffle furnace at 600 °C for 3 h. During calcination, β -Cyclodextrin in the nanocomposite material carbonized and transformed into porous carbon.

Using the same procedure, nanocomposites with 2, 5, and 10 % MoO_3 namely (2 β MZ), (5 β MZ), and (10 β MZ) were synthesized with the appropriate amounts of precursors. Pristine MoO_3 and ZrO_2 nanocomposites were also prepared using similar methods, with ammonium heptamolybdate tetrahydrate (8.58 g) and zirconium oxychloride octahydrate (2.61 g), respectively.

4. Materials characterization

The structural phase and crystallinity of nanocomposites were determined by using X-Ray Diffraction analysis (XRD, Rigacu MiniFlex 600) with $Cu K\alpha$ radiation ($\lambda = 0.154$ nm). Fourier Transform Infrared spectroscopy (FTIR, PerkinElmer Spectrum 2) was investigated in the range 4000 to 450 cm^{-1} . The surface morphology was examined using Field-Emission Scanning Electron Microscopy (FESEM, FEI Nova Nano SEM 450) and High-Resolution Transmission Electron Microscopy (HRTEM, Tecnai G2 20). UV-Visible Diffused Reflectance Spectra (UVDRS, Lab India UV-Vis spectrophotometer 3092) was used to analyze the optical properties. Raman analysis was done by a Renishaw Raman analyzer. The surface area was measured using Brunauer-Emmett-Teller analysis (BET, Microtrac MRB BELSORP MAX II).

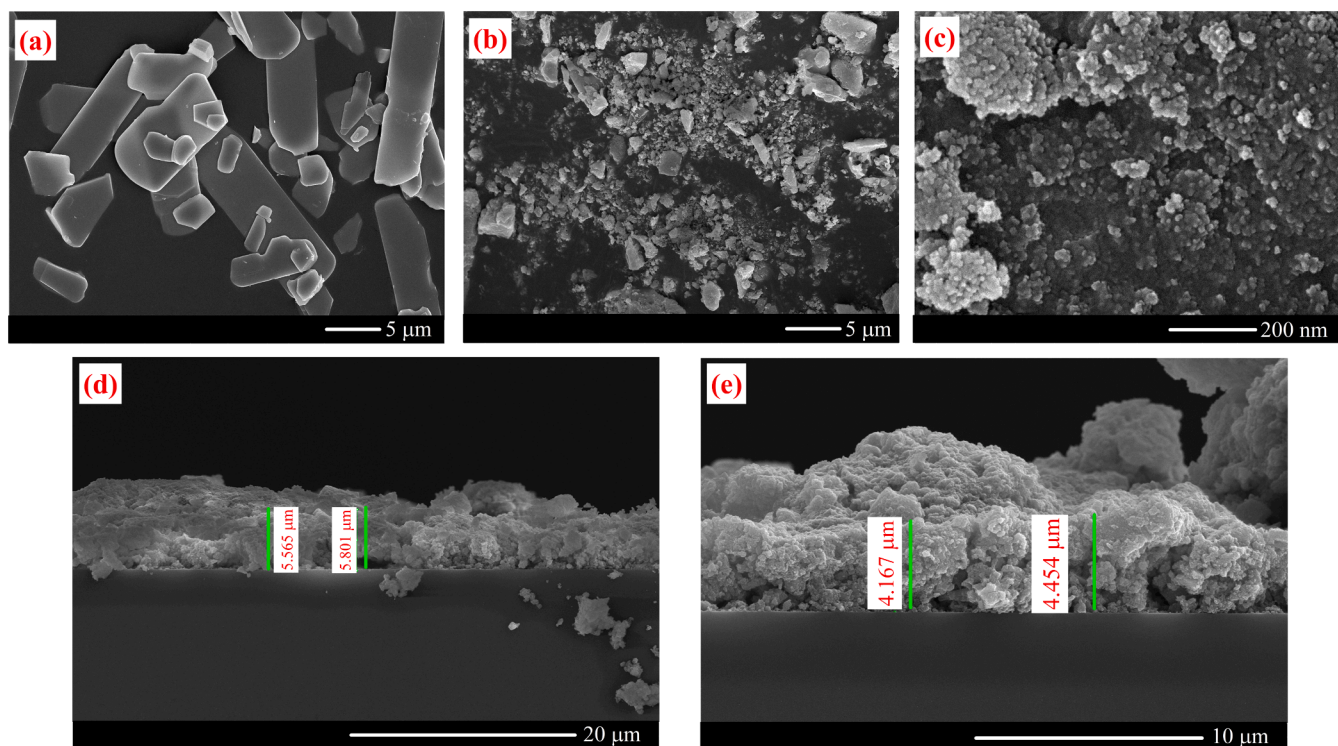


Fig. 4. FE-SEM images of (a) Pristine MoO_3 , (b) Pristine ZrO_2 , and (c) $10\beta\text{MZ}$; (d and e) cross-section of sensing film of $10\beta\text{MZ}$ nanocomposite material.

Surface chemical compositions were analyzed using X-ray photoelectron Spectroscopy (XPS, Thermo Scientific NEXA surface analyzer).

5. Gas sensing activity

To evaluate the gas sensing properties of the nanocomposites, thick films were prepared using the doctor-blade method on a clean glass substrate. The glass substrate were immersed in a 0.5 M HCl solution and sonicated for 30 min before cleaning. The nanocomposite powder was mixed with polyethylene glycol (PEG) as a binder to form a paste using a mortar and pestle. The resulting films were then dried at $300\text{ }^\circ\text{C}$ for three hours in an open-air muffle furnace. The gas sensing experiment was conducted in a 750 mL airtight glass chamber connected to a Keithley 2000 multimeter for recording the resistance of the nanocomposites. A static gas sensing method was used, where specific amount of test gas vapor was introduced into the test chamber. The gas sensing activity was performed at room temperature ($30\text{ }^\circ\text{C}$), and different concentrations of vapor were prepared using pure volatile organic compound (VOC) liquid. The concentration of VOC's in the glass bottle was calculated using Eq. (1), and the volume of gas transferred from the bottle using a syringe was calculated using Eq. (2) [5].

$$v = \frac{c \times M \times V \times 10^{-6}}{22.4 \times \rho} \quad (1)$$

Where v is the volume of the liquid (mL), c is the concentration of the target gas (ppm), ρ is the density of liquid (g/cm^3), M is the molecular weight of injected liquid (g mol^{-1}), and V is the volume of the glass bottle (mL).

$$v = c \times V \times 10^{-6} \quad (2)$$

Where v is the volume of the gas (mL), V is the volume of the testing chamber (mL), and c is the concentration of gas in the chamber (ppm).

Before conducting the sensing test, the gas sensor was stabilized in the air for 12 h, after which it was exposed to target volatile organic gas vapors. The response (S) was calculated by using the formula $\frac{R_g}{R_a}$ or $\frac{R_a}{R_g}$ for

reducing and oxidizing gases, where R_a is the resistance of the sensor in the air atmosphere and R_g is the resistance in the presence of the target gas. The response and recovery time of the gas sensor were defined as the time required achieving 90 % of the change in resistance.

6. Results and discussions

6.1. X-ray diffraction spectroscopy (XRD)

The crystallographic structure of pristine materials and nanocomposites were determined using X-ray diffraction (XRD) analysis, as shown in Fig. 1. The diffraction peaks of pristine ZrO_2 , depicted in Fig. 1 (a) appear at 2θ ($^\circ$) values of 30.2, 35.2, 50.2, 60.1 and 74.5 corresponding to the crystallite planes (111), (200), (202), (311) and (400). These planes align with JCPDS card No 14-0534, confirming a tetragonal crystal structure [26]. Fig. 1(b) shows the XRD pattern for orthorhombic MoO_3 , with sharp and intense peaks at 2θ ($^\circ$) values of 23.2, 26.0, 27.6, 34.0, and 39.3 corresponding to the (110), (120), (021), (111), and (150) diffraction planes, respectively. These match well with JCPDS card No 75-0912 [27].

For the nanocomposites with high loading of molybdenum, $5\beta\text{MZ}$, and $10\beta\text{MZ}$ the XRD pattern are shown in Fig. 1(e and f). The peaks at 2θ ($^\circ$) values of 23.2, 30.6, 35.3, 38.8, 47.4, and 50.1 correspond to the planes (112), (300), (220), (222), (224), and (116), respectively. These peaks match the values reported in JCPDS card No 38-1466, indicating the presence of a hexagonal phase of $\text{Zr}(\text{MoO}_4)_2$ material [28]. The gradual increase in intensity of the peak at 23.2 ($^\circ$) is attributed to the increasing MoO_3 concentration from $1\beta\text{MZ}$ to $10\beta\text{MZ}$. Additionally, a decrease in the intensity of the MoO_3 peak at 27.6 ($^\circ$) suggests the conversion of orthorhombic MoO_3 and the formation of the hexagonal $\text{Zr}(\text{MoO}_4)_2$ nanocomposite [29].

The crystallite sizes of the synthesized nanocomposites were estimated using the Debye-Scherrer equation, with the results are presented in Table S1. [30,31]. The Eq. (3) used for the calculation is as follows:

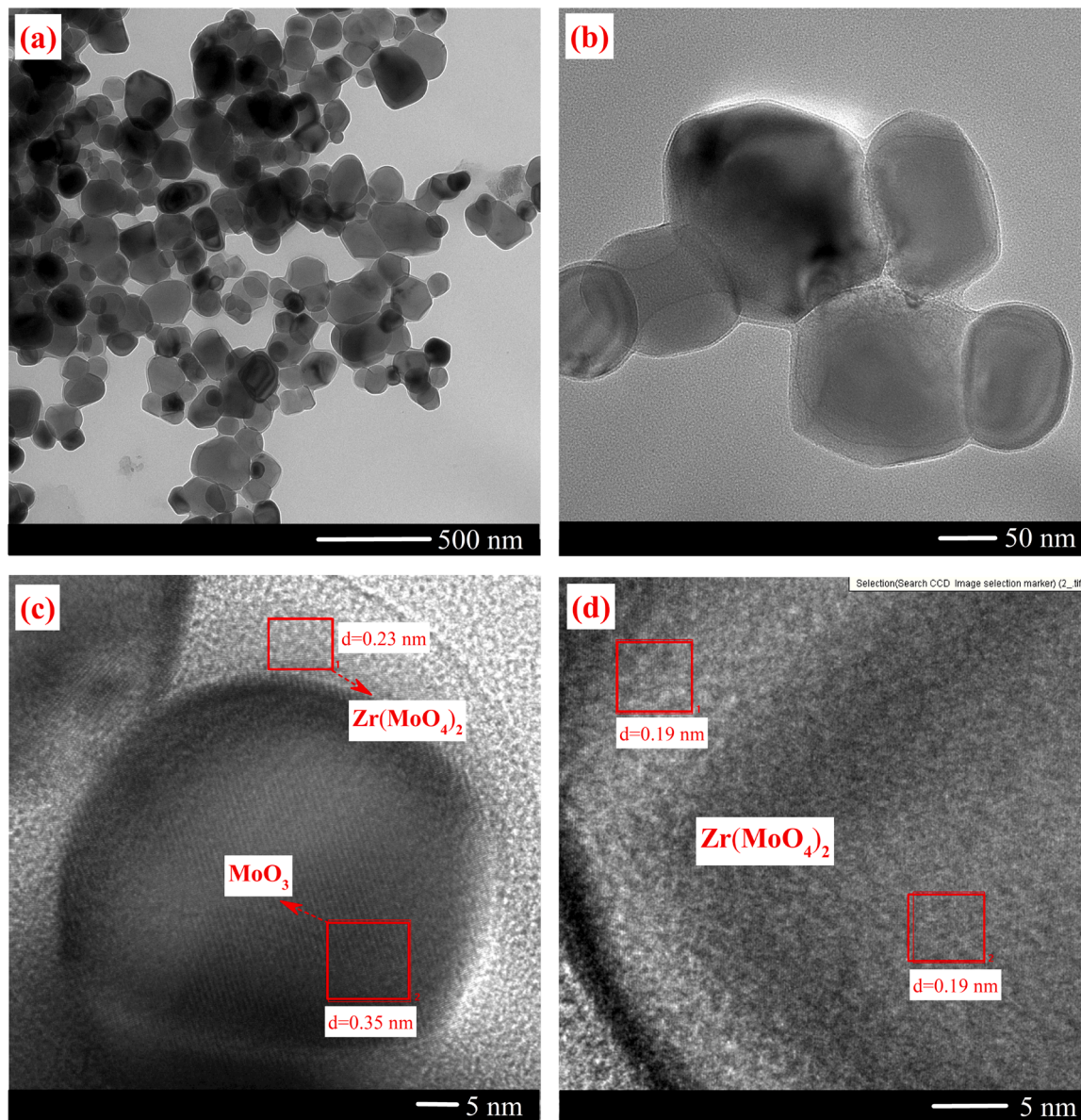


Fig. 5. (a-b) TEM image and (c-d) HRTEM image of 10βMZ nanocomposite.

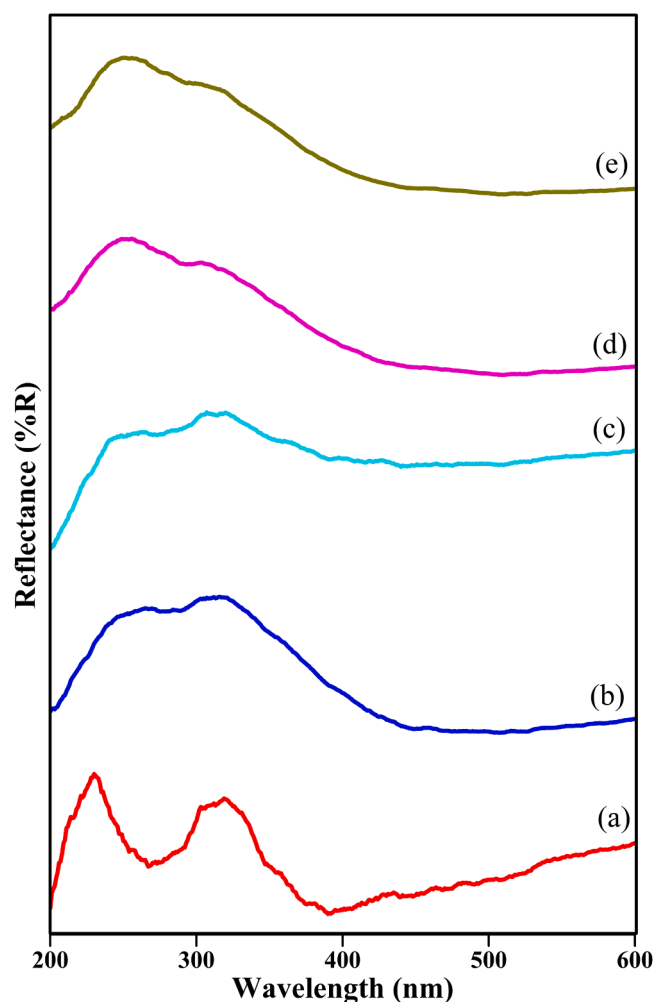


Fig. 6. UV-DRS reflectance spectra of (a) Pristine ZrO_2 , (b) 1β MZ, (c) 2β MZ, (d) 5β MZ, and (e) 10β MZ.

$$D = \frac{0.9 \lambda}{\beta \cos \theta} \quad (3)$$

Where, λ is the wavelength of Cu $K\alpha$ radiation (0.1514 nm), θ indicates the angular position of the peak, and β is the full width at half maximum (FWHM) of the most intense diffraction peak, measured in radians. The crystallite size of nanocomposites ranged from 7.72 to 27.61 nm, indicating strong interactions between the incorporated MoO_3 and ZrO_2 species.

6.2. RAMAN spectroscopy

Fig. 2 shows the Raman spectra, providing insights into the vibrational modes and crystal phase of both pristine and nanocomposite materials. Fig. 2(a) presents the Raman spectrum of pristine ZrO_2 . The intense peak at 147 cm^{-1} corresponds to the symmetric stretching vibration mode of Zr-O bonds in the tetragonal phase of ZrO_2 . Additional peaks at 268 and 316 cm^{-1} are attributed to the Zr-O-Zr bending vibration or the asymmetric stretching mode of oxygen atoms. The peak at 460 cm^{-1} corresponds to the symmetric stretching mode of the Zr-O-Zr bonds, while peaks at 601 and 645 cm^{-1} are associated with the bending mode of the O-Zr-O bond present on ZrO_2 [32].

In Fig. 2(b), the Raman spectrum of pristine MoO_3 is shown, with prominent peaks at 197 , 244 , and 283 cm^{-1} , corresponding to the symmetric stretching mode of Mo-O-Mo bonds in the orthorhombic MoO_3 lattice. The peaks at 335 , 378 , and 425 cm^{-1} are mainly due to the

bending vibrations of Mo-O bonds or may relate to the stretching mode of terminal Mo=O bonds. The band at 665 cm^{-1} corresponds to the symmetric stretching mode of the Mo-O bond, while peaks at 817 and 994 cm^{-1} illustrate the stretching vibration of Mo-O-Mo and Mo=O bonds, respectively [33,34].

The Raman spectra of β -CD coated MoO_3 - ZrO_2 nanocomposite indicate the presence of hexagonal phases. Fig. 2(c-F) shows the vibrational modes within the crystal lattice for 1β MZ, 2β MZ, 5β MZ, and 10β MZ nanocomposites. A low-frequency band is observed, resulting from the lattice vibrational and translational modes of the hexagonal structure. The peak at 319 cm^{-1} corresponds to the symmetric stretching vibrations of Mo-O and Zr-O bonds in the crystal lattice. Additionally, the intense peaks at 749 , 945 , and 1003 cm^{-1} correspond to the symmetric $\nu(O-Mo-O)$, antisymmetric $\nu(O-Mo-O)$ and $\nu(Mo=O)$ vibrational modes, respectively. The decrease in intensity of the corresponding peaks of pristine MoO_3 and ZrO_2 in the composite material further confirms the formation of hexagonal $Zr(MoO_4)_2$ nanocomposites [35-38].

6.3. Fourier transform infrared spectroscopy (FT-IR)

The Fourier Transform Infrared (FT-IR) spectrum, shown in Fig. 3, provides essential insights into the chemical bonding in the samples. In Fig. 3(a), the pristine ZrO_2 spectrum features peaks at 761 and 606 cm^{-1} , corresponding to Zr-O stretching vibration and a peak at 559 cm^{-1} , suggesting the O-Zr-O bending vibration, characteristic of the ZrO_2 [39-41]. The FT-IR spectrum of pristine MoO_3 shows a peak at 980 cm^{-1} , representing the terminal Mo=O and a peak at 809 cm^{-1} , associated with antisymmetric O-Mo-O or Mo-O-Mo stretching vibrations.

For the β -CD coated MoO_3 - ZrO_2 nanocomposite, a significant new absorption band emerges in the range of 500 to 810 cm^{-1} , likely corresponding to the M-O-M or O-M-O bonding. The peak at 809 cm^{-1} indicates the $M = O$ bonding mode. These results suggest the successful formation of $Zr(MoO_4)_2$ [39,42,43].

6.4. Field emission scanning electron microscopy (FE-SEM)

The surface morphology of both pristine materials and nanocomposites was analyzed using FE-SEM images, as depicted in Fig. 4. Fig. 4(a), shows that pristine MoO_3 has a 2-D nanosheet structure with a width ranging from 2 to $5 \mu\text{m}$ and a length of 10 – $20 \mu\text{m}$. Fig. 4(b) displays the pristine ZrO_2 , which exhibits agglomerated nanoparticle-like morphology. Fig. 4(c) reveals the uniform and smooth surface morphology of 10β MZ nanocomposite.

Fig. 4(d and e) illustrate the cross-sectional view of the sensing film made from the 10β MZ nanocomposite. The film's thickness ranges between 4 and $6 \mu\text{m}$, which is more favorable for fast response times and high sensitivity in gas sensing applications [44].

6.5. High resolution transmission electron microscopy (HR-TEM)

Fig. 5 presents the transmission electron micrograph (TEM) image the 10β MZ nanocomposite, revealing the presence of hexagonal crystal structure of $Zr(MoO_4)_2$. The size of the nanocomposite particles ranges from 70 to 180 nm . The high-resolution transmission electron microscopy (HRTEM) image also shows d-spacing values of 0.19 and 0.23 nm , corresponding to the (224) and (222) lattice planes of the $Zr(MoO_4)_2$ phase, respectively, along with d-spacing of 0.35 for the (120) lattice plane of residual MoO_3 in nanocomposite. Additionally, due to the high temperature calcination of the nanocomposite, β -CD was carbonized into porous carbon [19]. These findings are consistent the XRD analysis of 10β MZ nanocomposite material.

6.6. Ultra Violet- Visible and diffuse reflectance spectroscopy (UV-Vis DRS)

The UV-Vis diffuse reflectance spectrum offers critical insights into

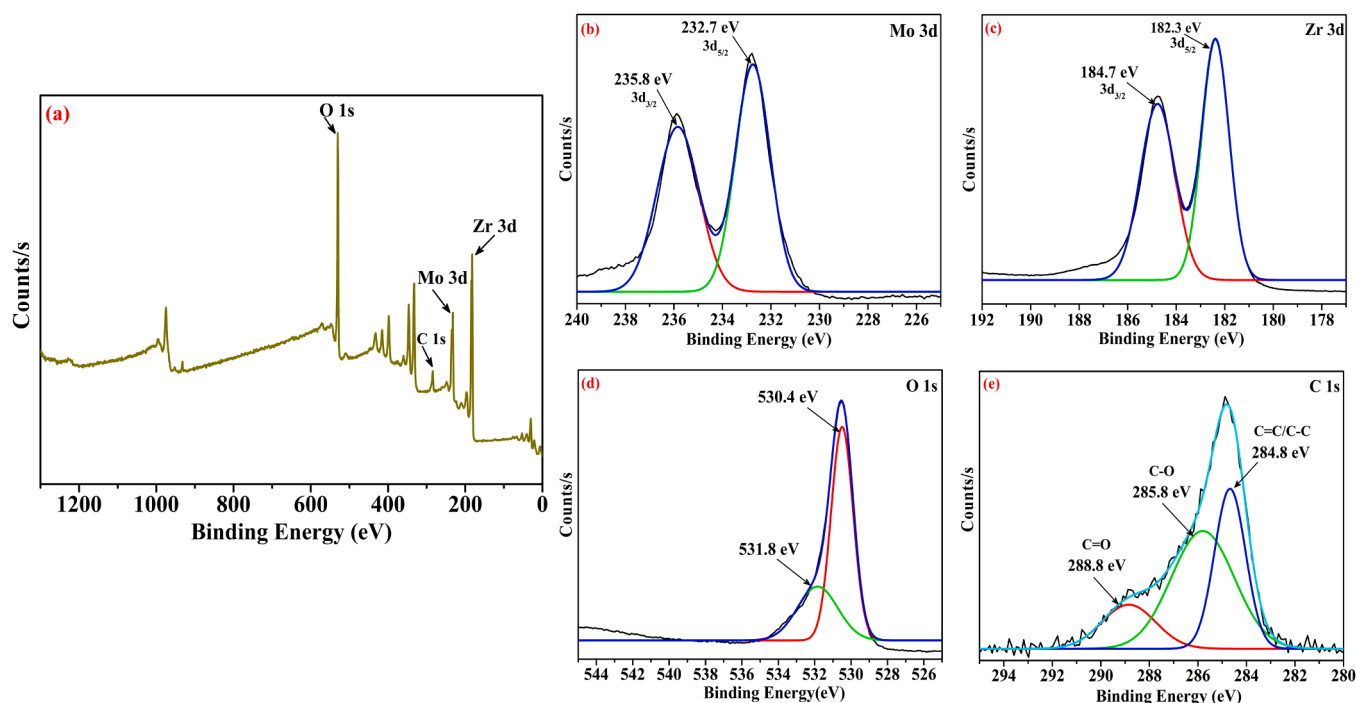


Fig. 7. XPS of (a) full scan spectrum of 10 β MZ, (b) Mo 3d, (c) Zr 3d, (d) O 1 s, and (e) C 1 s spectra.

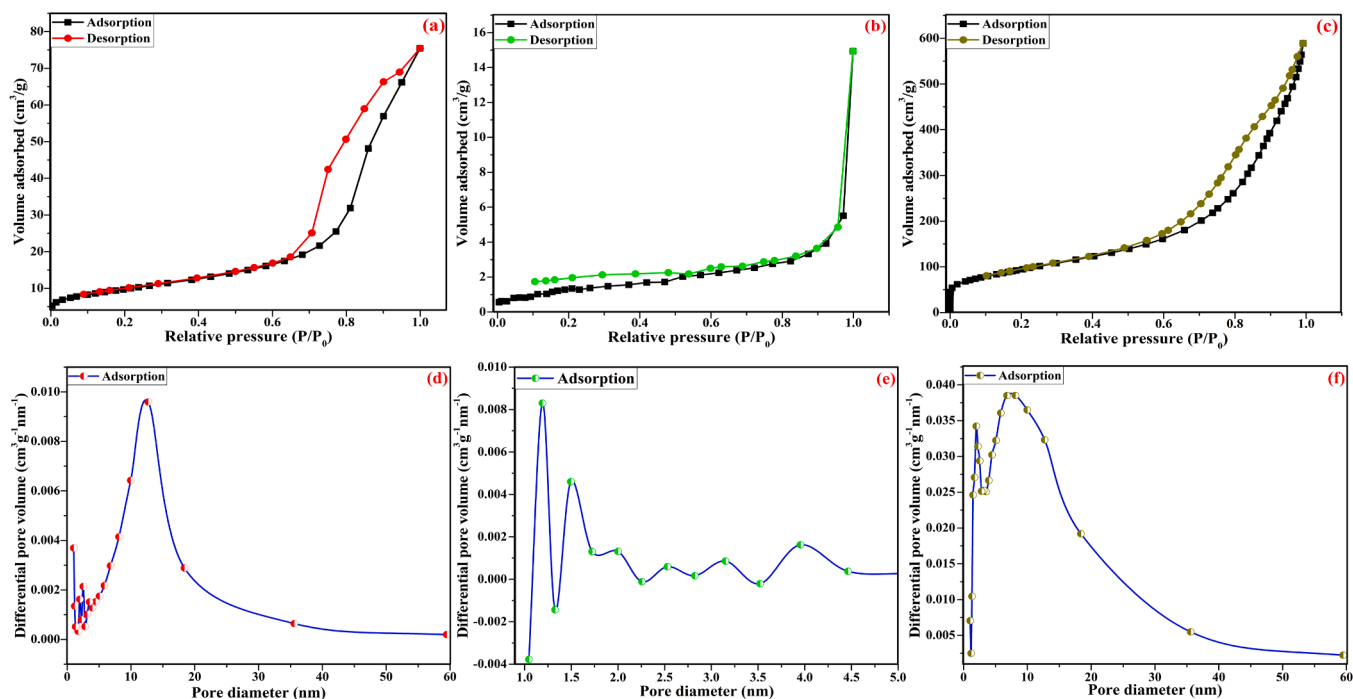


Fig. 8. BET Surface area plot, N₂ adsorption-desorption isotherms of (a) Pristine ZrO₂, (b) Pristine MoO₃, (c) 10 β MZ, BJH plot of pore size distribution (d) Pristine ZrO₂, (e) Pristine MoO₃, and (f) 10 β MZ.

the optical properties of nanocomposite materials. This spectrum captures both absorption and remission within the materials. As illustrated in Fig. 6(a-e), the reflectance spectra for the pristine ZrO₂, 1 β MZ, 2 β MZ, 5 β MZ, and 10 β MZ nanocomposites were recorded across a wavelength range of 200 nm to 800 nm at room temperature. Notably, the reflectance spectrum exhibits a peak shift towards the longer wavelength, which can be attributed to the increasing concentration of metal (Mo⁺) ions in the composites.

By converting the reflectance spectra into equivalent absorbance spectra, the optical absorption coefficient (α) was determined using the Kubelka-Munk method [45]. This absorption coefficient ' α ' was then modified by multiplying it by the incident beam light intensity. The effective band gap of the ZrO₂ and MoO₃-ZrO₂ series were calculated by extrapolating the linear region of the plot, as shown in Fig. 6. The analysis revealed an indirect optical band gap energy of pristine ZrO₂ and nanocomposites samples, with detailed values shown in Table S2

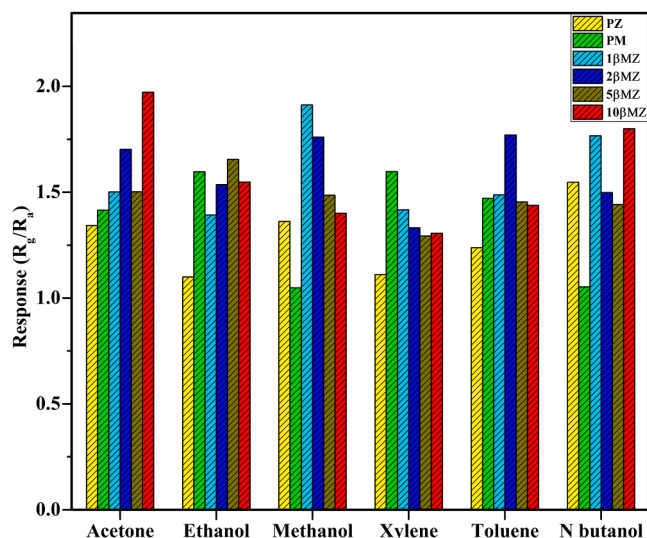


Fig. 9. Room temperature sensing response of the pristine ZrO_2 , pristine MoO_3 , and series of nanocomposite sensors towards different target gases at concentrations of 100 ppm.

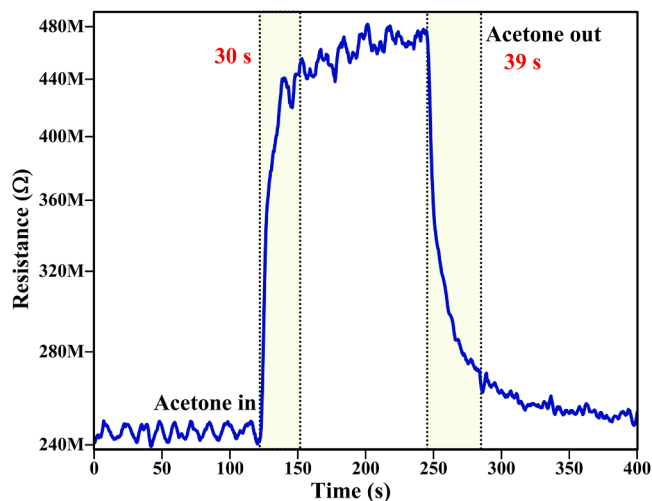


Fig. 10. Response and recovery curve of a 10 β MZ sensor towards 100 ppm acetone at room temperature.

[46]. The pristine ZrO_2 displayed an optical band gap of 4.02 eV, while in nanocomposites exhibited a ranges from 3.42 eV to 2.70 eV.

The incorporation of $Zr(MoO_4)_2$ significantly narrows the optical band gap, especially with higher Mo^{6+} ion concentration in nanocomposites. This narrowing is due to the formation of a narrow electronic band structure, likely resulting from localized defect states in the sub-band gap region. The absorption coefficient edge shifts towards the visible region (310 to 460 nm), enhancing the suitability of these nanocomposites for sensor applications [47].

6.7. X-ray photoelectron spectroscopy (XPS)

The surface elemental composition of 10 β MZ nanocomposites was analyzed using X-ray Photoelectron Spectroscopy (XPS). The comprehensive XPS spectrum, presented in Fig. 7(a), reveals the presence of Mo, Zr, C, and O elements on the nanocomposite surface, with atomic percentages of 7.15, 16.5, 57.42, and 18.31 %, respectively. The Mo 3d spectrum, shown in Fig. 7(b) features peaks at 232.7 and 235.8 eV, corresponding to the Mo 3d_{5/2} and Mo 3d_{3/2} of Mo^{6+} in MoO_3 [48].

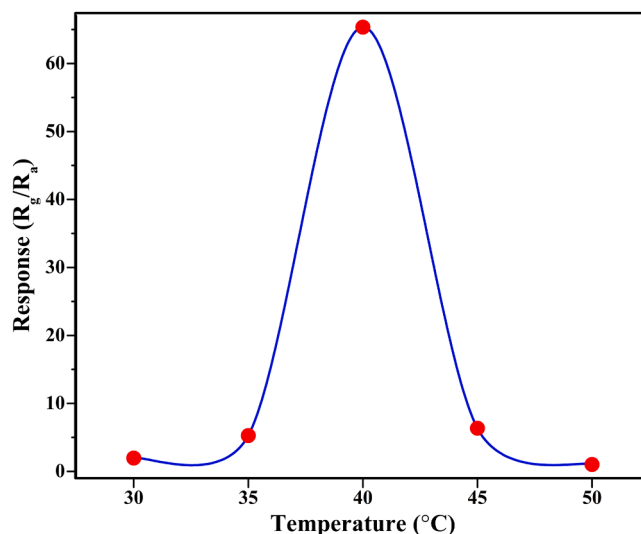


Fig. 11. Relationship between working temperature and the response of a 10 β MZ sensor to 100 ppm acetone.

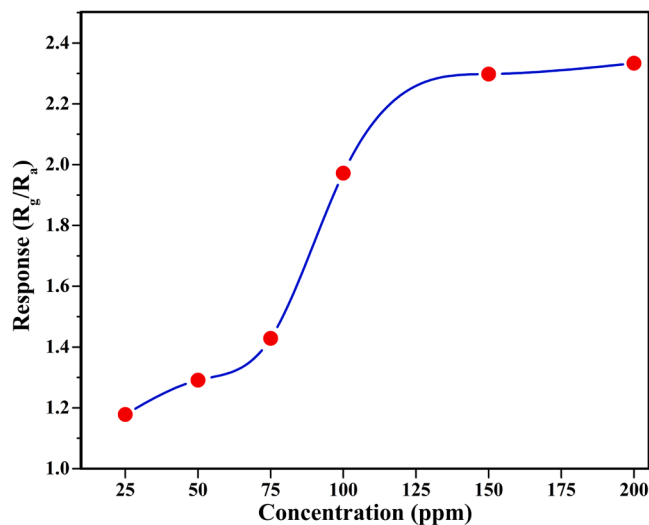


Fig. 12. Response of a 10 β MZ sensor to various concentrations of acetone (25–200 ppm) at room temperature.

Similarly, the Zr 3d spectrum shown in Fig. 7(c) display characteristic peaks at 184.7 and 182.3 eV for Zr 3d_{3/2} and Zr 3d_{5/2}, respectively, which are consistent with the Zr^{4+} oxidation state in the nanocomposite, as corroborated by literature [49]. The deconvoluted O 1s spectrum in Fig. 7(d) shows prominent peaks at 530.4 and 531.8 eV, representing O^{2-} ions within the lattice and surface-adsorbed oxygen or hydroxyl groups in nanocomposites, respectively [49,50].

Fig. 7(e) displays the C 1s spectrum, with peaks at 284.8, 285.8, and 288.8 eV, corresponding to C = C/C—C, C—O, and C = O bonds in graphite-like carbon atoms [51,52]. The detection of Mo 3d, Zr 3d, C 1s, and O 1s elements in the XPS survey confirms the formation of Zr (MoO_4)₂ nanocomposite, along with the attachment of carbon atoms.

6.8. Brunauer-Emmett-Teller (BET) Analysis

The Brunauer-Emmett-Teller (BET) analysis of the Pristine ZrO_2 , Pristine MoO_3 and 10 β MZ nanocomposite is summarized in Fig. 8. The analysis of pore size distribution, pore volume and specific surface area was conducted using nitrogen adsorption-desorption isotherms and the

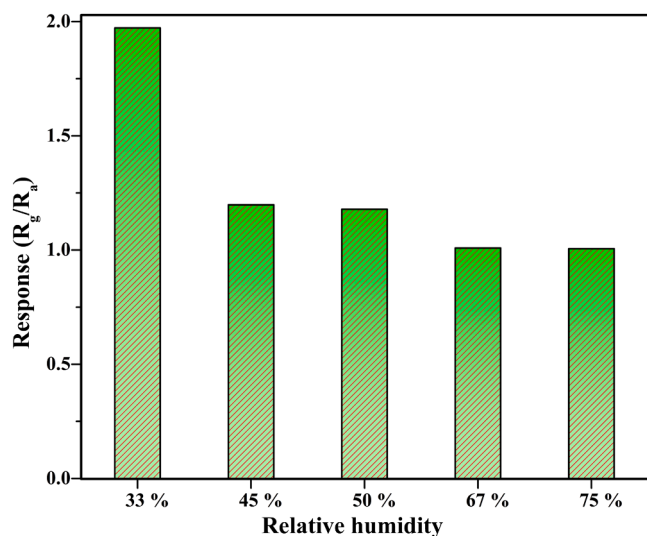


Fig. 13. Room temperature (30 °C) response of a 10βMZ sensor to various relative humidity (%) at 100 ppm acetone.

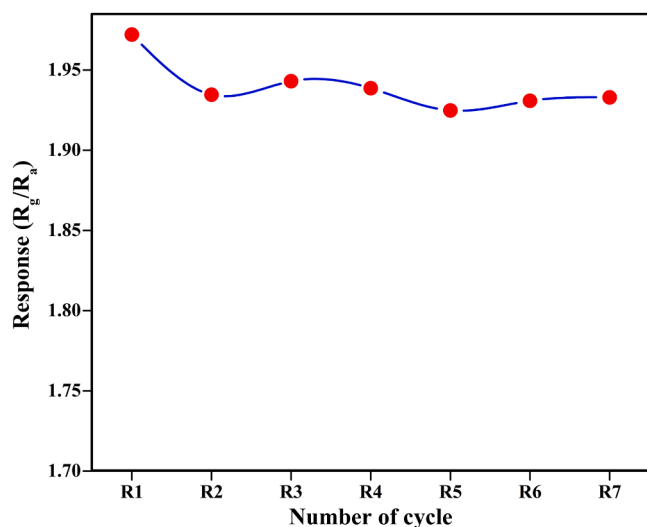


Fig. 14. Response of repetitiveness of a 10βMZ sensor at 100 ppm of acetone at room temperature.

Barrett-Joyner-Halenda (BJH) method. The specific surface area is a crucial factor that influencing the gas sensing properties of material.

Fig. 8(a-c) displays a type IV isotherm and a type H₃ hysteresis loop for both pristine and nanocomposite samples, indicating the mesoporous nature of the materials. The corresponding BJH plot in Fig. 8(d-f) further confirms this mesoporosity. Table S3 provides a summary of the specific surface area, pore size and pore volume for both pristine and nanocomposite samples. The results indicate that an increase in specific surface area correlates with a decrease in pore size, demonstrating that doping MoO₃ on ZrO₂ enhances the performance of the nanocomposite. This improvement is primarily due to the larger surface area, which plays a significant role in enhancing the sensing properties of the material [53-55]. The addition of β-CD further contributes to the increase in surface area, leading to enhanced sensor activity.

7. Gas sensing activity studies

The gas sensing experiment was conducted to evaluate the selectivity of the synthesized materials for various volatile organic compounds

(VOCs), as well as key factors such as response and recovery time, the effect of operating temperature, concentration dependence, and reusability. The material tested including pristine MoO₃, pristine ZrO₂ and a series of βMZ nanocomposites. Selecting appropriate target gases is crucial for evaluating sensor selectivity. Fig. 9 illustrates the responses of various VOCs (acetone, ethanol, methanol, xylene, toluene, and N-butanol) at a concentration of 100 ppm, tested at room temperature (30 °C) for both pristine and nanocomposites samples.

Among all the synthesized catalytic materials, the 10βMZ nanocomposite demonstrated the highest gas sensing response (1.97) towards acetone vapors, outperforming other tested gases. In comparison, pristine ZrO₂ and pristine MoO₃ exhibited lower responses of 1.34 and 1.41, respectively, highlighting the superior sensing activity of the 10βMZ nanocomposite. Several factors contribute to the enhanced performance of the 10βMZ nanocomposite. Firstly, high specific surface area (343.26 m²/g) provides more active sites for adsorption-desorption gas reaction, crucial for effective sensing [56]. Additionally, bond dissociation energy plays a significant role in determining selectivity towards acetone gas. Acetone, bond dissociation energy of 352 kJ/mol, has lower energy requirement compared to other testing gases such as ethanol (462 kJ/mol), methanol (462 kJ/mol) and toluene (370 kJ/mol) [57]. The high dipole moment of acetone, indicating high polarity, facilitates its easy adsorption onto sensors surface, resulting in a stronger sensing response [58].

8. Response and recovery time

One of the main characteristic features of gas sensors is their ability to respond and recover quickly. As depicted in Fig. 10, the change in resistance of the sensor when exposed to 100 ppm acetone vapors is shown. The 10βMZ nanocomposite material exhibits a rapid response time of 30 s and recovers within 39 s. Upon the injection of acetone vapors into the test chamber, the resistance of the film rapidly increases, indicating a swift detection response.

9. Optimum operating temperature

Determining the optimum operating temperature is crucial for maximizing the gas sensor's performance. The response of the sensor at various temperatures is illustrated in Fig. 11. As the temperature increases, the resistance R_a of the sensor also increases, leading to a higher response. The 10βMZ sample shows the highest response of 65.34 for 100 ppm acetone at 40 °C, which is nearly 33 times higher than the response observed at room temperature (30 °C). However, at 50 °C, the response decreases to 1.02 due to the reduced adsorption ability of acetone molecules at higher temperatures, which adversely affects the sensing activity [59].

10. Concentration effect

The effect of varying acetone vapor concentrations on the 10βMZ nanocomposite is illustrated in Fig. 12. The sensor was tested with concentrations ranging from 25 to 200 ppm. The response shows a linear increase with increasing concentration, but beyond 150 ppm, the rate of increase slows down, reaching a saturation point. This behavior is attributed to the reduced availability of surface-adsorbed oxygen species in the nanocomposite as it becomes increasingly covered with acetone vapors. Consequently, the reaction rate decreases, leading to a slower rise in response [60].

11. Effect of relative humidity

Fig. 13 illustrates how varying levels of relative humidity (RH) at room temperature (30 °C) influence the response of the 10βMZ nanocomposite to 100 ppm acetone vapor. The response at different RH levels 33, 45, 50, 67 and 75 % decrease from 1.97 to 1.006. As the relative

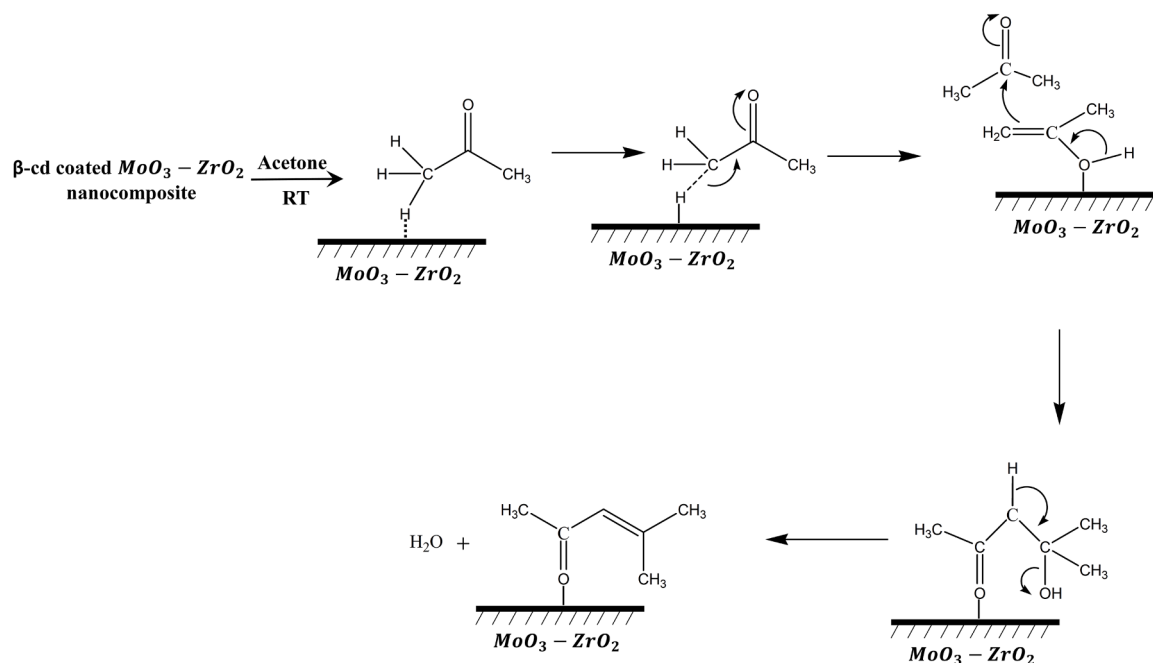


Fig. 15. Proposed acetone gas sensing mechanism of a β -Cd coated $\text{MoO}_3\text{-ZrO}_2$ nanocomposites sensor.

humidity increases, the gas sensor's response decreases. This is because the surface of nanocomposite absorbs more water molecules at higher humidity levels, which reduces the adsorption of oxygen. As a result, both the reaction rate and the sensor response are diminished [57].

12. Repeatability and reusability

Repeatability is a critical factor in evaluating the reliability and quality of a gas sensor. The $10\beta\text{MZ}$ films were tested for repeatability by recycling them at 100 ppm acetone vapor concentrations over seven cycles, as depicted in Fig. 14. After each cycle, the sensor's resistance returned to the baseline, with only a slight decrease in response observed before stabilization. This consistent performance across multiple cycles suggests that the $10\beta\text{MZ}$ nanocomposite exhibits excellent reusability and stability as a gas sensor material (Fig. 15).

13. Gas sensing mechanism

When $\text{MoO}_3\text{-ZrO}_2$ nanocomposites are exposed to air, they absorb O_2 from the atmosphere. The absorbed oxygen species (O_2^- or O^-) undergo chemisorption, drawing electrons (e^-) from the conduction band of $\text{MoO}_3\text{-ZrO}_2$. Upon exposure to acetone vapors, the acetone molecules adsorb onto the surface of the $\text{MoO}_3\text{-ZrO}_2$. The α -H of acetone, which is slightly acidic, interacts with the oxygen atom 'O' in $\text{MoO}_3\text{-ZrO}_2$, forming an intermediate enolate species through the elimination of α -H from the acetone molecule ($\text{M-O-H-CH}_2\text{COCH}_3$). This interaction leads to the formation of O—H bonds on the $\text{MoO}_3\text{-ZrO}_2$ film, a phenomenon that is confirmed by the FT-IR spectra, where an increase in the -OH frequency is observed in the presence of adsorbed acetone (as shown in Fig. 16b). Additionally, the enolate species can further interact with a second acetone molecule to form diacetone alcohol. The formation of the O—H bond on the $\text{MoO}_3\text{-ZrO}_2$ film involves the utilization of electrons from the conduction band, thereby increasing the resistance of

the film upon acetone adsorption. During the desorption process, the O—H bond on the $\text{MoO}_3\text{-ZrO}_2$ dissociates, restoring the H to the acetone species, which leads to a decrease in film resistance as acetone is removed [61,62].

The β -CD coated $\text{MoO}_3\text{-ZrO}_2$ nanocomposite exhibits excellent gas sensing performance towards acetone at room temperature, with quick response and recovery times. The enhancement in gas sensing properties towards acetone vapors is mainly attributed to several factors: the large specific surface area, the formation of heterojunctions, and the porous nature of the sensor [63]. The incorporation of β -CD significantly improves the specific surface area and porosity of the nanocomposite, providing more active sites, which in turn increases the sensor's response. Additionally, the Mo content loaded onto ZrO_2 nanocomposites exhibits high catalytic activity due to the formation of Brønsted acid sites, which enhance surface activity [36]. The high dipole moment and low bond dissociation energy of acetone also contribute to the selectivity and enhancing sensing performance.

Overall, the gas sensing mechanism relies on the adsorption-desorption reaction between the sensor's surface and the gas molecule. A highly porous sample performs better due to the availability of more active sites for the reaction. Therefore, the presence of β -Cyclodextrin in the sample enhances the sensing activity of nanocomposite material.

14. Comparison of acetone gas sensing performance with other gas sensors

Table 1 summarizes the performance of various gas sensors for acetone detection, highlighting key metrics such as response, operating temperature, response time, and recovery time.

β -CD coated $\text{MoO}_3\text{-ZrO}_2$ nanocomposite exhibits a high response of 1.97 at 100 ppm acetone at room temperature (RT), with a rapid response time of 30 s and a recovery time of 39 s. ZnO nanofibers

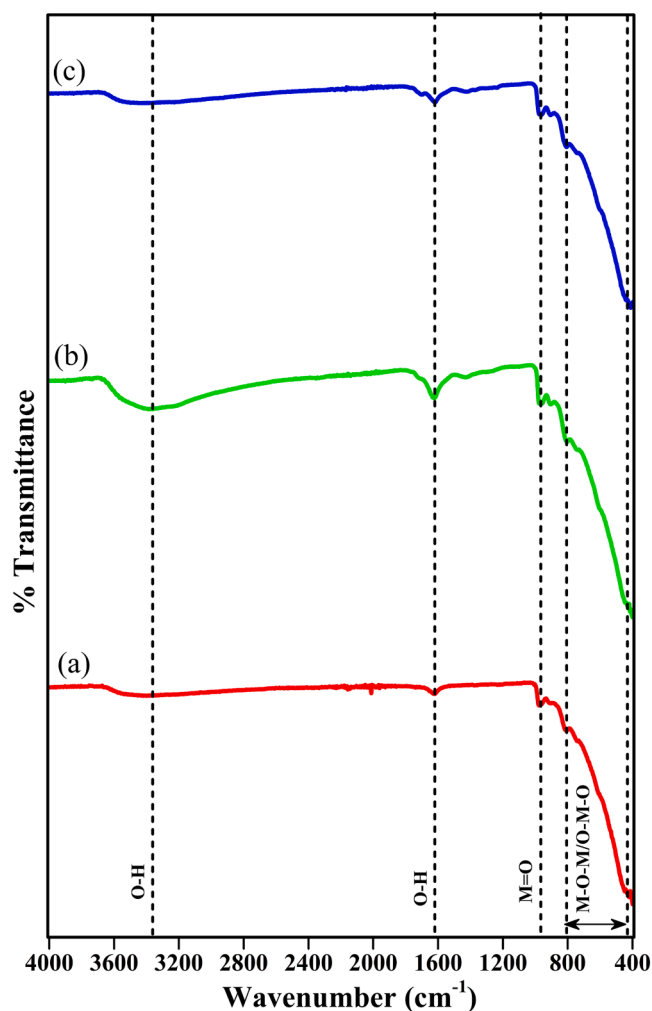


Fig. 16. FT-IR spectrum of (a) $\text{MoO}_3\text{-ZrO}_2$ nanocomposites before acetone vapor passes; (b) $\text{MoO}_3\text{-ZrO}_2$ nanocomposites after immediate acetone vapor passes; and (c) $\text{MoO}_3\text{-ZrO}_2$ nanocomposites after 10 min of acetone vapor passing.

(PZ_4G_0) show a slightly higher response of 2.30 at 200 ppm acetone, but require a high operating temperature of 400 °C and have longer response (31 s) and recovery (144 s) times. ZnO-RGO nanofibers (PZ_4G_7) achieve a significantly higher response of 4.00 at 200 ppm acetone, with a response time of 36 s and recovery time of 167 s, operating at 200 °C. Co_3O_4 nanoparticles demonstrate a high response of 8.61 at 100 ppm acetone, with a response time of 43 s and recovery time of 92 s, at an operating temperature of 200 °C. $\text{N-C@SnO}_2\text{-Co}_3\text{O}_4\text{-HNBs}$ (2 %) achieves a remarkable response of 14.00 at 50 ppm acetone, but the response and recovery times are not specified, and it operates at 160 °C. Cu-MOF400 provides a response of 2.60 at 40 ppm acetone, operating at 250 °C, with unspecified response and recovery times. Co_3O_4 Nanowire array has a response of 1.60 at 100 ppm acetone, with long response (206 s) and recovery times (over 190 s), at 250 °C. The Cu doped ZnO shows a response of 3.50 at 10 ppm acetone, operating at room temperature with a prolonged response time (~400 s) and recovery time (~100 s). Au loaded Co_3O_4 porous hollow nanocages demonstrate the highest response of 14.50 at 100 ppm acetone, but have the longest response (319 s) and recovery times (280 s) at 190 °C.

Our $\beta\text{-CD}$ coated $\text{MoO}_3\text{-ZrO}_2$ nanocomposite compares favorably, offering a strong balance of performance metrics with a high response and fast response and recovery times at room temperature.

15. Conclusion

This study successfully synthesized and characterized pristine MoO_3 , pristine ZrO_2 , and a series of $\beta\text{-CD}$ coated $\text{MoO}_3\text{-ZrO}_2$ nanocomposites using a cost-effective sol-gel method for gas sensing applications, particularly at room temperature (30 °C). The incorporation of $\beta\text{-Cyclodextrin}$ significantly enhanced the surface morphology and porosity of nanocomposite, as confirmed by extensive characterization techniques (XRD, RAMAN, FT-IR, SEM, HR-TEM, UV-DRS, XPS, and BET).

The gas sensing experiments demonstrated that the $\beta\text{-Cd}$ coated $\text{MoO}_3\text{-ZrO}_2$ nanocomposites exhibited superior performance compared to pristine MoO_3 and ZrO_2 . The $10\beta\text{MZ}$ nanocomposite, in particular, displayed remarkable sensing capabilities with rapid response time of 30 s and recovery time 39 s for 100 ppm acetone vapors. The nanocomposites displayed good selectivity and repeatability, with the response strongly influenced by operating temperature and acetone concentration. Notably, the $10\beta\text{MZ}$ nanocomposite demonstrated the highest response to acetone vapors (1.97) among the tested gases. This enhanced performance is attributed to the increased specific surface area, abundance of active sites, and the porous nature of the composite, which facilitated efficient gas adsorption. Additionally, the low bond dissociation energy and high dipole moment of acetone further contributed to the improved sensing response.

In comparison with existing materials reported in the literature, the $10\beta\text{MZ}$ nanocomposite not only operates effectively at room temperature but also offers competitive advantages in terms of response and recovery times, as well as overall sensitivity to acetone vapors. These findings underscore the potential of this nanocomposite as an efficient gas sensor for VOC detection, making it a promising candidate for applications in environmental monitoring and industrial safety.

However, while the $10\beta\text{MZ}$ nanocomposite demonstrated excellent acetone sensing performance, its effectiveness across a broader spectrum of VOCs and in real-world environments remains to be fully explored. Future research should focus on optimizing the nanocomposite

Table 1

Comparison of acetone gas sensing performance with other sensing materials.

Gas sensor	Acetone Concentration (ppm)	Response	Operating Temperature (°C)	Response Time (s)	Recovery Time (s)	Reference
$\beta\text{-Cd}$ coated $\text{MoO}_3\text{-ZrO}_2$ nanocomposite	100	1.97	RT	30	39	This work
ZnO nanofibers (PZ_4G_0)	200	2.30	400	31	144	[64]
ZnO-RGO nanofibers (PZ_4G_7)	200	4.00	200	36	167	[64]
Co_3O_4 nanoparticles	100	8.61	200	43	92	[65]
$\text{N-C@SnO}_2\text{-Co}_3\text{O}_4\text{-HNBs}$ (2 %)	50	14.00	160	-	-	[66]
Cu-MOF400	40	2.60	250	-	-	[67]
Co_3O_4 Nanowire array	100	1.60	250	206	>190	[68]
Cu doped ZnO	10	3.50	RT	~400	~100	[69]
Au loaded Co_3O_4 porous hollow nanocages	100	14.50	190	319	280	[70]

composition, exploring additional VOC targets, and assessing the material's long-term stability and reusability in diverse conditions. Such efforts will be crucial in expanding the practical applications of this promising material and addressing the ongoing challenges in VOC detection.

CRediT authorship contribution statement

Akash Nagare: Writing – original draft, Investigation, Formal analysis, Data curation. **Amol Dhadage:** Investigation, Formal analysis. **Pravin Ghare:** Data curation. **Ramesh Naval:** Supervision. **Anil Athare:** Supervision. **Parikshit Gogoi:** Writing – review & editing, Supervision. **Ashok Datir:** Writing – review & editing, Supervision. **Madhukar Navgire:** Conceptualization, Writing – review & editing, Supervision.

Declaration of competing interest

The authors declare the following financial interests/personal relationships which may be considered as potential competing interests:

Akash Nagare and Amol Dhadage reports financial support was provided by MAHAJYOTI Nagpur, India. If there are other authors, they declare that they have no known competing financial interests or personal relationships that could have appeared to influence the work reported in this paper.

Data availability

No data was used for the research described in the article.

Acknowledgments

Akash Nagare and Amol Dhadage are heartily acknowledged for providing financial support from MAHAJYOTI Nagpur, India [Fellowship/2021–22/1042 (431)] and [Fellowship/2021–22/1042 (227)], respectively. The authors are thankful to the Principals of New Arts Commerce and Science College, Ahmednagar; Jijamata College of Science and Arts, Bhende, as well as Nowgong College (Autonomous), Nagaon, Assam, India, and Agasti Arts, Commerce, and Dadasaheb Rupwate Science College, Akole, India, for providing all the required facilities to carry out this work. Special thanks to Dr. D. R. Shinde, Prof. Ramkrishna More College, Pune, for valuable guidance. Also, thank you to the Department of Physics, Jijamata College of Science and Arts in Bhende for granting permission to utilize a muffle furnace for the calcination of all synthesized materials.

Supplementary materials

Supplementary material associated with this article can be found, in the online version, at [doi:10.1016/j.surfin.2024.105068](https://doi.org/10.1016/j.surfin.2024.105068).


References

- S.S. Anand, B.K. Philip, H.M. Mehendale, *Encycl. Toxicol.* (2014) 967, <https://doi.org/10.1016/B978-0-12-386454-3.00358-4>.
- W.E. Luttrell, A.L. LaGrow, *J. Chem. Heal. Saf.* 21 (2014) 29, <https://doi.org/10.1016/j.jchas.2014.03.006>.
- J.H.E. Arts, J. Mojet, L.J. van Gemert, et al., *Crit. Rev. Toxicol.* 32 (2002) 43, <https://doi.org/10.1080/20024091064174>.
- C. Lou, Z. Li, C. Yang, et al., *Sensors Actuators B Chem* 333 (2021) 129572, <https://doi.org/10.1016/j.snb.2021.129572>.
- Y. Yan, Z. Ma, J. Sun, et al., *Nano Mater. Sci.* 3 (2021) 268, <https://doi.org/10.1016/j.nanoms.2021.02.001>.
- N. Kumari, S. Sareen, M. Verma, et al., *Nanoscale Adv* 4 (2022) 4210, <https://doi.org/10.1039/D2NA00367H>.
- I.N.A. Jannah, H.F. Sekarsari, S. Mulijani, et al., *Catalysts* 12 (2022) 609, <https://doi.org/10.3390/catal12060609>.
- A. Dankeaw, G. Pongchan, M. Panapoy, B. Ksapabutr, *Sensors Actuators B Chem* 242 (2017) 202, <https://doi.org/10.1016/j.snb.2016.11.055>.
- G.P. Nagabhushana, D. Samrat, G.T. Chandrappa, *RSC Adv.* 4 (2014) 56784, <https://doi.org/10.1039/C4RA05135A>.
- M.E. Navgire, M.K. Lande, A.B. Gambhire, et al., *Bull. Mater. Sci.* 34 (2011) 535, <https://doi.org/10.1007/s12034-011-0108-2>.
- M. Navgire, A. Yelwande, B. Arbad, M. Lande, *Chinese J. Chem.* 29 (2011) 2049, <https://doi.org/10.1002/cjoc.201180355>.
- M. Lande, M. Navgire, S. Rathod, et al., *J. Ind. Eng. Chem.* 18 (2012) 277, <https://doi.org/10.1016/j.jiec.2011.11.048>.
- M. Navgire, A. Yelwande, D. Tayde, B. Arbad, M. Lande, *Chinese J. Catal.* 33 (2012) 261, [https://doi.org/10.1016/S1872-2067\(10\)60298-7](https://doi.org/10.1016/S1872-2067(10)60298-7).
- M.E. Navgire, P. Gogoi, B. Malleshm, et al., *RSC Adv* 6 (2016) 28679, <https://doi.org/10.1039/C5RA25966E>.
- M.E. Navgire, S.R. Bhitre, A.A. Yelwande, M.K. Lande, *Russ. J. Org. Chem.* 58 (2022) 394, <https://doi.org/10.1134/S1070428022030198>.
- H. Fu, X. Yang, Z. Wu, et al., *Sensors Actuators B Chem* 352 (2022) 131007, <https://doi.org/10.1016/j.snb.2021.131007>.
- E. Ghaleghafi, M.B. Rahmani, *Diam. Relat. Mater.* 137 (2023) 110174, <https://doi.org/10.1016/j.diamond.2023.110174>.
- N. Tarannum, Suhani, D. Kumar, *J. Polym. Res.* 27 (2020) 89, <https://doi.org/10.1007/s10965-020-02058-9>.
- C. Liu, P. Wang, X. Liu, et al., *ACS Sustain. Chem. Eng.* 7 (2019) 14479, <https://doi.org/10.1021/acssuschemeng.9b01911>.
- A. Palaniappan, X. Li, F.E.H. Tay, J. Li, X. Su, *Sensors Actuators B Chem* 119 (2006) 220, <https://doi.org/10.1016/j.snb.2005.12.015>.
- P. Berwal, S. Sihag, S. Rani, et al., *Ind. Eng. Chem. Res.* 62 (2023) 14835, <https://doi.org/10.1021/acs.iecr.3c02288>.
- J. Zhang, X. Jia, T. Liu, et al., *Sensors Actuators B Chem* 359 (2022) 131601, <https://doi.org/10.1016/j.snb.2022.131601>.
- L. Qiu, P. Wang, S. Zhang, et al., *Sensors Actuators B Chem* 324 (2020) 128648, <https://doi.org/10.1016/j.snb.2020.128648>.
- S. Xu, M. Wang, C.-P. Chen, S. Feng, *Sensors Actuators B Chem* 379 (2023) 133288, <https://doi.org/10.1016/j.snb.2023.133288>.
- S. Shao, X. Chen, Y. Chen, M. Lai, L. Che, *Appl. Surf. Sci.* 473 (2019) 902, <https://doi.org/10.1016/j.apsusc.2018.12.208>.
- Z. Komissarova, L.N. Yu P Simanov, *Russ. J. Inorg. Chem. (Engl. Transl.* 5 (1960) 687.
- N. Wooster, *Zeitschrift für Krist. - Cryst. Mater.* 80 (1931) 504, <https://doi.org/10.1524/zkri.1931.80.1.504>.
- M. Auray, M. Quarton, P. Tarte, *Powder Diffr* 2 (1987) 36, <https://doi.org/10.1017/S0885715600012215>.
- H.-J. Huang, M.-C. Wang, *Ceram. Int.* 39 (2013) 1729, <https://doi.org/10.1016/j.ceramint.2012.08.019>.
- B. Malleshm, P. Sudarsanam, B. Venkata Shiva Reddy, B. Govinda Rao, B. Reddy, *ACS Omega* 3 (2018) 16839, <https://doi.org/10.1021/acsomega.8b02008>.
- P. Intaphong, A. Phuruangrat, H. Yeebu, et al., *Russ. J. Inorg. Chem.* 66 (2021) 2123, <https://doi.org/10.1134/S0036023621140047>.
- L. Shi, K.C. Tin, N.B. Wong, *J. Mater. Sci.* 34 (1999) 3367, <https://doi.org/10.1023/A:1004681015331>.
- S. Phadungdhithada, P. Mangkorntong, S. Chooipun, N. Mangkorntong, D. Wongratanaphisan, *Mater. Lett.* 65 (2011) 568, <https://doi.org/10.1016/j.matlet.2010.10.074>.
- S. Phadungdhithada, P. Mangkorntong, S. Chooipun, N. Mangkorntong, *Ceram. Int.* 34 (2008) 1121, <https://doi.org/10.1016/j.ceramint.2007.09.093>.
- B. Zhao, X. Wang, H. Ma, Y. Tang, *J. Mol. Catal. A Chem.* 108 (1996) 167, [https://doi.org/10.1016/1381-1169\(96\)00008-8](https://doi.org/10.1016/1381-1169(96)00008-8).
- B. Samaranch, P. Ramirez de la Piscina, G. Clet, M. Houalla, N. Homs, *Chem. Mater.* 18 (2006) 1581, <https://doi.org/10.1021/cm052433c>.
- Z. Liu, L. Dong, W. Ji, Y. Chen, *J. Chem. Soc. Faraday Trans.* 94 (1998) 1137, <https://doi.org/10.1039/a707725d>.
- S. Xie, K. Chen, A.T. Bell, E. Iglesia, *J. Phys. Chem. B* 104 (2000) 10059, <https://doi.org/10.1021/jp002419h>.
- V.K. Krut'ko, A.I. Kulak, O.N. Musskaya, *Inorg. Mater.* 53 (2017) 429, <https://doi.org/10.1134/S0020168517040094>.
- L. Ciolek, Z. Jaegermann, E. Zaczynska, et al., *Bioinorg. Chem. Appl.* 2022 (2022), <https://doi.org/10.1155/2022/9574245>.
- G.K. Sidhu, A.K. Kaushik, S. Rana, S. Bhansali, R. Kumar, *Appl. Surf. Sci.* 334 (2015) 216, <https://doi.org/10.1016/j.apsusc.2014.10.036>.
- S. Maity, M. Rana, B. Srinivas, et al., *J. Mol. Catal. A Chem.* 153 (2000) 121, [https://doi.org/10.1016/S1381-1169\(99\)00311-8](https://doi.org/10.1016/S1381-1169(99)00311-8).
- V. dos, C.P. Bergm, *Adv. Cryst. Process., InTech* (2012), <https://doi.org/10.5772/36385>.
- E. Cao, Z. Chu, H. Wang, et al., *Ceram. Int.* 44 (2018) 7180, <https://doi.org/10.1016/j.ceramint.2018.01.163>.
- R. Aher, A. Punde, P. Shinde, et al., *ACS Omega* 7 (2022) 31877, <https://doi.org/10.1021/acsomega.2c02666>.
- S. Pandharkar, S. Rondiya, A. Bhorde, et al., *J. Mater. Sci. Mater. Electron.* 30 (2019) 14781, <https://doi.org/10.1007/s10854-019-01851-7>.
- A.M. Amanulla, R. Sundaram, K. Kaviyarasu, *Surfaces and Interfaces* 16 (2019) 132, <https://doi.org/10.1016/j.surfin.2019.06.001>.
- X. Hou, M. Ruan, L. Zhou, et al., *J. Energy Chem.* 78 (2023) 91, <https://doi.org/10.1016/j.jechem.2022.11.011>.
- C.V. Reddy, B. Babu, I.N. Reddy, *J. Shim, Ceram. Int.* 44 (2018) 6940, <https://doi.org/10.1016/j.ceramint.2018.01.123>.

- [50] T. Thomas, N. Jayababu, J. Shruthi, et al., *Thin Solid Films* 722 (2021) 138575, <https://doi.org/10.1016/j.tsf.2021.138575>.
- [51] A. Raja, N. Son, M. Kang, *Environ. Res.* 199 (2021) 111261, <https://doi.org/10.1016/j.envres.2021.111261>.
- [52] L.-H. Meng, X.-P. Tan, L. Chen, et al., *Appl. Surf. Sci.* 541 (2021) 148476, <https://doi.org/10.1016/j.apsusc.2020.148476>.
- [53] Y. Yu, S. Liu, *Front. Mater. Sci.* 16 (2022) 220585, <https://doi.org/10.1007/s11706-022-0585-9>.
- [54] S. Singh, J. Deb, U. Sarkar, S. Sharma, *ACS Sustain. Chem. Eng.* 9 (2021) 7328, <https://doi.org/10.1021/acssuschemeng.1c01527>.
- [55] K. Xu, S. Duan, Q. Tang, et al., *CrystEngComm* 21 (2019) 5834, <https://doi.org/10.1039/C9CE00742C>.
- [56] S. Zhang, Y. Ding, Q. Wang, P. Song, *Sensors Actuators B Chem* 393 (2023) 134122, <https://doi.org/10.1016/j.snb.2023.134122>.
- [57] F. Li, J. Jing, J. Li, et al., *Sensors Actuators B Chem* 400 (2024) 134887, <https://doi.org/10.1016/j.snb.2023.134887>.
- [58] J. Liu, F. Jia, Y. Yang, et al., *Vacuum* 216 (2023) 112443, <https://doi.org/10.1016/j.vacuum.2023.112443>.
- [59] H. Yan, P. Song, S. Zhang, et al., *Sensors Actuators B Chem* 236 (2016) 201, <https://doi.org/10.1016/j.snb.2016.05.139>.
- [60] T. Zhou, T. Zhang, J. Deng, et al., *Sensors Actuators B Chem* 242 (2017) 369, <https://doi.org/10.1016/j.snb.2016.11.067>.
- [61] M.I. Zaki, M.A. Hasan, L. Pasupulety, *Langmuir* 17 (2001) 768, <https://doi.org/10.1021/la000976p>.
- [62] J. Gao, A.V. Teplyakov, J. Catal. 319 (2014) 136, <https://doi.org/10.1016/j.jcat.2014.08.014>.
- [63] Q. Xie, Y. Ding, Q. Wang, P. Song, *Sensors Actuators B Chem* 405 (2024) 135338, <https://doi.org/10.1016/j.snb.2024.135338>.
- [64] T. Salehi, A. Taherizadeh, A. Bahrami, A. Allafchian, V. Ghafarinia, *Adv. Eng. Mater.* 22 (2020), <https://doi.org/10.1002/adem.202000005>.
- [65] X. Fan, Y. Xu, C. Ma, W. He, J. Alloys Compd. 854 (2021) 157234, <https://doi.org/10.1016/j.jallcom.2020.157234>.
- [66] M. Huang, S. Wang, H. Fu, et al., J. Alloys Compd. 863 (2021) 158341, <https://doi.org/10.1016/j.jallcom.2020.158341>.
- [67] C. Arul, K. Moulae, N. Donato, et al., *Sensors Actuators B Chem* 329 (2021) 129053, <https://doi.org/10.1016/j.snb.2020.129053>.
- [68] K. Xu, C. Lai, Y. Yang, et al., *Sensors Actuators B Chem* 329 (2021) 129095, <https://doi.org/10.1016/j.snb.2020.129095>.
- [69] S. Brahma, Y.-W. Yeh, J.-L. Huang, C.-P. Liu, *Appl. Surf. Sci.* 564 (2021) 150351, <https://doi.org/10.1016/j.apsusc.2021.150351>.
- [70] Z. Li, Y. Zhang, H. Zhang, J. Yi, *Sensors Actuators B Chem* 344 (2021) 130182, <https://doi.org/10.1016/j.snb.2021.130182>.



Architecture of γ -WO₃ nanosheets-like electrode material for super capacitor application

Rahul S. Diggikar^{1,*}, Mohaseen S. Tamboli², S. K. Shinde³ , Shamkumar P. Deshmukh⁴, Shoyebmohamad F. Shaikh⁵, Hassnain Abbas Khan⁶, and Nguyen Tam Nguyen Truong^{7,*}

¹ Department of Chemistry, New Arts, Commerce and Science College, Parner, Ahmednagar, Maharashtra 414302, India

² Korea Institute of Energy Technology (KENTECH), 21 KENTECH-gil, Naju, Jeollanam-Do 58330, Republic of Korea

³ Department of Physics, Arts, Science and Commerce College, Indapur, Maharashtra 413106, India

⁴ Department of Chemistry, D.B.F. Dayanand College of Arts and Science, Solapur, MS 413002, India

⁵ Department of Chemistry, College of Science, King Saud University, P.O. Box 2455, 11451 Riyadh, Saudi Arabia

⁶ Clean Energy Research Centre, Korea Institute of Science and Technology, Cheongryang, PO Box 131, Seoul 02-792, Republic of Korea

⁷ School of Chemical Engineering, Yeungnam University, 280 Daehak-Ro, Gyeongsan 38541, Republic of Korea

Received: 3 April 2023

Accepted: 28 July 2023

Published online:

30 August 2023

© The Author(s), under exclusive licence to Springer Science+Business Media, LLC, part of Springer Nature 2023

ABSTRACT

The present work demonstrated simple, cost-effective, and efficient synthetic approach for producing two-dimensional (2D) nanosheets (NSs) of oxygen-deficient monoclinic γ -tungsten oxide (γ -WO₃), which exhibit desirable properties used for super capacitor application. The hydrothermal method was employed at a temperature of 120 °C for 12 h to synthesize γ -WO₃. Structural and optical properties of the γ -WO₃ NSs were analyzed by using various techniques such as X-ray diffraction, Raman spectroscopy, diffused reflectance spectroscopy, and photoluminescence analysis. Morphological characterization was performed using field emission-scanning electron microscopy and high-resolution transmission electron microscopy. Furthermore, the electrochemical properties of the γ -WO₃ NSs were evaluated for supercapacitor applications. The as-synthesized γ -WO₃ NSs electrode exhibited a remarkable specific capacitance of 386 F g⁻¹ at a low current density of 5 mA cm⁻². Also, the γ -WO₃ NSs electrode displayed excellent stability, emphasizing its potential for energy storage device applications (ESDA).

Address correspondence to E-mail: diggikarrs@gmail.com; tamnguyentn@ynu.ac.kr

1 Introduction

Nanomaterial with two-dimensional (2D) structures have received immense attention owing to their specific structural anisotropy and several fascinating electrical properties [1–3]. The transition metal oxide (TMO) semiconductors [4–11] with well-known physical and chemical properties in hierarchical nanostructures have attentive for wide applications in electrochemical energy storage devices (EESDs). However, the electrochemical activity of nanostructure tungsten oxides (WO_3) strongly depends on morphology and crystal system based on synthesis techniques, besides this, are also useful in water splitting, [12] visible light driven photo catalysts, photochromic devices, buffer layer in organic light-emitting diodes and sensor. EESDs play the central role in ongoing sustainable carbon-free energy technologies such as solar cells, batteries, and super capacitors, where the key factor in up and down streams of energy and power density devices trying to be resolved for both the purpose of TMOs are preferred. Due to the excellent electrochemical stability, low cost and easy to obtained WO_3 motivated to the material scientist to make a new avenue in the field of EESDs [13]. The recognition of these technologies heavily trusts on the fundamental properties of the electrode materials that are being used to fabricate EESDs. WO_3 has been materialized as a projecting metal oxide for next EESDs development by its inherently tunable nonstoichiometric, surface-active redox states augmented to improve the electrode kinetics in super capacitor applications. For the same, various synthesis techniques have been employed to engineer 2D materials with designated and controllable morphology. [14, 15] Recently, Mandal et al. [16] reported the lack of synthesis techniques with high quality WO_3 nanostructures. Yin et al. [17] presented the NSs of anchored WO_3 . The quality of nanostructures used for the supercapacitor is depends on the contact between electrode and electrolyte, the NSs possesses the sufficient area for the contact due to aspect ratio. Yang et al. [18] reported the NSs of WO_3 doped with MnO_2 for super capacitor. The quality of nanophase WO_3 also been improved by compositing with post transition metals [19].

In the context, the 2D γ WO_3 Nano sheets (NSs) is synthesized by hydrothermal technique in mild conditions and tested for electrode material in super capacitor applications resulting as a promising

material. By using the nanostructures reported the enhanced nano-technological applications. The super capacitor is one of the most important EESD which works as a faster delivery of energy than batteries and is superior to conventional capacitors [20]. To date, various electrode materials have been synthesized for use in supercapacitors, including conducting polymers, metal–organic frameworks, siloxenes, transition metal oxides, transition metal sulfides, carbonaceous materials, chalcogenides, polyoxometalates [5, 9, 11], Tungsten oxides in the forms of NSs is an n-type semiconductor with an indirect bandgap having good optical, chemical, and thermal stability, making it appropriate for super capacitor applications [21–23]. Extensive research and numerous studies have focused on WO_3 based super capacitors, highlighting their notable pseudo capacitive behavior arising from the presence of multiple oxidation states, rapid surface reactions, and a crystal structure conducive to the intercalation of electrolyte ions. Huang et al. [24] observed a high specific capacitance of WO_3 NSs.

In this work, we report the synthesis of stable, cost-effective, and oxygen deficient 2D- γ - WO_3 NSs by hydrothermal method and their performance in super capacitor applications. The synthesized materials were characterized by different spectroscopic techniques. Then, the as-synthesized materials were tested for super capacitive properties in the three-electrode system with the potential window of 0.0–0.6 V in the presence of 3 M KOH. The as-synthesized 2D NSs of γ - WO_3 demonstrated excellent electrochemical performance with the specific capacitance of 386 F g^{-1} at a constant current density of 5 mA cm^{-2} .

2 Experimental section

2.1 Synthesis of γ -Tungsten oxide nanosheet (γ - WO_3 NSs)

The precursors used in this synthesis are of analytical grade and utilized as received. In a typical reaction, an equivalent amount of lead acetate $\text{Pb}(\text{C}_2\text{H}_3\text{O}_2)_2$ and sodium tungstate (Na_2WO_4) (2 mmol) were dissolved in 50 ml 0.1 M nitric acid (HNO_3) solution. The mixture was stirred vigorously for 75 min in a hot water bath and obtained a white color suspension. This white color suspension of lead tungstate

(PbWO₄) turns to yellow at pH 2.9 [15] which is subjected to the hydrothermal treatment at 120 °C for 12 h in a Teflon reactor jacketed with stainless steel autoclave. After the completion of the reaction, the product was filtered at room temperature and then washed with DI water and dried at 100 °C for 2 h.

2.2 Characterizations

The structural analysis and phase purity of the sample was examined by X-ray diffraction (XRD) on a Bruker D8 Advance X-ray diffractometer. X-ray photoelectron spectroscopy (XPS) analysis was performed using an ESCALAB-MKII spectrometer. The absorption properties were measured by a UV–Vis diffuse reflectance spectrophotometer (UV-3600, Shimadzu). The Photoluminescence properties were measured by a spectrofluorophotometer (RF-5301PC, Shimadzu). Room-temperature micro-Raman scattering analysis was performed using an HR 800-Raman spectrometer (Horiba Jobin Yvon), with excitation at 532 nm. The morphological features of the synthesized samples were analyzed by Field-Emission Scanning Electron Microscopy (HITACHI S4800) and Transmission Electron Microscopy (FEI Technai T20, Netherlands). For SEM analysis, the sample was mounted on an aluminum stub using conductive sticky pads. For TEM analysis, the as-synthesized sample was dispersed onto TEM grids using ethanol, and air-dried before imaging.

2.3 Electrochemical measurement

Electrochemical properties of the electrodes fabricated from nanosheet-like γ -WO₃ were measured through a three-electrode assembly in 3 M KOH electrolyte using a Versa STAT 3 electrochemical workstation. The three-electrode assembly was composed of WO₃ as a working electrode, platinum as a counter electrode, and saturated calomel electrode (SCE) as a reference electrode. The cyclic voltammetry (CV) analysis was performed by varying the scan rates from 5 to 100 mV s⁻¹ within a potential window of 0–0.6 V vs. SCE. A Galvanostatic charge–discharge (GCD) investigation was carried out at various current densities ranging from 5 to 10 mA cm⁻². The electrochemical impedance spectroscopy (EIS) was conducted over a frequency range of 1 Hz–100 kHz.

3 Results and discussion

Figure 1a–d illustrates the XRD, Raman, DRS, and PL study of γ -WO_{3-x} NSs, respectively. The peak positions in Fig. 1a correspond to the monoclinic structure of WO₃ (γ -WO₃) with lattice parameters, $a = 0.7301$, $b = 0.7539$, and $c = 0.7688$ nm (JCPDS Card No 01-083-0950). The monoclinic structure of WO₃ is referred to as the gamma phase of tungsten oxide (γ -WO₃). The strong intensity peak located at 23.1° indicates domination of the (002) crystal plane as a preferred orientation [25]. Comparison to the XRD pattern of bulk WO₃ reported by Boruah et al., [26] corresponds to γ -WO₃ NSs. In addition, the shape of the peak located at 34.19° is not the same as bulk WO₃. This could indicate the oxygen deficiency in WO₃ NSs [15]. The Raman peaks observed at 720 and 813.5 cm⁻¹ in Fig. 1b correspond to the stretching vibrations [ν (O–W–O)] and the peak at 280.5 cm⁻¹ belongs to the bending vibrations [δ (O–W–O)] of the γ -WO₃ NSs [27–29]. Unlike in the bulk WO₃, the peaks are slightly blue-shifted, this again could attribute to the oxygen deficiency in the NS [23]. From the UV–Vis diffuse reflectance spectrum shown in Fig. 1c., the electronic band gap of the NSs is estimated as 2.86 eV. The band gap was evaluated by the Tauc method using the following Eq. (1):

$$(\alpha \cdot hv)^{1/\gamma} = B(hv - E_g) \quad (1)$$

where, α is the absorption coefficient, h is the Planck constant, ν is the photon's frequency, E_g is the band gap energy and B is a constant. The γ factor depends on the nature of the electron transition and is equal to 1/2 for direct and 2 for indirect band gaps. [26] The band gap of the NSs is higher than that of the commercial bulk WO₃ (2.54 eV) partially due to quantum confinement effects [15]. The major cause of the enhancement in the band gap is due to the shortage of O²⁻ ions at the intrinsic sites, although oxygen deficiency ultimately helps in the formation of the NSs [26, 27]. Fig. 1d reveals the PL spectrum of γ -WO₃ NSs obtained at an excitation wavelength of 325 nm in dichloromethane. The strong peak at 433 nm reveals a bandgap of 2.86 eV (\sim transparent WO₃) and other weak peaks are at the border of quantum confinement. However, quantum confinement is difficult to attain in metal oxides because their exciton Bohr radii are of the order of a nanometer [28]. This border quantum confinement

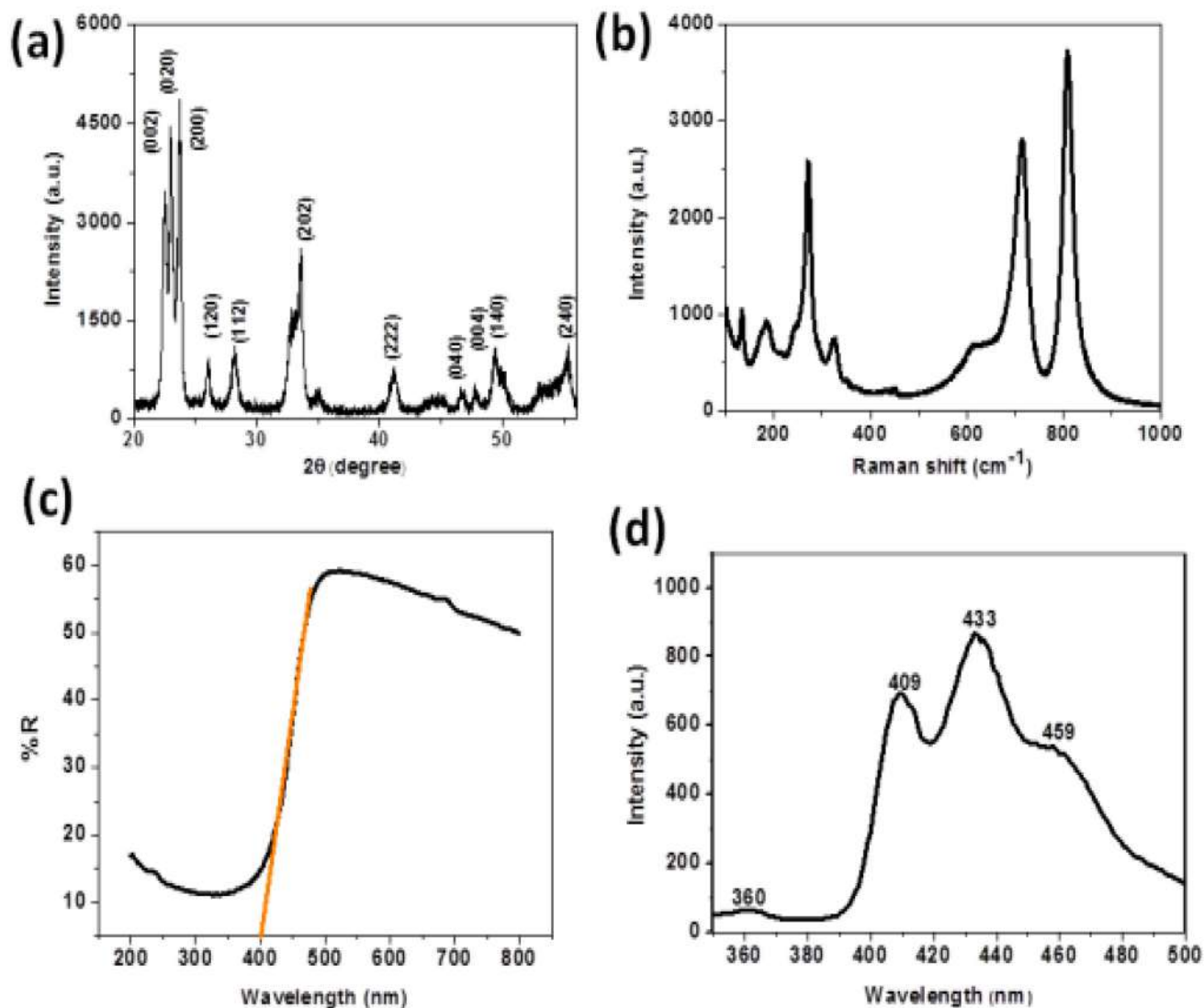
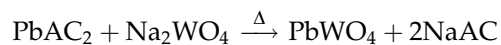


Fig. 1 a XRD, b Raman spectra, c Diffused reflectance spectra (DRS), and d Photoluminescence (PL) of γ - WO_3 NSs

and oxygen deficiency are indicated by the peaks at 433 and 459 nm, respectively.

The possible reaction of our as-prepared samples is given as follows. The reactions involved as,

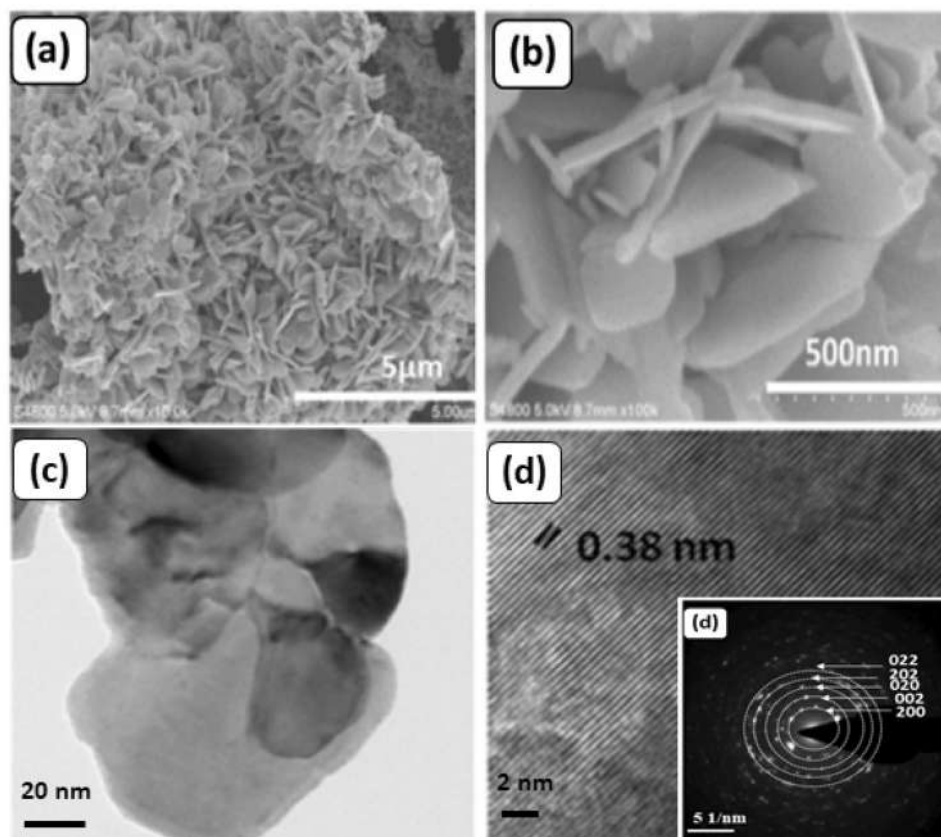


FE-SEM images of the γ - WO_3 NSs with different magnifications are displayed in Fig. 2a and b. From Fig. 2a, the morphology of the as-synthesized γ - WO_3 can be concluded as NSs. From the high magnification image provided in Fig. 2b, the average lateral size and thickness of the NSs are estimated to be 50

and 100 nm respectively. It shows that these NSs are loosely stacked together leading to a large mesoporosity, which could be one of the factors contributing to the good electrochemical properties. The surface area plays an important role in enhancing the supercapacitor properties. Therefore, the 2D NSs can provide better optimization routes including the modulation of the materials' activity, surface polarization, and rich oxygen vacancies. Hence, this is synthesized γ - WO_3 NSs could be very effective for supercapacitor applications.

The TEM images of γ - WO_3 NSs are given in Fig. 2c and d show the growth of a thin layer of uniform γ - WO_3 NSs. Figure 2c show γ - WO_3 NSs with irregular morphology. By analyzing the TEM images (Fig. 2c),

Fig. 2 a–b FESEM images of γ -WO₃ NSs c TEM images of γ -WO₃ NSs d high resolution image and SAED pattern (inset) of γ -WO₃ NSs synthesized by hydrothermal method



it is estimated that γ -WO₃ NSs have a broad distribution in lateral size ranging from 20 to 100 nm. The observed NSs-like morphology is favorable for supercapacitor application. HR-TEM images of the NSs displayed in Fig. 2d, clearly show lattice fringes, whose resolution is estimated to be 0.38 nm. This corresponds to the interplanar distance of the (002) planes of WO₃ (in good agreement with JCPDS data 01-083-0950), supporting the dominance of (002) peaks in the XRD patterns shown in Fig. 2a. The SAED pattern of the NS is given in inset Fig. 2d. From the figure, it is clear that the NS are crystalline and the corresponding planes match very well with the XRD data given in (Fig. 1a).

Elemental and oxidation state analysis was performed using XPS and are presented in Fig. 3a–c. The XPS survey spectrum of the NSs presented in Fig. 3a displays no other peaks than that of ‘W’ and ‘O’. The W4f spectrum with spin–orbit doublet 7/2–5/2 for the ‘W’ valance state is demonstrated in Fig. 3b. In Fig. 3c, the deconvoluted O1s spectra of the γ -WO₃-NSs are displayed. The peak located at 529.6 and 530 eV corresponds to the stoichiometric O₂[−] ions, while the slightly shifted peak located at

532.5 eV corresponds to oxygen deficiency [15]. The XPS results further support the XRD and Raman data to confirm the presence of oxygen deficiency in the nanosheet [29].

Figure 4 shows the supercapacitive properties of the γ -WO₃ thin films prepared using the hydrothermal method at a temperature of 120 °C for a constant deposition time of 12 h. Figure 4a shows the CV measurements of the γ -WO₃ thin films with various scan rates from 5 to 100 mV s^{−1} in the potential window of 0 to −0.6 V, respectively. The CV curves indicate the scan rates increase in the area under the CV curves and the reduction peaks intensity also increases. The values of specific capacitances of the γ -WO₃ thin film can be calculated using standard relations [29]. The calculated values of the C_s are shown in Fig. 4b, the obtained C_s values of 451, 409, 314, 190, 171, and 161 F g^{−1} for 5, 10, 20, 50, 80, and 100 mV s^{−1}, respectively. The C_s values of the γ -WO₃ thin film show larger than the reported values in the literature review. The calculated values of C_s are more than the previously reported values because the vertical growth of the nanoplates like surface morphology provided higher surface area and easy axis

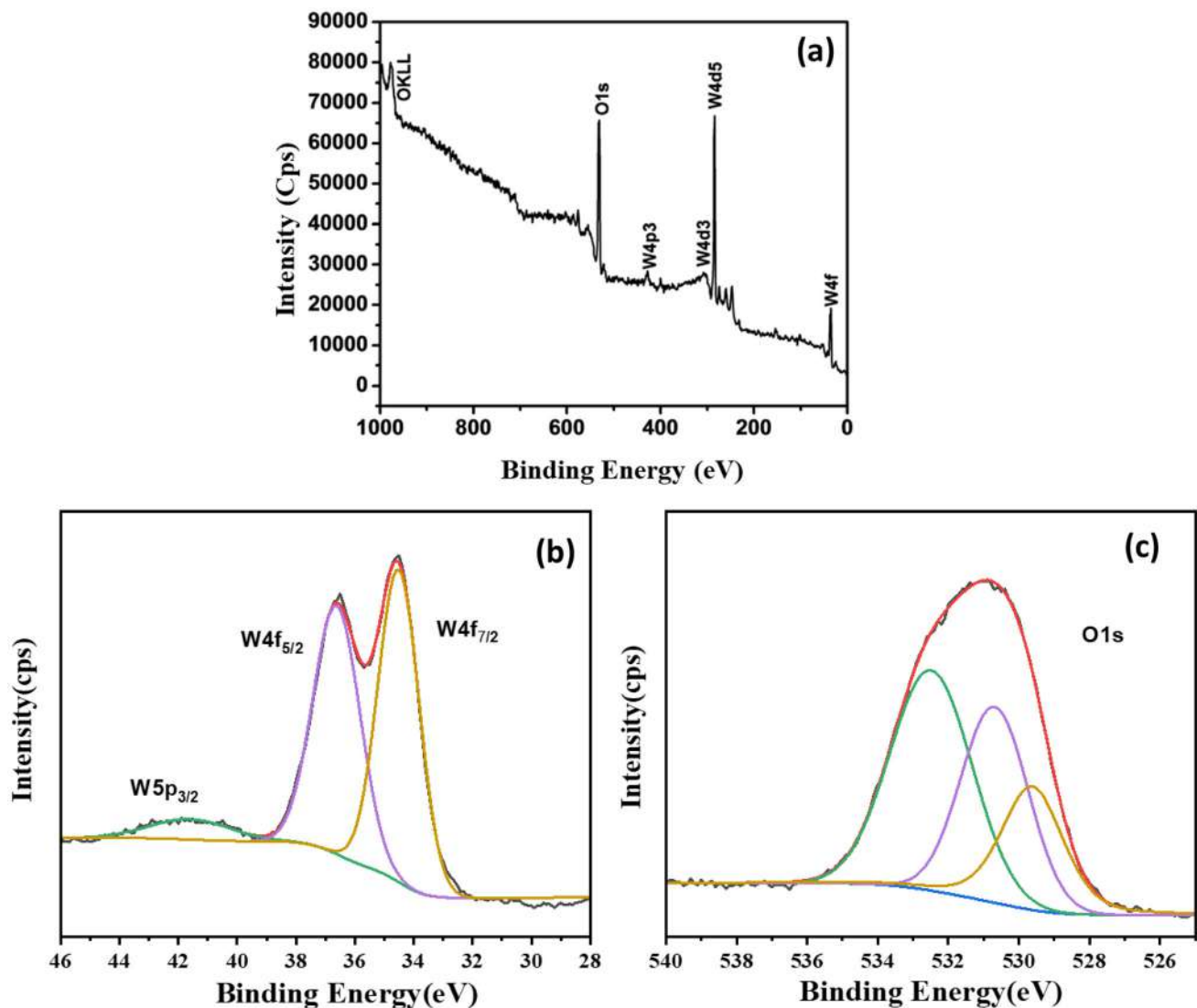


Fig. 3 a XPS survey scan spectrum b W4f XPS spectrum, and c O1s XPS spectrum of γ - WO_3 NSs

of the ions transfer from the electrode/electrolyte interface. Numerous researchers are currently engaged in the study of WO_3 nanomaterial for its potential use in electrochemical applications [30]. Sun et al. [31] synthesized the hexagonal nanorod-like WO_3 electrodes for negative electrode material by hydrothermal method for the supercapacitors application, and they reported a higher specific capacitance of 415.3 F g^{-1} at 0.5 A g^{-1} . Mineo et al. [32] reports the WO_3 electrode material using hydrothermal method. Also they reported the value specific capacitance of 325 F g^{-1} at fixed scan rate 2 mV s^{-1} with hexagonal nanostructures. Also, they reported the effect of, structural morphology and electrical properties of WO_3 electrodes. Similarly, the

supercapacitor properties of the as-synthesized nanoplates like the nanostructure of γ - WO_3 thin films were studied by GCD measurements with the same potential window (0.0 to -0.6 V) in the 3 M KOH electrolyte. Figure 4c shows the typical GCD measurements of γ - WO_3 thin films at different current densities from 5 to 10 mA cm^{-2} in the constant potential windows of 0.0 to $0-0.6 \text{ V}$, respectively. The charging-discharging curves show a non-linear-like nature which is typical behavior of electrical double layer capacitor (EDLC) super capacitors. This types of behavior indicate the presence of faradaic reaction in the as-synthesized nanoplates like γ - WO_3 thin films and electrolytes. The calculated values of the C_s of the as-synthesized nanoplates like γ - WO_3 thin films

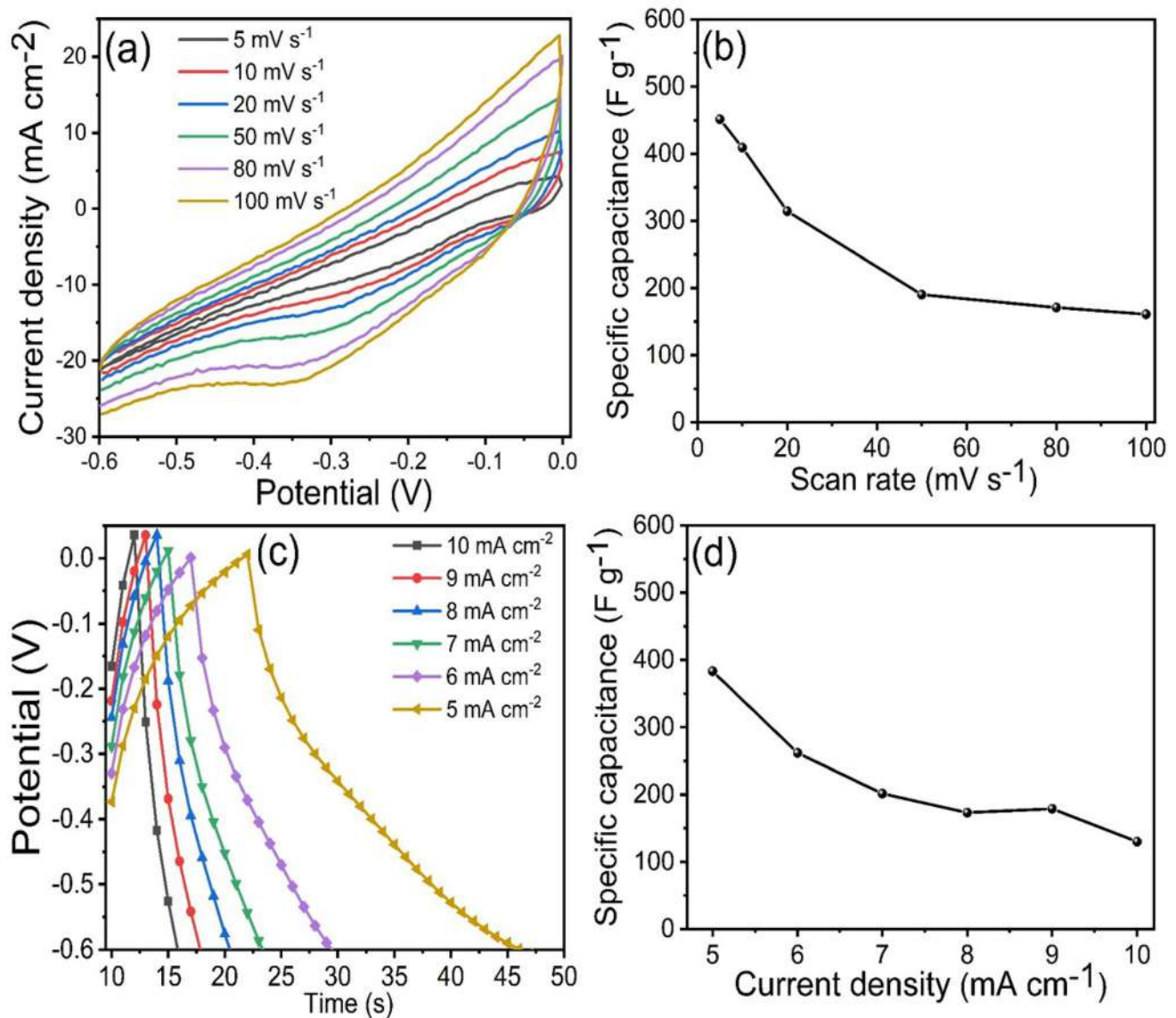


Fig. 4 **a** CV curves of WO₃ electrodes at various scan rates, **b** specific capacitance with scan rates, **c** GCD curves of WO₃ electrodes at different current densities, and **d** specific capacitance with different current density

using standard relations. The calculated C_s values were 383, 261, 201, 173, 179, and 130 F g⁻¹ at different current densities of 5, 6, 7, 8, 9, and 10 mA cm⁻² (as shown in Fig. 4d) [32–35]. Kumar and Karupuchamy [36] prepared the Co doped WO₃ electrode composite with CNT using solution growth method. They mentioned the value of the specific capacitance of 60 F g⁻¹ at 1 A g⁻¹, respectively. The calculated C_s values are better than the previously mentioned study [37], which indicates the highly porous-like

surface supply more active surface area for electrochemical properties, which is useful for faster ion transformation during the electrochemical reaction [33, 34].

For more details study of the electrical mechanism of the as-synthesized nanoplates like a γ -WO₃ thin film as shown in Fig. 5. We used the EIS techniques in the constant frequency of 1–100 kHz with an open-potential 0.39 V. The calculated values of the solution resistance (R_s) and charge-transfer resistance (R_{ct}) of

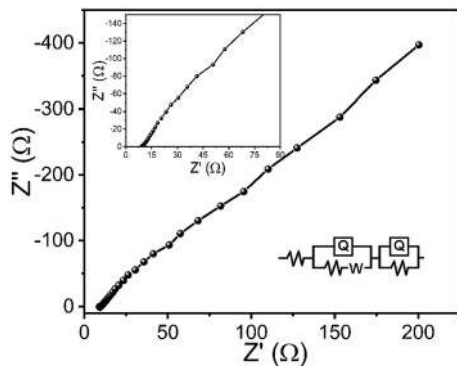


Fig. 5 EIS plots of WO₃ electrode, inset shows zoom image of the EIS and equivalent circuit

γ -WO₃ thin film fitted data with the Z-SimpWin software. The fitted data provided the values of the R_s and R_{ct} are 9.1 and 1.19 Ω , respectively. The calculated values of the charge-transfer resistance indicate the as-synthesized nanoplates like γ -WO₃ electrode provided higher conductivity for the enhanced electrochemical properties [34, 35].

4 Conclusions

In conclusion, high-quality γ -WO₃ NSs were synthesized by an inexpensive hydrothermal route at low temperatures. The as synthesized materials were characterized by different techniques such as X-ray diffraction, Raman spectroscopy, diffused reflectance spectroscopy, and photoluminescence analysis, field emission-scanning electron microscopy and high-resolution transmission electron microscopy. The as-prepared γ -WO₃ NSs have a monoclinic structure with the (002) plane as the preferred orientation. The as-synthesized γ -WO₃ has nanosheet-like morphology having a thickness of \sim 50 nm. The band gap of the nanosheet is calculated to be 2.86 eV using DRS results. In the Raman study of γ -WO₃ NSs, the peaks at 720 and 813.5 cm^{-1} corresponds to the stretching vibrations [ν (O-W-O)] and 280.5 cm^{-1} belong to the bending vibrations [δ (O-W-O)]. Furthermore, γ -WO₃ NSs were tested for electrochemical properties for supercapacitor application. The as-synthesized γ -WO₃ NSs electrode shows a high specific capacitance of 451 F g^{-1} at a scan rate of 5 mV s^{-1} . In addition, the γ -WO₃ nanosheet electrode displayed excellent stability, emphasizing its potential for energy storage applications. It opens up a new avenue to produce a new phase of WO₃ that will be extremely useful for

supercapacitor applications as well as other optoelectronic applications such as a photodetector, photo-switches, high-performance ultraviolet radiation sensors, optical keys, optical memory, etc. Further research in this direction is highly anticipated.

Author contributions

Conceptualization, writing-original draft, and methodology, RSD; formal analysis, MST, and SKS; resources, SPD; HK; writing—review and editing, SFS and NTNT funding acquisition, SFS, All authors have read and agreed to the published version of the manuscript.

Funding

The authors extend their sincere appreciation to the Researchers Supporting Project number (RSP2023R370), King Saud University, Riyadh, Saudi Arabia for the financial support.

Data availability

Not Applicable.

Declarations

Conflict of interest The authors declare that they have no conflict of interest.

Research involving human and animal participants This article does not contain any studies with human participants or animals performed by any of the authors. In this experiment, we did not collect any samples of human and animals.

References

1. S. Chen, J. Duan, Y. Tang, B. Jin, S.Z. Qiao, Molybdenum sulfide clusters-nitrogen-doped graphene hybrid hydrogel film as an efficient three-dimensional hydrogen evolution electrocatalyst. *Nano Energy* **11**, 11–18 (2015)
2. X. Wang, G. Li, F.M. Hassan, M. Li, K. Feng, X. Xiao, Z. Chen, Building sponge-like robust architectures of CNT-graphene-Si composites with enhanced rate and cycling

- performance for lithium-ion batteries. *J. Mater. Chem. A* **3**, 3962–3967 (2015)
- J. Low, S. Cao, J. Yu, S. Wageh, Two-dimensional layered composite photocatalysts. *Chem. Commun.* **50**, 10768–10777 (2014)
 - P. Velusamy, R. Ramesh Babu, K.T., Aparna, effect of Sm doping on the physical properties of ZnO thin films deposited by spray pyrolysis technique. *AIP Conference Proceedings* **1832**, 080085 (2017). <https://doi.org/10.1063/1.4980545>
 - R.S. Diggikar, M.V. Kulkarni, G.M. Kale, B.B. Kale, Formation of multifunctional nanocomposites with ultrathin layers of polyaniline (PANI) on silver vanadium oxide (SVO) nanospheres by in situ polymerization. *J. Mater. Chem. A* **1**, 3992–4001 (2013)
 - S.P. Deshmukh, K.R. Sanadi, R.S. Diggikar, V.B. Koli, A.V. Mali, Structural, magnetic, and electrical properties of manganese-substituted magnesium chromate spinel structure. *J. Mater. Sci.: Mater. Electron.* **32**, 6810–6819 (2021)
 - P. Velusamy, R.R. Babu, K. Ramamurthi, Structural, microstructural, optical and electrical properties of spray deposited rare-earth metal (Sm) ions doped CdO thin films. *J. Mater. Sci.: Mater. Electron.* **26**, 4152–4164 (2015)
 - P. Velusamy, R. Ramesh Babu, K. Ramamurthi, M.S. Dahlem, E. Elangovan, High transparent conducting cerium incorporated CdO thin films deposited by spray pyrolytic technique. *RSC Adv.* **0**, 1–3 (2013)
 - R.S. Diggikar, J.D. Ambekar, M.V. Kulkarni, B.B. Kale, Nanocrystalline silver vanadium sulfide (SVS) anchored polyaniline (PANI): new nanocomposite system for supercapacitor, 2013. *New J. Chem.* **37**(10), 3236–3243 (2013)
 - P. Velusamy, R. Ramesh Babu, K. Ramamurthi, E. Elangovan, J. Viegas, Effect of La doping on the structural, optical and electrical properties of spray pyrolytically deposited CdO thin films. *J. Alloys Compd.* **708**, 804–812 (2017)
 - R.S. Diggikar, V.M. Dhavale, D.B. Shinde, N.S. Kanbargi, M.V. Kulkarni, B.B. Kale, Morphology controlled synthesis of LiV₂O₅/Ag nanocomposite nanotubes with enhanced electrochemical performance. *RSC Adv.* **2**, 3231–3233 (2012)
 - P. Velusamy, X. Liu, M. Sathiyaa, N.S. Alsaiari, F.M. Alzahrani, M. Tariq Nazir, M. Elangovan Elamurugu, Senthil Pandian, Fuchun Zhang, Investigate the suitability of g-C₃N₄ nanosheets ornamented with BiOI nanoflowers for photocatalytic dye degradation and PEC water splitting. *Chemosphere* **321**, 138007 (2023)
 - G. Mineo, E. Bruno, S. Mirabella, Advances in WO₃-Based Supercapacitors: State-of-the-Art Research and Future Perspectives. *Nanomaterials* **13**, 1418 (2003)
 - A.V. Salkar, S.V. Bhosale, P.P. Morajkar, Nanostructured WO_{3-x} based advanced supercapacitors for sustainable energy applications, in *Advances in Metal Oxides and Their Composites for Emerging Applications*. (Elsevier, Amsterdam, 2022), pp.213–238
 - F. Zhan, Y. Liu, K. Wang, X. Yang, M. Liu, X. Qiu, J. Li, W. Li, Oxygen-deficient nanofiber WO_{3-x}/WO₃ homojunction photoanodes synthesized via a novel metal self-reducing method. *ACS Appl. Mater. Interfaces* **11**, 39951–39960 (2019)
 - D. Mandal, P. Routh, A.K. Nandi, A New facile synthesis of tungsten oxide from tungsten disulfide: structure dependent supercapacitor and negative differential resistance properties. *Small* **1**, 1702881 (2017)
 - Z. Yin, Y. Bu, J. Ren, S. Chen, D. Zhao, Y. Zou, S. Shen, D. Yang, Triggering superior sodium ion adsorption on (2 0 0) facet of mesoporous WO₃ nanosheet arrays for enhanced supercapacitance. *Chem. Eng. J.* **345**, 165–173 (2018)
 - G. Yang, X. Xia Liu, Electrochemical fabrication of interconnected tungsten bronze nanosheets for high performance supercapacitor. *J. Power Sources* **383**, 17–23 (2018)
 - V.C. Lokhande, T. Hussain, A.R. Shelke, A.C. Lokhande, Taeksoo Ji, Substitutional doping of WO₃ for Ca-ion based supercapacitor. *Chem. Eng. J.* **424**, 130557 (2021)
 - P. Velusamy, S. Liu, R. Xing, M. Sathiyaa, A. Ahmad, M.D. Albaqami, R.G. Alotabi, E. Elamurugu, M.S. Pandian, P. Ramasamy, Enhanced photo-electrocatalytic performance of the nano heterostructures based on Pr³⁺ modified g-C₃N₄ and BiOI. *Int. J. Hydrogen Energy* **47**, 32903–32920 (2022)
 - M. Aravind, M. Amalanathan, S. Aslam, A.E. Noor, D. Jini, S. Majeed, P. Velusamy, A.A. Alothman, R.A. Alshgari, M.S. Mushab, M. Sillanpaa, Hydrothermally synthesized Ag-TiO₂ nanofibers (NFs) for photocatalytic dye degradation and antibacterial activity. *Chemosphere* **321**, 138077 (2023)
 - S.P. Gupta, M.A. More, D.J. Late, P.S. Walke, High-rate quasi-solid-state hybrid supercapacitor of hierarchical flowers of hydrated tungsten oxide NSs. *Electrochim. Acta* **366**, 137389 (2021)
 - M.S. Tamboli, D.P. Dubal, S.S. Patil, A.F. Shaikh, V.G. Deonikar, M.V. Kulkarni, N.N. Maldar, A.M. Asiri, P. Gomez-Romero, B.B. Kale, D.R. Patil, Mimics of microstructures of Ni substituted Mn_{1-x}Ni_xCo₂O₄ for high energy density asymmetric capacitors. *Chem. Eng. J.* **307**, 300–310 (2017)
 - C. Huang, Q. Zhu, W. Zhang, P. Qi, Q. Xiao, Y. Ying, Facile preparation of W5O14 nanosheet arrays with large crystal channels as high-performance negative electrode for supercapacitor Author links open overlay panel. *Electrochim. Acta* **330**, 135209 (2020)
 - B. Moshofsky, T. Mokari, Length and diameter control of ultrathin nanowires of substoichiometric tungsten oxide with insights into the growth mechanism. *Chem. Mater.* **25**(8), 1384–1391 (2013)

26. P.J. Boruah, R.R. Khanikar, H. Bailung, Synthesis and characterization of oxygen vacancy induced narrow bandgap tungsten oxide (WO_{3-x}) nanoparticles by plasma discharge in liquid and its photocatalytic activity. *Plasma Chem. Plasma Process* **40**, 1019–1036 (2020)
27. P. Ivanoff Reyes, C.J. Ku, Z. Duan, Y. Xu, E. Garfunkel, Y. Lu, Reduction of persistent photoconductivity in ZnO thin film transistor-based UV photodetector. *Appl. Phys. Lett.* **101**(3), 031118 (2012)
28. B. Moshofsky, T. Mokari, Length and diameter control of ultrathin nanowires of substoichiometric tungsten oxide with insights into the growth mechanism. *Chem. Mater.* **25**, 1384–1391 (2013)
29. S.K. Shinde, D.P. Dubal, G.S., Ghodake, D.Y. Kim, V.J. Fulari, Nanoflower-like $\text{CuO}/\text{Cu}(\text{OH})_2$ hybrid thin films: Synthesis and electrochemical supercapacitive properties. *J. Electroanal. Chem.* **732**, 80–85 (2014)
30. S.K. Shinde, M.B. Jalaka, G.S. Ghodake, N.C. Maile, V.S. Kumbhar, D.S. Lee, V.J. Fulari, D.-Y. Kim, Chemically synthesized nanoflakes-like NiCo_2S_4 electrodes for high-performance supercapacitor application. *Appl. Surf. Sci.* **466**, 822–829 (2019)
31. K. Sun, F. Hua, S. Cui, Y. Zhu, H. Peng, G. Ma, An asymmetric supercapacitor based on controllable WO_3 nanorod bundle and alfalfa-derived porous carbon. *RSC Adv.* **11**, 37631–37642 (2021)
32. G. Mineo, E. Bruno, S. Mirabella, Advances in WO_3 -Based Supercapacitors: State-of-the-Art Research and Future Perspectives. *Nanomaterials* **13**, 1418 (2023)
33. S.K. Shinde, D.P. Dubal, G.S. Ghodake, V.J. Fulari, Hierarchical 3D-flower-like CuO nanostructure on copper foil for supercapacitors. *RSC adv.* **5**, 4443–4447 (2015)
34. Z. Khan, B. Senthilkumar, S. Lim, R. Shanker, Y. Kim, H. Ko, Redox-additive-enhanced high capacitance supercapacitors based on $\text{Co}_2\text{P}_2\text{O}_7$ Nanosheets. *Adv. Mater. Interfaces* **4**, 1700059 (2017)
35. H. Pang, Z. Yan, Y. Ma, G. Li, J. Chen, J. Zhang, W. Du, S. Li, Cobalt pyrophosphate nano/microstructures as promising electrode materials of supercapacitor. *J. Solid State Electrochem.* **17**, 1383–1391 (2013)
36. R.D. Kumar, Y.A.S. Karuppuchamy, Facile Synthesis of $\text{Co}-\text{WO}_3$ / functionalized carbon nanotube nanocomposites for supercapacitor applications. *J. Mater. Sci. Mater. Electron.* **28**, 5425–5434 (2017)
37. J. Jia, X. Liu, R. Mi, N. Liu, Z. Xiong, L. Yuan, C. Wang, G. Sheng, L. Cao, X. Zhou et al., Self-Assembled Pancake-like Hexagonal Tungsten Oxide with Ordered Mesopores for Supercapacitors. *J. Mater. Chem. A* **6**, 15330–15339 (2018)

Publisher's Note Springer Nature remains neutral with regard to jurisdictional claims in published maps and institutional affiliations.

Springer Nature or its licensor (e.g. a society or other partner) holds exclusive rights to this article under a publishing agreement with the author(s) or other rightsholder(s); author self-archiving of the accepted manuscript version of this article is solely governed by the terms of such publishing agreement and applicable law.

शब्दाली
प्रकाशन
पुणे-५८

वर्ष : १३ वे अंक : दुसरा

जुलै - ऑगस्ट - सप्टेंबर २०२३

ISSN : 2231 4377
(Peer Reviewed Journal)

SAKSHAM SAMIKSHA त्रैमासिक
सक्षम समीक्षा

मराठी भाषा-वाङ्मय व संधोषक यासाठी असलेला ग्रंथ

संपादक : प्रा. डॉ. शैलेश विश्वनाथ त्रिभुवन



लेखक,
विचारवंत

प्रा. हरी नरके

साहित्य
विशेषांक



वितरण क्षेत्र : * राज्य : पश्चिम बंगाल (कलकत्ता), उत्तर प्रदेश (वाराणसी), केरळ, गोवा, गुजरात (बडोदा), तेलंगणा (हैदराबाद)
* जिल्हा : पुणे, अहमदनगर, नाशिक, मुंबई, ठाणे, सिधुदूर्य, रत्नागिरी, रायगड, कोल्हापूर, सातारा, सांगली, सोलापूर, यवतमाळ,
लातूर, परभणी, जालना, औरंगाबाद, नागपूर, अमरावती, नांदेड, जळगाव, धुळे, नंदूरबार, चंद्रपूर, गडचिरोली, चाशिम

अं | त | रं | ग

३०. ध्येय घेडाची ६० वर्षे	प्रा. डॉ. शैलेश विश्वनाथ त्रिभुवन (पुणे)	०२
१. मा. श्री. छगन भुजबळ यांची श्रद्धाजली!	मा. श्री. छगन भुजबळ (मुंबई)	०४
२. परिवर्तनवादी विचारवंत	डॉ. आ. ह. साळुंगे	०६
३. महात्मा जोतीराव फुले पर्यायी समाजव्यवस्थेचे शिल्पकार	प्रा. हरी नरके (दिवंगत)	०७
४. समर्पक युक्तिवाद	गोविंद तळवलकर (नागपूर)	२३
५. हरी नरके: काही आठवणी	डॉ. जनार्दन बाघमारे (लातूर)	२५
६. हरी नरके : अवेळी निघून गेलेला माझा मित्र	प्रा. दत्ता भगत (नांदेड)	२६
७. बावांचा सहवास अल्पवेळ मिळाला	प्रणिती नरके (पुणे)	२९
८. 'हरी काका म्हणजे चालता बोलता ज्ञानकोश'	अनिल नरके (तळेगांव ढमढेरे)	३२
९. हरीभाऊ नरके आणि मी	संजय सोनवणी (पुणे).....	३६
१०. हरी नरके : साहित्य, संस्कृती आणि अभिजात मराठी भाषा	डॉ. अनिल सपकाळ (मुंबई)	३९
११. प्रागतिक विचारांचा दीपस्तंभ: प्रा. हरी नरके	डॉ. प्रतिभा सुरेश जाधव (लालसगांव)	४४
१२. सत्यशोधक हरी नरके	प्रा. डॉ. नाना झगडे (पुणे).....	५१
१३. वीटवीन द लाईन्स...	प्रा. डॉ. सतीश शिरसाठ (पुणे)	५७
१४. प्रा. हरी नरके सत्यशोधकीय विचारांचे एकनिष्ठ व्यक्तीमत्त्व	डॉ. जितेंद्र शामसिंग गिरासे (धुळे).....	५८
१५. थॉमस पेन यांचे धर्मचिंतन आणि म. फुले यांची सामाजिक समता : हरी नरके	डॉ. जितेंद्र कदम (खटाव)	६०
१६. सत्यशोधक केशवराव विचारे समग्र वाङ्मय : सत्यशोधनाचे कुतूहल जागवणारे संपादन	डॉ. संदीप भुयेकर (वाराणसी)	६३
१७. एक दुर्लक्षित खजिना - सत्यशोधक केशवराव विचारे समग्र वाङ्मय	प्रा. गणेश राऊत (पुणे).....	६७
१८. डॉ. हरी नरके : 'टेलको'तील प्रशिक्षणार्थी ते महाराष्ट्राचा विचारवंत पर्यंतचा अनोखा प्रवास..	उज्वला मेहेंदळे (पुणे)	६९
१९. हरी नरके : एक झंझावात !	शुद्धोदन आहेर (मुंबई).....	७३
२०. नव्या वाटा शोधणारा ज्ञानार्थी...	डॉ. प्रवीण बनसोड (यवतमाळ)	७६
२१. सत्यशोधनाची आस !	डॉ. श्रद्धा कुंभोजकर (पुणे).....	७८
२२. अभिजात मराठी भाषा आणि प्रा. हरी नरके	डॉ. हरेश संपत शेळके (अहमदनगर)	८०
२३. प्रा. हरी नरके यांच्या यत्कृत्याचे विशेष	प्रा. डॉ. सुभाष दिनकर आहेर (शिरवळ)	८३
२४. महात्मा फुलेंची बदनामी एक सत्यशोधन	प्रा. डॉ. शीला दत्तात्रय गाढे (श्रीरामपूर)	८६
२५. फुले विचारधारेचे चिकित्सक अभ्यास :	प्रा. डॉ. गोपीनाथ पां. बोडखे (बीड)	९०
२६. सावित्रीबाई फुले हिंदू संस्कृतीच्या इतिहासातील एका नव्या युगाचा आरंभ	डॉ. आश्लेषा मुंगी (बारामती)	९४
२७. विचारवंत हरी नरके	डॉ. मिलिंद कसबे (नारायणगांव)	९६
२८. फुले आंबेडकर विचारांचा वृहद कोश- हरी नरके	डॉ. वंदना महाजन (मुंबई)	९८
२९. प्रतिगाभ्यांना निरुत्तर करणारा आमचा हरि (भाऊ) प्रा. डॉ. धनंजय बाबुराय लोखंडे (पुणे).....		१००

अभिजात मराठी भाषा आणि प्रा. हरी नरके



प्रा. डॉ. हरीश संपत शेळके

सहाय्यक प्राध्यापक व मराठी
विभागप्रमुख, मराठी विभाग व
संशोधन केंद्र, न्यू आर्ट्स कॉमर्स अँड
सायन्स कॉलेज, पारनेर, ता. पारनेर,
जि. अहमदनगर ४१४३०२

दूरभाष : ९७६७१७६६५१

harieshelke@gmail.com

harieshelkecas@gmail.com

६६

खरं तर भाषा हा प्रत्येकाच्याच आस्थेचा
विषय असतो. भाषा ही समाजाला समृद्ध
करत असते. भाषा विचार देत असते. समाज
पुढे जाण्यासाठी, समाज घडण्यासाठी,
समाजातील माणसं जोडण्यासाठी,
समाजातील नाती समृद्ध होण्यासाठी भाषा
सातत्याने प्रयत्न करत असते आणि म्हणूनच
भाषेसाठी संघर्ष करणारी, भाषेसाठी संशोधन
करणारी, भाषेचा अभ्यास करणारी, भाषेवर
प्रेम करणारी, भाषा टिकण्यासाठी अहोरात्र
झगडणारी अशी जी अनेक थोर माणसं या
महाराष्ट्रात होऊन गेली किंवा आजही आहेत
त्यातील एक महत्त्वाचं नाव म्हणून प्रा. हरी
नरके यांची आपल्याला विशेष दखल ही
प्यायीच लागेल असे मला वाटते.

२२

मराठी भाषेला अभिजात भाषेचा दर्जा मिळावा यासाठी प्रा. हरी नरके
यांनी केलेले अथक प्रयत्न किंवा मराठी भाषेला अभिजात भाषेचा दर्जा मिळावा
यासाठी प्रयत्नांची पराकाष्ठा करणारे प्रा. हरी नरके

मराठी भाषेला अभिजात भाषेचा दर्जा मिळावा यासाठी
महाराष्ट्रामधील ज्येष्ठ साहित्यिक, विचारवंत, कवी, लेखक, समीक्षक,
अभ्यासक, संशोधक राजकीय क्षेत्रातील महत्त्वाचे व्यक्तिमत्त्व अशा विविध
क्षेत्रातील नामवंतांनी मराठी भाषेला अभिजात दर्जा मिळावा यासाठी प्रयत्न
केलेले आहेत. सद्यःस्थितीतही हे प्रयत्न चालू आहेत. ही सर्व मान्यवर मंडळी
मराठीला अभिजात भाषेचा दर्जा मिळावा यासाठी सातत्याने क्रियाशील
आहेत. मराठी भाषेला अभिजात भाषेचा दर्जा मिळावा यासाठी अहोरात्र मेहनत
घेणारे, कष्ट करणारे, प्रचंड संदर्भांचे पुरावे सादर करणाऱ्या मराठी भाषा अभिजात
समितीतील एक महत्त्वाचे सदस्य, अभ्यासक, विचारवंत म्हणून ज्यांची
महाराष्ट्राला ओळख आहे असे प्रा. हरी नरके सर यांच्याबद्दल लिहिणे मला वाटते
आपली नैतिक जबाबदारी आहे.

मराठी भाषेचा वैश्विक स्तरावर प्रचार, प्रसार व्हावा, सर्वत्र मराठीतून
संवाद करण्याची गोडी निर्माण व्हावी, दैनंदिन व्यवहारांमध्ये मराठी भाषेचा
अधिकाधिक वापर करण्यासाठी सर्वांनाच प्रोत्साहन मिळावे, अभिजात मराठी
साहित्याचे श्रवण, पारंपरिक कलांची नवी अभिव्यक्ती, नाविन्यपूर्ण उद्योग,
कल्पनांचे आदान - प्रदान व्हावे, आपली जी माय - मराठी आहे त्या माय -
मराठीला नवे दिवस यावेत, तिच्यामध्ये नवचैतन्य यावं, खऱ्या अर्थाने भारतीय
भाषांमधील तिचं जे महत्त्वाचं स्थान आहे ते अधिक अधोरेखित व्हावं या उद्देशाने
गेली दोन दशके प्रा. हरी नरके हे मराठी भाषा अभिजात कशी आहे या संदर्भात
अत्यंत महत्त्वाचे संशोधन, संदर्भ आणि विशेष म्हणजे त्या संदर्भातील व्याख्याने
सातत्यपूर्णरीत्या देत होते. मराठी भाषा, साहित्य, संस्कृती आणि कला यांना एक
प्रदीर्घ अशी परंपरा असून जगभर सर्वत्र मराठी संस्कृतीची आगळीवेगळी ओळख
आहे या पार्श्वभूमीवर या प्रदीर्घ परंपरेचा गौरव करत मराठी संस्कृतीचे महात्म्य
जगभर नव्याने अधोरेखित करण्यासाठी शासनाने वेळोवेळी पाऊल उचलावे व
मराठी भाषेसाठी अधिक चांगले कार्य करावे यासाठी मराठी भाषा अभिजात
कशी आहे यासाठी सातत्याने प्रयत्न करणारे प्रा. हरी नरके सर मला विशेष
महत्त्वाचे वाटतात.

मराठी भाषेबद्दल विचार प्रगट करताना श्री. वि. वा. शिरवाडकर उर्फ
कुसुमाग्रज १२, १३ ऑगस्ट १९८९ रोजी मुंबई येथे भरलेल्या जागतिक मराठी
परिषदेतील त्यांच्या अध्यक्षीय भाषणात असं म्हणतात, की "भाषा बंदीखान्यात
वाढत नाही. आजही जी मराठी प्रचलित आहे तीही अनेक भाषांतील शब्दांचे
आणि व्यावहारिक संज्ञांचे नजराणे घेऊनच संपन्न झाली आहे. कोणत्याही जिवंत
समाजाची भाषा तळ्यासारखी साचीव नसते तर कालमानानं निर्माण होणाऱ्या
नव्या ज्ञानाचे, विचारांचे, जाणिवांचे पाझर आत्मसात करित पुढे जाणाऱ्या
नदीसारखी प्रवाही असते. इतर प्रगत भाषांशी संपर्क ठेवूनच ती प्रगती करू
शकते. शुद्धतेच्या कर्मकांडात रुतलेल्या आणि त्यामुळेच प्रगतीला पराडूःमुख
झालेल्या भाषा मृत या सद्दरात कशा जमा होतात हे इतिहासानं दाखवलेलं आहे.
हे भान मराठीनं आपल्या पंधरा शतकांच्या प्रयासात राखलेलं आहे आणि

म्हणूनच नव्या युगाची आव्हाने पेलण्याच्या सामर्थ्यासंबंधी साशंक असलेली आम्ही तिची अपत्ये मात्र दुबळी आहेत. "असे अतिशय संघेदनशील विचार कवी कुसुमाग्रज आपल्या अध्याक्षीय भाषणात व्यक्त करतात. ते पुढे म्हणतात," भाषा म्हणजे शब्दांचे संकलन नव्हे. समाजाचे वैचारिक आणि जाणिवात्मक संचित काळातून पुढे नेणारी आणि परिणामतः समाजाच्या बदलत्या जीवनाला अखंडता आकार आणि आशय देणारी भाषा ही एक महाशक्ती असते. सूत्रात ओवलेल्या मण्यांप्रमाणे समाजजीवनाच्या सान्या धारणा आणि विकासाच्या प्रेरणा तिच्यात ओवलेल्या असतात म्हणून मराठीवरील संकट हे तिच्या शब्दकोशावरील वा साहित्यावरील संकट नाही; ते महाराष्ट्राच्या अस्मितेवरील, मराठीपणावरील आणि येथील लोकांच्या भवितव्यावरही संकट आहे. समाजाची प्रगती च क्रांती स्वभाषेच्या किनाऱ्यावरच पेरता येते असे क्रांतिकारकांच्या प्रणेत्यांनं म्हटलेलं आहे." असे अतिशय आस्थापूर्ण विवेचन कवी कुसुमाग्रज आपल्या भाषणातून व्यक्त करतात. कवी कुसुमाग्रज यांचे हे विचार वाचल्यानंतर भाषेबद्दल अभ्यास करणाऱ्या, भाषेविषयी आस्था असणाऱ्या आणि भाषेवर प्रेम करणाऱ्या कोणत्याही व्यक्तीला हे विचार सहज पटतील असे आहेत.

प्रा. हरी नरके सरांनी 'लोकराज्य' फेब्रुवारी २०२० च्या अंकात 'अभिजात मराठी' हे घ्या पुरावे नावाचा एक दीर्घ लेख लिहिलेला आहे. त्या लेखात त्यांनी असे म्हटलेले आहे की, "थोर संशोधक श्री.व्यं. केतकर, राजाराम शास्त्री भागवत, वि.का.राजवाडे, इरावती कर्वे, कृ.पा. कुलकर्णी, दत्तो वामन पोतदार, वि.ल.भावे, रा.भि.जोशी आदींच्या संशोधनाच्या आधारे मराठी भाषा ही किमान अडीच हजार वर्षे जुनी असल्याचे स्पष्टपणे दिसून येते. महाराष्ट्र मराठी भाषेचा अडीच हजार वर्षांचा प्रवास सादर उलगडला म्हणजे मराठी भाषा ही अभिजात भाषा असल्याचे निर्विवादपणे सिद्ध होते." भाषेबद्दलचा हा अतिशय व्यापक विचार सरांनी या लेखात मांडलेला आहे. शिलालेखांपासून ते प्राचीन संदर्भ ग्रंथांचे वेगवेगळे संदर्भ सरांनी या लेखात दिलेले आहेत. या त्यांच्या लेखातून मराठी अभिजात कशी यासाठी त्यांनी जे पुरावे संदर्भ गोळा केलेले आहेत, ते संदर्भ कोणत्याही भाषा-अभ्यासकाला विचारप्रयुक्त करणारे आहेत. खरं तर नरके सर हे कोणत्याही विषयावरचे विवेचन जेव्हा पुरायचे तेव्हा त्या विवेचनामध्ये सखोलता, चिंतनशीलता, व्यापकता, दूरदृष्टी, सहजता,

विशालता आणि रिलेव्हन्स अशा अनेक पैलूंची त्या विवेचनाला जोड असायची आणि त्यामुळे त्यांचे लेखन, त्यांचे विचार ज्यावेळेस आपण ऐकतो त्यावेळेस आपल्याला या सर्व गोष्टी त्यामध्ये स्पष्टपणे जाणवतात. मराठी भाषेसाठी विविध नावीन्यपूर्ण उपक्रम त्यांनी महाराष्ट्र शासनाच्या विविध ज्या सामाजिक संस्था आहेत त्यांना सुचविले होते. जेणेकरून त्या उपक्रमांद्वारे मराठी भाषेबद्दल, संस्कृतीबद्दल, अभ्यासक, विचारवंत, विद्यार्थी, हितचिंतक, वाचक या सर्वांमध्ये भाषेविषयी एक विशेष आवड निर्माण होईल व भाषेचा अभ्यास करण्याची अभिरुची निर्माण होईल हा दृष्टिकोन समाजामध्ये पेरण्यासाठी ते सातत्यपूर्ण प्रयत्नशील होते. या सर्व त्यांच्या वेगवेगळ्या पैलूंना स्पर्श केल्यानंतर लक्षात असे येत की, त्यांनी शोधलेले शिलालेखांपासून ते गाथा समशती (संपादक स. आ. जोगळेकर) इथपर्यंतचे सर्व संदर्भ हे मराठी भाषा अभिजात कशी आहे यासाठी खरे तर पुरेसे आहेत. त्यांचे हे संदर्भ महाराष्ट्र शासनाने लवकरात लवकर मान्य करून तसेच त्यांनी दिलेल्या पुराव्यांच्या बाजूने विचार करून मराठी भाषा ही अभिजात आहे असा दर्जा देण्यास काहीच हरकत नाही असे मला वाटते.

प्रा.हरी नरके सरांनी जे संदर्भ ग्रंथ शोधले त्याची नावे जरी आपण पाहिली तरी आपल्याला सहज त्यांनी घेतलेले जे परिश्रम आहेत ते किती अथक आहेत याची जाणीव होईल. नरके सरांनी तज्ज्ञांच्या जवळजवळ ३२ मौलिक संदर्भ ग्रंथांचा उपयोग लेखांसाठी केलेला दिसून येतो. प्राचीन महाराष्ट्र खंड १ व २, कथासंरिस्तागर, हाल सातवाहनाची, गाथा समशती (संपादक स. आ. जोगळेकर), गुणाढ्याचे बृहत्कथा, मराठी गद्याचा इंग्रजी अवतार, मराठी लोकांची संस्कृती, प्राचीन महाराष्ट्र, मराठी भाषा उद्गम व विकास, ज्ञानधरी असे अनेक संदर्भ ग्रंथ सरांनी त्यांच्या लेखासंदर्भात अभ्यासलेले दिसून येतात. सरांनी केलेल्या मांडणीतून इतर भारतीय भाषांना भारत सरकारने जो दर्जा दिलेला आहे तो दर्जा आपल्याही भाषेला सहजपणे मिळावा असे त्यांचा लेख वाचल्यानंतर आपल्याला वाटते.

खरंतर भाषा हा प्रत्येकाच्याच आस्थेचा विषय असतो. भाषा ही समाजाला समृद्ध करत असते. भाषा विचार देत असते. समाज पुढे जाण्यासाठी, समाज घडण्यासाठी, समाजातील माणसं जोडण्यासाठी, समाजातील नाती समृद्ध होण्यासाठी भाषा सातत्याने प्रयत्न करत असते आणि म्हणूनच भाषेसाठी संघर्ष करणारी,

भाषेसाठी संशोधन करणारी, भाषेचा अभ्यास करणारी, भाषेवर प्रेम करणारी, भाषा टिकण्यासाठी अहोरात्र झगडणारी अशी जी अनेक थोर माणसं या महाराष्ट्रात होऊन गेली किंवा आजही आहेत त्यातील एक महत्त्वाचं नाव म्हणून प्रा.हरी नरके यांची आपल्याला विशेष दखल ही घ्यावीच लागेल असे मला वाटते. कविवर्य सुरेश भट त्यांच्या एका कवितेत असे म्हणतात,

आमच्या मनामनात दंगते मराठी
अमुच्या रंगारंगत रंगते मराठी
आमच्या उराउरात स्पंदते मराठी,
आमच्या नसानसात नाचते मराठी

सुरेश भटांच्या कवितेतील या ओळी आपल्या मराठी भाषेची थोरवी समर्थपणे व्यक्त करतात. मराठी आपला श्वास आहे आणि आपला अभिमान आहे. तुम्हा - आम्हास मराठी बोलता येते, ऐकता येते हे भाग्य मोठे आहे. ज्ञानेश्वरांनी मराठीला अमृताची उपमा दिली. अमृता सारखी किंवा त्याहूनही गोड असलेली माझी - तुमची मराठी ही तारांमध्ये बारा राशी ख सप्तवारांमध्ये रवी - शशि ख या दीपिचेया भाषांमध्ये तैसी ख बोलती मराठीया अशी श्रेष्ठ आहे. हे श्रेष्ठत्व फादर स्टीफन्स यांनी या ओळींतून ठसठसतीरित्या अधोरेखित केले आहे.

मराठी भाषेला दोन हजाराहून अधिक काळाचा वैभवशाली इतिहास आहे. त्याचे विविध पुरावे मिळाले आहेत. हे पुरावे आपल्या मराठीला अभिजात भाषेच्या परिघात येऊन ठेवण्यास समर्थ आहेत. मराठी भाषेला अभिजात भाषेचा दर्जा मिळावा यासाठीचे आमचे प्रयत्न लवकरच फळाला येतील याची मला खात्री आणि विश्वास सुद्धा आहे. "डौलात रायगडावर फडकलेला भगवा आणि दिल्लीच्या तक्ताला हादरवून सोडणारे मराठी भाषेचे तेज व

सत्य, छत्रपती शिवाजी महाराजांच्या भवानी तलवारीसारखे तळपणारे आहे" असे मत फेब्रुवारी २०२० 'लोकसंवा' अंकाचे अतिथी संपादक तत्कालीन मराठी भाषा मंत्री सुभाष देसाई यांनी त्यांच्या संपादकीय भाषणामध्ये व्यक्त केले आहे. या अंकातील विचारांचे, लेखनाचे वाचन केल्यानंतर जाणवते की, लोकसंवा जानेवारी २०२०, व लोकसंवा फेब्रुवारी २०२३ हे अंक मराठी भाषेसंदर्भातील प्रकाशित करण्यामध्ये प्रा.हरी नरके सरांचाच सिंहाचा वाटा होता. मराठी भाषेला अभिजात भाषेचा दर्जा मिळावा यासाठीची चर्चा सर्व स्तरावर व्हावी, समाजामध्ये या संदर्भातील जाणीव - जागृती घडून यावी आणि विशेष करून मराठीचा अध्यापन करणारे, मराठीचे अध्ययन करणारे विद्यार्थी, लेखक, विचारवंत, कवी, हितचिंतक व भाषा अभ्यासक अशा सर्व लोकांमध्ये मराठी भाषेसंदर्भातील जाणीव जागृती घडून यावी हा अतिशय पारदर्शी हेतू नरके सरांच्या विचारांच्या केंद्रवर्ती होता आणि म्हणूनच महाराष्ट्र शासनाने हे दोन्ही अंक खास करून मराठी भाषा अभिजात कशी आहे, मराठी भाषा अभिजात भाषा कशी ठरू शकते, तिला अभिजात भाषेचा दर्जा मिळायलाच हवा यासाठी खरंतर या अंकातून खूप व्यापक असे विचार वेगवेगळ्या लेखकांनी व्यक्त केलेले आहेत, समीक्षकांनी व्यक्त केलेले आहेत, विचारवंतांनी व्यक्त केलेले आहेत हे विचार प्रत्येकाने वाचावे असे वाटते.

शेवटी मी एवढेच म्हणून की, प्रा. हरी नरके सरांनी केलेले लेखन, भाषणे, वाचन व चिंतन हे सर्व अभ्यासकांसमोर या या अंकाच्या निमित्ताने निश्चितच येईल, या अंकाचे संपादक डॉ. शैलेश त्रिभुवन सरांनी आम्हाला आमचे विचार व्यक्त करण्याची संधी दिली त्याबद्दल त्यांचे मनःपूर्वक आभार.

(पान नं. ६९ वरून) व 'आजचे सत्यशोधक' हे दोन्ही लेख मुळातून वाचण्यासारखे आहेत. भारतीय सत्यशोधक समाजाची घटनाही त्यात दिलेली आहे.

हरी नरके यांनी कष्टपूर्वक साधने गोळा करून समाजाला एक अत्यंत उद्बोधक ग्रंथ प्राप्त करून दिला आहे. जांभूळवाडी को-ऑपरेटिव्ह, इंडस्ट्रियल कॉलनी प्रकल्पावर 'त्रांबे क्रॉनिकल मध्ये ६ जानेवारी १९३५ ला जो लेख आला होता, तो पुस्तकाच्या पुढील आवृत्तीत समाविष्ट केल्यास पुस्तकाचे संदर्भमूल्य अधिक वाढेल, तत्कालीन सभांचे फोटोही घावेत.

कै. विचारे यांच्या संपूर्ण जीवनाचा भागोषा

घेणारा मोठा लेख पुस्तकात समाविष्ट करणे आवश्यक आहे. त्यामुळे सर्वसामान्य वाचकाला कै. केशवराव विचारे यांचे चरित्र समजावून घेण्यास मदत होईल. सत्यशोधक चळवळीची माहिती देणे आवश्यक ठरेल. त्या अर्थाने हे पुस्तक समग्र वाङ्मयाच्या जवळ जाते, परंतु समग्र वाङ्मय म्हटल्यावर अपेक्षित असणारे सारे संदर्भ येणे आवश्यक आहे. कै. विचारे यांचा पत्रव्यवहार, भाषणे, त्यांच्याबद्दलचे लेख हे सारे पुढील आवृत्तीत समाविष्ट झाल्यास सत्यशोधक समाजाचा अधिकृत संदर्भ कोश तयार होईल.

January - 2024

E-ISSN : 2348-7143

International Research Fellows Association's
RESEARCH JOURNEY

International E-Research Journal

Peer Reviewed, Referred & Indexed Journal

ISSUE : 335

Multidisciplinary Issue



Chief Editor -

Dr. Dhanraj T. Dhangar,
Assist. Prof. (Marathi)
MGV's Arts & Commerce College,
Yeola, Dist - Nashik [M.S.] India.

Executive Editors :

Dr. Tejesh Beldar, Nashikroad (English)
Dr. Gajanan Wankhede, Kinwat (Hindi)
Smt. Bharati Sonawane, Bhusawal (Marathi)
Dr. Swati Lawange, Yeola (Marathi)
Dr. Rajay Pawar, Goa (Konkani)

For Details Visit To : www.researchjourney.net

SWATIDHAN PUBLICATIONS

I
N
T
E
R
N
A
T
I
O
N
A
L

R
E
S
E
A
R
C
H

F
E
L
L
O
W
S

A
S
S
O
C
I
A
T
I
O
N



'RESEARCH JOURNEY' International E- Research Journal

Impact Factor 6.625

Issue 335 : Multidisciplinary Issue

Peer Reviewed Journal

E-ISSN :

2348-7143

January 2024

January 2024

E-ISSN : 2348-7143

International Research Fellows Association's

RESEARCH JOURNEY

International E-Research Journal

Peer Reviewed, Referred & Indexed Journal

Issue : 335

Multidisciplinary Issue

Chief Editor -

Dr. Dhanraj T. Dhangar,

Assist. Prof. (Marathi)

MGV's Arts & Commerce College,

Yeola, Dist - Nashik [M.S.] India.

Executive Editors :

Dr. Tejesh Beldar, Nashikroad (English)

Dr. Gajanan Wankhede, Kinwat (Hindi)

Smt. Bharati Sonawane, Bhusawal (Marathi)

Dr. Swati Lawange, Yeola (Marathi)

Dr. Rajay Pawar, Goa (Konkani)

Our Editors have reviewed papers with experts' committee, and they have checked the papers on their level best to stop furtive literature. Except it, the respective authors of the papers are responsible, answerable and accountable for their content, citation of sources and the accuracy of their references and bibliographies/references. Editor in chief or the Editorial Board cannot be held responsible for any lacks or possible violations of third parties' rights. Any legal issue related to it will be considered in Yeola, Nashik (MS) jurisdiction only.

- Chief & Executive Editor

SWATIDHAN INTERNATIONAL PUBLICATIONS

For Details Visit To : www.researchjourney.net

*Cover Photo Source : https://en.wikipedia.org/wiki/Ram_Mandir#/media/

File : Ayodhya_Ram_Mandir_Inauguration_Day_Picture.jpg

© All rights reserved with the authors & publisher

Price : Rs. 1000/-



Editorial Board

Chief Editor -

Dr. Dhanraj T. Dhangar,

Assist. Prof. (Marathi)

MGV's Arts & Commerce College,

Yeola, Dist - Nashik [M.S.] INDIA

Executive Editors :

Dr. Tejesh Beldar, Nashikroad (English)

Dr. Gajanan Wankhede, Kinwat (Hindi)

Mrs. Bharati Sonawane, Bhusawal (Marathi)

Dr. Swati Lawange, Yeola (Marathi)

Dr. Rajay Pawar, Goa (Konkani)

Co-Editors -

- ❖ Prof. Mohan S. - Dean faculty of Arts, Delhi University, **Delhi, India**
- ❖ Prof. Milena Brotaeva - Head, Classical East Department, Sofia University, **Sofia, Balgeria**
- ❖ Dr. R. S. Sarraju - Center for Translation Studies, University of Hydeabad, **Hydrabad, India**
- ❖ Mr. Tufail Ahmed Shaikh- King Abdul Aziz City for Science & Technology, Riyadh, **Saudi Arabia.**
- ❖ Dr. Anil Dongre - Head, Deptt. of Management, North Maharashtra University, Jalgaon [M.S.] **India**
- ❖ Dr. Shailendra Lende - R.T.M. Nagpur University, Nagpur [M.S.] **India**
- ❖ Dr. Dilip Pawar - BoS Member (SPPU), Dept. of Marathi, KTHM College, Nashik. [M.S.] **India**
- ❖ Dr. R. R. Kazi - North Maharashtra University, Jalgaon [M.S.] **India**
- ❖ Prof. Vinay Madgaonkar - Dept. of Marathi, Goa University, **Goa, India**
- ❖ Prof. Sushant Naik - Dept. of Konkani, Govt. College, Kepe, **Goa, India**
- ❖ Dr. G. Haresh - Associate Professor, CSIBER, Kolhapur [M.S.] **India**
- ❖ Dr. Munaf Shaikh - N. M. University, Jalgaon & Visiting Faculty M. J. C. Jalgaon [M.S.] **India**
- ❖ Dr. Sanjay Kamble - BoS Member Hindi (Ch.SU, Kolhapur), T.K. Kolekar College, Nesari [M.S.] **India**
- ❖ Prof. Vijay Shirsath- Nanasahab Y. N. Chavhan College, Chalisgaon [M.S.] **India**
- ❖ Dr. P. K. Shewale - BoS Member (SPPU), MGV's LVH College, Panchavati-Nashik [M.S.] **India**
- ❖ Dr. Hitesh Brijwasi - Librarian, K.A.K.P. Com. & Sci. College, Jalgaon [M.S.] **India**
- ❖ Dr. Sandip Mali - Sant Muktabai Arts & Commerce College, Muktainagar [M.S.] **India**
- ❖ Prof. Dipak Patil - S.S.V.P.S.'s Arts, Sci. and Com. College, Shindhkheda [M.S.] **India**
- ❖ Prof. K. M. Waghmare - Librarian, Anandibai Raorane College, Sawantwadi [M.S.] **India**
- ❖ Prof. Vidya Surve-Borse- MGV's LVH Arts, Sci. & Com. College, Panchavati-Nashik [M.S.] **India**

Advisory Board -

- ❖ Dr. Marianna Kosic - Scientific-Cultural Institute, Mandala, **Trieste, Italy.**
- ❖ Dr. M.S. Pagare - Director, School of Languages Studies, North Maharashtra University, Jalgaon
- ❖ Dr. R. P. Singh - HoD, English & European Languages, University of Lucknow [U.P.] **India**
- ❖ Dr. S. M. Tadkodkar - Rtd. Professor & Head, Dept. of Marathi, Goa University, **Goa, India.**
- ❖ Dr. Pruthwiraj Taur - Chairman, BoS, Marathi, S.R.T. University, Nanded.
- ❖ Dr. N. V. Jayaraman - Director at SNS group of Technical Institutions, **Coimbatore**
- ❖ Dr. B. V. Game - Principal, MGV's Arts and Commerce College, Yeola, Dist. Nashik.

Review Committee -

- ❖ Dr. J. S. More - BoS Member (SPPU), Dept. of Hindi, K.J.Somaiyya College, Kopergaon
- ❖ Dr. S. B. Bhambar, BoS Member Ch.SU, Kolhapur, T.K. Kolekar College, Nesari
- ❖ Dr. Uttam V. Nile - BoS Member (NMU, Jalgaon) P.S.G.V.P. Mandals ACS College, Shahada
- ❖ Dr. K.T. Khairnar- BoS Member (SPPU), Dept. of Commerce, L.V.H. College, Panchavati
- ❖ Dr. Vandana Chaudhari KCE's College of Education, Jalgaon
- ❖ Dr. Sayyed Zakir Ali, HoD, Urdu & Arabic Languages, H. J. Thim College, Jalgaon
- ❖ Dr. Sanjay Dhondare - Dept. of Hindi, Abhay Womens College, Dhule
- ❖ Dr. Amol Kategaonkar - M.V.P.S.'s G.M.D. Arts, B.W. Commerce & Science College, Sinnar.
- ❖ Dr. R.D. Shinde, HoD, Marathi, KPG Arts, Commerce & Science College, Igatpuri.

Published by -

© Mrs. Swati Dhanraj Sonawane, Director, Swatidhan International Publication, Yeola, Nashik

Email : swatidhanrajs@gmail.com Website : www.researchjourney.net Mobile : 9665398258

INDEX

No.	Title of the Paper	Author's Name	Page No.
English Section			
1	Historical Hues: Analyzing the Depiction of the Mughal Era in Indian English Fiction	Prof. Dilip Kute	4
2	Innovative Dramatic Techniques: New Dimensions of the Indian English Drama	Dr. Hemantkumar Patil	14
3	Pain as Literary Art: A Reading of Illness Memoirs to Understand the use of the Figurative Language to Define Illness, Life and Mortality	Mr. Ankit Banpurkar	19
4	Language: A Sociocultural System	Dr. Sanju Jadhav	23
5	An Analytical Study of Baby Kamble's Memoir 'The Prison We Broke' As	Prof. Minakshi Ingole	27
6	The Role of Keshavrao Jedhe and Dinkarrao Javalkar in Impact of Chhatrapati Mela in Pune Maharashtra	Dr. Sanjay Shelar	31
7	A Critical Study of Teaching and Learning With Knowledge Resources in Higher Education	Dr. Sanjay Kulkarni	38
8	Implementation of Mahatma Gandhi Tantamukt Village Campaign	Dr. Suresh Shahapure	41
9	Impact of Social Media on Politics	Saurabh Kolhe	45
हिंदी विभाग			
10	विपश्यना: तन और मन को स्वस्थ बनाने की प्राचीन भारतीय साधना पद्धति की प्रासंगिकता	प्रा.शांताराम वळवी	48
11	बोल री कठपुतली' में नारी के विविध रूप	अनिता शेजोळे, डॉ. शिवाजी सांगोळे	54
मराठी विभाग			
12	संत तुकाराम आणि कृषि : एक अनुबंध	डॉ. सुनिल निगडे, कल्पना घुगे	59
13	वि. का. राजवाडे यांचा समीक्षा विचार	अस्मिता कुंभार	63
14	वाडगीण : आदिवासींच्या जीवघेण्या संघर्षाची कहाणी	डॉ. सुलतान पवार	68
15	जुगाड : अस्तित्व संघर्षाची अनवट कहाणी	डॉ. सागर पाटील	75
16	आधुनिक तंत्रज्ञान व मराठी भाषा	डॉ. हर्देश शेळके	80
17	मराठी नियतकालिकाची स्वरूप आणि संकल्पना	डॉ. शरद दुधाट	88
18	तरसोद गावाचा ऐतिहासिक अभ्यास	डॉ. दिपक किनगे	94
19	मराठी माध्यमांच्या शाळांसमोरील आव्हाने	डॉ. राजेश्वर दुडूकनाळे	98
20	विद्यार्थ्यांच्या शब्दसंग्रह वाढवण्यासाठी शिक्षणात व्हॉट्सअॅपचा प्रभावि वापर	श्री खंडू मोरे	105
21	अध्यापनासाठीच्या संगणक प्रशिक्षण उपक्रमाच्या परीणामकारकतेच अभ्यास	डॉ. स्वाती चव्हाण	112
22	बँकेतर वित्तीय संस्थांची भारतीय अर्थव्यवस्थेतील भूमिका	डॉ. मेघा पाटोळे	115
23	पारंपारिक शेती व कृषी तंत्रज्ञान	डॉ. बी एम सोनवणे, संदिप अहिरे	121
24	गोटलां संग्रहांतले अस्तुरेचें चित्रण	प्रा. दिपा रायकर	126

Our Editors have reviewed papers with experts' committee, and they have checked the papers on their level best to stop furtive literature. Except it, the respective authors of the papers are responsible for originality of the papers and intensive thoughts in the papers. Nobody can republish these papers without pre-permission of the publisher. - Chief & Executive Editor

आधुनिक तंत्रज्ञान व मराठी भाषा

डॉ. हरीश संपत शेळके

सहाय्यक प्राध्यापक व मराठी विभागप्रमुख,
मराठी विभाग व संशोधन केंद्र,
न्यू आर्ट्स, कॉमर्स अँड सायन्स कॉलेज, पारनेर,
ता. पारनेर, जि. अहमदनगर. ४१४३०२
भ्रमणध्वनी - ९७६७१७६६५१

ई - मेल -- hareshelke@gmail.com, hareshelkecas@gmail.com

प्रास्ताविक :-

आज आपण पाहतो माहिती तंत्रज्ञानाच्या क्षेत्रात अतिशय वेगाने प्रसार आणि प्रचार होताना दिसतो आहे. या सर्व पार्श्वभूमीवर इ - संवाद कौशल्यांच्या माध्यमातूनही आपण मराठी भाषेतून चांगल्या प्रकारे इतरांबरोबर संवाद साधत आहोत. माहिती तंत्रज्ञानाचे युग सुरू झाल्यापासून मराठी भाषा आणि साहित्यतही बदलाचे वारे वाहू लागले आहेत. महाराष्ट्र शासनाच्या अखत्यारीतील महाराष्ट्र राज्य साहित्य संस्कृती मंडळ, राज्य मराठी विकास संस्था, जागतिक मराठी साहित्य संस्था, मराठी भाषा आणि साहित्याचे जतन संवर्धन करीत आहेत जागतिकीकरण आणि नवजागतिकीकरणाला सामोरे जाताना आपल्यासारख्या मराठी भाषकांना साहित्याविषयी आस्था असणाऱ्या, लेखन वाचनाची आवड असणाऱ्या सर्वांना माहिती तंत्रज्ञान स्वीकारणे अपरिहार्य ठरलेले दिसून येते. त्यामुळे इ - संवाद कौशल्यांचा आता आपल्याला यशस्वी वापर करणे काळाची गरज आहे.

इ-संवाद कौशल्यांचा उपयोग करताना आपल्याला सुरुवातीला त्या माध्यमांची व्यवस्थित ओळख करून घ्यावी लागते इ- संवाद कौशल्यांचा उपयोग व्यवस्थित करता आला तर आपण मराठी भाषेचे संवर्धन खूप चांगल्या प्रकारे करू शकू. आता संगणक हा या नव्या शतकातील सर्वांच्याच प्रगतीचा मार्ग बनलेला आहे. आता विज्ञान, तंत्रज्ञान, संगणक प्रणालीचे शिक्षण, प्रशिक्षण मराठी मातृभाषेत उपलब्ध होऊ लागले आहे. इ-संवाद कौशल्यामुळे मराठी ज्ञानभाषा शिक्षणाचे माध्यम म्हणून उपयोजन होताना असे विषय रंजक आणि सोपे, विद्यार्थीभिमुख झाले आहेत. मराठी विज्ञान साहित्यावर लक्ष केंद्रित करण्यावर भर दिला जात आहे. मराठी भाषेत अनेक नवनवीन विषयांची ओळख आपल्याला या इ - संवादांच्या माध्यमातून होताना दिसत आहे. त्यामुळेच मराठी साहित्य संस्कृतीचे संवर्धन मोठ्या प्रमाणात होण्यास मदत होताना दिसत आहे.

उद्दिष्टे :-

1. अद्ययावत माहितीसाठी, ज्ञानप्राप्तीसाठी संगणकाधिष्ठित माहिती तंत्रज्ञानाची उत्तम प्रकारे ओळख होण्यास मदत होईल.
2. मराठी ज्ञानभाषा शिक्षणाचे माध्यम म्हणून उपयोजन होताना असे विषय रंजक आणि सोपे, विद्यार्थीभिमुख झाले आहेत.
3. नवे तंत्रज्ञान वापरण्याच्या प्रणाली मराठीतून विकसित होण्यास मदत झाल्यामुळे ज्ञानार्जनासाठी त्याची खूप चांगली मदत होणार आहे.
4. इंटरनेट आणि सोशल मीडियाच्या वाढत्या प्रभावामुळे व इ - संवाद कौशल्यांच्या माध्यमातून वाचन संस्कृती वाढण्यास मदत होताना दिसत आहे.

5. इ- संवाद कौशल्यांच्या नव्या माध्यमांमुळे लेखन संस्कृती विकसित होण्यास मोठ्या प्रमाणात मदत होत आहे.
6. इंटरनेटच्या माध्यमातून मराठी प्रकाशक, जागतिक पुस्तक प्रदर्शन, विश्व मराठी साहित्य संमेलन, जागतिक मराठी परिषद, विविध ग्रंथजत्रा यांमधून इंटरनेटद्वारा आपल्या पुस्तकांची माहिती व विक्री करत आहेत.
7. अनेक प्रकारचे वाचक इ- कौशल्यांच्या (इंटरनेट, टॅब, लॅपटॉप) च्या माध्यमातून नवनवीन पुस्तके वाचत आहेत.
8. अगदी गाव तालुका पातळीवर देखील ही वाचनालये सुरू करून वाचनाची संधी उपलब्ध उपलब्ध करून देण्यात येत आहे.
9. आधुनिक तंत्रज्ञान युगातील मराठीचे अस्तित्व आणि भवितव्य उज्वल असलेले दिसून येत आहे.

आता आपण सविस्तरपणे इ - संवाद कौशल्यांची ओळख करून घेऊ

१. वेबसाईट :

आज इंटरनेटच्या युगात आपण सर्वजण कोणत्याही माहितीसाठी इंटरनेटवर अवलंबून आहोत. आज सर्व प्रकारची माहिती इंटरनेटच्या माध्यमातून आपल्यासमोर उपलब्ध आहे. ही माहिती पाहण्यासाठी आपल्याला वेबसाईटला भेट द्यावी लागते. वेबसाईट म्हणजे असे एक स्थान आहे; जेथे वेब पेजेसमध्ये बरीच माहिती संग्रहित केलेली असते आणि वेबसाईटवर ठेवली जाते. वेबसाईटची व्याख्या करायचीच म्हटले तर अशी करता येईल की, वेबसाईट हे एक मध्यवर्ती स्थान आहे; जिथे माहिती बऱ्याच वेबपृष्ठांमध्ये संग्रहित केली जाते. कोणताही वापरकर्ता त्या वेबसाईटच्या वेब पेजेसवर कनेक्ट होऊ शकतो आणि ती माहिती पाहू शकतो. जगभरातील कोणत्याही प्रकारची माहिती आपल्याला मिळवायची असेल तर वेबसाईट हा सर्वोत्तम पर्याय आहे. आज प्रत्येक घरी मोबाईलवर इंटरनेट उपलब्ध असल्यामुळे कोणीही जगातील कोणत्याही वेबसाईटला भेट देऊ शकतो आणि त्या डिवाइसवर वेबसाईट उघडू शकतो.

२. ई-मेल :

इलेक्ट्रॉनिक मेल किंवा ई-मेल हे इलेक्ट्रॉनिक माध्यमांच्या साहाय्याने संदेश पाठवण्याचे तंत्रज्ञान आहे. सध्याच्या बहुतांश ई-मेल यंत्रणा इंटरनेटचा वापर करतात. इलेक्ट्रॉनिक मेल ज्याला आपण रोजच्या वापरात ई-मेल या नावाने ओळखतो. ती एका प्रकारची डिजिटल संदेशाची देवाण - घेवाण आहे. ई-मेलने एका व्यक्तीने संगणकावर टंकलिखित करून पाठवलेला मजकूर अगदी थोड्याच वेळात दुसऱ्या एका किंवा अनेक वाचकांपर्यंत पोहोचतो. जर कोणाला एस.एम.एस करायचा असेल तर आपण तो फोन नंबर माध्यमातून पाठवतो त्याचप्रमाणे जर आपल्याला ई -मेल सेंड करायचा असेल तर ई-मेल ऍड्रेस आवश्यक आहे. ई-मेल संदेशाचे दोन भाग असतात पहिला भाग असतो हेडर म्हणजे ठळकपणे लिहिलेले संदेशाचे नाव, पाठवणार याचा ई -मेलचा पत्ता तसेच ज्याला संदेश पाठवला आहे त्याच्याही ई-मेलचा पत्ता हे सगळे असते. दुसरा भाग म्हणजे मेसेज बॉडी यामध्ये संदेश लिहिलेला असतो.

३. ब्लॉग :

ब्लॉग हा एखाद्या व्यक्तीने आंतरजालवर लिहिलेली स्फुटे (छोटे छोटे लेख) यांना दिलेली संज्ञा आहे. इंग्रजी शब्द ब्लॉग हा वेब (आंतरजाल) आणि ब्लॉग (नोंद) या दोन शब्दांपासून तयार केला गेला आहे. ब्लॉग हे एक प्रकारे संकेतस्थळ किंवा संकेतस्थळाचा भाग आहे. स्वतःचे विचार, एखाद्या कार्यक्रमाची माहिती,

रेखाचित्रे व चित्रफिती वगैरे गोष्टी इंटरनेटच्या आधारे सर्वापर्यंत पोहोचवता येतात ब्लॉग बहुदा एका व्यक्तीने तयार केलेला असतो. ब्लॉगवरील नोंदी बहुतेक वेळा उलट्या कालक्रमानुसार टाकलेले असतात. ब्लॉगची काळजी घेणे म्हणजे त्यातील नोंदीमध्ये सातत्यपूर्ण सुधारणा करणे होय. नवीन नोंदी न झाल्यास अनेक ब्लॉग कालबाह्य होतात. ब्लॉगचा शोध 23 ऑगस्ट 1999 रोजी प्यारा लॅम्स या व्यक्तीने लावला.

ब्लॉगचे प्रकार

1. वैयक्तिक ब्लॉग :

एखादी व्यक्ती स्वतःच्या ब्लॉगवर तिच्या आवडीनुसार जेव्हा मजकूर प्रसिद्ध करते तेव्हा तो वैयक्तिक ब्लॉग असतो. हा ब्लॉग कसा असावा किंवा त्याची आकर्षकता कशी असावी ही पूर्णता त्याच्यावर अवलंबून असते. वैयक्तिक ब्लॉगवर आपल्याला सातत्याने किंवा गरजेनुसार लेखन करता येते.

2. सहयोगी ब्लॉग :

जेव्हा एकापेक्षा अधिक ब्लॉगर्स वेब ब्लॉगमध्ये पोस्ट लिहितात तेव्हा त्याला सहयोगी ब्लॉग असे म्हणतात. यामध्ये अनेक विषयांचे एकत्रीकरण वाचायला मिळते.

3. मायक्रो ब्लॉगिंग :

डिजिटल सामग्रीचे लहान लहान तुकडे पोस्ट करण्यासाठी मायक्रोब्लॉगिंगचा उपयोग होतो. लहान पोस्ट वाचणे किंवा टाकणे काही वेळा फार गरजेचे असते. उदाहरणार्थ मीटिंग, निवडणूक प्रचार, पुस्तकांचा संदर्भ इत्यादी.

4. संस्थात्मक ब्लॉग :

खाजगी किंवा सरकारी संस्थात्मक कामासाठी याचा वापर केला जातो. आपल्या कर्मचाऱ्यांना अद्यावत माहिती पोहोचवण्यासाठी या ब्लॉगचे महत्त्व आहे.

४. ई. बुक्स (पुस्तक) :

ई - पुस्तक म्हणजे एखाद्या पुस्तकाचे केलेले डिजिटल किंवा इलेक्ट्रॉनिक रूपांतर असते. पुस्तकाची पाने पीडीएफ किंवा चित्ररूपात न ठेवता ती वेगवेगळ्या प्रकारच्या टंकात साठवलेली असतात. जेणेकरून वाचकाजवळ असणाऱ्या कोणत्याही प्रकारच्या साधनांमध्ये, माध्यमांमध्ये तो मजकूर सहजपणे उघडू शकतो आणि वाचकाला वाचन करता येऊ शकते. आपल्या जवळील असलेल्या मोबाईल, संगणक जर आंतरजालला जोडलेले असेल तर हे पुस्तक आपल्याला डाऊनलोडही करता येते आणि मग आपण सहज पुस्तकाचे वाचन करू शकतो.

५. ऑडिओ बुक्स (बोलती पुस्तके) :

आजच्या धकाधकीच्या जगात आपल्यासारख्या खाऊन पिऊन सुखी असणाऱ्या माणसांना सर्वात जास्त चणचण जर कुठल्या गोष्टीची भासत असेल तर ती म्हणजे फावला वेळ. वेळेअभावी आपण अशा अनेक महत्त्वाच्या गोष्टींना मुक्तो. ज्यांची मजा एकेकाळी आपण खूप लुटली. अनेकांसाठी यातली एक गोष्ट असते पुस्तक वाचन रोजचं वर्तमानपत्र वाचायला वेळ नसतो तर पुस्तक कसं वाचणार पण ज्या नव्या युगाने हा प्रश्न निर्माण केला त्यानंच त्याचे उत्तर दिलं ते आहे अर्थात बोलती पुस्तक. आता तुम्हाला पुस्तकाची मजा लुटायला एका जागी बसायची गरज नाही रस्त्याने चालताना, बसमध्ये बसल्याबसल्या, स्वयंपाक करताना किंवा रात्री झोपी जाताना तुम्ही ही पुस्तकं ऐकू शकता.

६. ई - पेपर (ऑनलाईन न्यूज पेपर) :

आज दैनंदिन जीवनात आपल्याला दररोजचे वर्तमानपत्र वाचल्याशिवाय स्वस्थता लाभत नाही कारण वर्तमानपत्र हा खूप लोकांच्या आयुष्याचा भागच बनलेला असतो. त्यामुळे वर्तमानपत्र आज ऑनलाईन पद्धतीने वाचणाऱ्या व्यक्तींची संख्या हजारो पटीने वाढलेली आहे. आज जवळजवळ सर्व वर्तमानपत्र आपल्याला ऑनलाईन पद्धतीने उपलब्ध असलेली दिसून येतात. मागील काही वर्षात आपण पाहिले तर वृत्तपत्र क्षेत्रातही नव्याने वेगाने बदल होत आहेत. वर्तमानपत्राचा वाचक हा वेगवेगळ्या थरातील असतो त्यामुळे वर्तमानपत्र वाचणाऱ्याचे प्रमाण जास्त असते आज ई - पेपरमध्ये जवळजवळ सर्वच पेपर आपण इंटरनेटवर जाऊन वाचू शकतो त्यातील जो भाग अतिशय महत्त्वाचा आहे तो संग्रही करून करू शकतो.

७. यु-ट्युब :

फेसबुक, ट्विटर, व्हाट्सअप बरोबरच जगात सर्वाधिक वापरले जाणारे माध्यम म्हणून युट्युबकडे पाहिले जाते. आता आपण युट्युब विषयी सविस्तर माहिती जाणून घेऊ व्हिडिओ म्हटल्यावर युट्युब चे समीकरण आता पक्के झाले आहे. युट्युबचा शोध 14 फेब्रुवारी 2005 रोजी लागला तसेच 23 एप्रिल 2005 रोजी युट्युबवर पहिला व्हिडिओ टाकला गेला. नुकतीच 23 एप्रिल 2020 ला youtube ला पंधरा वर्षे पूर्ण झाली दिवसेंदिवस youtube चे महत्त्व अधिकच वाढताना दिसत आहे. आपल्यापैकी प्रत्येक जण युट्युबवर रोज कमीत कमी एखादा तरी व्हिडिओ पाहत असतो. अनेक अभ्यासाचे व्हिडिओ, प्रेरणादायी भाषणे, मुलाखती, आपल्या आवडत्या विषयावरील माहिती, ज्ञान तसेच सिनेमांचे ट्रेलर्स सिनेमा व गाणी बघण्यासाठी आपण युट्युबचा वापर करतो एखादी पाककृती हवी असेल तर गुगल सर्च बरोबर youtube वरही सर्च करतो पुस्तकांचे परीक्षण, एखादे गणित कसे सोडवायचे या प्रश्नांची उत्तरे सुद्धा आपल्याला युट्युबवर मिळतात. आपण पोस्ट केलेले व्हिडिओ शेअर करता येतात त्यावर प्रतिक्रियाही देता येते. याचाच अर्थ youtube फक्त व्हिडिओ पोस्ट करायची जागा नाही तर सदस्य एकमेकांशी संपर्क करू शकतात. युट्युब असे एक उत्तम सामाजिक माध्यम आहे. एक अब्जाहून जास्त अधिक सदस्य असलेल्या या youtube चा वापर दिवसातून कित्येक तास व्हिडिओ पाहण्यासाठी होतो हे आपल्या सर्वांना परिचित आहे. युट्युबची सदस्य संख्या, जगभरात पाहिले जाणारे व्हिडिओ यांची संख्या खूप जास्त आहे. अनेक युट्युब चॅनेलच्या आर्थिक प्राप्तीमध्ये दरवर्षी वाढ होत असते असे दिसून येते. युट्युबवर आपल्या व्हिडिओला कसा प्रतिसाद मिळतो हे चटकन कळते. युट्युब एक सोशल मीडिया म्हणून वापरता येते., सर्च इंजिन म्हणून त्याचा वापर करता येतो., आपल्या युट्युब चॅनलवर आपल्याला संपर्क शेअरिंग, खरेदी विक्री या संबंधी माहिती देता येते. फेसबुक ट्विटर असा सर्व सोशल मीडिया आपल्याला आपल्या युट्युब चॅनलला जोडता येतो.

८. फेसबुक :

ही एक लोकप्रिय सोशल नेटवर्किंग संकेतस्थळ आहे. सर्वसामान्यतः तेरा वर्षाहून मोठ्या कोणालाही फेसबुकवर सदस्य म्हणून नोंदणी करता येते. सदस्यांना ओळखीच्या व फेसबुक सदस्य असलेल्या इतर व्यक्तींच्या खात्याशी मित्र, मैत्रीण म्हणून जोडणी करता येते. आपल्या मित्रमंडळींना संदेश, फोटो पाठवता येतात. सर्व मित्र मंडळींना दिसेल कळेल अशा पद्धतीने आपले मत मांडता येते. अशा अनेक सुविधा, सोयी,

फेसबुकवर उपलब्ध आहेत. मार्क झुकरबर्ग ने फेसबुकची निर्मिती 2000 साली केली. फेसबुकवर प्रवेश करताच पहिले पान उघडते त्याला मुखपृष्ठ म्हणतात. या पानावर सदस्यांच्या मित्रमंडळींनी प्रकाशित केलेल्या पोस्ट व फोटो दिसतात. या पोस्ट व फोटोवर सदस्य आपली मते मांडू शकतात. फेसबुकवरील दुसऱ्या पेजला प्रोफाइल पेज म्हणतात प्रोफाइल पेज चार भागात विभागलेले असते.

१. माहिती पानावर सदस्यांची माहिती दिसते.
२. सदस्यांचे फोटो अल्बम या पानावर दिसतात.
३. सदस्यांच्या फेसबुकवरील मित्र मंडळींची सूची फ्रेंड्स या पानावर दिसते.
४. सदस्यांच्या मित्रांनी सदस्यांकरता लिहिलेल्या पोस्ट वॉल या पानावर दिसते.

९. व्हाट्सअप :

व्हाट्सअपची निर्मिती 2009 मध्ये ब्रायन ऍक्टन व जॅन कोम यांनी केली. व्हाट्सअपला सध्याच्या काळातील जगातील सर्वात लोकप्रिय संदेशप्रणाली म्हणून ओळखले जाते. आपल्या स्मार्टफोनद्वारे आपण इंटरनेट वापरून दुसऱ्या व्हाट्सअप वापरकर्त्याला त्वरित संदेश पाठवता व वाचता येतो. संदेशासोबत चित्रे, गाणी, व्हिडिओ व इतर प्रकारच्या फाईल्स देखील एकमेकांसोबत शेअर करता येतात. व्हाट्सअप प्रणाली आयफोन, अँड्रॉइड, विंडोज फोन इ. सर्व आघाडीच्या स्मार्टफोनवर उपलब्ध असून सप्टेंबर 2015 मध्ये जगभर whatsapp चे 90 कोटी वापर करते झालेले आहेत. मार्क झुकरबर्ग हे सध्या व्हाट्सअप या कंपनीचे मालक आहेत.

१०. टेलिग्राम :

टेलिग्राम हे 2013 साली निकलाई व पवेलदुरव या दोन भावांनी एकत्र येऊन तयार केले आहे. टेलिग्राम हे मेसेजिंग ॲप आहे टेलिग्रामद्वारे व्हाट्सअप सारखेच मित्रमंडळी बरोबर आपण बातचीत करू शकतो तसेच telegram चे फीचर्स व्हाट्सअप पेक्षा अधिक चांगले व सुरक्षित आहेत टेलिग्राम ॲप हे अँड्रॉइड विंडोज फोन, आय.ओ.एस, विंडोज मॅक ,ओ.एस आणि लिनक्ससाठी उपलब्ध आहे. एप्रिल 2020 पर्यंत टेलिग्राममध्ये 400 दशलक्ष प्रतिमहिना सक्रिय वापर करणारे लोक आहेत. टेलिग्राम ॲपमध्ये आपण नवीन गुप, सुरक्षित संदेश, नवीन चॅनल, सेव मेसेज, कॉल इत्यादी सुविधा उपलब्ध आहेत.

११. ट्विटर :

ट्विटर या सोशल नेटवर्क साईटमध्ये खूप ताकद आहे. आपण ट्विटरवरून जगभरातील मिलियन लोकांना कनेक्ट करू शकतो. याचा मुख्य फायदा म्हणजे जगभरात जे काही घडते ते अगदी काही सेकंदात ट्विटरच्या माध्यमातून येते. ट्विटर जर आपण वापरले तर न्यूज चॅनेल, टीव्ही शो, सिरीयल काही पाहण्याची, किंबहुना त्याची गरज भासत नाही. सर्व माहिती आपल्याला ट्विटरवर उपलब्ध असलेली दिसून येते. ट्विटर म्हणजे ट्विट पोस्ट करणे होय. ट्विटर हे संवादाचे उत्तम साधन आहे ते वास्तवावर आधारित असून काही क्षणात आपल्यापर्यंत योग्य ती माहिती पोहोचते. ट्विटर हे जगातील असा प्लॅटफॉर्म आहे की जिथे आपण सर्वांशी बोलू शकतो. हवे असलेले प्रश्न विचारू शकतो. त्यांचे उत्तर सहज आणि जलदपणे मिळू शकणारे ठिकाण म्हणजे ट्विटर होय. ट्विटर वापर कर्ते ट्विटर करतात ब्रेकिंग न्यूज पोस्ट करतात. तर बरेच जण माहितीपर ट्विट करतात. तर काहीजण सेलिब्रिटींशी संवाद साधतात. इत्यादी सुविधा ट्विटरवरती उपलब्ध असलेल्या दिसून येतात.

१२. गुगल मीट :

गुगल मीट हे व्हिडिओ कॉन्फरन्स सेवा देण्याचे महत्त्वपूर्ण कार्य करते. गुगल मीटमध्ये एका वेळी तब्बल 100 जण सहभागी होऊ शकतात. गुगलने सध्याच्या काळात वाढत चाललेली व्हिडिओ कॉन्फरन्सिंग सेवांची मागणी लक्षात घेऊन त्यांची गुगल मीट ही सेवा आता सर्वांसाठी मोफत उपलब्ध करून दिली आहे. गुगल मीट सेवा वापरण्यासाठी तुम्ही meet.Google.com वर जाऊ शकता किंवा त्यांचे अँड्रॉइड व ios वापरू शकता, गुगल मीट वापरण्यासाठी गुगल अकाउंट असणे गरजेचे आहे.

१३. गुगल क्लासरूम:

गुगल क्लासरूमचा प्रारंभ 6 मे 2014 रोजी झालेला आहे. गुगल क्लासरूम हे शैक्षणिक माहितीचे आदान प्रदान करण्यासाठी बनवलेले दिसून येते. गुगल क्लासरूम ही एक वेब सेवा आहे. गुगल क्लास रूमचा प्राथमिक उद्देश हा शिक्षक आणि विद्यार्थ्यांमध्ये शिकवण्याची प्रक्रिया अधिक सुलभ कशी करता येईल यासाठी आहे. ऑनलाइन शिक्षण व्यवस्थापन वृद्धिंगत करण्याच्या हेतूने गुगल क्लासरूमची निर्मिती करण्यात आली. या टूलच्या माध्यमातून शिक्षक आणि विद्यार्थी, अभ्यास घटकासंदर्भात सहजपणे ऑनलाईन संवाद साधू शकतात. सध्याच्या काळात अनेक शाळा महाविद्यालयांनी त्यांचे ऑनलाइन क्लास सुरू केले आहेत. यासाठी प्रामुख्याने वापरला जाणारा पर्याय म्हणजे गुगल क्लासरूम. शैक्षणिक सुविधांनी युक्त अशी गुगलची गुगल क्लासरूम सेवा आहे. गुगलने काही दिवसांपूर्वी या गोष्टीचा आणखी चांगल्या प्रकारे वापर करता यायला हवा यासाठी यामध्ये नव्या सोयींच्या समावेश केला आहे. त्यामुळे विद्यार्थी आणि शिक्षक दोघांनाही गुगल क्लास रूम वापरण्यास अधिक सोयीचे झालेली दिसून येते.

काय आहे गुगल क्लासरूम : गुगल क्लासरूम म्हणजे वर्गाचीच ई - प्रतिकृती. गुगल क्लासरूम हे शिक्षणाकरता वापरले जाणारे नवीन माध्यम आहे. गुगल क्लासरूमच्या साहाय्याने शिक्षक एका वेळी कमाल 250 विद्यार्थ्यांसाठी ऑनलाईन तासिका घेऊ शकतात. यामध्ये गृहपाठ, वर्गपाठ मूल्यांकन देखील ऑनलाईन केले जाते. विद्यार्थ्यांना घरी देण्यात आलेला अभ्यास ऑनलाईन पद्धतीने तपासण्याची सुविधा यामध्ये देण्यात आली आहे. गुगल क्लासरूम मध्ये मराठीसह दहा भाषांचा सपोर्ट जोडण्यात आलेला आहे सध्या एकूण 54 भाषांना गुगल मार्फत या सेवेमध्ये जोडण्यात आलेले आहे. यामुळे शिक्षकांना विद्यार्थ्यांना मराठीतून सुद्धा सहज शिकवता आणि समजावता देखील येते.

गुगल क्लासरूमचे फायदे :

गुगल क्लासरूम या अॅपचा उपयोग अध्यापन करणाऱ्या शिक्षकांबरोबरच अध्ययन करणाऱ्या विद्यार्थ्यांनाही मोठ्या प्रमाणात होत आहे. गुगल क्लासरूम या अॅप्लिकेशनच्या माध्यमातून शिक्षक अभ्यासक्रमाचे नियोजन करू शकतात. विद्यार्थ्यांच्या सर्व ऍक्टिव्हिटींचेही नियोजन करू शकतात. विद्यार्थी प्रत्यक्ष वर्गात नसले तरी घरी राहून या अॅप्लिकेशनच्या माध्यमातून शिक्षण घेऊ शकतात. या अॅप्लिकेशनच्या माध्यमातून गुगलने ही सर्वात चांगली सोय उपलब्ध करून दिलेली आहे. गुगल क्लासरूमचा वापर करून आपण आधुनिक पद्धतीने शिक्षण द्यायला सुरुवात केली आहे. त्यामुळे शिक्षण आणि शिक्षक आणि विद्यार्थी यांच्या चांगल्या पद्धतीने संवाद घडून येताना दिसत आहे. गुगल क्लासरूमचे मुख्यतः चार फायदे दिसून येतात. नोट्स उपलब्ध करून देणे, प्रोजेक्ट संदर्भात माहिती देणे, व्हिडिओ उपलब्ध करून देणे आणि नोट्स उपलब्ध करून देण्यामध्ये महत्त्वाची भूमिका बजावणे.

१४. सिस्को वेबेक्स :

सिस्को वेबेक्स हे ऑप कॉन्फरन्सिंग आणि व्हिडिओ कॉन्फरन्सिंगसाठी तयार करण्यात आले आहे. त्याची निर्मिती 1995 मध्ये वेबेक्स म्हणून केली गेली होती. हे ऑप अँड्रॉइड आणि ios हे ऑपरेटिंग सिस्टिमसाठी उपलब्ध आहे.

१५. स्काईप :

स्काईप हे सॉफ्टवेअर इंटरनेटचा उपयोग करून व्हॉइस व व्हिडिओ कॉल करण्यासाठी वापरले जाते. त्याद्वारे त्वरित संदेश फाईल पाठवणे आणि व्हिडिओ कॉन्फरन्सिंग करता येते. स्काईपद्वारे अगोदरचे संदेश संपादन करता येतात. स्काईप हे विंडोज, मॅक, ओएस, एक्स, लिनक्स यावर वापरता येते.

१६. लिंकडइन :

लिंकडइन एक वेब पोर्टल असून वाणिज्य क्षेत्र, उद्योग धंद्यामधील व्यावसायिक भेटीसाठी ते प्रामुख्याने ओळखले जाते. या संकेतस्थळाचा शोध 28 डिसेंबर 2002 लागला आणि 5 मे 2003 रोजी ते सर्वांसाठी उपलब्ध झाले. फेसबुकवर ज्याप्रमाणे मित्रांची यादी असते तशीच यादी लिंकडइन येथे देखील असते. पण त्याला कनेक्शन असे म्हणतात इतर सोशल नेटवर्किंग साईडप्रमाणे यात देखील व्हिडिओ शेअरिंग, फोटो शेअरिंग, म्युझिक शेअरिंग, लॉर्ड ब्लॉगिंग, मायक्रो ब्लॉगिंग अशा सुविधा उपलब्ध आहेत.

मात्र फक्त व्यावसायिक जनसंपर्क तसेच भेटी गाठींसाठी वापर केली जाणारी लिंकडइन ही एक मात्र वेबसाईट आहे. व्यावसायिक जगात लिंकडइन या वेबसाईटवर माहिती अद्यावत असणे महत्त्वाचे आहे.

१७. पिन टेरिस्ट :

पिन टेरिस्ट हे सॉफ्टवेअर करताना कल्पना जतन करणे, टेरिस्ट व शोध सक्षम करण्यासाठी डिझाईन केलेले आहे. वेबसाईटवरील लहान प्रमाणात इमेजेस आणि व्हिडिओ पिनबोर्डवर असतात.

१८. मोबाईल फोन :

मोबाईल फोन म्हणजेच भ्रमणध्वनी हे एक इलेक्ट्रॉनिक उपकरण असून याचा दूरसंचारासाठी उपयोग केला जातो. याला इंग्रजीमध्ये मोबाईल फोन किंवा सेल फोन असे म्हणतात. भ्रमणध्वनीच्या सहाय्याने संभाषणाची व माहितीची देवाण-घेवाण करता येते. आधुनिक काळातील मोबाईल फोन हे संभाषणाखेरीज महाजाल न्याहाळणे, लेखी लघु संदेशाची देवाण -घेवाण, गाणी ऐकणे, छायाचित्र काढणे, रेडिओ ऐकणे, जीपीएस वापरणे, पैसे देणे, पैसे काढणे इत्यादी कामाकरता वापरले जाते. नोकिया, मोटोरोला, अॅप्पल, सॅमसंग या मोबाईल फोन उत्पादक कंपन्यांपैकी सर्वात मोठ्या कंपन्या आहेत. दूरसंचार विषयक सेवांसाठी मोबाईल फोनमध्ये सिमकार्ड वापरणे आवश्यक आहे. भ्रमणध्वनीमुळे माणसे जोडली गेली आहेत. मोबाईलमुळे सर्व जग जवळ आले

१९. इंस्टाग्राम :

इंस्टाग्राम हे ऑनलाइन चित्र शेअर करण्याचे ऑप आहे. हे ऑप अँड्रॉइड आयफोन, नोकिया या ऑपरेटिंग सिस्टिम वर चालते. अशाप्रकारे आपल्याला ही संवाद कौशल्यांमध्ये मराठी भाषेचा अधिकाधिक वापर करताना एकूण विद्यार्थ्यांचा होणारा सर्वांगीण विकास हा कौशल्याधिष्ठीत विकासाच्या मार्गाने कसा जाणार आहे. याची एक तोंड ओळख होण्यास मदत होते. आजच्या काळात भाषेला तंत्रज्ञानाची जोडून घेणे

अपरिहार्य आहे आणि जर आपण भाषेला तंत्रज्ञानाशी जोडून घेऊ शकलो तर उद्याचा काळ हा ज्ञानरचनावादी आणि राष्ट्रीय शैक्षणिक धोरणात सांगितल्याप्रमाणे कौशल्याला अधिक महत्त्व असणारा आहे आणि म्हणून आजच्या मराठी भाषा शिकणाऱ्या विद्यार्थ्यांमध्ये आपल्याला अधिकाधिक कौशल्याधिष्ठित रोजगाराच्या संधी निर्माण करायच्या असतील तर आपल्याला भाषेला तंत्रज्ञानाशी जोडून घेणे काळाची नितांत गरज आहे.

संदर्भग्रंथ यादी

1. राजाध्यक्ष विजया, (संपा), मराठी वाङ्मय कोश खंड चार, महाराष्ट्र राज्य साहित्य आणि संस्कृती मंडळ, मुंबई प्रथम आवृत्ती, नोव्हेंबर 2002.
2. मोकाशी मधुकर, व्यावहारिक व व्यावसायिक लेखन प्रणाली, स्नेहवर्धन प्रकाशन, पुणे, प्रथम आवृत्ती 1 मे 2013
3. वाळुंज महादेव. व्यासपीठ, अक्षर मानव प्रकाशन, पुणे, प्रथम आवृत्ती मे 2011
4. नसिराबादकर ल. र. व्यावहारिक मराठी, फडके प्रकाशन, कोल्हापूर, आठवी विस्तारित आवृत्ती 2008
5. सांगळे संदीप, व्यावहारिक उपयोजित मराठी व प्रसारमाध्यमांची कार्यशैली, डायमंड पब्लिकेशन, पुणे प्रथम आवृत्ती डिसेंबर 2013.

